PAUL SCHERRER INSTITUT

PSI

International Intercomparison Exercise of Airborne Gamma-Spectrometric Systems of the Czech Republic, France, Germany and Switzerland in the Framework of the Swiss Exercise ARM17

Gernot Butterweck, Benno Bucher, Lubomir Gryc, Christophe Debayle, Christopher Strobl, Stéphane Maillard, Michael Thomas, Alexandra Helbig, Inge Krol, Sonia Chuzel, Céline Couvez, Marcel Ohera, Ladislaus Rybach, Cristina Poretti, Bénédicte Hofstetter-Boillat, Sabine Mayer, Gerald Scharding

International Intercomparison Exercise of Airborne Gamma-Spectrometric Systems of the Czech Republic, France, Germany and Switzerland in the Framework of the Swiss Exercise ARM17

Gernot Butterweck[1], Benno Bucher[2], Lubomir Gryc[3], Christophe Debayle[4], Christopher Strobl[5], Stéphane Maillard[6], Michael Thomas[5], Alexandra Helbig[5], Inge Krol[5], Sonia Chuzel[4], Céline Couvez[4], Marcel Ohera[3], Ladislaus Rybach[7], Cristina Poretti[8], Bénédicte Hofstetter-Boillat[1], Sabine Mayer[1], Gerald Scharding[8]

1   Department of Radiation Safety and Security, Paul Scherrer Institute (PSI), 5232 Villigen PSI, Switzerland

2   Swiss Federal Nuclear Safety Inspectorate (ENSI), Industriestrasse 19, 5200 Brugg, Switzerland

3   National Radiation Protection Institute (NRPI), Bartoskova 28, 140 00 Praha 4, Czech Republic

4   Institute for Radiological Protection and Nuclear Safety (IRSN), 31, avenue de la Division Leclerc, 92260 Fontenay-aux-Roses, France

5   Bundesamt für Strahlenschutz (BfS), Ingolstädter Landstrasse 1, 85764 Oberschleissheim, Germany

6   Nuclear Biological Chemical - Explosive Ordnance Disposal (NBC-EOD) Centre of Competence, 3700 Spiez, Switzerland

7   Institute of Geophysics, Swiss Federal Institute of Technology Zürich (ETHZ), 8092 Zürich, Switzerland

8   Swiss National Emergency Operations Center (NEOC), 8044 Zürich, Switzerland

Abstract

Participants in this international intercomparison exercise performed from June 26th to June 30th were seven measuring teams of the Czech Republic, Germany, France and Switzerland.

In advance to the intercomparison exercise, two measuring areas around the nuclear power plants Gösgen and Mühleberg were inspected by Swiss teams CH01 and CH02 on June 22nd and June 23rd following a bi-annual schedule on behalf of the Swiss nuclear safety inspectorate (ENSI). No artificial radionuclides were detected outside the premises of the power plants.

The main measurement task for the international exercise tried to simulate a scenario in which the deployment of airborne gamma-spectrometry is essential and international support would be requested. The scenario assumes a theft of a strong radioactive ^{137}Cs-source. The get-away car including the empty source shielding was found abandoned by the police, suggesting that the thieves took flight on foot taking the source with them. Police investigations determined a perimeter inside which the thieves and the source should be located. The associated area adds up to seven percent of Switzerland (2900 km^2).

Two ^{137}Cs-sources were placed in the search area. Both sources were identified and located during the exercise.

Additional tasks consisted in combining the measured data in the source search area into composite maps of the natural radioactivity and in several reference areas for a direct comparison of system performance. The results of the measurements showed some minor differences between the results of the measuring teams.

Several supplementary tasks were included into the exercise to provide informations for potential optimisation of data evaluation to the participants. An altitude profile over a Swiss lake yielded information on system background and the influence of cosmic radiation. A reference area with mainly flat topography measured prior to the exercise with in-situ gamma-spectrometry on the ground by staff of the Nuclear Biological Chemical - Explosive Ordnance Disposal (NBC-EOD) Centre of Competence was introduced to check on individual calibration factors and the influence of different ground clearances on the measurement results. A second reference area with alpine topography and a transversal going from flat to alpine terrain was introduced to provide information on the influence of topography on the measurement results. The detailed analysis of the results of the supplementary tasks in combination with post-processing of raw data after the exercise helped to reduce some of the differences in the composite mapping observed during the exercise.

Contents

List of Figures

List of Tables

1 Integration of airborne gamma-spectrometry into National Emergency Response Organisations

1.1 Czech Republic

The National Radiation Protection Institute (SÚRO) is a public research institution engaged in professional activities in the field of population protection against ionizing radiation and it was established by the decision of the chairman of the State Office for Nuclear Safety (SÚJB). SÚRO is involved in radiation monitoring network of the Czech Republic whose major component constituent Mobile groups. The SÚRO Mobile group performs also airborne measurements for quick and large-scale monitoring of radioactivity on the soil surface. These tasks are fulfilled together with Armed Forces of the Czech Republic which provide in particular air resources. Joint training of SÚRO and Armed Forces of the Czech Republic (314th Weapons of Mass Destruction Warning Centre and 24th Transport Air Force Base) takes place regularly twice a year.

1.2 France

Since its creation in 2002, instituted by Decree 2002-254 of 22 February 2002, IRSN ensures a permanent watch in the field of radiation protection, in particular by contributing to the environmental radiological monitoring. As a technical expert on radiological and nuclear risks, IRSN participates in the French emergency management system.
In this context, IRSN develops, operates and maintains in operational conditions the Téléray remote sensing network, ensuring the permanent in-situ measurement of the ambient gamma dose equivalent rate. This network, which today is composed of more than 400 probes, has been modernized, but has also undergone a significant geographical redeployment from 2009 to 2016. In this context, it was decided to increase the number of probes around French nuclear sites. These probes thus play the role of sentinel by being pre-positioned in case of radioactive fallout following a nuclear accident. Nevertheless, 20 deployable probes have been developed and are intended to replace existing faulty probes or to fill persistent geographical gaps.
In spite of this arsenal of resources, possibly supplemented by the equipment of the operators and public authorities, a large part of the territories affected by a possible large-scale radioactive contamination may not be sufficiently covered by this type of fixed equipment. For this reason, IRSN introduced in 2010 a mobile in-situ measurement system capable of covering large areas of territory in order to rapidly characterize the state of environmental contamination. Comparing to the Téléray network which provides temporal data, this kind of system provides a large instantaneous picture of the contamination, even where no probe is located. This system, called ULYSSE, was first tested in December 2011 during a mission in collaboration with the Japan Atomic Energy Agency (JAEA) in Japan in a contaminated environment and participated in an intercomparison with the already existing measurements of the Japanese (JAEA) and US Department of Energy (DOE) counterparts. A second mission took place in Japan as part of the Response and Assistance Network (RANET) of the International Atomic Energy Agency (IAEA) in May 2013, in which the system was successfully used for carborne measurements in the forbidden zone, a few hundred meters from the Fukushima plant.
In 2012, the ULYSSE system was loaded aboard an aircraft (Cessna Skymaster) for the first time and has performed several surveys in France (Esterel, Camargue, Massif Central)

on natural radioactivity since then.

In parallel, contacts with Civil Protection led to two joint missions, the first one in the framework of the national exercise in Cattenom in June 2013 and the second in the framework of a feasibility test in Brittany in January 2014. Finally, IRSN took part in the European airborne radiometric exercise AGC15 in Chemnitz (Germany) in 2015 and another similar exercise ARM17 in Zurich (Switzerland) in 2017, during which intercomparison of the monitoring systems and methods of Germany, Switzerland, Czech Republic and France were carried out.

1.3 Germany

In the Federal Office for Radiation Protection (BfS), German competences in the field of radiation protection have been concentrated. The BfS executes manifold tasks in the field of nuclear emergency preparedness. These include the quick and large-scale measurement of radioactivity on the soil surface from the air. The BfS is subordinated to the Federal Ministry for the Environment, Nature Conservation, Building and Nuclear Safety.

The Flying Corps of the Federal Police with its four Federal Police flying squadrons that are separately located all over Germany, sees itself as a comprehensive service provider for the Federal Police bureaus and other national and international public agencies (among others for the BfS) and performs a multitude of tasks on a daily, mostly 24/7 basis.

1.4 Switzerland

The civil branch of Swiss airborne gamma spectrometry measurements started in 1986. Besides constructing the first measuring equipment, the methodology and software for calibration, data acquisition and mapping were developed at the Institute of Geophysics of the Swiss Federal Institute of Technology Zurich (ETHZ). Between 1989 and 1993 the environs of Swiss nuclear installations were measured annually on behalf of the Swiss Federal Nuclear Safety Inspectorate (ENSI). This schedule was changed to biannual inspections in 1994, together with an organizational inclusion of the airborne gamma-spectrometric system into the Emergency Organization Radioactivity (EOR) of the Federal Office for Civil Protection (FOCP). The deployment of the airborne gamma-spectrometric system is organized by the National Emergency Operations Centre (NEOC). NEOC is also responsible for the recruitment and instruction of the measurement team and the operational readiness of the system. Aerial operations are coordinated and performed by the Swiss Air Force. The gamma-spectrometric equipment is stationed at the military airfield of Dübendorf. The gamma-spectrometry system can be airborne within four hours. Responsibility for scientific support, development and maintenance of the aeroradiometric measurement equipment passed from ETHZ to the Radiation Metrology Section of the Paul Scherrer Institute (PSI) in 2003 in cooperation with ENSI. General scientific coordination and planning of the annual measuring flights is provided by the Expert Group for Aeroradiometrics (FAR). FAR was a working group of the Swiss Federal Commission for NBC-protection (ComNBC) and consists of experts from all Swiss institutions concerned with aeroradiometry. FAR was reorganized as an expert group of the NEOC in 2008. Additional information can be found at `http://www.far.ensi.ch/`.

The main missions of the Swiss armed forces are defence against military aggressions, peace support operation abroad and support of civilian authorities. The support of civilian

authorities is provided on request if the civilian forces are unable to provide this particular service themselves and if this service is not already engaged in favour of military forces (prioritisation). In the specific case of radiological emergency situations, the Nuclear Biological Chemical - Explosive Ordnance Disposal (NBC-EOD) centre of competence is able and allowed to support civilian authorities with radiological reconnaissance, sampling and field measurements, decontamination of persons, patients, vehicles and equipment and analysis of samples in mobile or stationary laboratories. Some of these services are provided within short deadlines (1-6 hours) by professionals and others require the prior mobilisation of military militia forces (12-24 hours). For example, in-situ gammaspectrometry services have been used to obtain reference measurements in the Linth Plain prior to this intercomparison exercise (see section 9). Since 2002 the NBC defence forces perform an ambitious modernisation program and capacity improvement. For example, the cold war era military radiation detection helicopters have been replaced with fewer more sensitive and gamma spectrometric systems. These systems were first integrated in vehicles for the reconnaissance in urban areas (2008) thereafter also in helicopters (2016). Activities and methods are coordinated with other Swiss organisations like the Emergency Organisation Radioactivity (EOR) and the Expert Group for Aeroradiometrics (FAR).

2 Measuring Systems

2.1 Team CH01

The measuring system ARM consists of four NaI-detectors with a total volume of 16.8 l. The measurements were performed with detector package (Detector D, Radiation Solutions RSX4) which includes digital spectrometers with a maximum resolution of 1024 channels for each detector. To render the data evaluation compatible to the old systems, the spectral resolution is reduced to 256 channels. The measurement control, data acquisition and storage are performed with an industrial grade personal computer. A second, identically configured PC is present in the electronics rack (figure 1) as redundancy. Under normal operation conditions, this PC is used for real-time evaluation and mapping of the data. The positioning uses GPS (Global Positioning System) in the improved EGNOS (European Geostationary Navigation Overlay Service) mode. Together with spectrum and position, air pressure, air temperature and radar altitude are registered. The measuring system is mounted in an Aerospatiale AS 332 Super Puma helicopter of the Swiss Air Force (Figure 2). This helicopter has excellent navigation properties and allows emergency operation during bad weather conditions and night time. The detector is mounted in the cargo bay below the centre of the helicopter. The cargo bay is covered with a lightweight honeycomb plate to minimize photon absorption losses.

The airborne gamma-spectrometry system used for emergency preparedness in Switzerland is currently modernised. The hitherto used measuring system ARM will be replaced in 2018 with the new RLL (Radiometrie Land Luft) system, which will then be used both by the National Emergency Operations Centre (NEOC) and the Swiss army. After prototype tests of the RLL system the last years, four systems were purchased by the Swiss army. Both systems participated in the exercise ARM17 and are described separately.
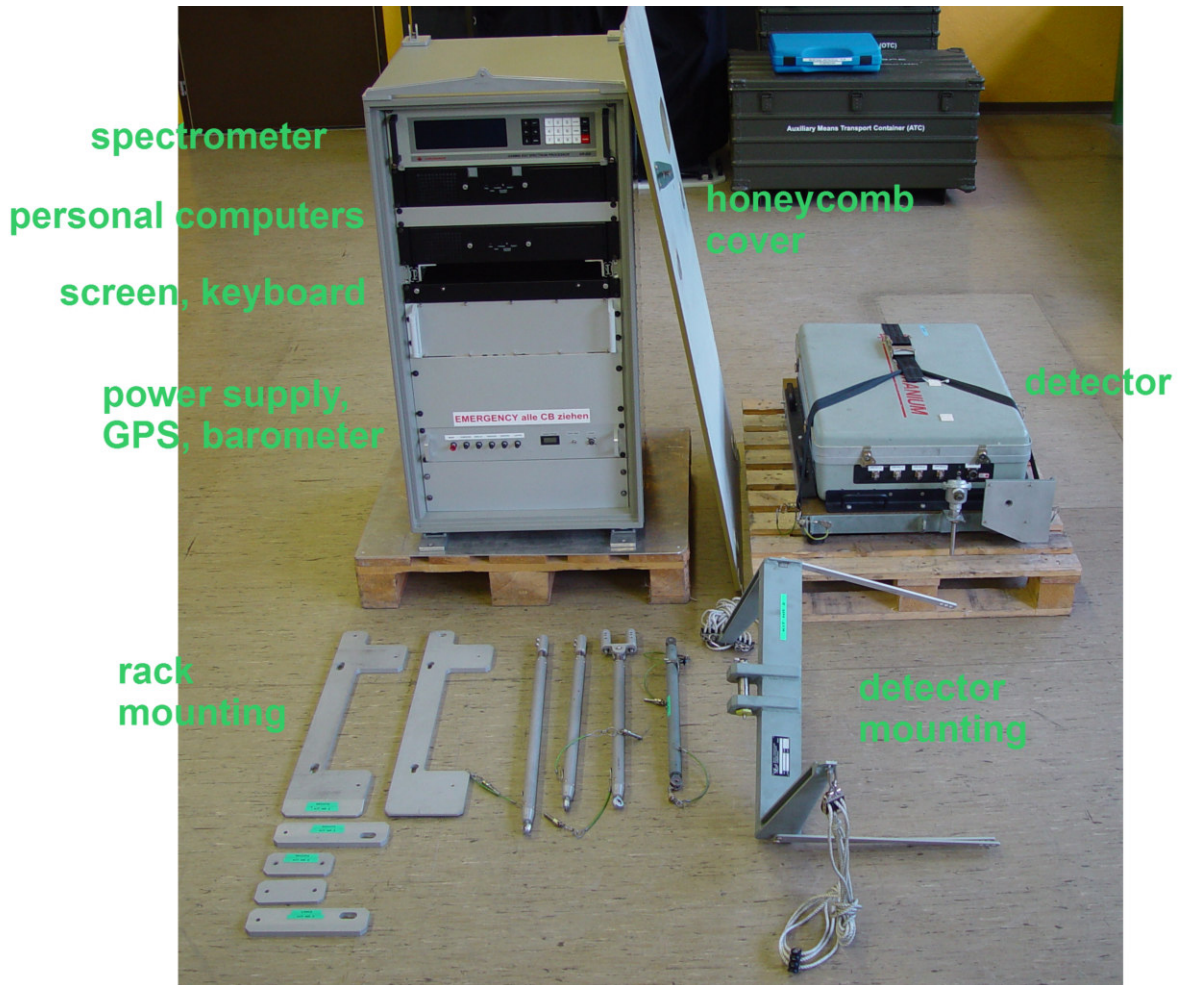
Figure 1: Measurement system of the Swiss team.

Figure 2: Super Puma helicopter of the Swiss Air Force.

2.2 Team CH02

The measuring system RLL (Radiometrie Land Luft) consists of four NaI(Tl) radiation detectors and associated photo-multipliers and multichannel analysers for low level measurements and one Geiger-Müller tube and associated electronics for high-level dose rate measurement. Detectors, Geiger-Müller tube and associated electronics are installed in an aluminium case with thermal insulation foam. The detection container is mounted in the cargo bay below the centre of the helicopter. The RLL system uses position, air pressure, air temperature and radar altitude provided by the helicopter via the internal ARINC bus. Figure 3 shows the complete system packaged for storage. The equipment control, data acquisition and storage are performed with an rugged computer working as a data server. Two further rugged redundant client computers are used as operator interface for real-time evaluation, data mapping and communication. All computers are installed in an equipment rack including a battery backed-up power supply. Both operators can operate the system with their associated client computer, display, keyboard and trackball. The additional third central display of the operator's console is mirrored in the cockpit on a screen located between both pilots and is used for information exchange with the pilots and general radiological situation awareness (figure 4). The measuring system RLL is mounted in an Aerospatiale AS 332 Super Puma helicopter (TH 06) of the Swiss Air Forces (figure 5). This helicopter has excellent navigation properties and allows emergency operation during bad weather conditions and night time. Table 1 summarises the specifications of the RLL system.

Figure 3: Components of the RLL system. 1. Lifting platform for the installation of the detection container. 2. Floor plates and accessories case. 3. Monitors and operator console. 4. Detection container. 5. Operator seats and equipment rack.

Figure 4: Operator console of the RLL system. 1. Displays of the client computers. 2. Common display (mirrored in the cockpit). 3. Control panel with switches for power, lighting and communication and USB ports for file exchange.
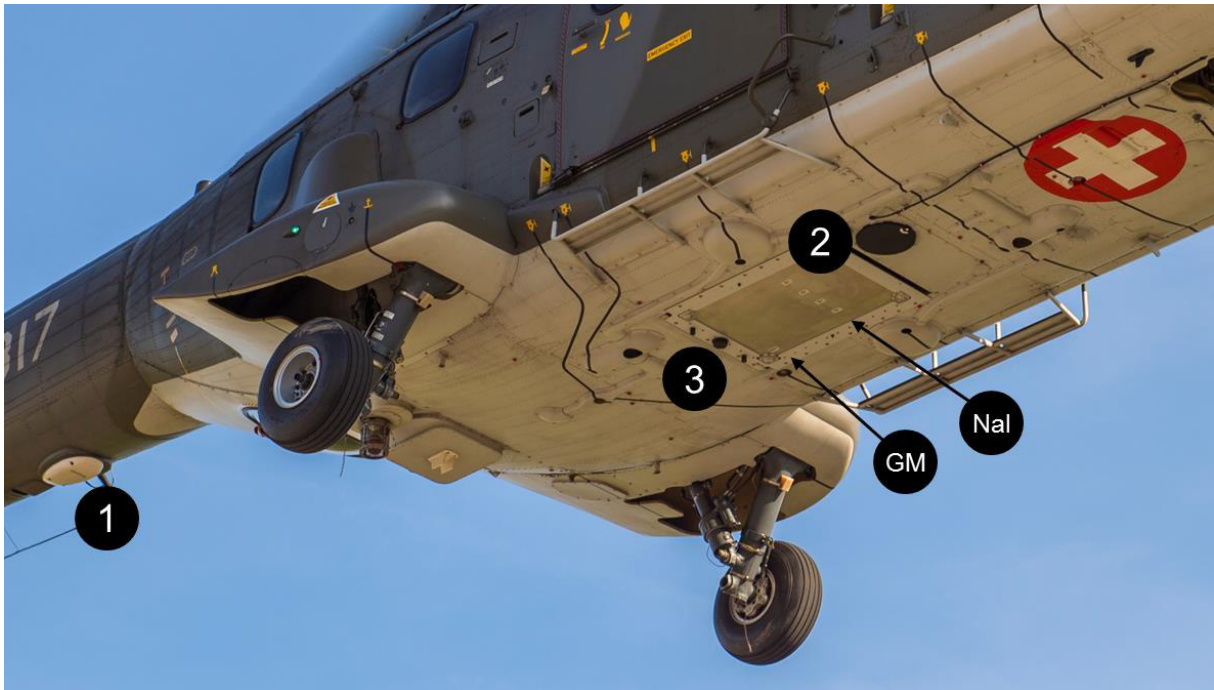
Figure 5: RLL detector mounted in the cargo bay of a Superpuma helicopter. 1. Radar altimeter. 2. Detection container marked with detector reference points. 3. UMTS antenna for data upload.

Table 1: Specifications of RLL system.

Detection systems	4 x 4 litres NaI(Tl) detector
	1 Geiger-Müller detector for high range dose rate
Sample time	1 s sampling
	5 s moving average for identification
Energy range	30 - 3000 keV
Spectrometer	1024 channels
Method of evaluation	Real time identification
	Calculation/extrapolation on ground, resp. 1 m above ground
Positioning system	Military GPS
	(Civilian GPS as backup)
Altimetry system	Radar
	(GPS as backup)
Computer	1 server for data acquisition
	2 client computers as user interface

2.3 Team CZ01

The IRIS airborne gamma-ray spectrometric system was developed by Pico Envirotec Inc. Company in Toronto, Canada. Two boxes (Master and Slave), each box with 2 NaI(Tl) crystals with dimensions 10x10x40 cm are used (figure 6). The gamma-ray spectrometer is provided with all electronics and additional accessories, i.e. GPS receiver, radar altimeter (figure 7), pilot guidance unit (PGU, figure 8) and software package for the project preparation, data browsing and the data post-processing. With the exception of power, the spectrometer is fully independent on all on-board systems and it can be easy installed in all airplanes or helicopters. In near future, a special battery pack will be used to be fully independent on power. Mainly, the IRIS airborne gamma-ray spectrometric system is installed on military Mi-17 helicopter (figure 9), however, it is also possible to install IRIS on board of Police Eurocopter EC-135 (figure 10) and Bell 412HP.
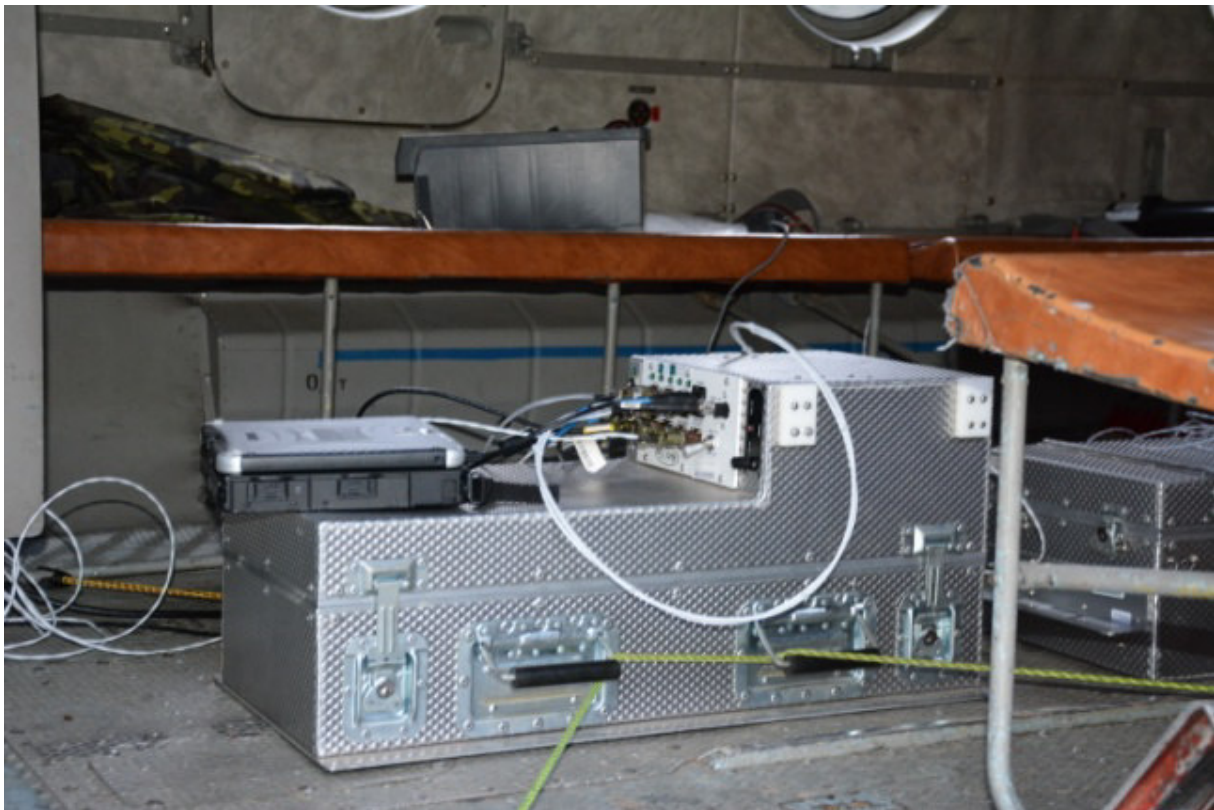
Figure 6: IRIS Master box with electronic aboard Mi-17 helicopter.

Figure 7: TR3000 radar altimeter aerial mounted below a Mi-17 helicopter.

Figure 8: XENARC 700^{TM}PGU display in the cockpit of a MI-17 helicopter.

Figure 9: MI-17 Helicopter of the Czech army.

Figure 10: EC 135 helicopter of the Czech police.

The energy range of the gamma-ray spectrometer is always set from approxmately 20 keV to 3 MeV in 256 or 512 channels. The last channel (channel 256 or channel 512, respectively) is used as cosmic window and collects all cosmic photons with energies higher than 3 MeV. This is used in the PRAGA4 post-processing program (see below) to eliminate the effect of cosmic radiation and airplane radiation contribution to the spectra. Each of the four NaI(Tl) crystals has dimensions of 10x10x40 cm with attached photomultiplier tubes (PMT) and analog-digital (A/D) converter electronics. The A/D converter applies special firmware for pulse height processing on the digital sampling principle (so-called digital peak detector). Each crystal has independent HV setting for PMT (set in PEICalib program). A special mathematical algorithm was developed by Pico Envirotec, Inc. which secures the spectrum stabilization and the independence of measurement with NaI(Tl) crystals on temperature in the operating temperature range. After starting, the system is tuned to the photopeak of ^{40}K and afterwards also to the photon emission of ^{208}Tl at 2615 keV. The gain of the individual photo-multipliers is adjusted automatically to maintain the peaks at pre-defined channels. The gain adjustment is performed in real time together with a procedure for linearisation of the energy calibration. Thus, the system does not require any radioactive calibration sources before and during flight.

Spectra, GPS positions, altitude and other parameters measured and the results of real-time data evaluation are saved in one-second intervals into a PEI-binary file for later data browsing and post processing. The internal firmware calculates on-line all important quantities, local air dose rate in nGy/h on board and the ground air dose rate recalculated to 1 m above the ground, activity concentrations of potassium , uranium and thorium in Bq/kg and surface activity of ^{137}Cs, ^{60}Co and ^{131}I in Bq/m^2. The data can be used as the preliminary information about the radiological situation, while a more precise gamma-ray spectrometric analysis can be achieved with PRAGA4 post processing software in which more sophisticated mathematical calculations are used (Least Squares Approximation (LSQ), Noise Adjusted Singular Value Decomposition (NASVD) or Maximum Noise Fraction (MNF)) including the corrections for aircraft/cosmics background and radon.

The IRIS operator has available three different types of screens on the monitor during the flight: Navigation (figure 11), spectrum (figure 12) and data (figure 13). All information about positions relative to the polygon and survey/tie lines including ground speed, altitude, survey lines, etc. are displayed on-line. The calculated air dose rates (local/ground) and activity concentrations and surface activities are shown in charts. Also, a so-called "waterfall" display is available to identify anomalies in the spectrometric data.
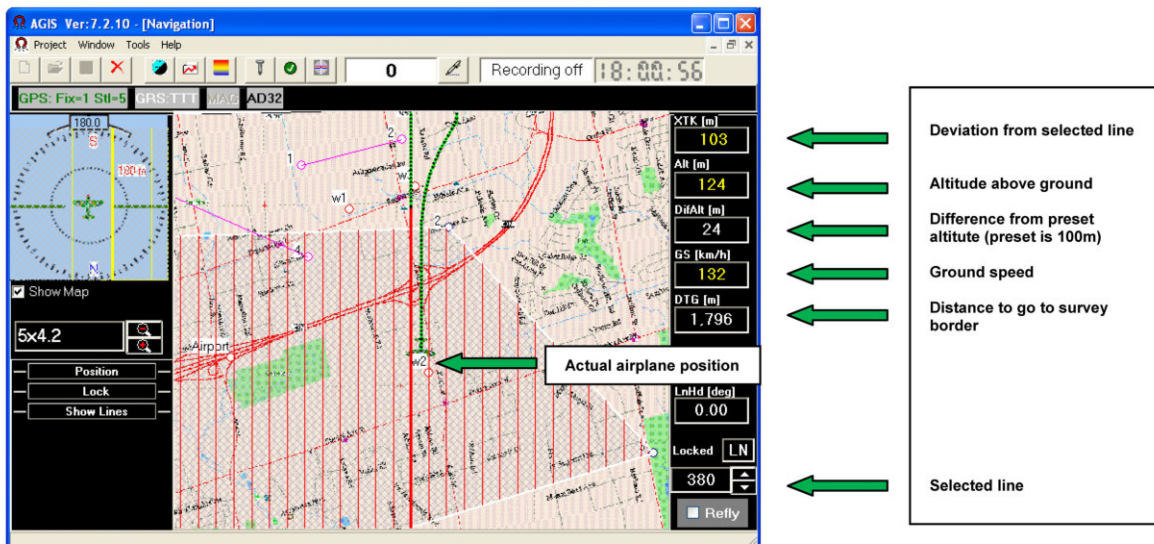
Figure 11: Navigation screen of the IRIS system.
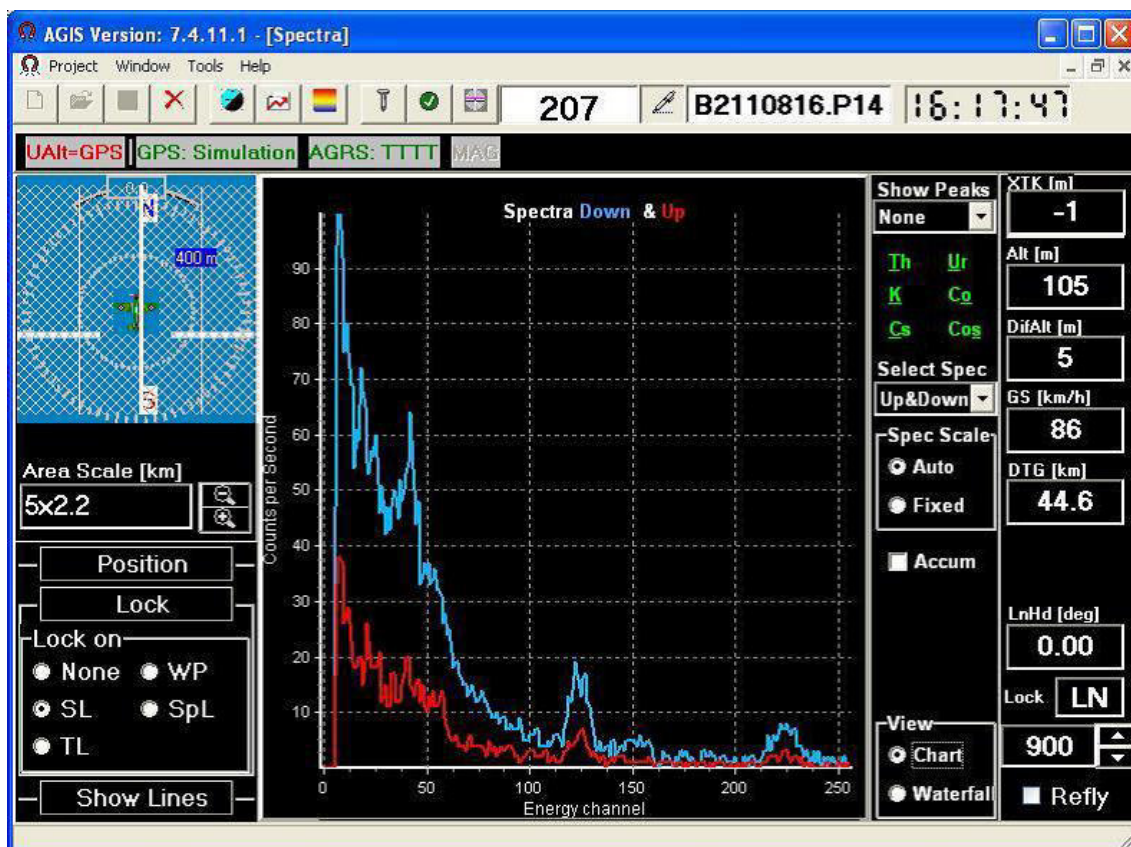
Figure 12: Spectrum screen of the IRIS system.
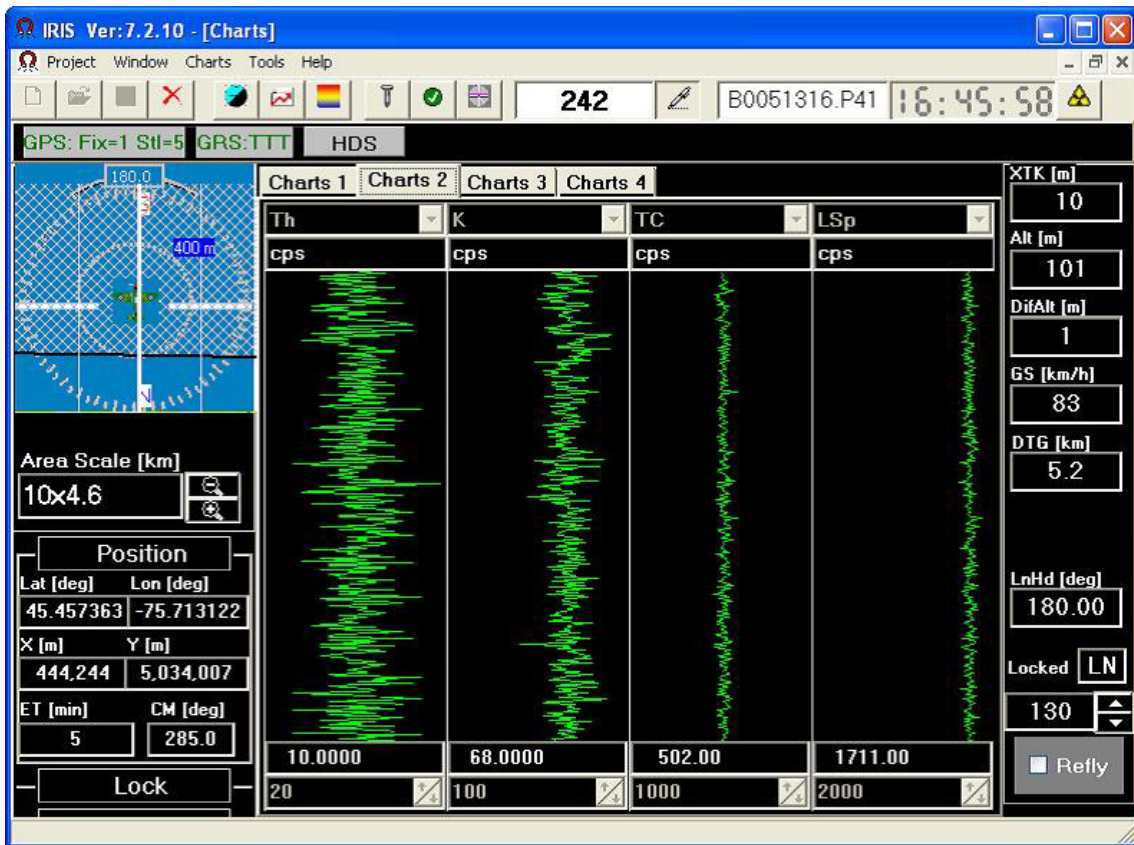
Figure 13: Data screen of the IRIS system.

2.4 Teams DE01 and DE02

Helicopters of the German Federal Police (figure 14) can be equipped with high resolution gamma-spectrometry systems from the Federal Office for Radiation Protection, which allows monitoring environmental radioactivity of large areas in a relatively short period of time. This offers an important tool for nuclear emergency management in case of accidental releases of radioactive material from a nuclear installation. Four of these measurement systems are available in Germany.

Figure 14: Helicopter of the German Federal Police equipped with gamma spectrometers during the measurement campaign ARM17.

Two types of detectors are used simultaneously for the detection of gamma emitting radionuclides, one high purity germanium detector (HPGe) with a very good energy resolution and four highly sensitive NaI(Tl) scintillation detectors with volumes of 4 dm^3 (figure 15). The high efficiency of the NaI(Tl)-detectors allows the detection of a radionuclide distribution at a high spatial resolution using integration times of one or two seconds. Data measured with the HPGe-detector usually has to be integrated over a longer period of time due to the lower efficiency of that type of detector. However, the high energy resolution of the HPGe-detector allows to unambiguously identify the individual radionuclides.

Figure 15: Measurement system mounted in an EC135.

The airborne spectrometers are calibrated according to the procedure used for the calibration of in-situ gamma-spectrometers which is described in more detail in Beck et al. 1972, Schötzig and Schrader 1993,DIN 25462 2000, DIN 25482 1991 and ICRU report 53 1994. The detector response and the angular dependency as a function of energy are determined using point sources. The attenuation of the gamma-rays due to the helicopter components is taken into account. The unscattered flux of photons depending on the distribution of radionuclides in soil and the position of the detector for the given altitude is calculated. The calibration is confirmed by measurements over areas with a known content of natural and artificial radionuclides.

2.5 Team FR01

The ULYSSE system consists of a hardened acquisition PC, a GPS and four large NaI detectors (between 2 and 4 liters, figure 16). However, the detectors can be used in different configurations from one to four NaI detectors. According to the needs or the intensity of the contamination to be characterised, it is possible to modulate the configuration of the system as well as the vector (plane, helicopter, car, etc.). For aerial use, the system can be mounted directly inside the aircraft, which allows a great flexibility of implementation. Figure 17 shows a set of four ULYSSE units with four litres NaI-detectors prior to installation into a Beechcraft King Air fixed wing airplane. Note that it is also possible, when the equipment is previously certified by Civil Aviation, to place the detectors on the outside of the aircraft in suitable baskets (figures 18 to 20).

The system performs measurement by gamma spectrometry every second, synchronized to the GPS position (latitude, longitude, altitude, speed, heading, etc.). A cumulative spectrum of each detector is thus analysed in real time to calculate the dose equivalent rate as well as to provide a radionuclide specific analysis. Isotope quantification can also be carried out online with a specific algorithm of the manufacturer (Mirion) for a time averaged spectrum with typically 5 s sliding average in order to improve the detection limit. Figure 21 shows a photograph of the graphical user interface of the ULYSSE system during a measuring flight.
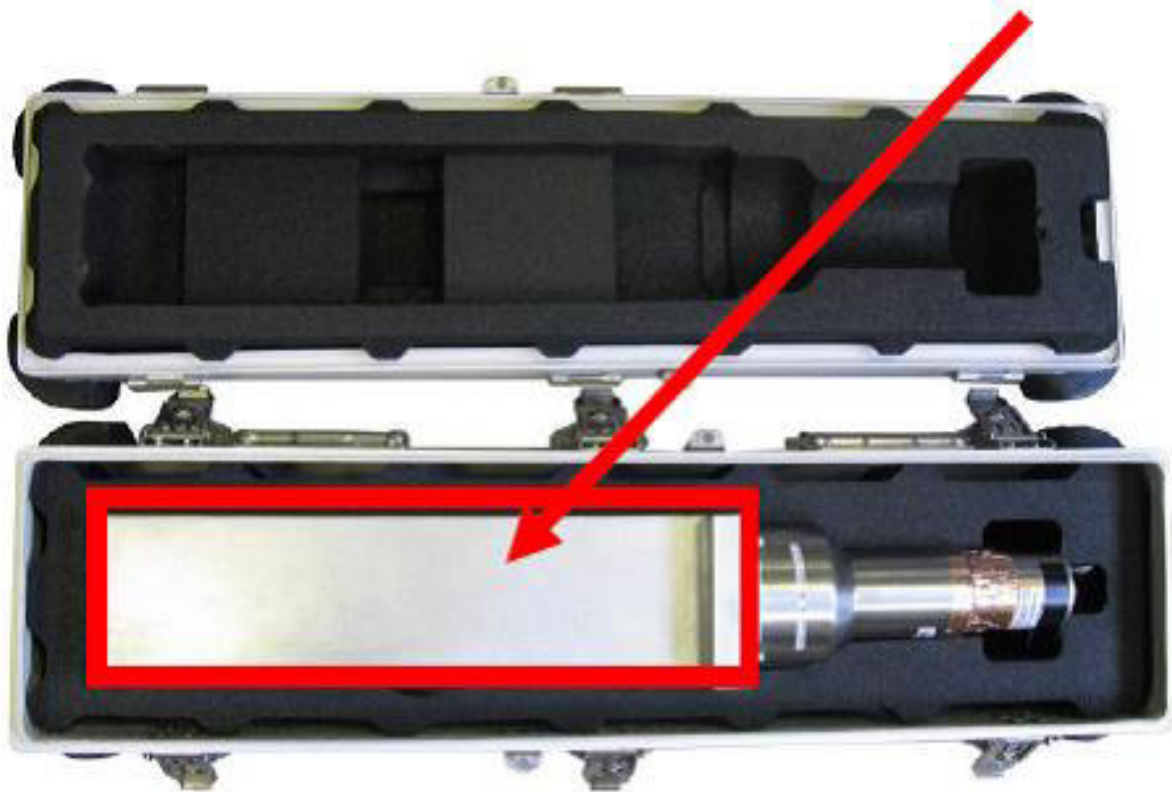
Figure 16: Four liters NaI-detector of the ULYSSE system.

Figure 17: Four ULYSSE units prior to installation into a Beechcraft King Air.

Figure 18: ULYSSE system installed on EUROCOPTER AS 350 B2 used during ARM17 viewed from the right side.

Figure 19: ULYSSE system installed on EUROCOPTER AS 350 B2 used during ARM17 viewed from the left side.

Figure 20: Rear view of the ULYSSE system installed on EUROCOPTER AS 350 B2 used during ARM17.
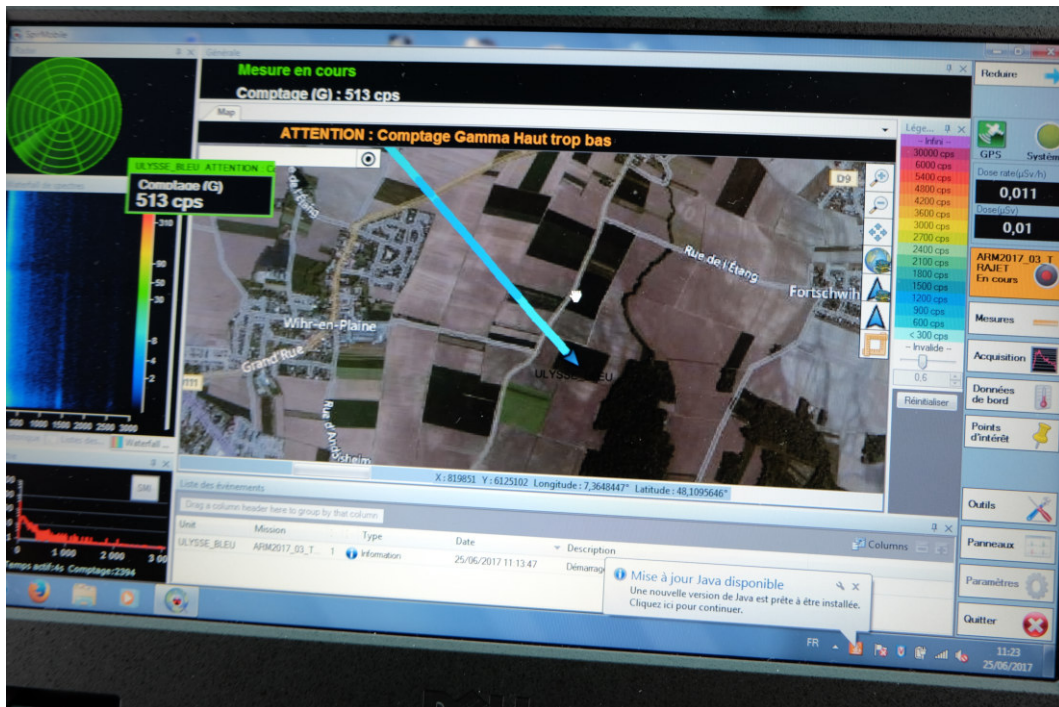
Figure 21: Screenshot of the ULYSSE system during a measuring flight.

Monitoring strategy

The measurements with a fixed-wing aircraft are usually carried out at altitudes around 200 m with a speed of about 400 km/h. By choosing a 2 km line spacing and applying geostatistical treatment to the data, it allows to characterize an area of approximately 2000 km^2 in just over two hours flight. In the event of a nuclear crisis, any French nuclear site could be reached within 6 to 8 hours. The data processing time from measurement to radiological maps requires approximately one hour. The global response time can be considered of the order of 12 hours from the beginning of an event to the first level product delivery.

The helicopter installation can provide the possibility to install the detectors outside in dedicated and certified baskets. This configuration provides better detection limit and the aircraft allows higher flexibility in the flight plan. This configuration is perfect for surveying contaminated sites or post-accidental activities.

Table 2 lists typical acquisition parameters for fixed wing aircrafts and helicopters. The detection limits for point source activities measured with a helicopter under optimal flight parameters are given in table 3.

Table 2: Acquisition parameters and minimum detectable ^{137}Cs activity concentration (LD).

Parameter	ULYSSE	
Aircraft	Fixed wing	Helicopter
Detector	16 litre NaI(Tl)	16 litre NaI(Tl)
Ground clearance	150 m to 300 m	50 m to 150 m
Acquisition time	1 Second	1 Second
LD ^{137}Cs	50 kBq/m^2	1 kBq/m^2 to 5 kBq/m^2
Speed	400 km/h	200 km/h
Hourly coverage	About 800 km^2/h with line spacing of 2 km	About 400 km^2/h with line spacing of 2 km

Table 3: Minimum detectable point source activities (MDA) for a ground clearance of 40 m and a speed of 70 km/h.

Nuclide	MDA
^{241}Am	700 MBq
^{131}I	70 MBq
^{137}Cs	30 MBq
^{60}Co	15 MBq
^{226}Ra	80 MBq

3 Data Evaluation

The advantage of aeroradiometric measurements lies in the high velocity of measurements in a large area, even over rough terrain. Uniform radiological information of an area is obtained from a regular grid of measuring points. This grid is composed from parallel flight lines which are 100 m to 500 m apart, depending on the scope of the measurement. The flight altitude above ground is aspired to be constant during the measuring flight. Typical values lie between 50 m and 150 m above ground. The spectra are recorded in regular time intervals of typical one second, yielding integration over 28 meters of the flight line at a velocity of 100 km/h.

3.1 Team CH01

The data evaluation follows the methodology described in Schwarz (1991 and 1997). Since the year 2000, software developed by the Research Group for Geothermics and Radiometry of the Institute of Geophysics of the Swiss Federal Institute of Technology Zurich (ETHZ) with on-line mapping options (Bucher, 2001) is used. The impulses in eight photon energy windows of each spectrum are summed for further evaluation (table 4). The right hand column of Table 4 notes the energy of the relevant photon emission. The "total" energy window sums counts for photon energies between 400 keV and 3000 keV.

Three energy windows are associated with natural radionuclides. The "potassium" window measures photon emissions of ^{40}K at 1461 keV. The determination of the activities of uranium and thorium utilises high energy emissions of the decay products ^{214}Bi and ^{208}Tl to minimize absorption losses in the air between ground and detector.

Four energy windows are employed for a determination of artificial radioactivity. Those at 662 keV and 1250 keV measure the emissions of ^{137}Cs and ^{60}Co, respectively. The remaining two MMGC (Man Made Gross Count) energy windows measure in the photon energy interval 400 keV to 1400 keV (MMGC1) radiation from artificial and natural radionuclides and in the photon energy interval 1400 keV to 3000 keV (MMGC2) mainly natural radionuclides. The ratio of the count rates in these energy windows can be used for the search of artificial radioactive sources.

Additional to the acquired spectra, a special channel is dedicated for the measurement of photon energies between 3000 keV and 6000 keV. This channel is used to determine the fraction of the measured counts in the spectra, which are correlated to cosmic radiation. Simplifying, this channel (measured separately from the spectrum) is called cosmic window.

Table 4: Energy windows for data evaluation.

Window	Lower energy limit [keV]	Upper energy limit [keV]	Peak energy [keV]
Total	400	3000	-
Potassium (^{40}K)	1369	1558	1461
Uranium (^{214}Bi)	1664	1853	1765
Thorium (^{208}Tl)	2407	2797	2615
Caesium (^{137}Cs)	600	720	662
Cobalt (^{60}Co)	1100	1400	1173, 1332
MMGC1	400	1400	-
MMGC2	1400	3000	-

The photons registered in the detector origin from several different sources. Goal of the measurement is the determination of the part of the signal, which is correlated to radionuclides in the soil. The signal has to be reduced in respect to other sources of photon radiation, which therefore have to be identified and quantified. Additionally, the measuring signal is dependent on several influencing parameters, which may vary during a measuring flight. For optimum quality of the derived results, the influence of these parameters has to be corrected. The steps for data processing are described in the following sections in detail. Corrections are applied either in the energy windows described above or for each channel of the spectrum separately.

3.1.1 Dead time correction

During the processing of an impulse, the detector and spectrometer are blocked from registering further impulses. This effect reduces the number of counted impulses at high count rates. The dead time of the spectrometer is measured directly and can be utilised for the according correction.

$$CR_{corr,t} = CR_{raw}\frac{t_{meas}}{t_{meas} - t_{dead}} \qquad (3.1.1.1)$$

with:

$CR_{corr,t}$:   Deadtime corrected count rate [cps]
CR_{raw}:   Measured count rate [cps]
t_{meas}:   Measuring time of the spectrometer (constant 990 ms) [s]
t_{dead}:   Time during which the spectrometer was blocked [s]

Typical values for t_{dead} lie between 40 ms (central Switzerland) and 200 ms (Swiss nuclear power plant Leibstadt) in 990 ms measuring time, yielding an associated correction factor between 1.04 and 1.25.

3.1.2 Detector background and cosmic radiation

The detector measures photons which originate from the detector itself and the surrounding helicopter. Both components are assumed constant for an individual detector and helicopter. To this background is added a second component generated by cosmic radiation. The primary cosmic radiation consists of 87% protons, of 12% alpha particles and of 1% heavy nuclei. Photons are generated during interaction of the primary cosmic radiation with the atmosphere. The effect of these photons on the measuring signal is dependent on elevation, air pressure and latitude. A linear relationship between the count rate produced by cosmic radiation in any channel of the spectrum and the count rate in the cosmic window was found experimentally. Thus, the count rate in the cosmic window can be used for the direct correction in other energy windows. The correction for background and cosmic radiation can be formulated as

$$CR_{corr,B} = CR_{corr,t} - (CR_B + S_c CR_c) \qquad (3.1.2.1)$$

with:

$CR_{corr,B}$: Background corrected count rate [cps]
CR_B: Background count rate of detector and helicopter [cps]
CR_c: Count rate in cosmic window [cps]
S_c: Cosmic correction factor [ ]

The two constants CR_B and S_c are determined with an ascent over large water bodies. Due to the absorption in water the terrestrial radiation is mainly shielded yielding a direct measurement of the term $CR_B + S_c CR_c$ for each energy window. The background is independent of the flight altitude, whereas the effect of cosmic radiation increases with altitude. Thus, both effects can be separated with a linear regression of the measured count rates. The measured count rates during an ascent over the British Channel in the year 2002 are summed in table 5. Figure 22 shows exemplarily the measured count rates and the respective linear regression for the caesium energy window. The constants CR_B and S_c are listed together with their uncertainties according to the Guide to the Expression of Uncertainty in Measurement (GUM, extension factor k=1) for all energy windows in table 6. This section was already published in the report of the international intercomparison exercise ARM07. Unfortunately, the then published values were obtained for an erroneous energy calibration. The correct values are presented below.

Table 5: Measured count rates in three different altitudes.

Altitude [m]	1888	2864	3750
Energy window	Count rate [cps]		
Cosmic	105.3	159.4	253.8
Total	205.6	255.8	362.8
Potassium	18.5	20.5	25.5
Uranium	7.2	9.3	13.3
Thorium	7.0	9.0	13.3
Caesium	26.5	30.2	40.4
Cobalt	20.1	24.1	35.3
MMGC1	157.5	193.8	274.2
MMGC2	48.1	62.1	88.6
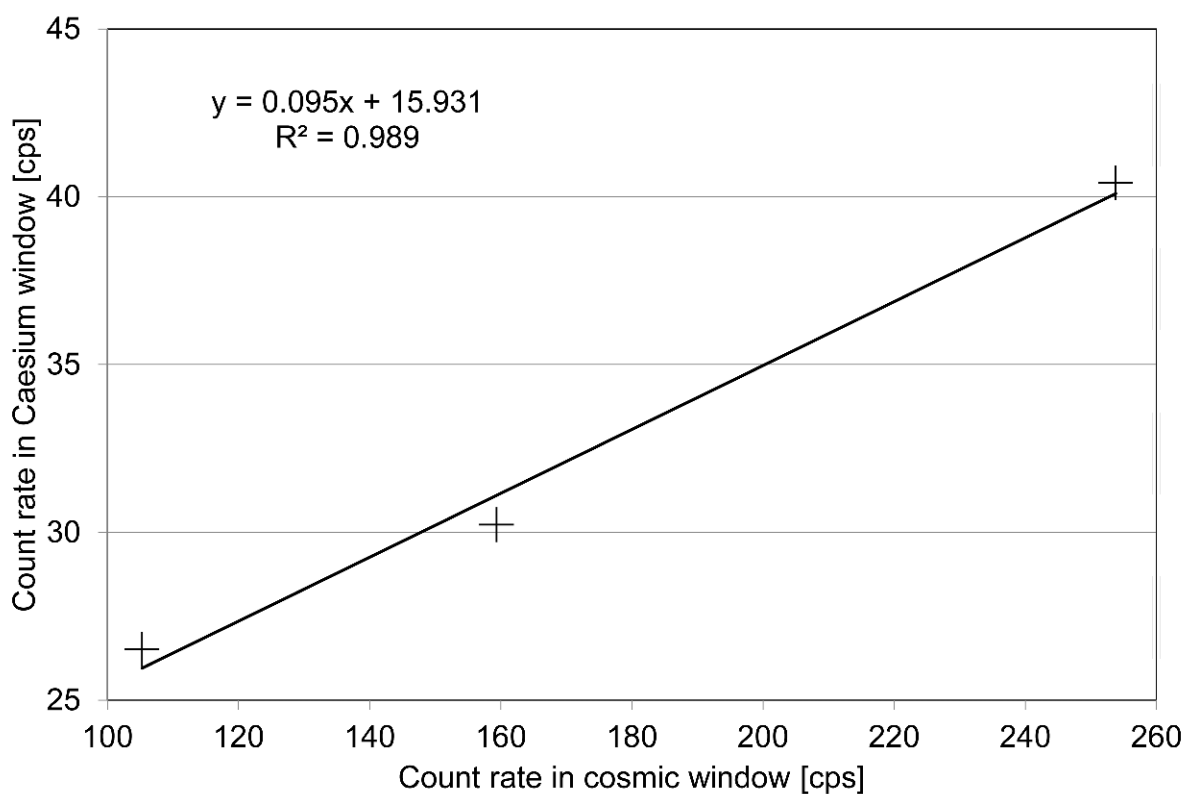
Figure 22: Count rate in the caesium energy window for three different altitudes and according linear regression.

Table 6: Correction factor S_c and background count rate CR_B determined by linear regression together with their uncertainties.

Energy window	S_c	$U(S_c)$	CR_B [cps]	$U(CR_B)$ [cps]
Total	1.067	0.054	90.4	9.8
Potassium	0.047	0.004	13.4	0.7
Uranium	0.041	0.000	2.8	0.1
Thorium	0.043	0.002	2.3	0.4
Caesium	0.095	0.010	15.9	1.9
Cobalt	0.104	0.012	8.5	2.2
MMGC1	0.793	0.048	71.4	8.7
MMGC2	0.274	0.006	19.0	1.1

3.1.3 Energy resolution and Compton scattering

Photons emitted from the soil are scattered due to the Compton effect in the soil, in buildings, in vegetation, in the air between surface and helicopter and in the detector. The associated energy loss may lead to a registration of the photon in a lower photon energy window. The poor energy resolution of a NaI(Tl)-detector compared to modern solid-state detectors causes the possibility that photons with energies near the energy limits of a photon energy window are registered in the adjacent energy window. The influence of both effects on the signal is determined experimentally. The count rate $CR_{korr,B}(i)$ in the energy window i is composed from contributions of all photon sources j, weighted with a stripping coefficient $f_{i,j}$

$$CR_{corr,B}(i) = \sum_{j=1}^{8} f_{i,j} CR_{corr,S}(j) \tag{3.1.3.1}$$

with:

$CR_{corr,B}(i)$: Background corrected count rate measured in energy window i [cps]
$CR_{corr,S}(j)$: Background corrected count rate measured in the energy
             window of source component j [cps]
$f_{i,j}$: Stripping coefficient of component j into energy window i [ ]

For the derivation of the contributions of the different photon sources $CR_{corr,S}(j)$ from measured count rates $CR_{corr,B}(i)$, the system of linear equations has to be solved. The equation above can be formulated as

$$\overline{CR}_{corr,B} = \overline{\overline{f}}\; \overline{CR}_{corr,S} \tag{3.1.3.2}$$

with:

$\overline{CR}_{corr,B}$: Vector of background corrected count rates in the eight energy windows [cps]
$\overline{CR}_{corr,S}$: Vector of background corrected count rates measured in the energy
             windows of source components [cps]
$\overline{\overline{f}}$: Matrix of stripping coefficients [ ]

Matrix $\overline{\overline{f}}$ is then inverted with the help of the LU-decomposition (reduction to two triangular matrices, L(ower) and U(pper)), which yields

$$\overline{CR}_{corr,S} = \overline{\overline{f}}^{-1} \; \overline{CR}_{corr,B} \qquad (3.1.3.3)$$

with:

$\overline{\overline{f}}^{-1}$:   Inverted matrix of stripping coefficients [ ]

The stripping coefficients $f_{i,j}$ can be determined with measurements of radioactive point sources near to the detector, which are then corrected for altitude and scattering in soil for the natural radionuclides.

$$f_{i,j} = g_{i,j} + f_{i,j,point} \qquad (3.1.3.4)$$

with:

$f_{i,j,point}$:   Stripping coefficients derived from measurements with point sources [ ]
$g_{i,j}$:   Correction for altitude and scattering in soil [ ]

These steps are demonstrated with a numerical example in the following paragraphs. Formally, the stripping factors are calculated for all energy windows and all radiation sources. The stripping correction is obsolete for the group energy windows Total, MMGC1 and MMGC2. Measurements showed that ^{137}Cs does not render counts in energy windows with higher photon energies. With these restrictions, the determination of stripping coefficients is reduced to the radioactive sources ^{60}Co, ^{40}K, uranium and thorium, the latter two in natural isotope composition. Table 7 summarises exemplarily results of measurements of these four radioactive sources together with a laboratory background measurement performed in the year 2000. After subtracting the background count rates, the net count rate is normalised to the component energy window (table 8). The matrix is completed with the given values in the group windows (table 9). After applying the corrections for altitude and soil scattering $g_{i,j}$, the system of equations can be solved by formation of the inverse matrix.

Table 7: Measured count rates with four different point sources in 1 m distance to the detector.

Energy window	Component count rate [cps]				
	Background	^{40}K	Uranium	Thorium	^{60}Co
Potassium	160	210	256	233	210
Uranium	40	39	173	83	43
Thorium	40	40	47	248	43
Caesium	200	211	720	578	256
Cobalt	156	174	429	264	378

Table 8: Relative fraction of count rates in the respective energy window.

Energy window	Relative fraction of component			
	^{40}K	Uranium	Thorium	^{60}Co
Potassium	1.00	0.72	0.35	0.23
Uranium	-0.02	1.00	0.20	0.01
Thorium	0.01	0.06	1.00	0.01
Caesium	0.21	3.92	1.81	0.25
Cobalt	0.36	2.06	0.52	1.00

Table 9: Extended matrix of relative count rate fractions in the respective energy windows.

Energy window	Relative fraction of component							
	Total	^{40}K	U	Th	^{137}Cs	^{60}Co	MMGC1	MMGC2
Total	1.00	0.00	0.00	0.00	0.00	0.00	0.00	0.00
Potassium	0.00	1.00	0.72	0.35	0.00	0.23	0.00	0.00
Uranium	0.00	-0.02	1.00	0.20	0.00	0.01	0.00	0.00
Thorium	0.00	0.01	0.06	1.00	0.00	0.01	0.00	0.00
Caesium	0.00	0.21	3.92	1.81	1.00	0.25	0.00	0.00
Cobalt	0.00	0.36	2.06	0.52	0.00	1.00	0.00	0.00
MMGC1	0.00	0.00	0.00	0.00	0.00	0.00	1.00	0.00
MMGC2	0.00	0.00	0.00	0.00	0.00	0.00	0.00	1.00

3.1.4 Altitude, air pressure, air temperature and atmospheric radioactivity

Normalisation of the measured data to a fixed altitude of 100 m above ground improves the comparability of the multitude of point measurements along the flight lines. An exponential dependence between photon attenuation and altitude is assumed.

$$CR_{corr,h} = CR_{corr,S} \frac{e^{-\mu_{ref} h_{ref}}}{e^{-\mu h}}; \quad \mu = \mu_{ref} \frac{T_{ref}}{T} \frac{P}{P_{ref}} \tag{3.1.4.1}$$

with:

$CR_{corr,h}$: Count rate corrected to reference altitude h_{ref} [cps]
μ_{ref}: Attenuation coefficient at reference conditions [m^{-1}]
μ: Attenuation coefficient at measurement conditions [m^{-1}]
h_{ref}: Reference altitude h_{ref} = 100 m
h: Altitude above ground [m]
T_{ref}: Reference temperature T_{ref} = 273.15 K
T: Air temperature [K]
P_{ref}: Reference pressure P_{ref} = 101325 Pa
P: Air Pressure [Pa]

A more complex method, which takes into account topographic effects with the help of the Swiss digital terrain model is used only in special cases. The attenuation coefficients for

the respective radiation components are determined with ascents over flat terrain. The measured net counts for different altitudes are fitted to an exponential curve using the least squares method. The so determined attenuation coefficient is extrapolated with the measured values of air temperature and air pressure to the reference conditions. The detector registers photon emissions from radionuclides contained in the atmosphere, mainly radon decay products attached to aerosol particles. The influence of these radionuclides can be observed during the determination of the attenuation coefficient of the uranium component. The measurement of this component including the expected temporal variation during a measuring flight with additional instrumentation is neither performed nor planned for the near future. Ascents for the determination of the attenuation coefficients are performed during the annual aeroradiometric exercises. The attenuation coefficients for the artificial radionuclides ^{137}Cs and ^{60}Co are revised only in the case that the peaks are clearly identifiable in the photon spectrum. Table 10 sums the results of an ascent over the airfield of the Swiss town Locarno measured during the exercise ARM05. Figure 23 shows the decrease of the ^{137}Cs count rate together with a approximated exponential interpretation of the measurement results. The attenuation coefficients determined from this flight and normalised to reference conditions are listed in table 11 together with the uncertainties according to GUM (extension factor k=1).

Table 10: Results of the ascent over the airfield of Locarno, 2005.

Altitude [m]	Count rate of component $CR_{corr,S}$ [cps]						
	Total	^{40}K	Uranium	Thorium	^{137}Cs	MMGC1	MMGC2
27.4	2436	162	38	55	184	2044	401
59.3	1952	122	30	44	118	1646	313
93.7	1571	96	26	34	75	1323	254
118.4	1358	79	25	30	45	1143	221
162.4	1064	59	22	22	22	894	175
247.4	726	33	16	14	8	613	116
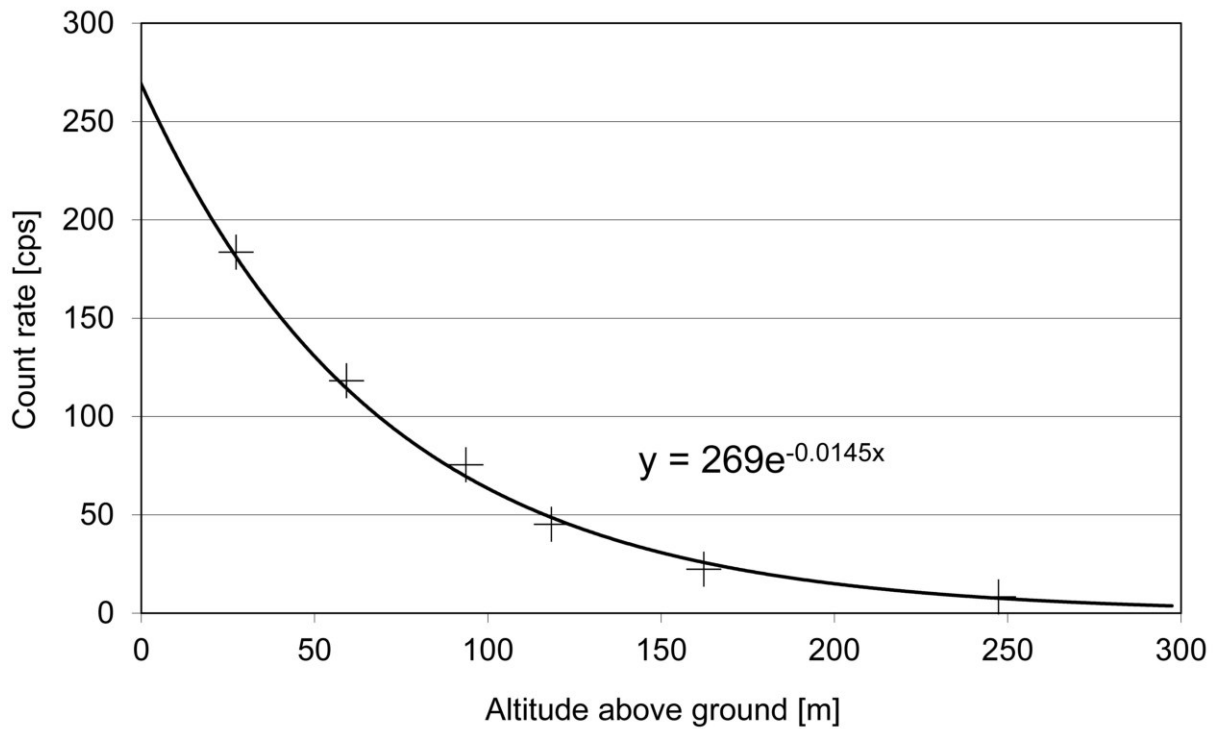
Figure 23: Decrease of ^{137}Cs count rate in dependence on flight altitude.

Table 11: Experimentally determined attenuation coefficients.

Component	μ_{ref} [m^{-1}]	$U(\mu_{ref})$ [m^{-1}]
Total	5.48E-03	2.53E-04
^{40}K	7.19E-03	1.66E-04
Uranium	3.53E-03	2.99E-04
Thorium	6.18E-03	2.99E-04
^{137}Cs	1.45E-02	5.83E-04
^{60}Co	not detectable	
MMGC1	5.46E-03	2.55E-04
MMGC2	5.54E-03	2.47E-04

3.1.5 Specific activity calibration

Activity concentrations of radionuclides in soil can be estimated from the normalised measured count rates $CR_{corr,h}$. In the case of natural radionuclides, a homogeneous distribution in soil is assumed, whereas for artificial radionuclides the activity is assumed to be located in a thin layer of topsoil. The calibration factors (table 12) are determined by comparing the measured count rates with results from radioanalytical measurement of soil samples and in-situ gamma-spectrometric measurements.

Table 12: Experimentally determined calibration factors.

Component	Nuclide	Calibration factor [Bq kg⁻¹ cps⁻¹]
Potassium	^{40}K	8.3
Uranium	^{214}Bi	4.0
Thorium	^{208}Tl	1.7
Caesium	^{137}Cs	2.0

3.1.6 Dose rate calibration

The specific activities determined in the prior paragraph can be used for a determination of terrestrial dose rate $H^*(10)$ at one meter above ground. As used for measurements with in-situ gamma-spectrometry, the air kerma is estimated using conversion factors listed in ICRU report 53. Further multiplication with factors 1.1 Sv/Gy (uranium- and thorium-decay series) or 1.2 Sv/Gy (Caesium) renders terrestrial dose rate $H^*(10)$, assuming radioactive equilibrium in the decay series (table 13).

Table 13: Dose rate conversion factors.

Nuclide	Conversion factor [nSv h⁻¹ Bq⁻¹ kg]
^{40}K	0.044
^{214}Bi	0.55
^{208}Tl	0.77
^{137}Cs	0.20

A second approach consist of a direct calculation of the terrestrial dose rate with the spectrum dose index (SDI) method. This method utilises the energy deposition in the detector as a direct measure of dose rate $dH^*(10)/dt$. The dose delivered by a photon is considered proportional to the energy of the photon. Due to the automatic gain stabilisation of the measuring system with the help of the ^{40}K photon emission, the assignment of channel to energy interval can be considered constant. The SDI is then calculated as sum of the products of channel number and net count rate.

$$SDI = \sum_{k=0}^{255} k\, CR_{raw}(k) \qquad (3.1.6.1)$$

with:

$CR_{raw}(k)$: Raw count rate in channel k [cps]
SDI: Spectrum dose index [cps]

In a next step the SDI is corrected for background and cosmic radiation.

$$SDI_{corr} = SDI - SDI_{back} - SDI_{cosmic} \qquad (3.1.6.2)$$

with:

SDI_{cosmic}: Contribution of cosmic radiation to SDI [cps]
SDI_{back}: Contribution of background to SDI [cps]
SDI_{corr}: Corrected SDI [cps]

The contribution of the background is calculated using a background spectrum of the aircraft and the equipment. The value used currently for SDI_{back} is 12640 cps.

$$SDI_{back} = \sum_{k=0}^{255} k\,CR_{back}(k) \qquad (3.1.6.3)$$

with:

$CR_{back}(k)$: Raw count rate of the background spectrum in channel k [cps]
SDI_{back}: SDI of the background spectrum [cps]

The contribution of the cosmic radiation is calculated using the count rate of the cosmic window and the cosmic stripping coefficients of each channel. The value of f_{cosmic} currently used is 95.5.

$$SDI_{cosmic} = CR_{cosmic}f_{cosmic} = CR_{cosmic} \sum_{k=0}^{255} k\,S(k) \qquad (3.1.6.4)$$

with:

SDI_{cosmic}: SDI derived from counts in the cosmic window [cps]
CR_{cosmic}: Raw count rate in the cosmic window [cps]
f_{cosmic}: Bulk stripping factor for the influence of cosmic radiation [ ]
$S(k)$: Cosmic stripping coefficient for channel k [ ]

The SDI reduced for backround and cosmic radiation is corrected to reference altitude h_{ref} = 100 m.

$$SDI_{alt} = SDI_{corr}e^{\mu_{air}(h-h_{ref})} \qquad (3.1.6.5)$$

with:

SDI_{alt}: SDI at reference altitude [cps]
μ_{air}: Attenuation coefficient in air [m^{-1}]
h: Flight altitude [m]
h_{ref}: Reference altitude [m]

A comparison to dose rate measurements at ground level yields directly the calibration factor to the dose rate $dH^*(10)/dt$.

$$DR_{terr} = \alpha SDI \qquad (3.1.6.6)$$

with:

DR_{terr}:   Terrestrial dose rate $dH^*(10)/dt$ at 1 m above ground [nSv h^{-1}]
α: Calibration factor α = 0.00096 [nSv h^{-1} cps^{-1}]

The total dose rate consists of two components, terrestrial and cosmic dose rate. The cosmic dose rate in dependence of height above sea level can be approximated with an exponential function. The total dose rate is then obtained by adding the cosmic dose rate to the terrestrial dose rate estimated with the SDI-method.

$$DR_{cosmic} = 37e^{0.38z} \qquad (3.1.6.7)$$

with:

DR_{cosmic}:   Cosmic dose rate $dH^*(10)/dt$ at height z above sea level [nSv h^{-1}]
z: Height above sea level [km]

Table 14 shows a comparison of dose rates in 1 m above ground estimated with both methods in the year 2006. The slight decrease of the dose rate estimated from specific activities can be assigned to the influence of airborne radon decay products, which led to an over-compensation of Compton scattering. Nevertheless, both methods agree well inside the uncertainties according GUM (extension factor k=1).

Table 14: Dose rate $H^*(10)$ in 1 m above ground.

Altitude	Dose rate [nSv h^{-1}]	
	Activities	SDI
45	130 ± 6	120 ± 6
60	126 ± 6	120 ± 6
89	125 ± 7	118 ± 6
120	120 ± 8	116 ± 8
149	119 ± 9	118 ± 10
175	119 ± 10	117 ± 10
209	118 ± 11	121 ± 10

3.1.7   Transition to RLL system

The two ARM measuring systems deployed by the National Emergency Operations Centre (NEOC) will be replaced in 2018 by two of four RLL measuring systems purchased by the Swiss Air Force. To achieve continuity of the measured data in this transition, the RLL system provides raw data for a re-evaluation using the software developed for the ARM system. Prior to the use of the ARM software, the interference between different radiation sources and energy windows (see section 3.1.3) had to be determined in the laboratory. Figure 24 shows RLL detector 002 mounted for irradiation at the calibration facility of PSI. Spectra measured with ^{40}K-, ^{137}Cs-, ^{60}Co-, natural uranium- and thorium-sources are depicted together with the energy windows used for analysis in figures 25 to 29. The energy resolution

of RLL detector 002 for the 662 keV peak of ^{137}Cs of 9.5 % is relatively large. Thus, the energy peaks are slightly broader than the associated energy windows. The under-performing energy resolution is caused by crystals 1 and 3 with energy resolutions of 9.9% and 11.6% respectively, which are compensated by crystals 2 and 4 with normal energy resolutions of 8.4% and 8.7%. The energy resolutions of crystals 1 and 3 will be reviewed during the next annual maintenance by the manufacturer of the system. The count rates in the different energy windows due to the different sources relative to the appropriate energy window are listed in table 15. The values are very similar to the values obtained with the latest ARM detector (table 8. The sub-optimal energy resolution of RLL detector 002 is mainly visible in the spillover of counts from a potassium source into the slightly overlapping cobalt energy window of 0.47 compared to 0.36. The stripping correction is listed with further parameters derived from the results of this exercise in section 18.5.

Figure 24: RLL detector 002 in the calibration laboratory at PSI.
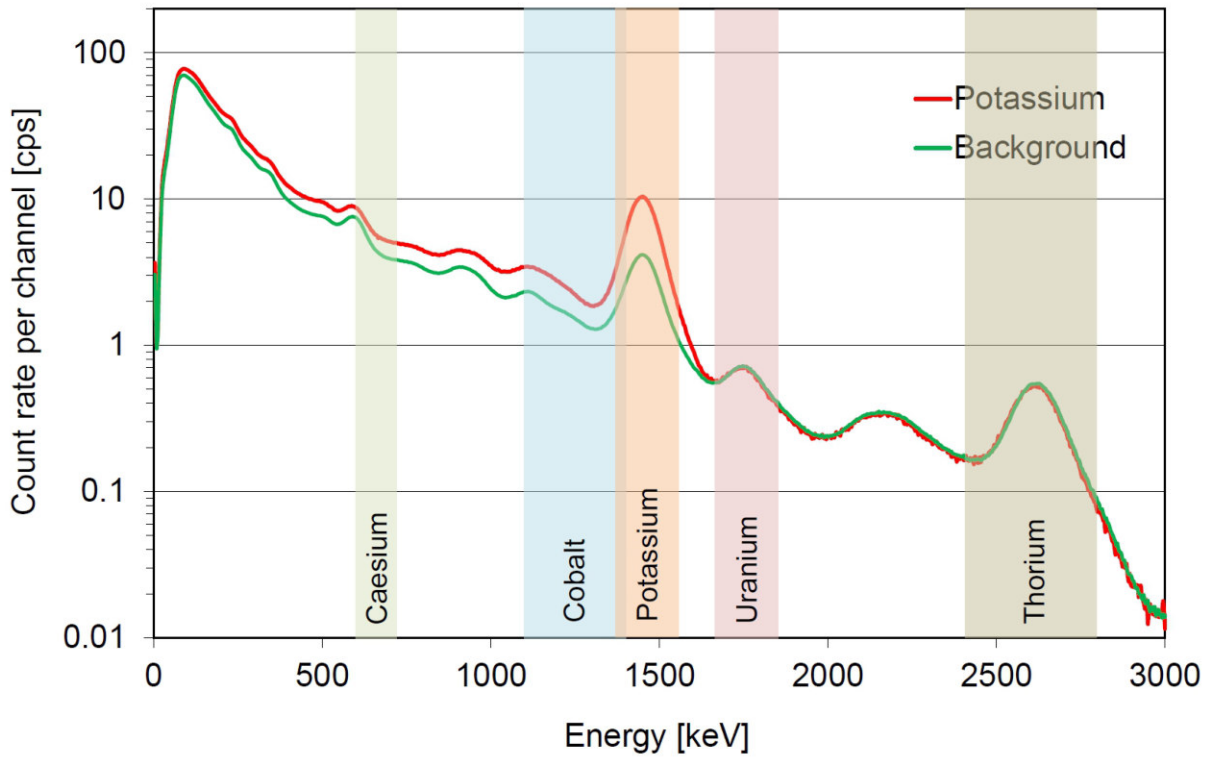
Figure 25: Spectrum of RLL detector 002 with a ^{40}K source compared to a background spectrum.
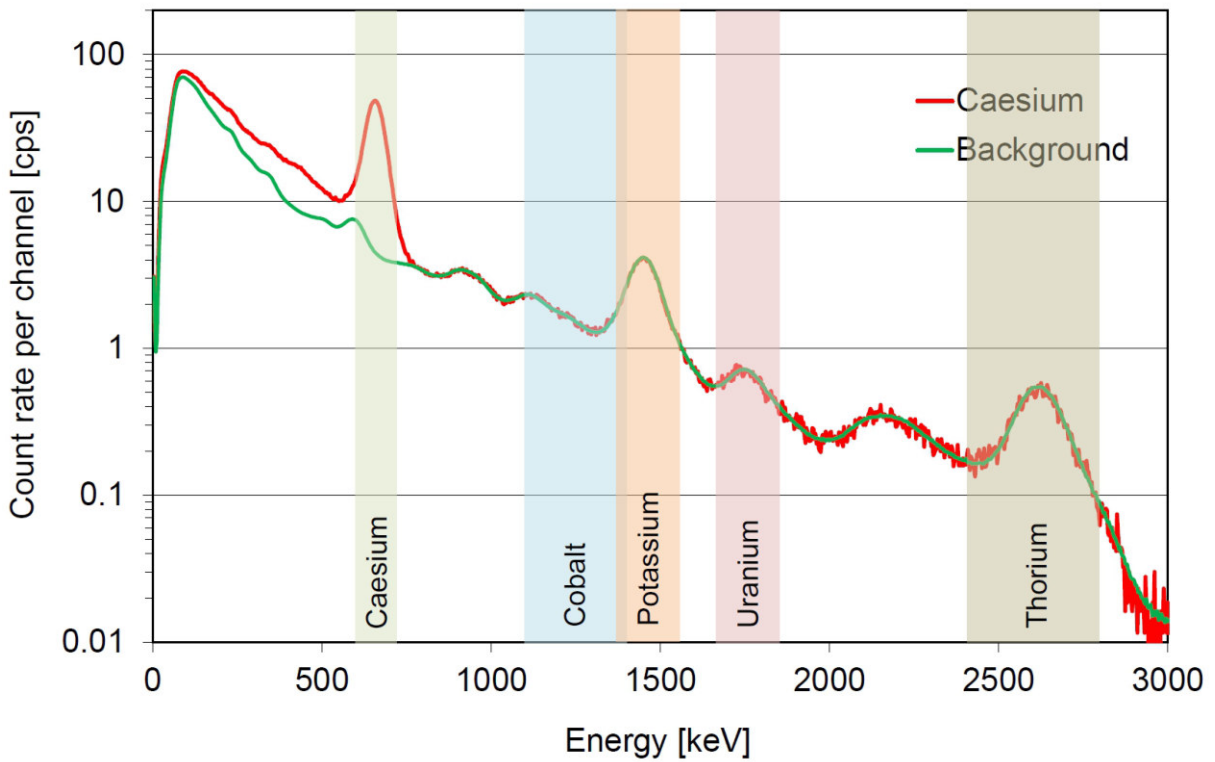
Figure 26: Spectrum of RLL detector 002 with a ^{137}Cs source compared to a background spectrum.
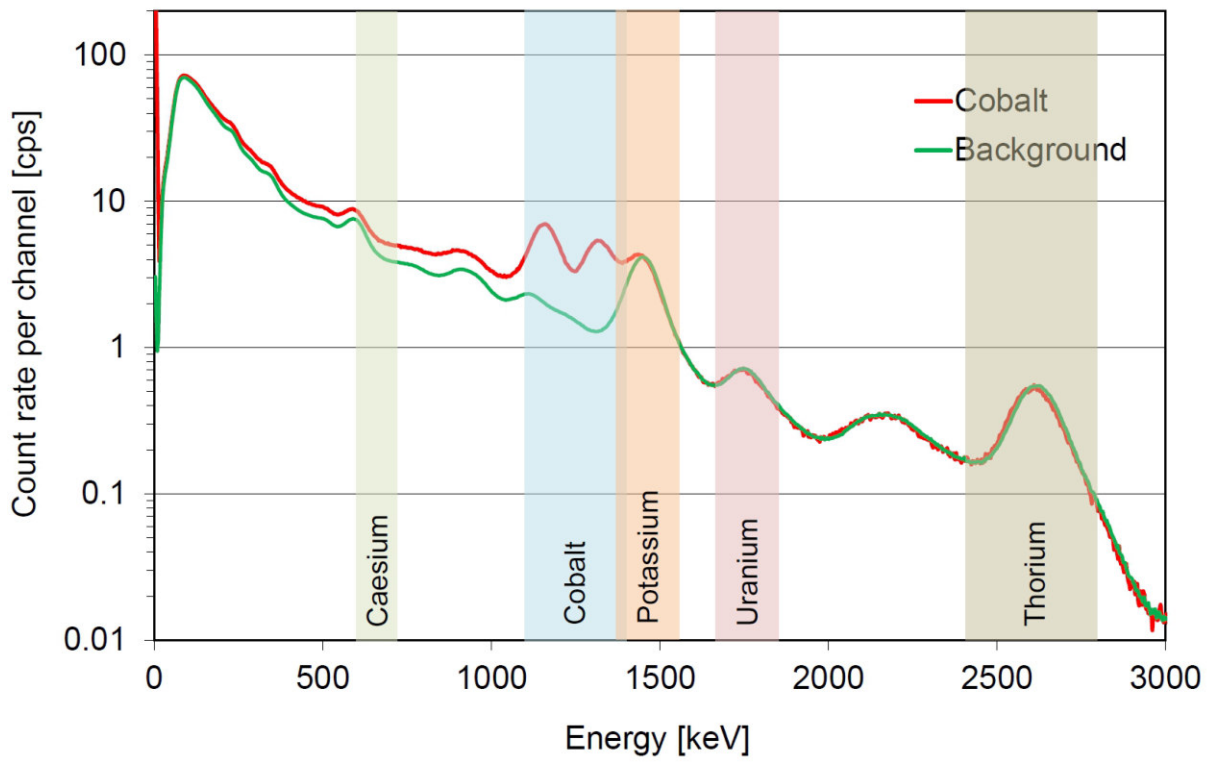
Figure 27: Spectrum of RLL detector 002 with a ^{60}Co source compared to a background spectrum.
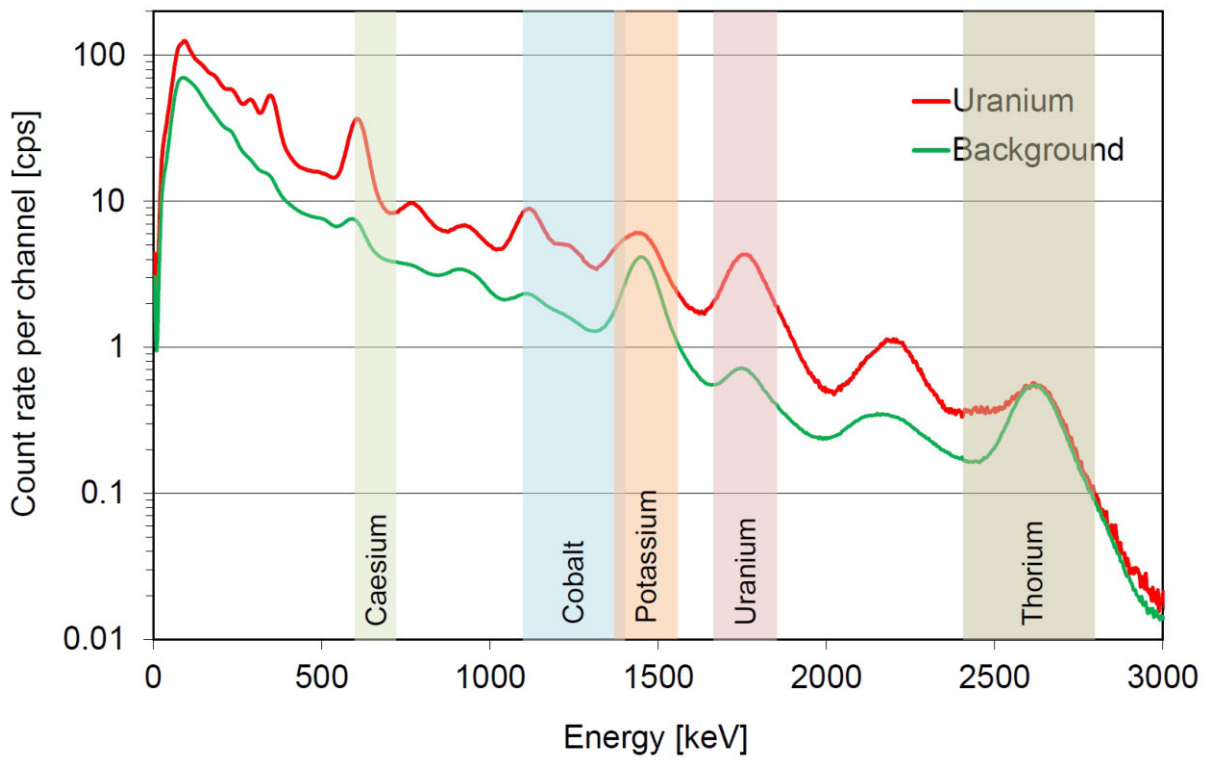
Figure 28: Spectrum of RLL detector 002 with a natural uranium source compared to a background spectrum.
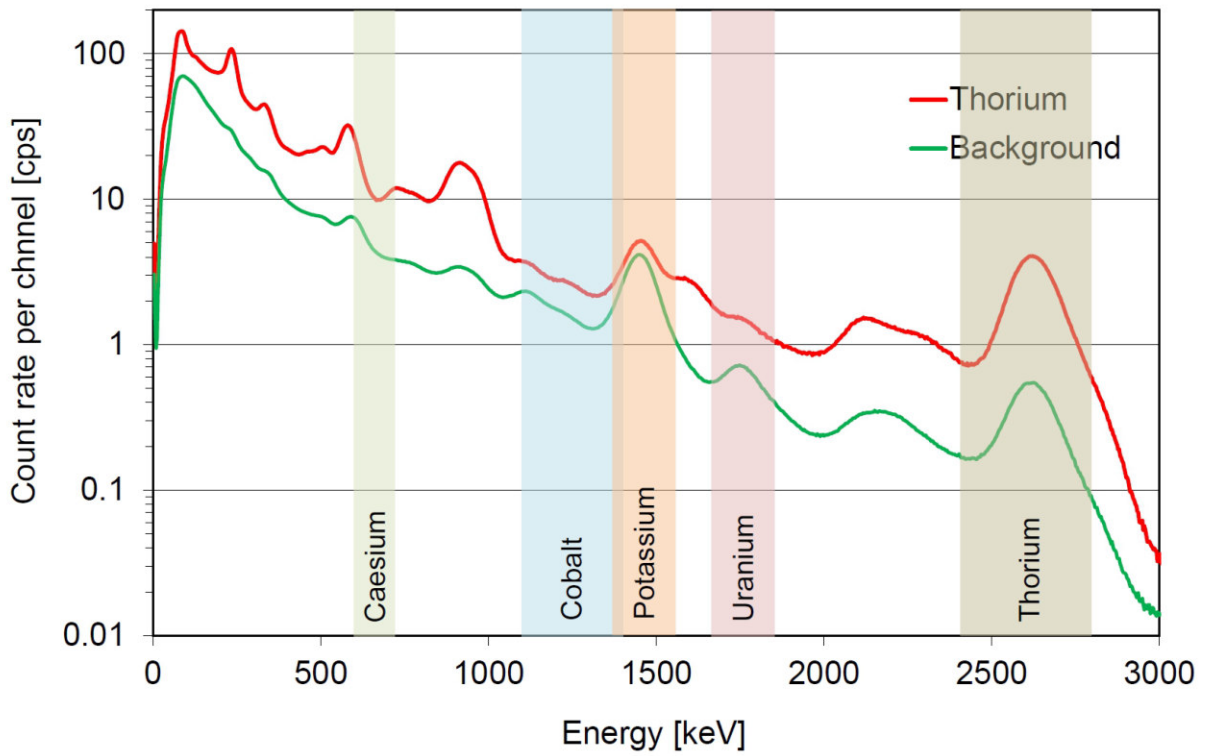
Figure 29: Spectrum of RLL detector 002 with a natural thorium source compared to a background spectrum.

Table 15: Relative fraction of count rates in the respective energy window for RLL detector 002.

Energy window	Relative fraction of component			
	^{40}K	Uranium	Thorium	^{60}Co
Potassium	1.00	0.79	0.33	0.09
Uranium	0.00	1.00	0.24	0.00
Thorium	0.00	0.06	1.00	0.00
Caesium	0.22	3.13	1.56	0.15
Cobalt	0.47	2.15	0.47	1.00

3.2 Team CH02

3.2.1 Signal processing and spectra analysis

Each of the four NaI(Tl) radiation detectors is associated with a 1024 channel spectrometer providing elementary spectra from approximately 0 to 3 MeV. The real accumulation time is 1 second. The first step of the signal processing is the energy stabilisation that corrects the effect of possible temperature changes (despite the excellent thermal insulation of the detection container) and a hypothetical ageing process of the detector assemblies. The stabilisation process uses the ^{40}K peak as reference (other NORM isotopes like ^{226}Ra or ^{232}Th are possible) and produces an offset and a slope for each spectra. Subsequently and based on the linearity characteristics obtained during the initial detector characterisation stored in the spectrometers, the elementary spectra are normalised to spectra without offset and with a fixed gain of 3 keV per channel. At this stage, the normalised spectra can be summed to build the total channel (other configurations like right and left channel are possible, e.g. in vehicle). The normalised total spectrum is then available for dose rate calculation and further analysis like isotope identification. The further signal processing depends of the situation and required mission type. The NBC-EOD centre of competence basically uses a standard configuration for background mapping and source search or an adapted configuration for contamination mapping. With the standard configuration the software uses a sliding accumulation of the normalised spectra (1 second) over 5 seconds in order to improve the confidence level of the isotope identification process. Some criteria or combination of criteria like increased count rate (full spectra or defined region of interest) or increased dose rate can trigger a longer accumulation in order to identify the detected isotopes (these events are named "detection"). For the mapping of a contaminated area the isotope is assumed to be identified and the operators don't need to be warned with continuous identification results. In this case, the used configuration doesn't require the sliding of the normalized spectra and doesn't trigger a longer accumulation. Therefore only the 1 second spectra are used.

3.2.2 Isotope identification

The used proprietary isotope identification algorithm (SIA IdentPro Identification Algorithm) has been specially optimized in order to provide fast decisions based on spectra with poor statistical features. It is based on the analysis of many regions of interest (over 70 ROIs), taking into account an interference matrix and an additional process by partial deconvolution. This algorithm does not require preliminary peak recognition: it takes into account large statistical fluctuations and does not require a calibrated efficiency. It also takes into account possible shielding and background variation. The algorithm is able to identify up to four isotopes from the isotope groups listed in table 16. Different filters or combination of filters allow discrimination of the alarms displayed and recorded. These filters can be set for example on isotope group, dose rate or count rate.

Table 16: Isotope groups used by the SIA algorithm. NORM: Naturally occuring radioactive materials. SNM: Special nuclear materials.

Isotope group	Isotopes
NORM	^{40}K, ^{238}U-series, ^{232}Th-series
Medical	^{18}F, ^{51}Cr, ^{67}Ga, ^{99}Mo, ^{99m}Tc, ^{103}Pd, ^{111}In, ^{123}I, ^{125}I, ^{131}I, ^{132}I, ^{133}I, ^{133}Xe, ^{153}Sm, ^{201}Tl
Industrial	^{22}Na, ^{57}Co, ^{60}Co, ^{106}Ru/Rh, ^{133}Ba, ^{134}Cs, ^{137}Cs, ^{152}Eu, ^{166}Ho, ^{192}Ir, ^{207}Bi, ^{241}Am, Bremsstrahlung, H(n,gamma)
SNM	^{233}U, ^{235}U, ^{237}U, ^{238}U, ^{237}Np, ^{239}Pu, ^{241}Pu

3.2.3 Ground dose rate

The system calculates the ground dose rates according to IAEA's technical note TECDOC 1363, 2003. The cosmic dose rate at the flight level, the detector background and the local radon background are subtracted from the actual dose rate at the flight level. The cosmic dose rate at the flight level is converted from the cosmic channel with a conversion factor of 0.002203 μSv/h per cps. The intrinsic detector background dose rate is estimated at 2 nSv/h and the radon dose rate set as 0 nSv/h. The measured altitude above ground is first corrected to standard conditions of air pressure and temperature according the outside air pressure and temperature provides by the helicopter. The dose rate at flight altitude resulting after subtraction of cosmic, intrinsic and radon dose rate is then extrapolated to ground level (1 m above ground) with an exponential correction.

$$DR_{1m} = DR_h e^{-0.0056h}$$

(3.2.3.1)

with:

DR_{1m}:   Terrestrial dose rate at 1 m above ground [nSv/h]
h: Height of detector above ground [m]
DR_h: Dose rate at flight altitude [nSv/h]

3.2.4 NORM concentration calculation

The activity concentration of naturally occurring radioactive materials (NORM) in the soil is assumed to be constant with depth. The used algorithm is based on a reverse matrix calculation. The matrix coefficients are specific for the different regions of interest (ROI) used for different NORM nuclides and are functions of the altitude above ground and of the attenuation of the vehicle. The matrix coefficients are estimated by Monte Carlo simulations with a uniform soil concentration in an infinite plate of 50 cm thickness.

Table 17: Energy ranges and algorithm parameters. BKGND: Intrinsic background count rate in ROI. Radon: Count rate in ROI due to airborne radon progeny. Cosmic: Count rate in ROI due to cosmic radiation.

NORM	Isotope	Main peak	Energy range (ROI)	BKGND [cps]	Radon [cps]	Cosmic [cps]
Potassium	^{40}K	1461 keV	1370 to 1570 keV	2.30	0.00	23
Uranium	^{214}Bi	1765 keV	1660 to 1860 keV	0.73	0.00	21
Thorium	^{208}Tl	2614 keV	2410 to 2810 keV	0.00	0.00	26

As a first step, the net count rates CR_K, CR_U and CR_{Th} in the NORM energy ranges are calculated by subtracting the intrinsic background count rate, the count rate due to airborne radon progeny and the count rate produced by cosmic radiation. The activity concentrations of the individual NORM components are calculated from a linear combination of alls of these net count rates multiplied with stripping correction factors.

$$C_K = CR_K a' + CR_U b' + CR_{Th} c' \qquad (3.2.4.1)$$

with:

C_K: Activity concentration of Potassium [Bq/kg]
a':   Stripping factor associated with potassium energy range and potassium activity concentration. [Bq kg^{-1} cps^{-1}]
b':   Stripping factor associated with uranium energy range and potassium activity concentration. [Bq kg^{-1} cps^{-1}]
c':   Stripping factor associated with thorium energy range and potassium activity concentration. [Bq kg^{-1} cps^{-1}]

$$C_U = CR_K d' + CR_U e' + CR_{Th} f' \qquad (3.2.4.2)$$

with:

C_U: Activity concentration of Uranium [Bq/kg]
d':   Stripping factor associated with potassium energy range and uranium activity concentration. [Bq kg^{-1} cps^{-1}]
e':   Stripping factor associated with uranium energy range and uranium activity concentration. [Bq kg^{-1} cps^{-1}]
f':   Stripping factor associated with thorium energy range and uranium activity concentration. [Bq kg^{-1} cps^{-1}]

$$C_{Th} = CR_K g' + CR_U i' + CR_{Th} k' \qquad (3.2.4.3)$$

with:

C_{Th}:   Activity concentration of Thorium [Bq/kg]
g':   Stripping factor associated with potassium energy range and thorium activity concentration. [Bq kg^{-1} cps^{-1}]
i':   Stripping factor associated with uranium energy range and thorium activity concentration. [Bq kg^{-1} cps^{-1}]
k':   Stripping factor associated with thorium energy range and thorium activity concentration. [Bq kg^{-1} cps^{-1}]

The stripping coefficients can be considered as elements of an inverse matrix $\overline{\overline{A}}^{-1}$ of matrix $\overline{\overline{A}}$.

$$\overline{\overline{A}}^{-1} = \begin{bmatrix} a' & b' & c' \\ d' & e' & f' \\ g' & i' & k' \end{bmatrix} ; \overline{\overline{A}} = \begin{bmatrix} a & b & c \\ d & e & f \\ g & i & k \end{bmatrix} \tag{3.2.4.4}$$

The coefficients of matrix $\overline{\overline{A}}$ are assumed proportional to a nuclide specific attenuation factor and inverse proportional to a nuclide and detector specific factor and a polynomial in dependence of ground clearance h. The coefficients of the polynomials determined with Monte Carlo calculations are listed in table 18.

$$a = \frac{\rho_{Potassium}}{a_1 h^4 + a_2 h^3 + a_3 h^2 + a_4 h + a_5} \frac{1}{\delta_{Potassium}} \tag{3.2.4.5}$$

with:

a: Count rate in potassium energy range due to potassium activity concentration. [cps Bq^{-1} kg]

a_1:   Polynomial coefficient [m^{-4}]

a_2:   Polynomial coefficient [m^{-3}]

a_3:   Polynomial coefficient [m^{-2}]

a_4:   Polynomial coefficient [m^{-1}]

a_5:   Polynomial coefficient [ ]

$\rho_{Potassium}$:   Attenuation factor for potassium photons [ ]

$\delta_{Potassium}$:   Detector specific calibration factor for potassium [Bq kg^{-1} cps^{-1}]

$$b = \frac{\rho_{Potassium}}{b_1 h^4 + b_2 h^3 + b_3 h^2 + b_4 h + b_5} \frac{1}{\delta_{Potassium}} \tag{3.2.4.6}$$

with:

b: Count rate in potassium energy range due to uranium activity concentration. [cps Bq^{-1} kg]

b_1:   Polynomial coefficient [m^{-4}]

b_2:   Polynomial coefficient [m^{-3}]

b_3:   Polynomial coefficient [m^{-2}]

b_4:   Polynomial coefficient [m^{-1}]

b_5:   Polynomial coefficient [ ]

$\rho_{Potassium}$:   Attenuation factor for potassium photons [ ]

$\delta_{Potassium}$:   Detector specific calibration factor for potassium [Bq kg^{-1} cps^{-1}]

$$c = \frac{\rho_{Potassium}}{c_1 h^4 + c_2 h^3 + c_3 h^2 + c_4 h + c_5} \frac{1}{\delta_{Potassium}} \tag{3.2.4.7}$$

with:

c: Count rate in potassium energy range due to thorium activity concentration. [cps Bq^{-1} kg]

c_1:   Polynomial coefficient [m^{-4}]

c_2:   Polynomial coefficient [m^{-3}]

c_3:   Polynomial coefficient [m^{-2}]

c_4: Polynomial coefficient [m^{-1}]

c_5: Polynomial coefficient [ ]

$\rho_{Potassium}$: Attenuation factor for potassium photons [ ]

$\delta_{Potassium}$: Detector specific calibration factor for potassium [Bq kg^{-1} cps^{-1}]

$$d = 0 \tag{3.2.4.8}$$

with:

d: Count rate in uranium energy range due to potassium activity concentration. [cps Bq^{-1} kg]

$$e = \frac{\rho_{Uranium}}{e_1 h^4 + e_2 h^3 + e_3 h^2 + e_4 h + e_5} \frac{1}{\delta_{Uranium}} \tag{3.2.4.9}$$

with:

e: Count rate in uranium energy range due to uranium activity concentration. [cps Bq^{-1} kg]

e_1: Polynomial coefficient [m^{-4}]

e_2: Polynomial coefficient [m^{-3}]

e_3: Polynomial coefficient [m^{-2}]

e_4: Polynomial coefficient [m^{-1}]

e_5: Polynomial coefficient [ ]

$\rho_{Uranium}$: Attenuation factor for uranium photons [ ]

$\delta_{Uranium}$: Detector specific calibration factor for uranium [Bq kg^{-1} cps^{-1}]

$$f = \frac{\rho_{Uranium}}{f_1 h^4 + f_2 h^3 + f_3 h^2 + f_4 h + f_5} \frac{1}{\delta_{Uranium}} \tag{3.2.4.10}$$

with:

f: Count rate in uranium energy range due to thorium activity concentration. [cps Bq^{-1} kg]

f_1: Polynomial coefficient [m^{-4}]

f_2: Polynomial coefficient [m^{-3}]

f_3: Polynomial coefficient [m^{-2}]

f_4: Polynomial coefficient [m^{-1}]

f_5: Polynomial coefficient [ ]

$\rho_{Uranium}$: Attenuation factor for uranium photons [ ]

$\delta_{Uranium}$: Detector specific calibration factor for uranium [Bq kg^{-1} cps^{-1}]

$$g = 0 \tag{3.2.4.11}$$

with:

g: Count rate in thorium energy range due to potassium activity concentration. [cps Bq^{-1} kg]

$$i = \frac{\rho_{Thorium}}{i_1 h^4 + i_2 h^3 + i_3 h^2 + i_4 h + i_5} \frac{1}{\delta_{Thorium}}$$ (3.2.4.12)

with:

i:	Count rate in thorium energy range due to uranium activity concentration. [cps Bq^{-1} kg]
i_1:	Polynomial coefficient [m^{-4}]
i_2:	Polynomial coefficient [m^{-3}]
i_3:	Polynomial coefficient [m^{-2}]
i_4:	Polynomial coefficient [m^{-1}]
i_5:	Polynomial coefficient [ ]
$\rho_{Thorium}$:	Attenuation factor for thorium photons [ ]
$\delta_{Thorium}$:	Detector specific calibration factor for thorium [Bq kg^{-1} cps^{-1}]

$$k = \frac{\rho_{Thorium}}{k_1 h^4 + k_2 h^3 + k_3 h^2 + k_4 h + k_5} \frac{1}{\delta_{Thorium}}$$ (3.2.4.13)

with:

k:	Count rate in thorium energy range due to thorium activity concentration. [cps Bq^{-1} kg]
k_1:	Polynomial coefficient [m^{-4}]
k_2:	Polynomial coefficient [m^{-3}]
k_3:	Polynomial coefficient [m^{-2}]
k_4:	Polynomial coefficient [m^{-1}]
k_5:	Polynomial coefficient [ ]
$\rho_{Thorium}$:	Attenuation factor for thorium photons [ ]
$\delta_{Thorium}$:	Detector specific calibration factor for thorium [Bq kg^{-1} cps^{-1}]

Table 18: Polynomial coefficients determined with Monte Carlo calculations.

	$_1$ [m^{-4}]	$_2$ [m^{-3}]	$_3$ [m^{-2}]	$_4$ [m^{-1}]	$_5$ [ ]
a	3.24E-11	-1.12E-08	3.84E-06	1.47E-04	2.08E-02
b	1.63E-10	-4.09E-08	2.26E-05	3.02E-03	3.41E-01
c	6.00E-10	-4.12E-07	1.40E-04	-2.32E-03	1.61E00
e	1.55E-10	4.59E-10	1.04E-05	3.95E-03	2.45E-01
f	-6.31E-10	5.44E-07	-9.89E-05	1.71E-02	1.69E00
i	2.69E-09	-1.17E-06	5.44E-04	5.81E-03	5.56E-00
k	2.37E-10	-9.51E-08	4.08E-05	3.69E-03	4.90E-01

3.2.5 Point source and contamination activity calculation

The RLL system calculates activity (point source and surface contamination) based on the results of the identification algorithm (SIA), which calculates the net counts per second for each identified isotope. First, the algorithm corrects the count rate with the attenuation of the vehicle and then converts the attenuated count rate into Bq/cm^2 or into MBq using a "sensitivity versus altitude" function. For each isotope, the sensitivity as a function of the ground clearance is estimated with Monte Carlo simulations. For the activity estimation of a point source, the algorithm assumes that the helicopter flies directly above the source. For a surface contamination, the used model assumes a uniform contamination on an infinite and flat surface. This method does not require stripping corrections or background corrections, because the identification algorithm already takes into account the interference between nuclides and provides net count rates. Table 19 exemplifies the detector factor $F_{Detector}(N)$ and the attenuation factor $F_{Attenuation}(N)$ for some radionuclides.

$$A(N) = \frac{Q(N)}{Q_{ref}(N)\frac{4}{h^2}e^{-0.129h\mu(N)}} \frac{F_{Detector}(N)}{F_{Attenuation}(N)} \tag{3.2.5.1}$$

with:

N:	Nuclide
$A(N)$:	Activity of a point source of nuclide N [MBq]
$Q(N)$:	Quantification for nuclide N provided by the SIA algorithm [ ]
h:	Ground clearance [m]
Q_{ref}:	Nuclide reference quantification [ ]
$\mu(N)$:	Attenuation coefficient for nuclide N [m^{-1}]
$F_{Detector}(N)$:	Detector factor for nuclide N depending on detector configuration [MBq m^{-2}]
$F_{Attenuation}(N)$:	Attenuation factor for nuclide N including detector shielding [ ]

$$CA(N) = \left(c_1 h^4 + c_2 h^3 + c_3 h^2 + c_4 h + \frac{1}{Q_{ref}(N)}\right) Q(N) \frac{F_{Detector}(N)}{F_{Attenuation}(N)} \tag{3.2.5.2}$$

with:

N:	Nuclide
$CA(N)$:	Surface activity concentration of nuclide N [Bq cm^{-2}]
$Q(N)$:	Quantification for nuclide N provided by the SIA algorithm [ ]
h:	Ground clearance [m]
c_1:	Polynomial coefficient [m^{-4}]
c_2:	Polynomial coefficient [m^{-3}]
c_3:	Polynomial coefficient [m^{-2}]
c_4:	Polynomial coefficient [m^{-1}]
Q_{ref}:	Nuclide reference quantification [ ]
$\mu(N)$:	Attenuation coefficient for nuclide N [m^{-1}]
$F_{Detector}(N)$:	Detector factor for nuclide N depending on detector configuration [MBq m^{-2}]
$F_{Attenuation}(N)$:	Attenuation factor for nuclide N including detector shielding [ ]

Table 19: Detector factor $F_{Detector}(N)$ and attenuation factor $F_{Attenuation}(N)$ for some radionuclides N.

Nuclide N	$F_{Detector}(N)$ [MBq m^{-2}]	$F_{Attenuation}(N)$ [ ]
^{40}K	2.16	1.0
^{60}Co	2.16	1.0
^{131}I	1.36	1.0
^{137}Cs	1.60	1.0
^{192}Ir	1.36	1.0
^{238}U	2.55	1.0
^{232}Th	2.46	1.0

3.3 Team CZ01

For the IRIS settings, project preparation, fast raw IRIS data browsing and post processing, the software package from Pico Envirotec (PEICalib, PEIConvert, PEIDataViewer, PRAGA4) is supplied. The Czech National Radiation Protection Institute has started the development of an advanced solution for the post-processing of airborne gamma-spectrometry data named AGAMA. The final data is usually processed in a mapping program (free available Q-GIS or MapInfo Professional GIS mapping application).

3.3.1 PEICalib - Settings

This program allows the operator to

- remotely set high voltage for each detector,

- remotely turn each detector on or off,

- assign "downward" or "upward" looking detectors,

- set the system threshold,

- watch each detector independently,

- watch all detectors in two groups - down/up,

- display Uncorrected/Corrected/Tracking spectra,

- observe an instant (one second) spectra or summed over period of time,

- calibrate (energy calibration) individual detectors for linearity with the help of natural background radiation and

- store all measured, calculated or pre-set parameters for later use with this program or with any data acquisition system.

3.3.2 PEICconvert - Survey preparation

This program is used to convert and to calibrate scanned maps into a *.BMP file that carries all of the information necessary for proper positioning of the map in airborne IRIS real time operation. This program ties the coordinates of the map with the coordinates coming in real time from the GPS/Glonass navigation receivers. It can be used on any PC compatible computer with Windows operating system.

In addition, the program allows to create and define the survey area file (AREA.XYZ) that is required for determining the coordinates of survey lines and tie lines. The survey area can be viewed with the survey and tie lines overlaid on the defined area.The survey area can also be displayed superimposed on the geographical map, if latter is available (figure 30). WGS84 coordinates are associated manually with the digital image. Once the coordinates of three to ten reference points are entered, the conversion of the map may be initialized. The PEIConvert program will adjust and rotate the map according to the entered points. The defined project flight path information, including survey polygon corner points, line spacing and direction, central meridian, way points and special line information is prepared and stored into XYZ or PLM file using the PEIConvert program supplied with

the system. The area file holds base navigation parameters: projection type (UTM, UPS, or Lambert), Central Meridian value or Lambert parameters, and distance, speed and altitude units (metric, imperial).
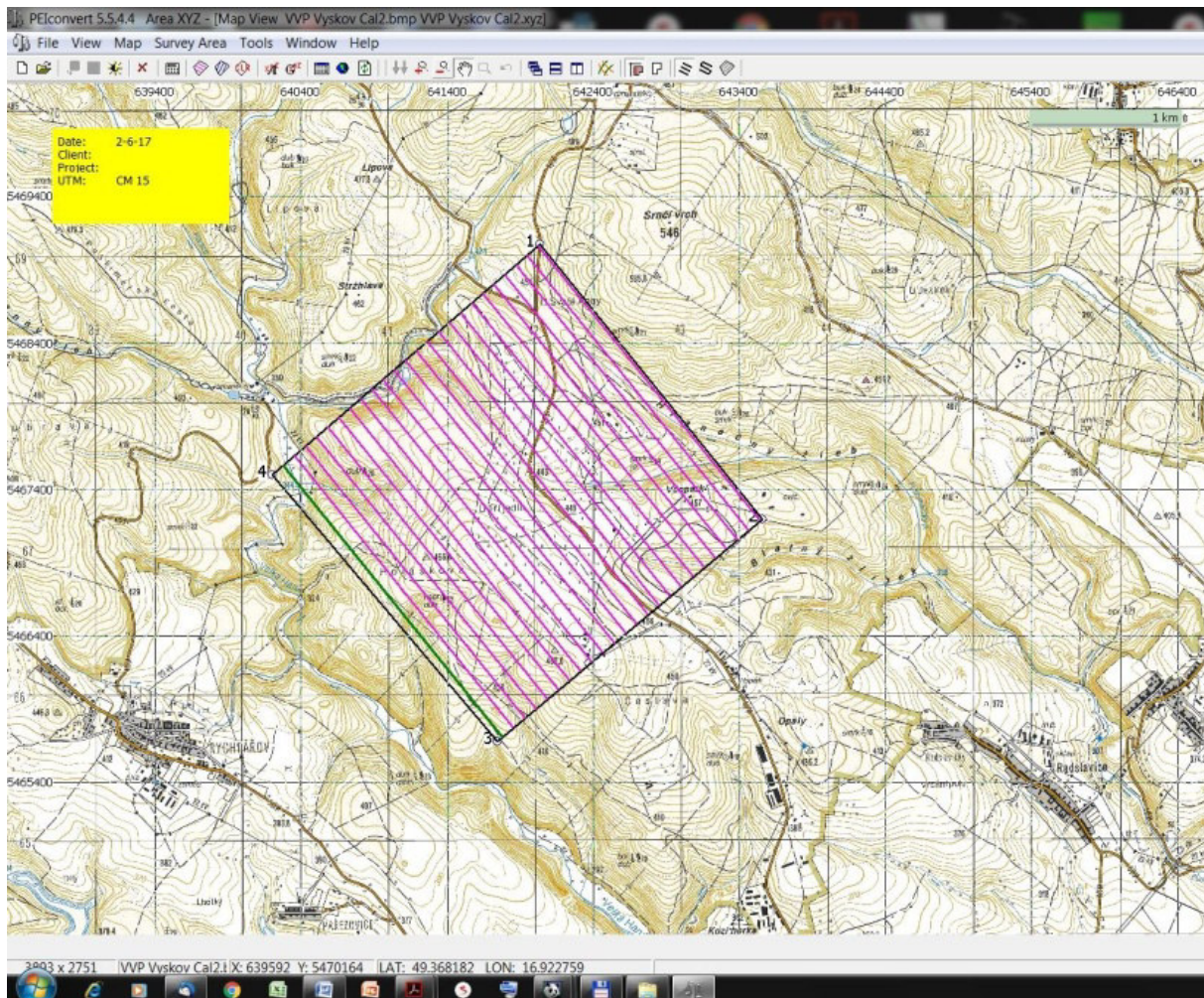
Figure 30: Survey preparation in PEIConvert (a polygon and 24 survey lines).

3.3.3 IRIS-AGIS - Preliminary data evaluation

The measured data are evaluated preliminarily in real time with the IRIS airborne spectrometer aboard the helicopter. All calculated results (local air dose rate, ground air dose rate, activity concentrations of ^{40}K, uranium-series (^{214Bi}), thorium-series (^{208}Tl), ^{137}Cs, ^{60}Co and ^{131}I (not corrected for stripping, aircraft and cosmic background, radon) including all raw data, geographical coordinates, altitudes are saved into the PEI binary file(s) for postprocessing.

3.3.4 PEIDataViewer - Fast data browsing

PEIDataViewer was designed to provide fast field data verification for Pico Envirotec Inc. (PEI) binary data format files (figure 31). It also provides conversion from PEI data format into ASCII, to be used with standard data base programs and into a Geosoft GBN format to be used with OASIS-MONTAJ data processing software. The program allows simple data

47

correction and provides functions such as calculation of stripping ratio and window sensi-tivities. "Waterfall spectra"(left panel in figure 31) are used to identify spectral anomalies.
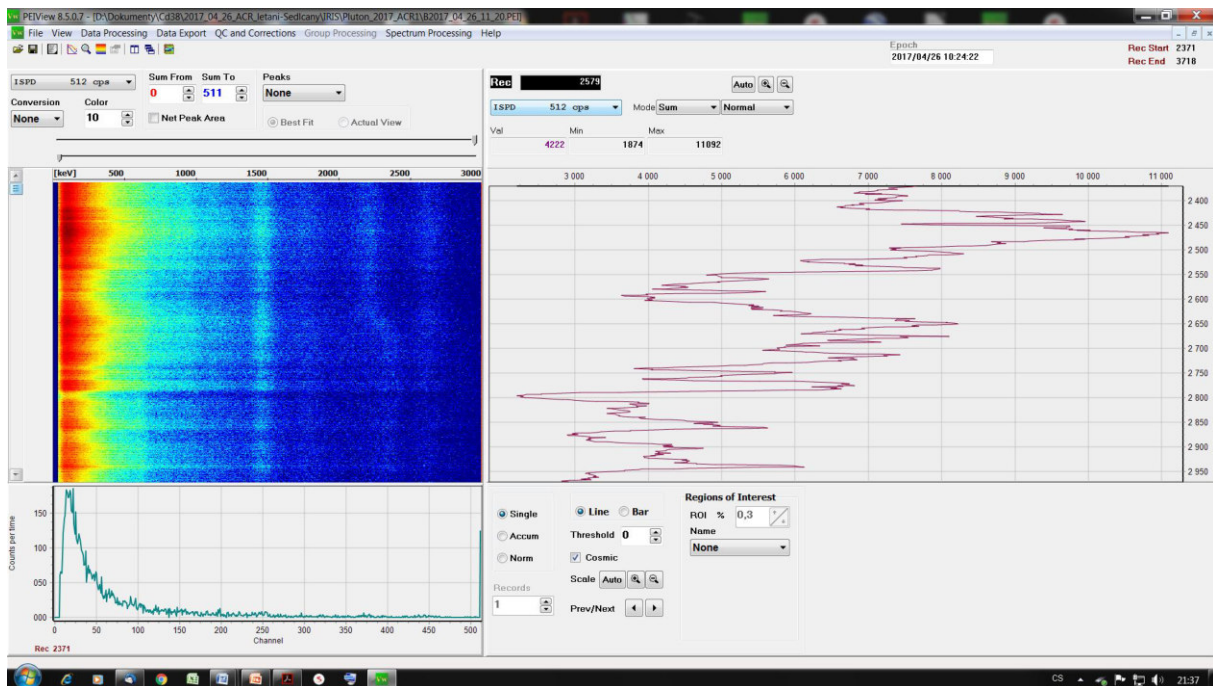
Figure 31: PEIDataViewer for data browsing.

3.3.5   PRAGA4 - Post processing

The PRAGA4 post processing software is based on IAEA TECDOC 1363 (2003) and Tech-nical Reports Series No 323 (1991). The latter report describes the standard energy win-dow method. Moreover, PRAGA4 applies other sophisticated statistical methods, for ex-ample a LSQ based on Monte Carlo spectra simulation, NASVD/MNF based on the prin-cipal component analysis using eigenvalues and eigenvectors and spectra reconstruction. PRAGA4 also makes aircraft/cosmics background removal, and furthermore for a huge package of spectra is able to correct the data for radon.

PRAGA4 (figure 32) provides an advanced solution for the mapping and processing of airborne gamma-ray spectrometry data acquired by modern spectrometers using NaI(Tl) detectors. PRAGA4 is a radiometric processing package that uses the maximum infor-mation stored in the gamma-ray spectrum to evaluate radiation of natural and man-made radioactive ground sources. The processing requires spectra at resolutions of 256 or 512 channels and auxiliary data channels such as live time, STP (standard temperature and pressure) and altitude channels. Spectra with higher resolution (1024 ch) are downsam-pled in PRAGA4 to 512 channels.
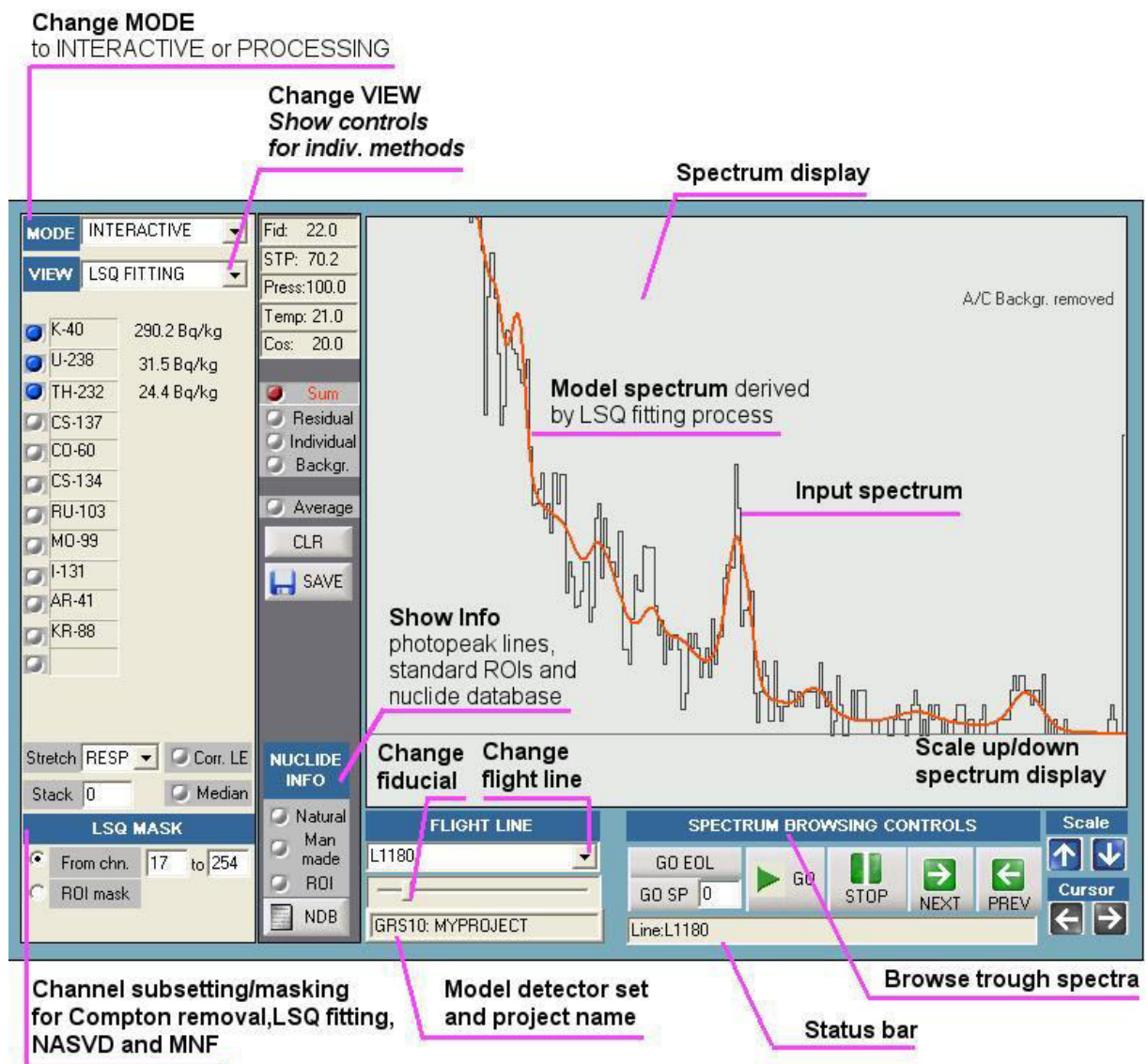
Figure 32: Main PRAGA4 screen.

PRAGA4 has the following features:

- Spectrum browser with tools for peak identification (Compton removal, peak deconvolution)

- Window (ROI) based processing following IAEA standards

- Advanced full-spectrum processing using least-squares fitting technique (LSQ)

- Principal component (NASVD or MNF) analysis and spectrum processing

- Advanced support for radon removal including extended spectral-ratio and full-spectrum techniques

Full-spectrum processing is the most significant feature of the Praga4 software. This function was designed specially for the processing of man-made (artificial) radiation data. Full-spectrum processing uses a weighted least-squares fitting algorithm to find contributions

of individual radionuclides into the input spectra. PRAGA4's full-spectrum technique includes a complete system of spectrum background removal. Aircraft, cosmic, and radon background components can be separately adjusted by the user via control of experimental calibration constants. Principal component (NASVD and MNF) analysis tools allow to investigate spectrum signatures included in the actual dataset. A spectrum dataset is converted into a limited set of spectrum components (eigenvectors) which are ordered by variance (NASVD) or by signal to noise ratio (MNF) Radon removal has a choice to use the window based, "spectral-ratio" method that compares count rates of low and high-energy uranium peaks or a method that uses full spectrum difference in responses of the radon and ground uranium sources. The window based "spectral-ratio" method has the option to use the low-energy ^{214}Pb (0.352 MeV) photopeak instead of commonly used ^{214}Bi (0.609 MeV) photopeak. This approach is beneficial in areas with substantial ^{137}Cs fall-out (Northern hemisphere) or for data with extreme thorium to uranium ratio.

3.3.6 Minimum detectable activities

Based on Currie's approach (see Currie, 1999), the minimum detectable activities were calculated at 95% confidence level (table 20). The minimum detectable activities were calculated for one-second spectra of a 4 x 4.2 liter NaI(Tl) detector in a MI-17 helicopter flying with a ground clearance of 100 m (figure 33).
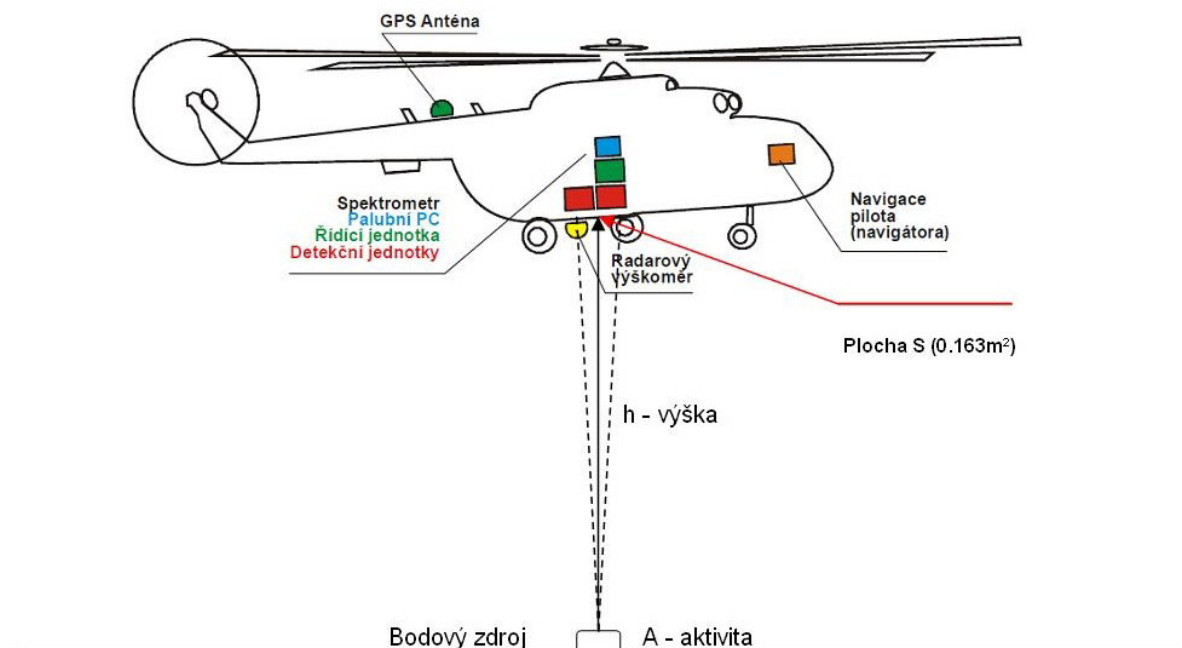
Figure 33: Measuring geometry (in Czech).

Table 20: Minimum detectable activities (MDA).

Nuclide	Distribution	MDA
^{40}K	Uniform	115 Bq/kg
^{238}U	Uniform	16 Bq/kg
^{232}Th	Uniform	8 Bq/kg
^{137}Cs	Exponential	2.7 kBq/m^2
^{137}Cs	Surface	1.6 kBq/m^2

3.3.7 QGIS - Geographical mapping

The free open-source geographical information system QGIS is used for the airborne data visualisation. The program is able to visualise the data exported from PEIDataViewer and PRAGA4 in comma separated value (CSV) format. Figures 34 and 35 show examples of maps generated with QGIS.
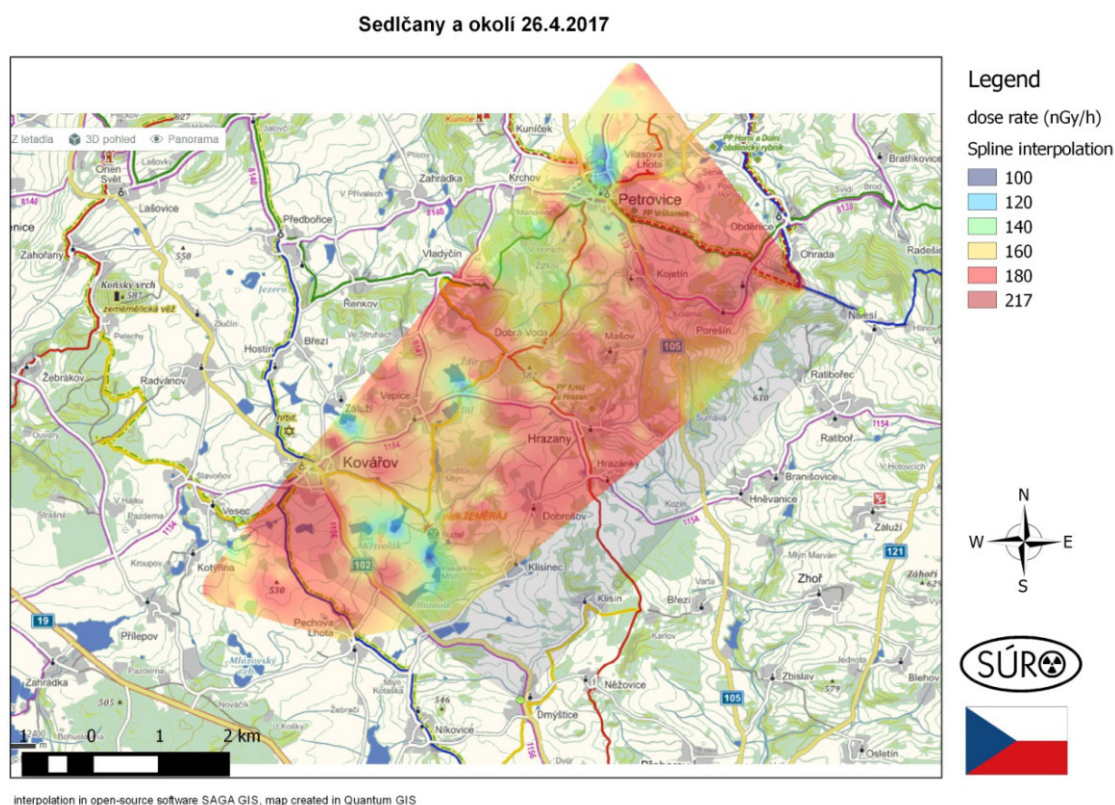
Figure 34: QGIS map example of a dose rate survey.
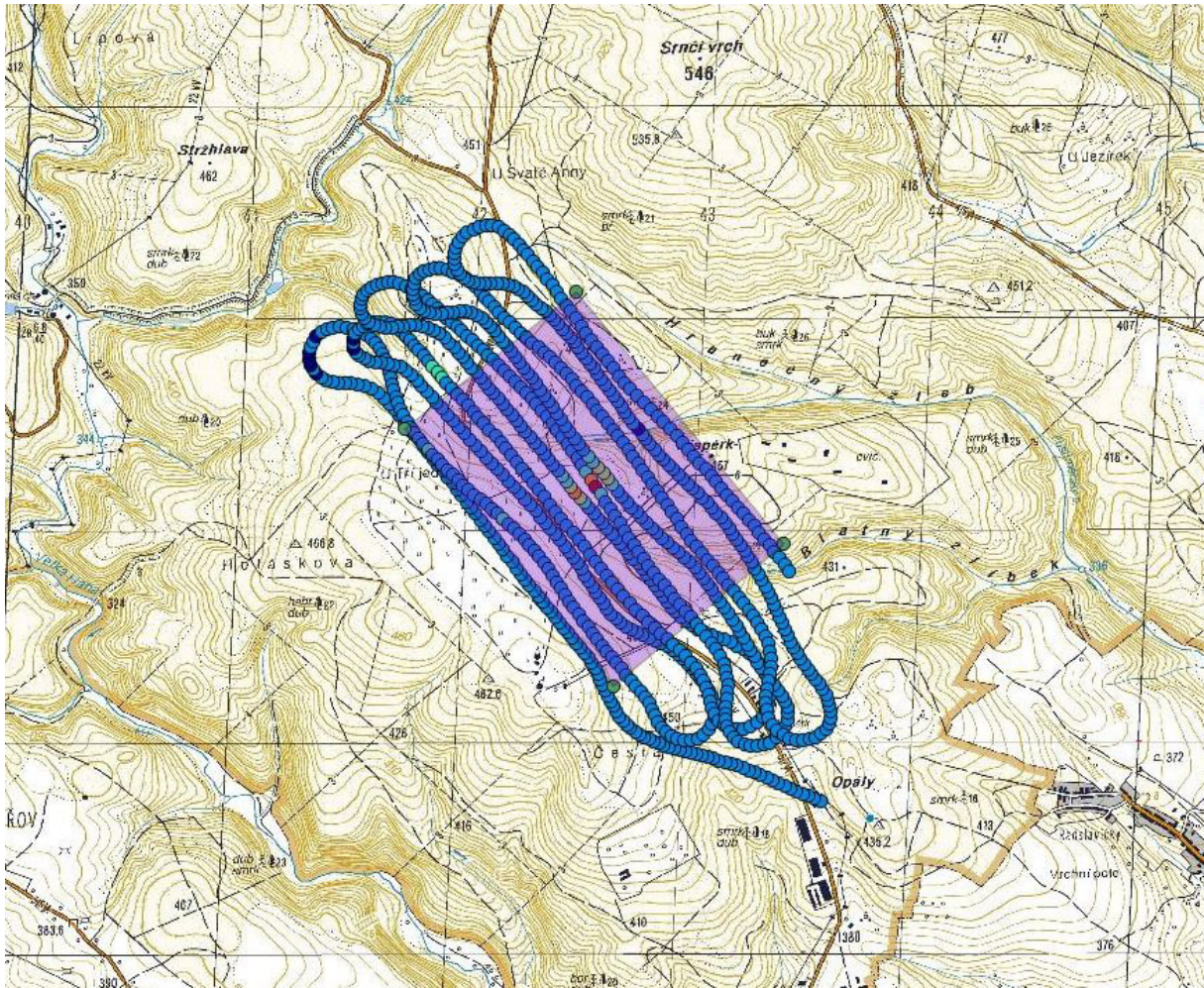
Figure 35: QGIS map example of a search for a ^{137}Cs source.

3.4 Teams DE01 and DE02

The energy spectra are measured simultaneously with the two types of detectors during the flight and the count rates in the specific energy windows are directly displayed on the screen, so that the operator can monitor the measured activities of the radionuclides online (figure 36). In addition, the position of the helicopter is monitored continuously via GPS to exactly allocate the radionuclide measurements. Furthermore, the flight altitude is recorded with a radar altimeter.
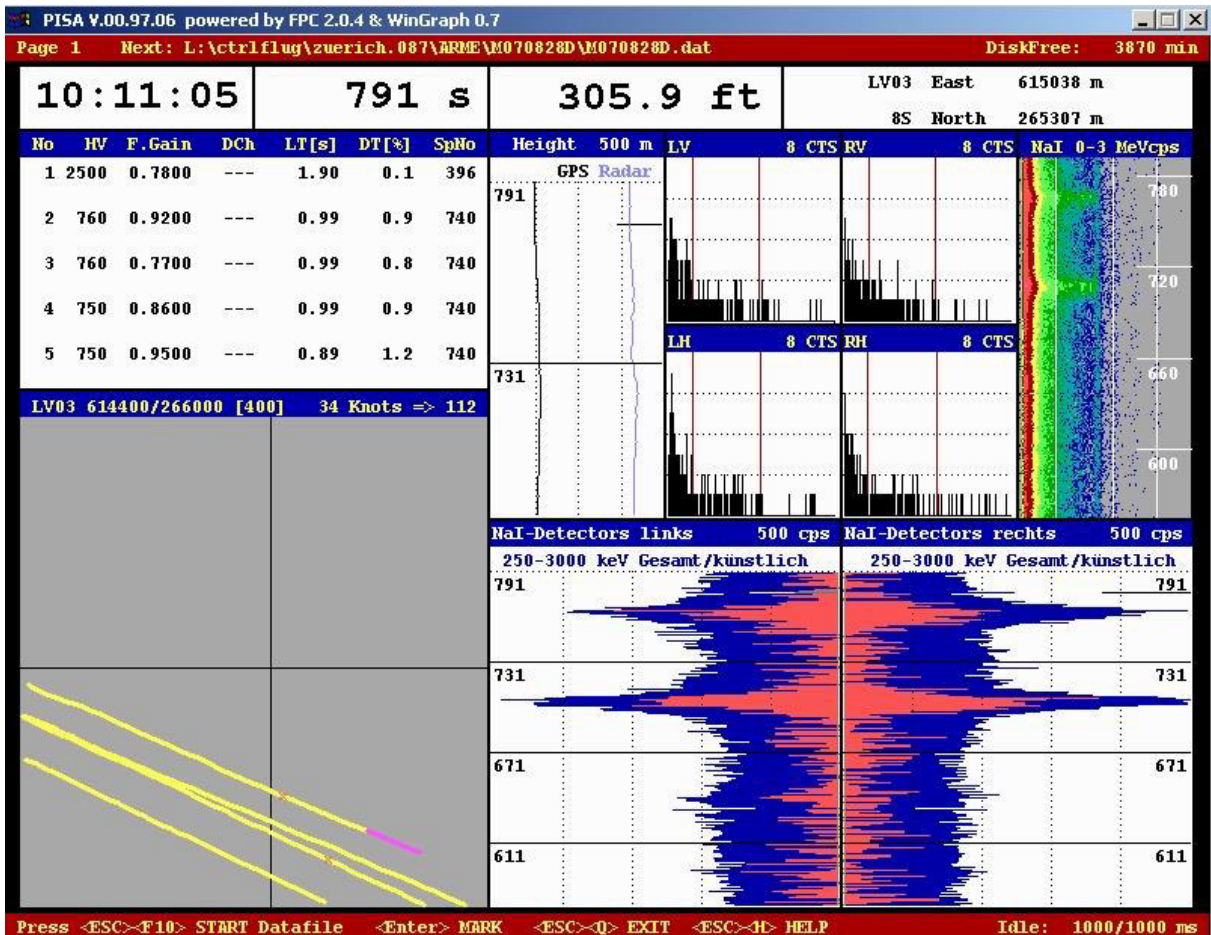
Figure 36: Screen shot of the data acquisition software.

3.4.1 Evaluation of NaI(Tl)-spectra

An energy window method is used for the evaluation of the specific activities of ^{137}Cs, ^{40}K, ^{238}U and ^{232}Th. Total count rates within the selected energy windows are determined. Separate flights over lakes and in high altitudes were performed to gain information on the background contributions due to the activity of the system itself, the helicopter components, the personnel, and the cosmic radiation to each energy window. The calibration factors for the determination of the specific activities of the selected radionuclides are calculated for a reference altitude.

Because of scattering processes in the air, in the ground and in the detector itself, the contribution of scattered photons originating from radionuclides with higher energies are also measured in lower energy windows. To obtain the net count rate of each energy window the amount of the scattered photons has to be removed by stripping each NaI(Tl)-spectrum.

The stripping coefficient matrix documented in table 21 is determined by measurements on a set of calibration pads doped with potassium, uranium and thorium.

Table 21: Matrix of stripping coefficients.

Source Destination	^{137}Cs	^{40}K	^{214}Bi	^{208}Tl
^{208}Tl	0.000	0.000	0.090	-
^{214}Bi	0.000	0.000	-	0.330
^{40}K	0.000	-	0.990	0.570
^{137}Cs	-	0.570	2.660	1.680

3.4.2 Evaluation of HPGe-spectra

The gamma lines listed in table 22 are used for the calculation of the specific activities of ^{238}U, ^{208}Tl, ^{40}K and ^{137}Cs in the HPGe-spectra. For the evaluation of the HPGe-spectra, a program especially adapted to low counting statistics is used. It identifies the total absorption peaks of the individual radionuclides and calculates their net count rate. The photopeak energies used for radionuclide identification in HPGe-spectra are listed in table 22.

Table 22: Parameters for the evaluation of the HPGe-spectra.

Nuclide	Energy [keV]	Unit	Photon emission probability, P_γ
^{208}Tl	2614	Bq/kg	0.999
^{214}Bi	609	Bq/kg	0.446
^{40}K	1460	Bq/kg	0.107
^{137}Cs	662	kBq/m^2	0.860

3.4.3 Detection limits

With the standard measuring time of 2 seconds for the NaI array and 60 seconds for the germanium detector, the spectra cover areas of 400 x 800 m and 400 x 1200 m, respectively. The detection limit for ^{137}Cs is 4 kBq/m^2 for a ground clearance of 150 m (table 23).

Table 23: Detection limit for the HPGe-Detector with a measuring time of 60 s.

^{137}Cs	Plane source			Exponential distribution (Relaxation mass parameter $\zeta = 1.5$ g/cm^{-2})		
Ground clearance [m]	50	100	150	50	100	150
Detection limit [kBq/m^2]	1.6	2.5	3.7	1.9	3.8	4.4

3.4.4 Evaluation examples

After landing the ambient dose rate, the specific activities of the natural radionuclides (^{40}K, ^{214}Bi and ^{232}Th) and the contamination due to artificial radionuclides (e.g. ^{137}Cs) which are determined from the NaI(Tl)- and HPGe-spectra at each point of the flight path are calculated with a software written by the Federal Office for Radiation Protection. A comparison between values of specific activity (^{40}K) calculated from NaI and HPGe data measured during the exercise ARM17 by the German team DE01 is plotted in figure 37.
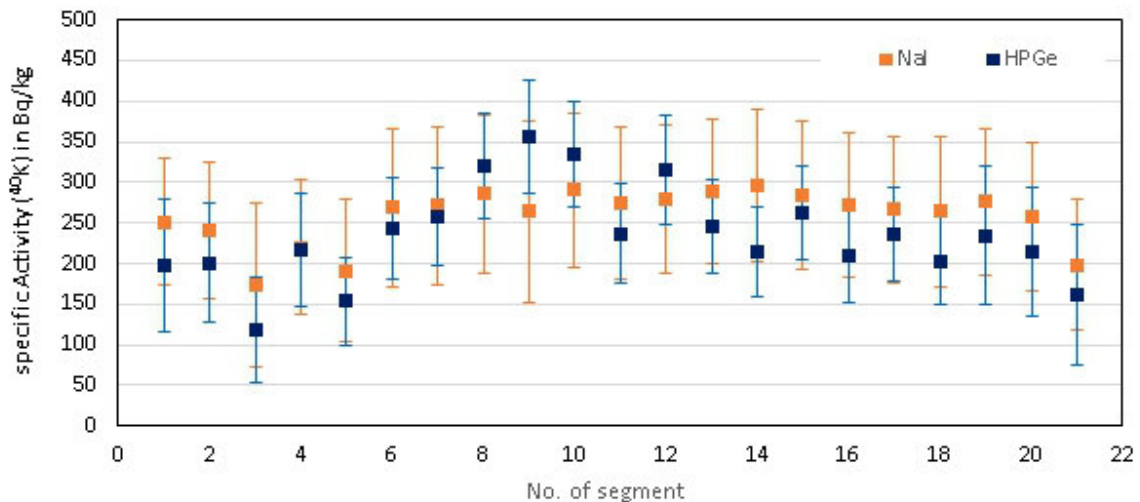
Figure 37: Comparison between values of specific activity (^{40}K) calculated from NaI and HPGe spectra measured by the German team DE01 (source search and composite mapping, see section 12)). Values are averages for segments of (5 x 5) km^2 (measurement area divided into 21 segments).

Within a time period of 10 minutes the radiological situation along the trajectory is present on the screen. Additional information (e.g. method of data evaluation (stripping, altitude correction, statistic values)) are given and provide an overview of the radiological data for each radionuclide. The data are further integrated into digital maps (figure 38), which are available at different scales. Thus regions of low or elevated concentrations of natural and artificial radionuclides can easily be located.
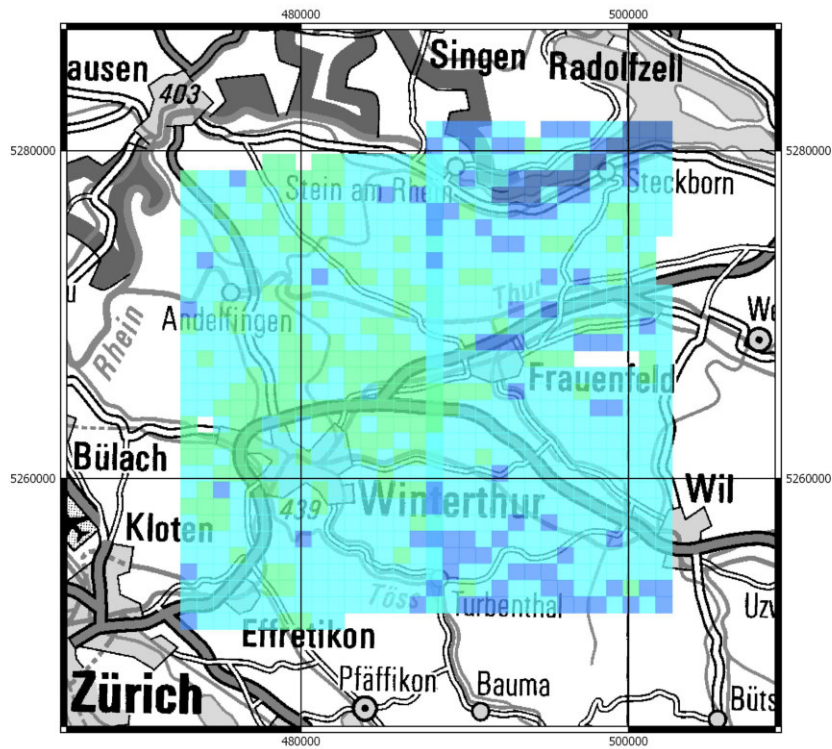
Figure 38: Ambient gamma dose rate (ODL) measured during the measurement exercise ARM17 by both German teams (task: CM+HS , between Lake Constance and Zurich).

3.5 Team FR01

IRSN uses the acquisition software provided by MIRION company in standard configuration to produce spectra synchronized with GPS position. The raw data acquired on-line are stored in a Structured Query Language (SQL) database. The raw data are then transferred with the help of scripts to one or more databases dedicated to gamma-spectrometry data, developed by a collaboration of the Department of Applied Physics of Aalto University, the Finnish Radiation and Nuclear Safety Authority (STUK), and the Radiation Protection Bureau, Health Canada (HC RPB) (see Aarnio et al, 2008). This original Linux based database LINSSI was adapted to a Microsoft windows environment and re-dubbed WINSSI. The WINSSI databases could be located inside the aircraft, at the ground station or close to Paris in the IRSN supervising center. Figure 39 shows a screenshot of the WINSSI user interface. Each spectrum is analysed to evaluate different quantities, like gross count rate, dose rate at 1 m height above ground, Man-Made-Gross-Count(MMGC)-ratio, windows net counting estimation, nuclide specific activities.
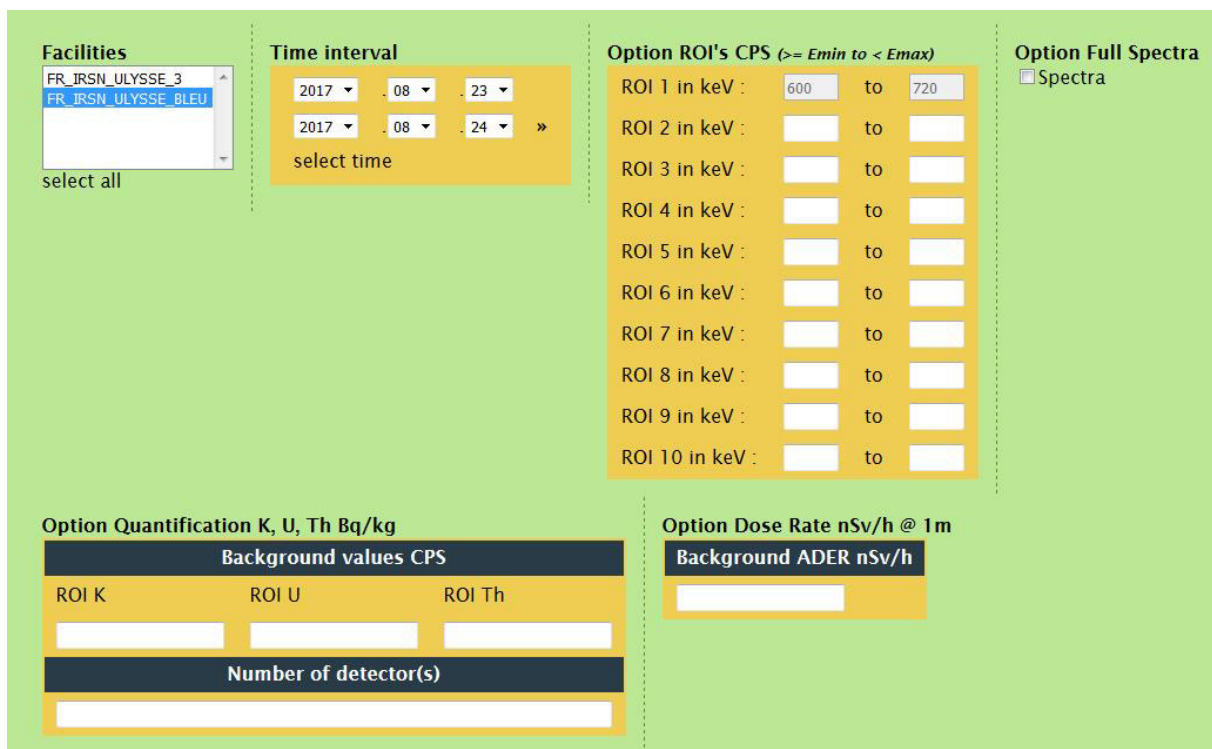
Figure 39: Screen shot of the WINSSI user interface.

3.5.1 Gross count rate

The gross count rate (C) extraction method calculates the integral count rate in a single spectral window covering the complete spectral range (equation 3.5.1.1).

$$CR_{GC}^{raw} = \frac{1}{t_{live}} \sum_{E=30}^{3000} n(E) \qquad (3.5.1.1)$$

with:

CR_{GC}^{raw}: Gross count rate at survey altitude [cps]
t_{live}:   Livetime of the acquired spectrum [s]

57

E: Photon energy associated with the spectrum channel [keV]

$n(E)$:   Counts in spectrum channel for photon energy E [ ]

3.5.2 Correction for attenuation in air

The gross count rate is corrected for non-terrestrial background and adjusted to the nominal flight ground clearance according to equation 3.5.2.1.

$$CR_{GC} = \frac{1}{t_{live}} \sum_{E=30}^{3000} (n(E) - n_N) e^{\beta(z-z_0)}$$
(3.5.2.1)

with:

CR_{GC}:   Corrected gross count rate at nominal survey altitude [cps]

n_N: Total count rate attributable to non-terrestrial sources [cps]

z: Measured ground clearance of the aircraft [m]

z_0:   Reference ground clearance [m]

β: Effective linear attenuation coefficient in air [m^{-1}]

The non-terrestrial background count rate, C_N, was determined initially from a test line altitude profile and adjusted on a flight-by-flight basis, determining contributions from cosmic rays, the aircraft system, and airborne radon. It should be noted that the use of an exponential form for the altitude dependence of the count rate is an empirical approximation. More correct expressions, which explicitly include geometrical effects, use a form of the exponential integral (see for example Kogan et al., 1971).
In this document we include a comparison of the corrections, but do not report corrected values. This will be deferred to a later publication.
The US National Nuclear Security Adminsistration (NNSA) operated Aerial Measuring System (AMS) derives routinely height attenuation coefficients from altitude spirals flown over test lines located in the Nevada National Security Site (NNSS) or near Lake Mohave in California. During an intercomparison campaign with AMS, the air attenuation coefficient, β, of the IRSN measuring system was determined from NNSS test line data to be 0.00541 m^{-1}.

3.5.3 Man-made gross count ratio (MMGC)

The MMGC-ratio is the ratio of low-energy counts to high-energy counts in the photon energy spectrum.

$$MMGC = \frac{\sum_{E=30}^{1360} n(E)}{\sum_{E=1360}^{3000} n(E)}$$
(3.5.3.1)

with:

$n(E)$:   Counts per channel [ ]

E: Energy of the channel [keV]

$MMGC$: Man-made gross count ratio [ ]

The MMGC-ratio is sensitive to low levels of man-made radiation even in the presence of large variations in the natural background. When man-made radioactivity has been identified, a detailed analysis of the gamma energy spectrum is conducted to ascertain which radionuclides are present.

3.5.4 Evaluation of ^{40}K, ^{238}U and ^{232}Th activity concentrations

The evaluation of the concentration of natural radionuclides in rock and soil by a high resolution spectrometer (high-purity germanium in-situ spectrometer) is typically made from the measurement of total absorption peaks produced by the photo effect. This method is not suitable for medium resolution NaI spectrometers. The alternative reference method for aerial measurements, described in IAEA Technical Report No. 323 (1991) is a method based on the counting rates of three energy windows centred on the major emission lines of the three main terrestrial radionuclides, ^{40}K and the decay chains of ^{232}Th and ^{238}U considered at secular equilibrium (figure 40 and table 24).

Table 24: Energy windows for the evaluation of natural radionuclides.

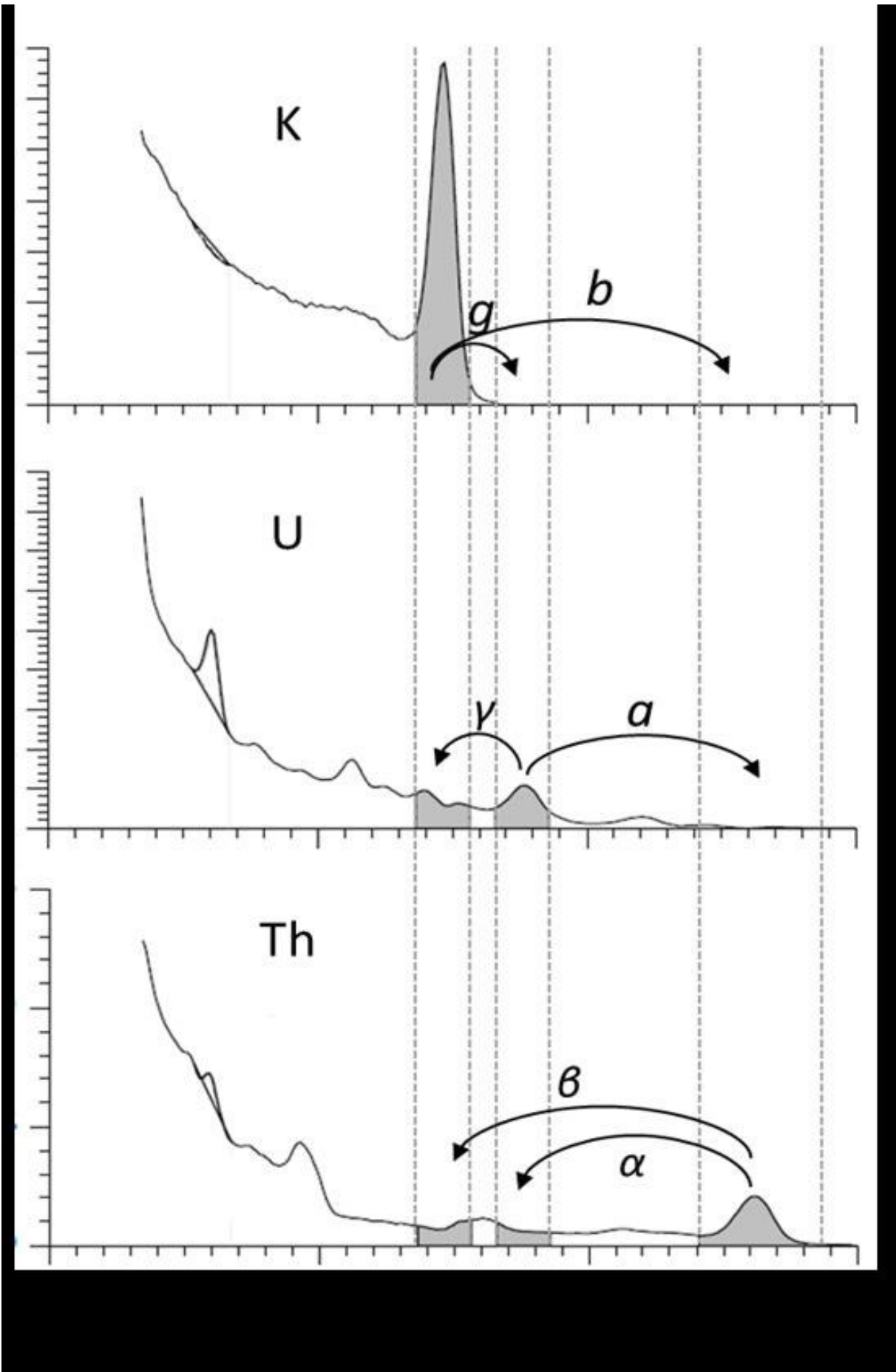| Energy window	K	U	Th
Radionuclide	^{40}K	^{214}Bi	^{208}Tl
Photon emission	1460 keV	1765 keV	2614 keV
Lower border	1370 keV	1660 keV	2410 keV
Upper border	1570 keV	1860 keV	2810 keV

Figure 40: Energy windows for the determination of natural radionuclides.

Due to the moderate energy resolution of the NaI(Tl)-detectors and Compton scattering, photons emitted by one of the natural radionuclides could be registered in an energy window associated with a different radionuclide. Assuming secular equilibrium, the counts in each energy window are correlated to the activity concentrations of ^{40}K, ^{232}Th and ^{238}U, resulting in a matrix equation (equation 3.5.4.1).

$$\begin{bmatrix} CR_K \\ CR_U \\ CR_{Th} \end{bmatrix} = \begin{bmatrix} S_{K,K} & S_{K,U} & S_{K,Th} \\ S_{U,K} & S_{U,U} & S_{U,Th} \\ S_{Th,K} & S_{Th,U} & S_{Th,Th} \end{bmatrix} \cdot \begin{bmatrix} c_K \\ c_U \\ c_{Th} \end{bmatrix} \qquad (3.5.4.1)$$

with:

CR_K: Count rate in Potassium (K) energy window [cps]
CR_U: Count rate in Uranium (U) energy window [cps]
CR_{Th}:   Counts in Thorium (Th) energy window [cps]
$S_{K,K}$:   Efficiency of Potassium (K) energy window for ^{40}K activity concentration [cps Bq^{-1} kg]
$S_{K,U}$:   Efficiency of Potassium (K) energy window for ^{238}U activity concentration [cps Bq^{-1} kg]
$S_{K,Th}$:   Efficiency of Potassium (K) energy window for ^{232}Th activity concentration [cps Bq^{-1} kg]
$S_{U,K}$:   Efficiency of Uranium (U) energy window for ^{40}K activity concentration [cps Bq^{-1} kg]
$S_{U,U}$:   Efficiency of Uranium (U) energy window for ^{238}U activity concentration [cps Bq^{-1} kg]
$S_{U,Th}$:   Efficiency of Uranium (U) energy window for ^{232}Th activity concentration [cps Bq^{-1} kg]
$S_{Th,K}$:   Efficiency of Thorium (Th) energy window for ^{40}K activity concentration [cps Bq^{-1} kg]
$S_{Th,U}$:   Efficiency of Thorium (Th) energy window for ^{238}U activity concentration [cps Bq^{-1} kg]
$S_{Th,Th}$:   Efficiency of Thorium (Th) energy window for ^{232}Th activity concentration [cps Bq^{-1} kg]
c_K: ^{40}K activity concentration [Bq kg^{-1}]
c_U: ^{238}U activity concentration [Bq kg^{-1}]
c_{Th}: ^{232}Th activity concentration [Bq kg^{-1}]

Assuming linear relations, the correction or stripping of the wrongly assigned photons can be performed using the counts in the energy window assigned to the radionuclide, as illustrated in figure 40.

$$CR_K = CR_{K,K} + \gamma CR_{U,U} + \beta CR_{Th,Th} \qquad (3.5.4.2)$$

$$CR_U = g CR_{K,K} + CR_{U,U} + \alpha CR_{Th,Th} \qquad (3.5.4.3)$$

$$CR_{Th} = b CR_{K,K} + a CR_{U,U} + CR_{Th,Th} \qquad (3.5.4.4)$$

with:

$CR_{K,K}$:   Count rate in Potassium (K) energy window attributable to ^{40}K emissions [cps]
$CR_{U,U}$:   Count rate in Uranium (U) energy window attributable to ^{238}U decay chain emissions [ ]
$CR_{Th,Th}$: Count rate in Thorium (Th) energy window attributable to ^{232}Th decay chain emissions [ ]
α: Stripping factor for correcting Counts in Uranium (U) energy window
       for counts attributable to ^{232}Th decay chain emissions [ ]
β: Stripping factor for correcting Counts in Potassium (K) energy window
       for counts attributable to ^{232}Th decay chain emissions [ ]
γ: Stripping factor for correcting Counts in Potassium (K) energy window
       for counts attributable to ^{238}U decay chain emissions [ ]
a: Stripping factor for correcting Counts in Thorium (Th) energy window
       for counts attributable to ^{238}U decay chain emissions [ ]
b: Stripping factor for correcting Counts in Thorium (Th) energy window

for counts attributable to ^{40}K emissions [ ]

g: Stripping factor for correcting Counts in Uranium (U) energy window
for counts attributable to ^{40}K emissions [ ]

If the stripping factors b and g are considered negligible, the net count rates can be determined according to equations 3.5.4.5, 3.5.4.6 and 3.5.4.7.

$$CR_{Th,Th} = \frac{CR_{Th} - aCR_U}{1 - a\alpha} \tag{3.5.4.5}$$

$$CR_{U,U} = \frac{CR_U - \alpha CR_{Th}}{1 - a\alpha} \tag{3.5.4.6}$$

$$CR_{K,K} = CR_K - \beta CR_{Th,Th} - \gamma CR_{U,U} \tag{3.5.4.7}$$

The concentrations in soil and rock are then calculated by equations 3.5.4.8, 3.5.4.9 and 3.5.4.10.

$$c_K = \frac{CR_{K,K}}{S_{K,K}} \tag{3.5.4.8}$$

$$c_U = \frac{CR_{U,U}}{S_{U,U}} \tag{3.5.4.9}$$

$$c_{Th} = \frac{CR_{Th,Th}}{S_{Th,Th}} \tag{3.5.4.10}$$

The stripping factors are related to the efficiencies by equations 3.5.4.11, 3.5.4.12, 3.5.4.13 and 3.5.4.14.

$$\alpha = \frac{S_{U,Th}}{S_{Th,Th}} \tag{3.5.4.11}$$

$$\beta = \frac{S_{K,Th}}{S_{Th,Th}} \tag{3.5.4.12}$$

$$\gamma = \frac{S_{K,U}}{S_{U,U}} \tag{3.5.4.13}$$

$$a = \frac{S_{Th,U}}{S_{U,U}} \tag{3.5.4.14}$$

3.5.5   WINSSI database

Following the adaptation to the Windows operating system made by IRSN, LINSSI, which means LINux System for Spectral Information, was renamed WINSSI. The very generic model of the database, which is initially based on the "sample-measurement" association, makes it possible to integrate the majority of data related to spectrometry measurements: gross measurement, analysis results, measurement conditions and other metadata.

Without any modification of the initial model but with a rigorous definition of the naming and data integration rules, all the devices used by IRSN and described in section 2.5 have been integrated into different interoperating and compatible databases (BDD), hosted on an IRSN internal server. Note also that the issue of international compatibility has already been addressed via the international working groups in which IRSN participates, like the European Radiation Dosimetry Group (EURADOS) and the Response and Assistance Network (RANET) of the International Atomic Energy Agency (IAEA).

3.5.6 LINSSI interface and architecture

The linux distribution LINSSI includes not only the definition and the tools of deployment of the database but also the scripts for the management of the integration of the data (written in the programming language Perl) as well as the skeleton of the Internet site allowing the access to data. The flexibility and intelligence in LINSSI's design has enriched the scripts and the basic web interface with internal developments.

The processing and analysis of spectra, directly from the BDD data, are made by other scripts, usually written in the script language PHP. These processes can be applied, either in post-processing to a set of specific spectra via dedicated pages of the web portal, or automatically in real time to any new measurement integrated in BDD. The dedicated pages display the result of the processing and allow the export for integration by other tools of the laboratoire de télédétection (LTD), in particular geographic information system (GIS) or geostatistical processing tools. Real-time processing is intended to integrate validation or warning logic.

3.5.7 Geostatistical software KARTOTRAK

In IRSN, the transition in 2012 from static measurements to mobile measurements was the trigger for a new way of communicating results. IRSN manages a large amount of data and have to report them to the public. The need arose for a tool helping to communicate results in a clear and concise way. Providing maps from data was a natural choice, but representativeness of such reporting has to be a priority.

For this purpose, IRSN has implemented a standard GIS which allows to quickly process data and get maps. However, the interpolation quality of the maps caused some scepticism because some parameters are often automatically set by the software to compute the maps, the software acting as a black box. IRSN then looked for a software solution which would allow communicating results quickly whilst enabling map analysis and quality control. After an extensive training in geostatistics, the standard GIS was replaced by the KARTO-TRAK software solution (figure 41). KARTOTRAK gives control on the key parameters for the calculation of a map by Kriging (named after Danie Gerhardus Krige, a pioneer in geostatistics). The software offers a geostatistical workflow which requires only a few hours of training before feeling comfortable with it. KARTOTRAK enables quick loading of data files and is able to process a huge quantity of data simultaneously. It also allows automatic streaming data acquisition, and is therefore perfectly adapted to mobile data acquisition systems. The software allows setting the interpolation grid according to the input data, especially the variance indicator, and adjusting the interpolation area to each project, so avoiding extrapolation and false results where data is missing.
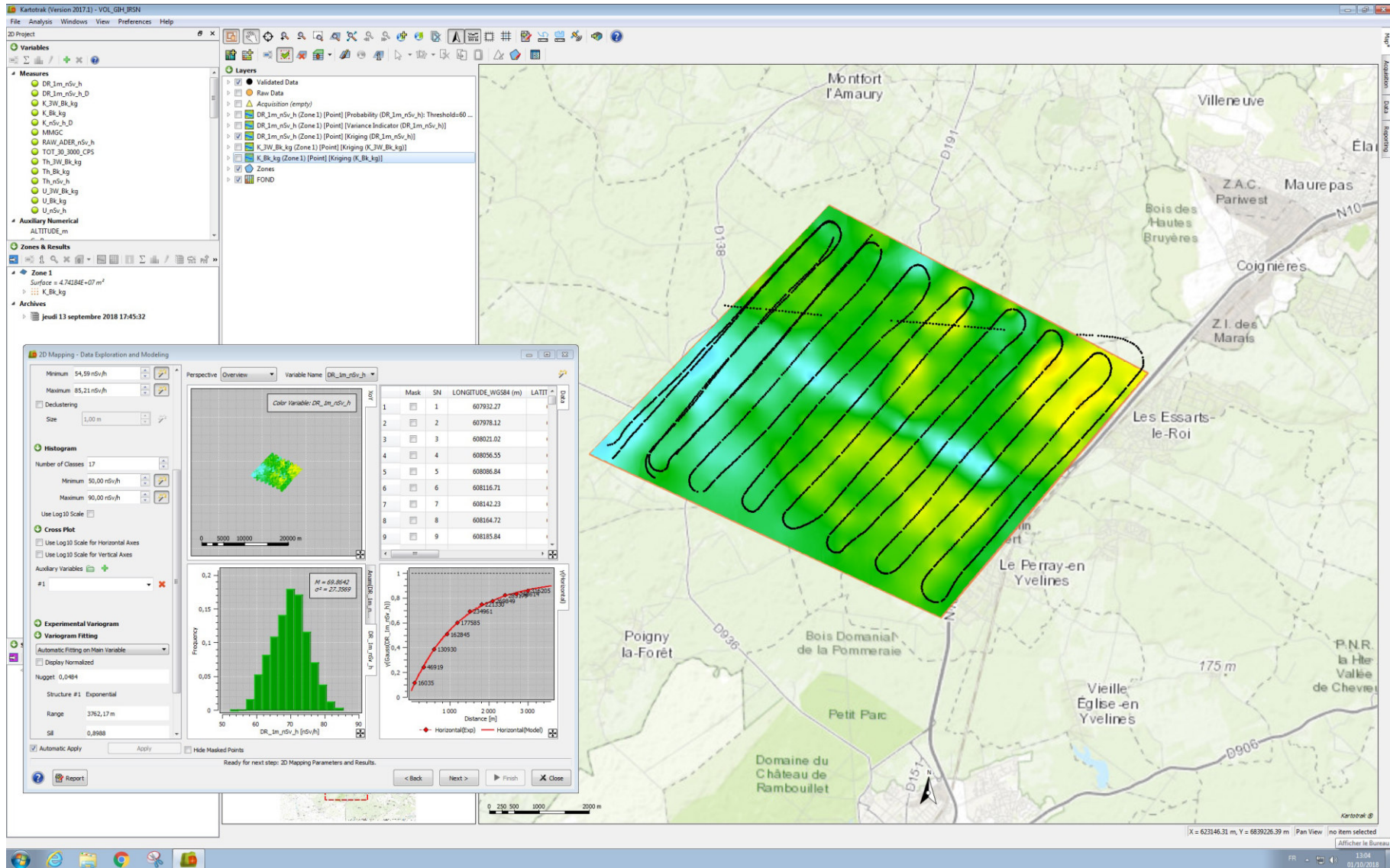
Figure 41: Screenshot of the KARTOTRAK software.

4 Data format

The data exchange between the participants utilised the European Radiometric and Spectrometry (ERS) format described already in detail (PSI-report 09-07, 2007). Quantities and units were specified according to table 25. The coordinates were reported in the World Geodetic System WGS84 reference system or in the Swiss National Grid reference system.
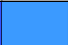
Table 25: Quantities and units used in the exercise.

Quantity	ERS identifier	Unit	distribution
Dose rate	DHSR	μSv s^{-1}	-
Activity concentration ^{40}K	AD_K-40	Bq kg^{-1}	Uniform
Activity concentration ^{238}U	AD_U-238	Bq kg^{-1}	Uniform
Activity concentration ^{232}Th	AD_Th-232	Bq kg^{-1}	Uniform
Surface activity ^{137}Cs	AA_Cs-137	Bq m^{-2}	Surface

5 Data presentation

In the standardized Swiss reports, a map of the total dose rate (measuring quantity $H^*(10)$ at 1 m above ground) and the flight lines is presented together with a map of the Man-Made-Gross-Count (MMGC) ratio for all measuring areas. A map of the ^{232}Th activity concentration (measuring quantity activity per dry mass) yields quality information as it can be expected that this quantity is constant over time. In the case of large changes of topography in the measured area, a map of the terrestrial dose rate consisting of the total dose rate reduced of the altitude dependent cosmic component is included. In the case of measuring flights with the main purpose of mapping natural radionuclide concentrations, a supplementary map of the ^{40}K activity concentration (measuring quantity activity per dry mass) is presented. All maps are projected from WGS84 coordinates into the Swiss National Grid (CH1903+_LV95). The maps use a gradual color scale from blue for low values to red for high values. The maximum and minimum values are specified in the legend together with the measurement unit of the depicted quantity. The colors for 10 percent steps between minimum and maximum values of the scale are given in table 26. Minimum and maximum of the color scale for the measured quantity are generally set to standard values to facilitate easier comparison of maps. Maps with different value ranges are added if considered helpful to the reader. The presentation of maps for the international intercomparison exercise is adapted where considered appropriate.

Table 26: Quantification of the color scale.

Percentage	$\leq$0	10	20	30	40	50	60	70	80	90	$\geq$100
Color											

6 Recurrent Swiss measurement tasks

On June 22nd and June 23rd, Swiss teams CH01 and CH02 performed measurements over the nuclear power plants Mühleberg (KKM) and Gösgen (KKG) prior to the international intercomparison exercise. The measurements over Swiss nuclear installations are performed in a bi-annual rhythm on request by the Swiss Federal Nuclear Safety Inspectorate (ENSI). The raw data were corrected for the faulty energy calibration of crystal three, as described in section 6.1. The parameters used in the evaluation documented in section 18.4 were modified due to result of the international intercomparison exercise described in sections 8.1 and 9.1.1. The survey of the environs of the KKM and KKG showed no artificial radionuclides outside of the plant premises.

6.1 Faulty detector of team CH01

The dose rate measured by team CH01 shows in the dose rate map of the source search area (figure 229) a horizontal line with lower values compared to the rest of the measuring area. The maps of the activity concentrations of natural radionuclides (figures 230 and 231) do not reproduce this effect. These lower dose rate values are associated with one and a half flight lines at the beginning of the second measuring flight. Figure 42 shows the averaged photon spectra over the suspicious flight line compared to the rest of the assigned measuring area. The count rates per channel are clearly lower. A temporal break down of one of the four NaI(Tl)-detectors could have been a possible cause for these lower count rates at the beginning of the second flight. This assumption was checked by comparing the count rate in the cosmic window (> 3 MeV) which should be independent on variations of ground activity. The count rate in the cosmic channel (figure 43) plotted versus the fiducial (number of the measuring point) shows clearly reduced values for the part of the flight associated with low dose rate values. All other flights of team CH01 were checked but did not show groups of successive points with lower count rates in the cosmic window. Unfortunately, the reduction of the cosmic count rate depicted in figure 43 lies within the statistical fluctuations, so single aberrant data points are still possible. The correction based on the assumption of a measurement with only three instead of four NaI(Tl) detectors, a division of the reported values by 0.75, would mitigate the aberrant dose rate values, but generate an overestimation of the ^{40}K and ^{232}Th activity concentration (figure 42). As the cause of the aberrant values could not be clearly identified, the spectra of the four single crystals were extracted from the log files stored in the Exploranium detector. The spectra in the log-files are stored with 1024-channel resolution. Figure 44 shows clearly a completely maladjusted average spectrum for the third crystal of the detector. Unfortunately, the effect on the sum of the spectra of all four crystals is surprisingly unremarkable, which was the reason for the late detection of the flawed raw data in the detailed analysis after the exercise. All logged spectra still available in the detector were retrieved and analysed after the detection of the problem. A slight degradation of the energy resolution of the third crystal could be traced starting in 2015 and the loss of energy calibration started with the measuring flights of 2017. The degradation of the energy resolution had a minor effect on the data evaluation using the windows method, whereas the faulty energy resolution had a major deteriorating effect on the results. Thus it was decided to reconstruct the raw data of all flights performed in 2017 without using the faulty signal of the third crystal. Crystals one and four are located on the outer faces of the detector having therefore a slightly different field of view compared to the inner detectors two and three. Therefore, the signal of the third crystal was replaced by

the signal of the second crystal rather than using the signal of the remaining three detectors divided by a factor of 0.75. The resulting reconstructed spectrum is depicted in figure 44.
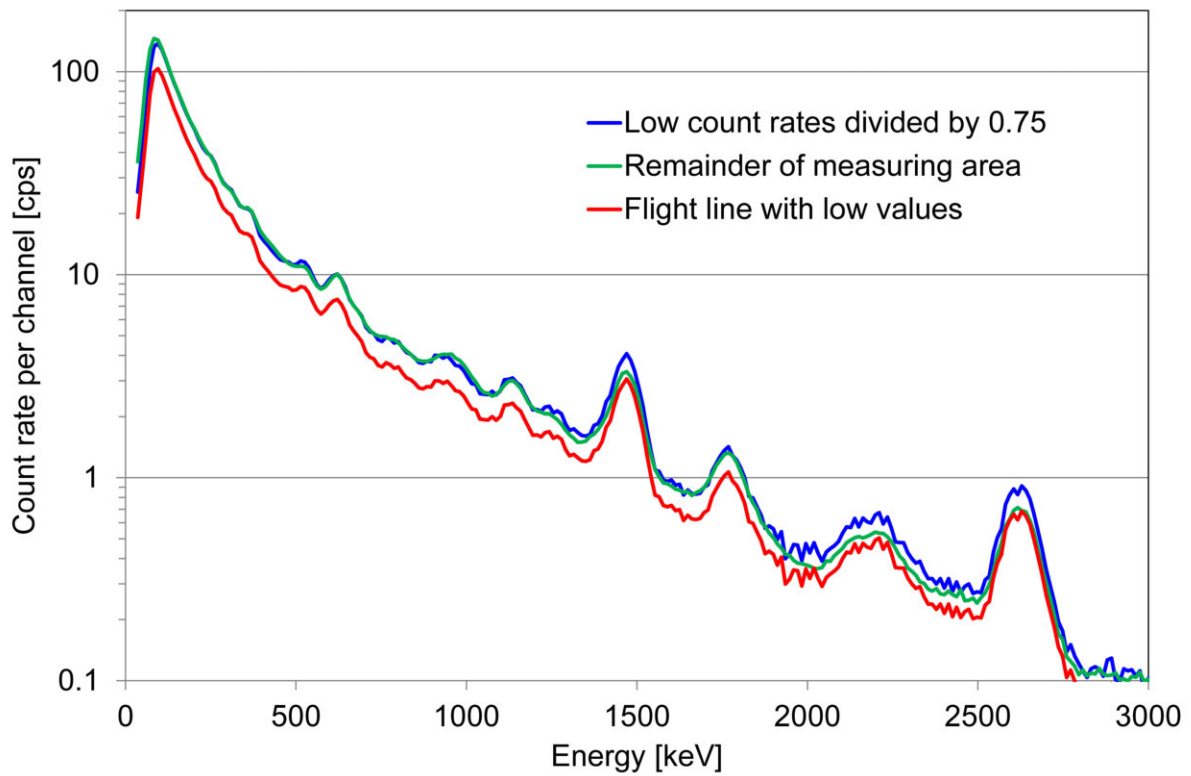

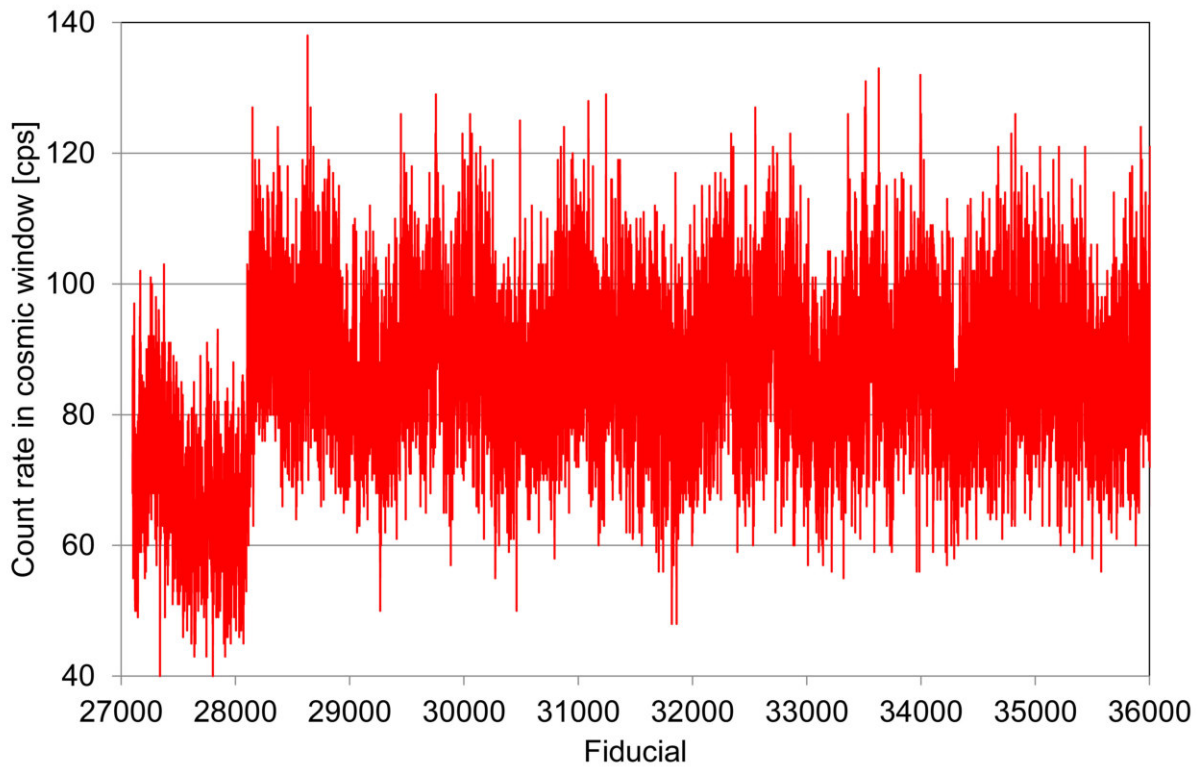Figure 42: Averaged photon spectra measured by team CH01 in the source search area.

Figure 43: Count rate in the cosmic window in dependence of the fiducial.
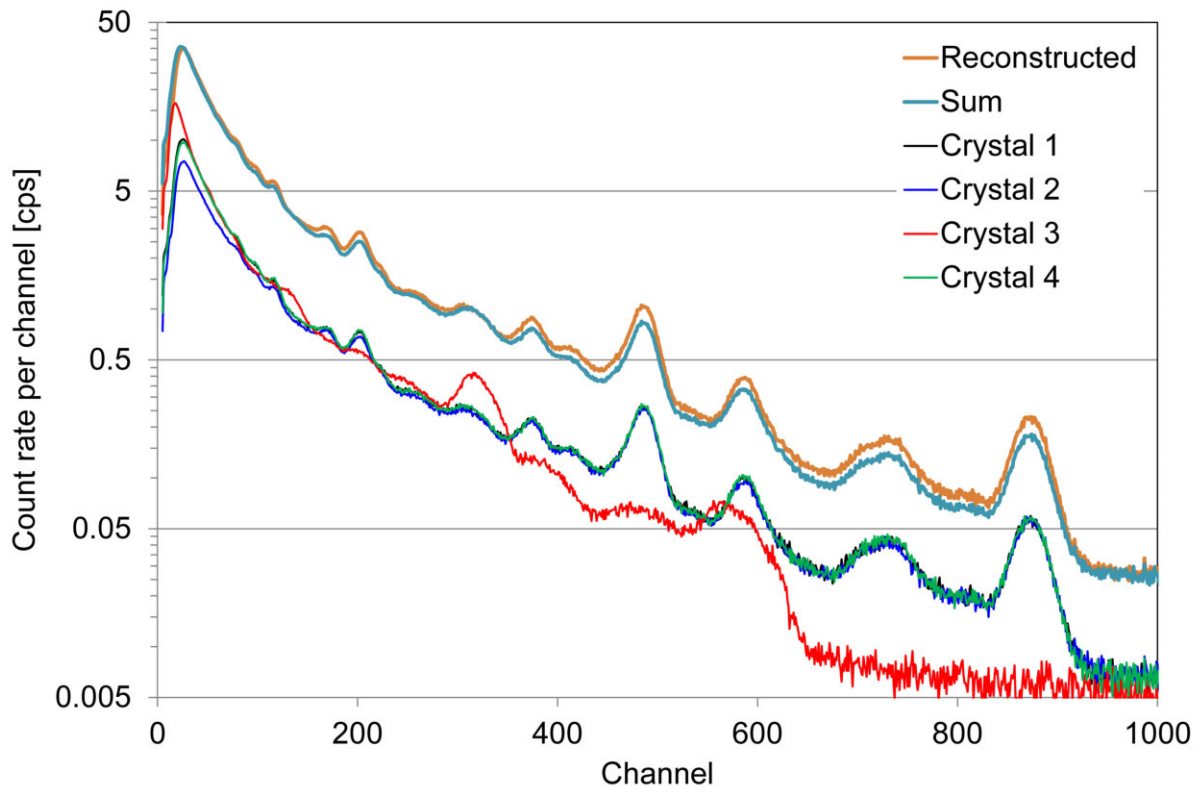
Figure 44: Spectra restored from detector log by team CH01 averaged over the source search area.

6.2 KKG

In the pressurised reactor of the nuclear power plant Gösgen (KKG), the radioactive steam of the primary circuit stays completely in the heavily shielded containment. Thus, neither the dose rate map (figure 45) nor the map of the MMGC-ratio (figure 48) as indicator for the presence of artificial radionuclides show increased signals at the site of the plant. The map of the natural radionuclide ^{232}Th (figure 51) is added for quality assurance purposes.

The area around KKG was also measured by team CH02. The results evaluated with the proprietary software of the manufacturer are in good agreement with the results of team CH01 (figures 46, 49 and 52). The raw data of the flights of team CH02 were also evaluated using the ARM-software used by team CH01, yielding also good agreement with the results of team CH01 and the data evaluated with the manufacturer software (figures 47, 50 and 53). The spectra of team CH02 were saved as sliding 5 second averages, thus the maps of the re-evaluated data show slightly less details compared to the evaluation of the 1 second raw spectra.

At coordinate 640060, 244809, a slight elevation of the MMGC-ratio can be observed (figure 48). The photon spectrum over this coordinate (figure 54) depicts no peaks which could be associated with a specific radionuclide, but generally elevated count rates for low energy photons. The same effect was already observed more pronounced during the exercise ARM11 (PSI report No. 12-04) near this location at coordinate 640000, 244850. A commercial irradiation facility is located at the coordinate under consideration. The photon spectrum leads to the assumption, that scattered radiation of the applied accelerators was observed. The dose rate map (figure 45) shows in this area no significantly elevated values.

Figure 45: Dose rate in the vicinity of KKG measured by team CH01. PK100©2017 swisstopo (JD100042).

Figure 46: Dose rate in the vicinity of KKG measured by team CH02. PK100©2017 swisstopo (JD100042).

Figure 47: Dose rate in the vicinity of KKG. Raw data measured by team CH02 were evaluated using the ARM software of team CH01. PK100©2017 swisstopo (JD100042).

Figure 48: MMGC-ratio in the vicinity of KKG measured by team CH01. PK100©2017 swisstopo (JD100042).

Figure 49: MMGC-ratio in the vicinity of KKG measured by team CH02. PK100©2017 swisstopo (JD100042).

Figure 50: MMGC-ratio in the vicinity of KKG. Raw data measured by team CH02 were evaluated using the ARM software of team CH01. PK100©2017 swisstopo (JD100042).

Figure 51: ^{232}Th activity concentration in the vicinity of KKG measured by team CH01. PK100©2017 swisstopo (JD100042).

Figure 52: ^{232}Th activity concentration in the vicinity of KKG measured by team CH02. PK100©2017 swisstopo (JD100042).

Figure 53: ^{232}Th activity concentration in the vicinity of KKG. Raw data measured by team CH02 were evaluated using the ARM software of team CH01. PK100©2017 swisstopo (JD100042).
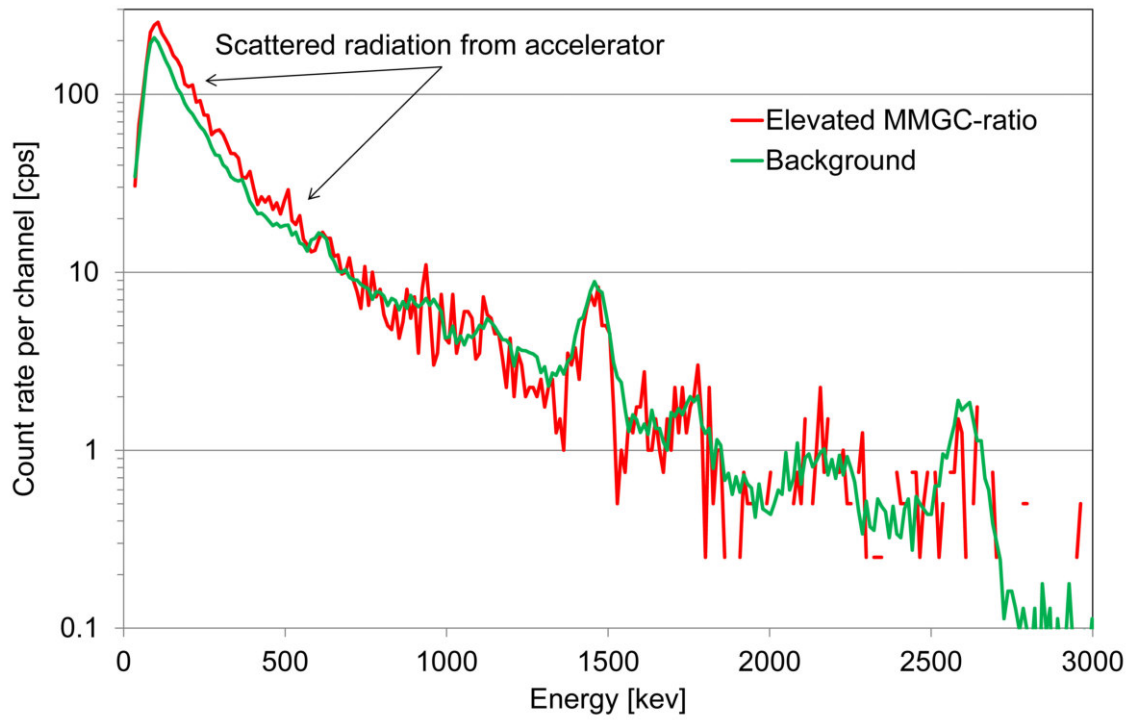
Figure 54: Photon spectrum over the coordinate with slightly elevated MMGC-ratio south of KKG measured by team CH01.

6.3 KKM

The nuclear power plant Mühleberg (KKM) is a boiling water reactor. Activated steam is passed from the containment to the turbines in the machine building. As the roof of the machine building is less shielded, the photon emissions from the primary steam pipe can be detected easily with airborne gamma-spectrometry. Both the map of the dose rate (figure 55) and the map of the MMGC-ratio (figure 58) as indicator of artificial radionuclides show distinct signals over the plant. The map of the natural radionuclide ^{232}Th (figure 61) depicts also elevated values at the location of the power plant. These elevated values are a known artefact of the spectrum evaluation in presence of the activation product ^{16}N. ^{16}N emits gamma-rays with energies above 6 MeV. Compared to a background spectrum averaged over a region outside of KKM premises, scattered photons originating from ^{16}N can be observed over KKM throughout the measured photon spectrum, affecting the evaluation of spectral energy windows (figure 64). Figure 64 shows additionally to the scattered photons from ^{16}N photons emitted by ^{60}Co, ^{137}Cs and annihilation radiation at 511 keV. During the measurement flights, KKM staff measured drums with radioactive waste from the KKM intermediate storage. Therefore, the lid of the intermediate storage facility was opened and the stored waste drums could be detected from above.

Team CH02 also measured the premises of KKM. The increase of dose rate and the artefact in the map of ^{232}Th at the site of KKM observed by team CH01 are reproduced both with the standard evaluation (figures 56 and 62) and re-analysis of the raw data with the ARM-software used by team CH01 (figures 57 and 63). Comparing the maps of the Man-Made-Gross-Count (MMGC) ratio, both evaluations of the spectra measured by team CH02 (figures 59 and 60) do not display the elevated values over the KKM site observed by team CH01 (58) in the color scale chosen for both maps. The maximum MMGC-ratio point value of 8.8 measured by team CH02 over KKM is lower compared to the respective value of 66 measured by team CH01. Reason for the difference is a more pronounced signal of ^{137}Cs in the spectra measured by team CH01 (figure 64). The change of the ^{137}Cs signal between both flights performed in the morning of June 23rd is likely caused by a relocation of waste drums performed by KKM staff between the flights.
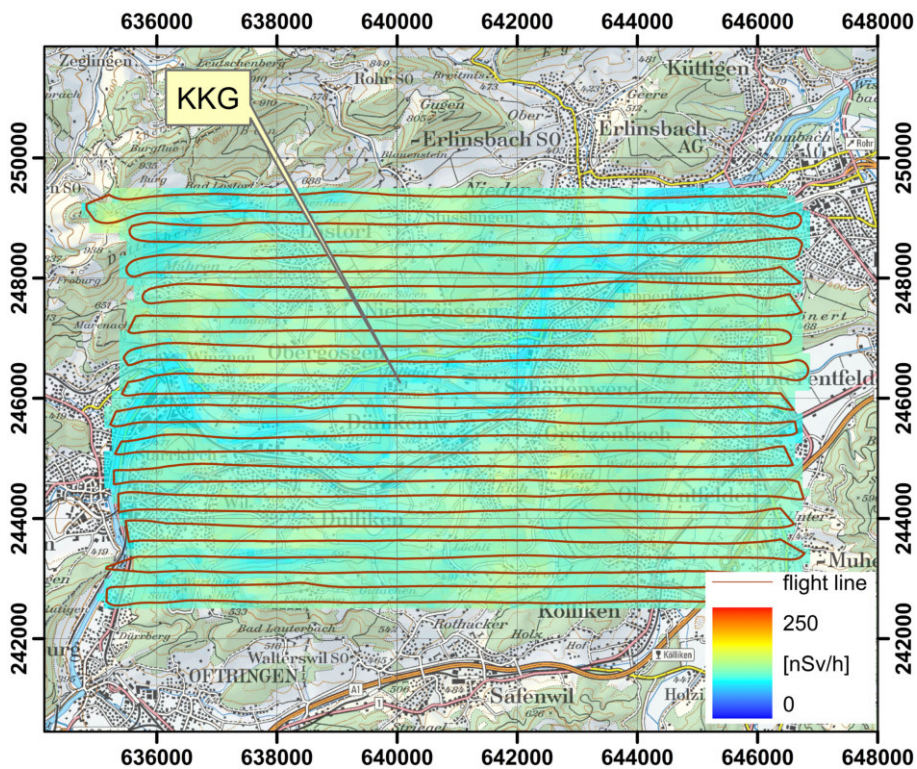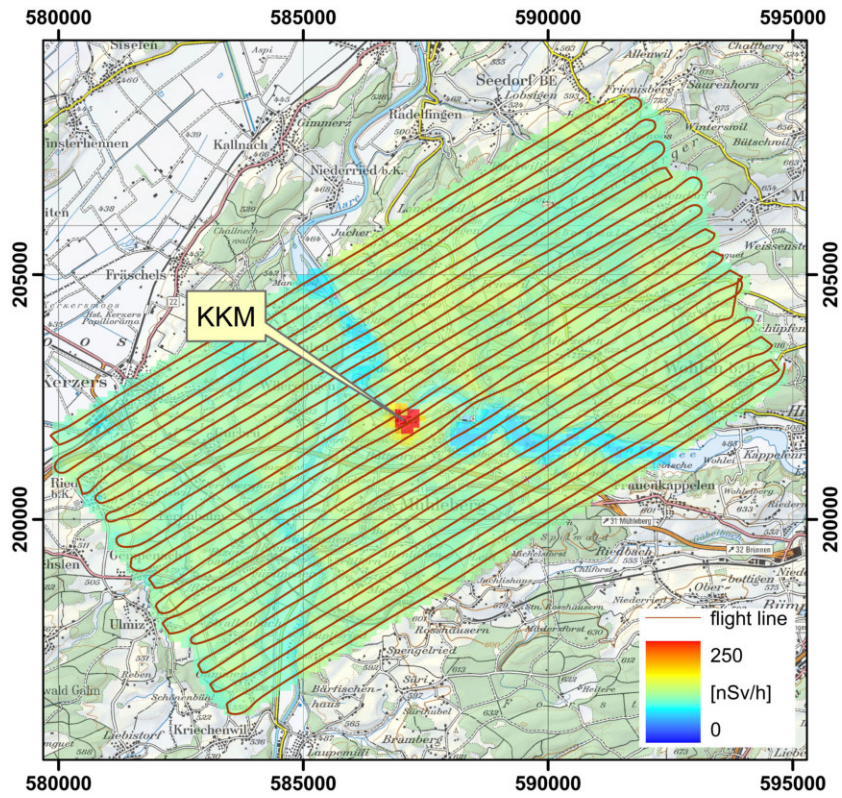
Figure 55: Dose rate in the vicinity of KKM measured by team CH01. PK100©2017 swisstopo (JD100042).
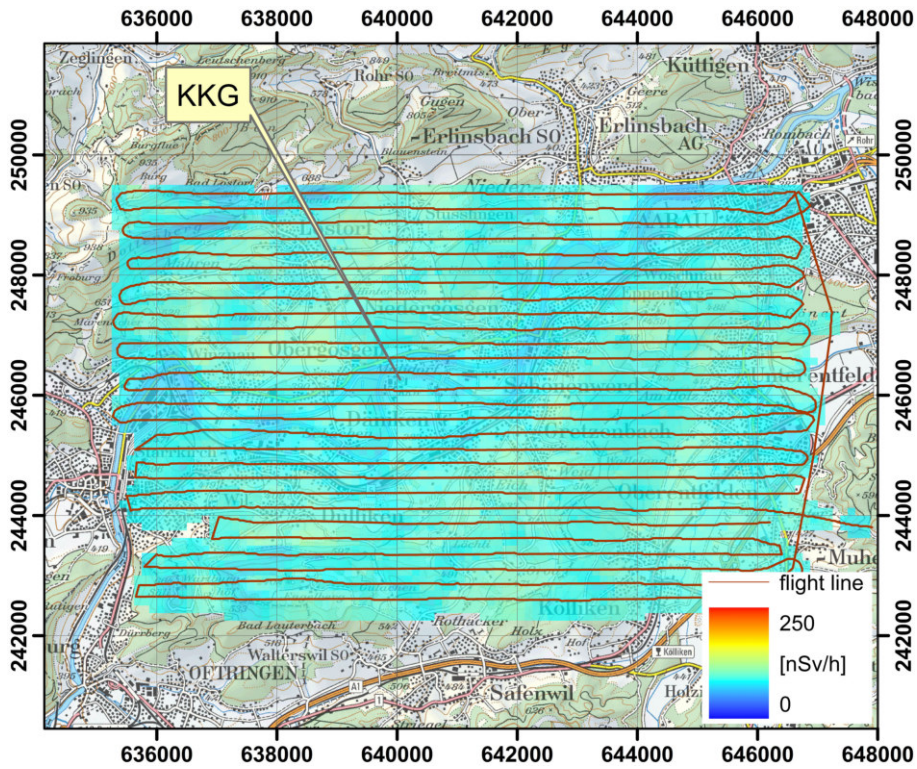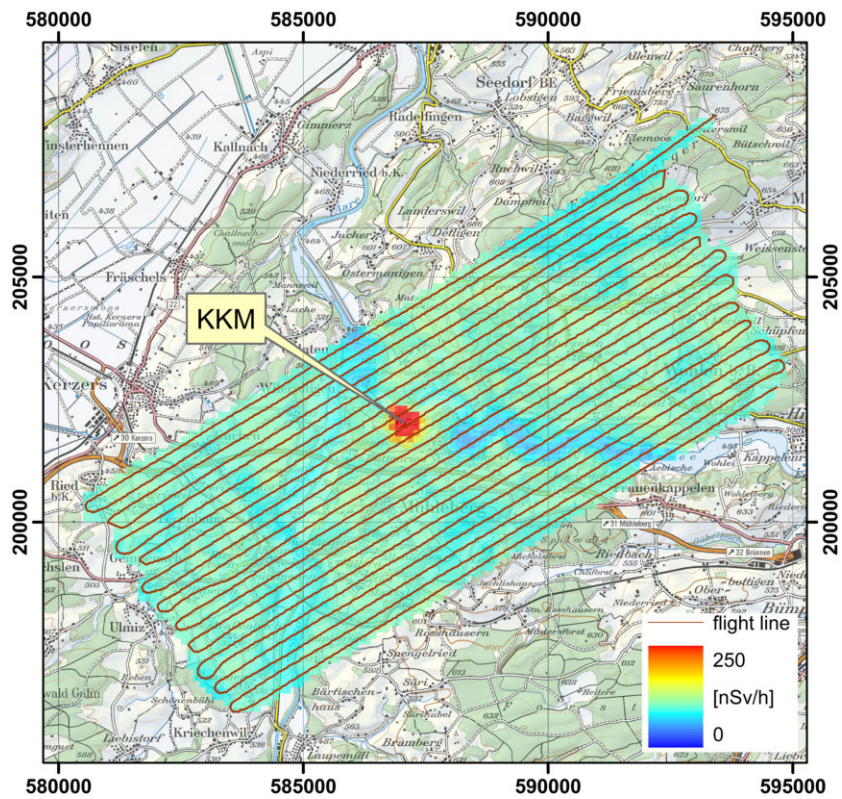

Figure 56: Dose rate in the vicinity of KKM measured by team CH02. PK100©2017 swisstopo (JD100042).
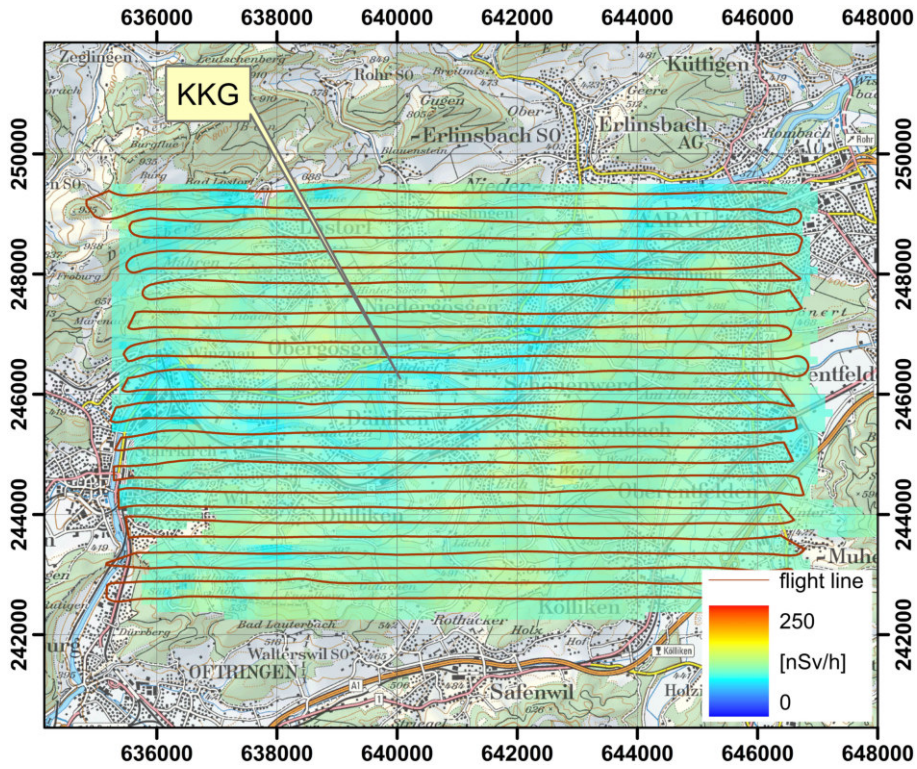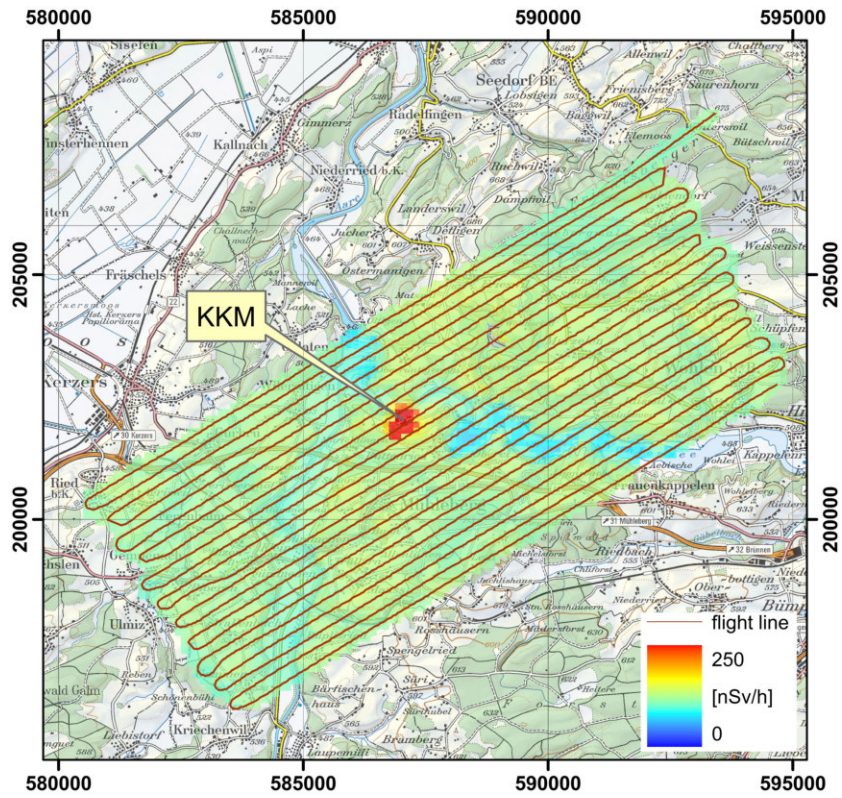
Figure 57: Dose rate in the vicinity of KKM. Raw data measured by team CH02 were evaluated using the ARM software of team CH01. PK100©2017 swisstopo (JD100042).
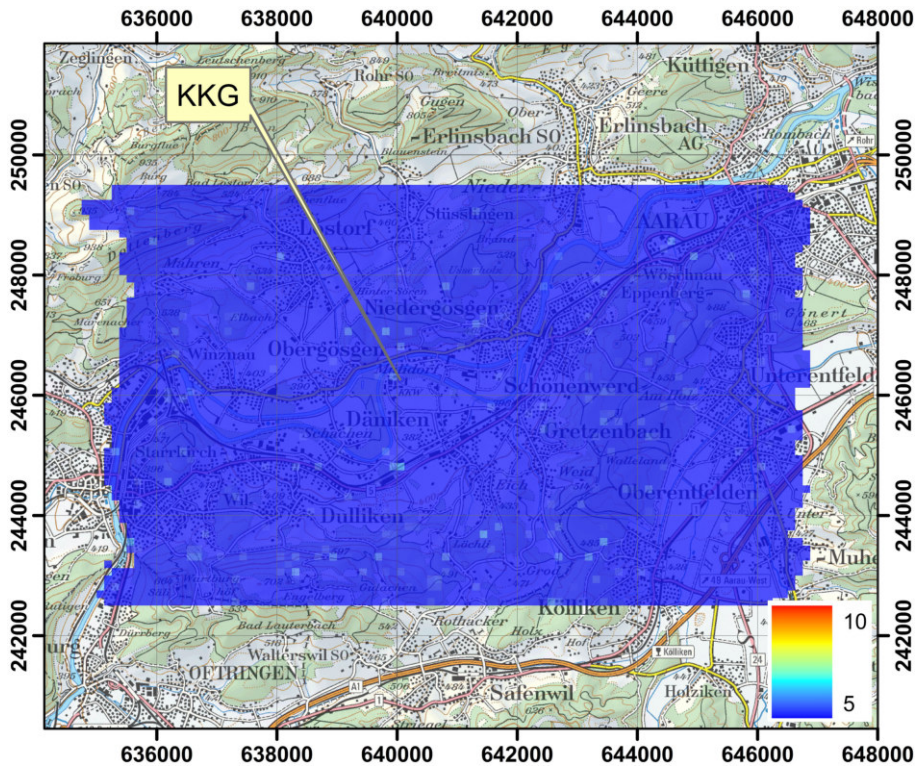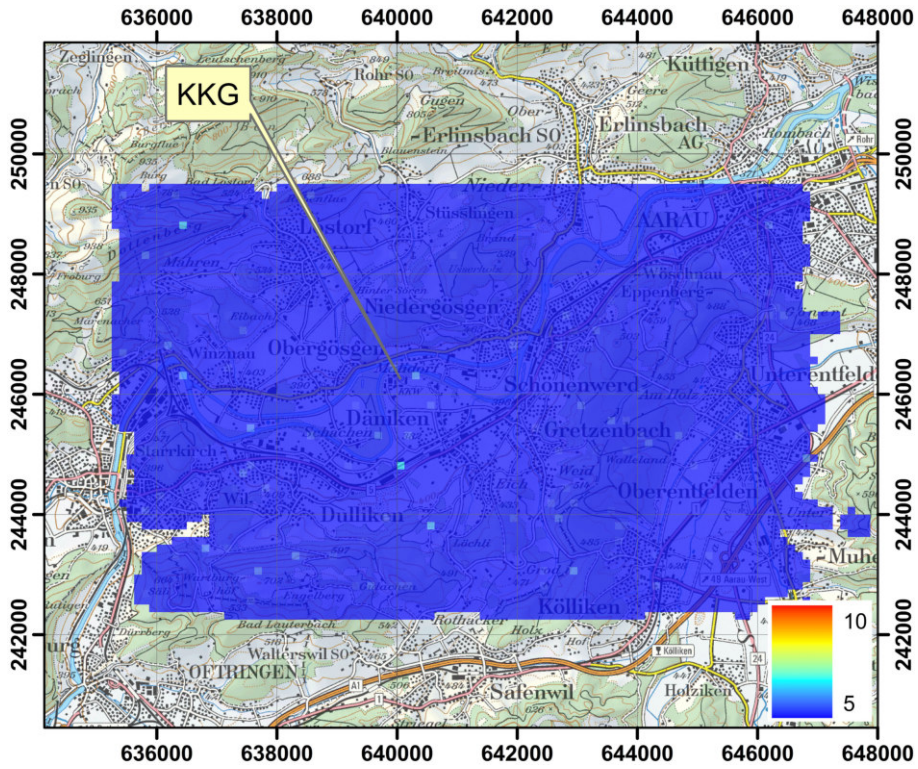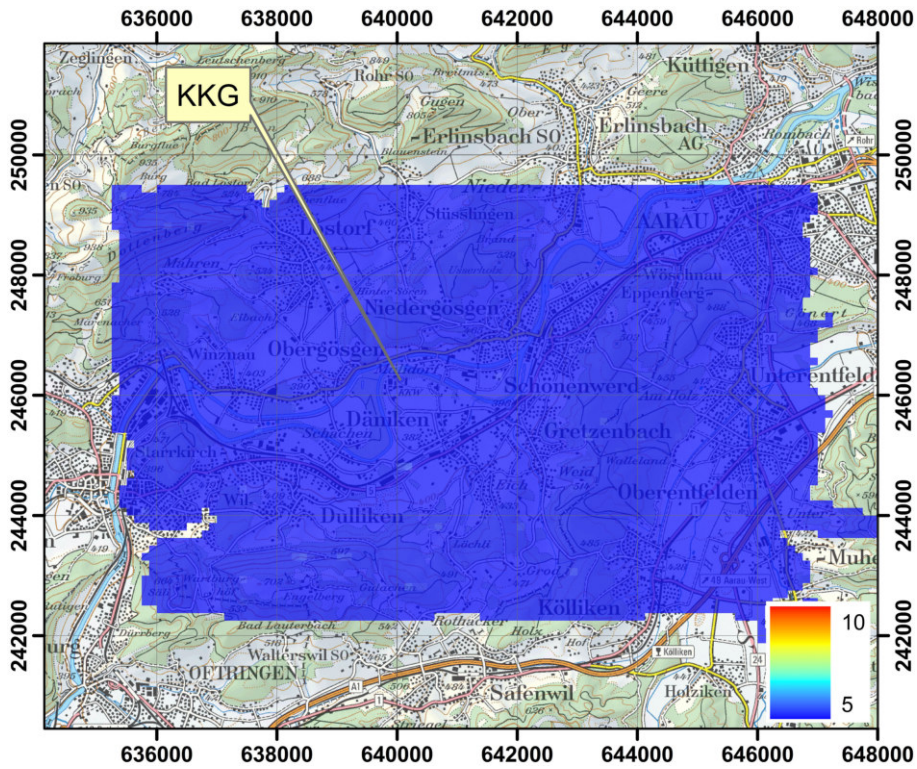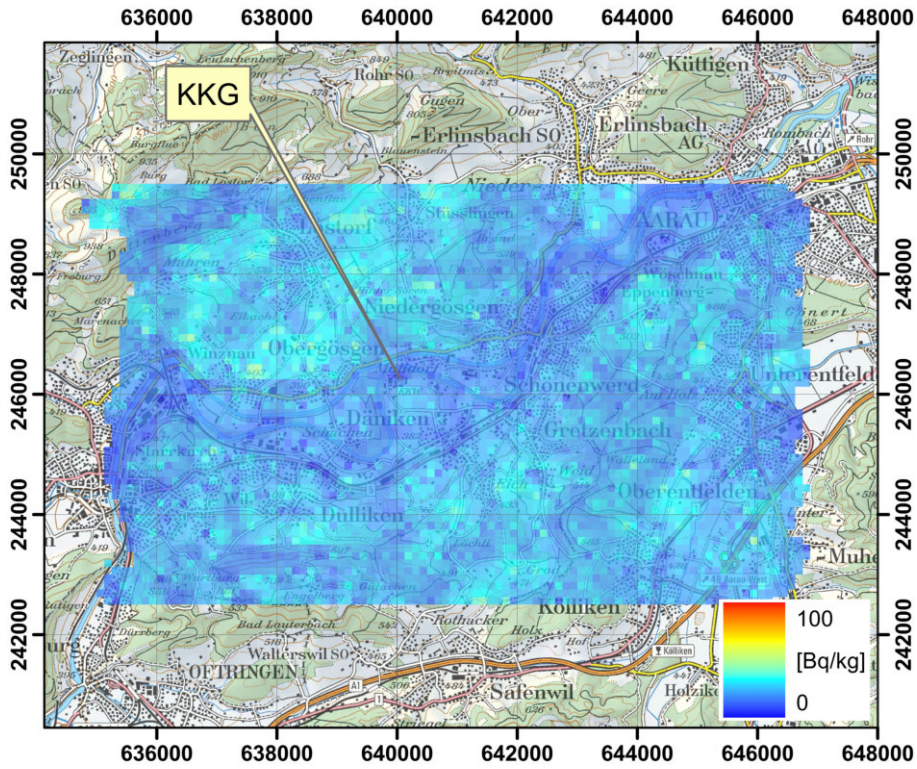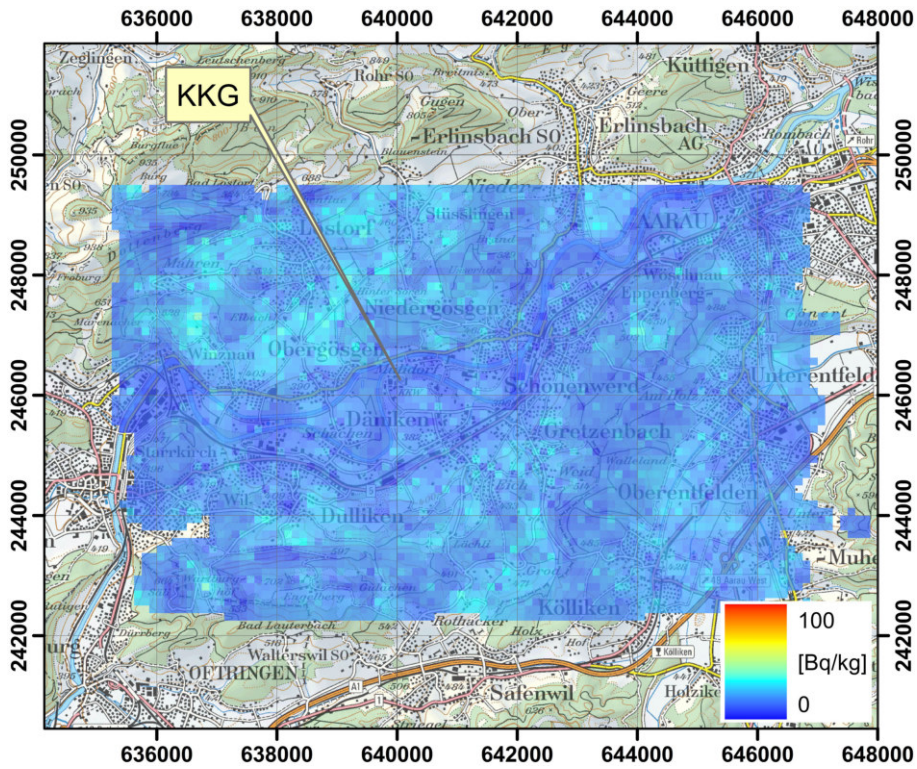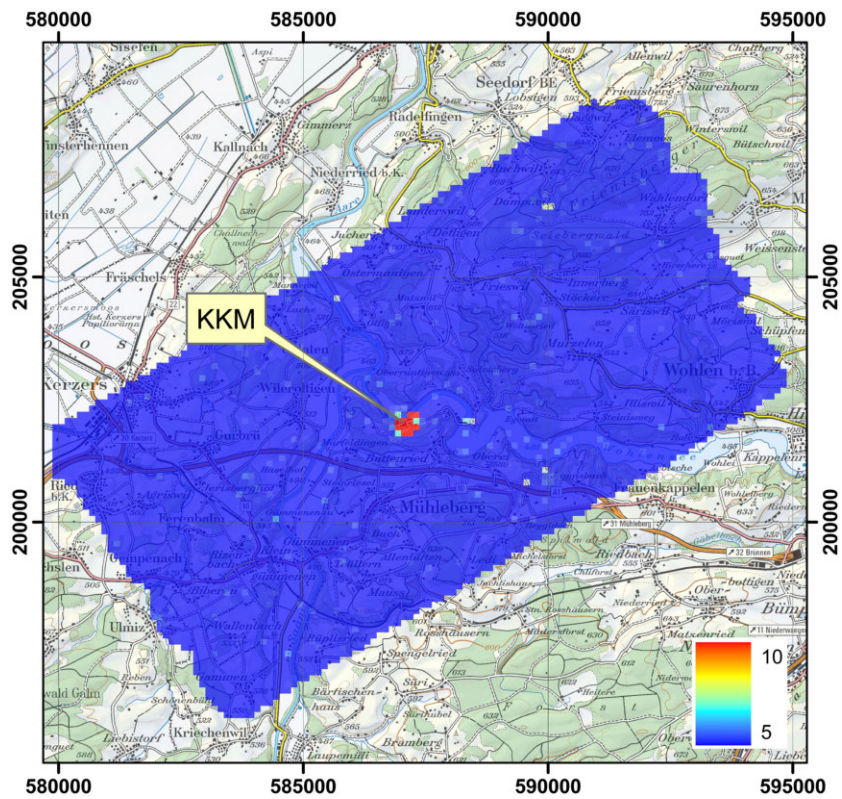

Figure 58: MMGC-ratio in the vicinity of KKM measured by team CH01. PK100©2017 swisstopo (JD100042).
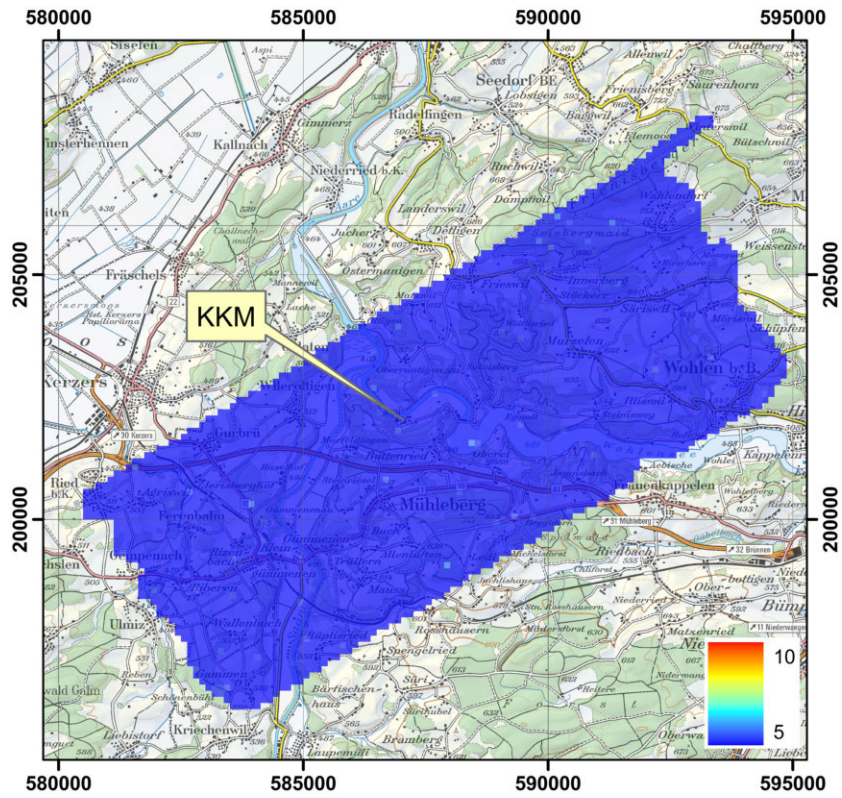
Figure 59: MMGC-ratio in the vicinity of KKM measured by team CH02. PK100©2017 swisstopo (JD100042).
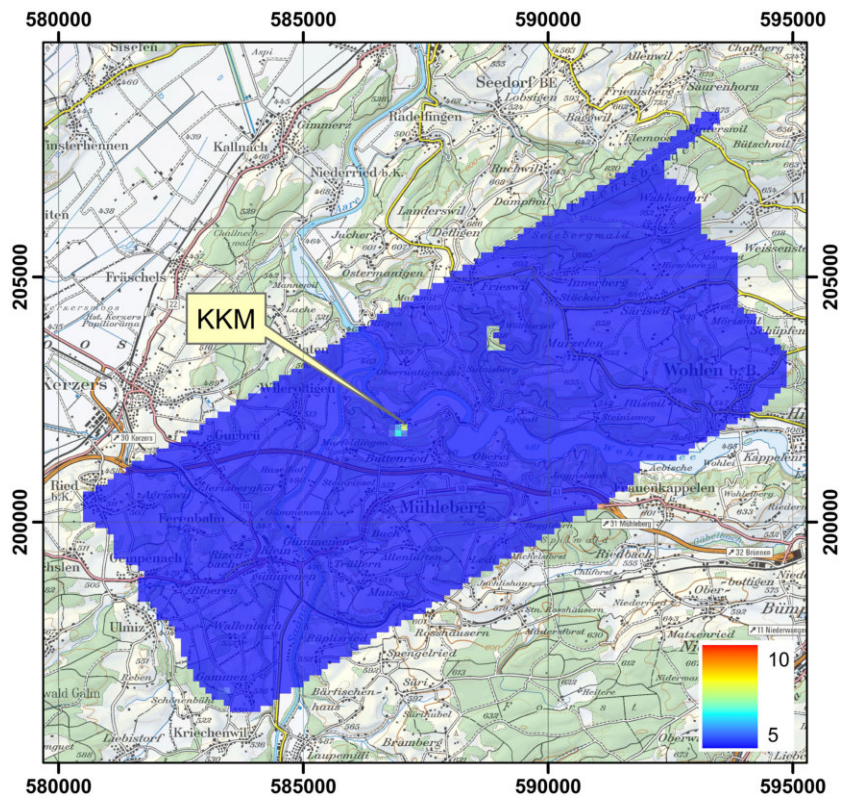
Figure 60: MMGC-ratio in the vicinity of KKM. Raw data measured by team CH02 were evaluated using the ARM software of team CH01. PK100©2017 swisstopo (JD100042).

Figure 61: ^{232}Th activity concentration in the vicinity of KKM measured by team CH01.
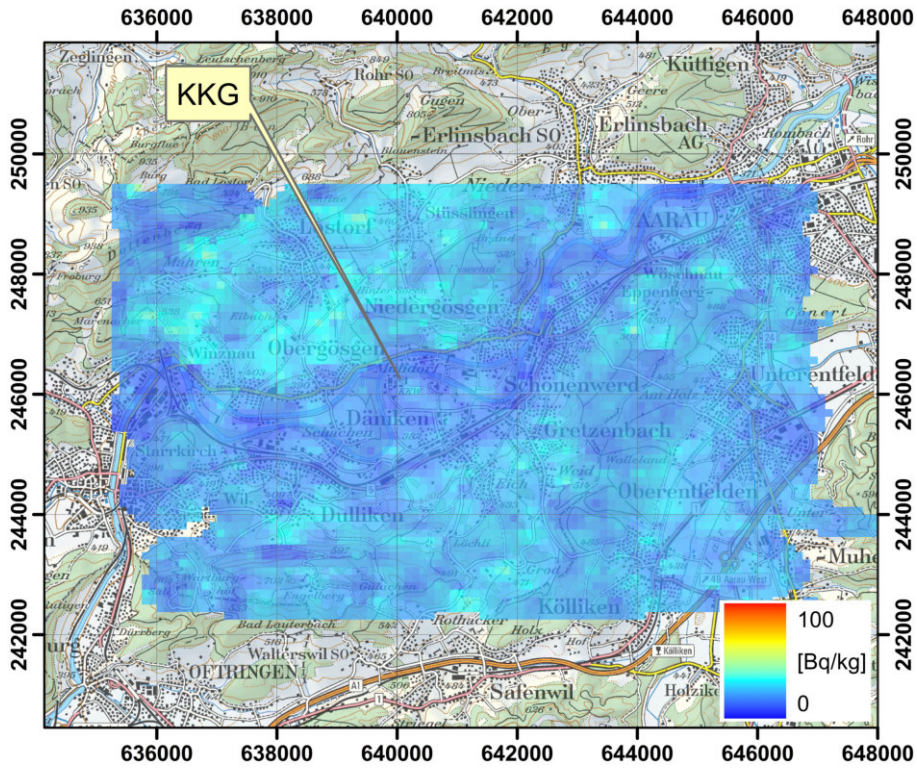PK100©2017 swisstopo (JD100042).

Figure 62: ^{232}Th activity concentration in the vicinity of KKM measured by team CH02.
PK100©2017 swisstopo (JD100042).

Figure 63: ^{232}Th activity concentration in the vicinity of KKM. Raw data measured by team CH02 were evaluated using the ARM software of team CH01. PK100©2017 swisstopo (JD100042).
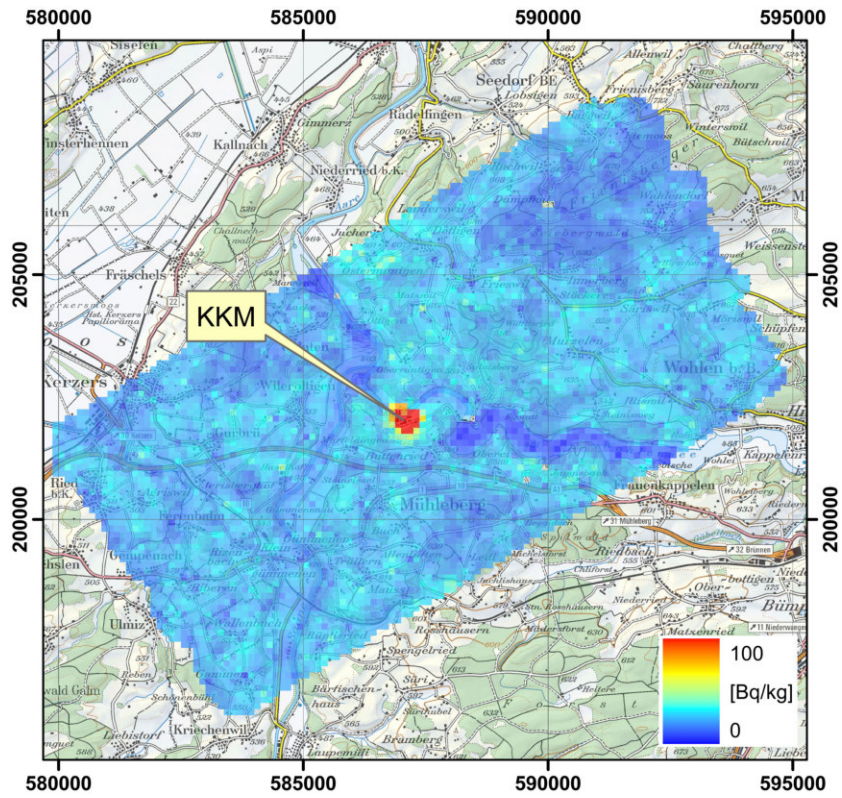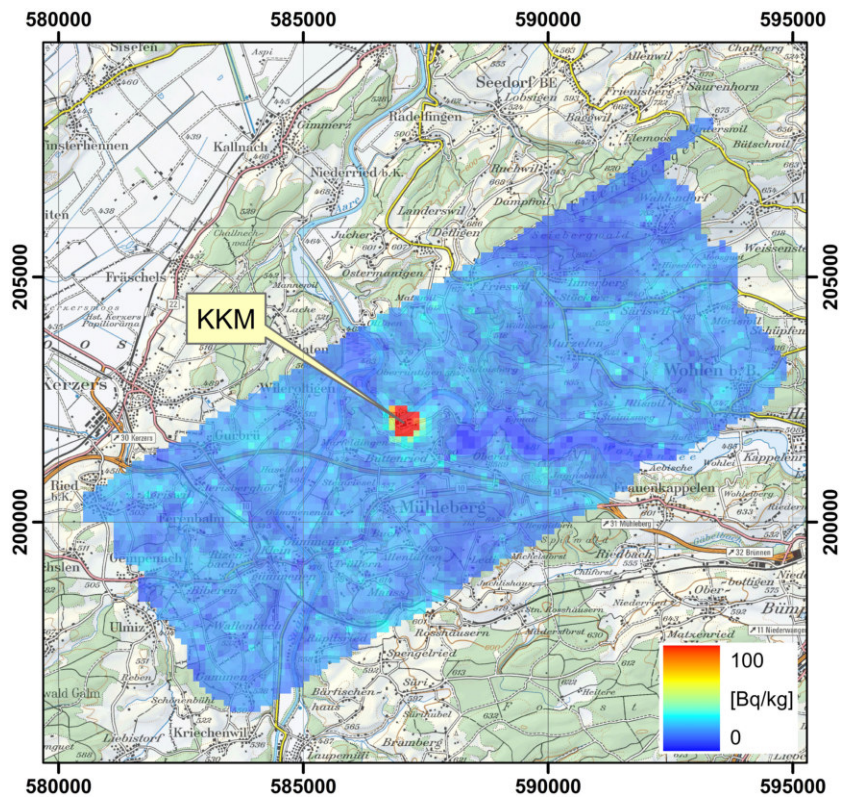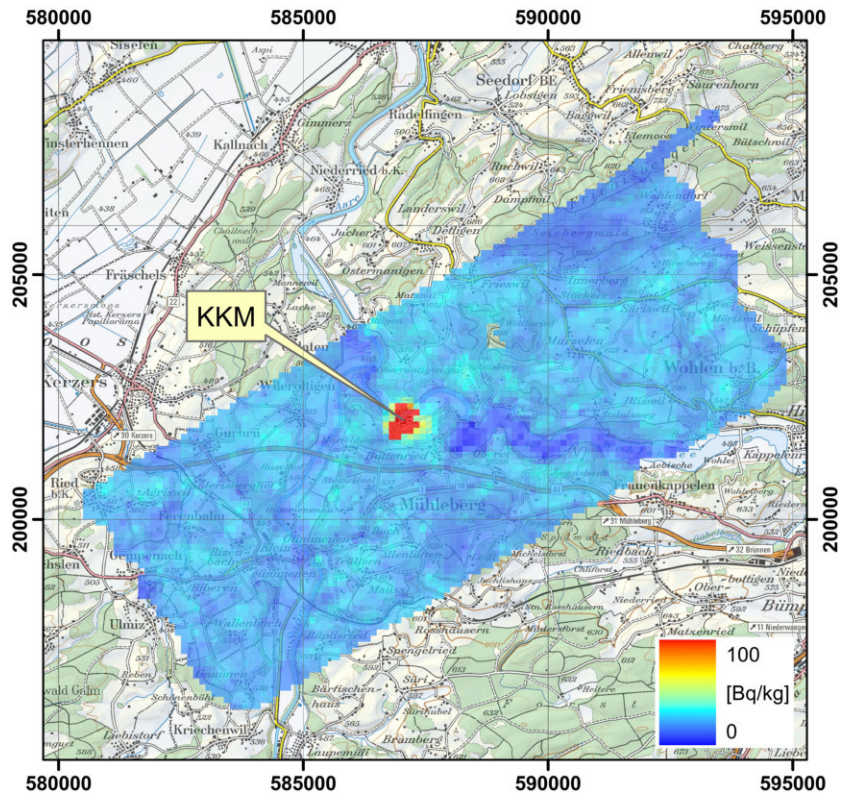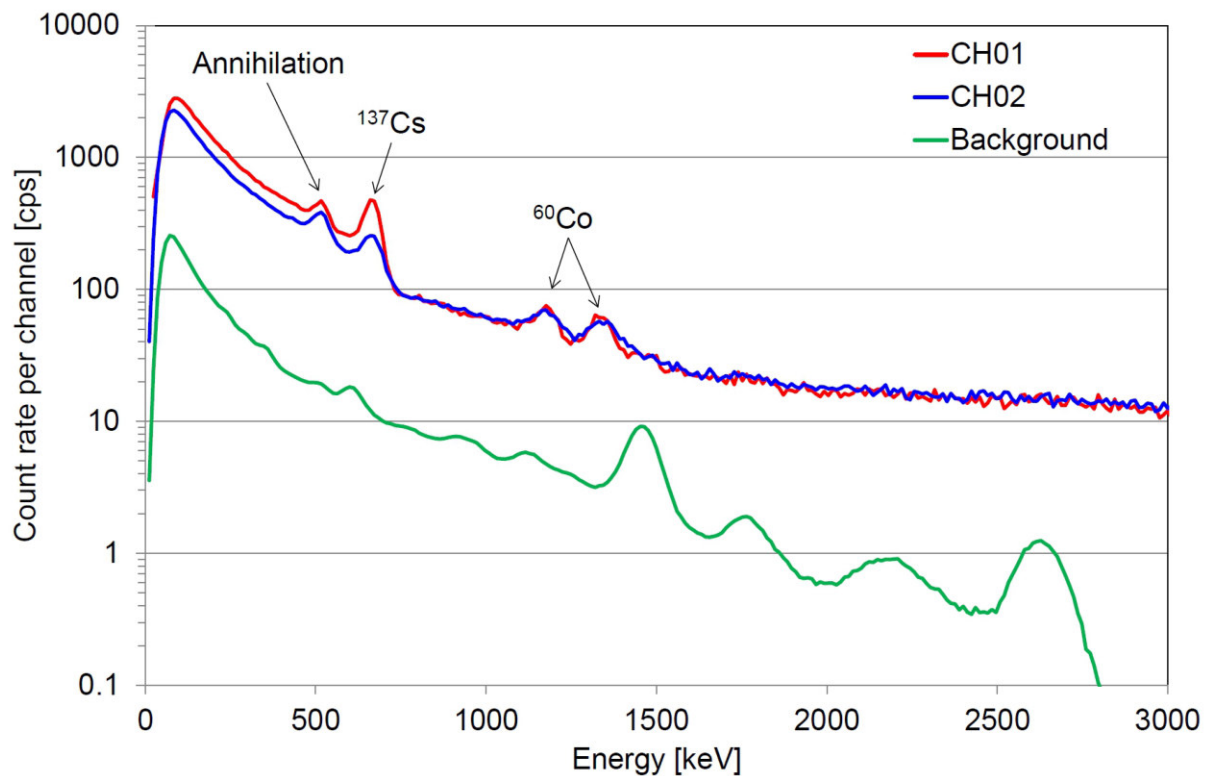

Figure 64: Photon spectra in the vicinity of KKM measured by teams CH01 and CH02.

7 Measurement tasks of the international exercise

The main measurement task for this international exercise tried to simulate a scenario in which the deployment of airborne gammaspectrometry is essential and international support would be requested.

The scenario assumes a theft of a strong radioactive ^{137}Cs-source. The get-away car including the empty source shielding was found abandoned by the police, suggesting that the thieves took flight on foot taking the source with them. Police investigations determined a perimeter inside which the thieves and the source should be located. Unfortunately, the associated area adds up to seven percent of Switzerland (2900 km^2). According to the significant public health risk in the vicinity of the radioactive source, a rapid location and recovery of the source was mandatory. As the search time decreases with the number of measuring aircrafts, the request of foreign assistance can be considered a reasonable assumption. Developing the exercise scenario further, no clear prescription of a search strategy was given in advance by the organisers. The search strategy, including flight altitude, line spacing and deployment of helicopters was determined during the exercise one day before the measuring flights by a command group formed from the heads of the participating measuring teams and the Swiss head pilot.

On the other hand, the focus on this realistic exercise scenario alone would lead to a frustrating exercise experience for most of the teams if the radioactive source were not placed in the assigned area of the team. The exercise was therefore expanded with additional objectives testing the performance of the participating systems. Typically, airborne gammaspectrometry is performed using standard flight parameters, for example a height above ground of 100 m with a line spacing of 250 m. Under these standard flight parameters, all participating teams perform well mapping natural background radiation as was shown in previous intercomparison exercises. For search of a strong radioactive source in a large area, a different set of flight parameters may be considered advantageous by the command group. The generation of a composite map of natural background radiation under these unusual and for this additional task suboptimal flight conditions can be considered as a challenge and success is on no account guaranteed. The measurement of two reference areas by all teams using both standard and modified flight parameters was included into the exercise to help analysing potential performance problems. An altitude profile over Lake Zug was scheduled to provide the opportunity to check on background and response to cosmic radiation of the measurement systems. A transversal going from flat to alpine terrain was included to give information on the influence of topography on the measurement results.

The requested results for each measuring task, data format, file naming conventions and colour scheme for maps were pre-defined during preparation of the exercise. A dedicated share point site for the exercise was supplied by the Federal Office of Information Technology, Systems and Telecommunications (BIT). The data transfer from participants to this central site worked without major issues. Nevertheless, the possibility to change and add files during and in the aftermath of the exercise had some disadvantages as no file tracking was established. A recommendation for future intercomparison exercise would be the introduction of a file inventory, where file names, a description of file contents and format are documented together with differences to potential previous versions of the files. With such an inventory, a strict file naming convention would be unnecessary.

8 Altitude profile over Lake Zug

The background of the measurement systems and the influence of cosmic radiation on the measured signal can be determined by measurements in different altitudes over a body of water which attenuates direct radiation of terrestrial radionuclides. The distance to the coast line should be sufficiently large to be outside the field of view of the detector at the maximum altitude intended for the measurement. Wind should preferably be landward to prevent interference of airborne radon progeny. Measurements located a couple of miles from an ocean coast would be ideal. Unfortunately, Switzerland does not provide such an ideal location. Most of the larger lakes of Switzerland are used as flight corridors with heavy air traffic, preventing permission for measuring altitude profiles. A location over Lake Zug was selected as best available option. Figure 65 shows the location of the altitude profiles over Lake Zug together with the flight path of team CH01 at the different altitudes.
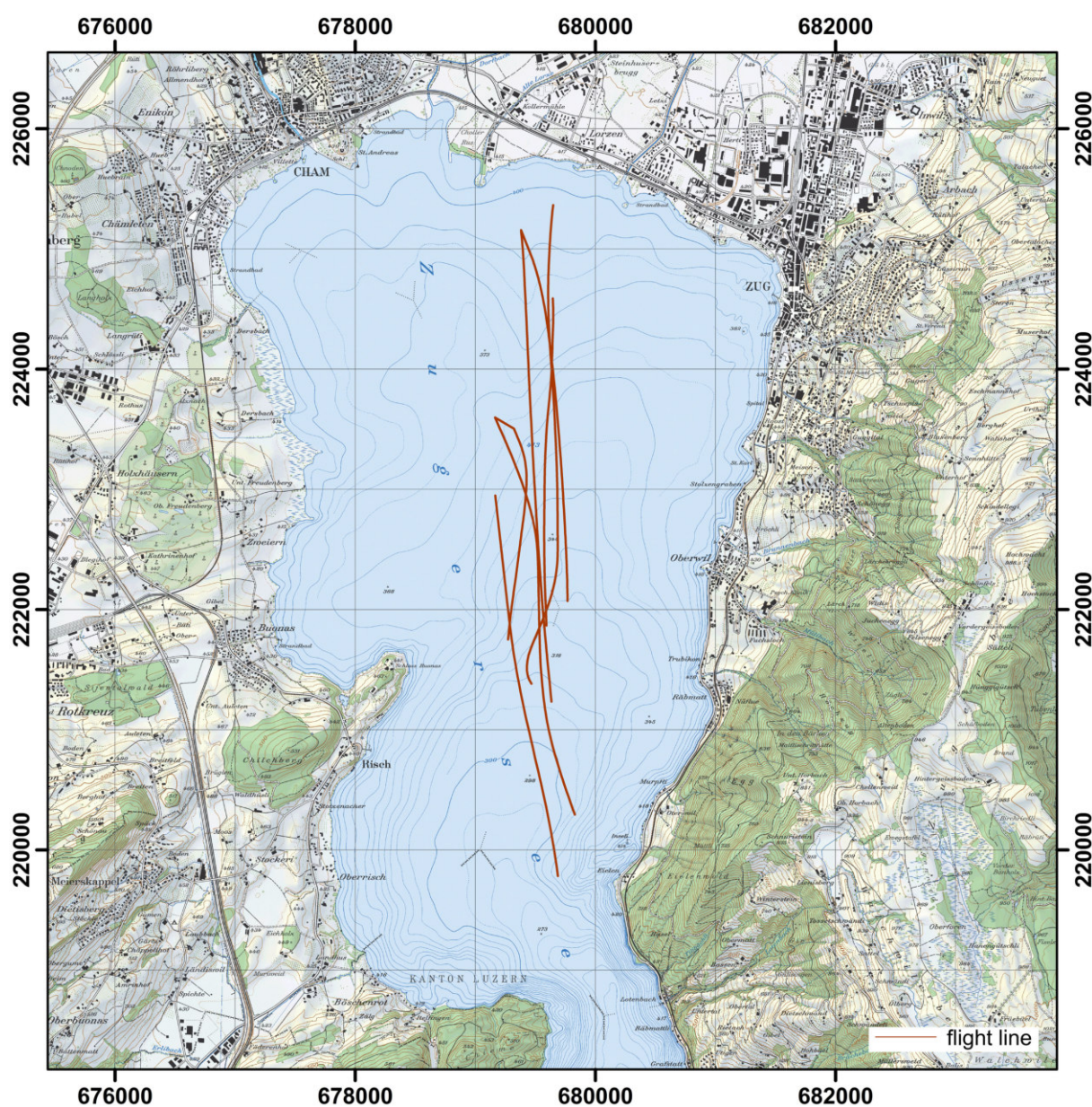
Figure 65: Location of the altitude profiles over Lake Zug with flight path of team CH01. PK25©2017 swisstopo (JD100042).

8.1 Results

Measurements were performed by team CH01 with flight lines over Lake Zug at seven altitude levels (figure 65). The measured data and spectra were averaged over the respective flight lines. The correction for the influence of cosmic radiation and instrument and helicopter background utilises the count rate in the cosmic window with photon energies above 3 MeV. This count rate can be expected to have a similar altitude dependence as the cosmic dose rate described in section 3.1.6. This assumption is tested in figure 66 with scaling the horizontal axis according to the altitude dependence of the cosmic dose rate. The resulting linear relationship with a 0.997 coefficient of determination confirms the assumption on the altitude dependence.

The correction of the cosmic and background contributions to the different energy windows is based on the cosmic count rate, as described in section 3.1.2. The count rate in the respective energy window above the lake should consist of an altitude dependent contribution representing the influence of cosmic radiation and a constant value due to natural radionuclides contained in detector and helicopter. Using the count rate in the cosmic window to represent the altitude, a linear relationship to the count rate in the respective energy window is expected. Figure 67 shows a good linearity between the count rates in the total window and the cosmic count rate. The location of the altitude profile over an inland lake is not optimal, as already stated in section 8. A potential influence of airborne radon progeny could be expected to induce a reduced linearity for the count rate in the uranium window with respect to the cosmic count rate. The coefficient of determination of the linear regression for this energy window of 0.985 is smaller than the value determined for the total count rate (0.995), but indicates still a good linearity (figure 68). The slopes and intercepts of the linear regression for each energy window are listed in table 27 together with their uncertainty. The values agree with data derived from a flight over the English Channel in 2002 (table 6), albeit indicating a lower background of detector and helicopter compared to the system used 15 years ago. The reason for the higher background measured in 2002 could be associated with additional gear like supplementary tanks and starter batteries in the helicopter used solely during missions outside of Switzerland.

Figure 66: Altitude dependence of cosmic count rate. Horizontal axis is scaled according to the altitude dependence of cosmic dose rate.

Figure 67: Relationship of total count rate to cosmic count rate.

Figure 68: Relationship of count rate in the uranium window to cosmic count rate.

Table 27: Correction factor S_c and background count rate CR_B determined by linear regression together with their uncertainties for the altitude profile over Lake Zug.

Energy window	S_c	$U(S_c)$	CR_B [cps]	$U(CR_B)$ [cps]
Total	1.096	0.071	74.8	9.7
Potassium	0.065	0.011	6.2	1.5
Uranium	0.048	0.005	2.6	0.7
Thorium	0.059	0.008	0.1	1.0
Caesium	0.072	0.009	16.6	1.3
Cobalt	0.096	0.006	9.6	0.9
MMGC1	0.751	0.049	67.7	6.6
MMGC2	0.345	0.024	7.1	3.3

The new airborne gamma-spectrometry system (RLL) employed by the Komp Zen ABC-KAMIR of the Swiss army (team CH02) will replace the old gamma-spectrometry system (ARM) used by the Swiss National Emergency Operations Centre (team CH01) in 2018. The measured raw data of the RLL system can be exported in the ERS-format and evaluated offline using the software developed for the ARM system to provide continuity during this transition. Besides measurements in the laboratory to determine stripping coefficients (see section 3.1.3), the altitude profile over Lake Zug is used to determine cosmic stripping and background of detector and helicopter (see section 3.1.2). Figure 69 shows the altitude dependence of the count rate in the cosmic energy window analogous to figure 66. The coefficient of determination of 0.994 confirms the assumed altitude dependence also for the

RLL system. The cosmic count rate is about 5 times lower compared to the ARM system. The difference of energy ranges assigned to the cosmic window (ARM: 3 MeV - 6 MeV; RLL: 2.9 MeV - 3.5 MeV) are assumed to be responsible for the difference in cosmic count rates between both systems. The lower cosmic count rate is also reflected in the slope of the linear regression between counts in the total energy window and the cosmic count rate, whereas the intercept indicating the background count rate of detector and helicopter are nearly identical (Figures 70 and 67). As the altitude profiles were measured at different times, the influence of airborne radon progeny could have changed. Fortunately, the co-efficient of determination for the linear regression of the count rate in the uranium energy window to the cosmic count rate of 0.976 matches the value derived for the ARM system (0.985) (figure 71). The values derived for correction of cosmic radiation and background (table 28) agree well with the values derived for the ARM system (table 27), if the different definitions of the cosmic window are considered. These values are used in the parameter file used to evaluate the raw data of RLL detector 002 with the existing ARM software (see section 18.5).
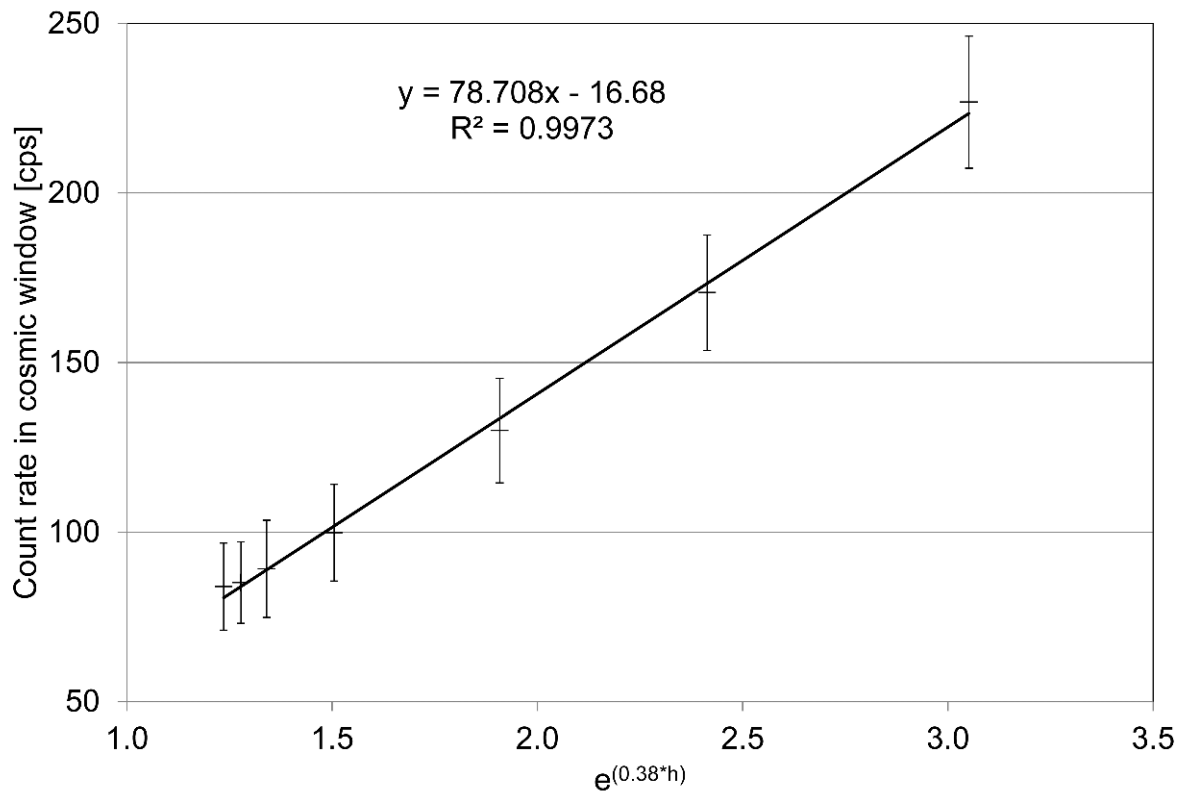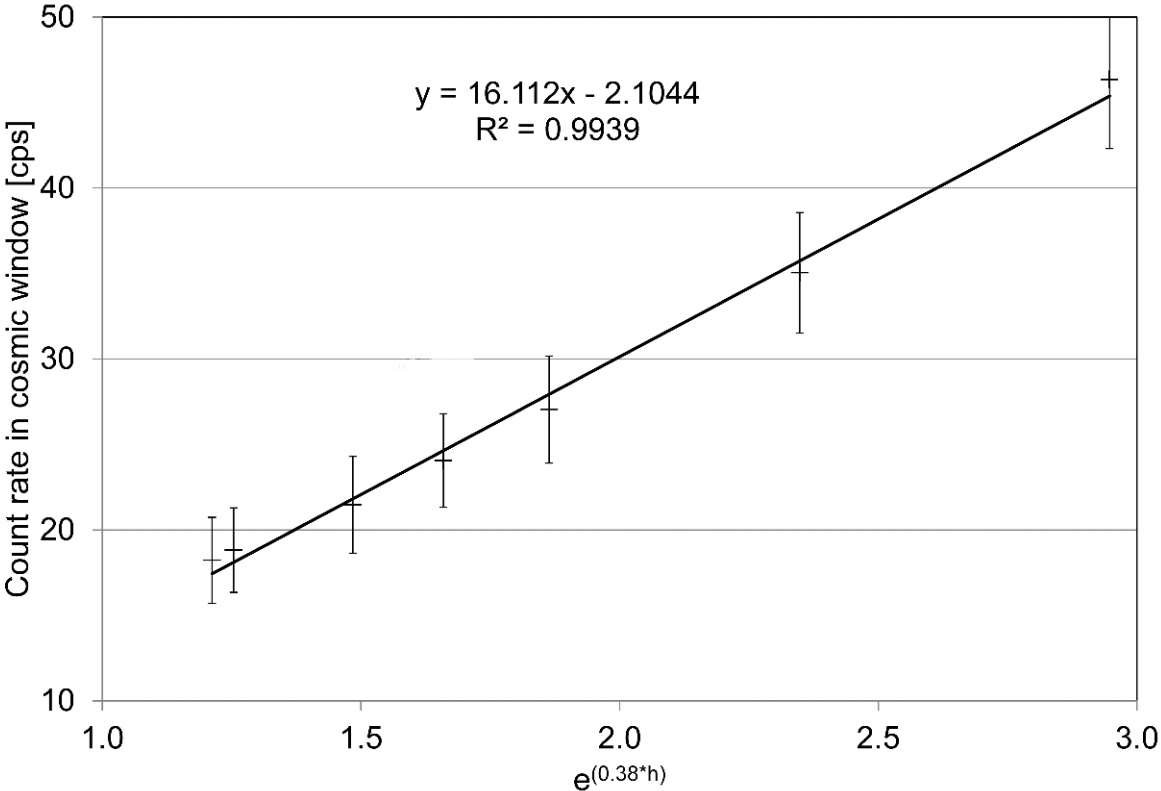

Figure 69: Altitude dependence of cosmic count rate. Horizontal axis is scaled according to the altitude dependence of cosmic dose rate.
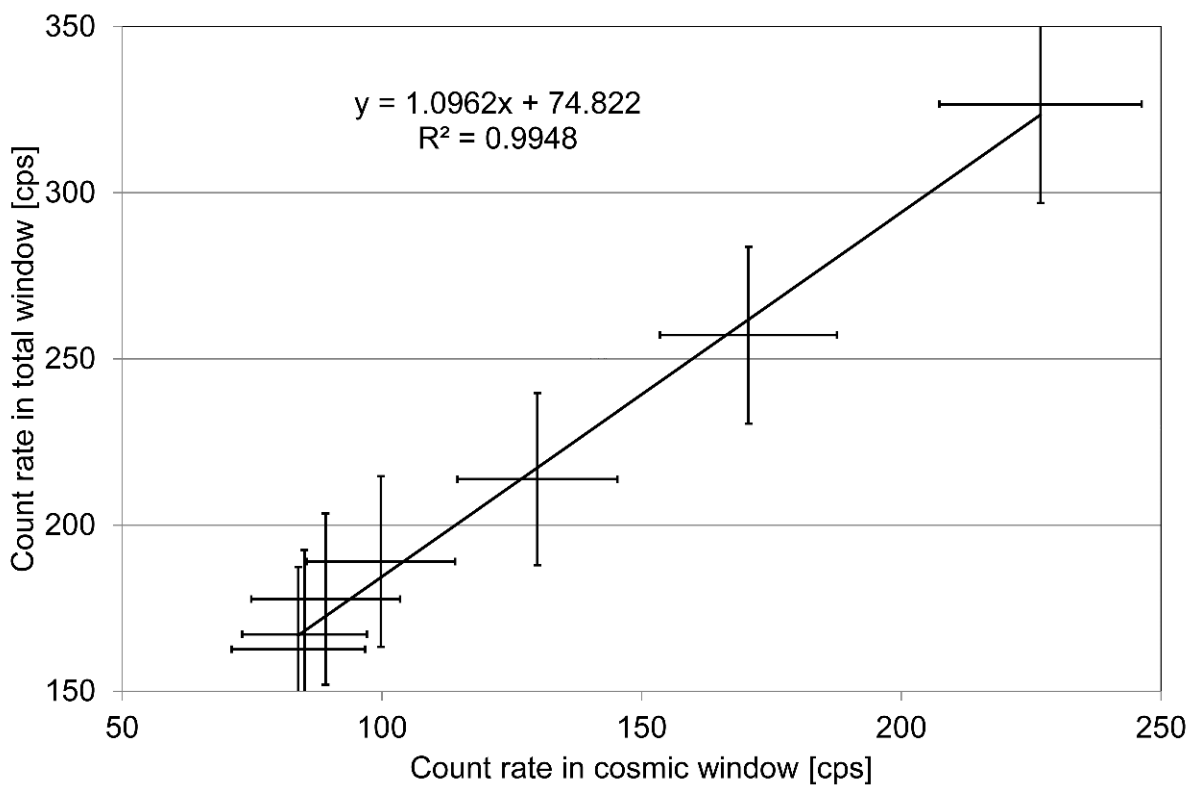
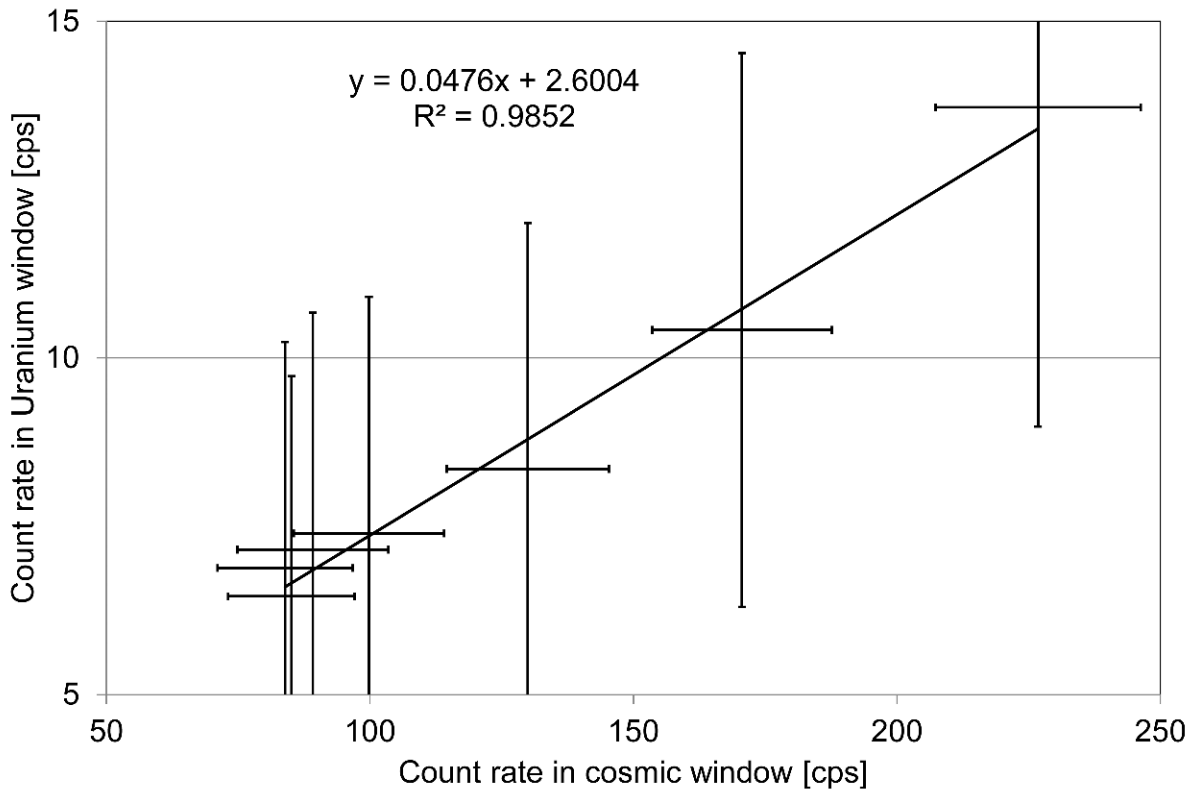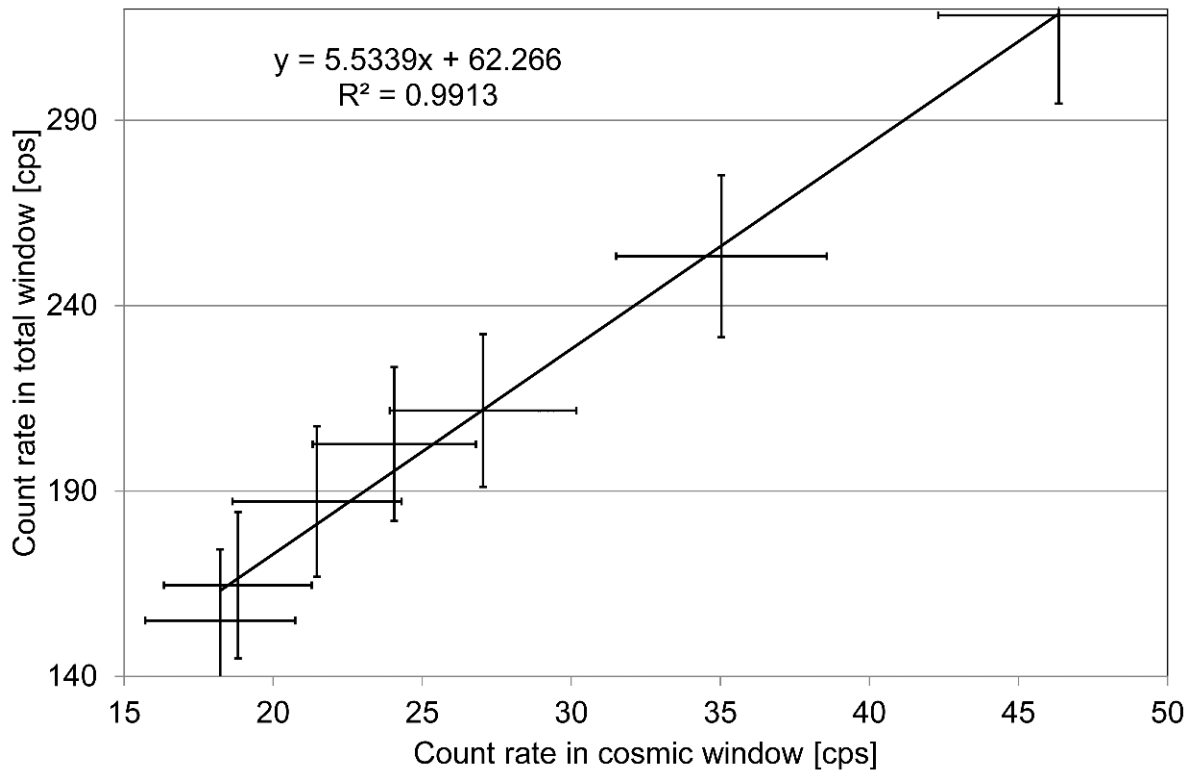Figure 70: Relationship of total count rate to cosmic count rate.
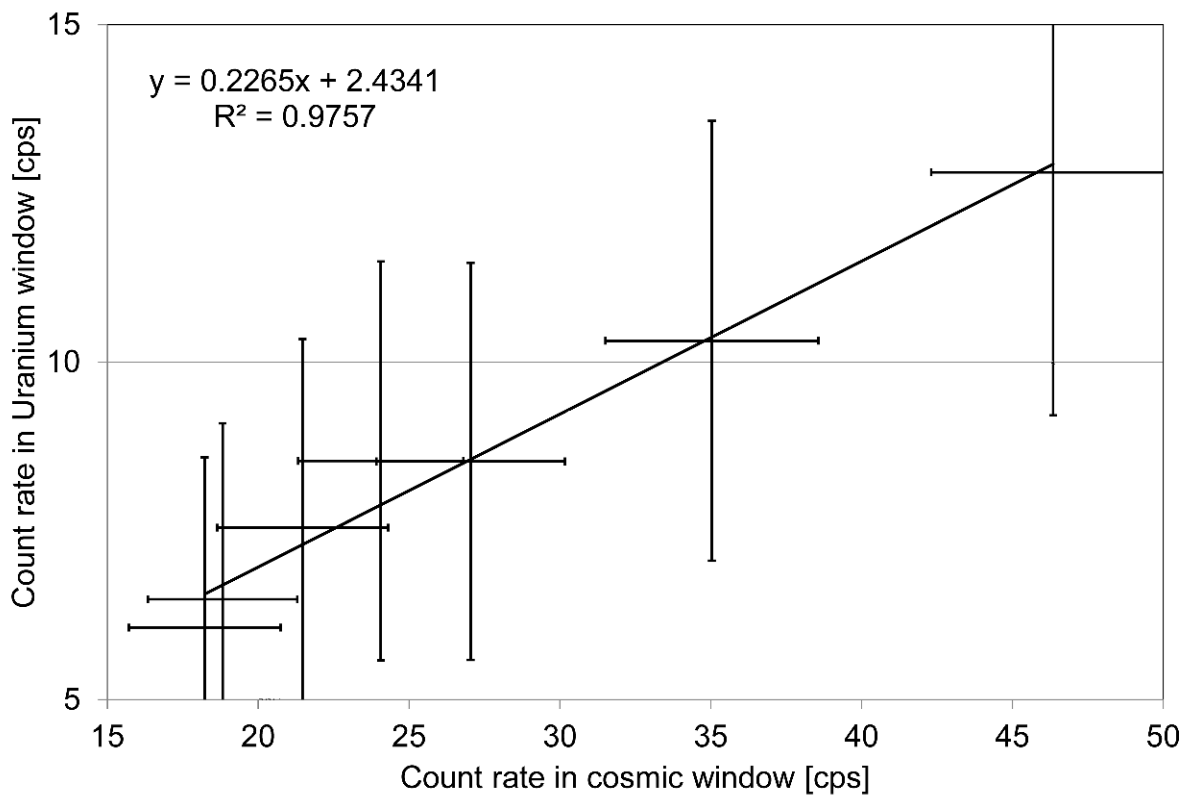
Figure 71: Relationship of count rate in the uranium window to cosmic count rate.

Table 28: Correction factor S_c and background count rate CR_B determined by linear regression together with their uncertainties for the altitude profile over Lake Zug.

Energy window	S_c	$U(S_c)$	CR_B [cps]	$U(CR_B)$ [cps]
Total	5.534	0.463	62.3	13.4
Potassium	0.270	0.033	6.5	0.9
Uranium	0.227	0.032	2.4	0.9
Thorium	0.294	0.029	0.0	0.8
Caesium	0.520	0.089	11.0	2.6
Cobalt	0.540	0.073	7.6	2.1
MMGC1	3.910	0.375	56.3	10.8
MMGC2	1.624	0.094	6.0	2.7

Team CZ01 used the altitude profile over Lake Zug to update the system background in the PRAGA post-processing software. Figure 72 shows the spectrum measured over Lake Zug at an altitude of 2400 m and figure 73 the background spectrum of helicopter and detector derived from the altitude profile. Based on the spectra measured at altitudes from 1200 m to 2400 m over Lake Zug, the helicopter background and cosmic contributions in the individual windows were calculated by the standard method recommended by IAEA. The count rates in individual windows can be described by the following formula, $CR_{bkgd} = CR_{B,Heli} + S_c * CR_{cos}$ where CR_{bkgd} is the background count rate in the appropriate window, $CR_{B,Heli}$ is the background helicopter contribution, S_c is the correction factor for the cosmic channel and CR_{cos} is the count rate in the cosmic channel. The values of $CR_{B,Heli}$ and S_c determined from the altitude profile over Lake Zug are listed in table 29.

Table 29: Background count rate $CR_{B,Heli}$ and correction factor S_c determined for the altitude profile over Lake Zug.

Window [IAEA]	$CR_{B,Heli}$ [cps]	S_c [ ]
Cs	14.5	0.1019
K	12.7	0.1971
U	4.1	0.0593
Th	0.0	0.0632
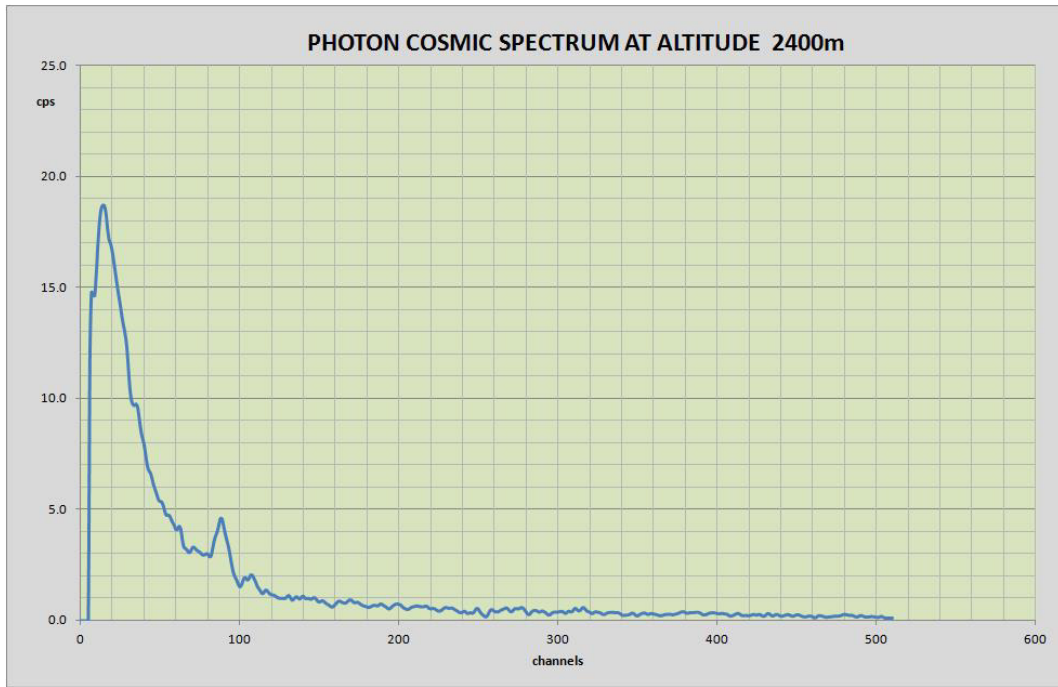
Figure 72: Spectrum at 2400 m altitude measured over Lake Zug by team CZ01.
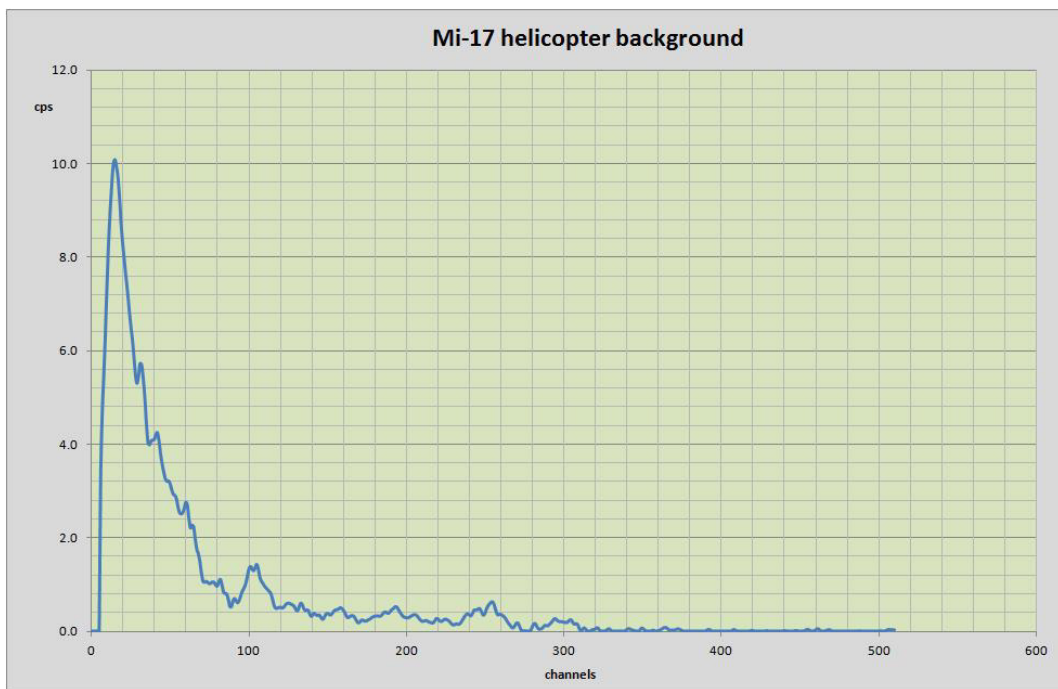
Figure 73: Background spectrum derived from the altitude profile over Lake Zug by team CZ01.

Figures 74 and 75 show the increase of the count rate associated with the most important radionuclides as a function of flight altitude over Lake Zug measured by teams DE01 and DE02, repectively [Helbig et al., 2017]. The background count rates were already used for the data evaluation during the exercise.

The types of detection system and helicopter of teams DE01 and DE02 were identical. Nevertheless, a significant difference between count rates over Lake Zug can be observed. Either airborne radon progeny concentrations were significantly different at the two flights

or background count rates and influence of cosmic radiation have to be determined for each detector-helicopter-combination separately.
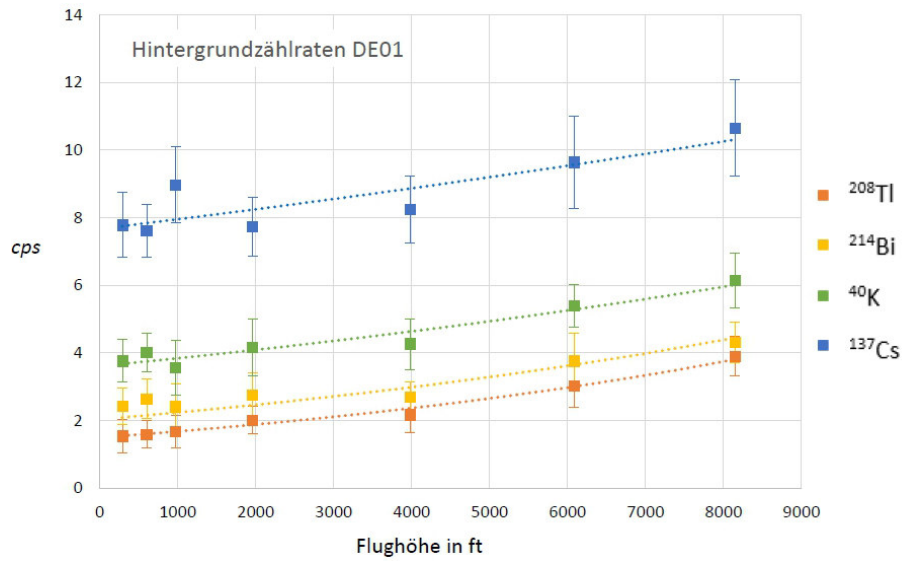
Figure 74: Count rates measured by team DE01 on the altitude profile over Lake Zug (in German).
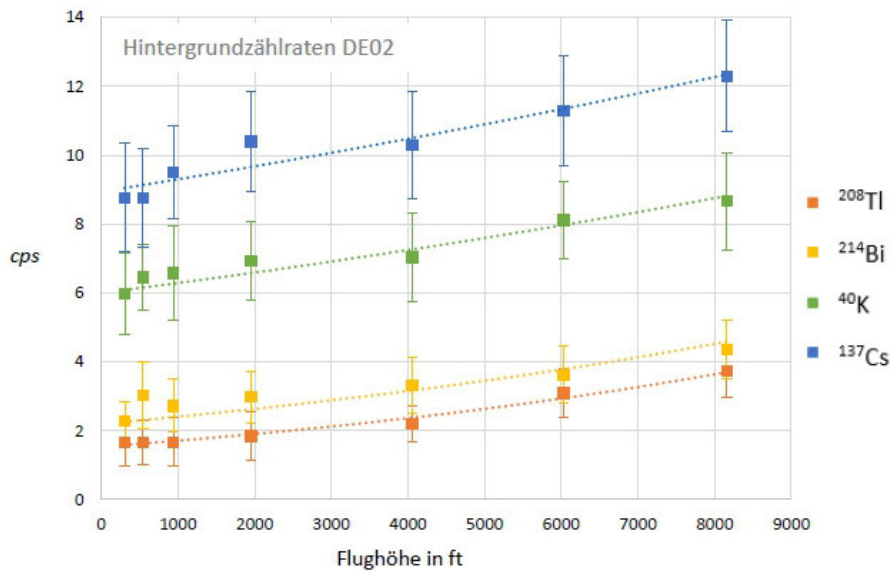
Figure 75: Count rates measured by team DE02 on the altitude profile over Lake Zug (in German).

9 Reference area Linth plain

The Linth plain was selected as one of the two reference areas (figure 76). The Linth plain is located between Lake Zurich and Lake Walen and was flooded as a connection between both lakes in the aftermath of the last ice age. The flooding lasted until the Renaissance. The terrain is rather flat for Swiss topography which is an advantage for the use as reference area. The plain consists largely of alluvial deposits yielding a homogeneous distribution of natural radionuclides. These alluvial deposits are depicted in white colour in the geological map of the area (figure77). Outcrops of various rocks are located around and within the alluvial deposit areas. The geological map "Geocover" is composed of a set of panels, which unfortunately were not completely cleared of inconsistencies. Such inconsistencies can be observed a the border of two panels located at y-coordinate 230000. A feature of the reference area disturbing the homogeneity of measurements is the non-uniform distribution of soil water content, manifesting in pools, marshes and courses of the Linth river, both historical and present day. For a better homogeneity of measurement results, polygons were defined which excluded surface water areas and a formation of calcareous sandstone (green and brown colours in figure 77) in the reference area, depicted with light blue colour in figure 78. Only measuring points falling into the restricting polygons were used in the data analysis described below.

Besides the airborne measurements in the Linth plain, a ground survey at 38 measurement points was performed with portable instruments (for details see section 9.1).

Two flights with different ground clearances were recommended for the reference area, at the standard ground clearance of the individual measuring team and at the ground clearance used for source search and composite mapping (section 12).
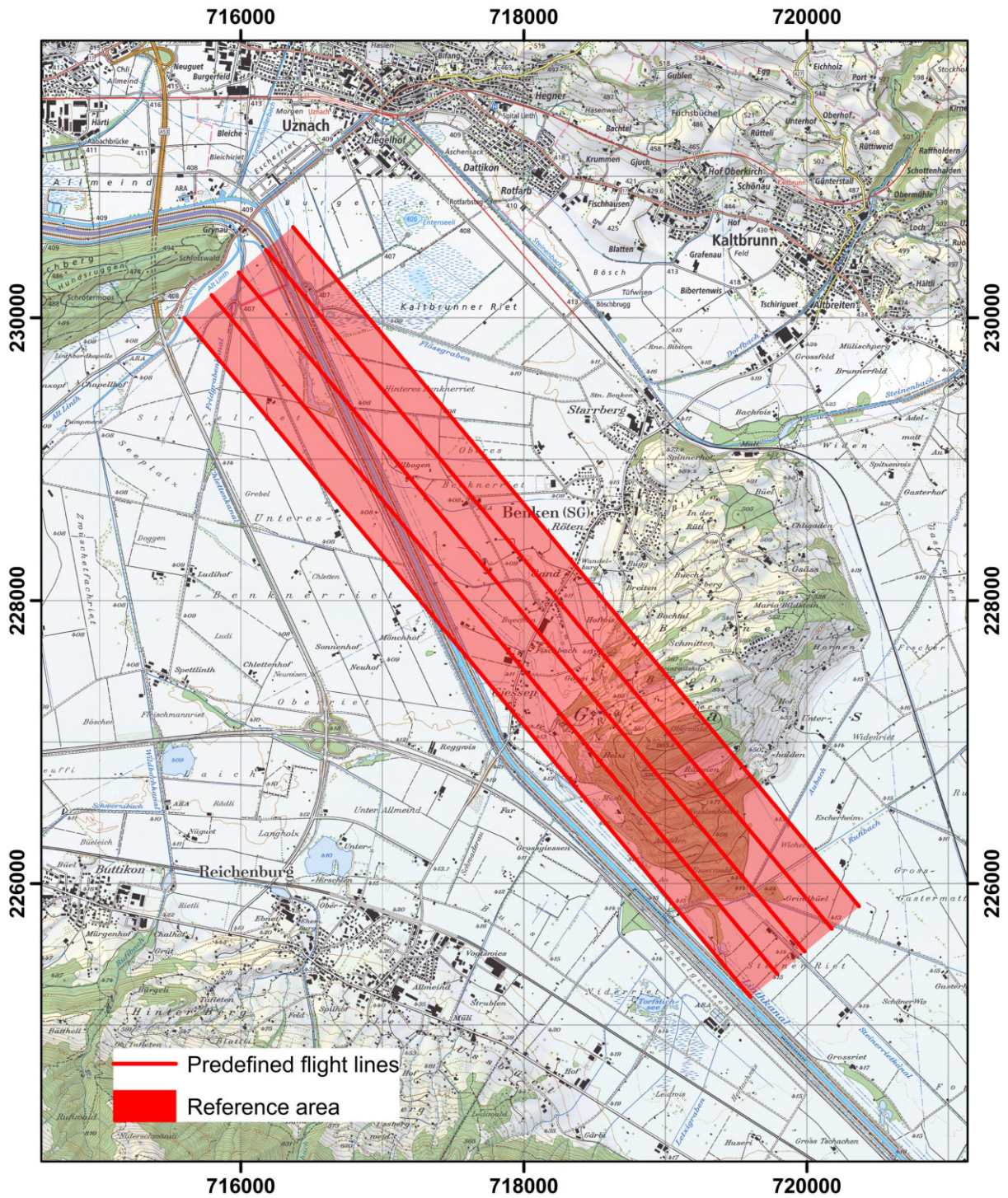
Figure 76: Location of the reference area in the Linth plain. PK25©2017 swisstopo (JD100042).
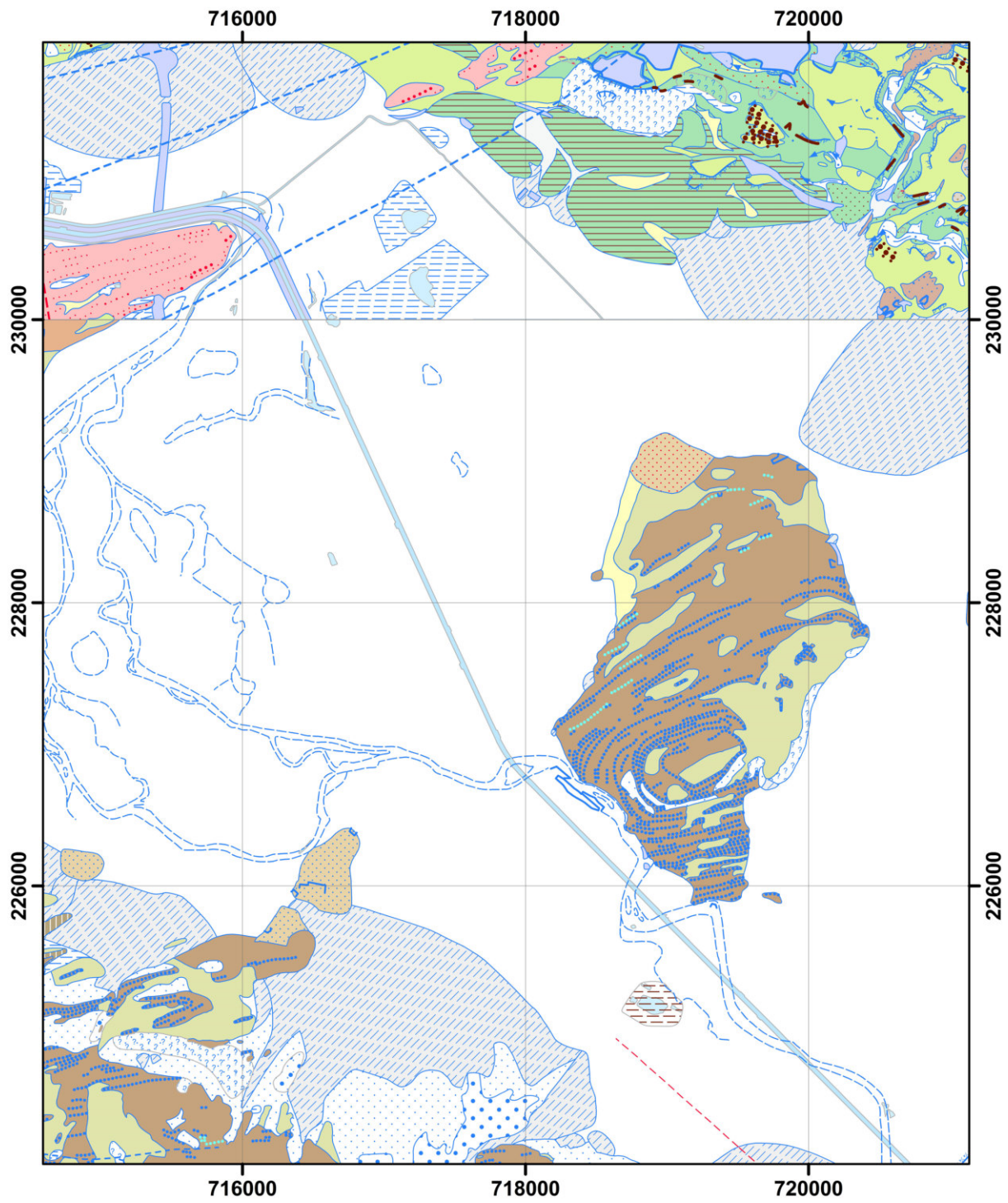
Figure 77: Geology of the reference area. Geocover©2017 swisstopo (JD100042).

Figure 78: Restricting polygons (light blue) in the reference area. PK25©2017 swisstopo (JD100042).

9.1 Results

The radionuclide content and the dose rate was measured with in-situ gamma-spectrometry and a high quality scintillation probe (Automess AD-b) at 54 points in or near the reference area by staff of the NBC-EOD centre of competence. Additionally, the dose rate was measured at one of these points (coordinate 717590, 229411) with the Swiss reference instrument for environmental dose rate, a high-pressure ionisation chamber extensively calibrated at the Physikalisch-Technische Bundesanstalt (PTB) in Germany. The reference dose rate dH*(10)/dt at the reference point was determined to (103 ± 7) nSv/h, consisting of 53 nSv/h due to Photons from terrestric radionuclides, 38 nSv/h due to charged particles and photons from cosmic radiation and 12 nSv/h due to neutrons from cosmic radiation.

The reference dose rate was determined using a height dependence of the cosmic dose rate including the dose rate originating from neutron radiation (see Bouville and Lowder,1988 and UNSCEAR, 2008):

$$DR_{cosmic} = DR_{neutron} + DR_{charged} = 8.963e^{0.78z} + 32.594e^{0.38z} \qquad (9.1.0.1)$$

with:

DR_{cosmic}: Cosmic dose rate $dH^*(10)/dt$ at height z above sea level [nSv h^{-1}]
$DR_{neutron}$: Cosmic dose rate $dH^*(10)/dt$ at height z above sea level
     originating from neutron radiation [nSv h^{-1}]
$DR_{charged}$: Cosmic dose rate $dH^*(10)/dt$ at height z above sea level
     originating from charged particles and photons [nSv h^{-1}]
z: Height above sea level [km]

The scintillation probe used by the NBC-EOD centre of competence measured 92 nSv/h at the reference point. The Automess AD-b probe is sensitive both to photons and charged particles but blind to neutron radiation. This sensitivity characteristic was determined during type testing of the probe performed in the PTB calibration laboratories. Thus, the measured dose rate had to be compared to the reference dose rate due to photons and charged particles of 53 nSv/h + 38 nSv/h = 91 nSv/h, which agrees well with the measured value yielding a correction factor of 0.99. As the Linth plain is sufficiently flat, the dose rate of 12 nSv/h due to neutrons was added to all measuring points after the correction factor was applied. 39 of the ground measurement points were located in the restricting polygons (figure 79). The corrected results of dose rate dH*(10)/dt at these selected measuring points are listed in table 30.

The radionuclide activity concentration at the ground measurement points was determined using high purity germanium (HPGe) detectors. The angular responses of the detectors were calibrated with [241]Am and [152]Eu point sources. The response to volume and surface source distributions was calculated from these data using transfer factors published in ICRU Report 53. The activity concentrations of [238]U and [232]Th were determined using Photon emissions of their radioactive decay products [214]Bi and [208]Tl. The activity concentrations at the points located in the restricting polygons are listed in table 30.
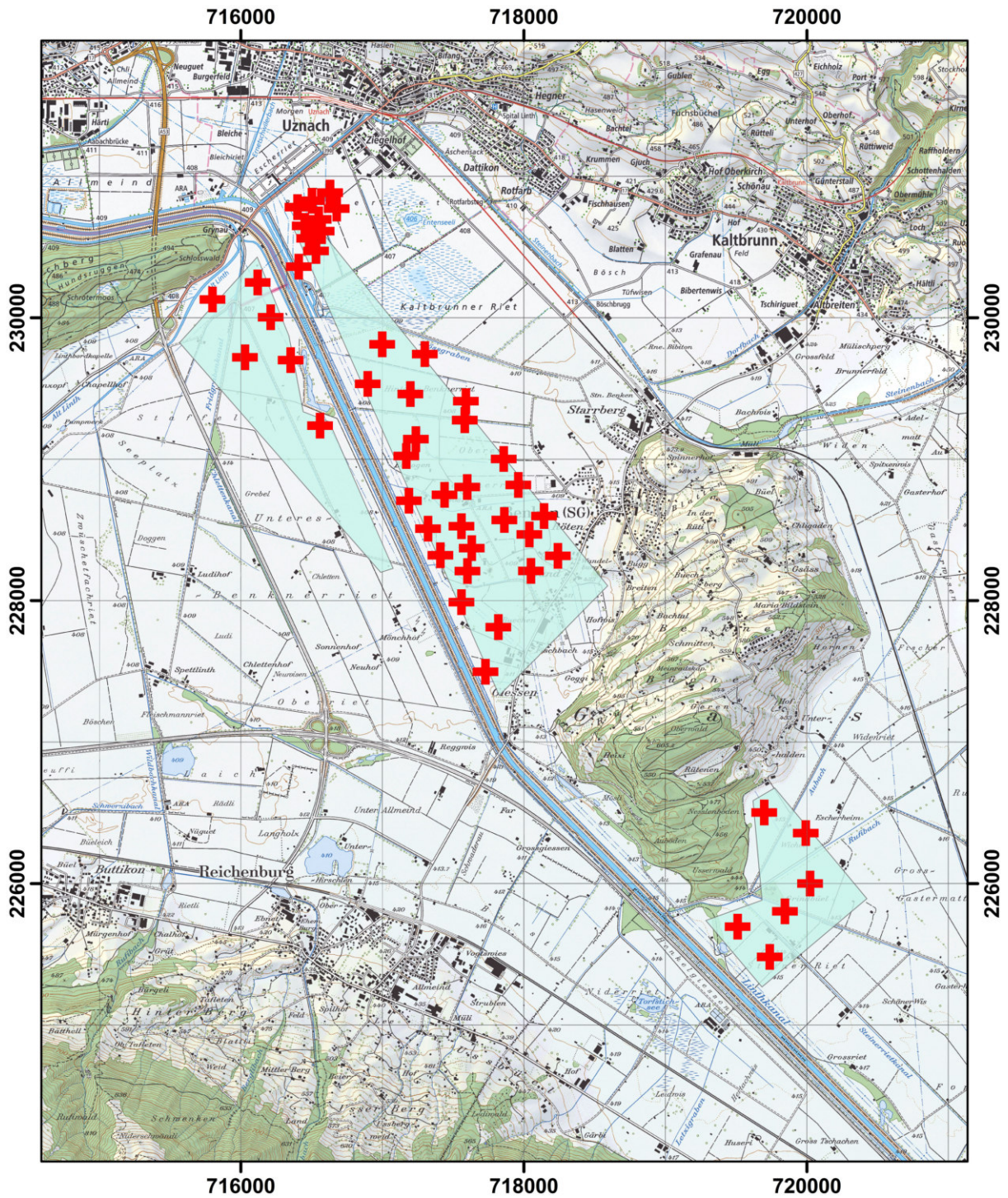
Figure 79: Locations of ground measurements in the reference area. PK25©2017 swisstopo (JD100042).

Table 30: Results of ground measurements.

Coordinate		Dose rate	Activity concentration			
x [m]	y[m]	[nSv/h]	^{40}K [Bq/kg]	^{238}U [Bq/kg]	^{232}Th [Bq/kg]	^{137}Cs [Bq/m^2]
716029	229721	109	365	16	21	1109
716119	230250	113	517	33	30	639
716211	230004	122	456	27	27	576
716352	229701	111	444	29	32	850
716452	230650	109	379	19	24	452
716483	230562	108	365	23	28	940
716531	230473	110	296	22	23	1271
716560	229238	116	433	29	31	929
716897	229533	103	248	19	16	1151
716999	229813	105	389	23	28	694
717170	229023	124	469	30	36	853
717198	229461	115	425	25	29	1049
717237	229143	114	282	19	19	874
717323	228510	118	434	29	38	962
717410	228322	113	414	29	29	622
717440	228749	102	347	26	24	1006
717559	227990	115	369	26	28	214
717559	228527	126	382	28	34	1158
717583	229277	85	238	17	11	639
717583	229277	85	373	22	27	994
717600	228804	99	377	26	22	577
717602	228210	125	390	28	31	1265
717632	228372	123	461	34	29	507
717820	227814	109	534	34	44	613
717858	229002	113	292	22	25	447
717862	228571	115	482	28	37	741
717938	227974	123	499	25	41	609
717961	228819	118	328	24	27	892
718039	228469	119	334	28	22	1115
718050	228211	126	491	28	36	510

Table 30: Results of ground measurements (continued).

Coordinate		Dose rate	Activity concentration			
x [m]	y[m]	[nSv/h]	^{40}K [Bq/kg]	^{238}U [Bq/kg]	^{232}Th [Bq/kg]	^{137}Cs [Bq/m^2]
718143	228599	113	444	26	36	563
718241	228317	118	405	31	38	1094
719511	225696	112	369	29	27	575
719699	226503	98	214	27	21	789
719738	225482	103	310	21	20	1546
719845	225804	103	478	29	32	826
719993	226358	96	206	18	13	697
720023	226001	113	378	28	21	552
Average		111	383	25	28	811
Standard deviation		10	83	5	7	279

The comparison of the results of airborne measurements by team CH01 to the ground measurements in the restricting polygons shows clearly the effect of the faulty detector described in section 6.1. The dose rate (-11%) and activity concentrations of ^{40}K (-27%) and ^{232}Th (-29%) are clearly underestimated, whereas the activity concentrations of ^{238}U and ^{137}Cs are overestimated by 81% and 12%, respectively (figure 80). The latter overestimation can be associated with the faulty energy calibration of crystal three. On the other hand, it is more probable that the overestimation of ^{238}U activity concentration is caused by the lack of a correction for airborne radon progeny in the evaluation procedures of team CH01. This assumption is confirmed by the results for the reconstructed data, lowering the relative deviation to the ground measurements to about three percent for all quantities except ^{238}U activity concentration.

Applying the values for cosmic stripping derived from the altitude profile over Lake Zug (section 8.1), the deviations between ground and airborne measurements increase for dose rate, potassium and thorium, making a revision of calibration factors necessary. The results calculated using both the revised cosmic stripping and the calibration factors show now agreement with the ground measurements (figure 80) for the standard ground clearance of 98 m. The revised parameter file for team CH01 is listed in section 18.4. The radiological maps derived for the reference area Linth plain after the corrections are depicted for both ground clearances in figures 93, 106, 132, 119, 94, 107, 133 and 120.
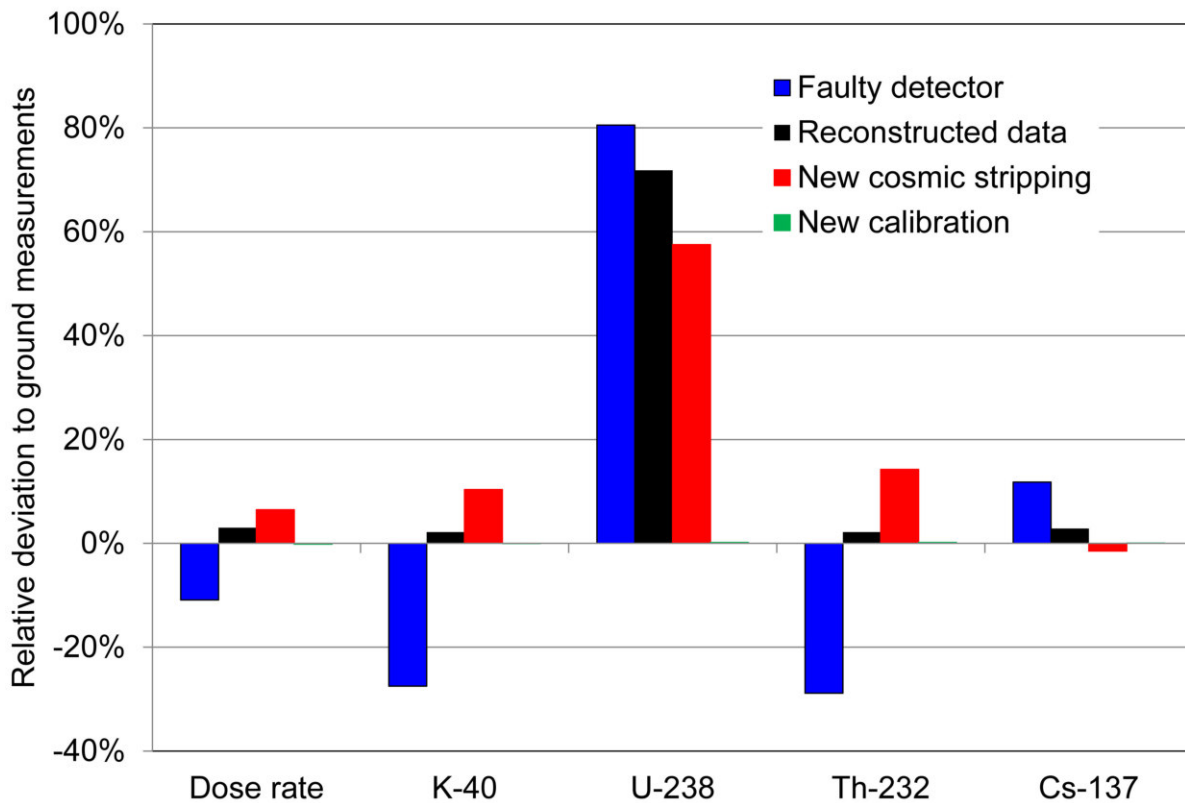
Figure 80: Influence of corrections for team CH01 at a ground clearance of 98 m.

Whereas adjustment of parameters used in the data evaluation with the RLL software (section 3.2) is principally possible, the man-power for a detailed analysis of measurement results and their impact for the individual evaluation parameters is not available at KompZen ABC-Kamir. Thus, no correction was performed based on the results of the ground measurements in the Linth plain reference area (figures 95, 108, 134, 121, 94, 107, 133, 120). Nevertheless, as the RLL system will replace the ARM system of team CH01 in 2018, the measurement results were used to determine calibration factors for RLL detector 002 to be used with the ARM evaluation software. The raw data were directly extracted from the respective data files (*.mdm) provided by the RLL software and stored in ERS 1.0 format. The correction of ground clearance and topography included in the ARM software are based on a digital elevation model with altitudes relative to the WGS84 ellipsoid. The altitude used in the RLL system is directly derived from the military GPS of the helicopter, which in contrast to the GPS of the ARM system is based on the geoid as reference surface. The RLL altitudes were referenced to the WGS84 ellipsoid interpolating an undulation table with one minute spacing published by the National Geospatial-Intelligence Agency (NGA) (Pavlis et al., 2008).

The calibration factors were determined using values determined for a detector of the ARM system with nearly identical geometry as a starting point. The relative deviation of the thus determined concentrations and dose rates over the reference area to the ground values was then used for adjustment. As ^{137}Cs-activity concentrations were below detection limit, the calibration factor was adjusted using the average deviation found for the natural radionuclides. Table 31 shows the resulting calibration factors for natural and man-made radionuclides, which are used in the according parameter file for the data evaluation (section 18.5). The results of the evaluation of the RLL raw data with the ARM software and the adapted calibration factors are shown in figures 97, 110, 136, 123, 98, 111, 137 and 124.

99

Table 31: Calibration factors derived for RLL detector 002 based on the ground measurements to be used in data evaluation with existing ARM software.

Nuclide	source geometry	ERS-Identifier	Calibration factor	Unit
^{40}K	homogeneous	AD_K-40	7.27	Bq kg^{-1} cps^{-1}
^{238}U	homogeneous	AD_U-238	2.63	Bq kg^{-1} cps^{-1}
^{232}Th	homogeneous	AD_Th-232	1.50	Bq kg^{-1} cps^{-1}
^{137}Cs	homogeneous	AD_Cs-137	2.00	Bq kg^{-1} cps^{-1}
^{137}Cs	surface	AA_Cs-137	34.99	Bq m^{-2} cps^{-1}
^{137}Cs	point	AP_Cs-137	7.53	MBq cps^{-1}
^{60}Co	point	AP_Co-60	2.61	MBq cps^{-1}

Team CZ01 used the measurements in the reference area to compare several evaluation procedures for post-processing (see section 3.3) with a background revised due to the measurements over Lake Zug (see section 8.1). For a comparison of results, averages over a part of the measuring area (figure 81) were calculated. The averaging area used by team CZ01 differs from the restricting polygons defined for the reference area (figure 78). As the water bodies were included in the averages of team CZ01, a bias toward lower dose rates and activity concentrations can be expected. Figures 82 and 83 show the results of different evaluation procedures for the measurement with 90 m and 150 m target ground clearance. The values of this comparison are listed in tables 32 and 33. Figures 99, 112, 138, 125, 100, 113, 139 and 126 show the corrected radiological maps for ground clearances of 105 m and 145 m after post-processing.
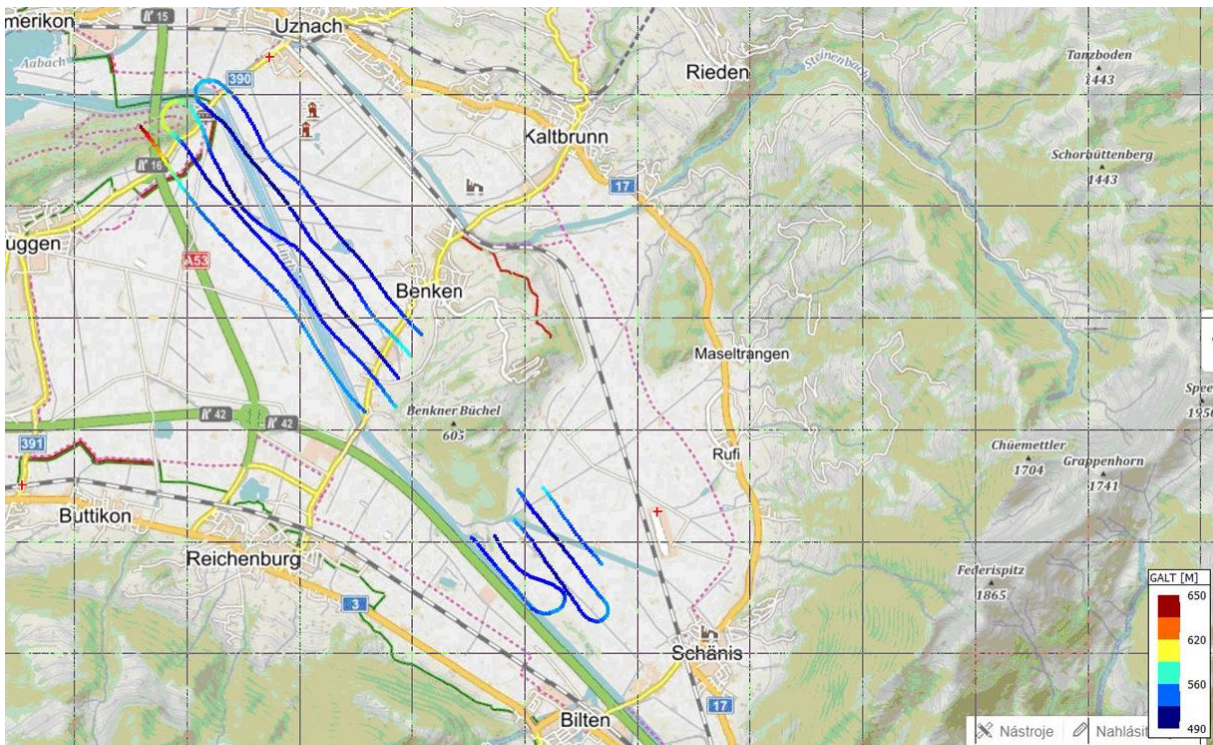
Figure 81: Averaging area used by team CZ01.

Figure 82: Comparison of the results of different evaluation procedures used by team
CZ01 for a target ground clearance of 90 m.

Table 32: Comparison of different evaluation procedures of team CZ01 for a
measurements with a target ground clearance of 90 m to ground measurements
(Swiss-GND).

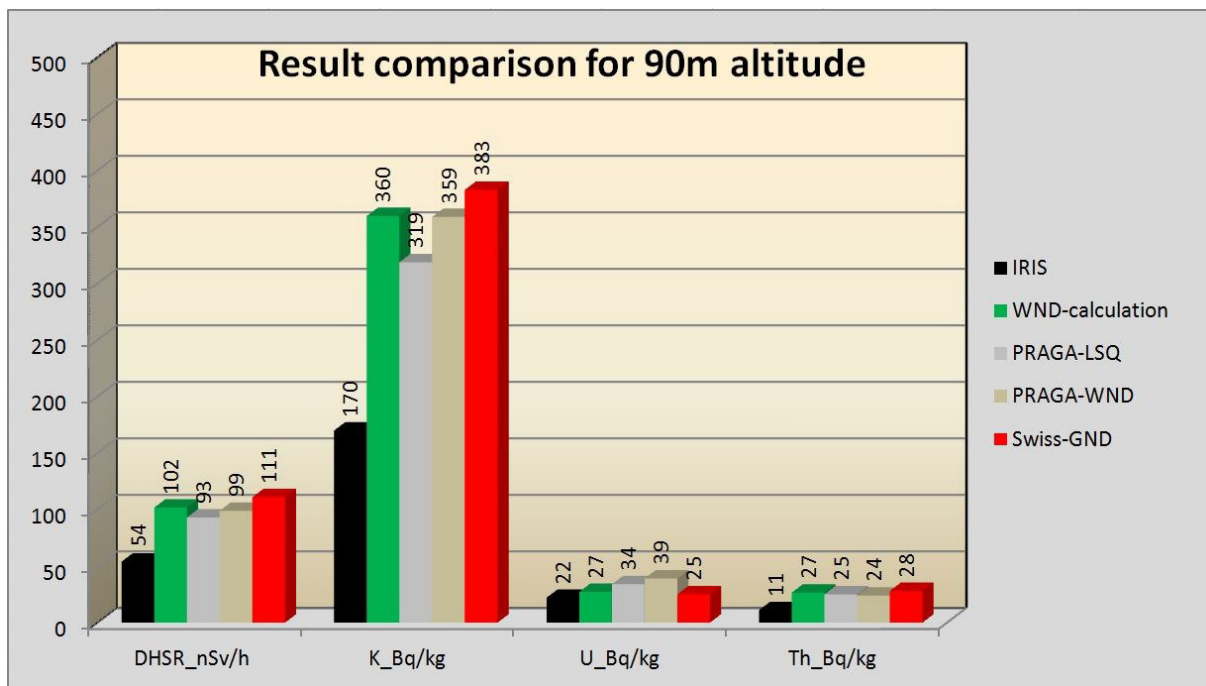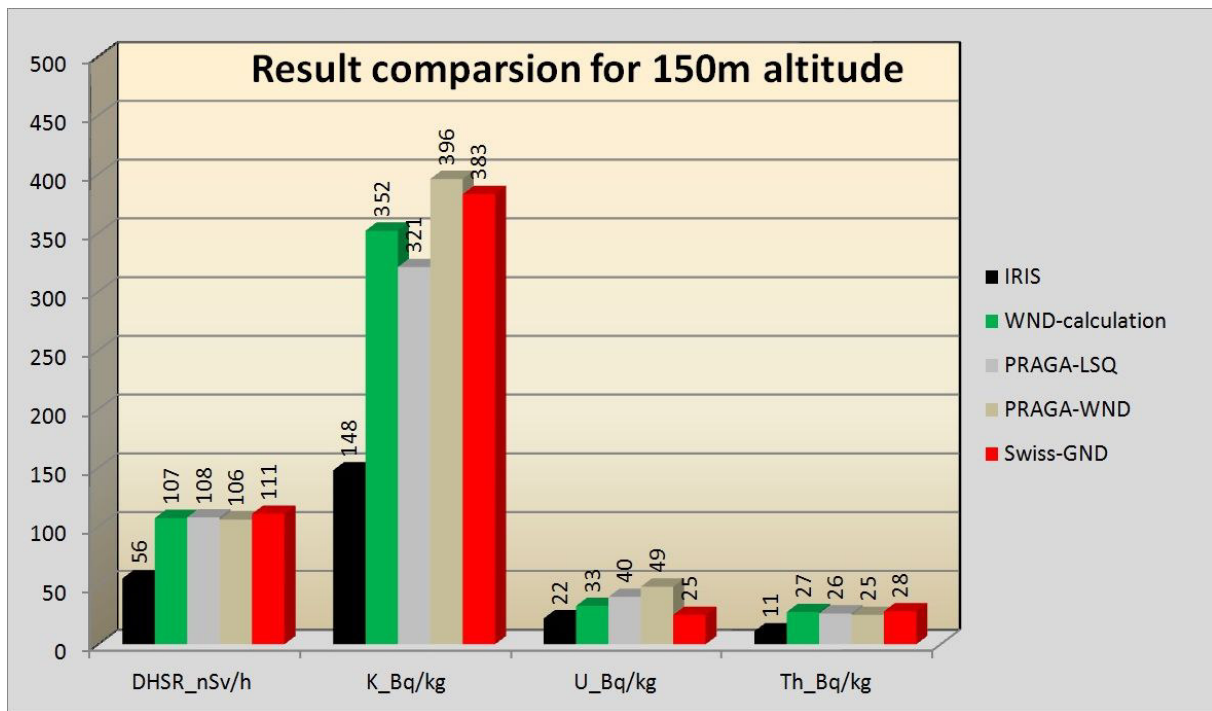| Procedure	DHSR [nSv/h]	K [Bq/kg]	U [Bq/kg]	Th [Bq/kg]
IRIS (raw)	54	170	22	11
AGAMA-WND	102	360	27	27
PRAGA-LSQ	93	319	34	25
PRAGA-WND	99	359	39	24
Swiss-GND	111	383	25	28

Figure 83: Comparison of the results of different evaluation procedures used by team CZ01 for a target ground clearance of 150 m.

Table 33: Comparison of different evaluation procedures of team CZ01 for a measurements with a target ground clearance of 150 m to ground measurements (Swiss-GND).

Procedure	DHSR [nSv/h]	K [Bq/kg]	U [Bq/kg]	Th [Bq/kg]
IRIS (raw)	56	148	22	11
AGAMA-WND	107	352	33	27
PRAGA-LSQ	108	321	40	26
PRAGA-WND	106	396	49	25
Swiss-GND	111	383	25	28

Teams DE01 and DE02 used the altitude profile over Lake Zug (see section 8.1) already for the results reported during the exercise. No further corrections based on the ground measurements were applied. Data points below the decision limit were excluded leading to gaps in the area coverage. Both teams measured in the reference area with target ground clearance of 100 m. The radiological maps with the results of team DE01 measured with an average ground clearance of 114 m and of team DE02 with an average ground clearance of 116 m are depicted in figures 101, 114, 140, 127, 103, 116, 142 and 129.

Team DE01 measured a second set of data with a ground clearance of 130 m and line spacing of 500 m as used in the source search and composite mapping (figures 102, 115, 141 and 128).

The radiological maps of team FR01 after post-processing are shown in figures 104, 117, 143, 130, 105, 118, 144 and 131 for ground clearances of 96 m and 159 m.

9.1.1 Comparison

Team CH01 used a correction for the faulty detector (section 6.1), revised cosmic stripping from the altitude profile over Lake Zug (section 8.1) and revised calibration factors derived from the comparison with the ground data (section 9.1.1). The values for team CH02 were evaluated using the software of the ARM system with parameters derived from laboratory measurements and results of this exercise (listed in section 18.5).

Team CZ01 used the PRAGA software for post-processing with a background revised due to the measurements over Lake Zug (see section 8.1). The post processed values were not adjusted using the ground measurements provided for the reference area in the Linth plain. Team FR01 used a different algorithm for post-processing. Teams DE01 and DE02 used the altitude profile over Lake Zug (see section 8.1) already for the results reported during the exercise. During post processing data points were eliminated according to quality criteria, especially values below the decision limit.

Figure 84 shows the average dose rate measured over the restricting polygons in the reference area of the Linth plain as reported during the exercise. The error bars depict the standard deviation of all measurements located in the restricting polygons. All dose rates derived from airborne measurements are somewhat lower (6% to 20%) compared to the value derived from ground measurements. A possible reason may be an inadequate consideration of the dose rate originating from neutrons produced by cosmic radiation.

The dose rates reported by the Czech team for both heights above ground during the exercise are significantly lower compared to all other results. The immediate data evaluation was performed with software provided by the manufacturer of the measuring system. Figure 85 repeats figure 84 after corrections were applied if applicable for the team. The dose rates evaluated by team CZ01 with PRAGA post-processing do not show the difference observed in the values reported during the exercise, indicating a maladjustment of the algorithms used by the manufacturer of the system. The dose rates obtained with post-processing overestimate the dose rate measured on the ground by 10% at a ground clearance of 100 m and 28% at a ground clearance of 140 m.

The average dose rate measured by team CH01 without corrections (figure 84) is lower compared to the result of the ground measurements due to the faulty crystal (figure 80). As should be expected, the values both for team CH01 and the evaluation of the raw data of team CH02 with the ARM software after corrections agree well with the ground measurements.

The uncorrected airborne results for the activity concentrations of ^{40}K (figure 86), ^{238}U (figure 90) and ^{232}Th (figure 88) show compared to the ground measurements lower values for teams CZ01, CH01 and CH02 and higher values for teams FR01, DE01 and DE02. After corrections and post-processing performed by teams FR01, CZ01, CH01 and CH02, the latter evaluated with the ARM Software of team CH01, better agreement with the ground measurements is mostly achieved (figures 87, 91) and 89). The overestimation of ^{40}K activity concentration observed in the uncorrected results of team FR01 (figure 86) is replaced with a slight underestimation after post-processing (figure 87). The quality assurance process of teams DE01 and DE02 eliminated values of ^{238}U activity concentration for all measured data points (figure 91).

The activity concentration of ^{137}Cs, originating from the Chernobyl accident, of 811 Bq/m^2 measured on the ground is well below the detection limit of the airborne systems. Figure 92 shows the results of team CH01 and team CH02 after corrections were applied. The values averaged over the reference area agree well with the ground measurements, albeit standard deviations over all points in the same magnitude as the reported averages.
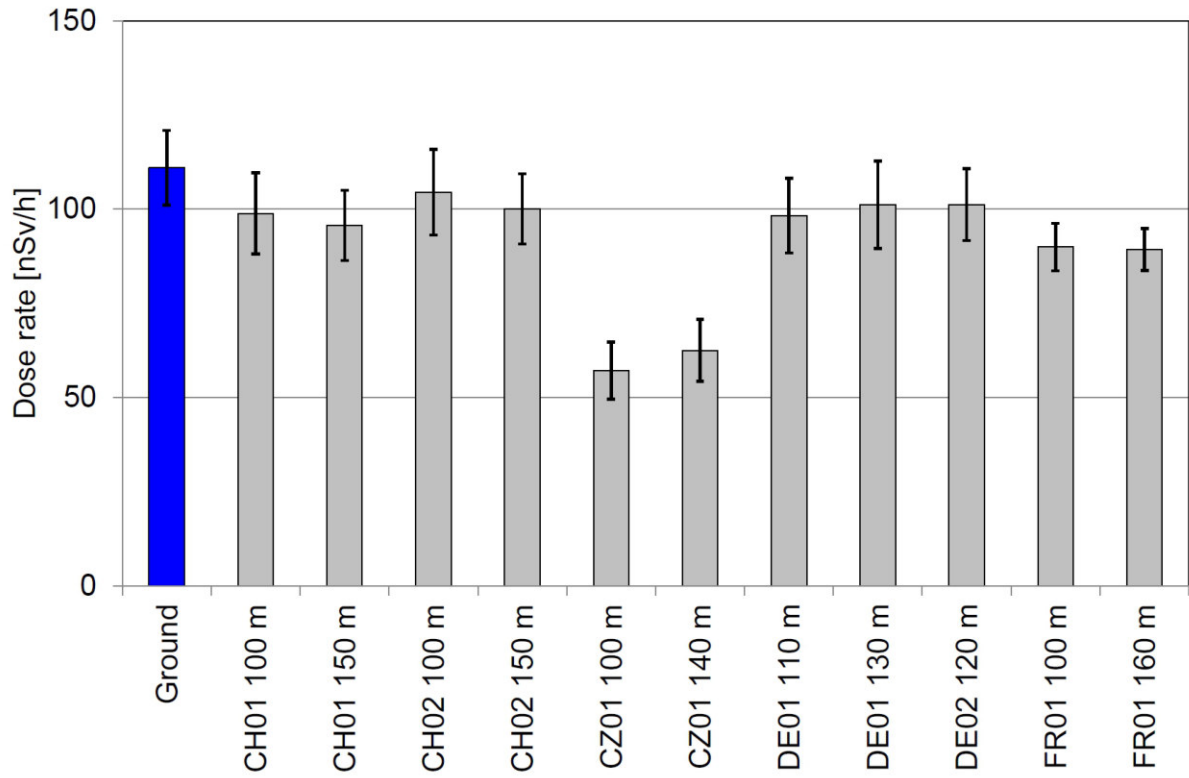
Figure 84: Comparison of dose rate measurements.
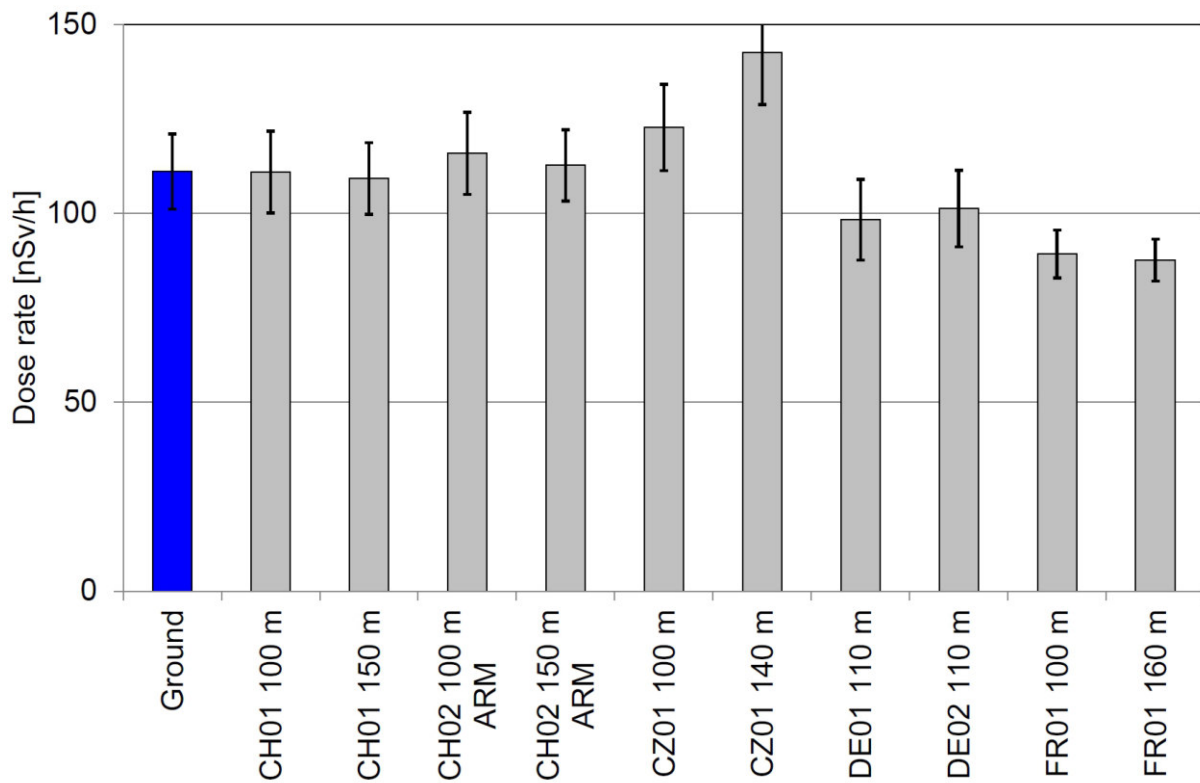

Figure 85: Comparison of dose rate measurements after corrections. Raw data measured by team CH02 were evaluated using the ARM software of team CH01.

Figure 86: Comparison of ^{40}K activity concentrations.

Figure 87: Comparison of ^{40}K activity concentrations after corrections. Raw data measured by team CH02 were evaluated using the ARM software of team CH01.
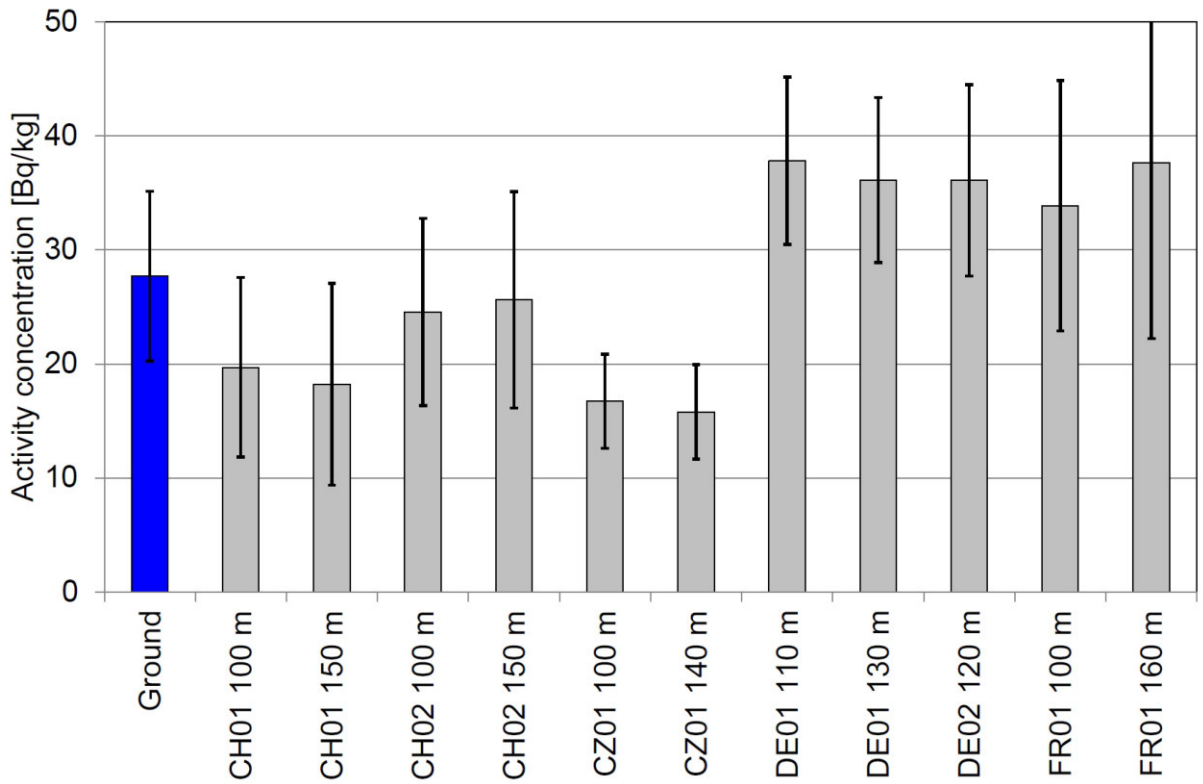
Figure 88: Comparison of ^{232}Th activity concentrations.
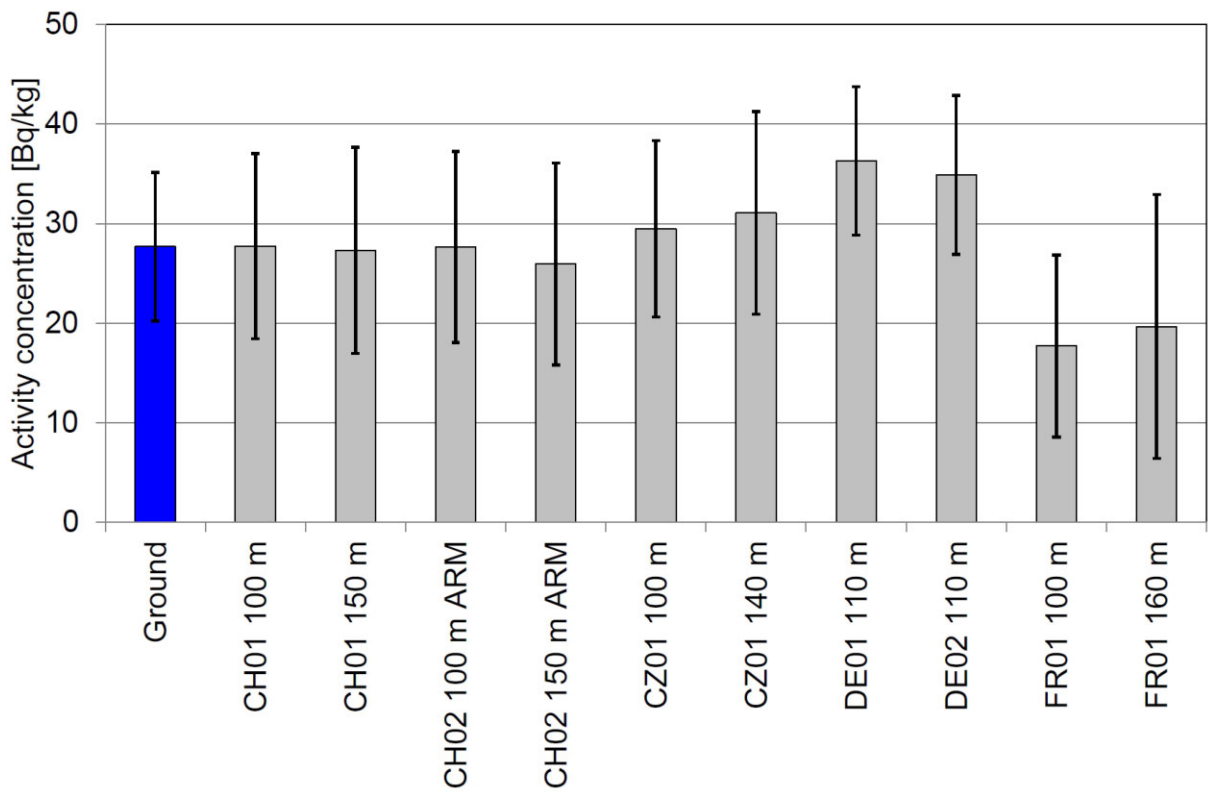
Figure 89: Comparison of ^{232}Th activity concentrations after corrections. Raw data measured by team CH02 were evaluated using the ARM software of team CH01.
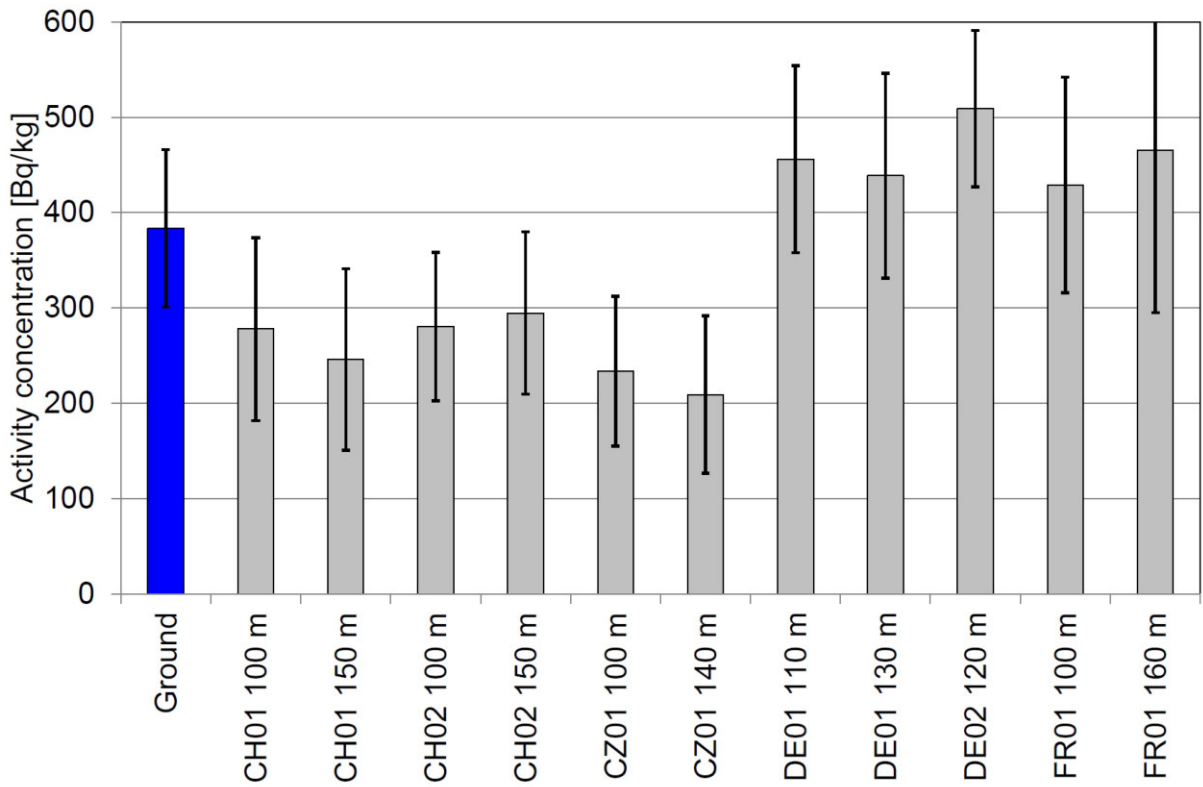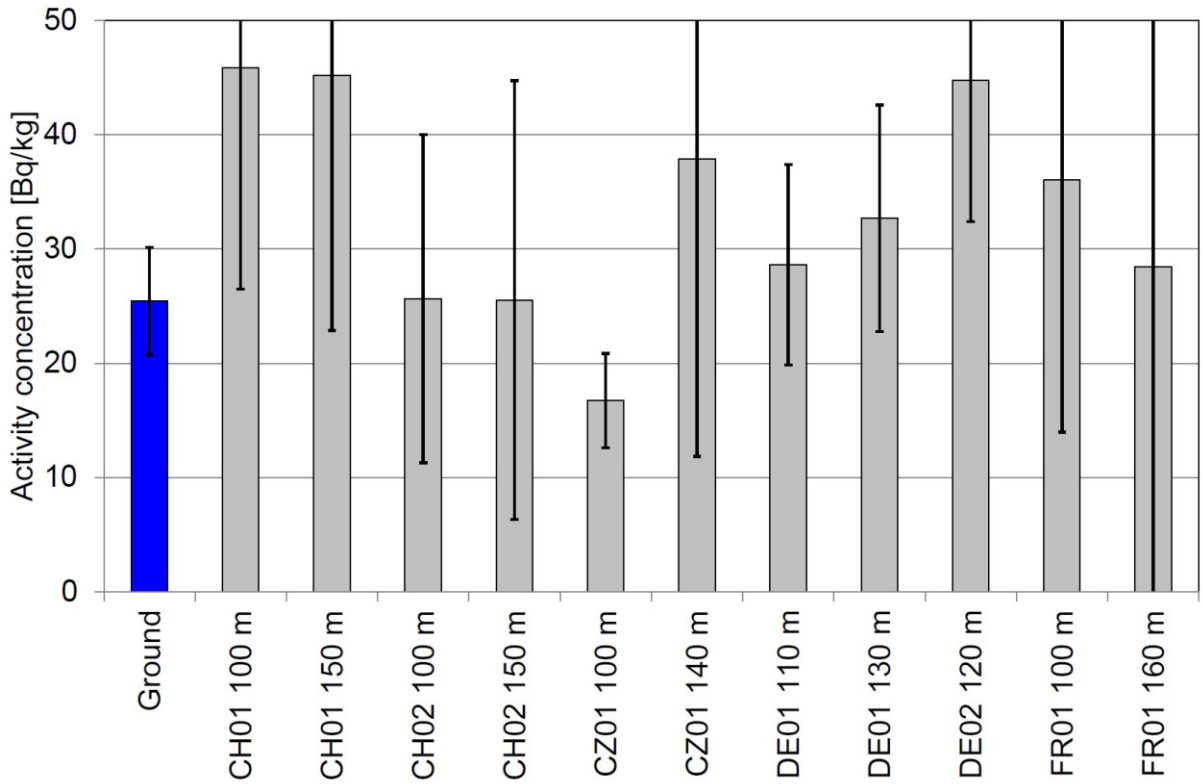
Figure 90: Comparison of ^{238}U activity concentrations.
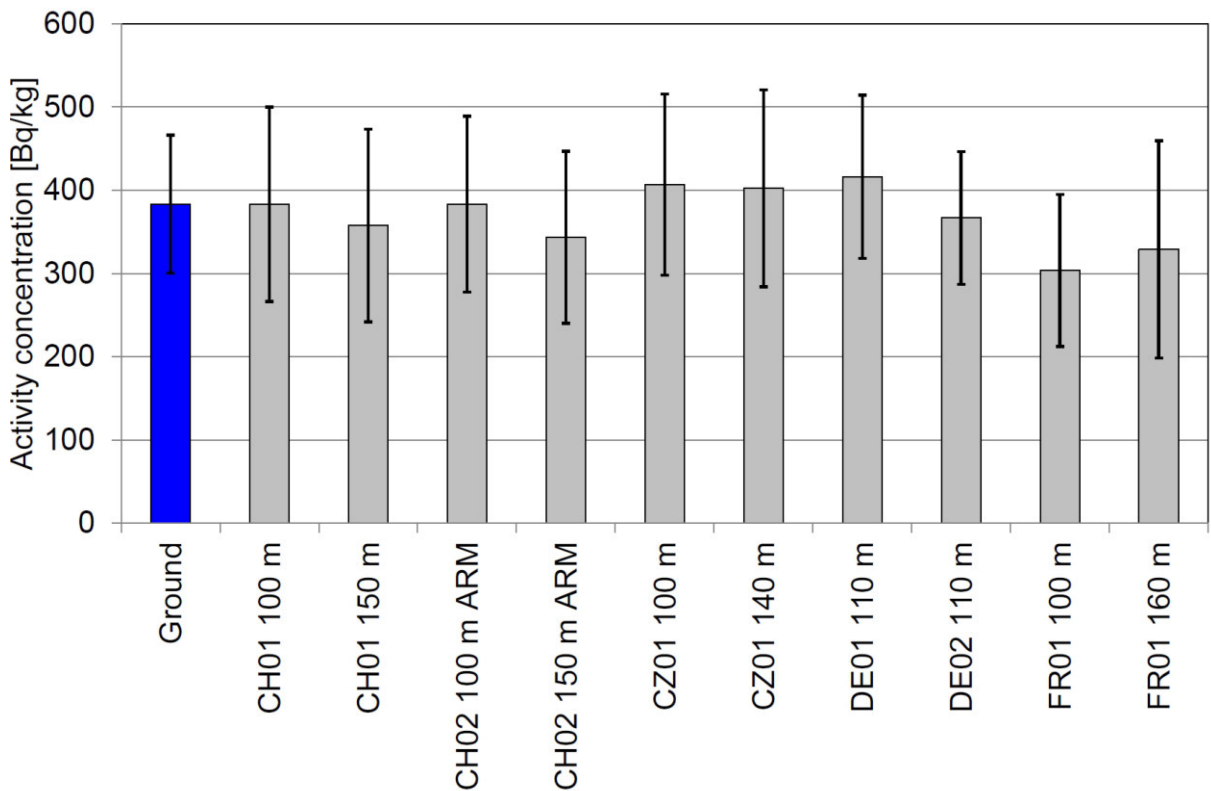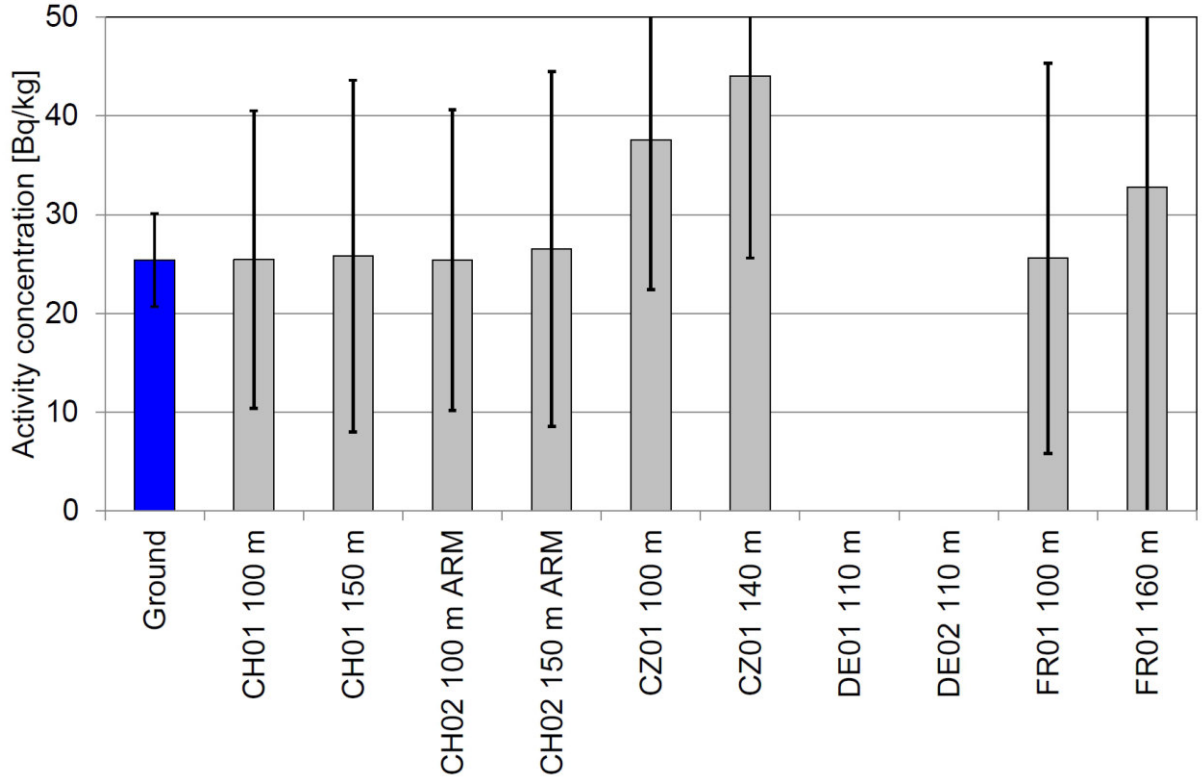

Figure 91: Comparison of ^{238}U activity concentrations after corrections. Raw data measured by team CH02 were evaluated using the ARM software of team CH01.
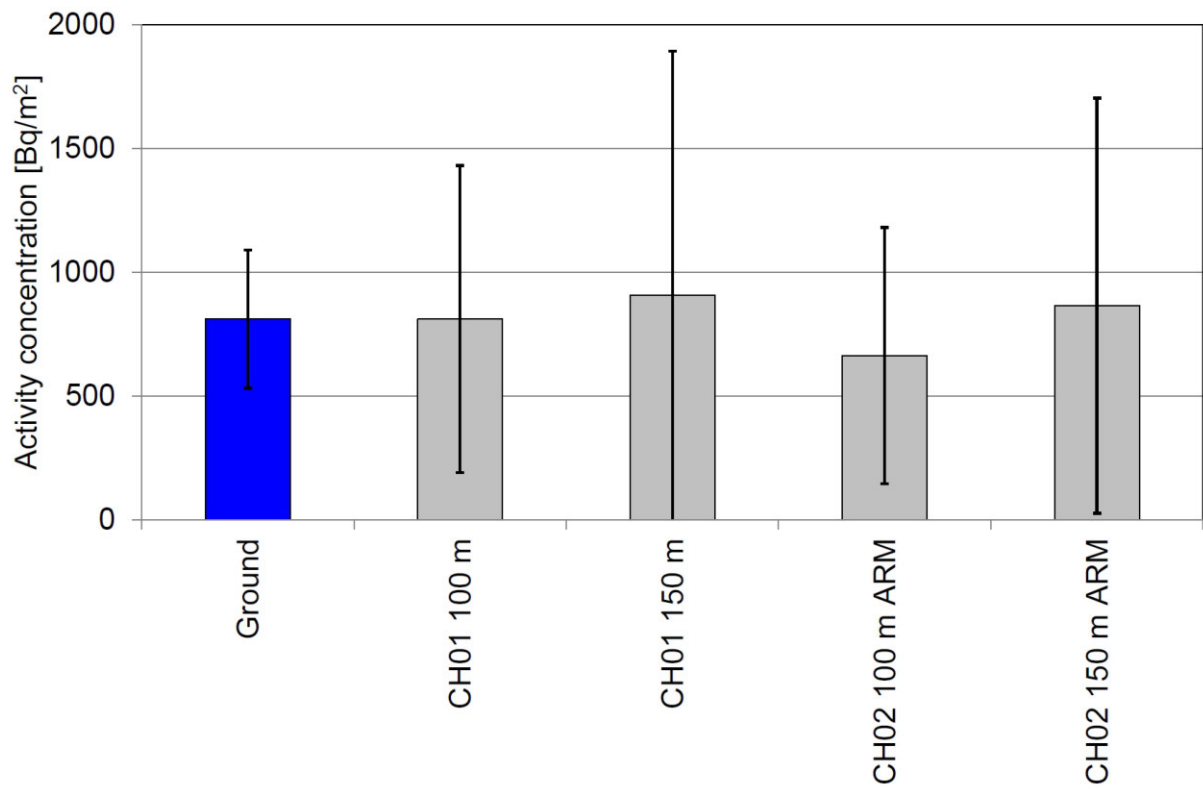
Figure 92: Comparison of ^{137}Cs activity concentrations after corrections. Raw data measured by team CH02 were evaluated using the ARM software of team CH01.

9.1.2 Maps

Figure 93: Dose rate measured by team CH01 over the Linth plain with ground clearance of 98 m after corrections. PK25©2017 swisstopo (JD100042).

Figure 94: Dose rate measured by team CH01 over the Linth plain with ground clearance of 151 m after corrections. PK25©2017 swisstopo (JD100042).

Figure 95: Dose rate measured by team CH02 over the Linth plain with ground clearance of 95 m without corrections. PK25©2017 swisstopo (JD100042).

Figure 96: Dose rate measured by team CH02 over the Linth plain with ground clearance of 152 m without corrections. PK25©2017 swisstopo (JD100042).

Figure 97: Dose rate measured by team CH02 over the Linth plain with ground clearance of 95 m. ARM data evaluation with corrections. PK25©2017 swisstopo (JD100042).

Figure 98: Dose rate measured by team CH02 over the Linth plain with ground clearance of 152 m. ARM data evaluation with corrections. PK25©2017 swisstopo (JD100042).

Figure 99: Dose rate measured by team CZ01 over the Linth plain with ground clearance of 105 m after post-processing. PK25©2017 swisstopo (JD100042).

Figure 100: Dose rate measured by team CZ01 over the Linth plain with ground clearance of 145 m after post-processing. PK25©2017 swisstopo (JD100042).
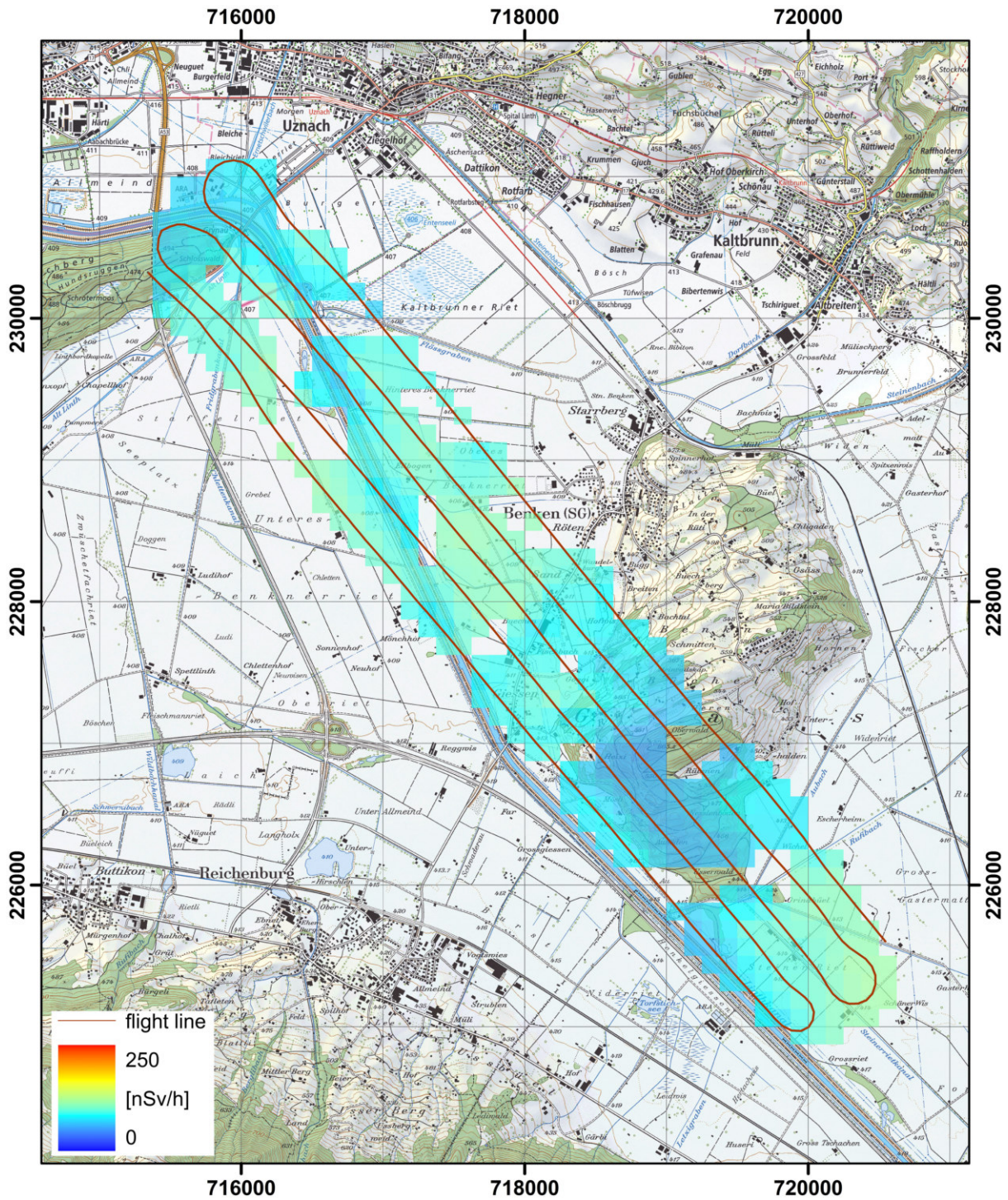
Figure 101: Dose rate measured by team DE01 over the Linth plain with ground clearance of 114 m. PK25©2017 swisstopo (JD100042).
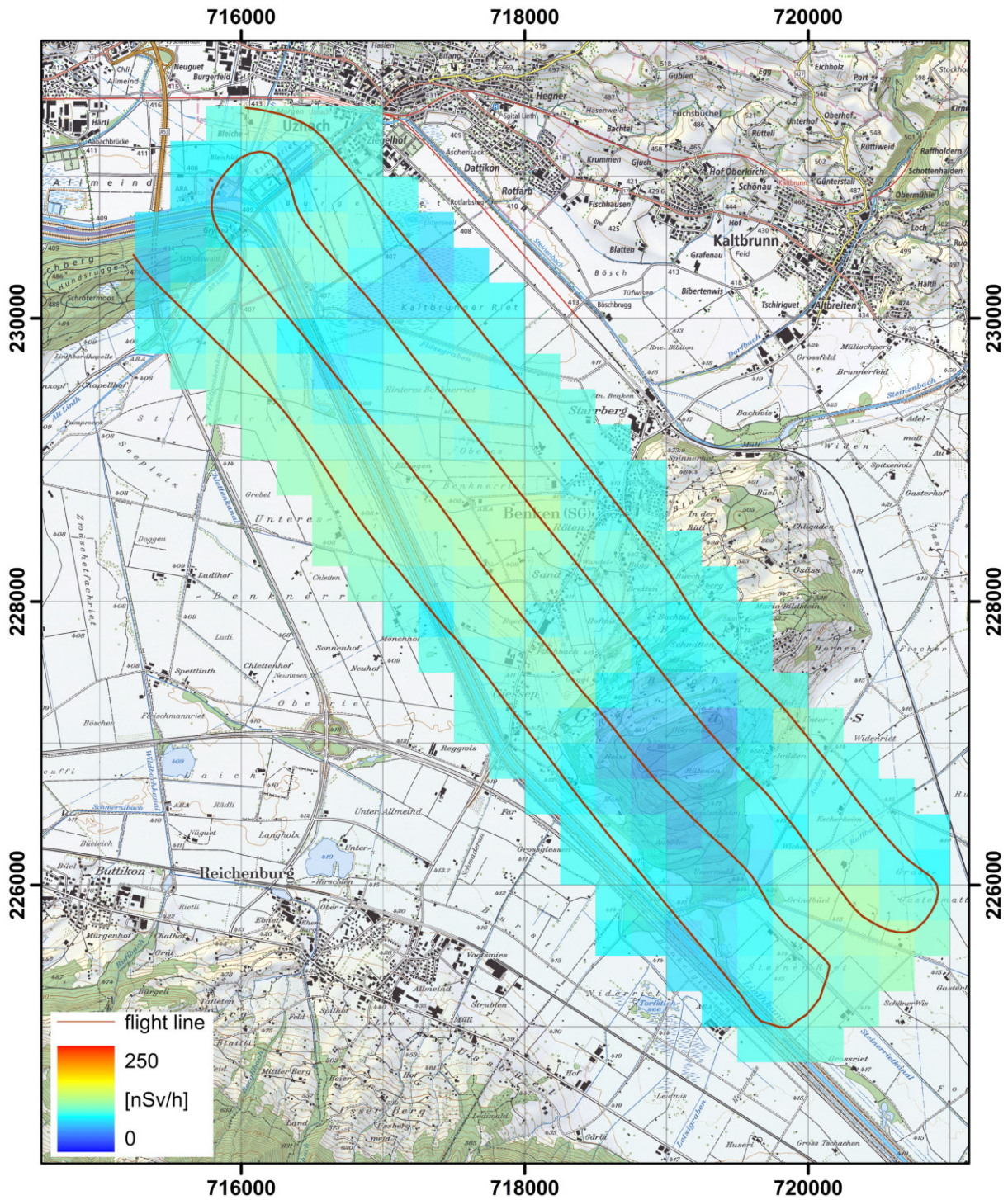
Figure 102: Dose rate measured by team DE01 over the Linth plain with ground clearance of 130 m. PK25©2017 swisstopo (JD100042).
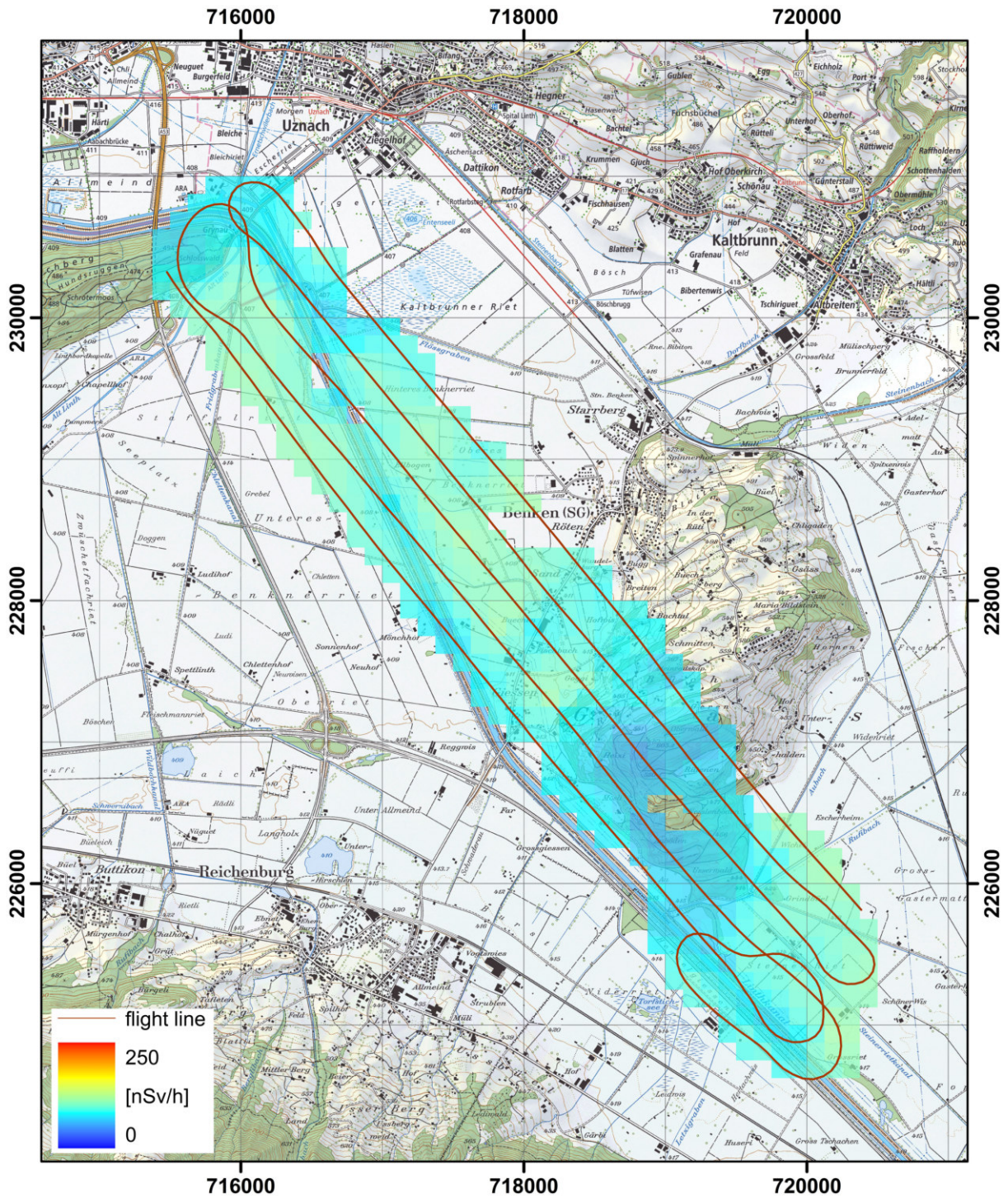
Figure 103: Dose rate measured by team DE02 over the Linth plain with ground clearance of 116 m. PK25©2017 swisstopo (JD100042).
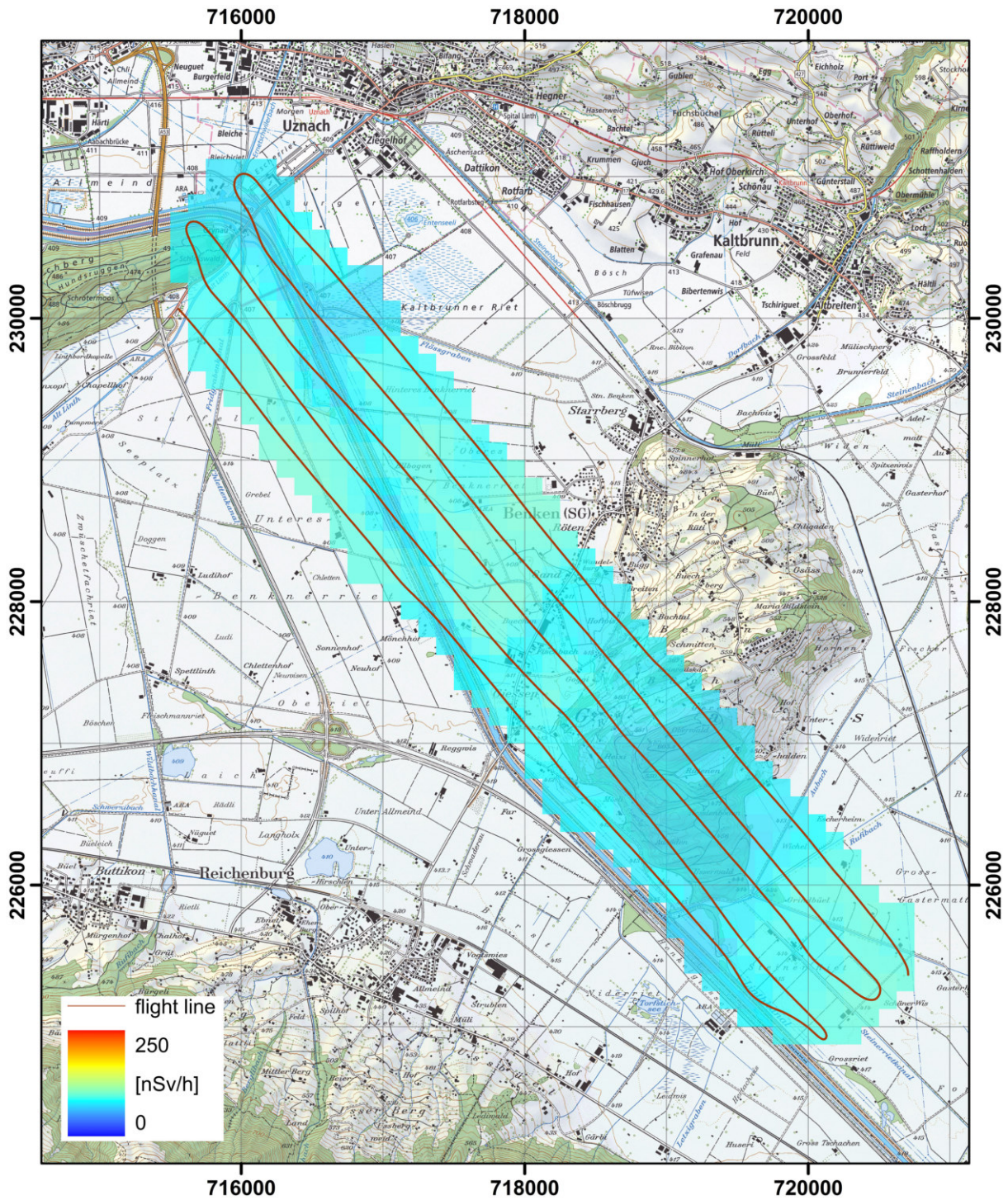
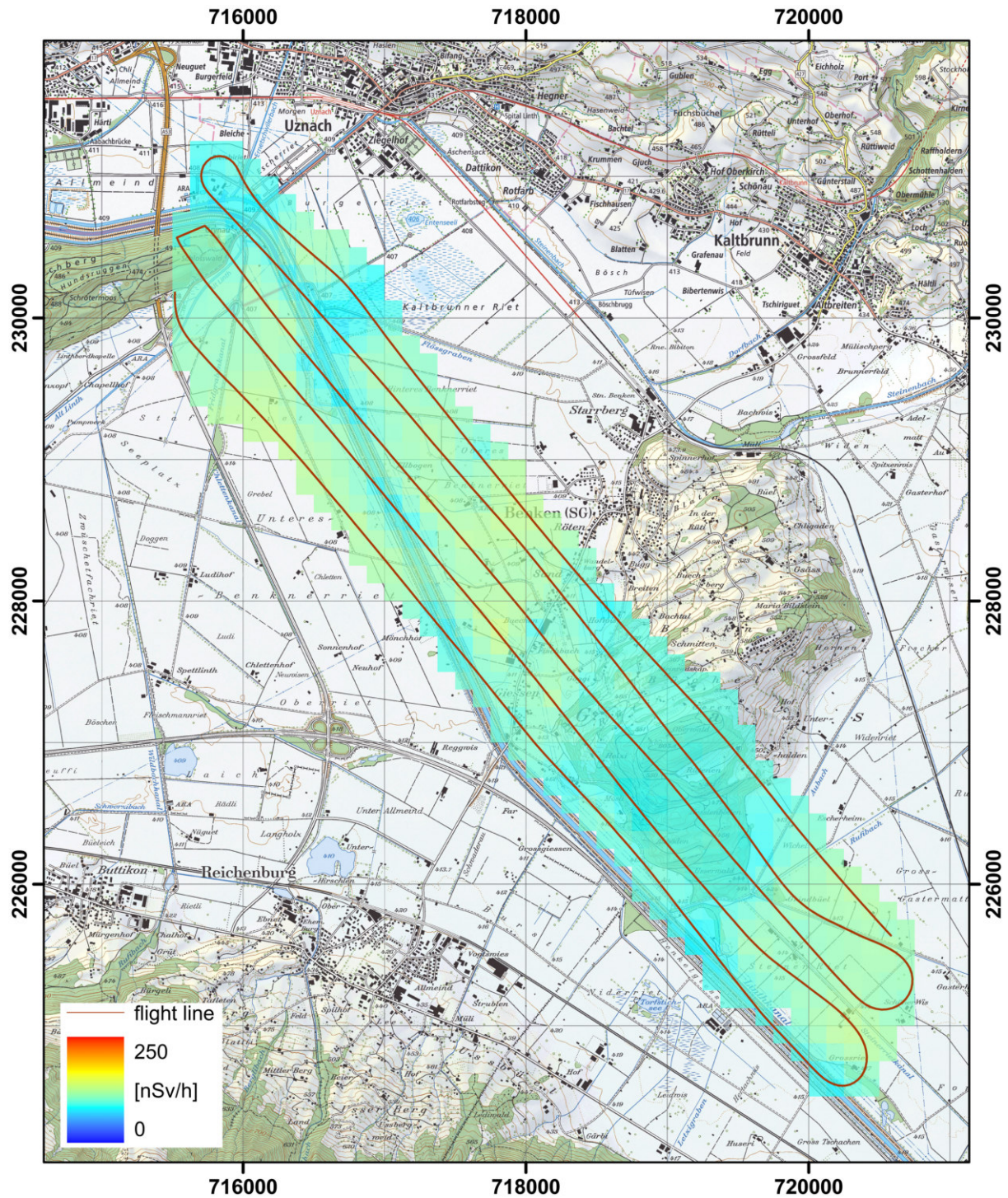Figure 104: Dose rate measured by team FR01 over the Linth plain with ground clearance of 96 m after post-processing. PK25©2017 swisstopo (JD100042).
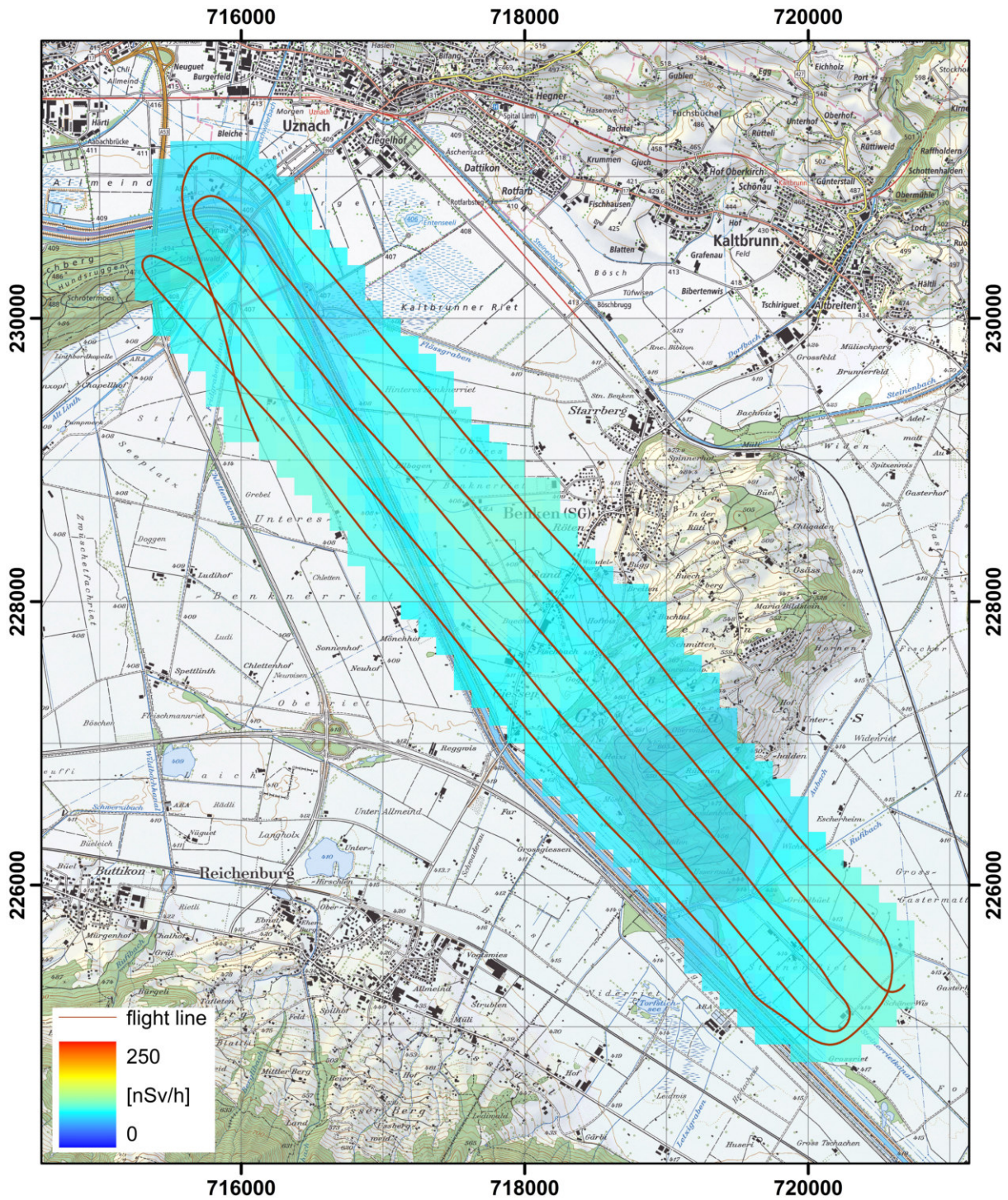
Figure 105: Dose rate measured by team FR01 over the Linth plain with ground clearance of 159 m after post-processing. PK25©2017 swisstopo (JD100042).

Figure 106: ^{40}K activity concentration measured by team CH01 over the Linth plain with ground clearance of 98 m after corrections. PK25©2017 swisstopo (JD100042).
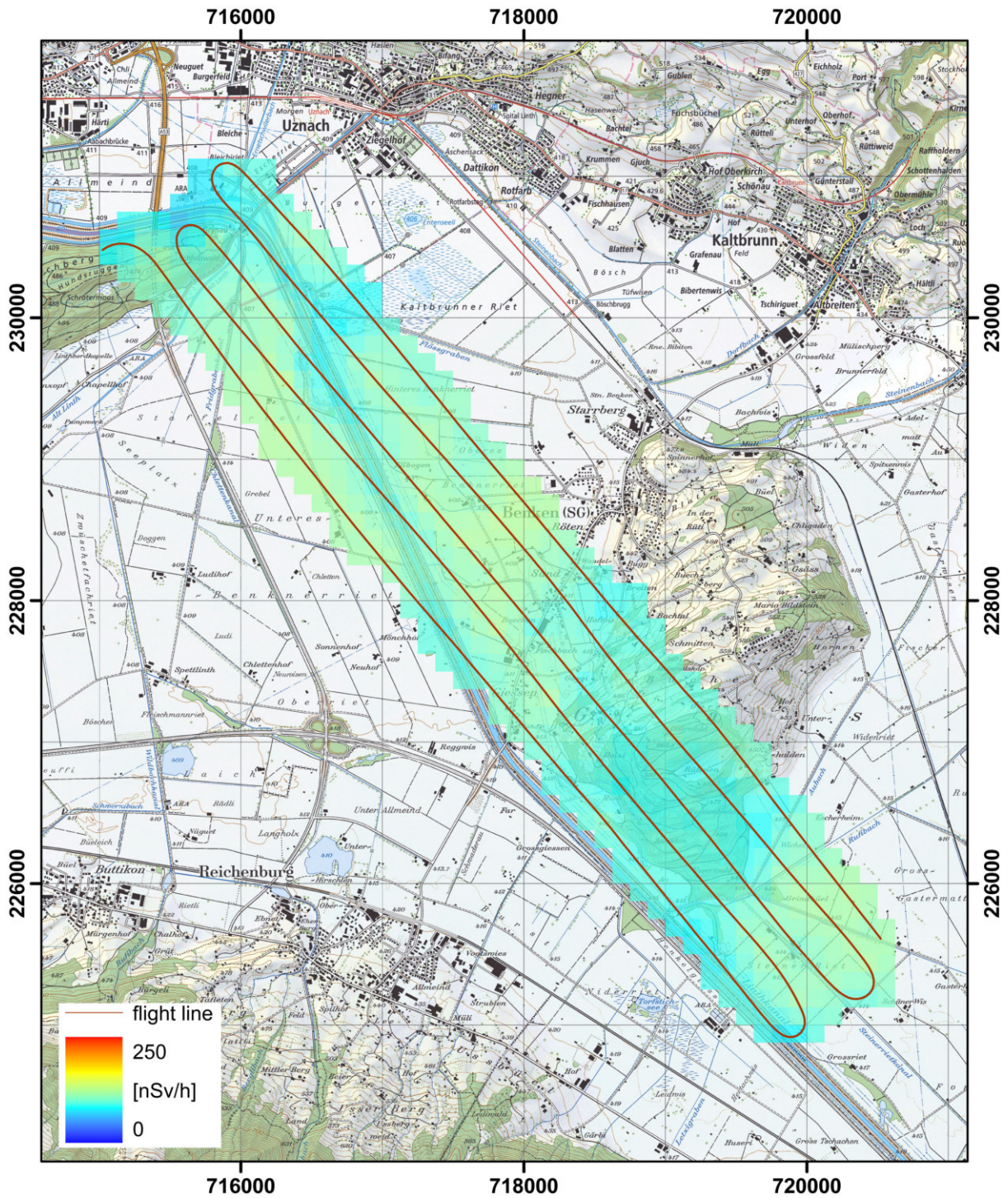
Figure 107: ^{40}K activity concentration measured by team CH01 over the Linth plain with ground clearance of 151 m after corrections. PK25©2017 swisstopo (JD100042).

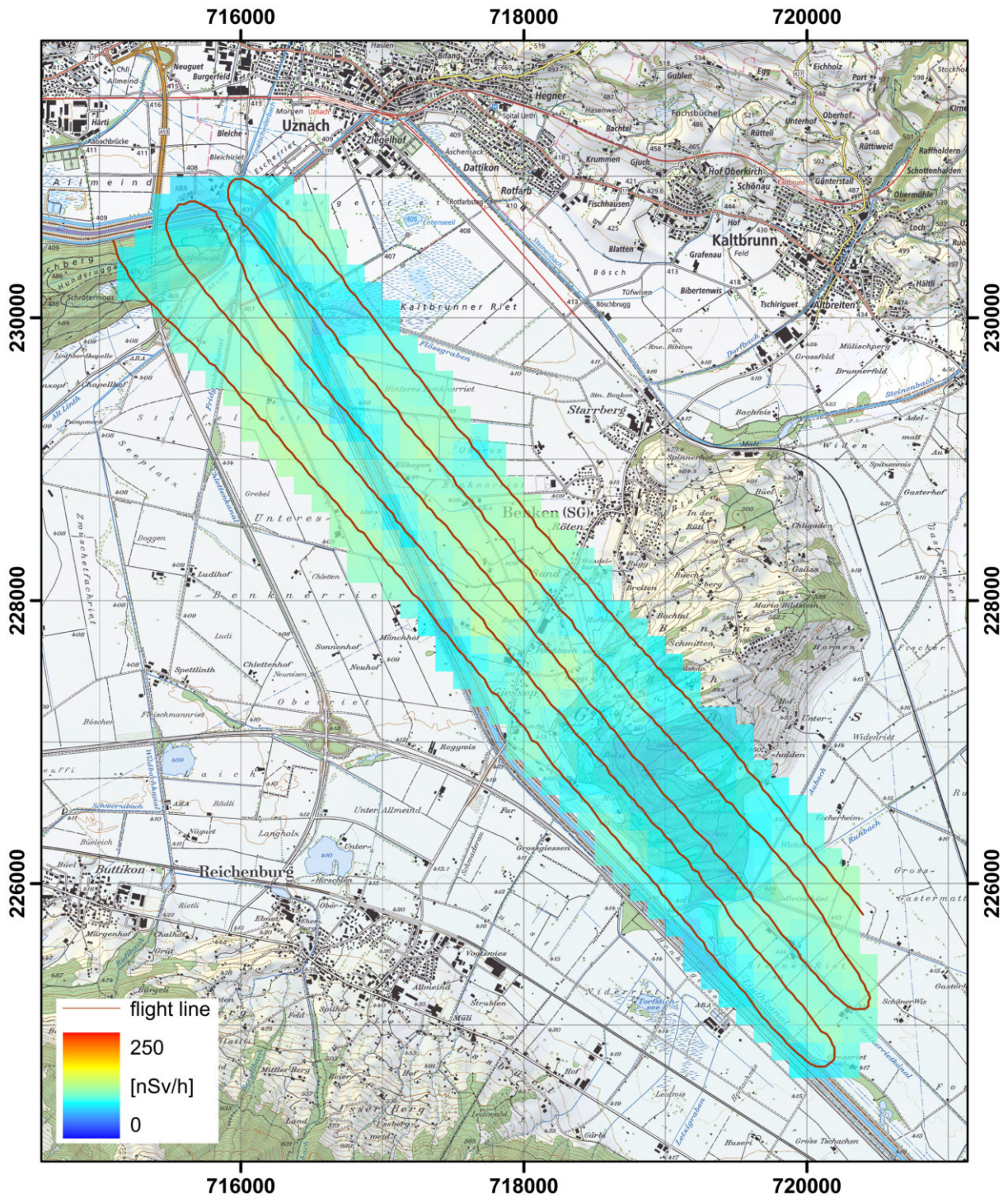Figure 108: ^{40}K activity concentration measured by team CH02 over the Linth plain with ground clearance of 95 m without corrections. PK25©2017 swisstopo (JD100042).
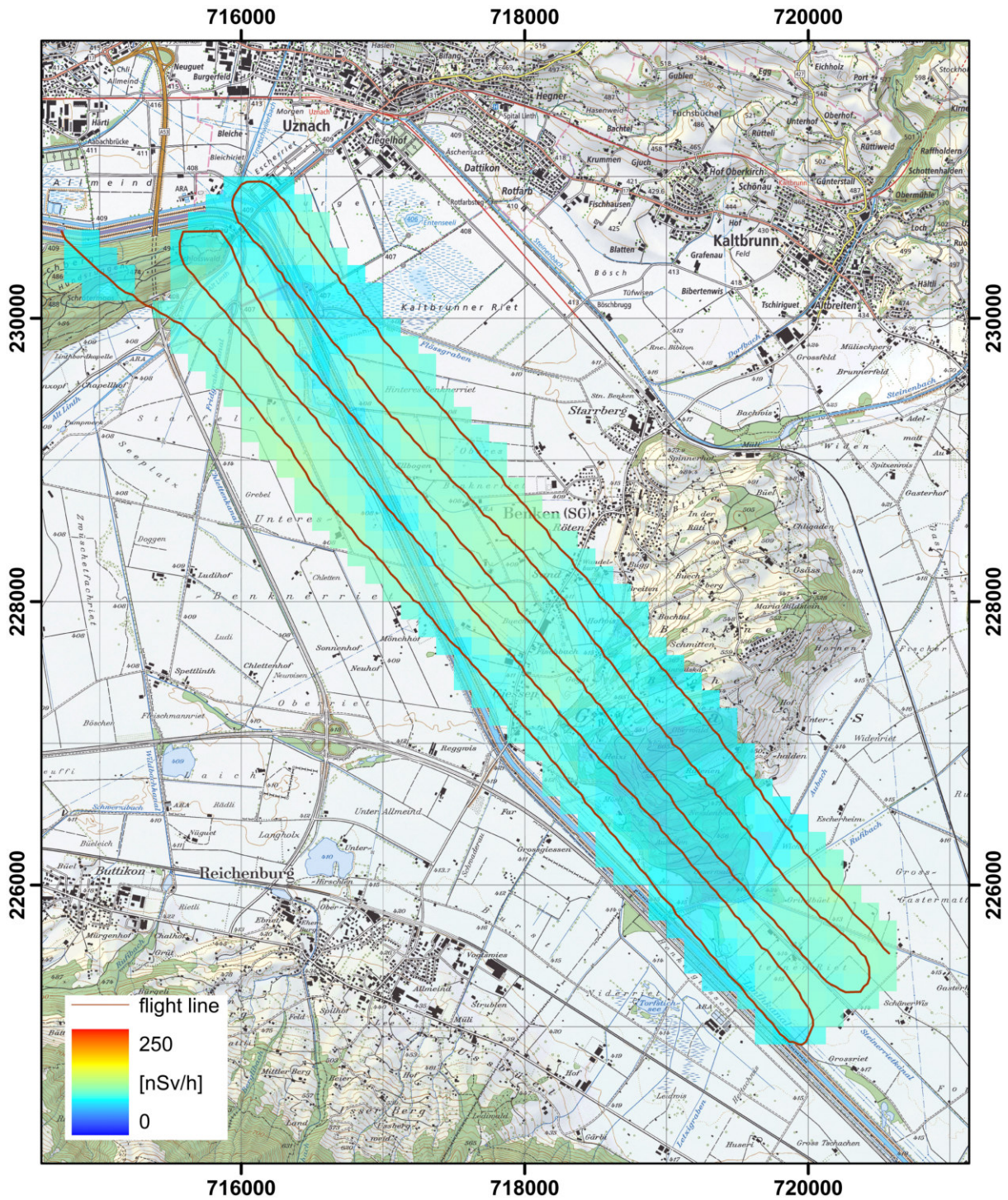
Figure 109: ^{40}K activity concentration measured by team CH02 over the Linth plain with ground clearance of 152 m without corrections. PK25©2017 swisstopo (JD100042).
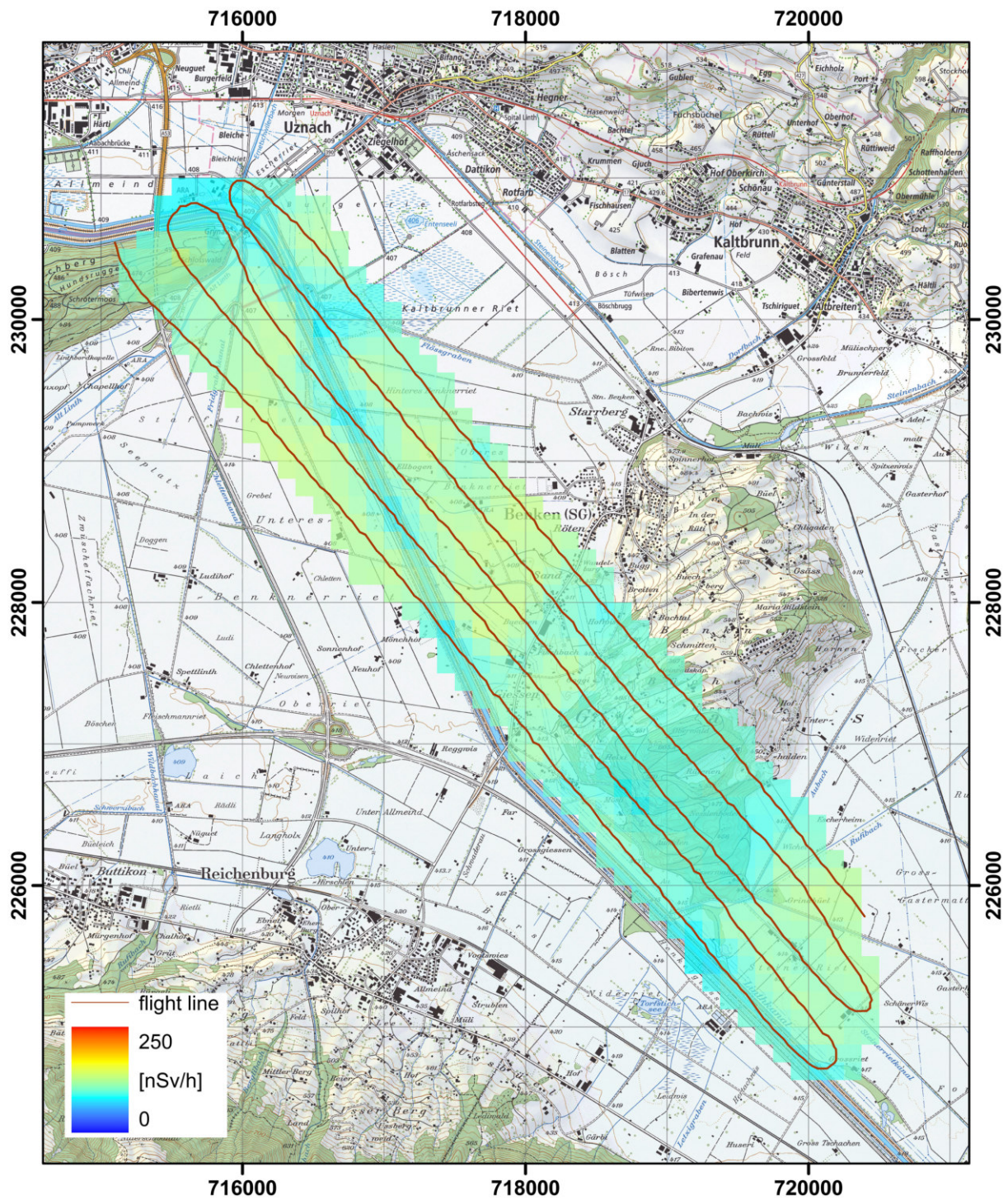
Figure 110: ^{40}K activity concentration measured by team CH02 over the Linth plain with ground clearance of 95 m. ARM data evaluation with corrections. PK25©2017 swisstopo (JD100042).

Figure 111: ^{40}K activity concentration measured by team CH02 over the Linth plain with ground clearance of 152 m. ARM data evaluation with corrections. PK25©2017 swisstopo (JD100042).
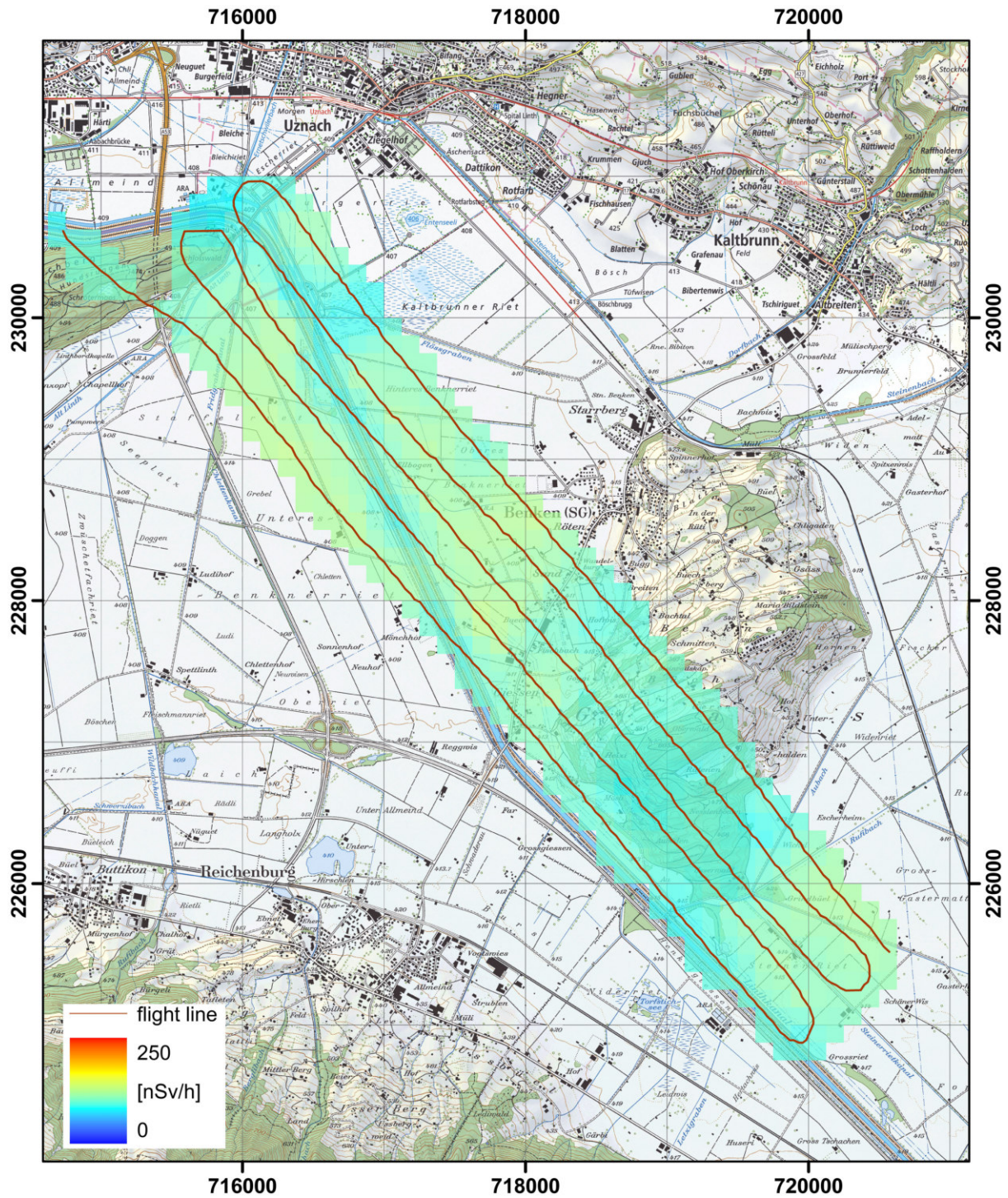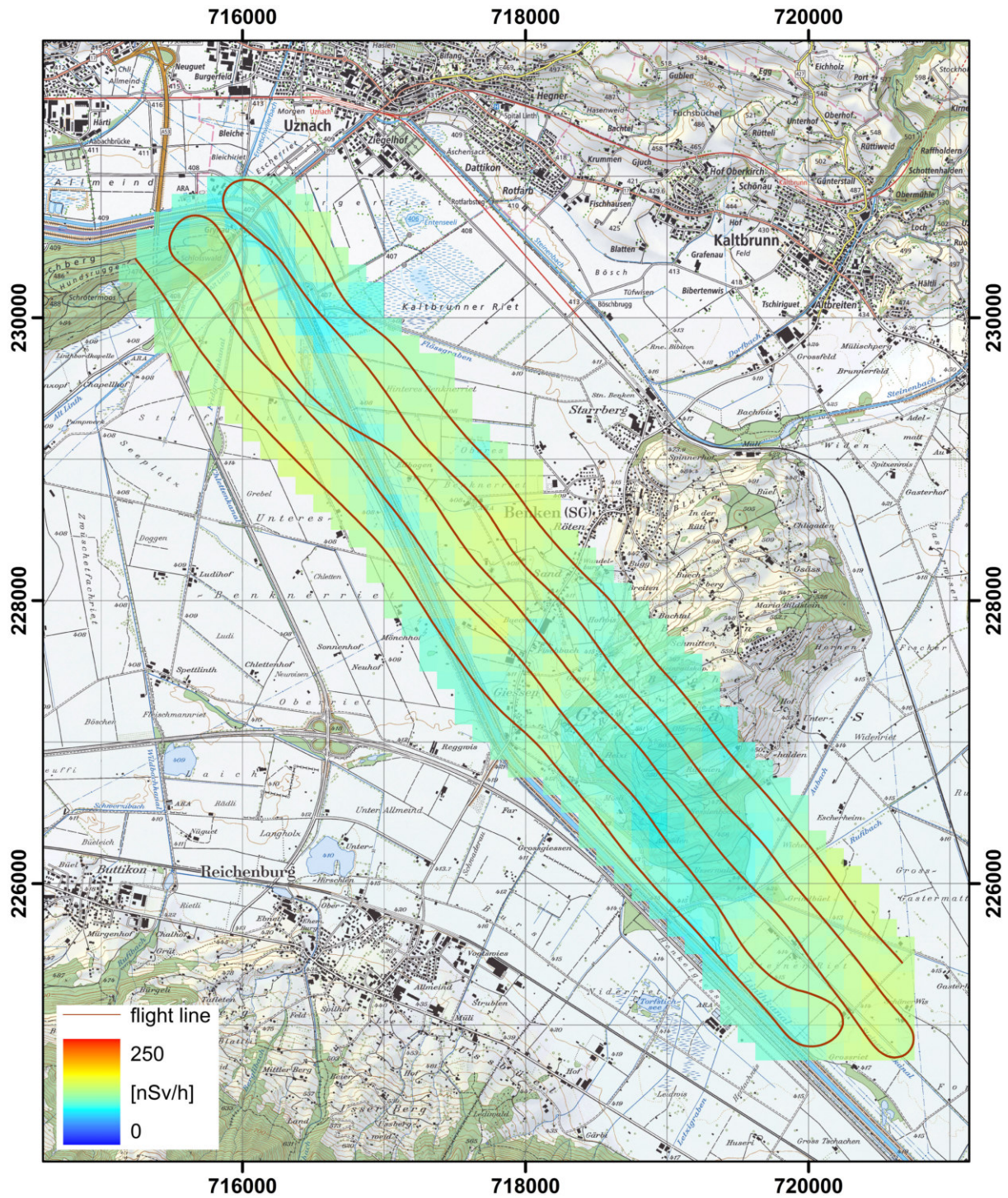
Figure 112: ^{40}K activity concentration measured by team CZ01 over the Linth plain with ground clearance of 105 m after post-processing. PK25©2017 swisstopo (JD100042).

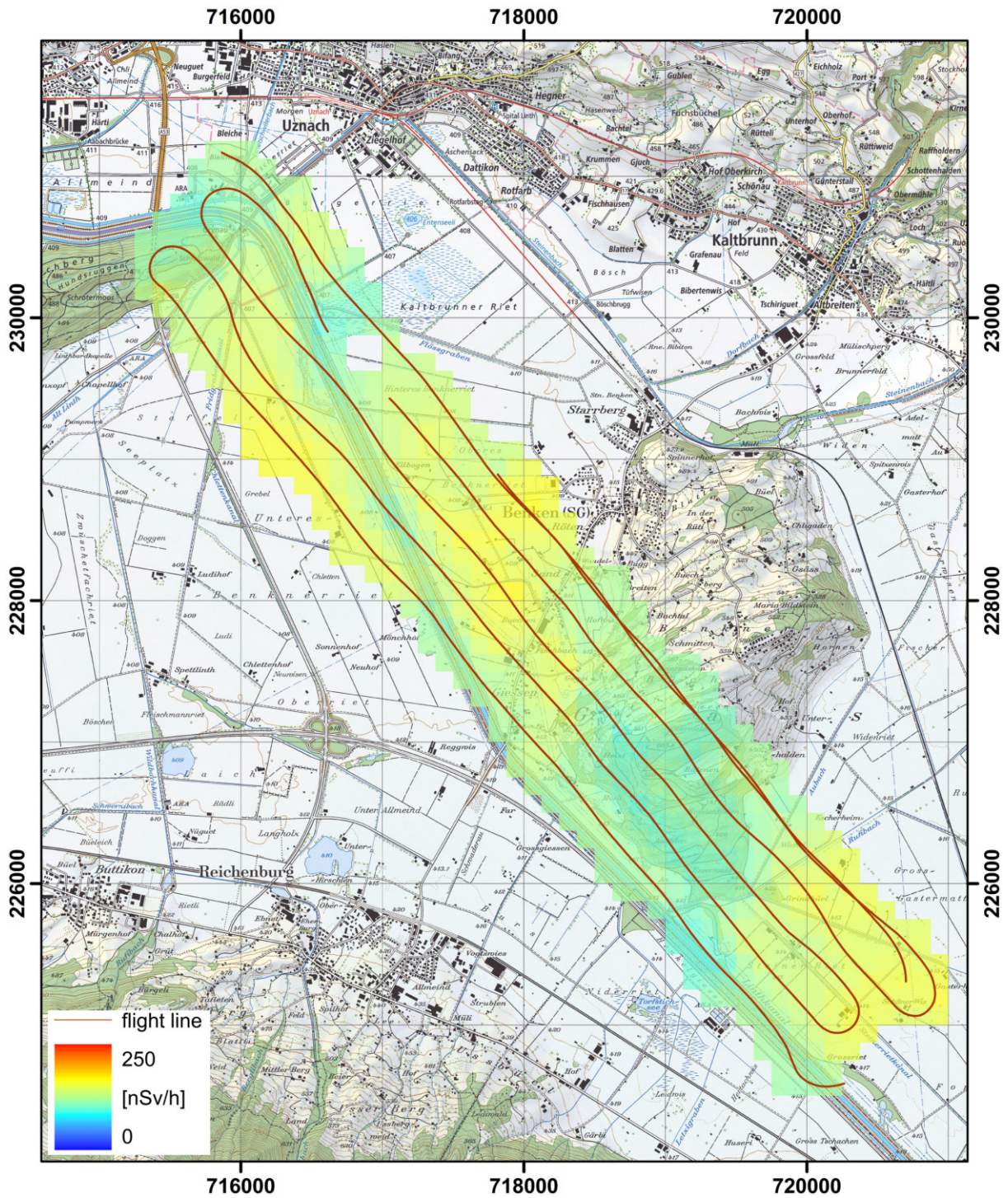Figure 113: ^{40}K activity concentration measured by team CZ01 over the Linth plain with ground clearance of 145 m after post-processing. PK25©2017 swisstopo (JD100042).

Figure 114: ^{40}K activity concentration measured by team DE01 over the Linth plain with ground clearance of 111 m after corrections. PK25©2017 swisstopo (JD100042).

Figure 115: ^{40}K activity concentration measured by team DE01 over the Linth plain with ground clearance of 130 m. PK25©2017 swisstopo (JD100042).

Figure 116: ^{40}K activity concentration measured by team DE02 over the Linth plain with ground clearance of 111 m after corrections. PK25©2017 swisstopo (JD100042).

Figure 117: ^{40}K activity concentration measured by team FR01 over the Linth plain with ground clearance of 96 m after post-processing. PK25©2017 swisstopo (JD100042).
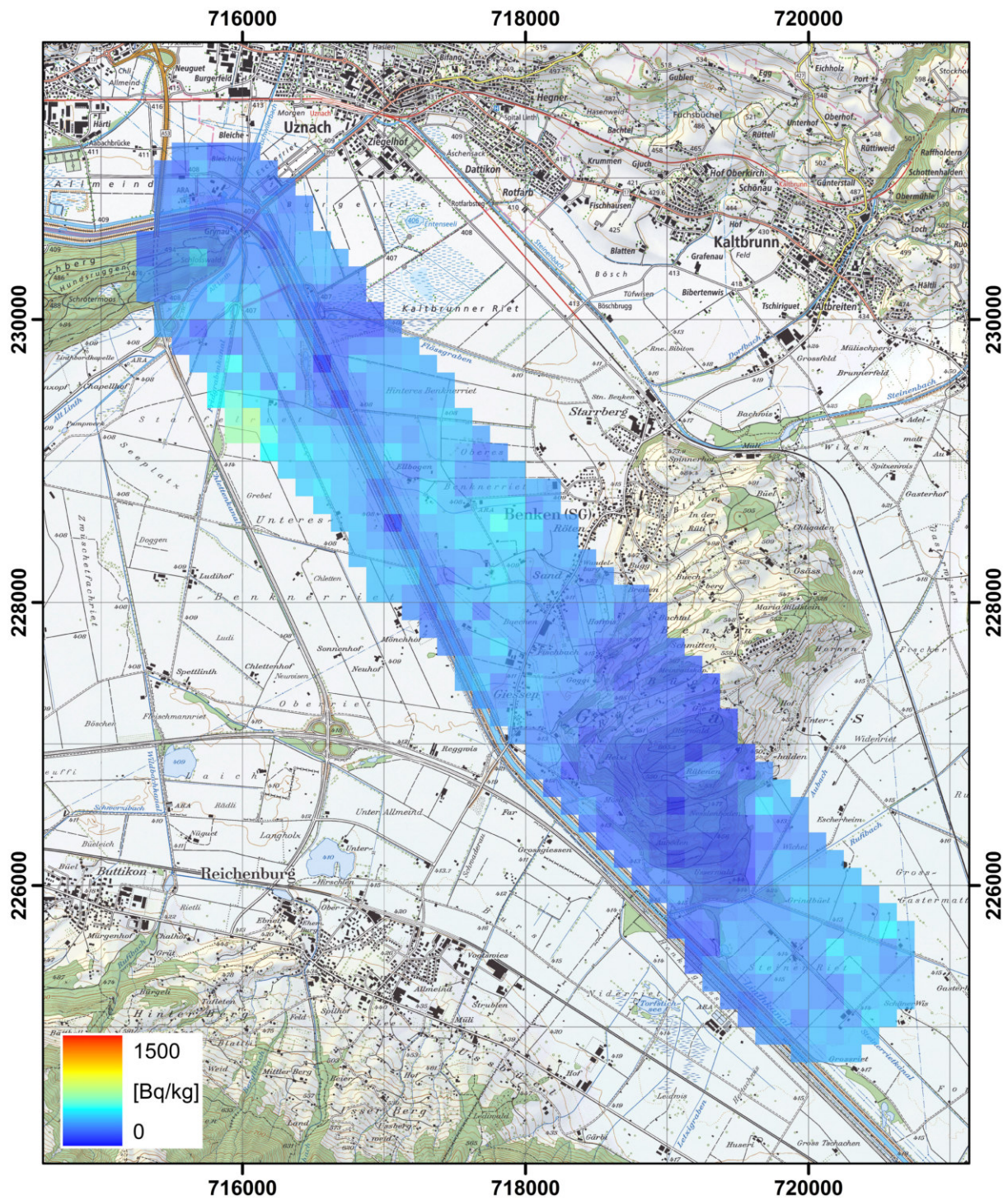
Figure 118: ^{40}K activity concentration measured by team FR01 over the Linth plain with ground clearance of 159 m after post-processing. PK25©2017 swisstopo (JD100042).
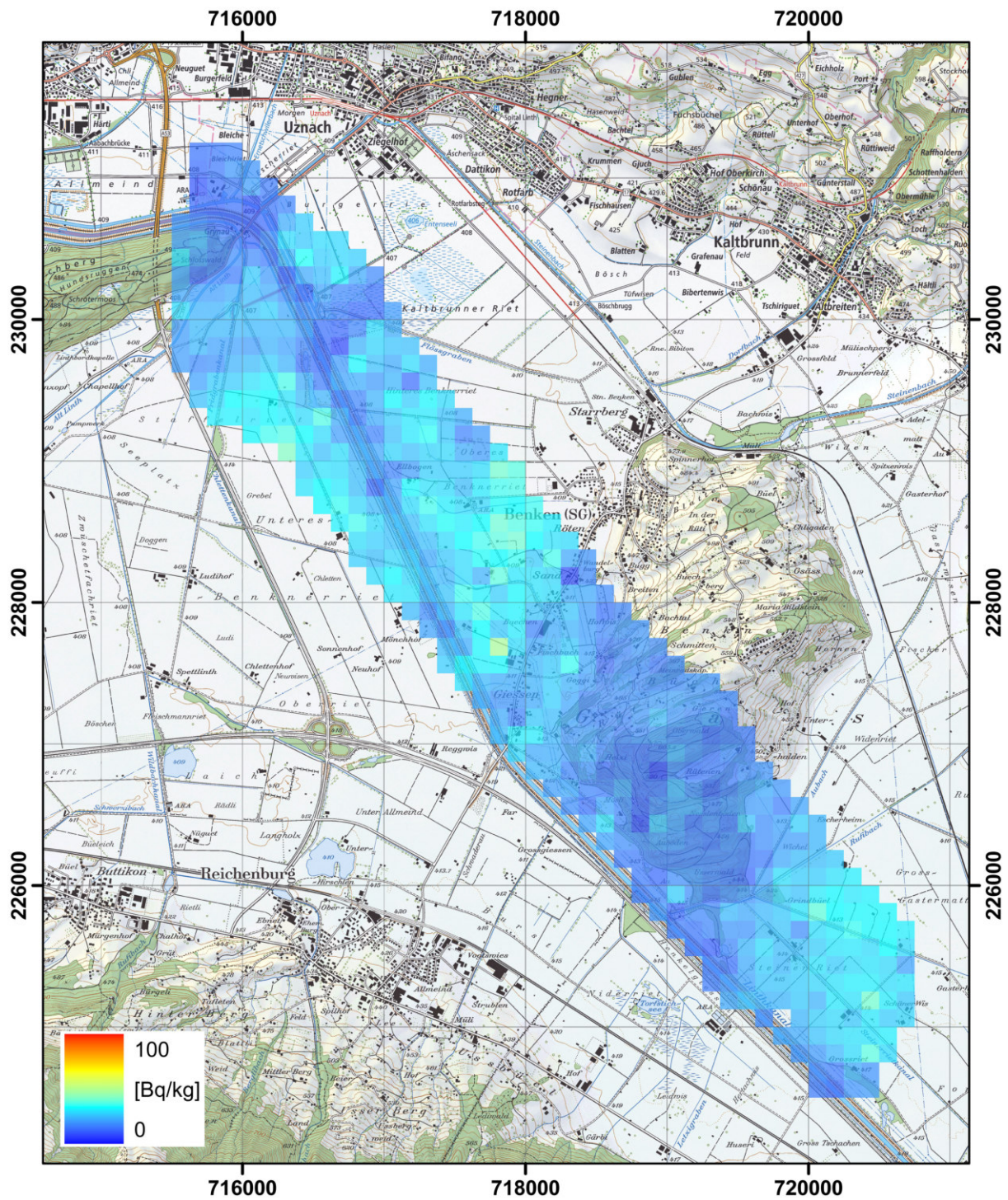
Figure 119: ^{232}Th activity concentration measured by team CH01 over the Linth plain with ground clearance of 98 m after corrections. PK25©2017 swisstopo (JD100042).
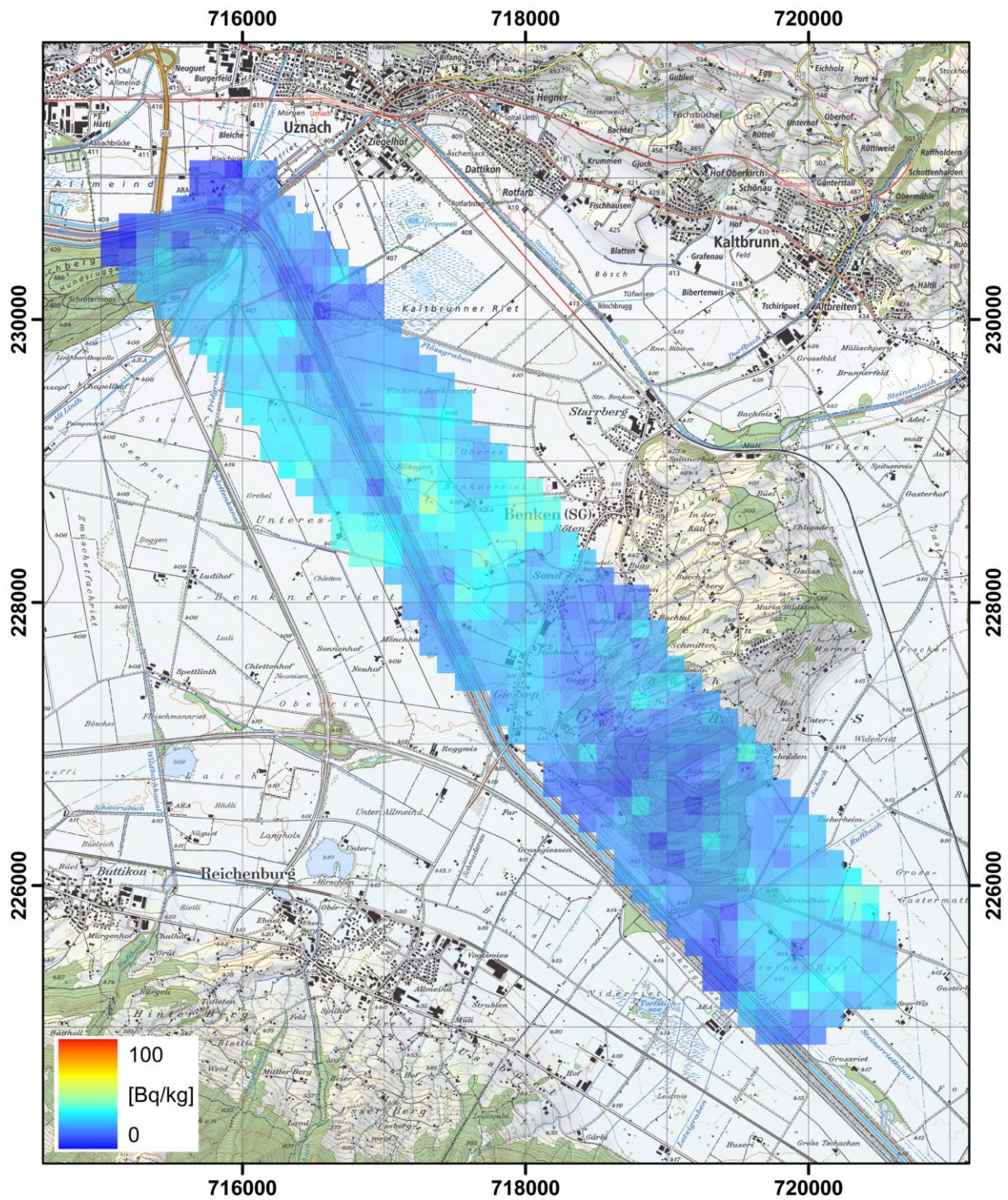
Figure 120: ^{232}Th activity concentration measured by team CH01 over the Linth plain with ground clearance of 151 m after corrections. PK25©2017 swisstopo (JD100042).
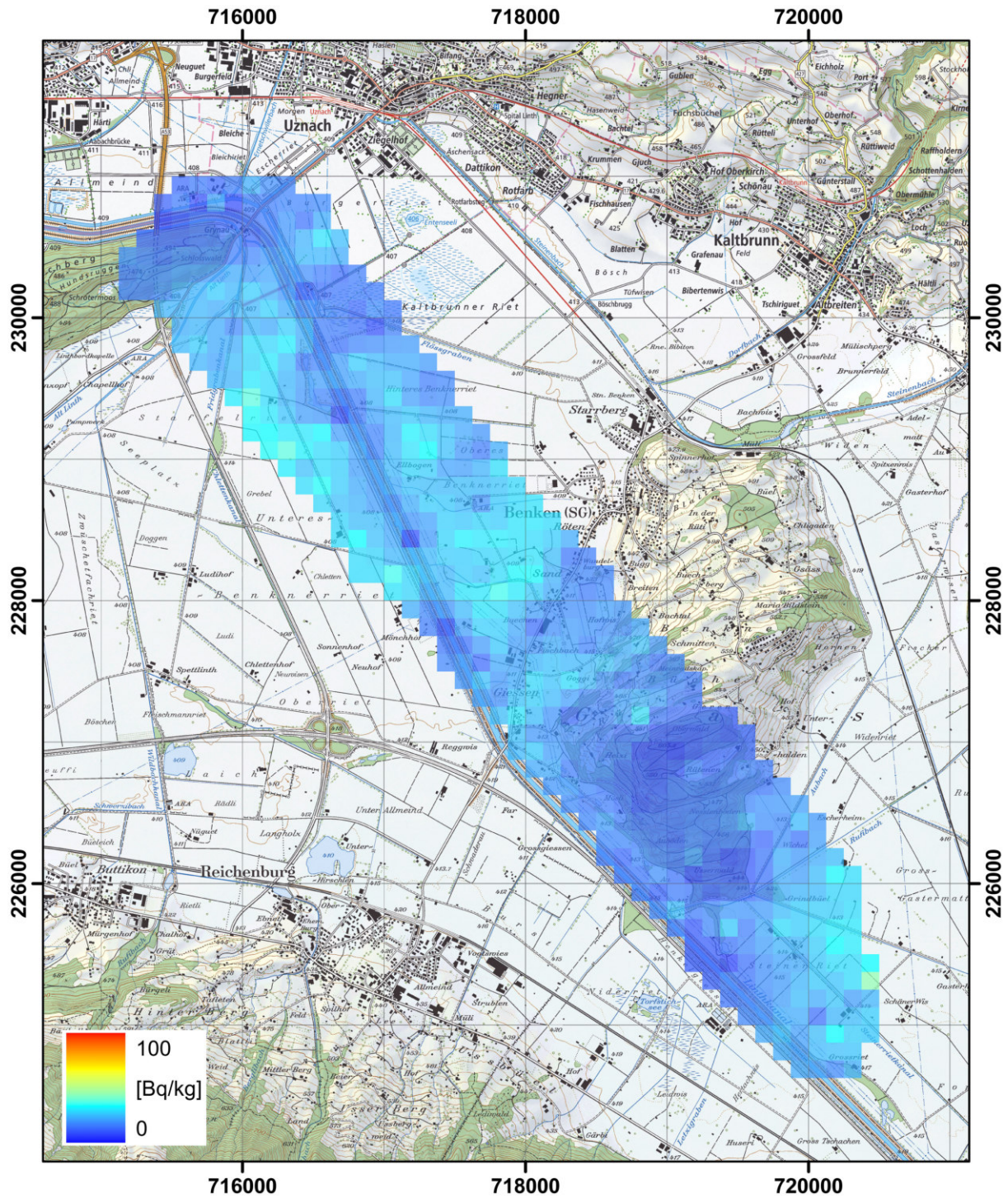
Figure 121: ^{232}Th activity concentration measured by team CH02 over the Linth plain with ground clearance of 95 m without corrections. PK25©2017 swisstopo (JD100042).
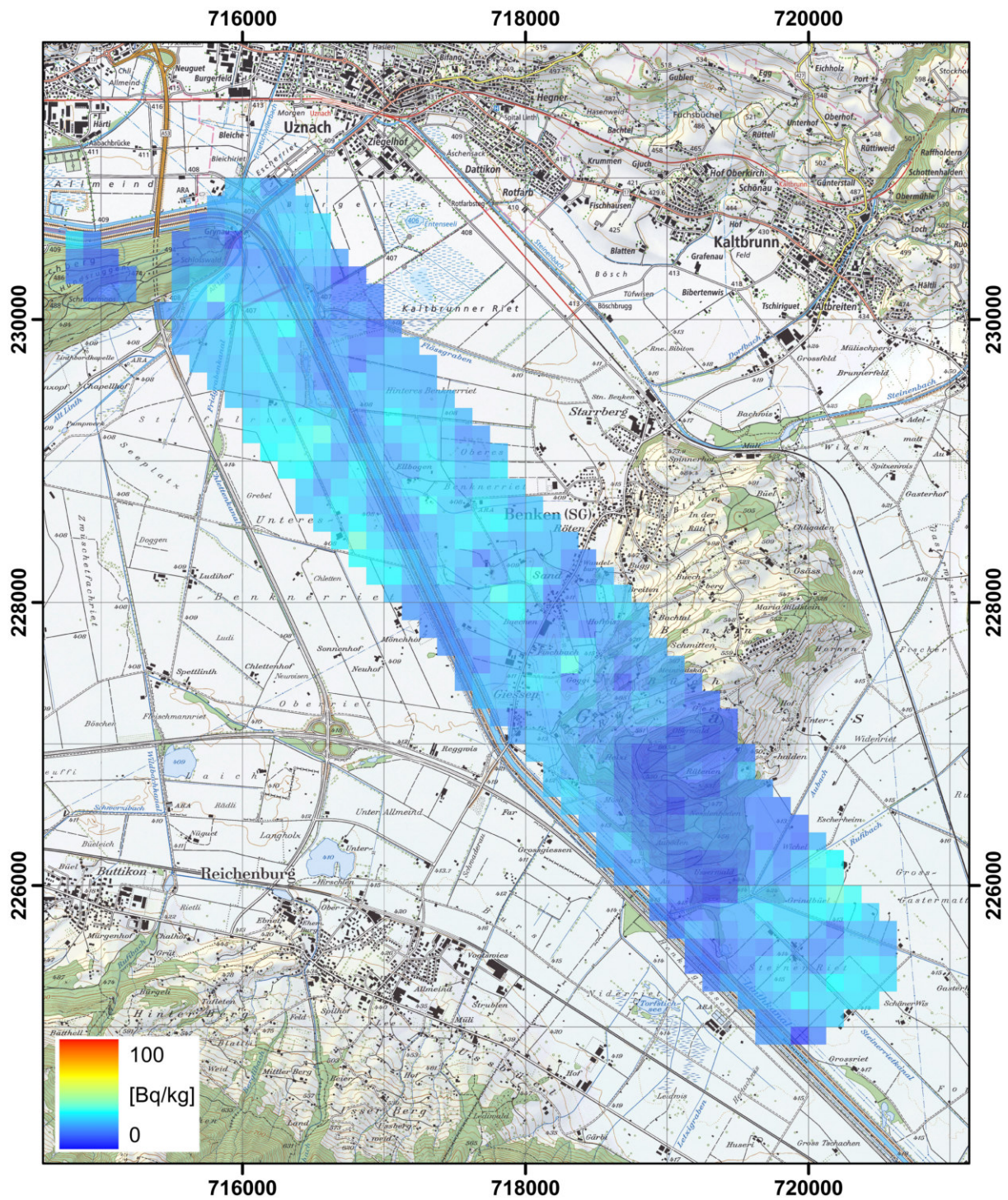
Figure 122: ^{232}Th activity concentration measured by team CH02 over the Linth plain with ground clearance of 152 m without corrections. PK25©2017 swisstopo (JD100042).

138
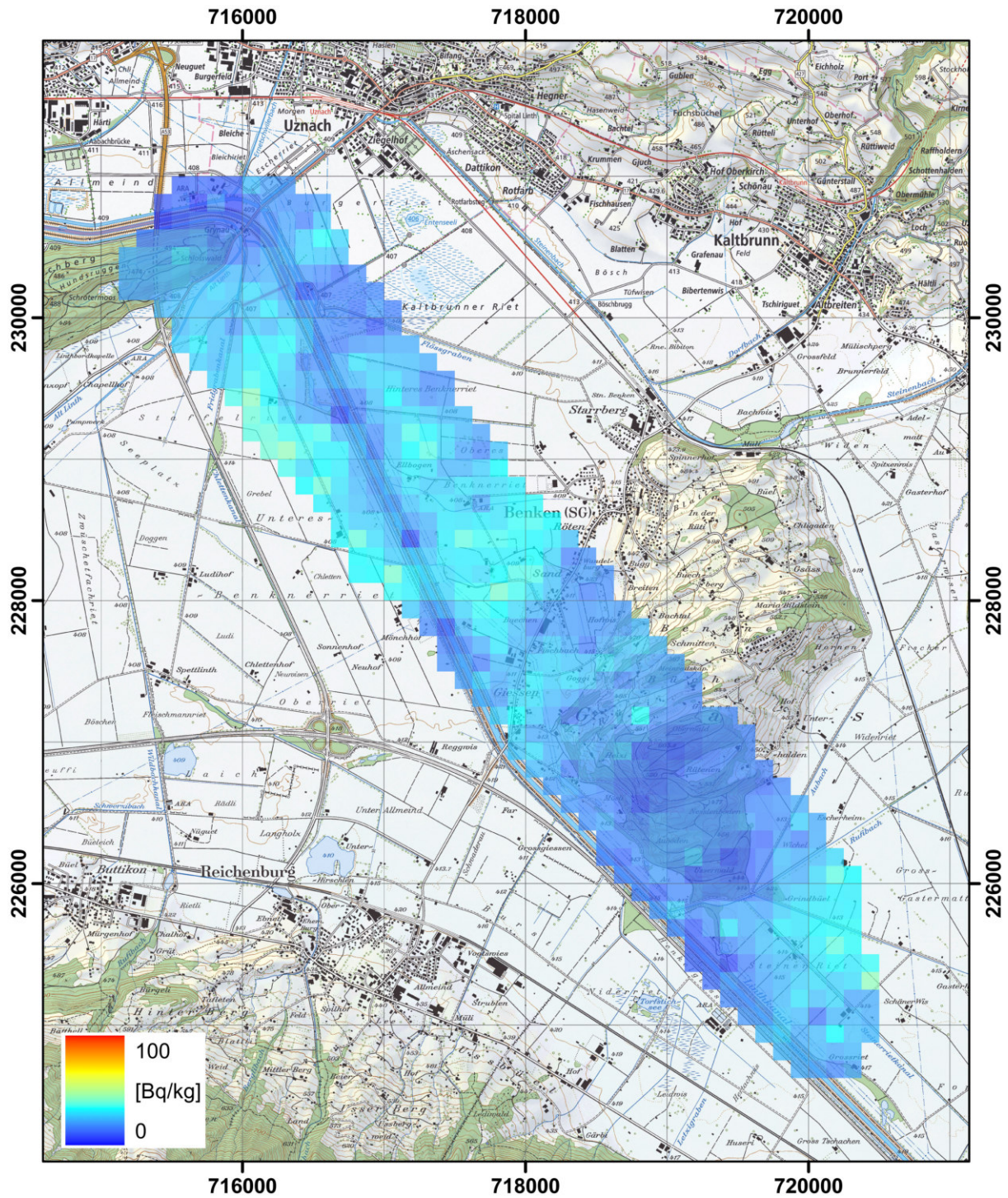
Figure 123: ^{232}Th activity concentration measured by team CH02 over the Linth plain with ground clearance of 95 m. ARM data evaluation with corrections. PK25©2017 swisstopo (JD100042).
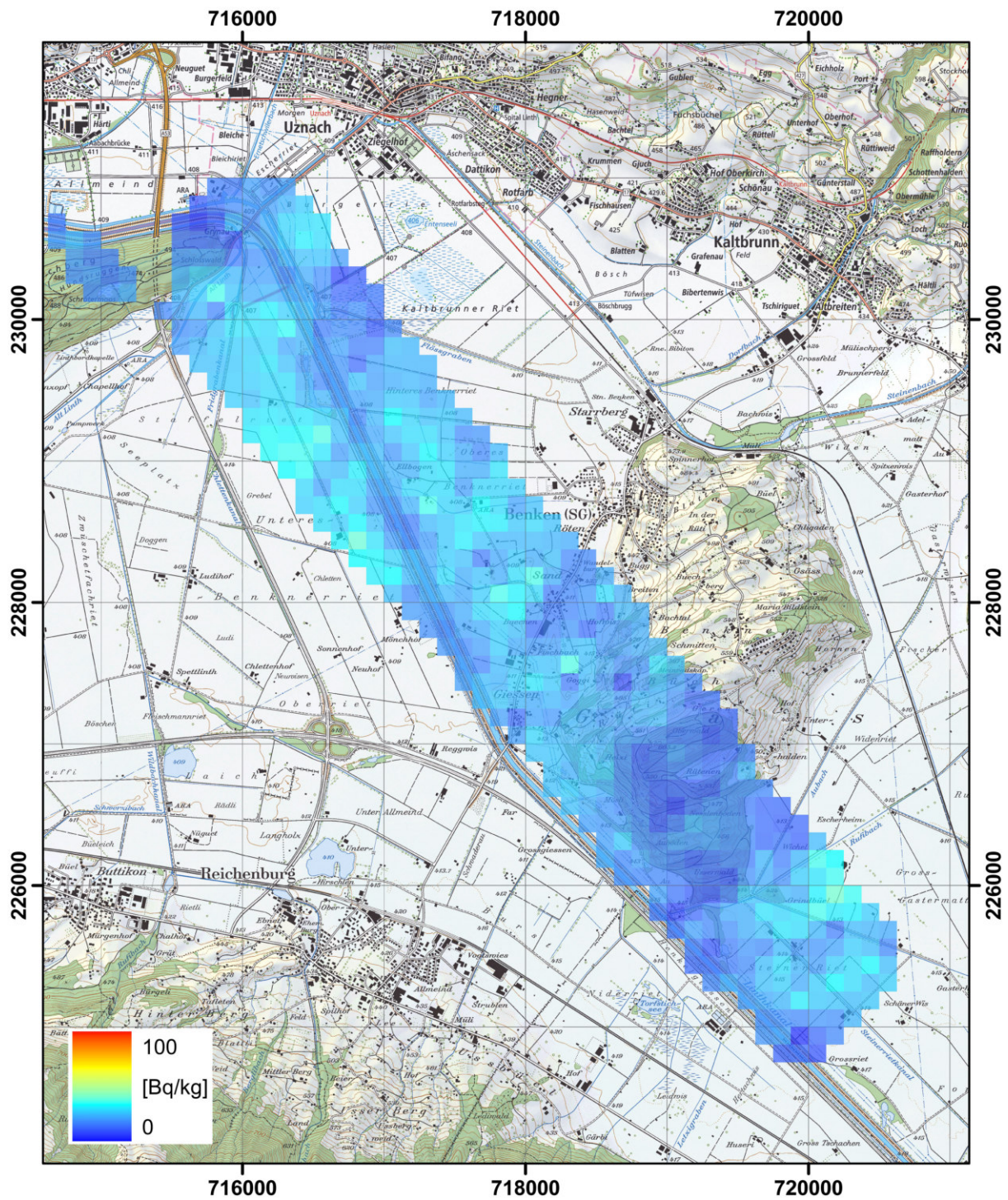
Figure 124: ^{232}Th activity concentration measured by team CH02 over the Linth plain with ground clearance of 152 m. ARM data evaluation with corrections. PK25©2017 swisstopo (JD100042).
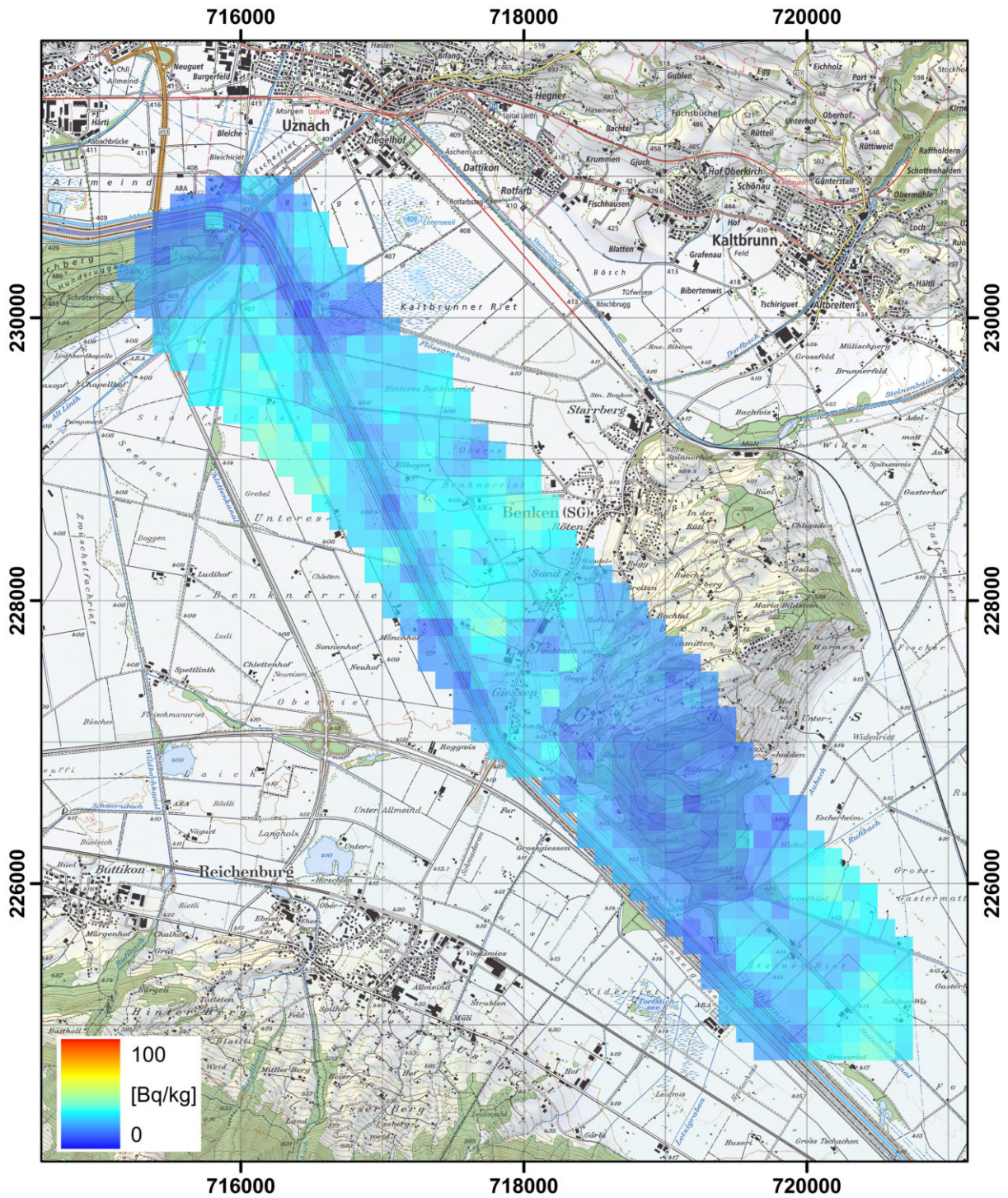
Figure 125: ^{232}Th activity concentration measured by team CZ01 over the Linth plain with ground clearance of 105 m after post-processing. PK25©2017 swisstopo (JD100042).
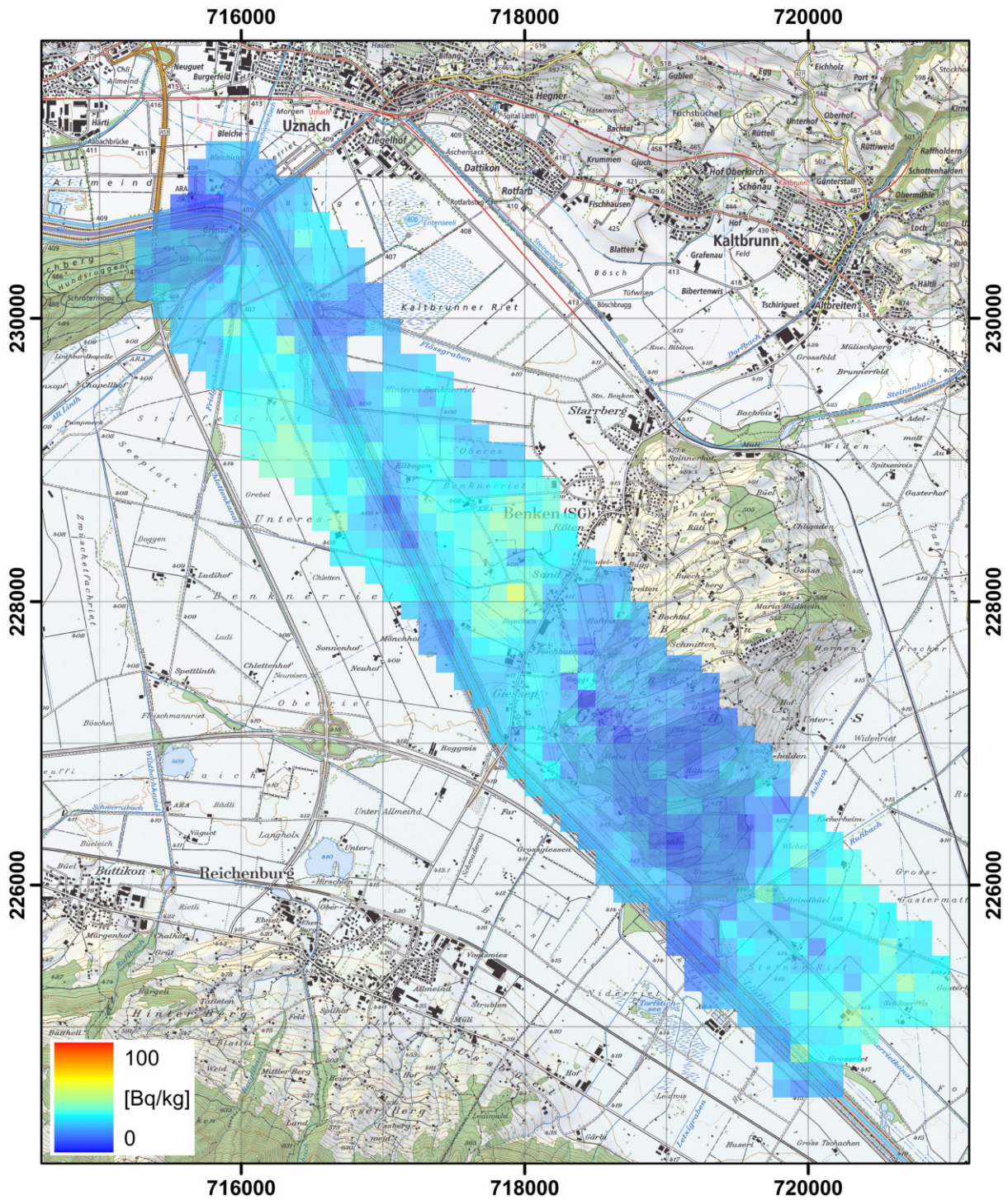
Figure 126: ^{232}Th activity concentration measured by team CZ01 over the Linth plain with ground clearance of 145 m after post-processing. PK25©2017 swisstopo (JD100042).

142
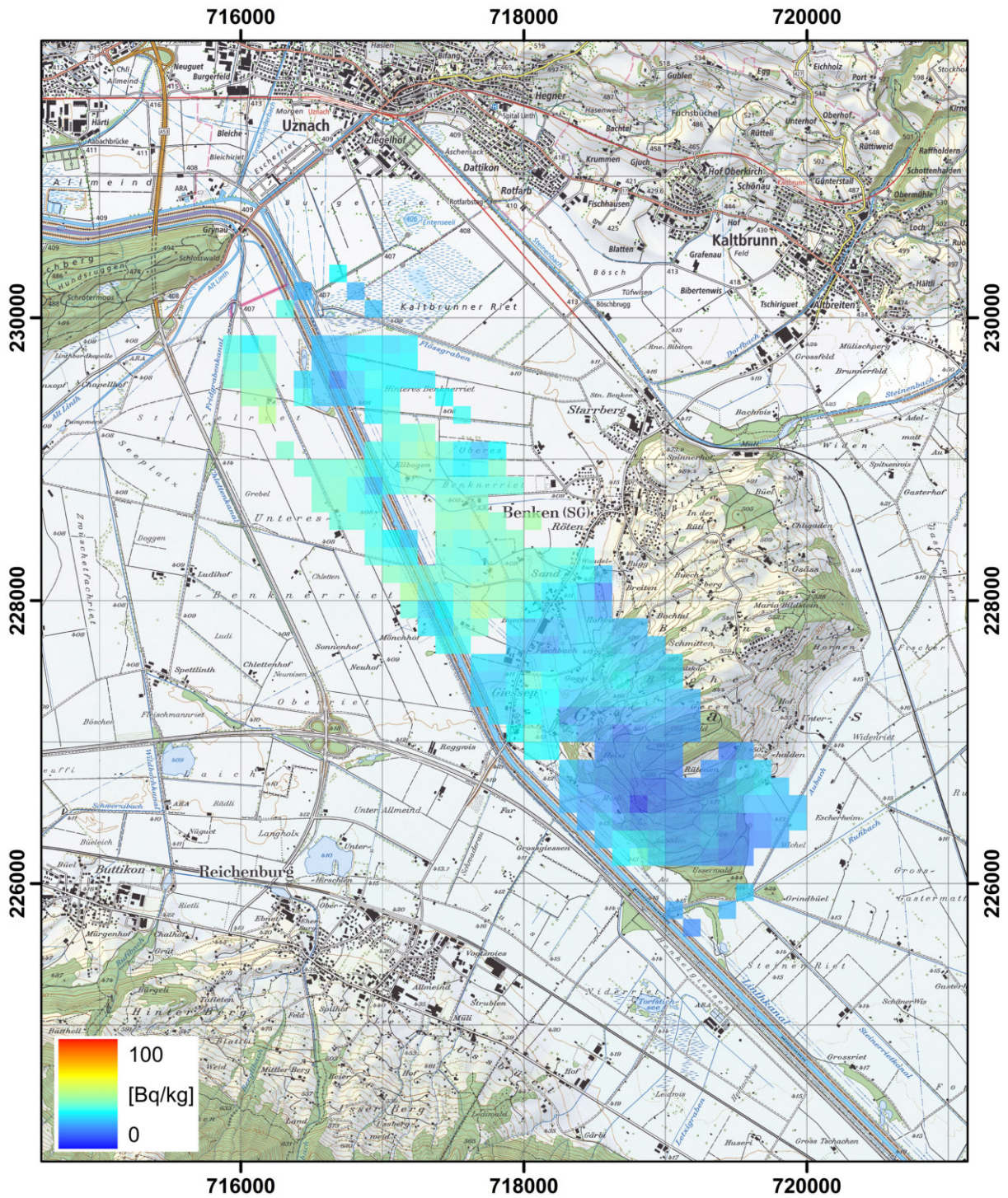
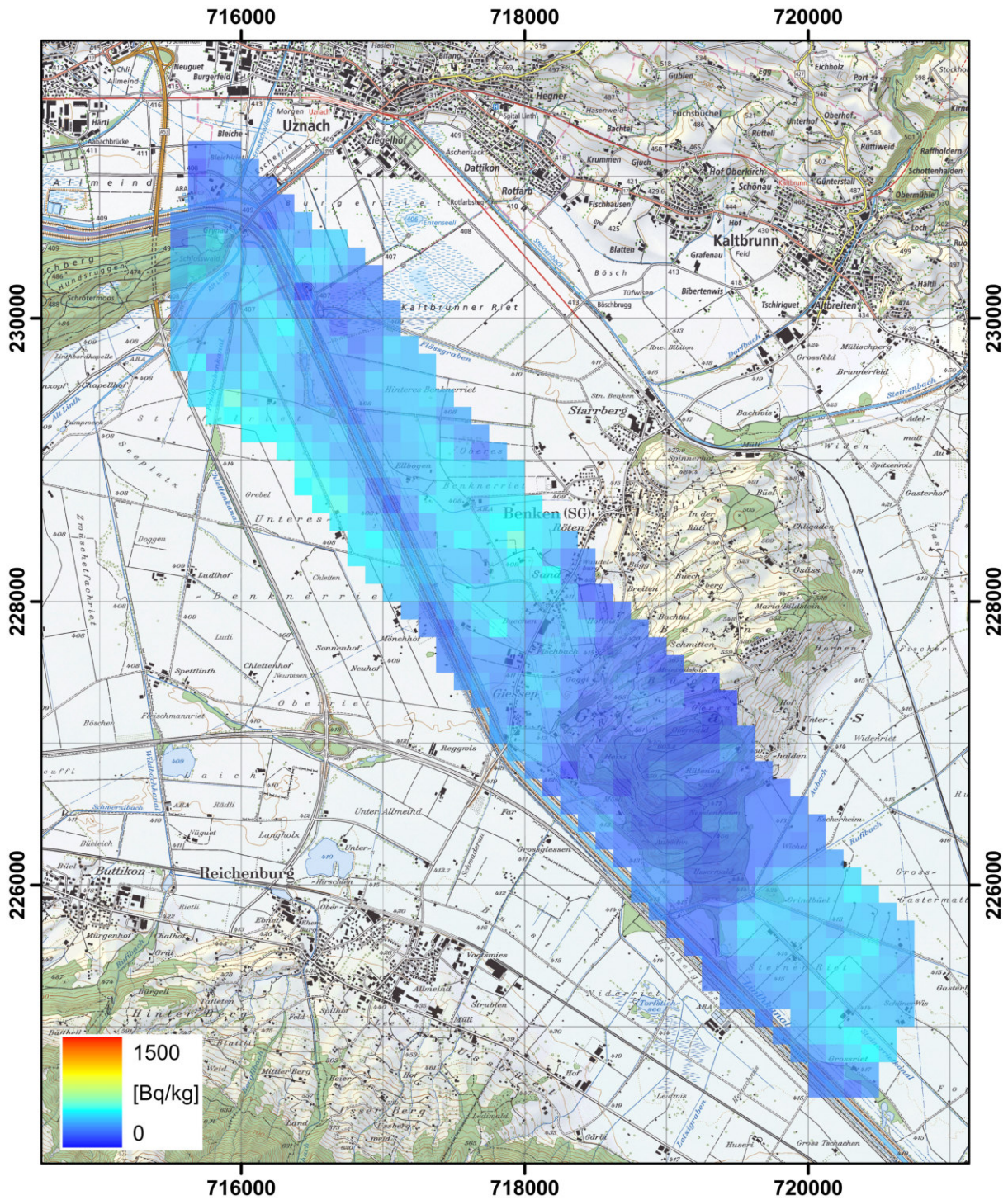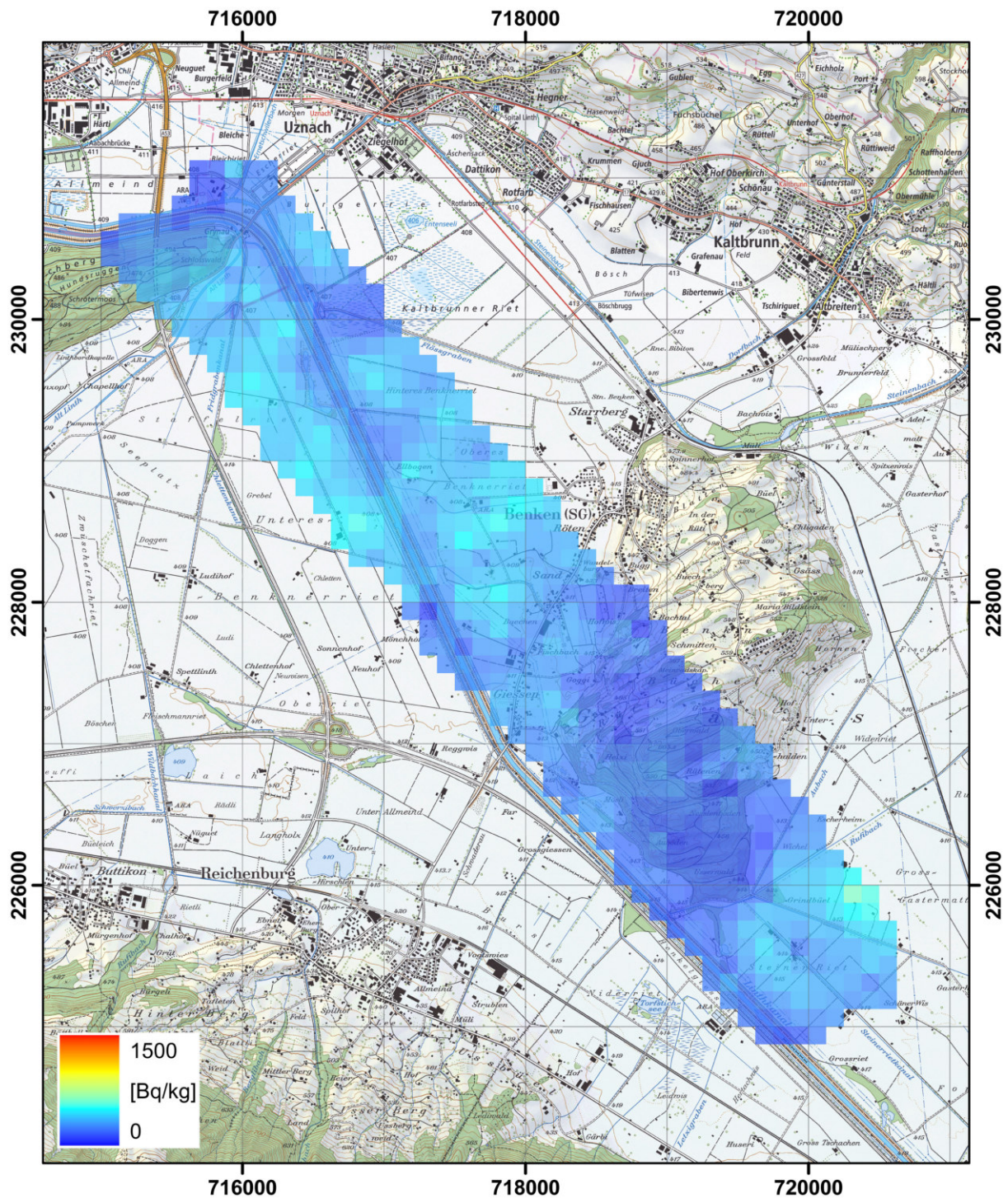Figure 127: ^{232}Th activity concentration measured by team DE01 over the Linth plain with ground clearance of 114 m. PK25©2017 swisstopo (JD100042).
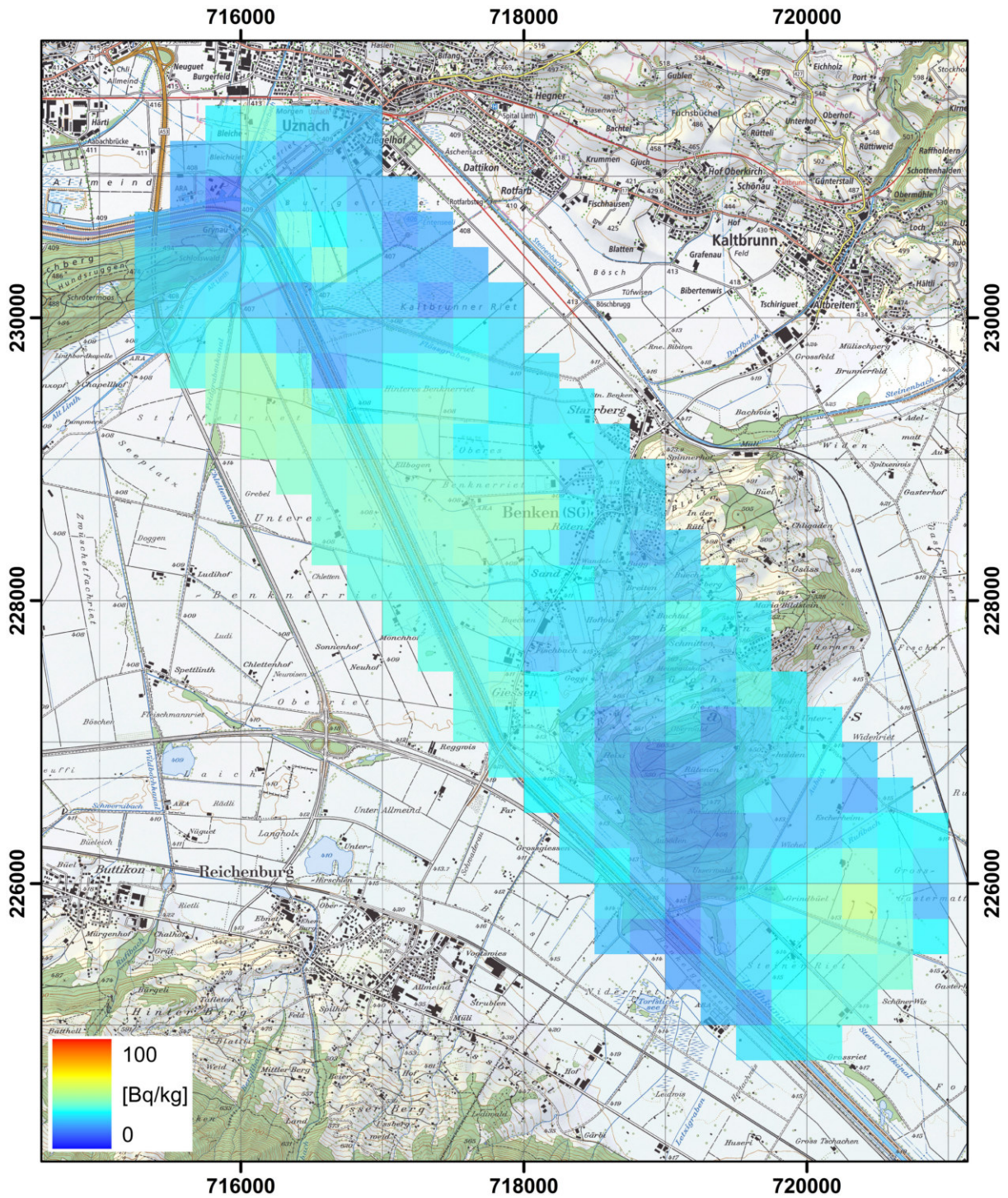
Figure 128: ^{232}Th activity concentration measured by team DE01 over the Linth plain with ground clearance of 130 m. PK25©2017 swisstopo (JD100042).
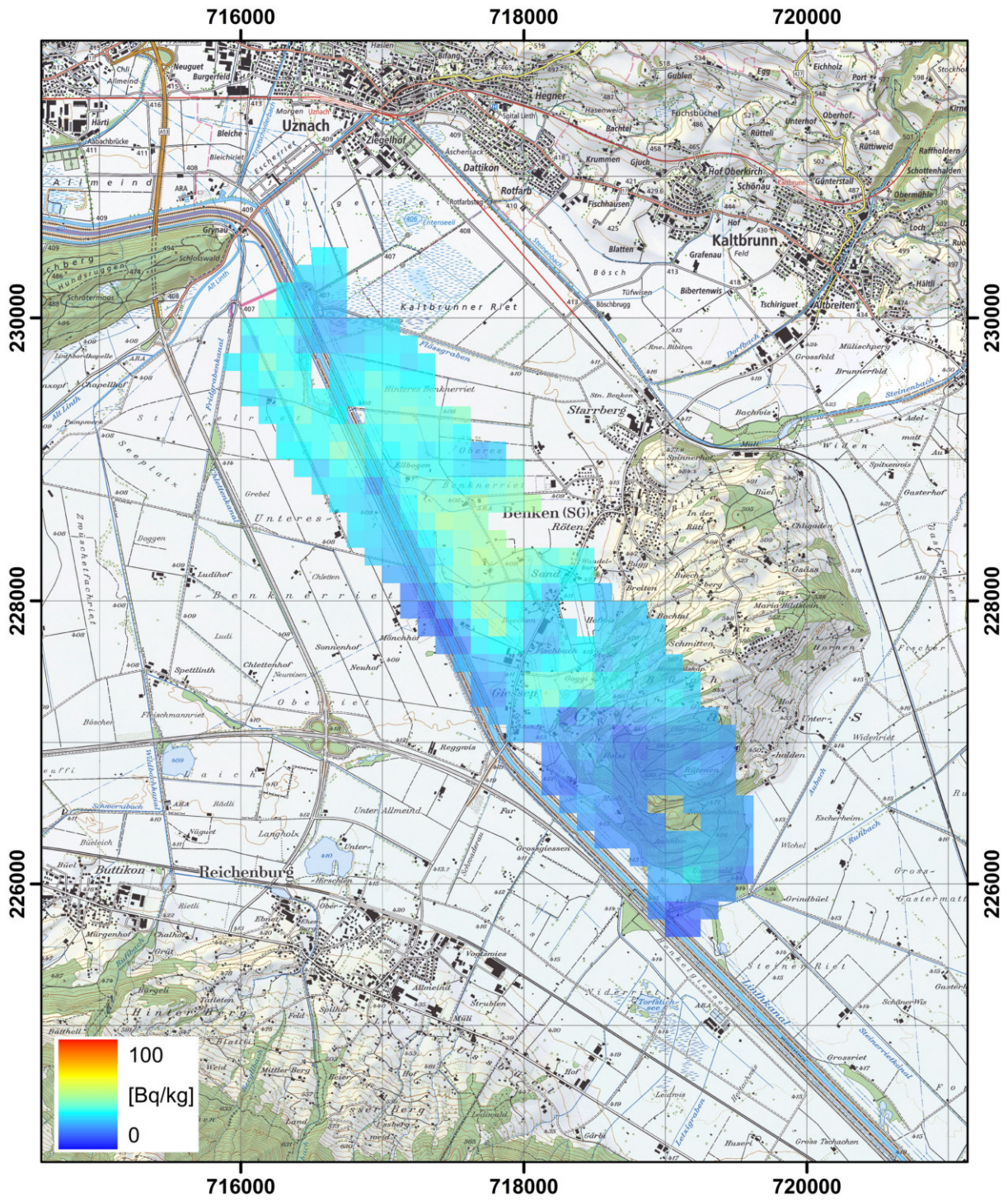
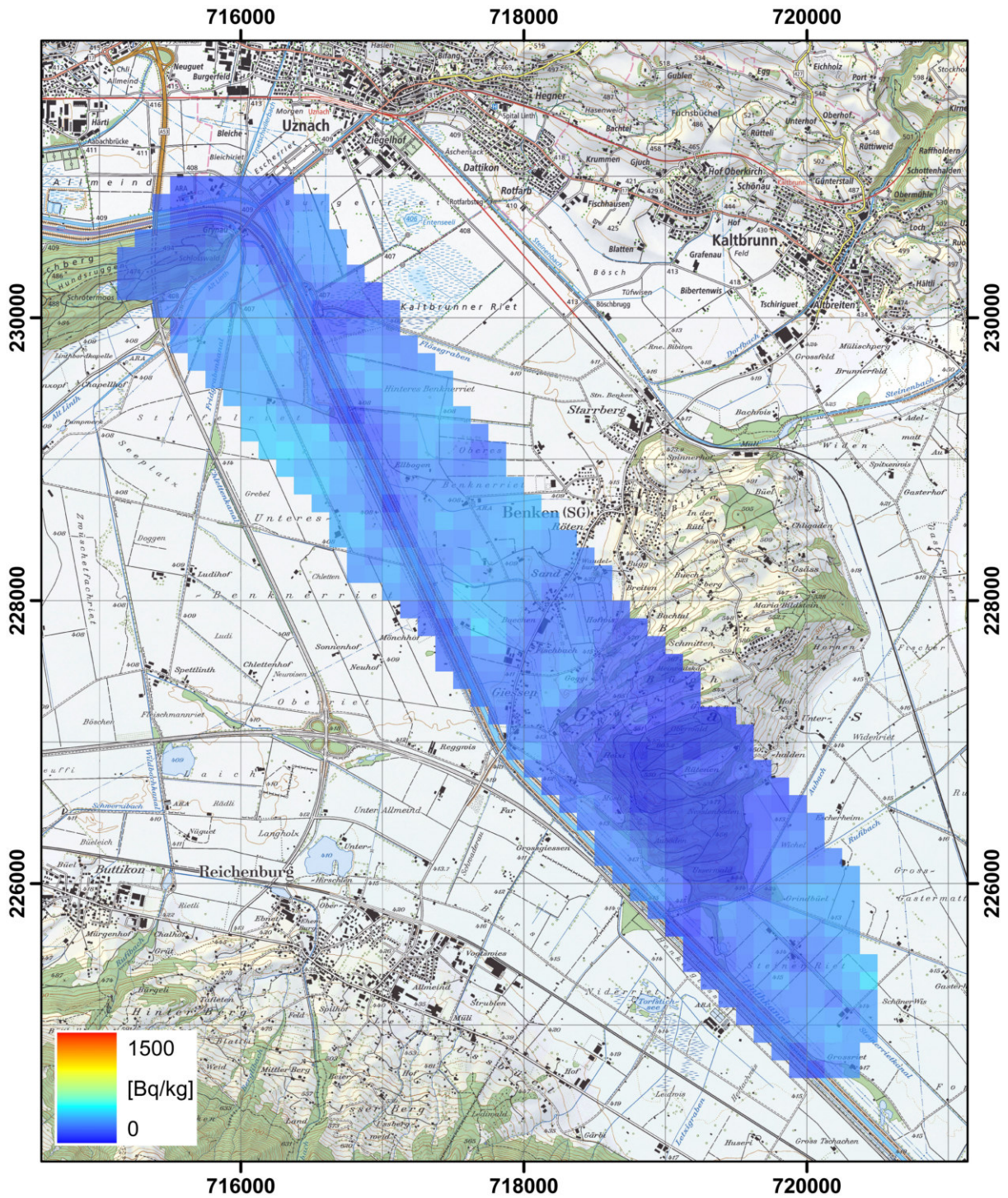Figure 129: ^{232}Th activity concentration measured by team DE02 over the Linth plain with ground clearance of 116 m. PK25©2017 swisstopo (JD100042).

145
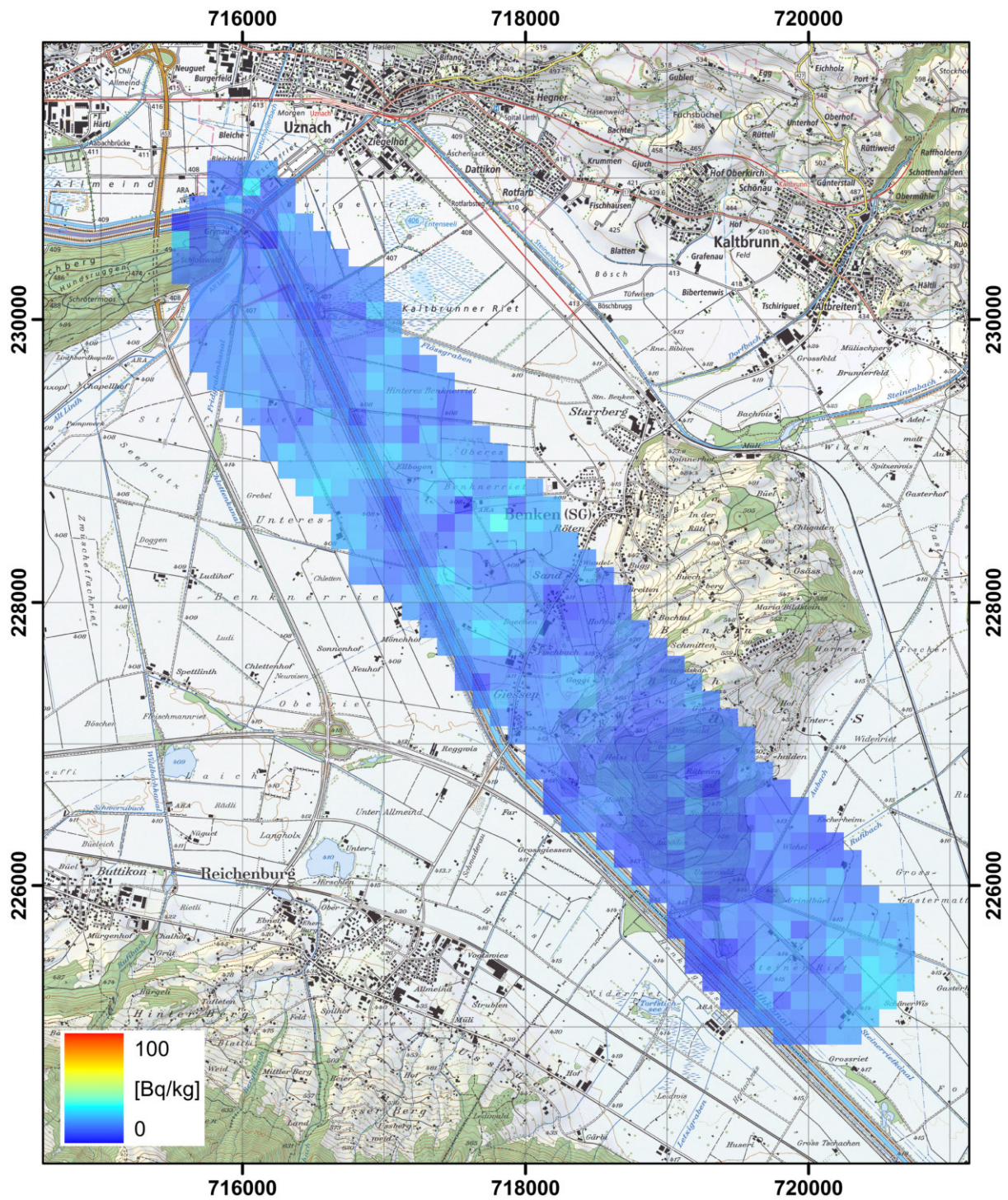
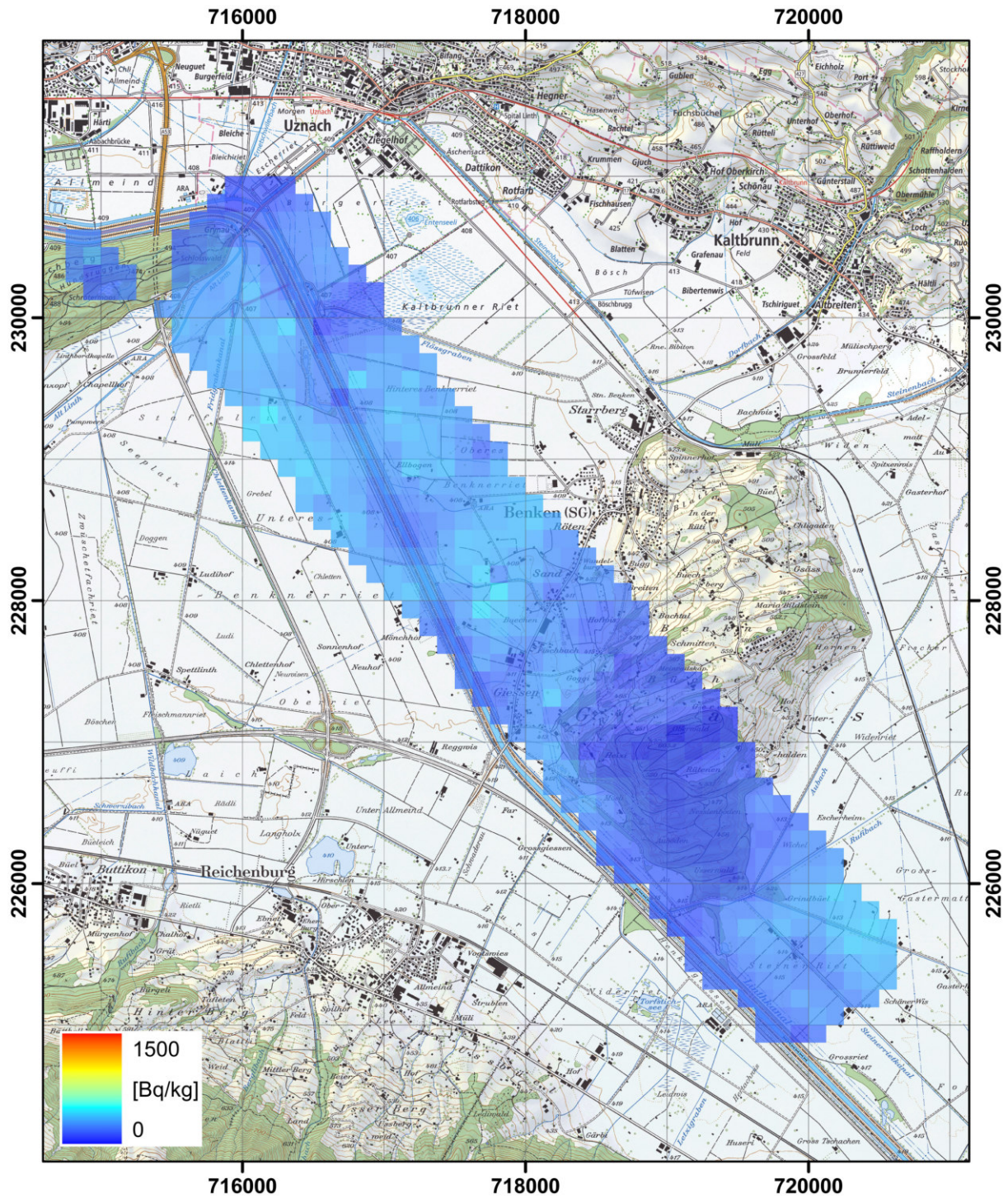Figure 130: ^{232}Th activity concentration measured by team FR01 over the Linth plain with ground clearance of 96 m after post-processing. PK25©2017 swisstopo (JD100042).
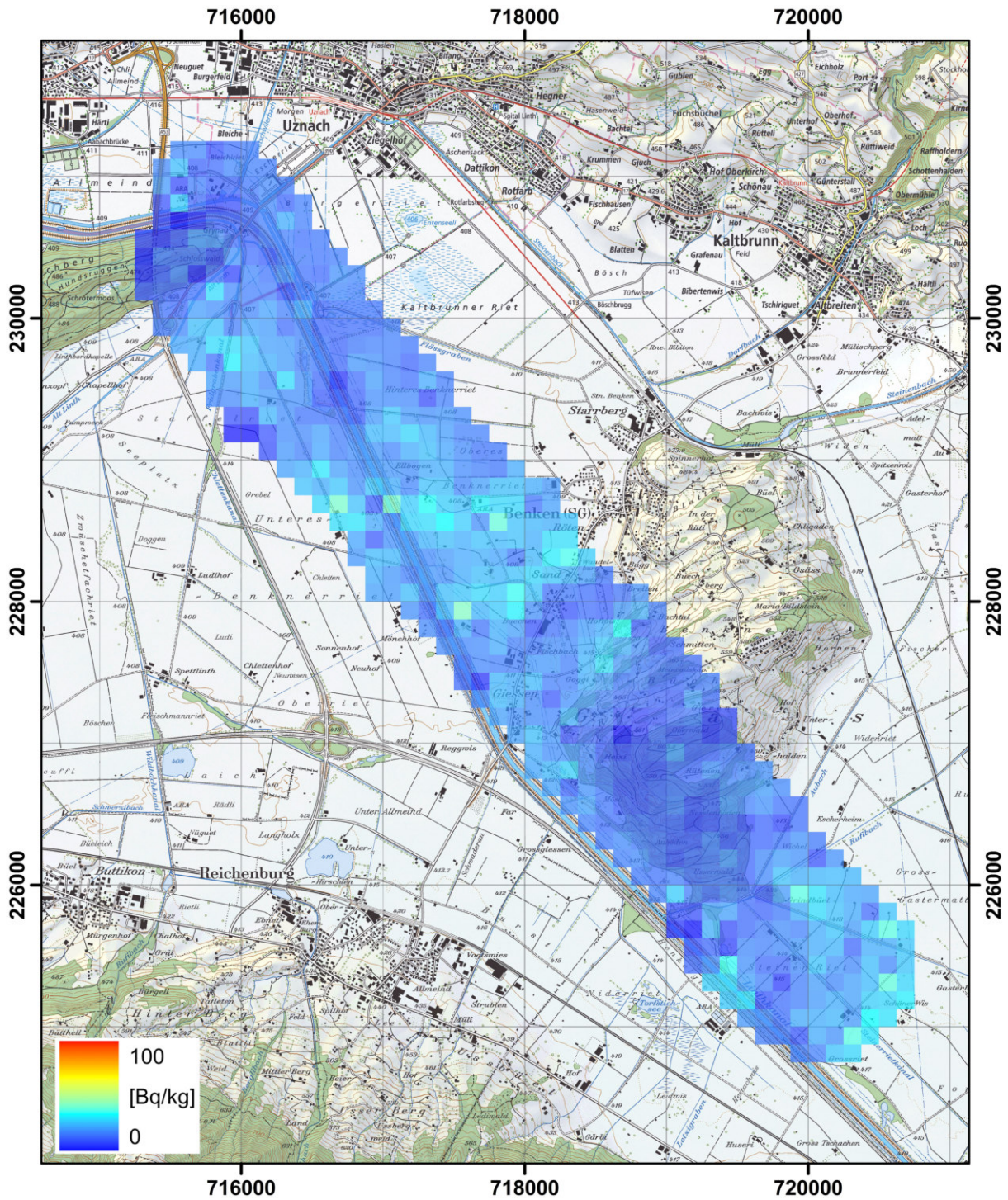
Figure 131: ^{232}Th activity concentration measured by team FR01 over the Linth plain with ground clearance of 159 m after post-processing. PK25©2017 swisstopo (JD100042).
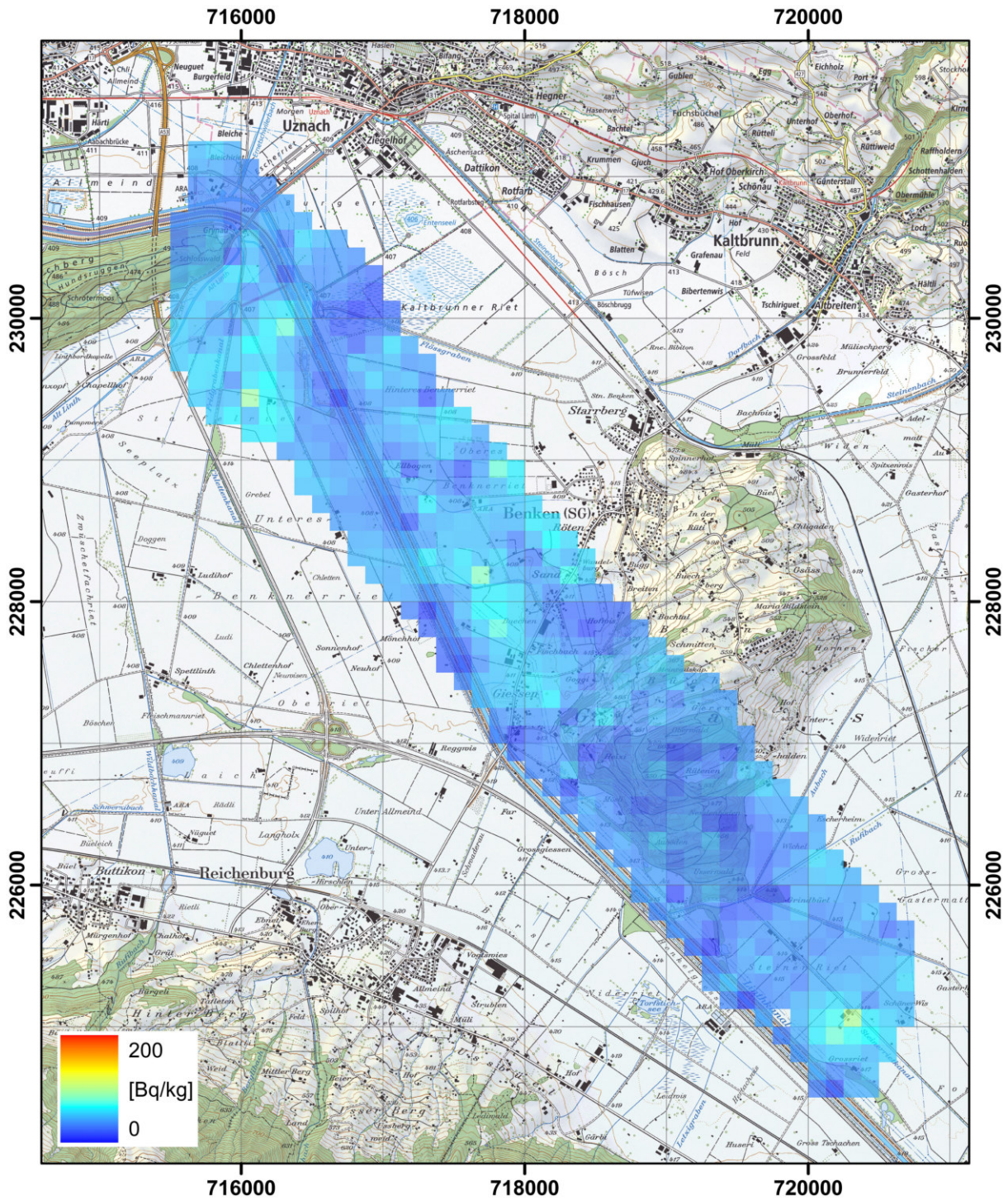
Figure 132: ^{238}U activity concentration measured by team CH01 over the Linth plain with ground clearance of 98 m after corrections. PK25©2017 swisstopo (JD100042).
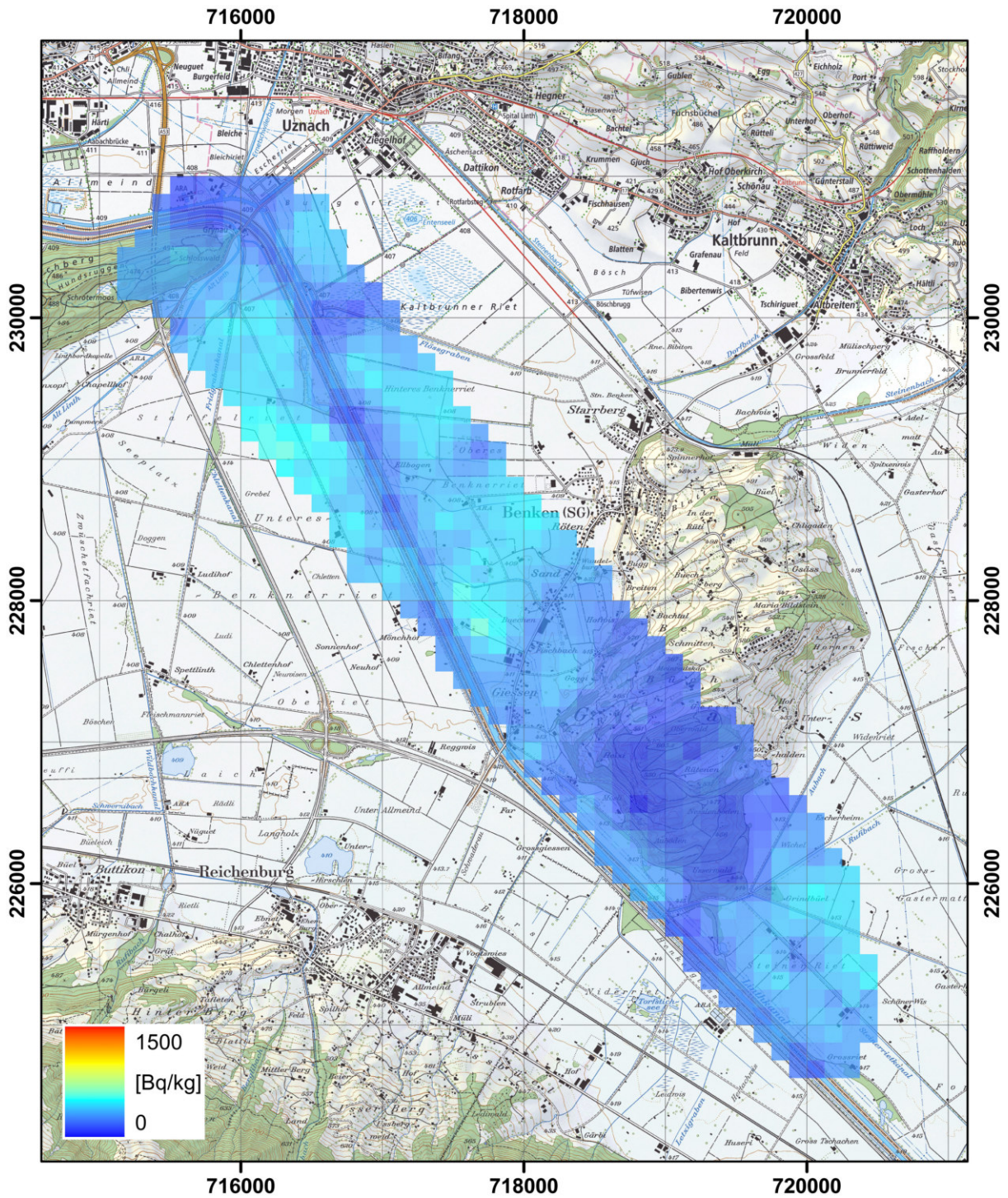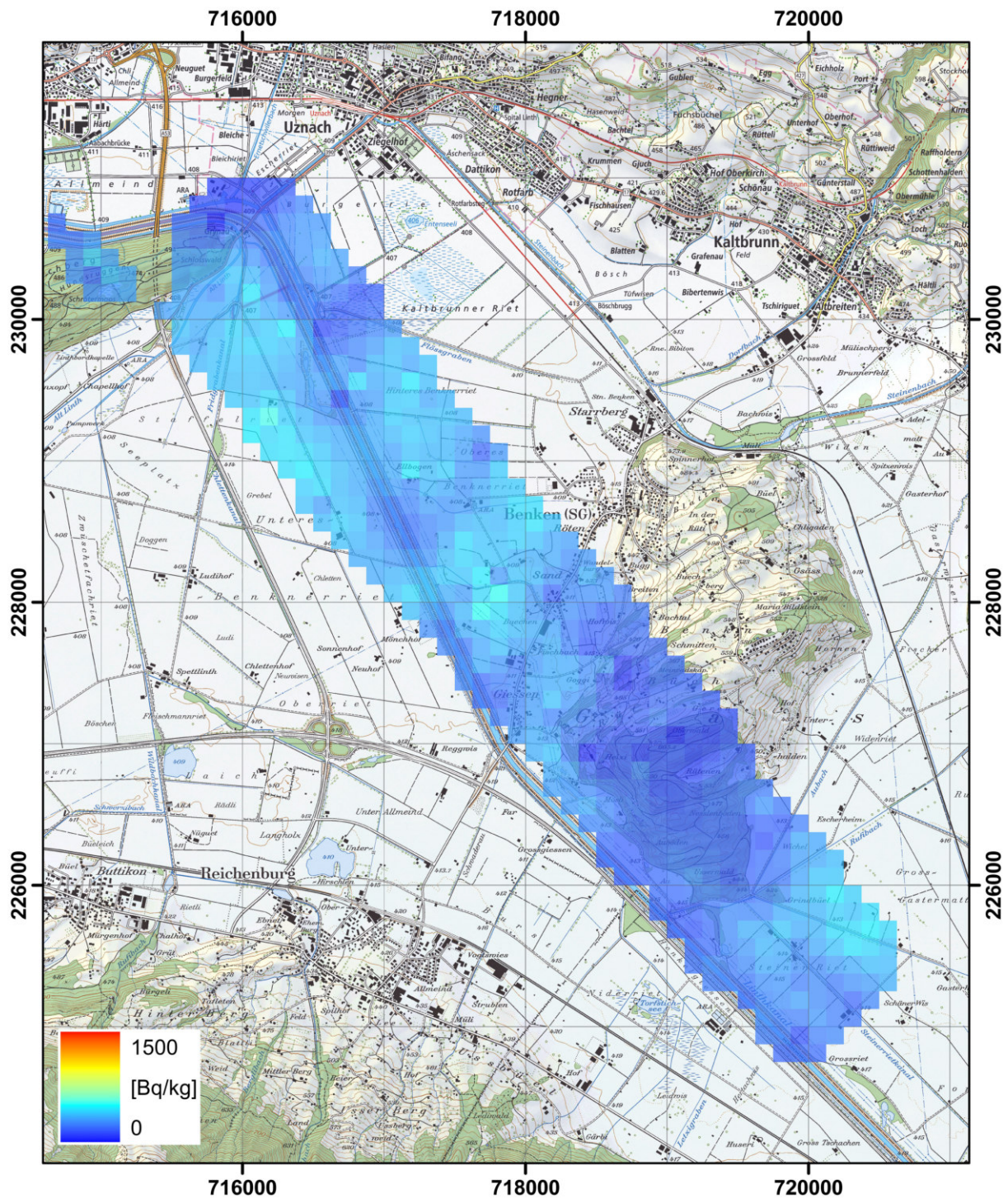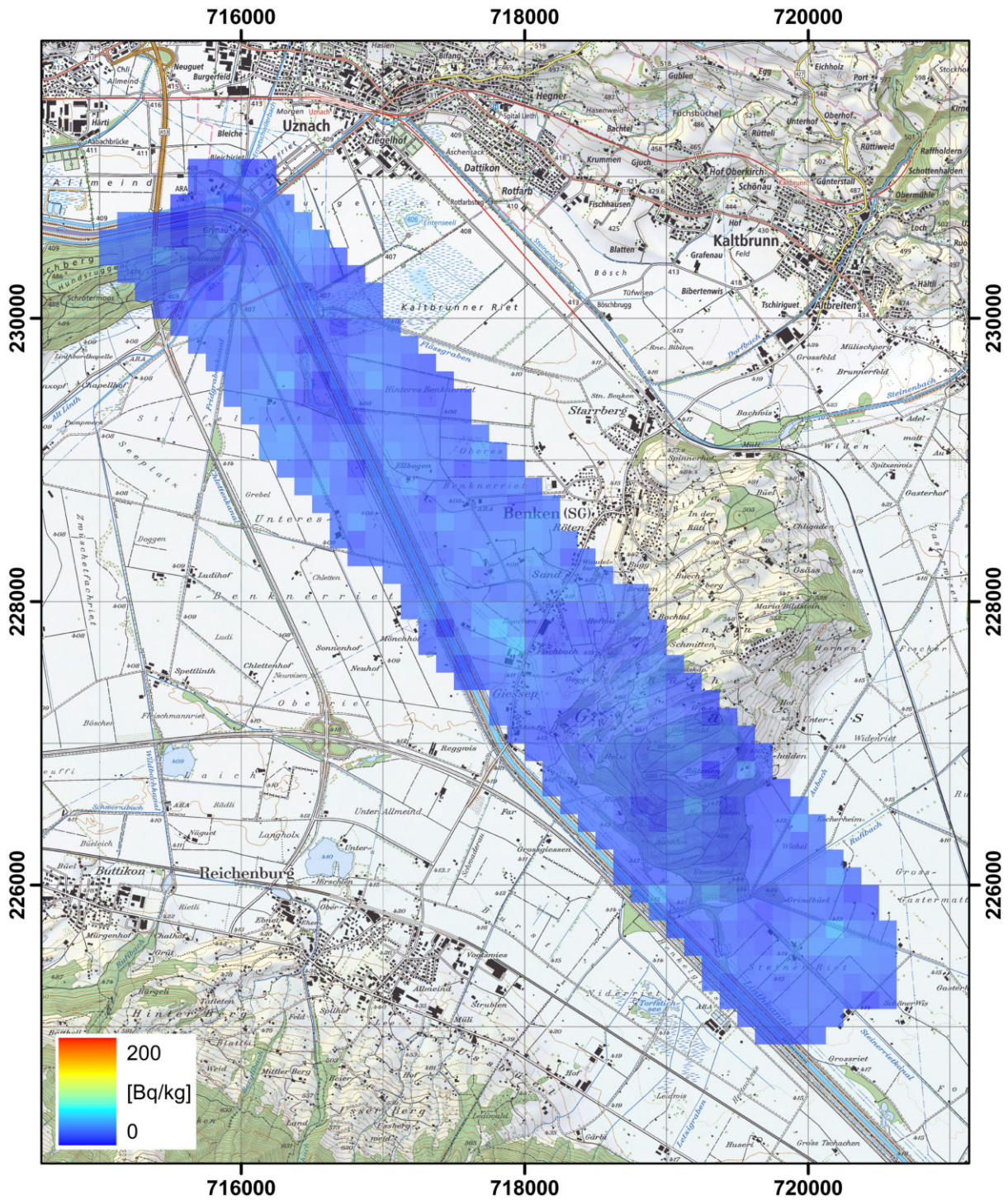
Figure 133: ^{238}U activity concentration measured by team CH01 over the Linth plain with ground clearance of 151 m after corrections. PK25©2017 swisstopo (JD100042).
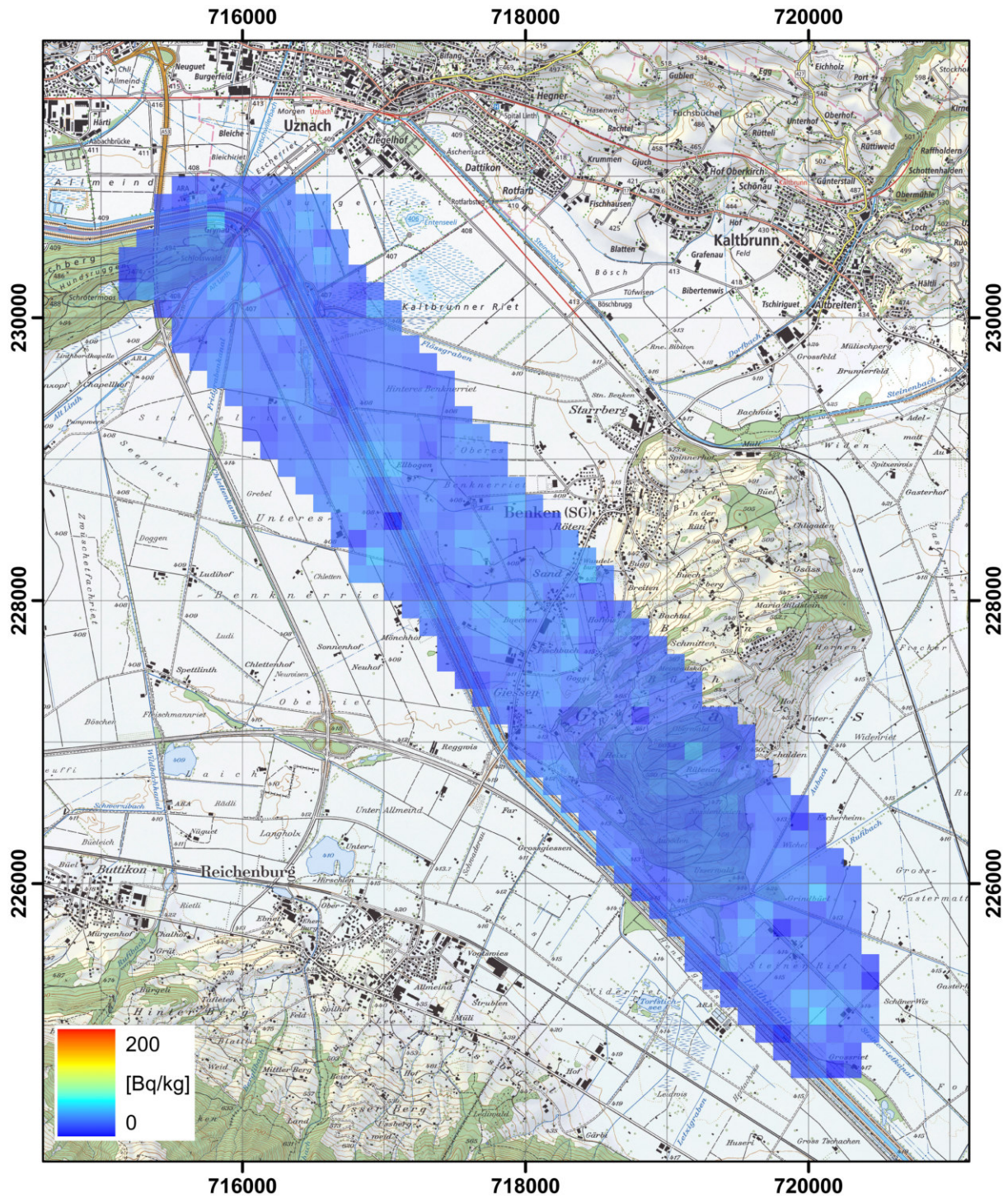
Figure 134: ^{238}U activity concentration measured by team CH02 over the Linth plain with ground clearance of 95 m without corrections. PK25©2017 swisstopo (JD100042).
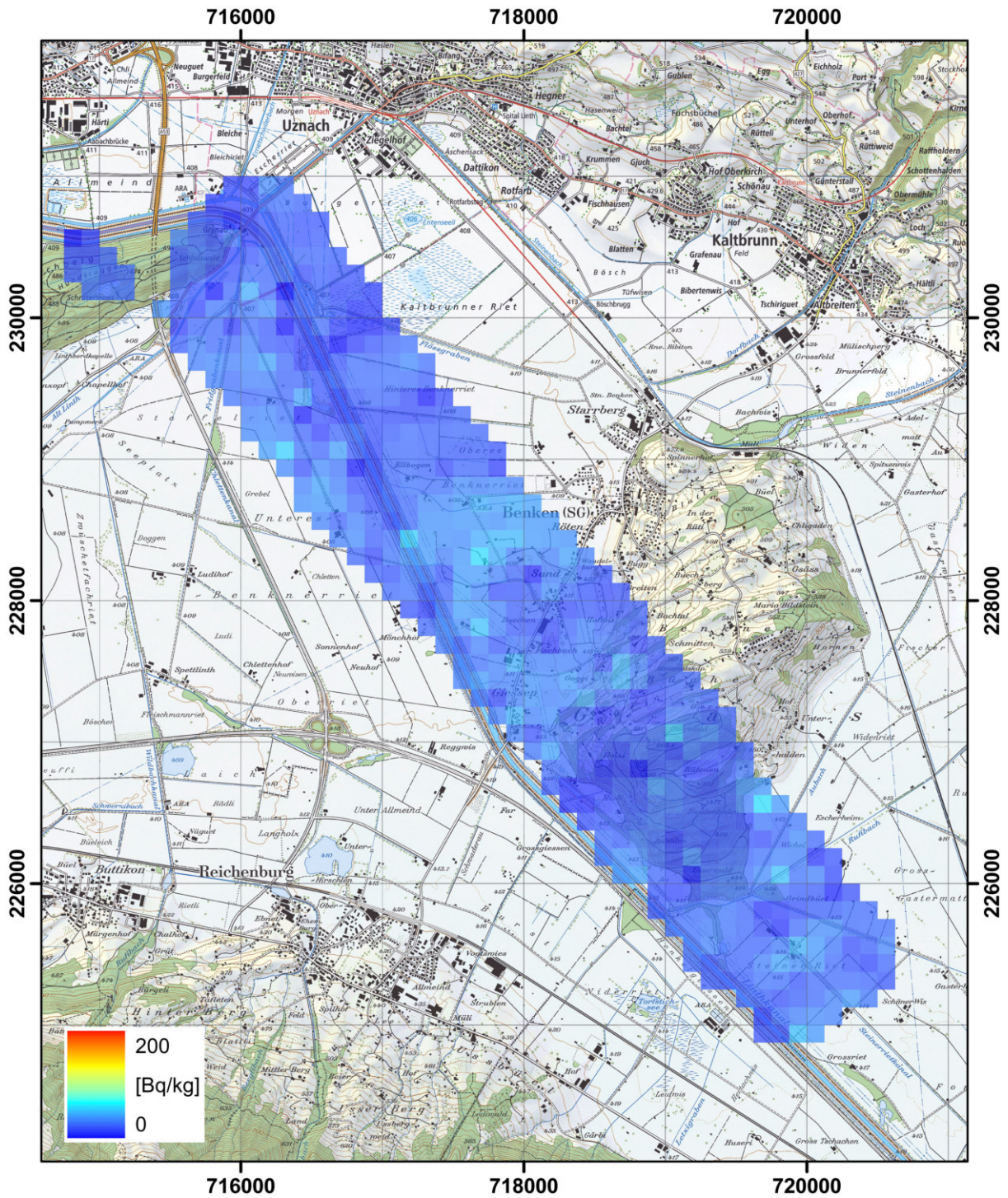
Figure 135: ^{238}U activity concentration measured by team CH02 over the Linth plain with ground clearance of 152 m without corrections. PK25©2017 swisstopo (JD100042).
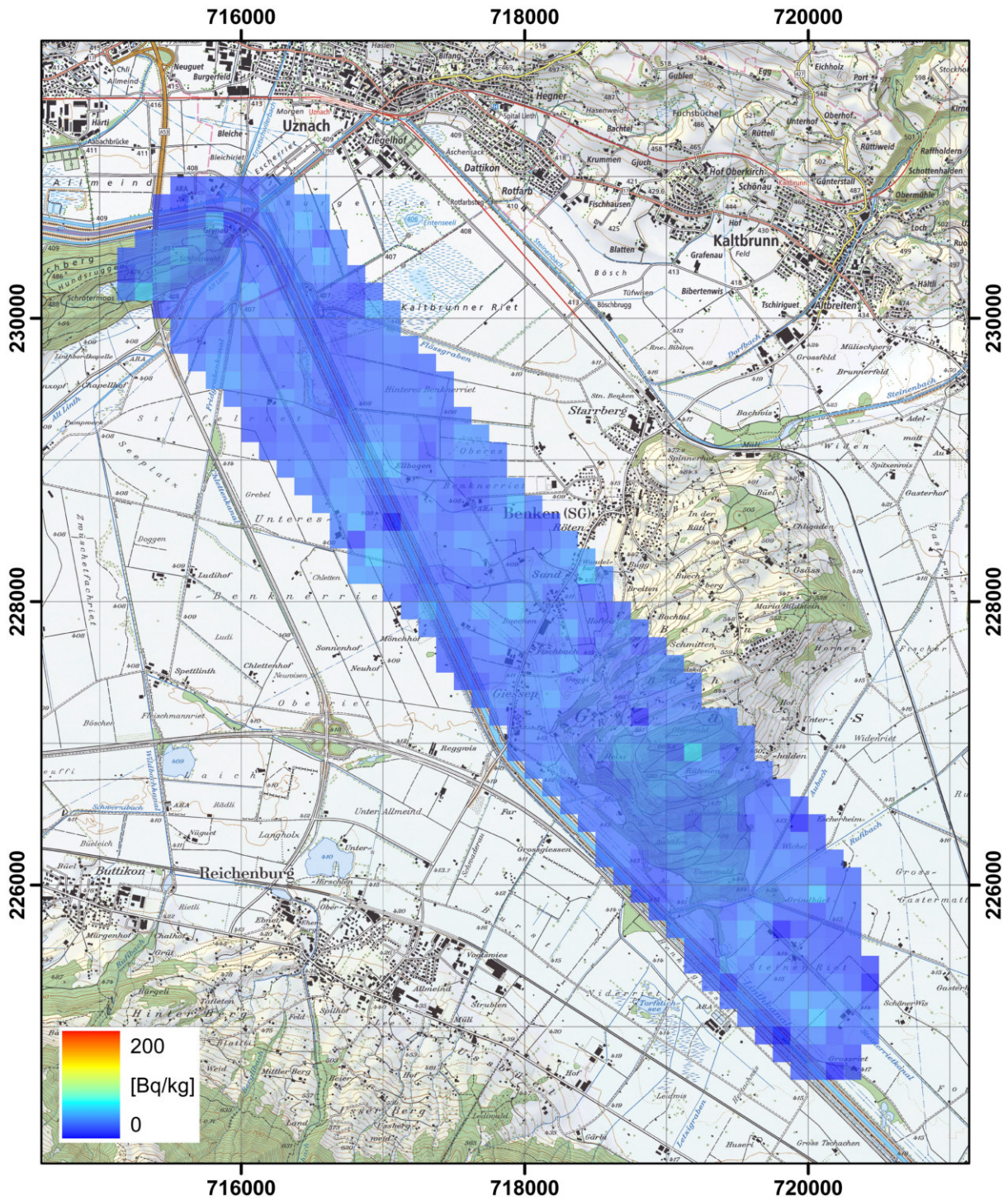
Figure 136: ^{238}U activity concentration measured by team CH02 over the Linth plain with ground clearance of 95 m. ARM data evaluation with corrections. PK25©2017 swisstopo (JD100042).
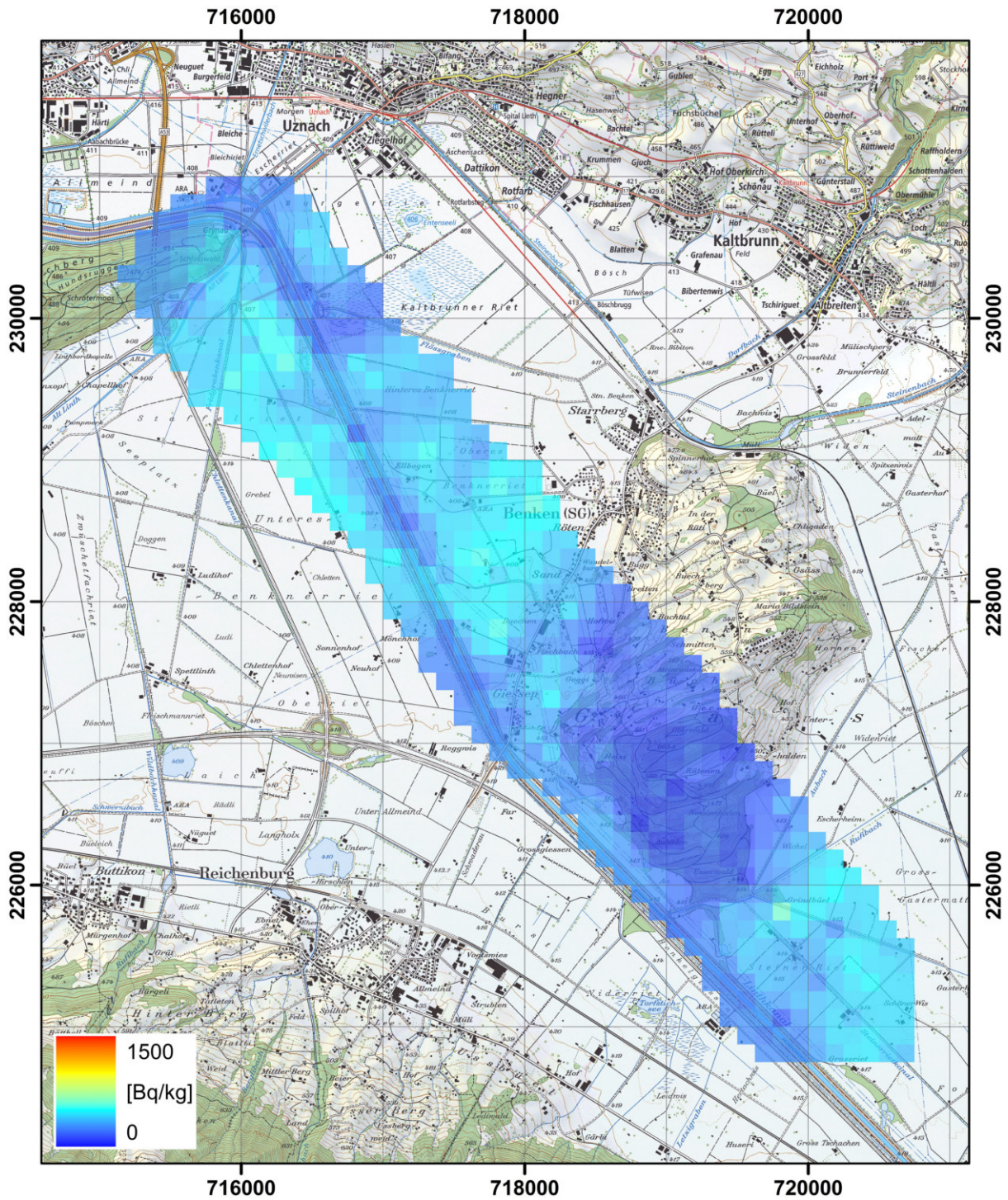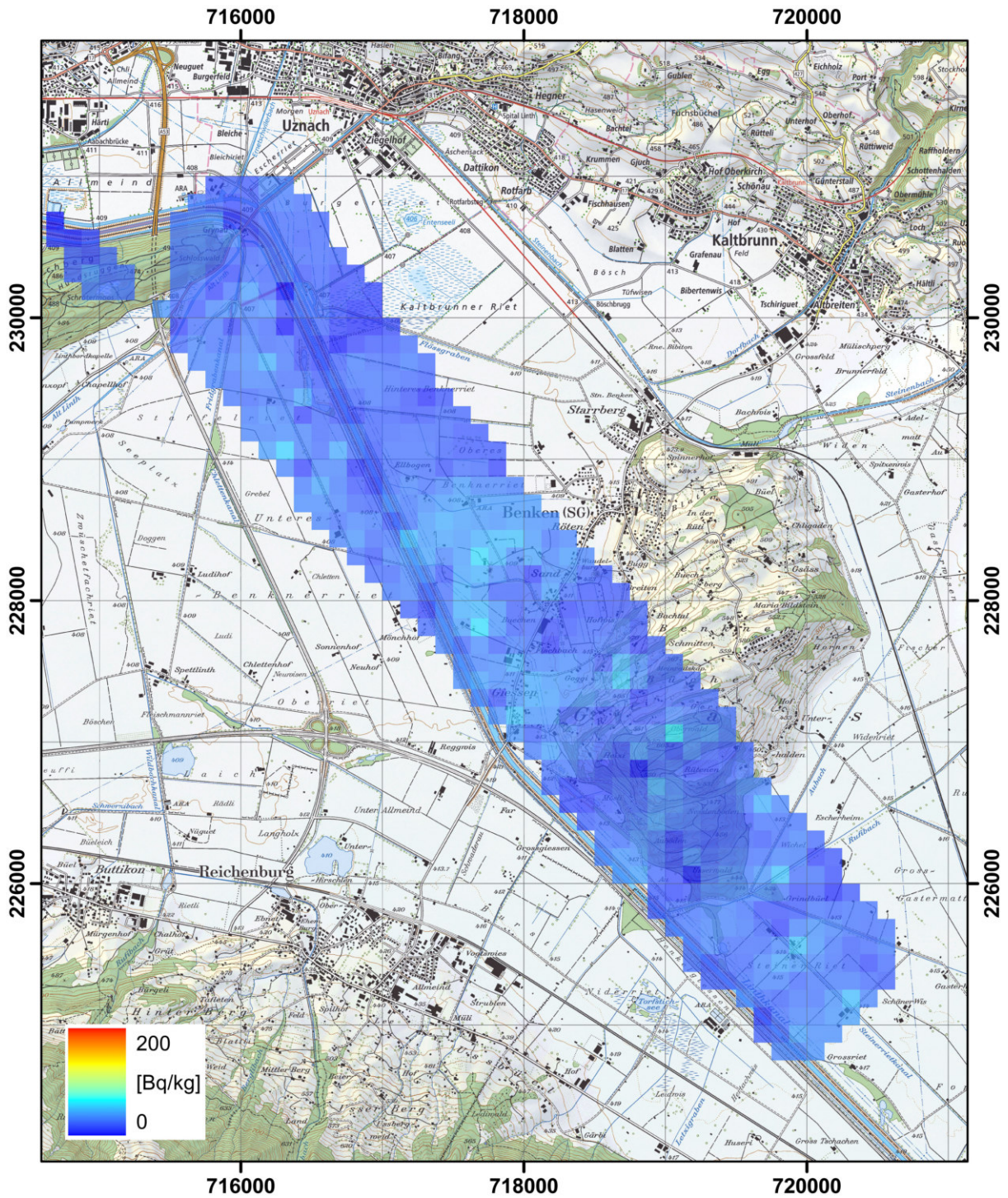
Figure 137: ^{238}U activity concentration measured by team CH02 over the Linth plain with ground clearance of 152 m. ARM data evaluation with corrections. PK25©2017 swisstopo (JD100042).

153
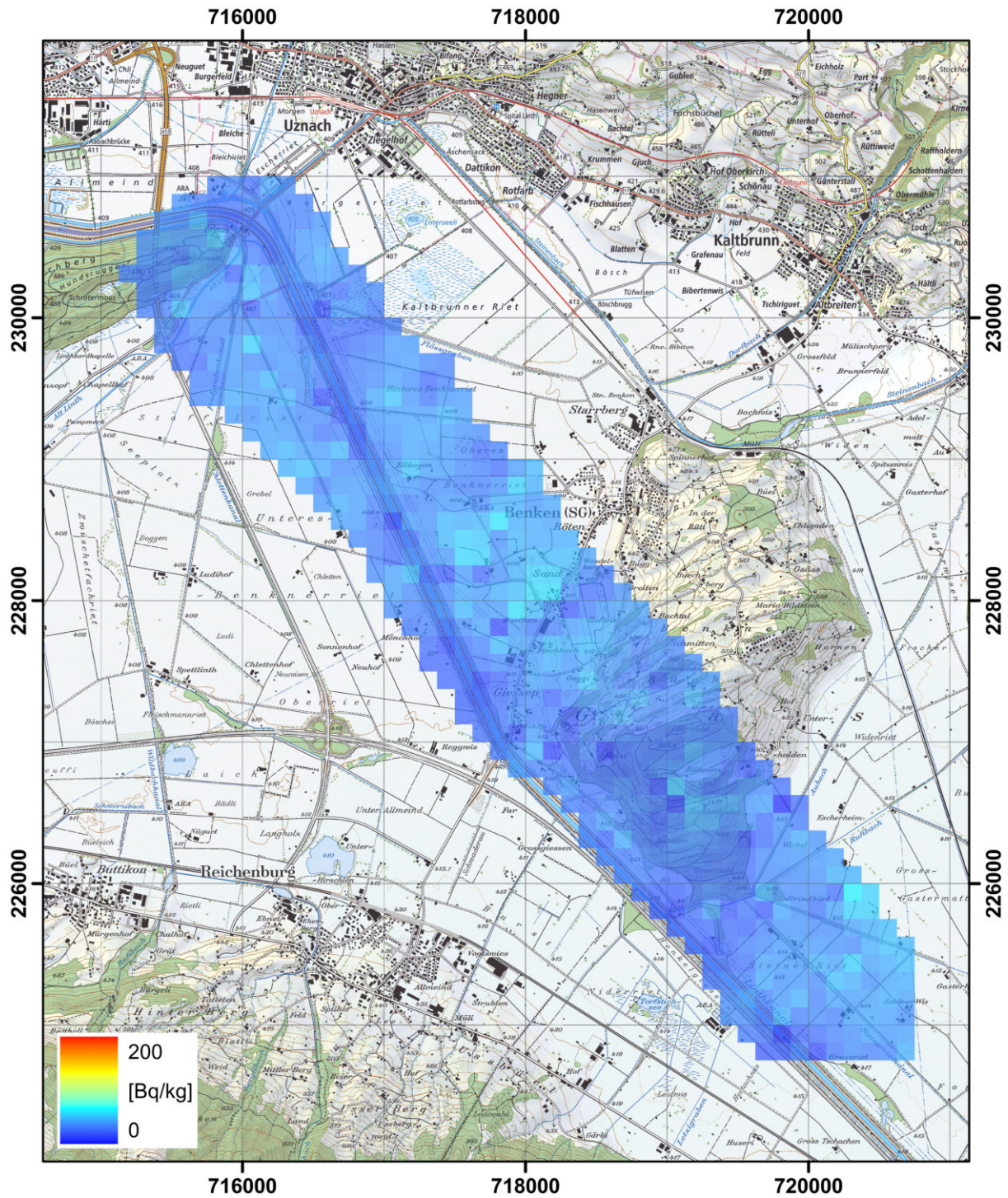
Figure 138: ^{238}U activity concentration measured by team CZ01 over the Linth plain with ground clearance of 105 m after post-processing. PK25©2017 swisstopo (JD100042).
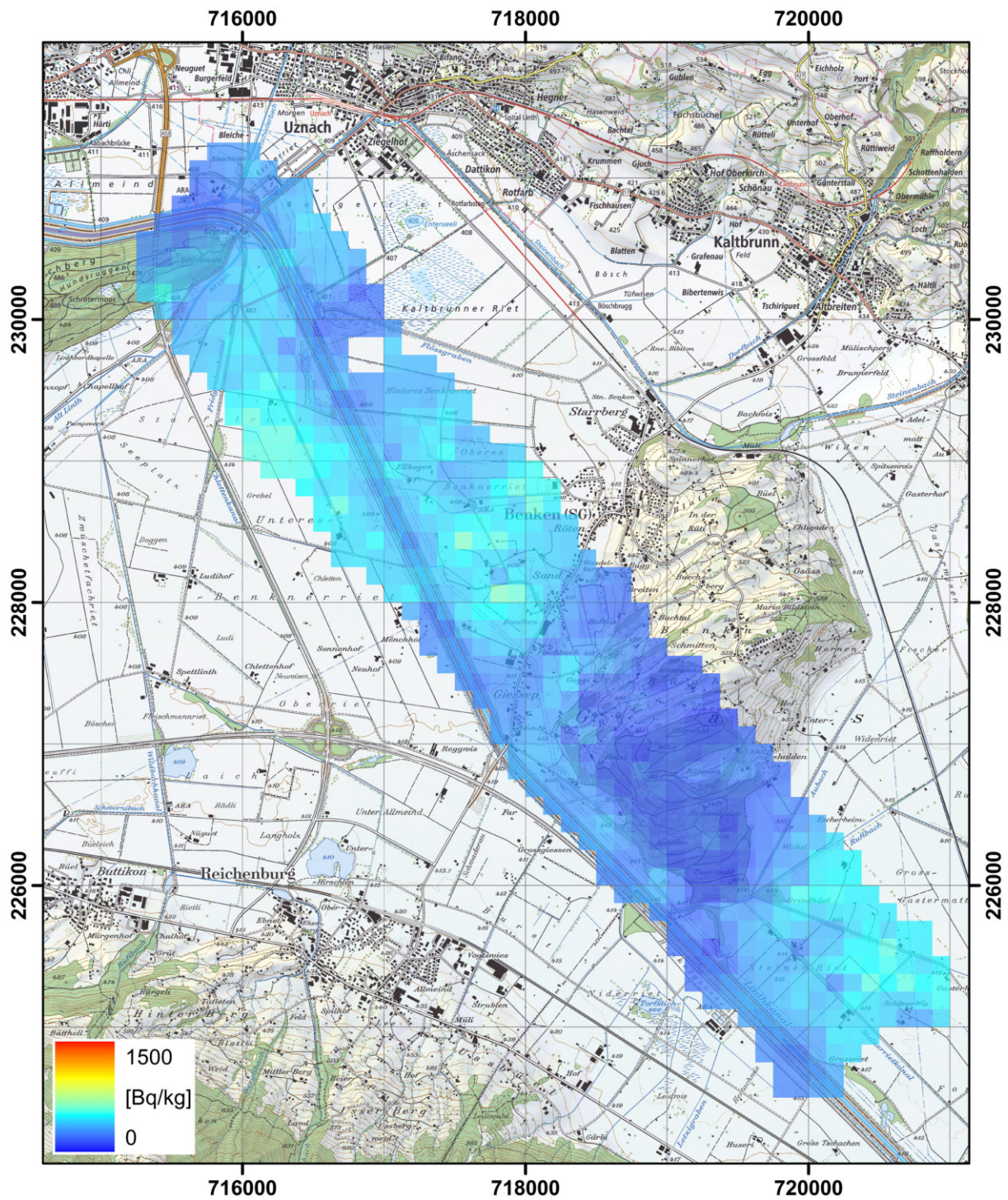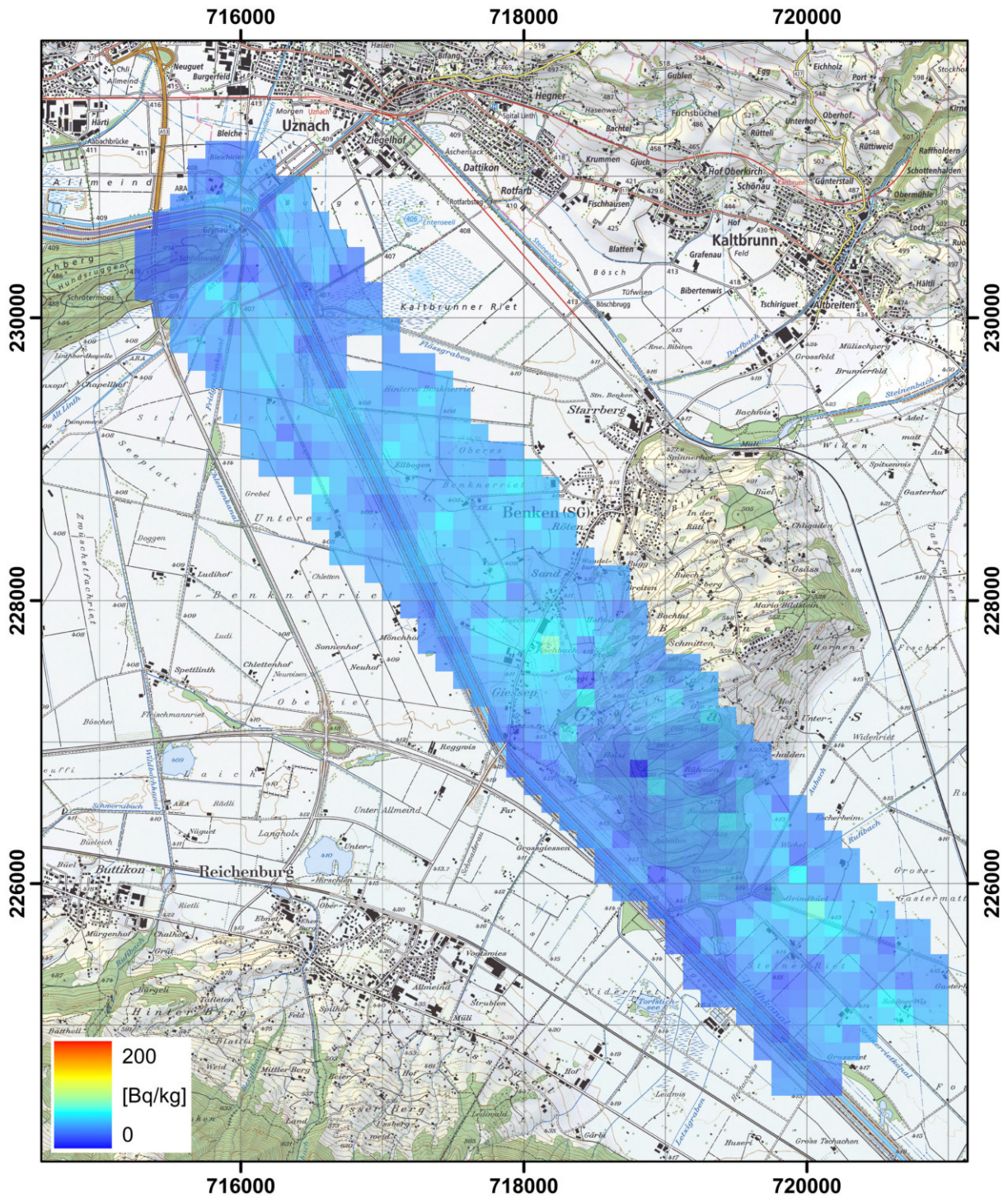
Figure 139: ^{238}U activity concentration measured by team CZ01 over the Linth plain with ground clearance of 145 m after post-processing. PK25©2017 swisstopo (JD100042).
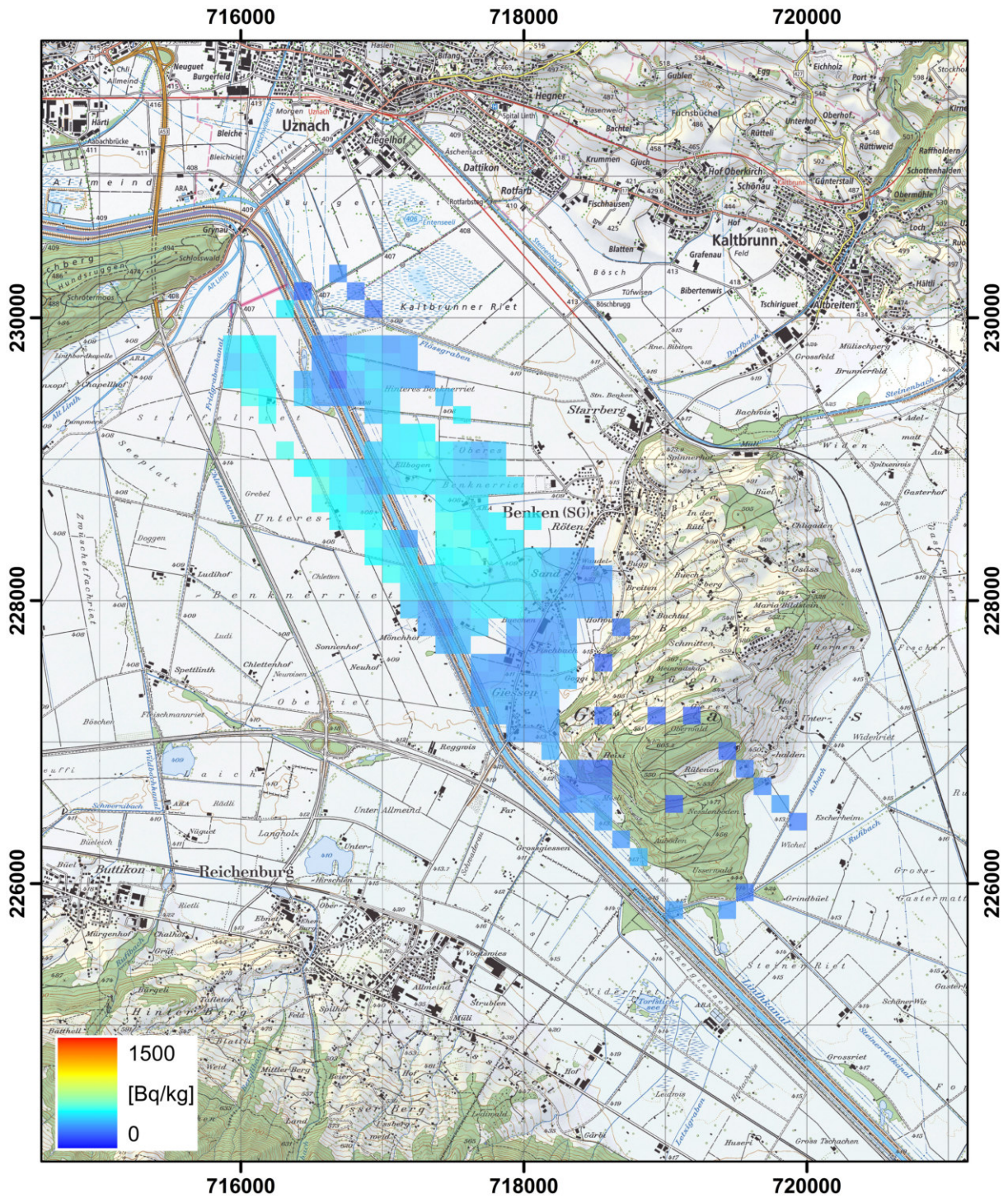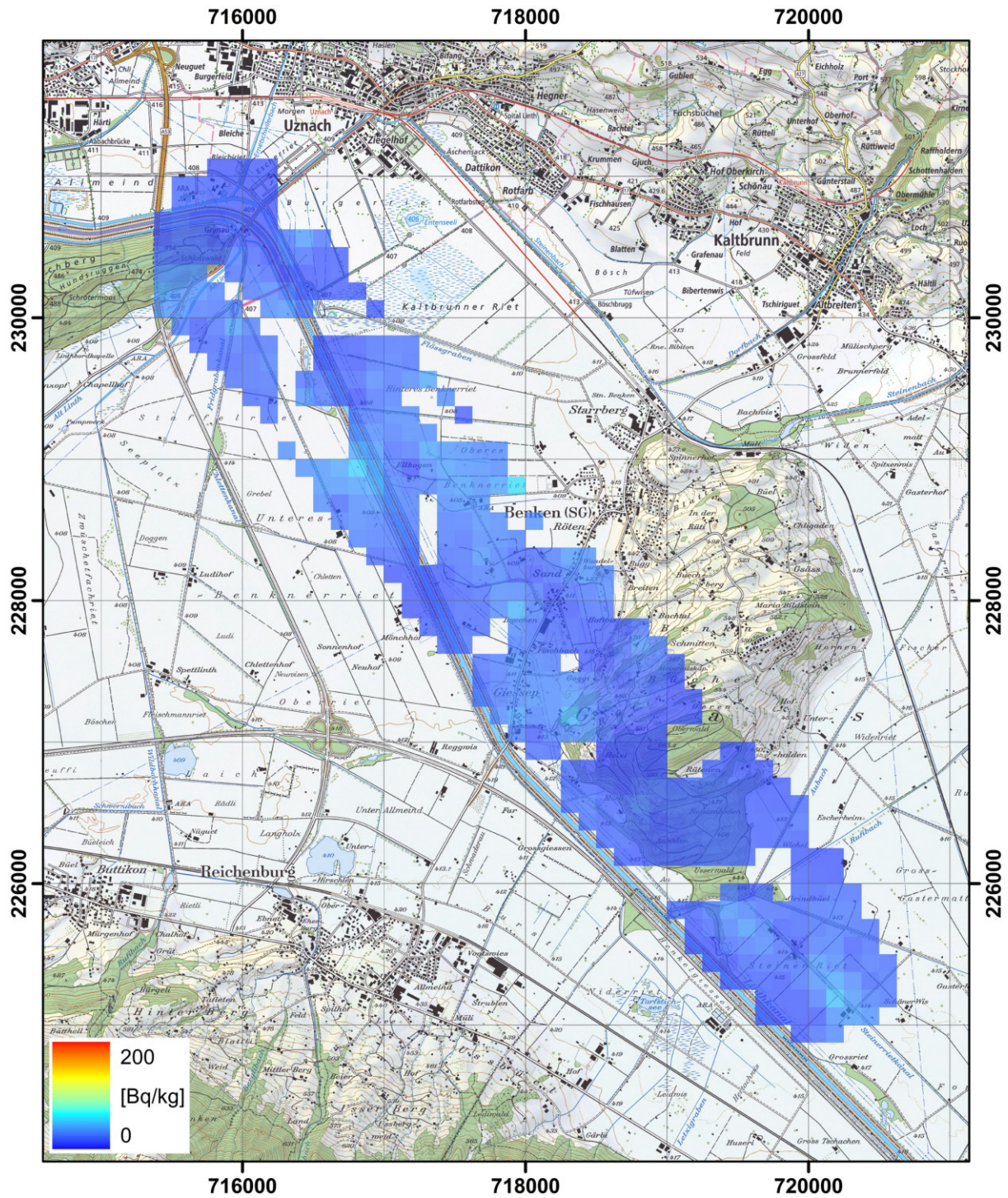
Figure 140: ^{238}U activity concentration measured by team DE01 over the Linth plain with ground clearance of 114 m. PK25©2017 swisstopo (JD100042).
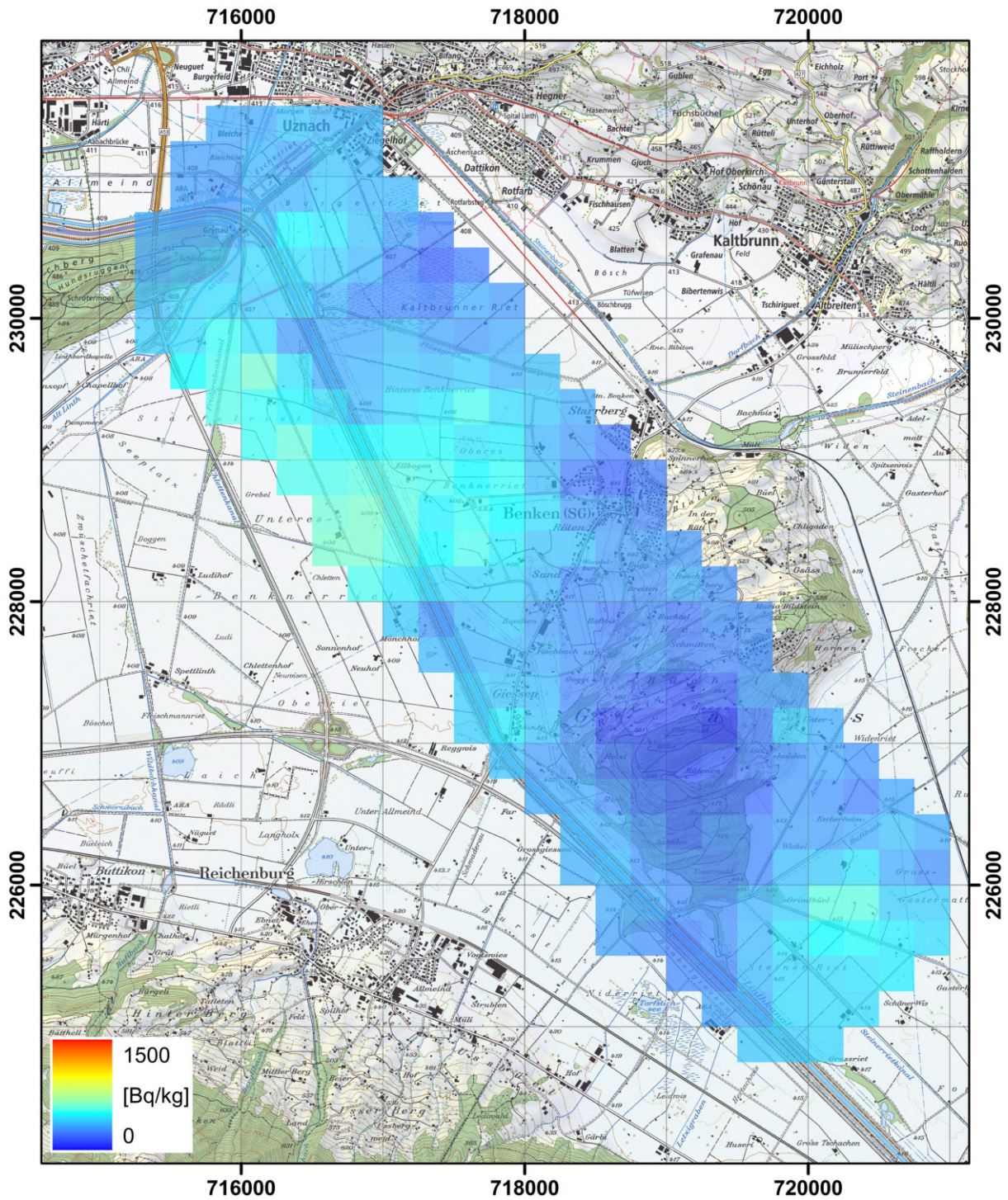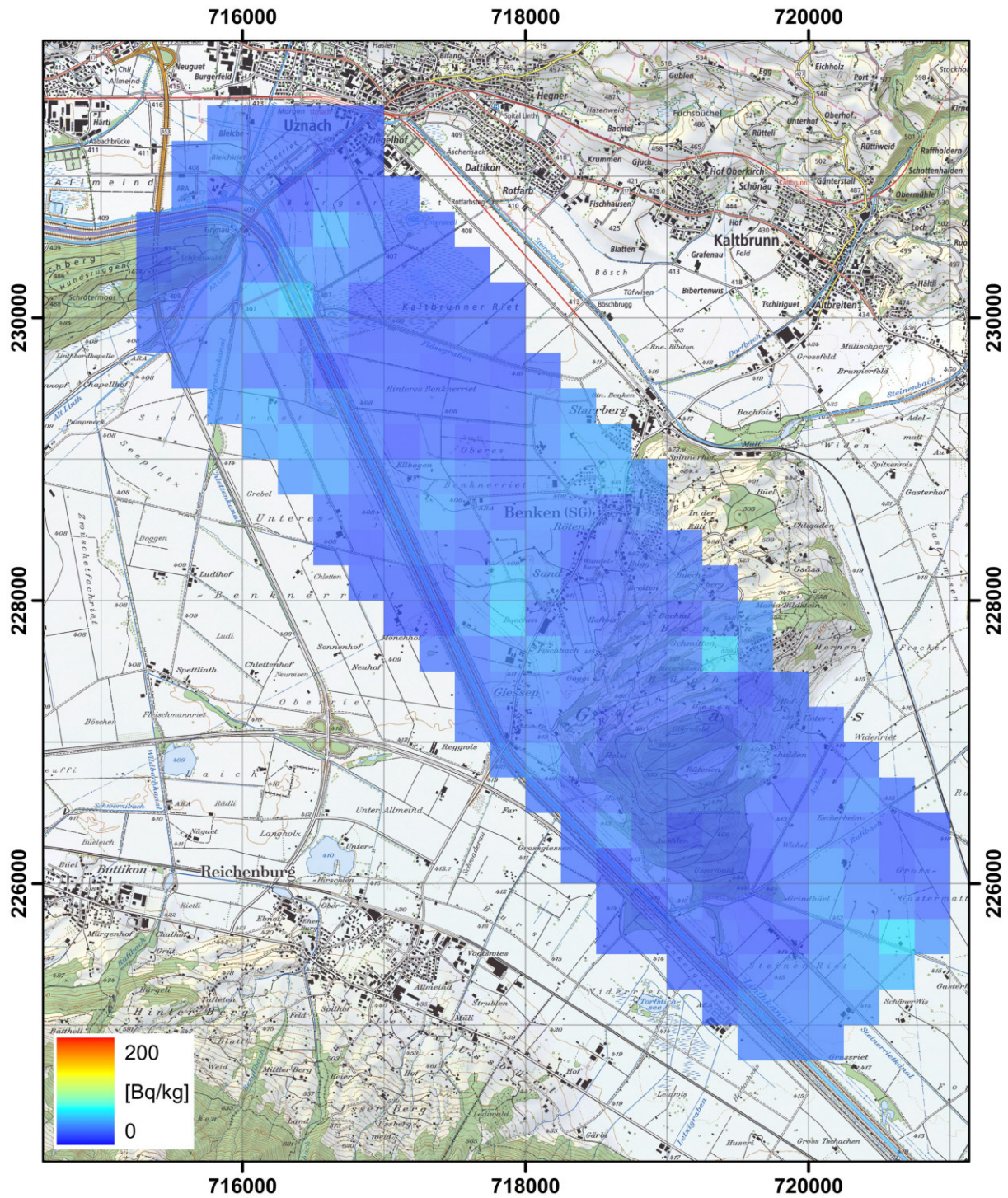
Figure 141: ^{238}U activity concentration measured by team DE01 over the Linth plain with ground clearance of 130 m. PK25©2017 swisstopo (JD100042).
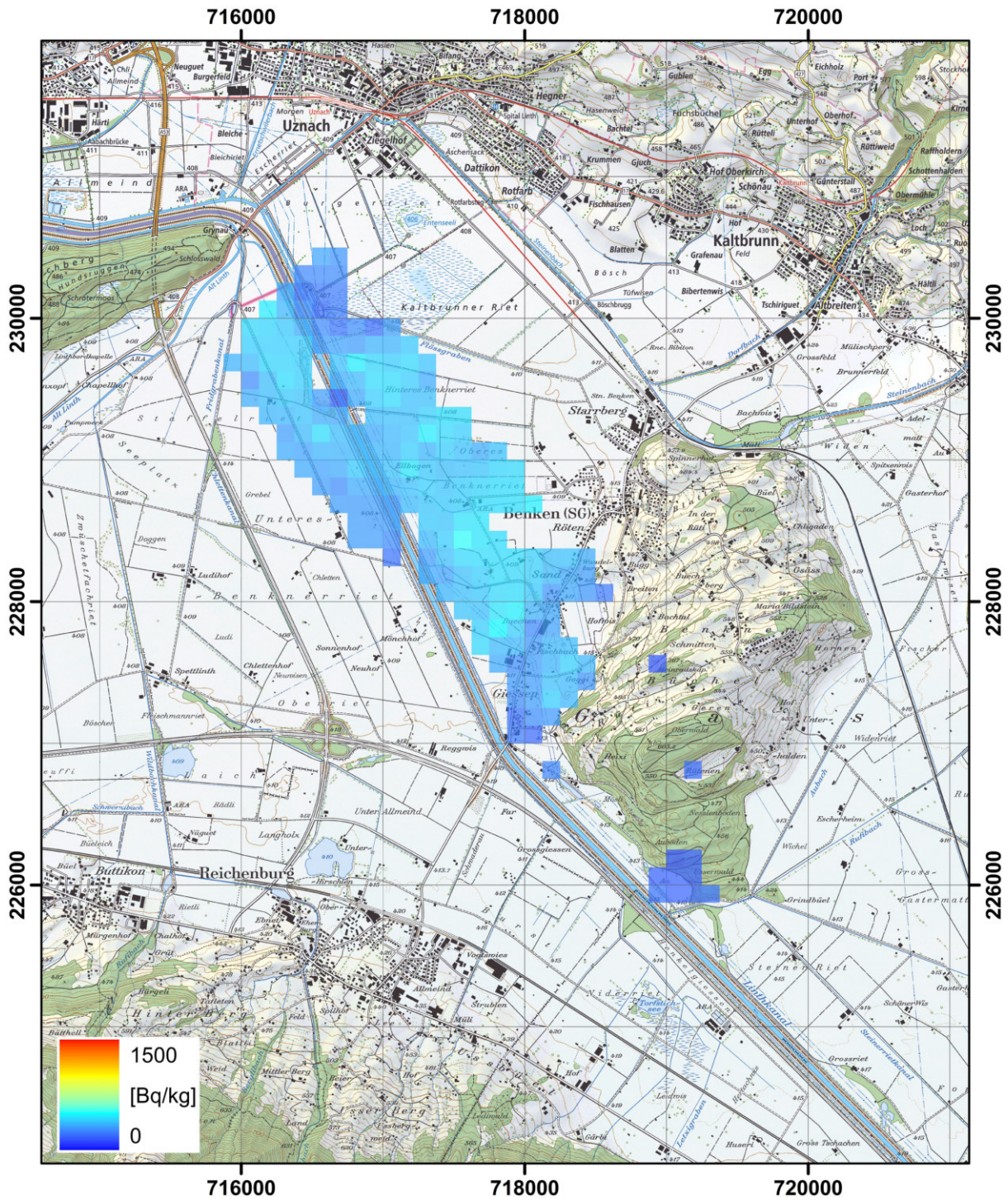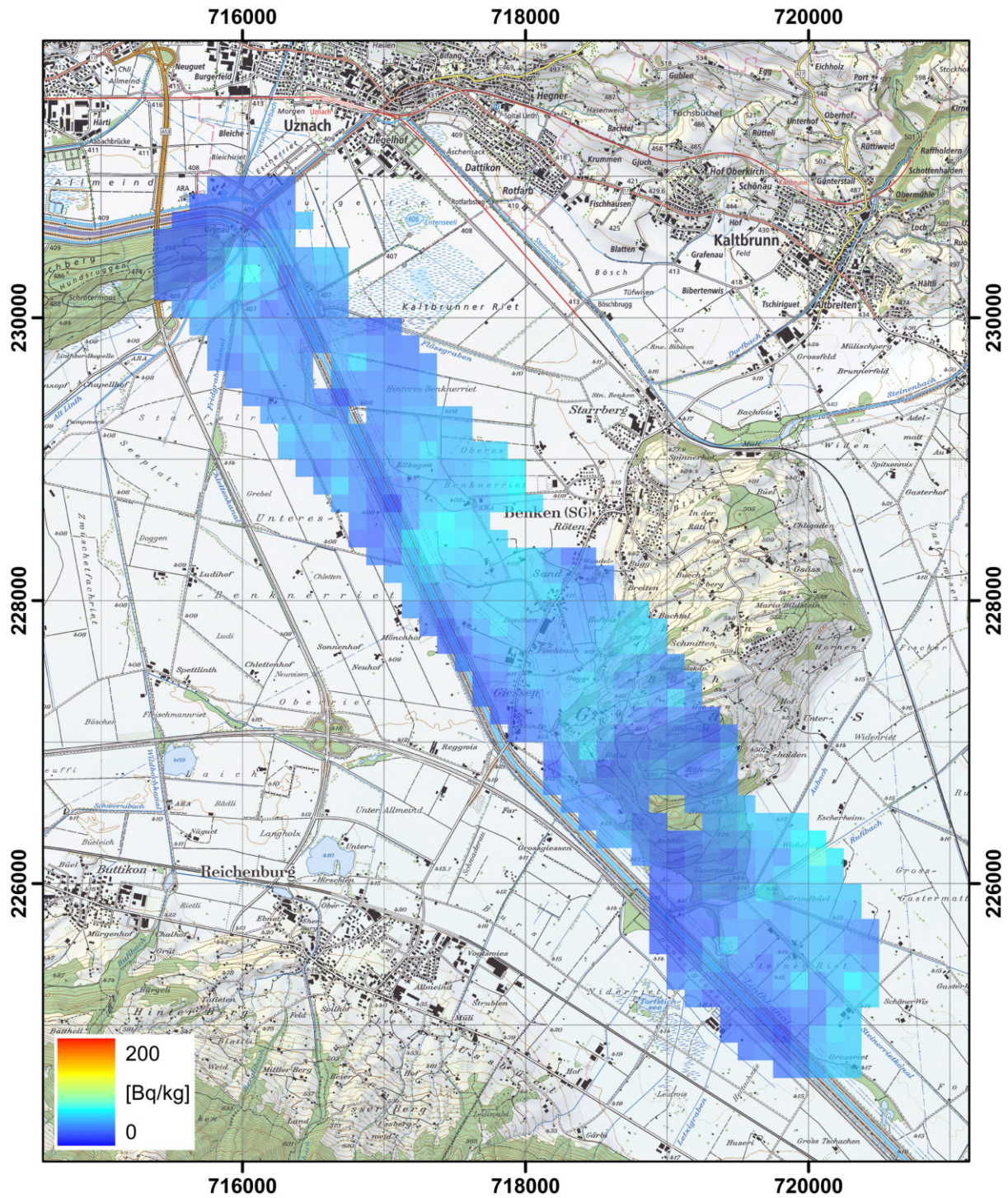
Figure 142: ^{238}U activity concentration measured by team DE02 over the Linth plain with ground clearance of 116 m. PK25©2017 swisstopo (JD100042).
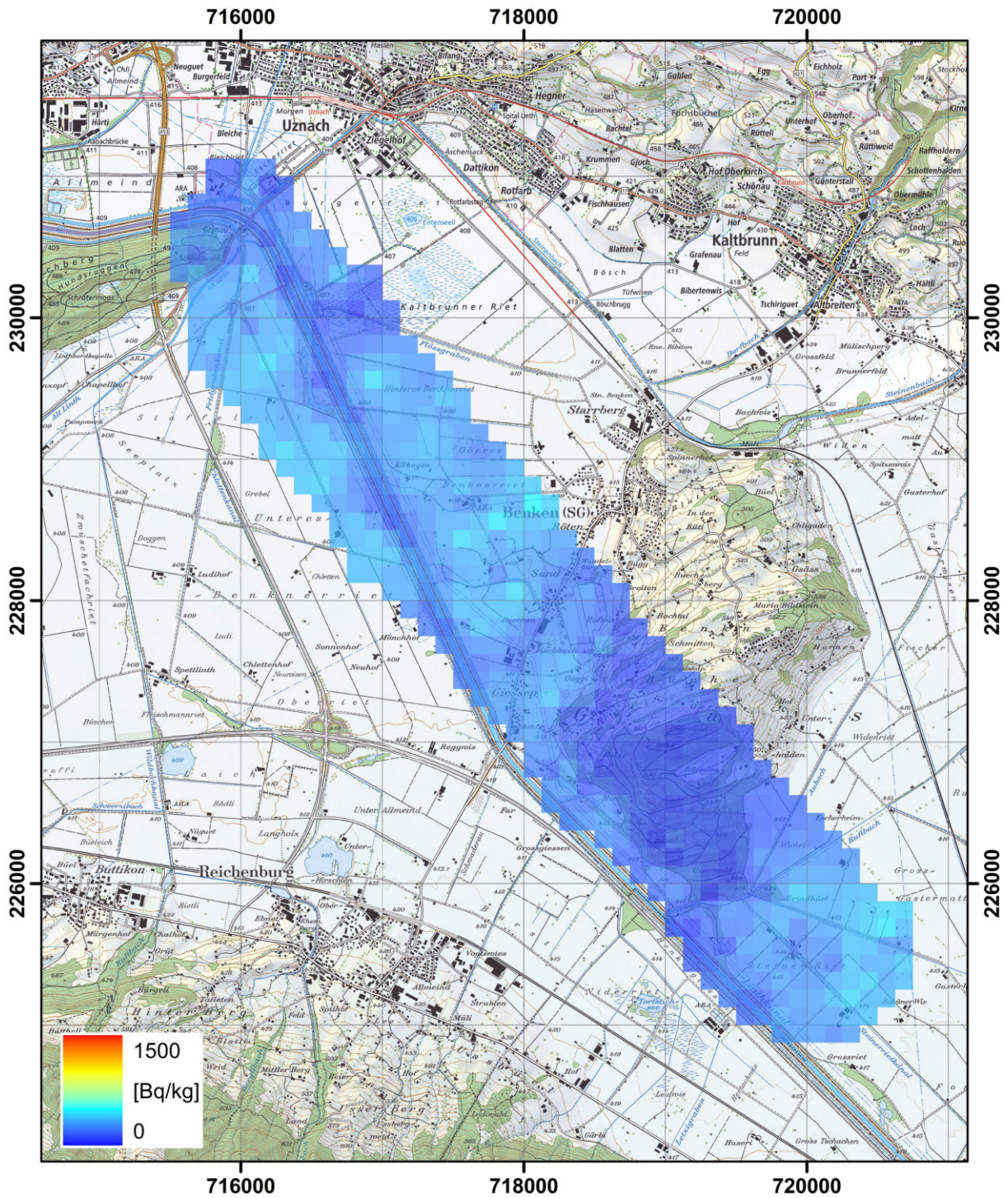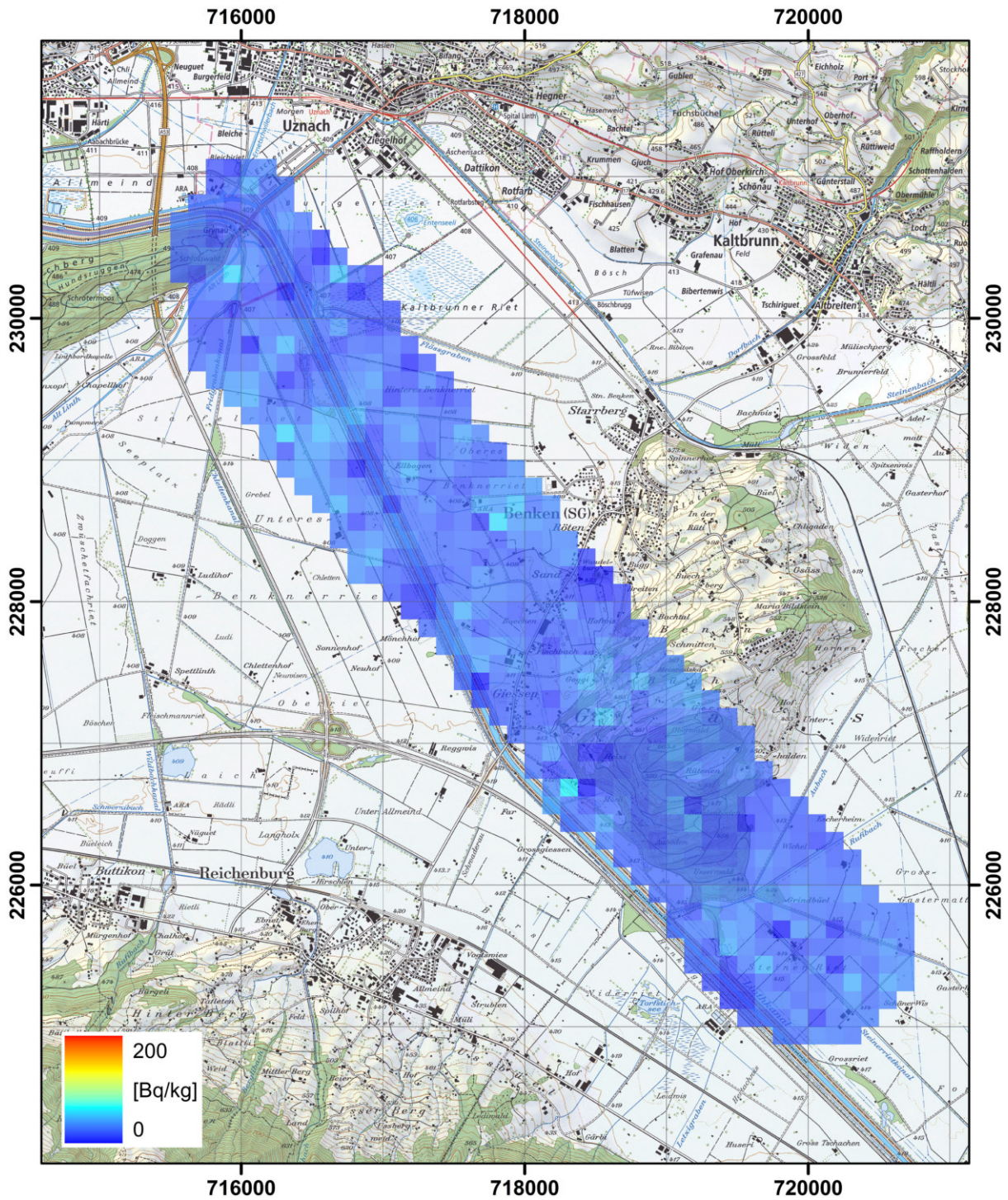
Figure 143: ^{238}U activity concentration measured by team FR01 over the Linth plain with ground clearance of 96 m after post-processing. PK25©2017 swisstopo (JD100042).
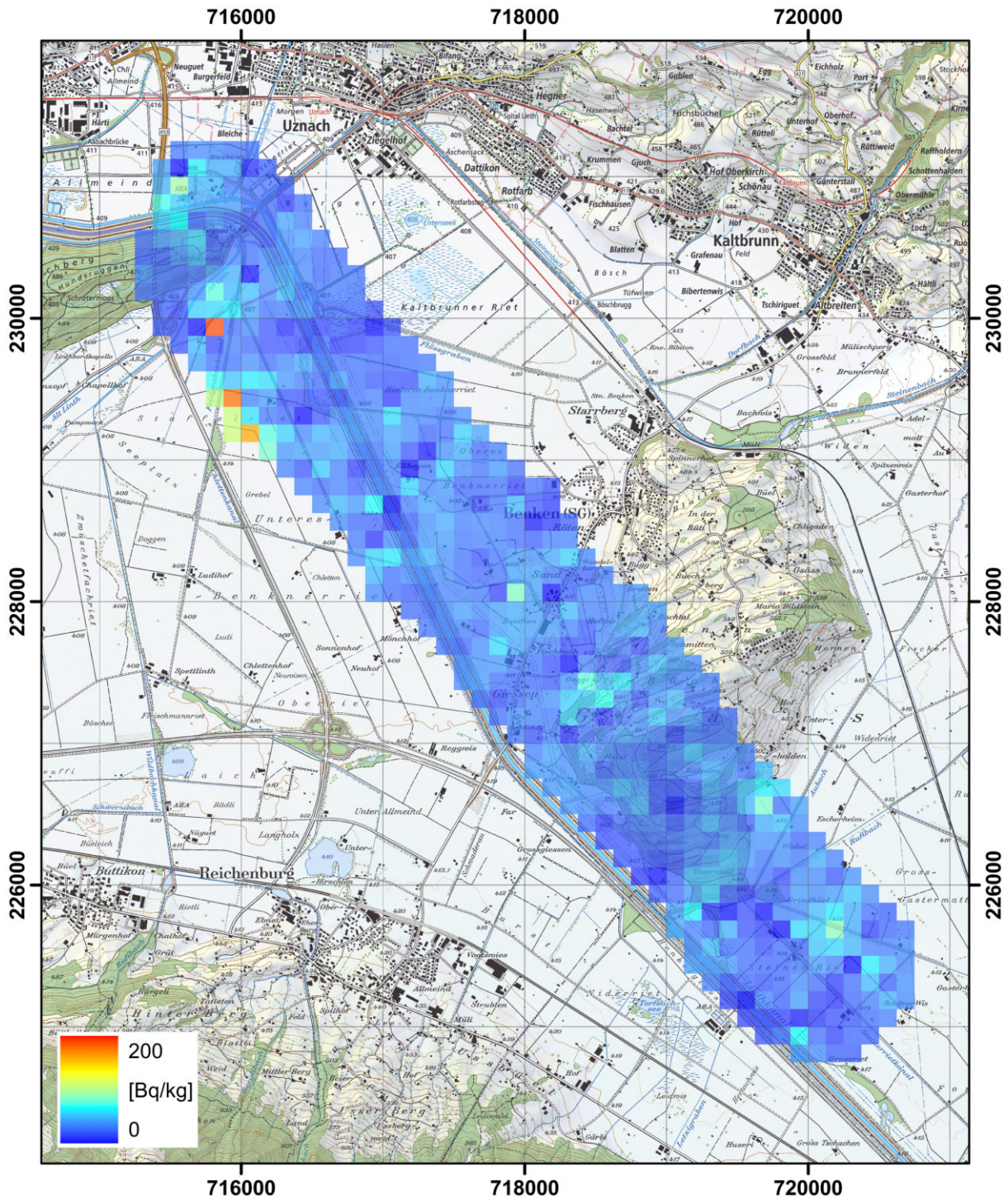
Figure 144: ^{238}U activity concentration measured by team FR01 over the Linth plain with ground clearance of 159 m after post-processing. PK25©2017 swisstopo (JD100042).

10 Reference area Murg valley

A second reference area was selected near the Murg valley to provide information on the influence of a larger variation in radionuclide content and topography on the results. Several radiometric anomalies of very limited lateral extent caused by uranium mineralisations are known from the reference area (see both publications of Gilliéron, 1988).

Figure 145 shows the placement of the reference area together with the scheduled flight lines. The terrain is challenging for the pilots as can be seen in the aerial view (figure 146) and the elevation map with elevation differences up to 1000 m (figure 147). Especially challenging is the deep valley to the north-east of the measuring area crossing the planned flight lines. Due to a low cloud cover, this valley could not be measured using the standard ground clearances. Thus, data comparison was restricted to a tetragon inside of the measuring area excluding the valley plotted as blue frame in figure 145.

Two flights with different ground clearances were recommended for the reference area, at the standard ground clearance of the individual measuring team and at the ground clearance used for source search and composite mapping (section 12).
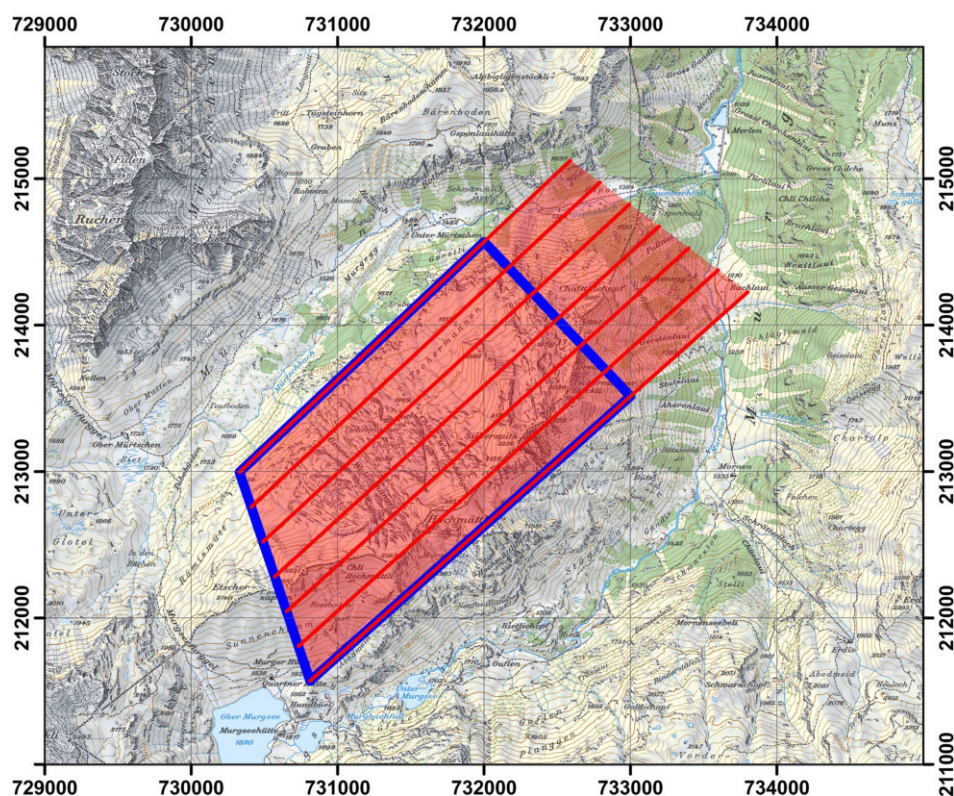
Figure 145: Reference area near the Murg valley. PK25©2017 swisstopo (JD100042).
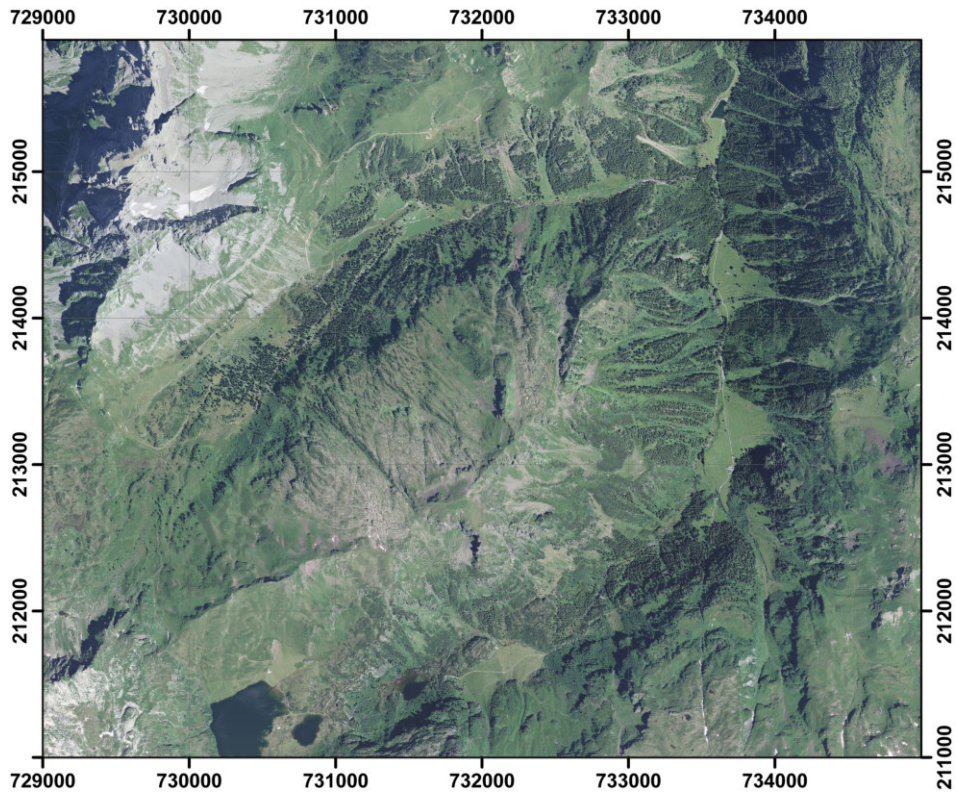
Figure 146: Aerial view of the reference area near the Murg valley. swissimage©2017 swisstopo (JD100042).
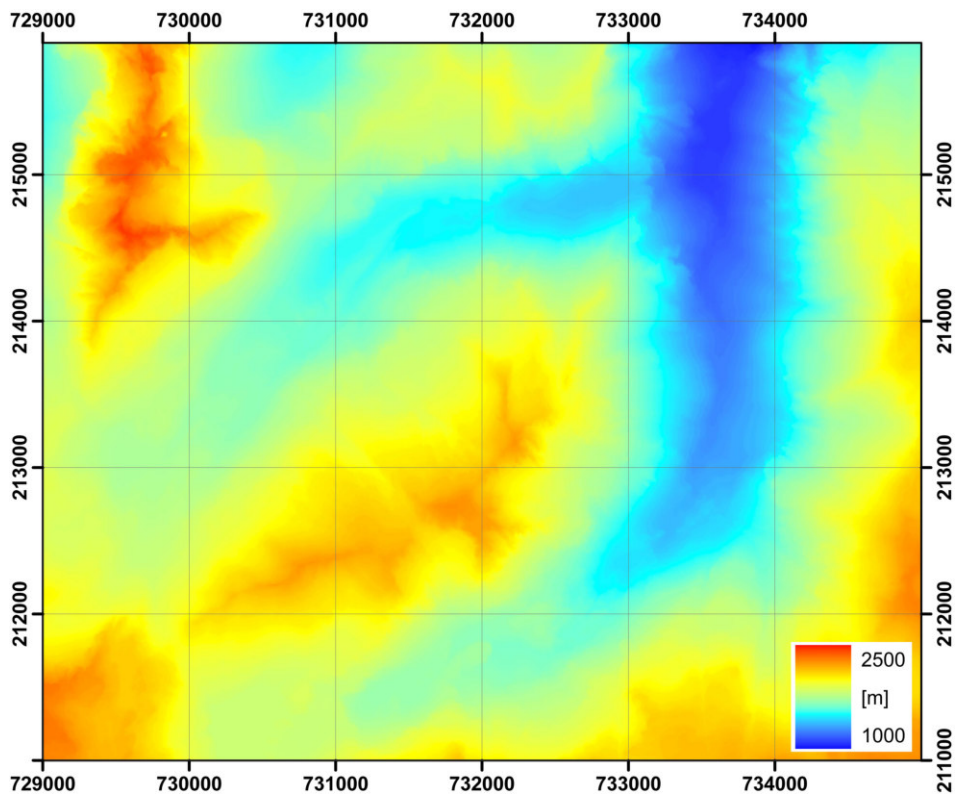
Figure 147: Elevation map of the reference area near the Murg valley. alti3D©2017 swisstopo (JD100042).
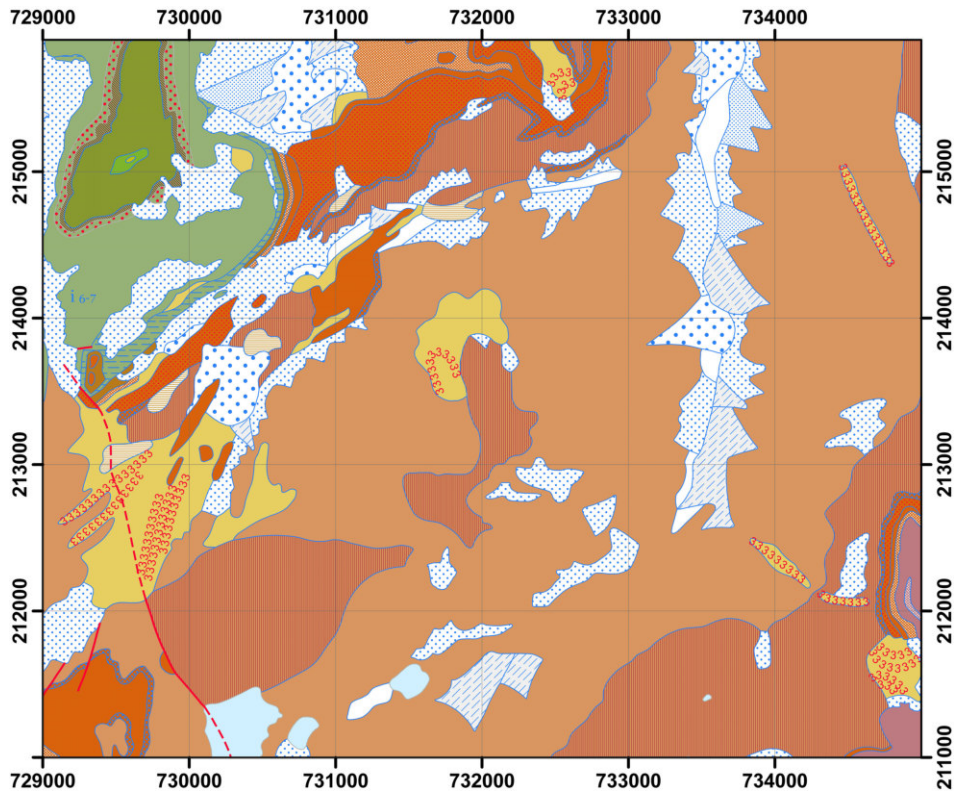
Figure 148: Geological map of the reference area near the Murg valley. Geocover©2017 swisstopo (JD100042).

The geology of this reference area is mainly dominated by conglomerates and breccia (Vorwiegend Konglomerate und Breccien, Sernifit; brown colour) and phyllites (Vorwiegend Phyllite; brown with vertical stripes). Local moraines (Lokalmoräne; yellowish colour), detrital slopes (Gehängeschutt; white color with small blue dots), rock slides (Bergsturz, Blockschutt; white colour with big blue dots)and alluvial fans (Bachschuttkegel; light blue colour with blue lines) can further be found in the reference area. Some local copper and uranium mineralisations, albeit not minable, were reported for the area (Bächtiger, 1963).

- - - - - - -	Mutmassliche geologische Kontur
———	Bruch beobachtet
- - - -	Bruch vermutet
⊥⊥⊥⊥⊥⊥	Abrissränder von Bergstürzen
———	Biegungen
3333333	Moränenwall
··········	Nummulitenschichten
··········	Orbitolinaschichten
·······	Korallenkalkfacies
··········	Melsersandstein
··········	Rauhwacke

	See
	Fluss
	Sackung

	Alluvialböden, Talsohlen
	Torfmoor
	Stauschotter
	Bachschuttkegel
	Gehängeschutt
	Trockene Schuttkegel
	Bergsturz, Blockschutt
	Schotter
	Lokalmoräne
	Linth- und Rheingletschermoräne

	Altdorfersandstein und Dachschiefer
	Stadschiefer, Globigerinenschiefer, z.T. incl. Pectinidenschiefer
	Nummulitenschichten
	Seewerkalk
	Turriliten-, Knollen- und Concentricusschichten
	Schrattenkalk i. allg.
	Unterer Schrattenkalk
	Drusberg- und Altmannschichten
	Kieselkalk (Hauterivien)
	Valanginienkalk
	Valanginienmergel
	Öhrlischichten i. allg. (z.T. Valanginienkalk-Öhrlischichten)
	Öhrlimergel
	Unterer Öhrlikalk
	Zementsteinschichten
	Lochseitenkalk
	Quintnerkalk i. allg.
	Schiltschichten
	Dogger i. allg.
	Posidonomyenschiefer, Oberer Lias
	Mittlerer und unterer Lias, z.T. Lias i. allg.
	Trias i. allg.
	Quartenschiefer
	Rötidolomit, z.T. Trias i. allg.
	Oberer Rötidolomit
	Rauhwacke
	Unterer Rötidolomit
	Melsersandstein
	Vorwiegend Konglomerate und Breccien, Sernifit
	Vorwiegend Phyllite

Figure 149: Legend to the geological map of the reference area near the Murg valley (in German). Geocover©2017 swisstopo (JD100042).

10.1 Results

The presented results for the reference area near the Murg valley include already corrections performed on the findings from the altitude profile over Lake Zug (section 8 and from the comparison with ground measurements in the Linth plain reference area (section 9).

There was some expectation to find clearly identifiable local maxima in the activity concentrations of natural radionuclides. Unfortunately, the only convincing local maximum of the natural radionuclides ^{40}K and ^{232}Th was observed at the Silberspitz. Generally, slightly higher values of the natural radionuclide concentrations can be found over the marl regions in the measurement area.

Two flights with intended ground clearances of 100 m and 150 m were performed over the reference area. The dose rate measured by team CH01 (figure 154) with a ground clearance of 105 m reflects the elevated alpine terrain with a higher contribution of cosmic radiation compared to measurements at sea level. Removing the contribution of cosmic radiation renders the terrestrial component of the dose rate (figure 174). The most distinct feature in this map is a region with elevated terrestrial dose rates in the north-east of the measured area. A map of the ^{137}Cs activity concentration seems to indicate remains of Chernobyl deposition as cause of the elevated dose rate values (figure 175). A closer look on the map of the count rate in the Caesium energy window (figure 176) shows lower than average count rates in the area yielding elevated ^{137}Cs activity concentrations, contradicting the according statement. This contradiction is resolved with a map of the ground clearance of the measuring flight (figure 177). The helicopter did not follow the terrain with standard ground clearance over the northeastern valley. The deviation from the standard procedure was caused by a low cloud cover, which was avoided for flight security reasons. The ground clearance of up to 600 m instead of the planned 100 m led to the observed artefacts of dose rate and ^{137}Cs activity concentration. The effect of large ground clearance can also be observed in large variations of ^{40}K, ^{238}U and ^{232}Th activity concentrations in the affected area (figures 159, 169 and 164). This stresses the importance of precisely keeping the predetermined ground clearance during the flight and a continuous check of data inconsistencies during the evaluation procedure. One parameter less influenced by the deviation from the standard ground clearance is the MMGC-ratio as indicator for the presence of artificial radionuclides (figure 178).

Only the eastern part of the measurement area was afflicted by the low cloud cover. Thus, data points from a reduced part of the measurement area in a tetragon (blue-framed in figure 145) between coordinates (730812,211570), (733000, 213514), (732000, 214569) and (730330, 212996) were used for a comparison of results. Table 34 shows reasonable agreement between measuring flights at different ground clearances for team CH01.

Table 34: Comparison of results measured near the Murg valley for predefined ground clearances of 100 m and 150 m measured by team CH01.

Parameter	Ground clearance 100 m		Ground clearance 150 m	
	Average	Stand. dev.	Average	Stand. dev.
Number of points	448	-	476	-
Ground clearance [m]	105	57	165	52
Altitude [m]	2152	142	2210	138
Dose rate [nSv/h]	222	30	220	26
Cosmic dose rate [nSv/h]	112	9	112	8
Terrestrial dose rate [nSv/h]	110	24	109	21
^{40}K activity concentration [Bq/kg]	679	165	636	157
^{232}Th activity concentration [Bq/kg]	46	15	43	15
^{238}U activity concentration [Bq/kg]	48	23	44	26
^{137}Cs activity concentration [Bq/m^2]	1468	1148	1997	1542

The effect of unplanned ground clearance in the north-east of the measuring area due to a low cloud cover can also be observed to a lesser extent in the radiological maps derived from the measurements of team CH02 (figures 155, 160, 170 and 165).

The radiological maps based on the measurements of team CZ01 (figures 156, 161, 171 and 166) do not show the clear influence of the low cloud cover in the north-east of the measuring area as observed by the Swiss teams.

From the German teams, only team DE01 performed a measuring flight in the Murg valley reference area. As in the Linth plain (section 9), measuring points below the decision limit were removed, leading to gaps in the area coverage. The data points affected by the low cloud cover in the north-eastern part of the measuring area were eliminated by post-processing data quality analysis from the measurements of team DE01 (figures 157, 162, 172 and 167).

In the radiological maps derived from the measurements of team FR01 (figures 158, 163, 173 and 168), regions in the north-east and outside of the measurement area can be identified where artefacts are produced due to ground clearances well above the target value.

10.1.1 Comparison

Differences in the maps derived from the data of the different measuring teams (section 10.1.2) can be clearly identified. Only a part of these differences can be assigned to unusual large ground clearances necessary for flight safety reasons and a low cloud cover. The further comparison of results is restricted to the tetragon between coordinates (730812,211570), (733000, 213514), (732000, 214569) and (730330, 212996) already introduced in section 10.1 to reduce the influence of these unusual flight conditions.

The average dose rates measured in the tetragon (figure 150) range from 178 nSv/h to 278 nSv/h. Re-evaluating the raw data of team CH02 with the software used by team CH01 increases the derived dose rates from around 180 nSv/h to 230 nSv/h, slightly above the value of 220 nSv/h obtained by team CH01. Comparing the results of all participating teams renders a ranking of values in the alpine site of the Murg valley (figures 150 to 153) similar

to the ranking of observed in the Linth plain (figures 84 to 91).
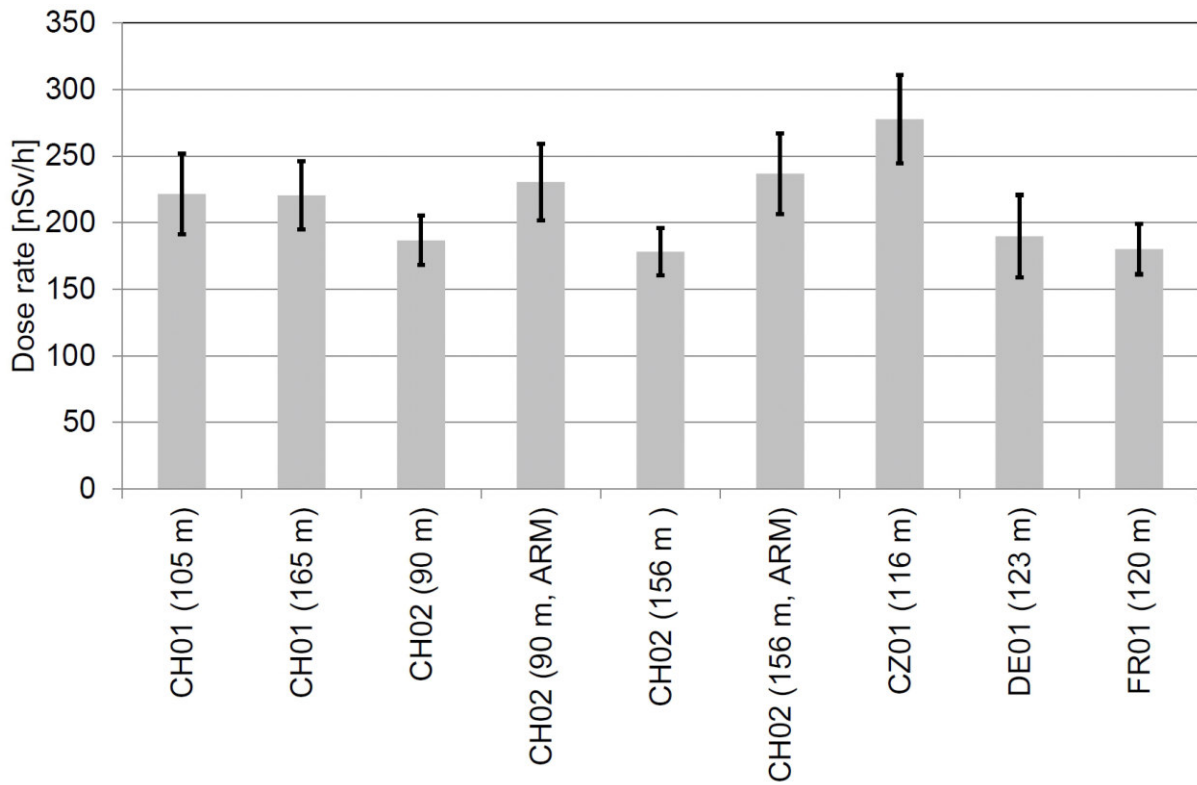
Figure 150: Comparison of dose rate measurements.
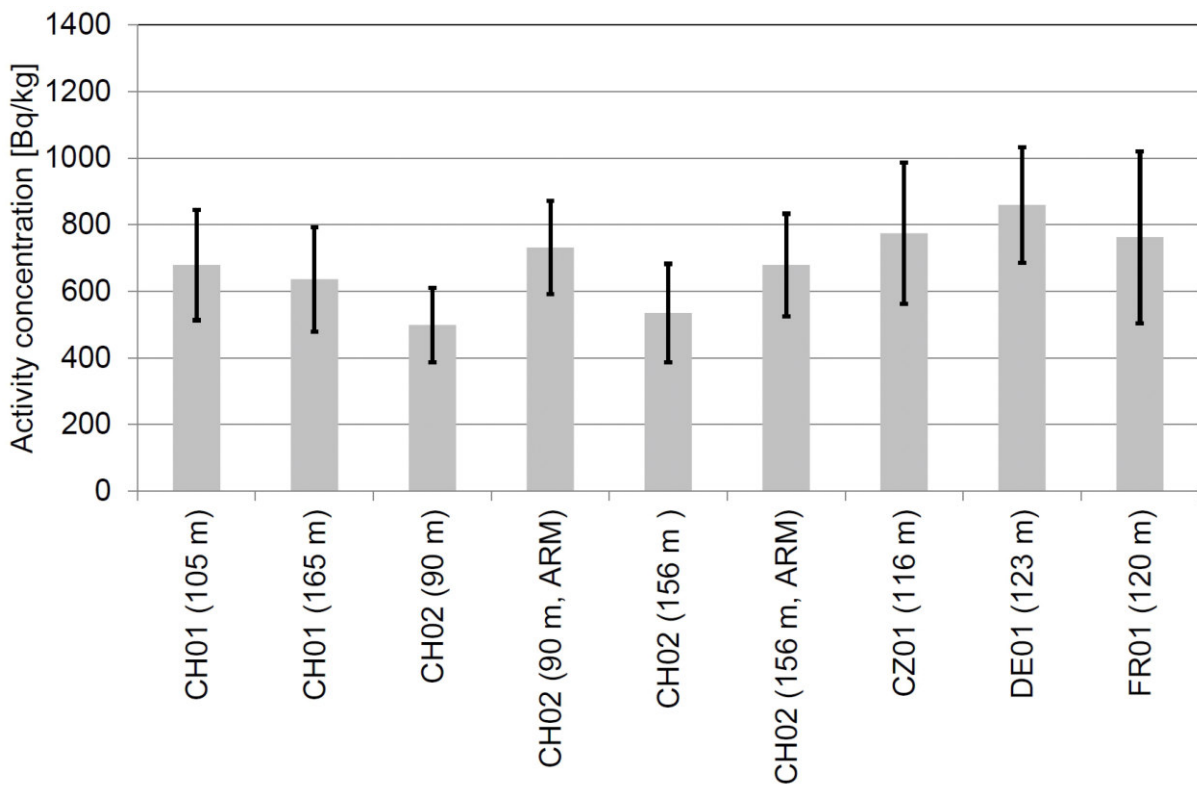
Figure 151: Comparison of ^{40}K activity concentrations.
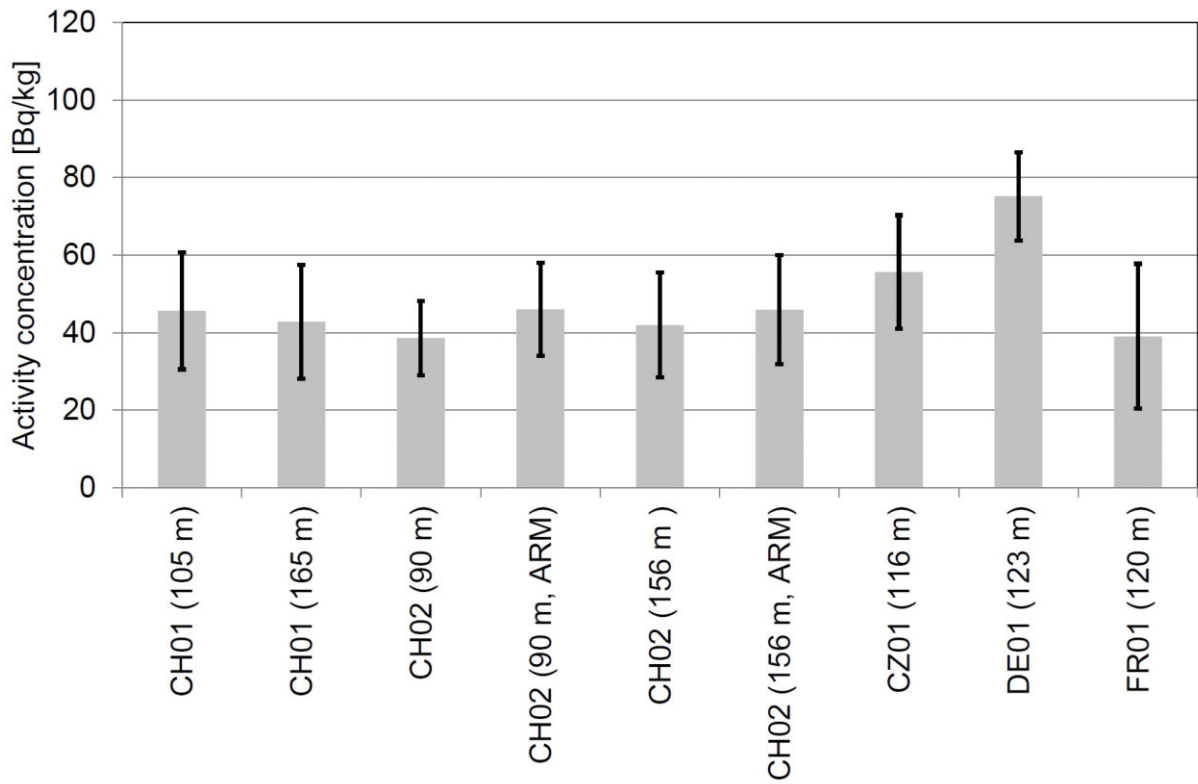
Figure 152: Comparison of ^{232}Th activity concentrations.
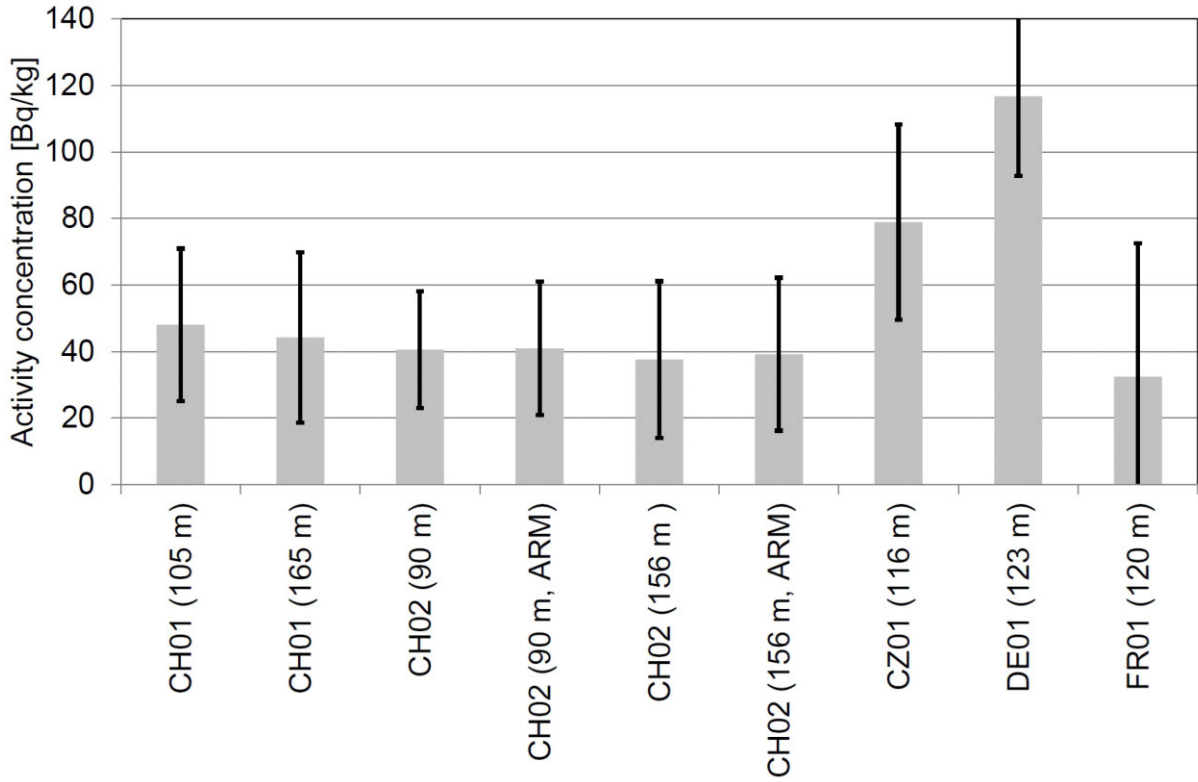
Figure 153: Comparison of ^{238}U activity concentrations.

10.1.2 Maps
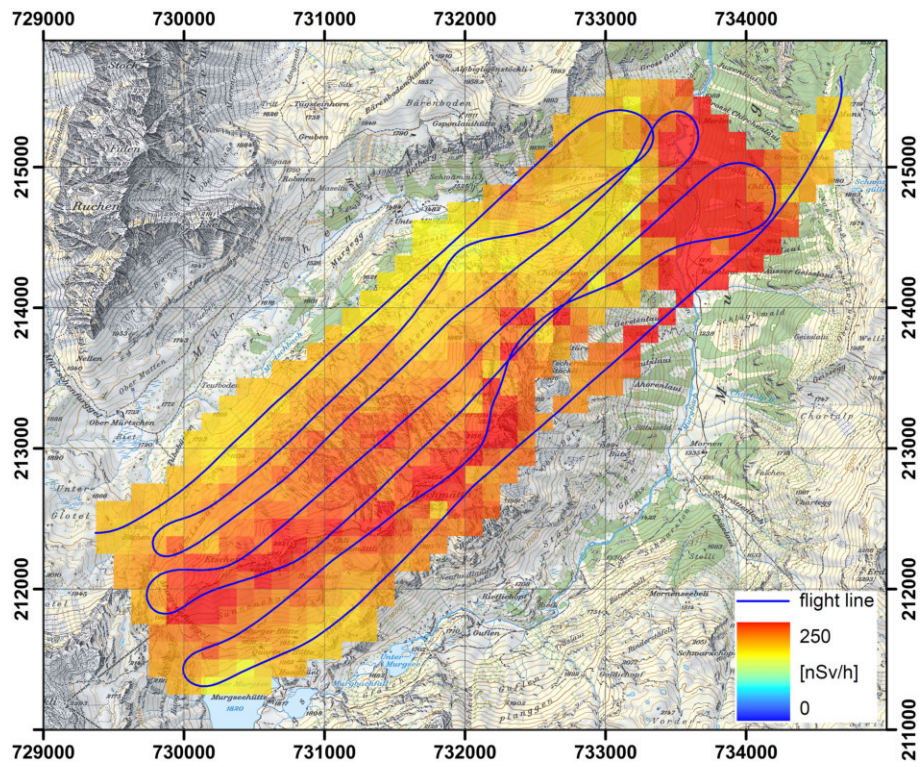
Figure 154: Dose rate near the Murg valley measured by team CH01 with a ground clearance of 105 m. PK25©2017 swisstopo (JD100042).
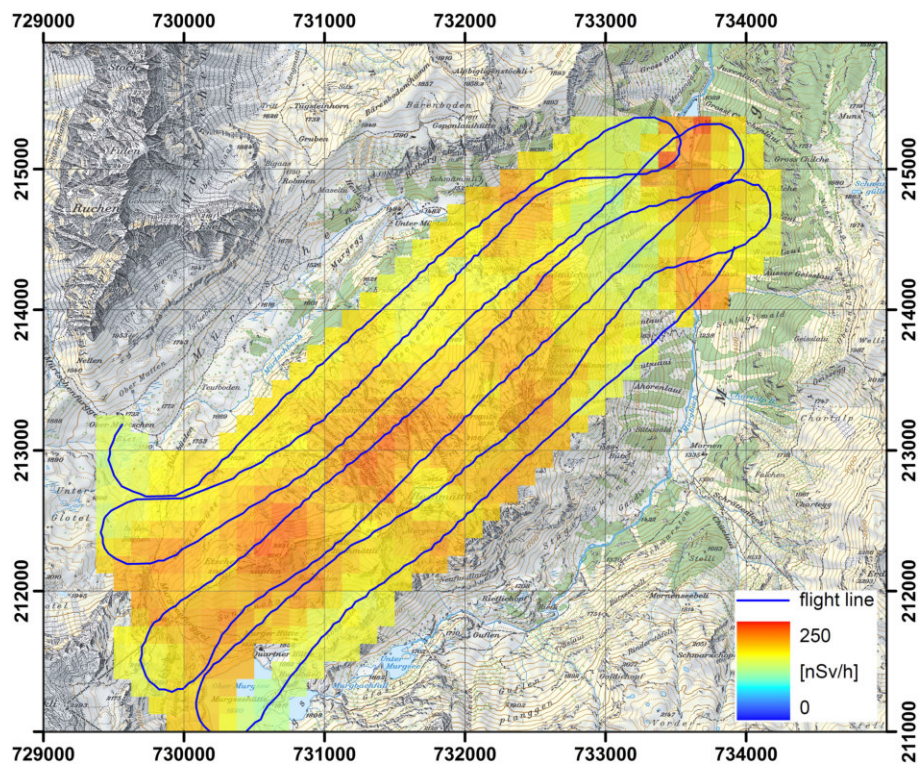
Figure 155: Dose rate near the Murg valley measured by team CH02 with a ground clearance of 90 m. PK25©2017 swisstopo (JD100042).
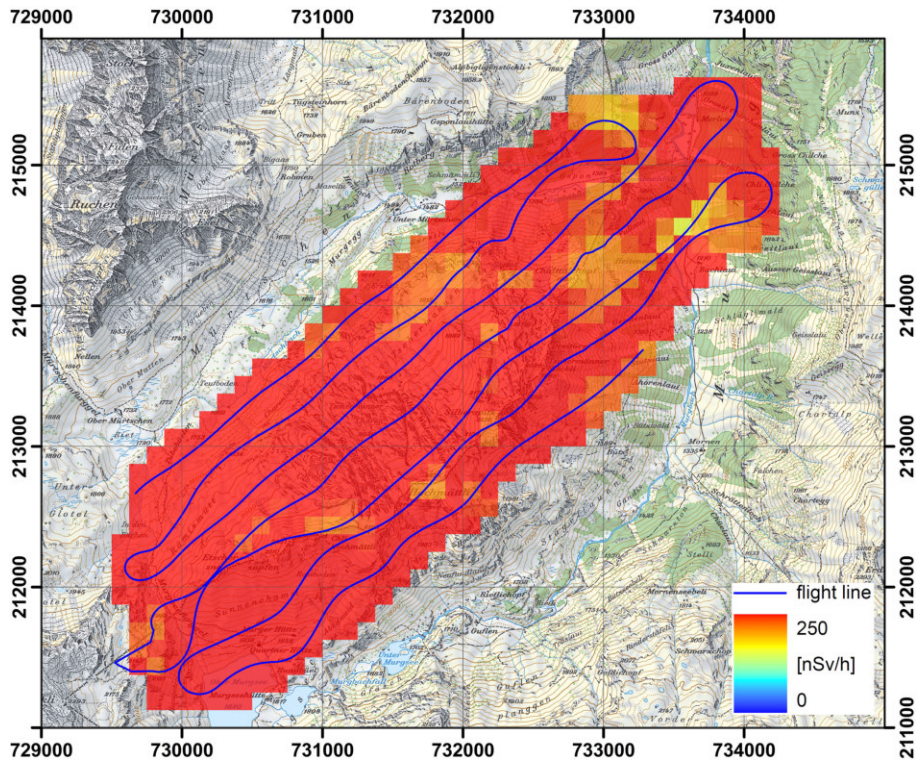
Figure 156: Dose rate near the Murg valley measured by team CZ01 with a ground clearance of 116 m. PK25©2017 swisstopo (JD100042).
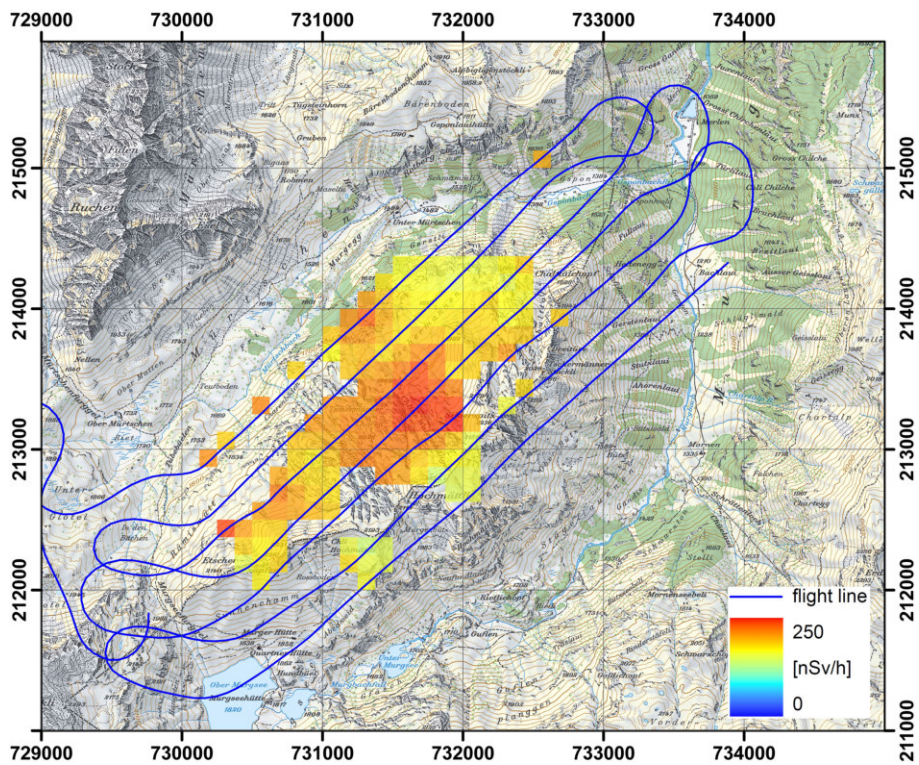
Figure 157: Dose rate near the Murg valley measured by team DE01 with a ground clearance of 123 m. PK25©2017 swisstopo (JD100042).
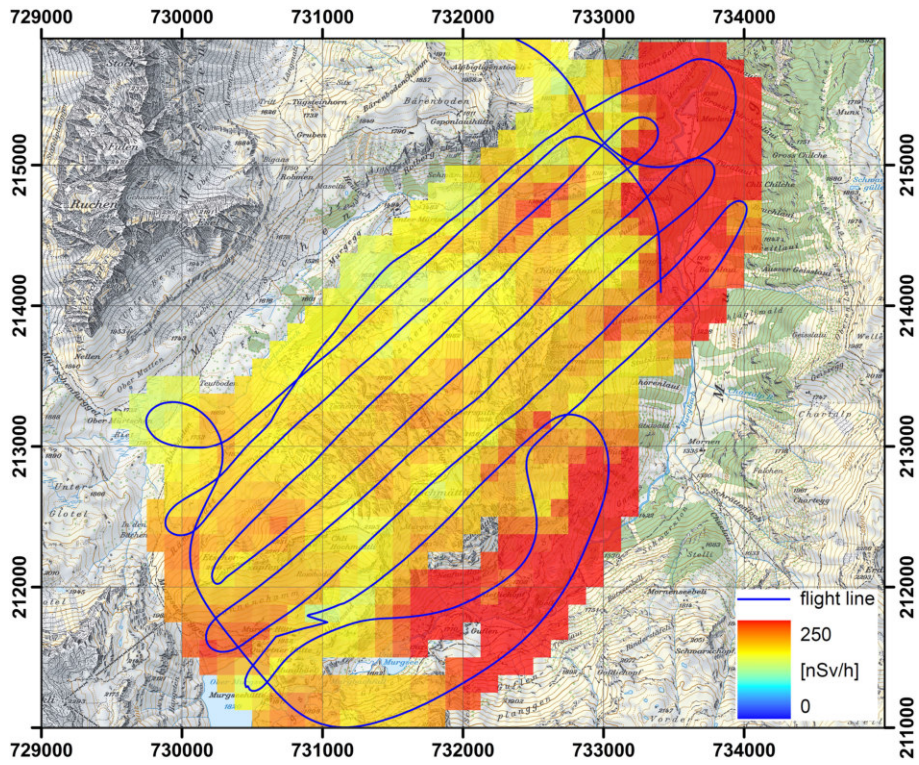
Figure 158: Dose rate near the Murg valley measured by team FR01 with a ground clearance of 120 m. PK25©2017 swisstopo (JD100042).
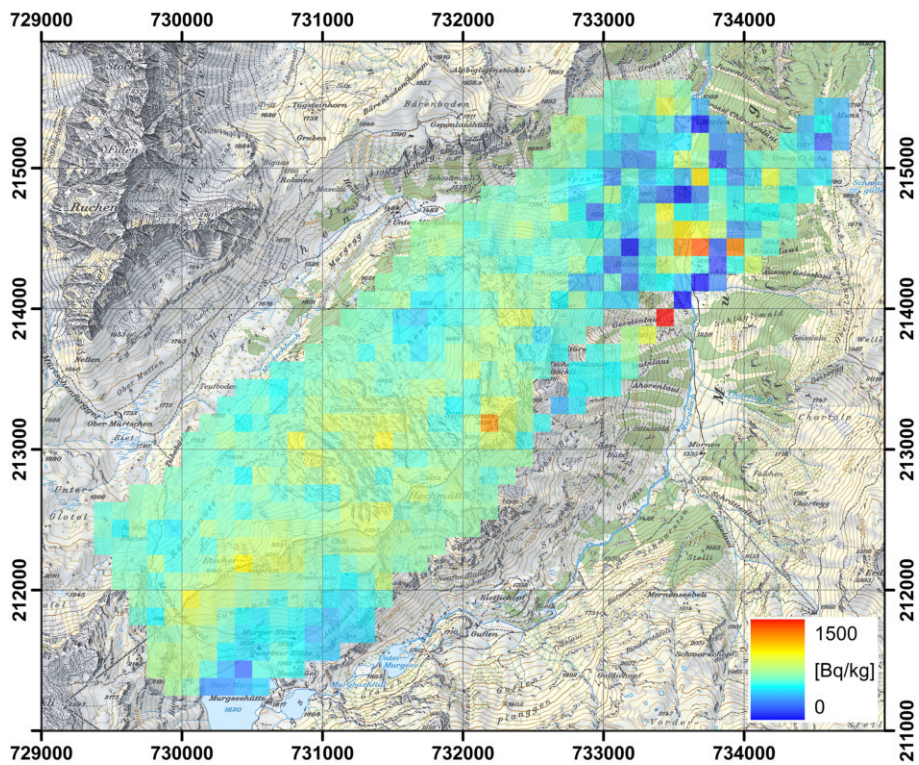
Figure 159: ^{40}K activity concentration near the Murg valley measured by team CH01 with a ground clearance of 105 m. PK25©2017 swisstopo (JD100042).
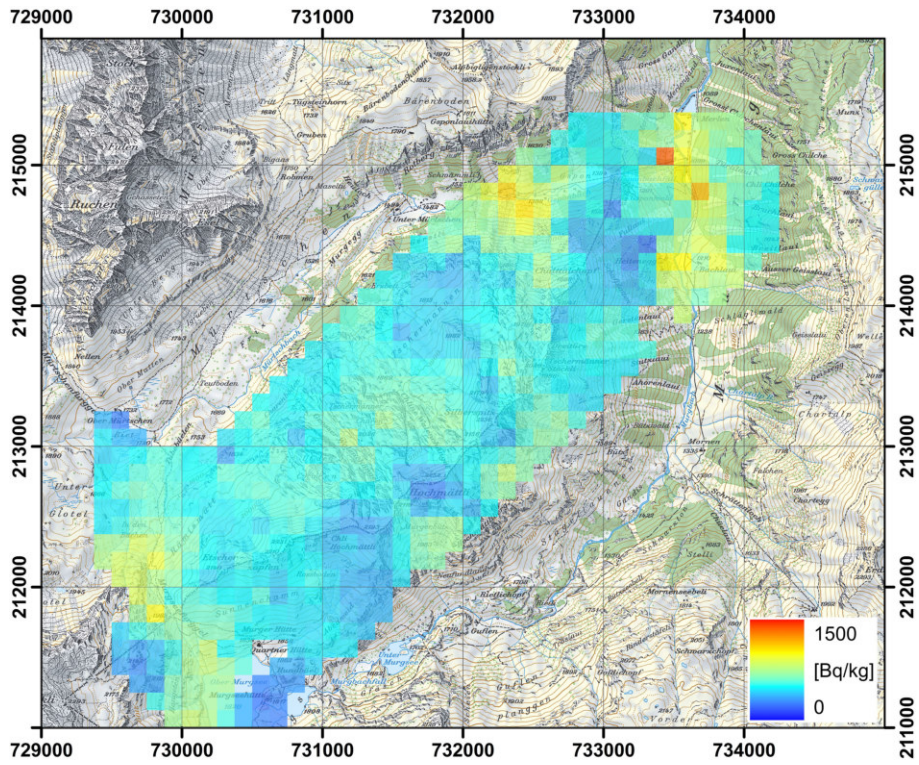
Figure 160: ^{40}K activity concentration near the Murg valley measured by team CH02 with a ground clearance of 90 m. PK25©2017 swisstopo (JD100042).
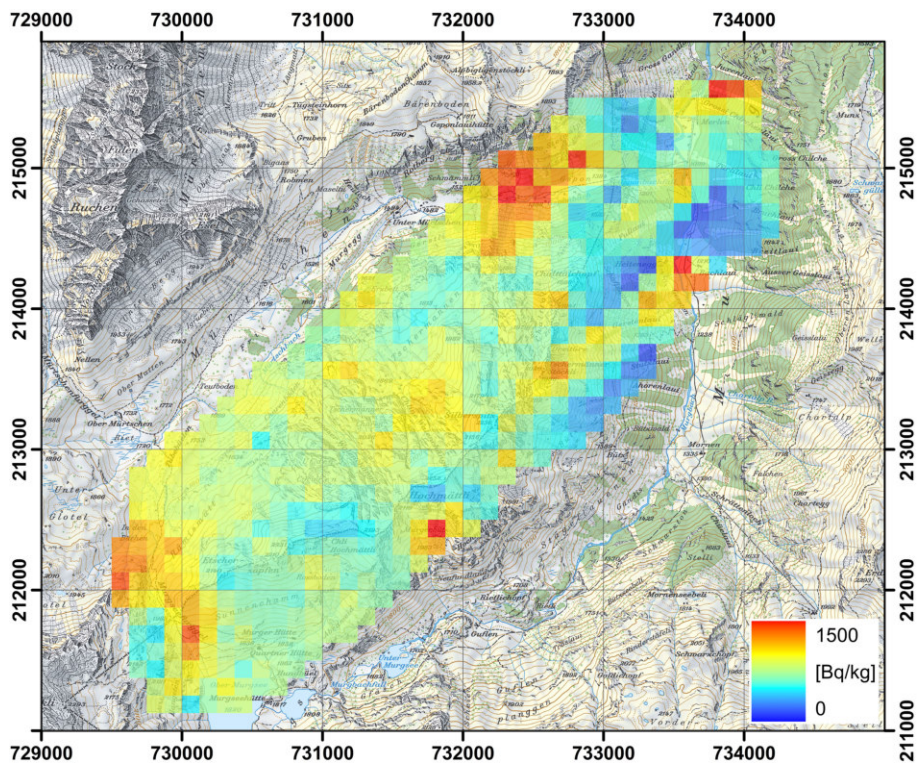
Figure 161: ^{40}K activity concentration near the Murg valley measured by team CZ01 with a ground clearance of 116 m. PK25©2017 swisstopo (JD100042).
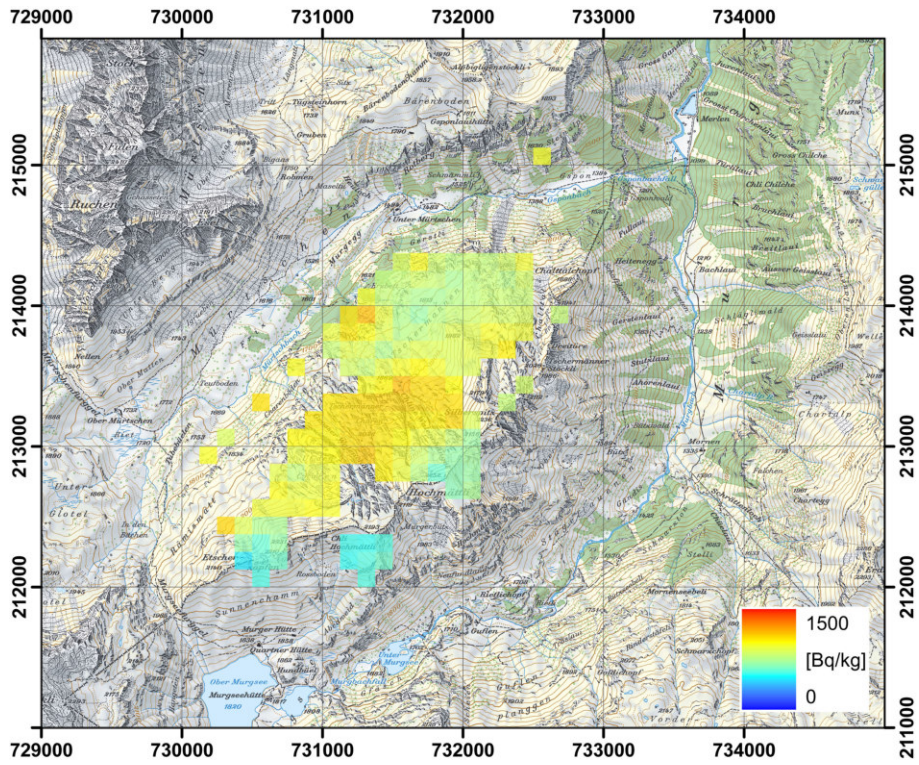
Figure 162: ^{40}K activity concentration near the Murg valley measured by team DE01 with a ground clearance of 123 m. PK25©2017 swisstopo (JD100042).
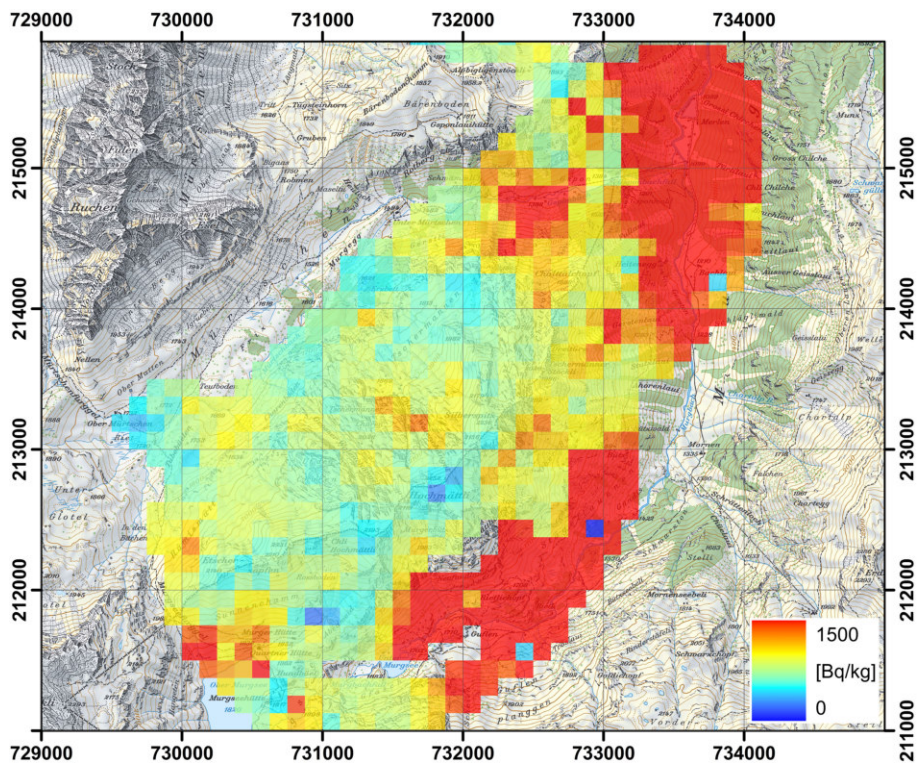
Figure 163: ^{40}K activity concentration near the Murg valley measured by team FR01 with a ground clearance of 120 m. PK25©2017 swisstopo (JD100042).
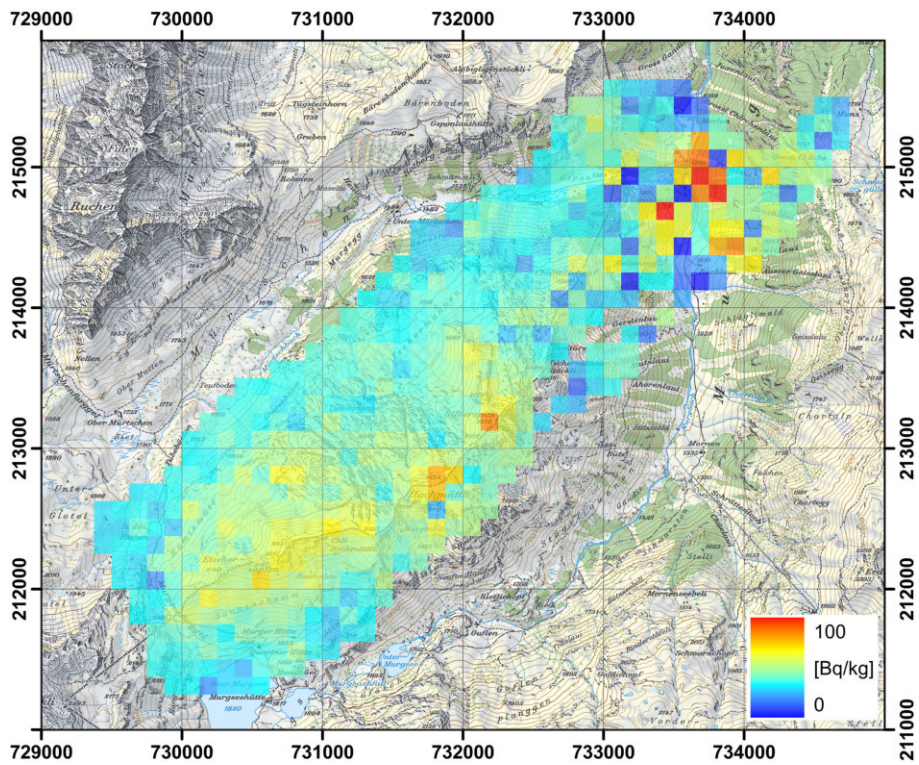
Figure 164: ^{232}Th activity concentration near the Murg valley measured by team CH01 with a ground clearance of 105 m. PK25©2017 swisstopo (JD100042).
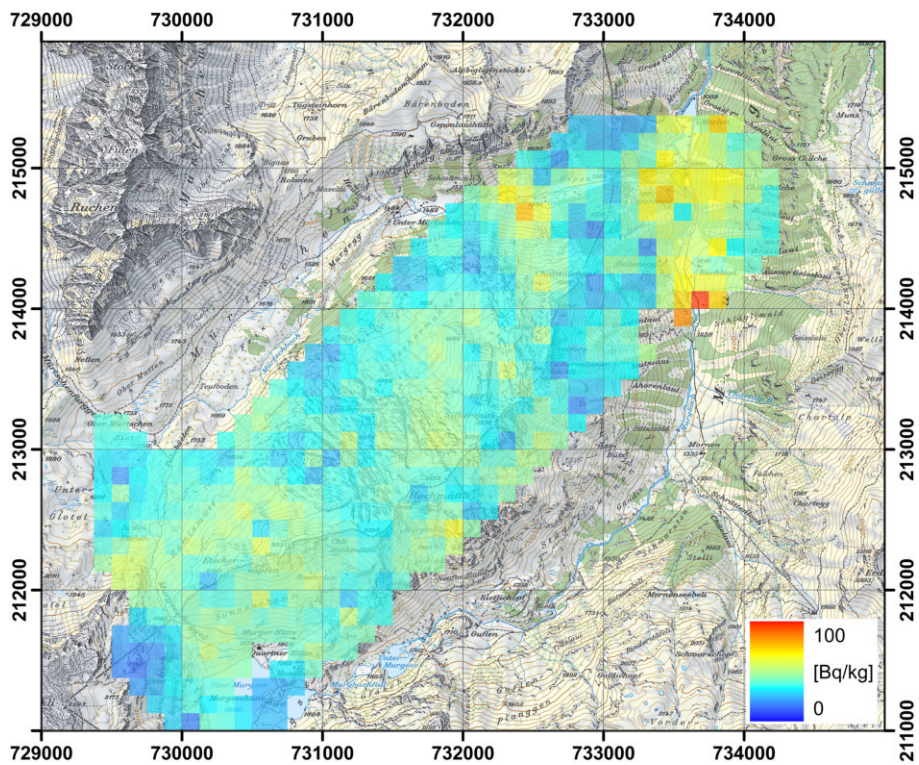
Figure 165: ^{232}Th activity concentration near the Murg valley measured by team CH02 with a ground clearance of 90 m. PK25©2017 swisstopo (JD100042).

174
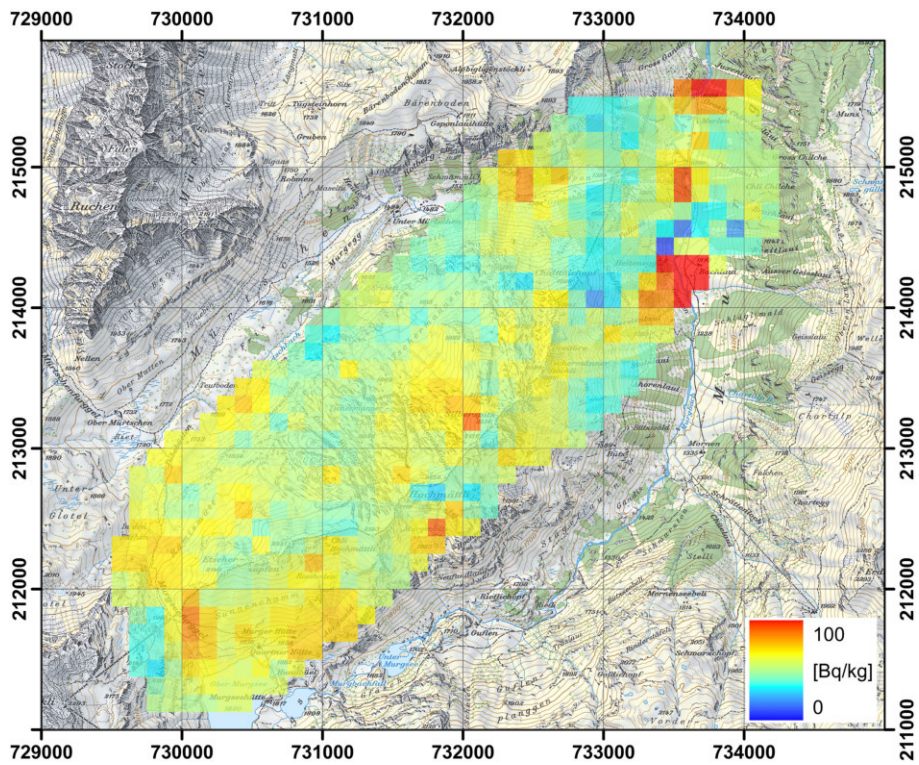
Figure 166: ^{232}Th activity concentration near the Murg valley measured by team CZ01 with a ground clearance of 116 m. PK25©2017 swisstopo (JD100042).
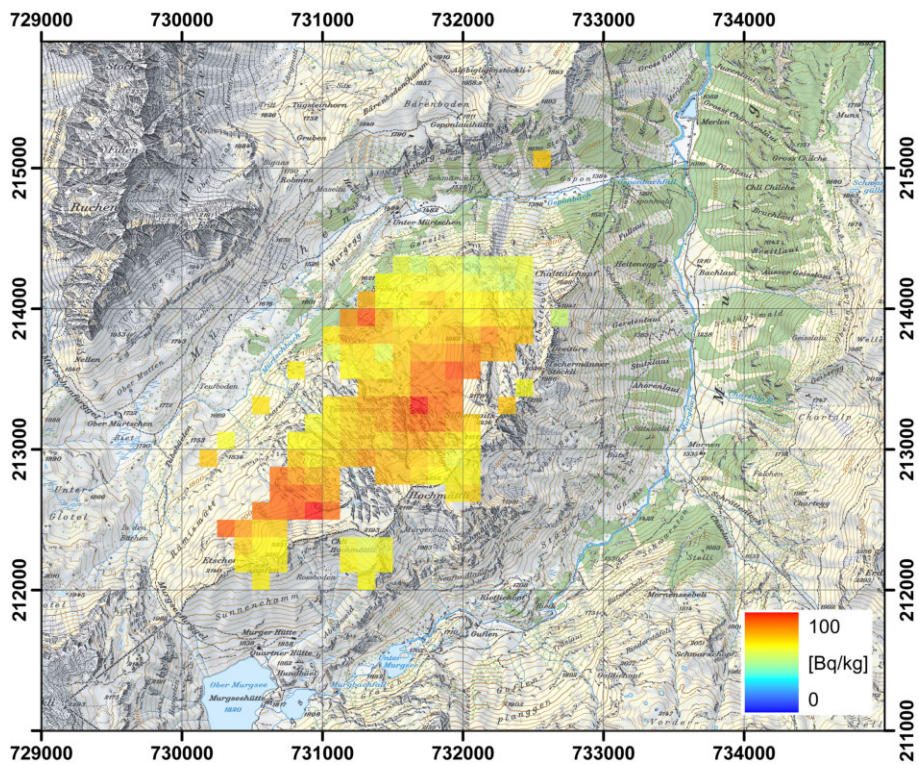
Figure 167: ^{232}Th activity concentration near the Murg valley measured by team DE01 with a ground clearance of 123 m. PK25©2017 swisstopo (JD100042).

175
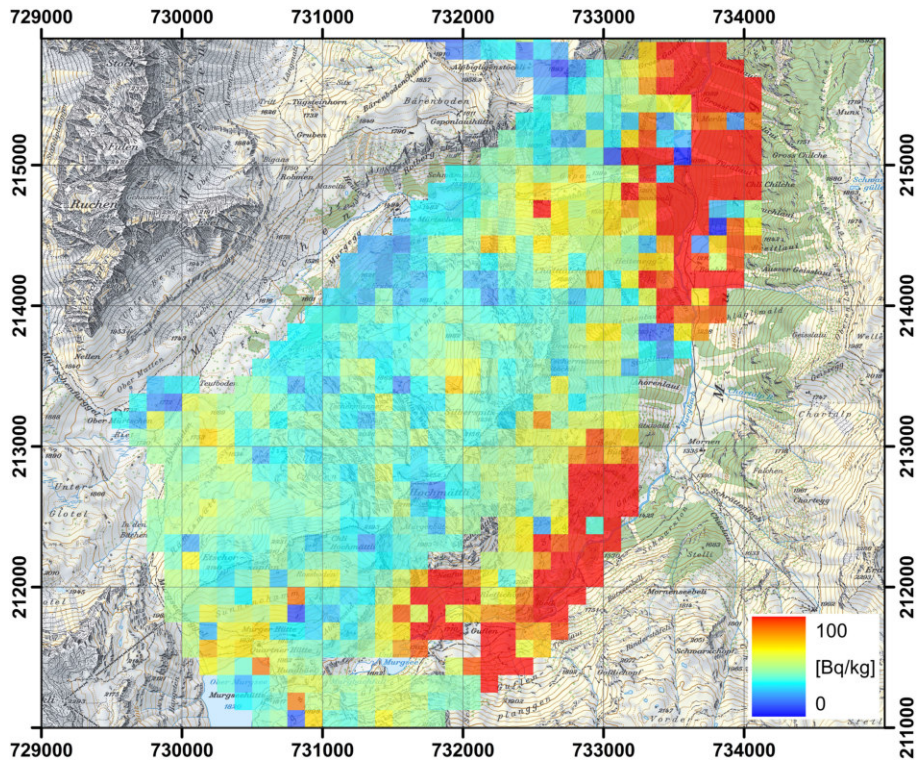
Figure 168: ^{232}Th activity concentration near the Murg valley measured by team FR01 with a ground clearance of 120 m. PK25©2017 swisstopo (JD100042).
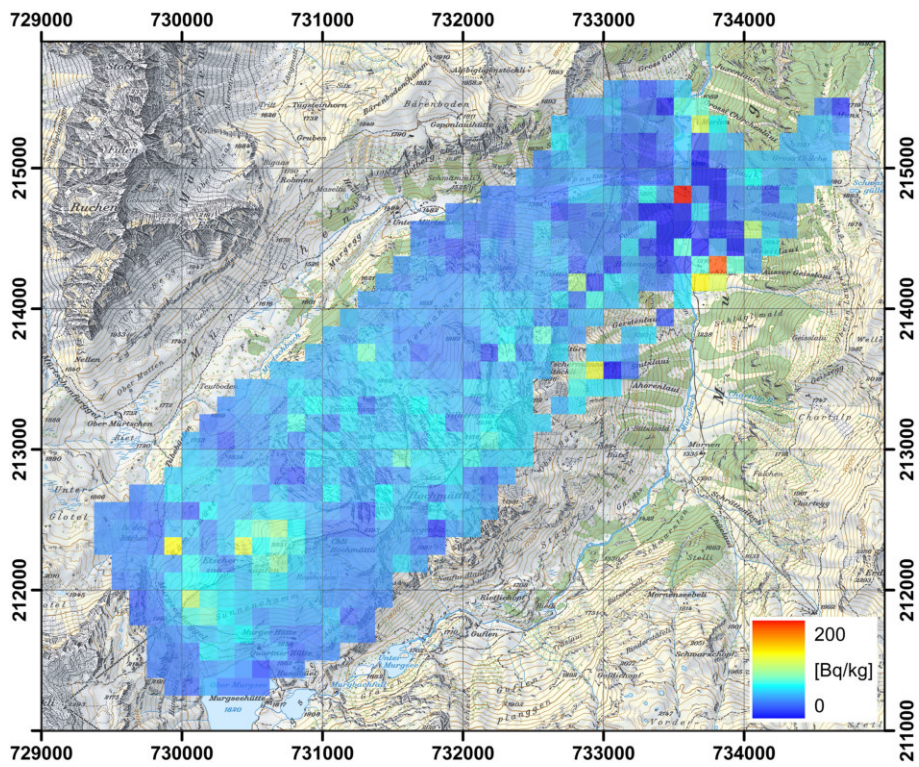
Figure 169: ^{238}U activity concentration near the Murg valley measured by team CH01 with a ground clearance of 105 m. PK25©2017 swisstopo (JD100042).
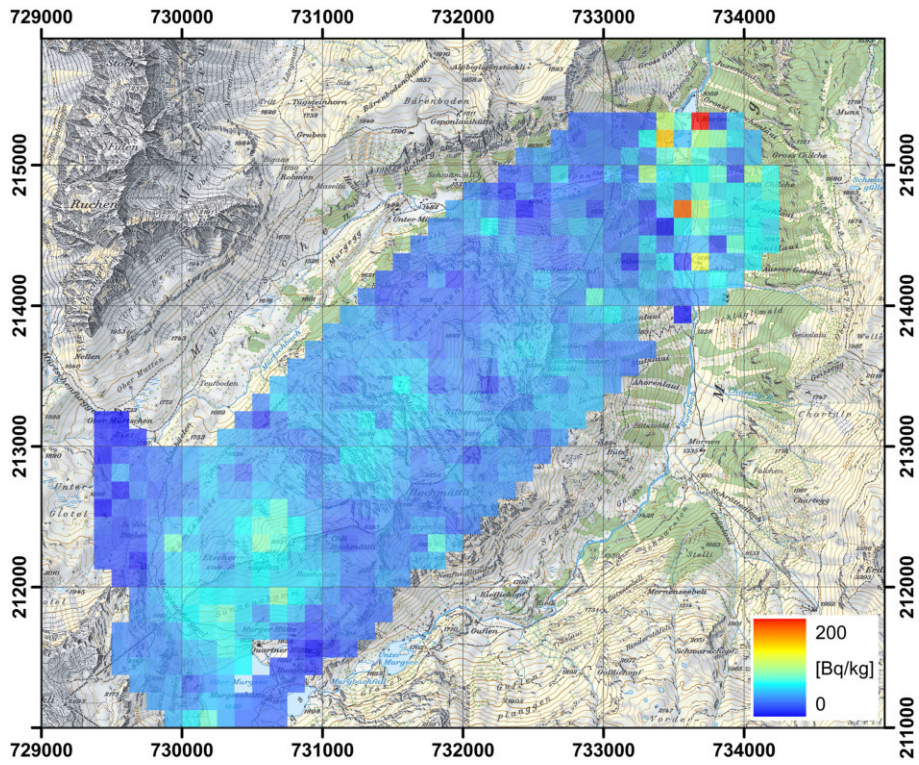
Figure 170: ^{238}U activity concentration near the Murg valley measured by team CH02 with a ground clearance of 90 m. PK25©2017 swisstopo (JD100042).
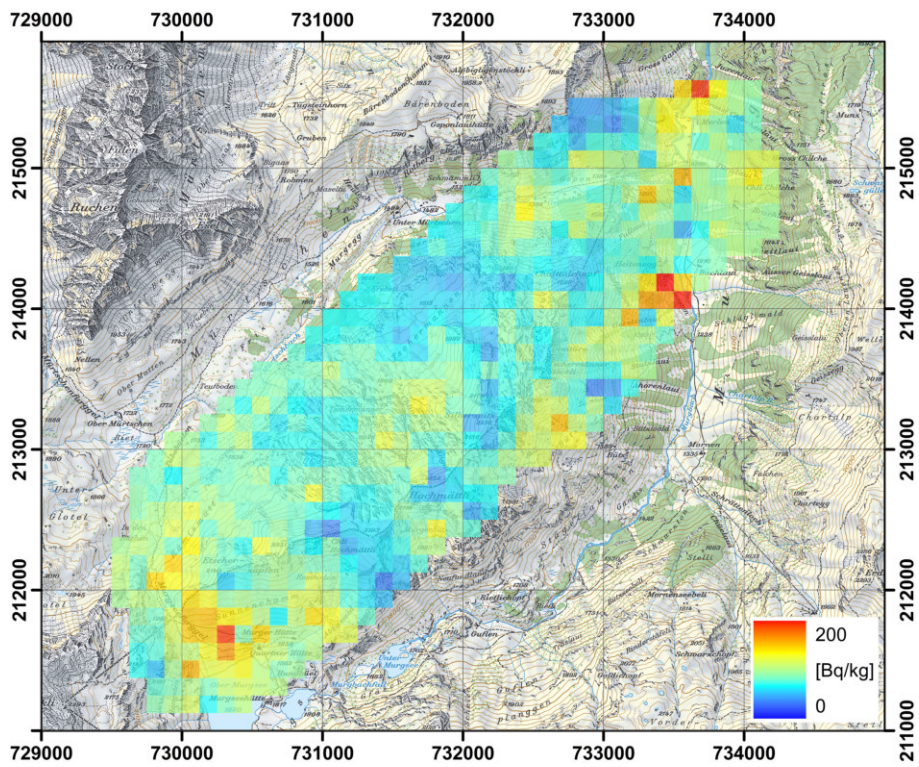
Figure 171: ^{238}U activity concentration near the Murg valley measured by team CZ01 with a ground clearance of 116 m. PK25©2017 swisstopo (JD100042).
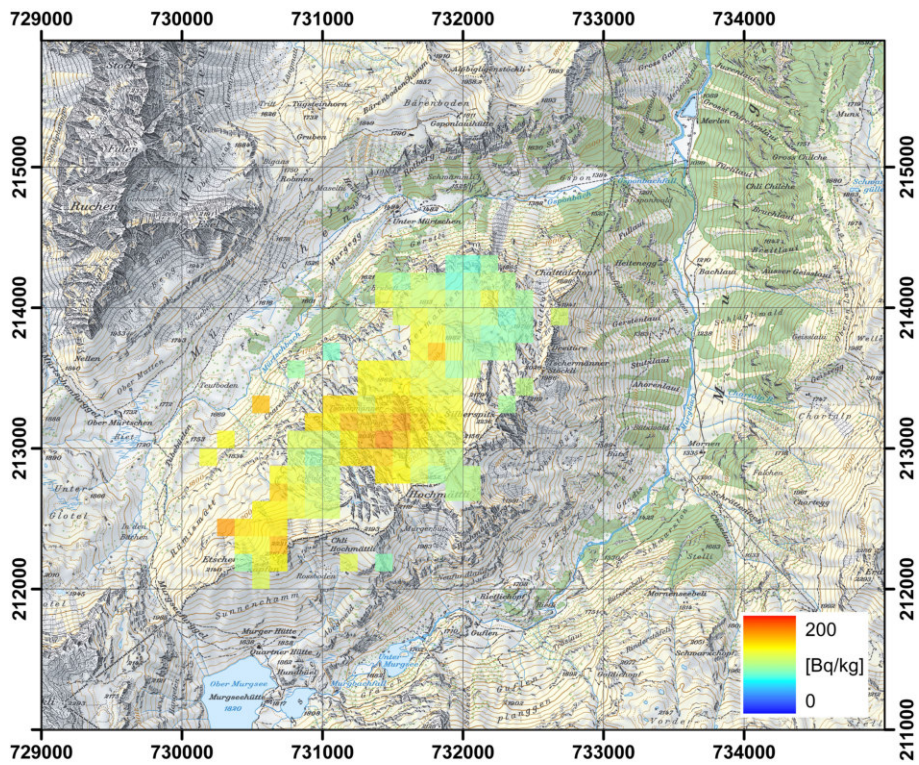
Figure 172: ^{238}U activity concentration near the Murg valley measured by team DE01 with a ground clearance of 123 m. PK25©2017 swisstopo (JD100042).
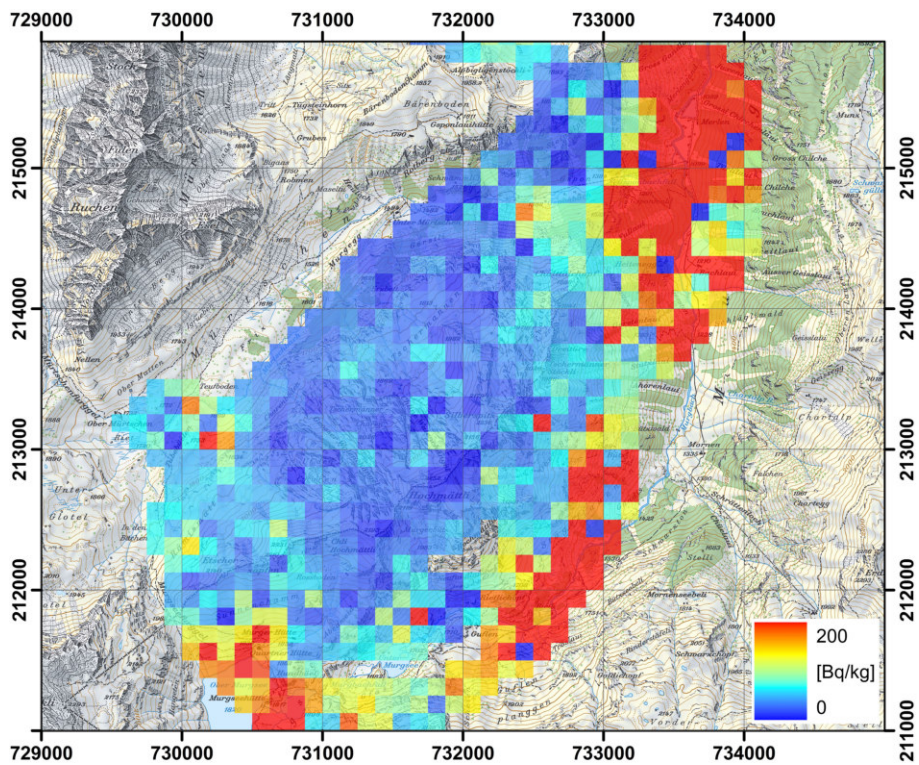
Figure 173: ^{238}U activity concentration near the Murg valley measured by team FR01 with a ground clearance of 120 m. PK25©2017 swisstopo (JD100042).

178
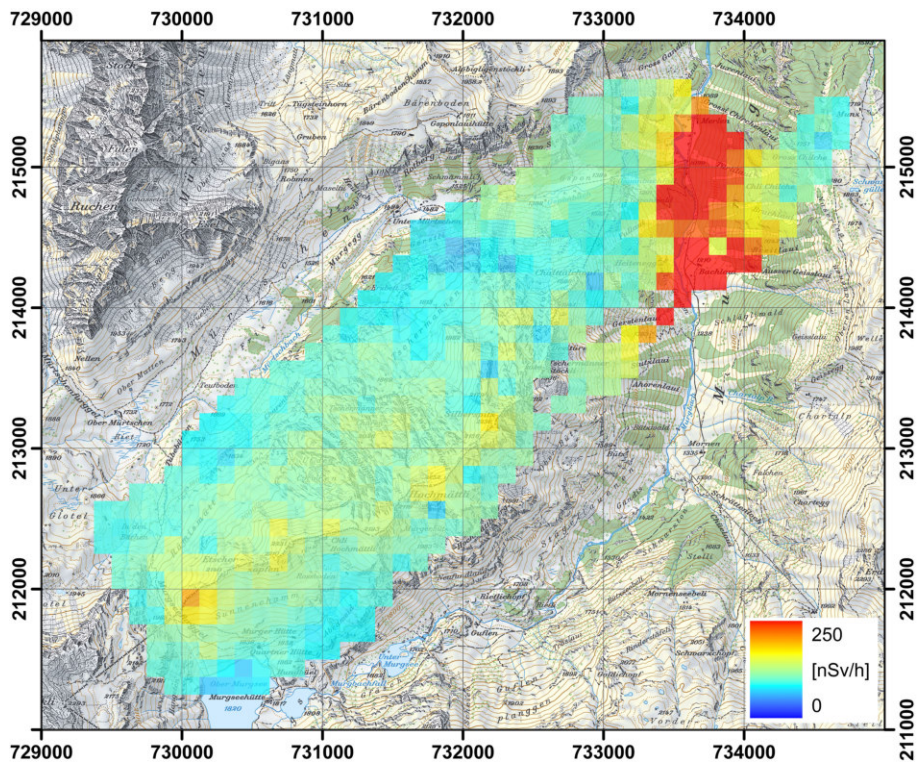
Figure 174: Terrestrial component of the dose rate near the Murg valley measured by team CH01 with a ground clearance of 105 m. PK25©2017 swisstopo (JD100042).
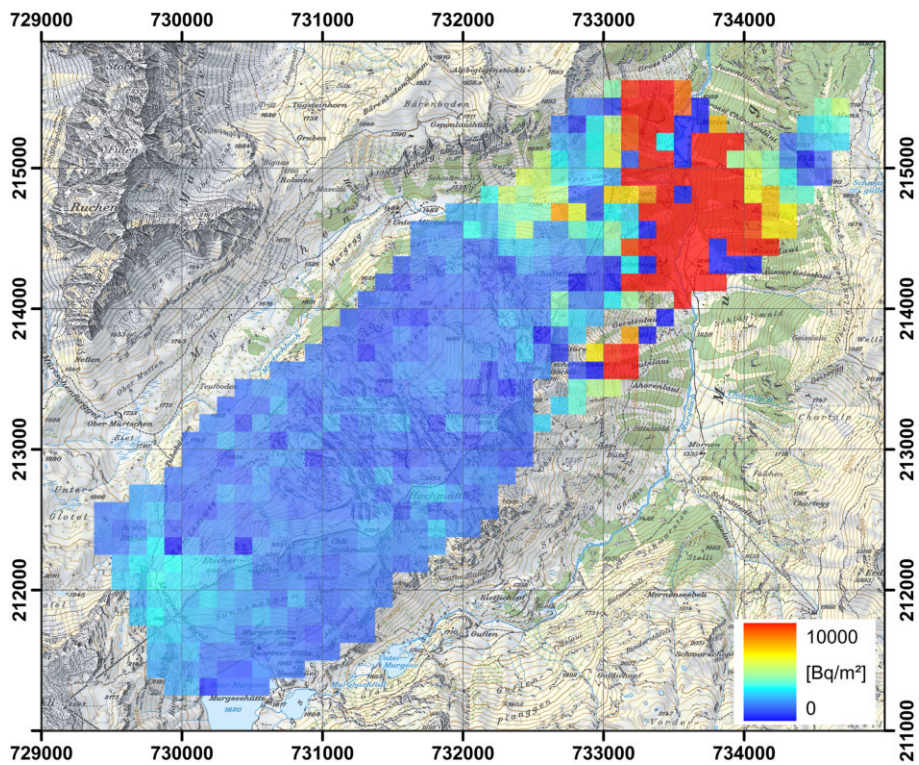
Figure 175: ^{137}Cs activity concentration near the Murg valley measured by team CH01 with a ground clearance of 105 m. PK25©2017 swisstopo (JD100042).
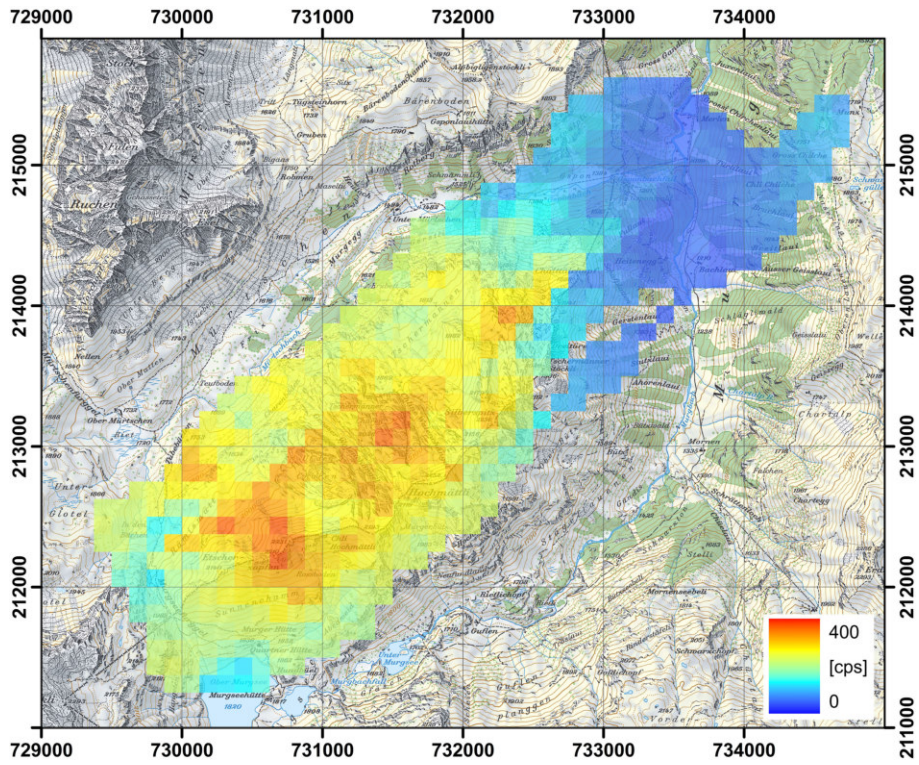
Figure 176: Count rate in the Caesium energy window near the Murg valley measured by team CH01 with a ground clearance of 105 m. PK25©2017 swisstopo (JD100042).
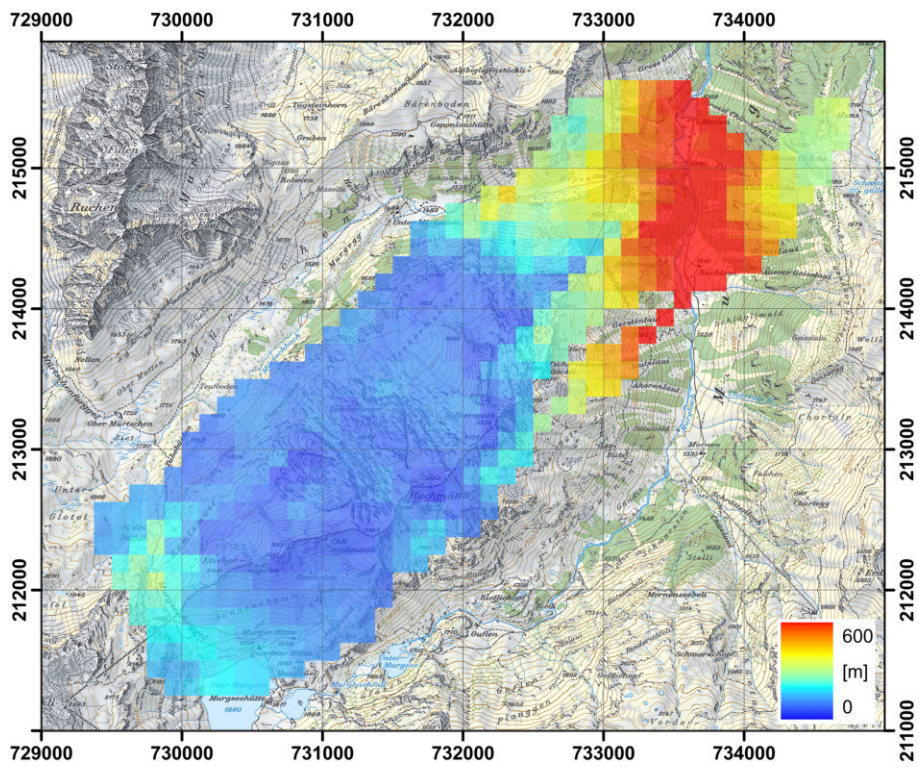
Figure 177: Ground clearance of the measuring flight near the Murg valley measured by team CH01 with a predetermined ground clearance of 100 m. PK25©2017 swisstopo (JD100042).
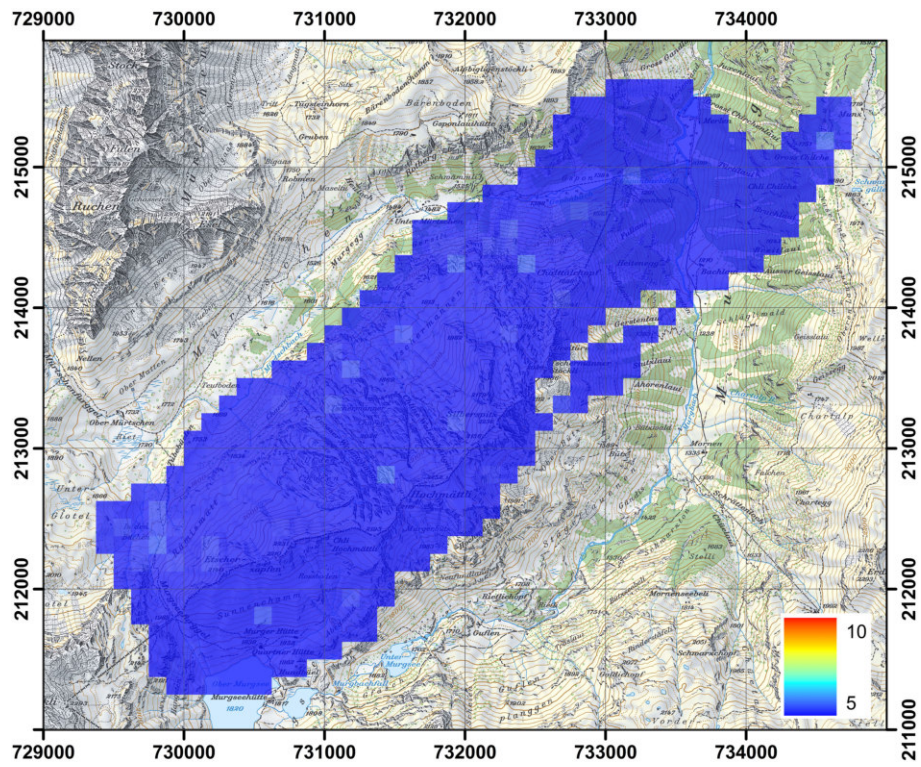
Figure 178: Man-made gross-count ratio (MMGC) near the Murg valley measured by team CH01 with a ground clearance of 105 m. PK25©2017 swisstopo (JD100042).

11 Transversal

A second task for testing the influence of topography on the results was a transversal from Neubrunn to Wartau (figure 179). The profile was referenced to a fictive starting point at coordinate (705000 m, 259000 m) marked in the upper left of figure 179 with a blue star. The elevation of the ground along the 60 km flight line varies between 600 m and 2000 m (figure 180).
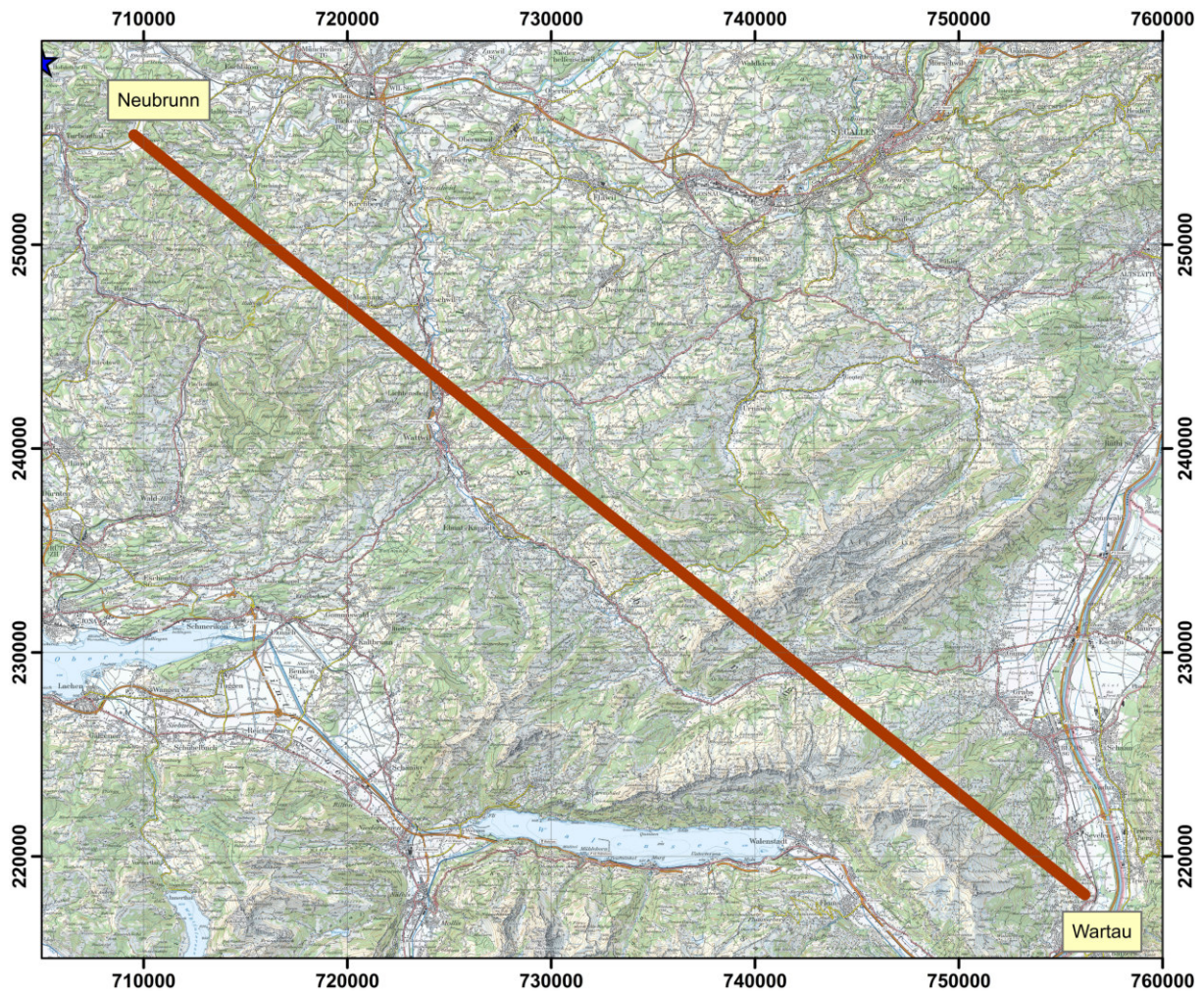
Figure 179: Predefined flight line of the transversal from Neubrunn to Wartau. The fictive starting point of the profile is marked with a blue star. PK100©2017 swisstopo (JD100042).
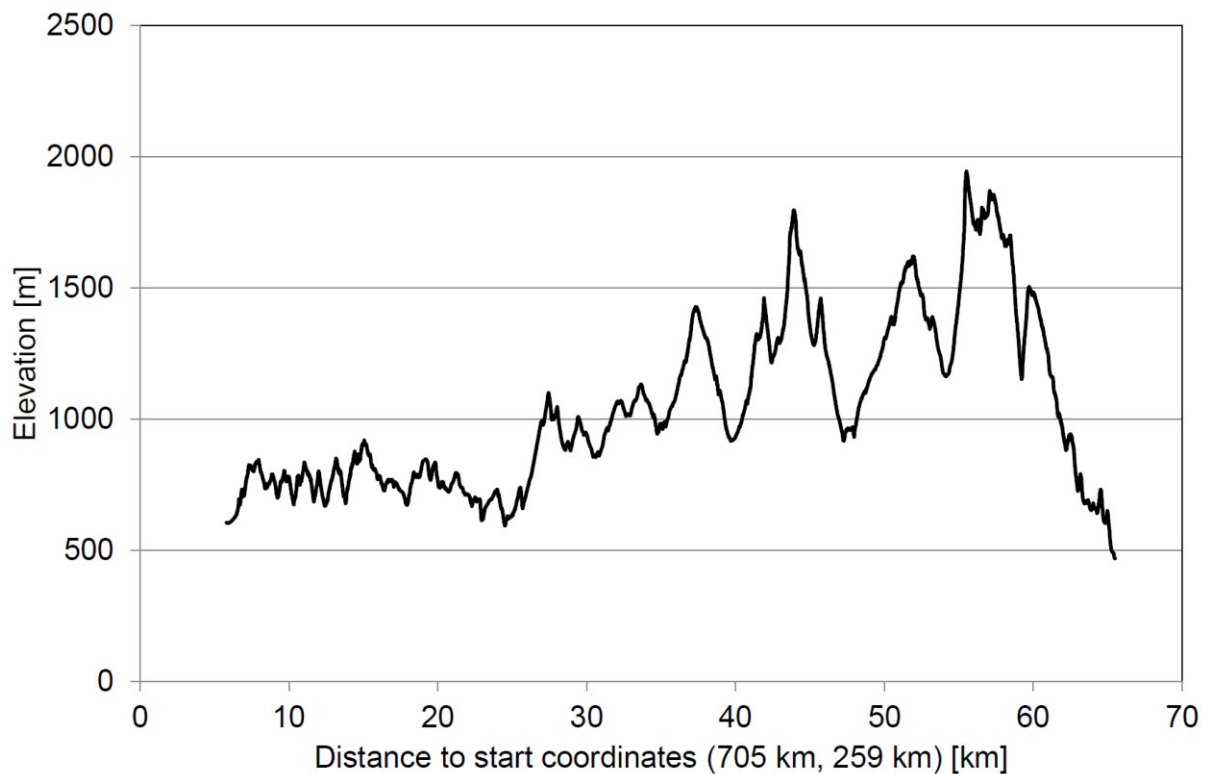
Figure 180: Elevation profile along the transversal from Neubrunn to Wartau derived from the Swiss digital elevation model DHM25©2017 swisstopo (JD100042).

11.1 Results

The flight altitude of team CH01 (figure 210) follows largely the elevation of ground (figure 180) with a major exception at 54.2 km, where the steep incline of the terrain required a detour to gain height. This caused additionally a deviation from the nominal ground clearance of 100 m to values up to 400 m.

The dose rate along the transversal reflects the altitude profile and passages over water bodies attenuating terrestrial photon radiation. Two crossings of the Thur river at 24.5 km and 52.2 km can be identified (figure 186). The terrestrial component of the dose rate (figure 216) shows besides the attenuation effect of water bodies slight variations due to fluctuations in the content of natural radionuclides. The maximum observed at 30.3 km can be related to elevated concentrations of Potassium and Thorium (figures 191 and 198), whereas the Uranium content shows elevated values in the south-eastern part of the profile (figure 205). These increased ^{238}U-concentrations may be artefacts caused by a unusual high ground clearance (figure 210).

Figure 211 shows flight altitude and ground clearance measured by team CH02. The loop at the beginning is caused by the inclusion of data from the approach to the start of the transversal. Steep inclines between 50 km and 60 km caused deviations to the target ground clearance.

The raw data measured by team CH02 were evaluated with the proprietary software provided by the manufacturer of the RLL system and the software of the old ARM system used by team CH01 (see sections 3.2, 3.1 and 9.1.1). The dose rates (figures 187 and 188) show in the ARM-evaluation 20 nSv/h to 40 nSv/h larger values, indicating a difference in calibration factors. The potassium activity concentrations agree well between both evaluation methods (figures 192 and 193). In the results of the ARM evaluation, a smoothing

can be observed compared to the RLL evaluation. The measurement settings (use case) of the RLL system applied by team CH02 does store only spectra averaged over 5 seconds, which were then used as raw spectra in the ARM evaluation. Besides the smoothing effect of the spectrum average, Uranium and Thorium activity concentrations agree well between both evaluation methods (figures 206, 207, 199 and 200). Two peaks with elevated ^{238}U activity concentrations at 56 km and 59 km coincide with peaks in ground clearance (figure 211), indicating a possible artefact produced by the evaluation algorithms. The elevated ^{40}K and ^{232}Th activity concentrations observed at 30.3 km by team CH01 are also visible in the results of team CH02 (figures 192, 193, 199 and 200).

The ground clearance measured by team CZ01 along the profile from Neubrunn to Wartau is depicted in figure 212. Rather large deviations to the target ground clearance cannot be explained with an insufficient rate of climb and rate of descent of the MI-17 helicopter for measurements in alpine terrain. The value of 480 m/min for the MI-17 is comparable to the helicopters used by the other teams (Superpuma (CH) 492 m/min, EC-135 (DE) 457 m/min and AS-350 (FR) 597 m/min). Values of flight altitude were not reported. Dose rate and activity concentrations of the natural radionuclides are shown in figures 189, 194, 208 and 201.

Teams DE01 and DE02 reported results of the transversal measurements based on the UTM 32T projected coordinates. The fictive starting point of the profile at Swiss national grid coordinates (705000 m, 259000 m) was translated to UTM 32T coordinates using an on-line coordinate conversion application (https://www.deine-berge.de/Rechner/Koordinaten/Dezimal/51,10), which gave the reference point as (32487306 m, 5257786 m) and the distance to the starting point was calculated in UTM coordinates.

Dose rate values along the transversal were not reported by teams DE01 and DE02. Values of other quantities were already reviewed according to data quality criteria, thus gaps are visible in the diagrams. All values measured for ^{238}U activity concentration were rejected for both teams according to the quality criteria, especially the decision limit of the measuring system. Figures 213 and 214 show that unusual ground clearances as reported by the other teams were eliminated during quality assurance. The elevated ^{40}K activity concentrations observed at 30.3 km by the Swiss teams are also visible in the results of the German teams (figures 195 and 196). The values reported for the activity concentration of the natural radionuclides along the transversal agree well between both German teams (figures 195, 196, 202 and 202).

As for the Swiss and Czech teams, the ground clearance of team FR01(figure 215) shows large deviations from the standard ground clearance in the vicinity of strong inclines of the terrain. These unusual ground clearances have only a small effect on the measured dose rate (figure 190). The activity concentrations of the natural radionuclides (figures 197, 209 and 204) show a larger influence on unusual ground clearances. The increase of ^{40}K activity concentration 30 km along the profile was also observed by team FR01 (figure 197).

11.1.1 Comparison

The frequency distributions of the ground clearance of all values reported for the transversal (figure 181) illustrate the already mentioned deviations to the target ground clearance of team CZ01 (see section 11.1) as a flatter distribution compared to the other teams. The distributions of teams DE01 and DE02 are the narrowest distributions around the target ground clearance. This can be caused by the massive reduction of measuring points due to quality assurance aspects.

The frequency distributions of the measured dose rates (figure 182) show asymmetric distributions for all participants. The frequency distribution of team CH02 evaluated with the proprietary software of the manufacturer of the RLL system is quite close to the distribution observed by team FR01. After re-evaluation with the ARM-software used by team CH01, the distribution agrees with the distribution observed by team CH01. Teams DE01 and DE02 did not report dose rates for the transversal measurement.

The frequency distributions of the ^{40}K activity concentration (figure 183) are very similar. Again, the distributions of teams DE01 and DE02 are narrower due to the reduction of reported measuring points. The distribution measured by team CZ01 shows a peak at zero, whereas the distribution of teams CH01, CH02 and FR01 show few negative concentration values. This effect can be seen more clearly in the frequency distribution of the ^{238}U activity concentration (figure 185).

During data evaluation (see section 3), raw count rates are corrected for various perturbations. Like the raw count rates, these corrections are typically prone to statistical variations, which could lead to values considered nonsensical (e.g. negative activities) or unreliable (e.g. below the detection limit). Different treatments of such results for a single data point are used:

- Report values independent on the statistical significance.

- Set negative values to zero.

- Report only values above zero.

- Report only values above the detection limit.

The peaks of the frequency distributions at a value of zero suggest that team CZ01 uses the second alternative. The reported negative values imply the application of the first alternative by teams CH01, CH02 and FR01, whereas teams DE01 and DE02 seem to use the fourth alternative.

Evaluated parameters at a measuring point can be considered as samples from a probability distribution around the true value. Uncertainty analysis of the measurement and evaluation describes the according probability distribution, using indicators like e.g. the detection limit. The latter three alternatives listed above cut off a part of this probability distribution. The problem generated with this cut-off is the introduction of a bias in the resulting probability distribution. In consequence, if we assume an area as homogeneous (i.e. all measured data points are members of the same population), the average over all points considered valid in the area will be larger than the mean value of the unbiased distribution. The frequency distributions of the ^{232}Th activity concentration (figure 184) of all participants agree well.
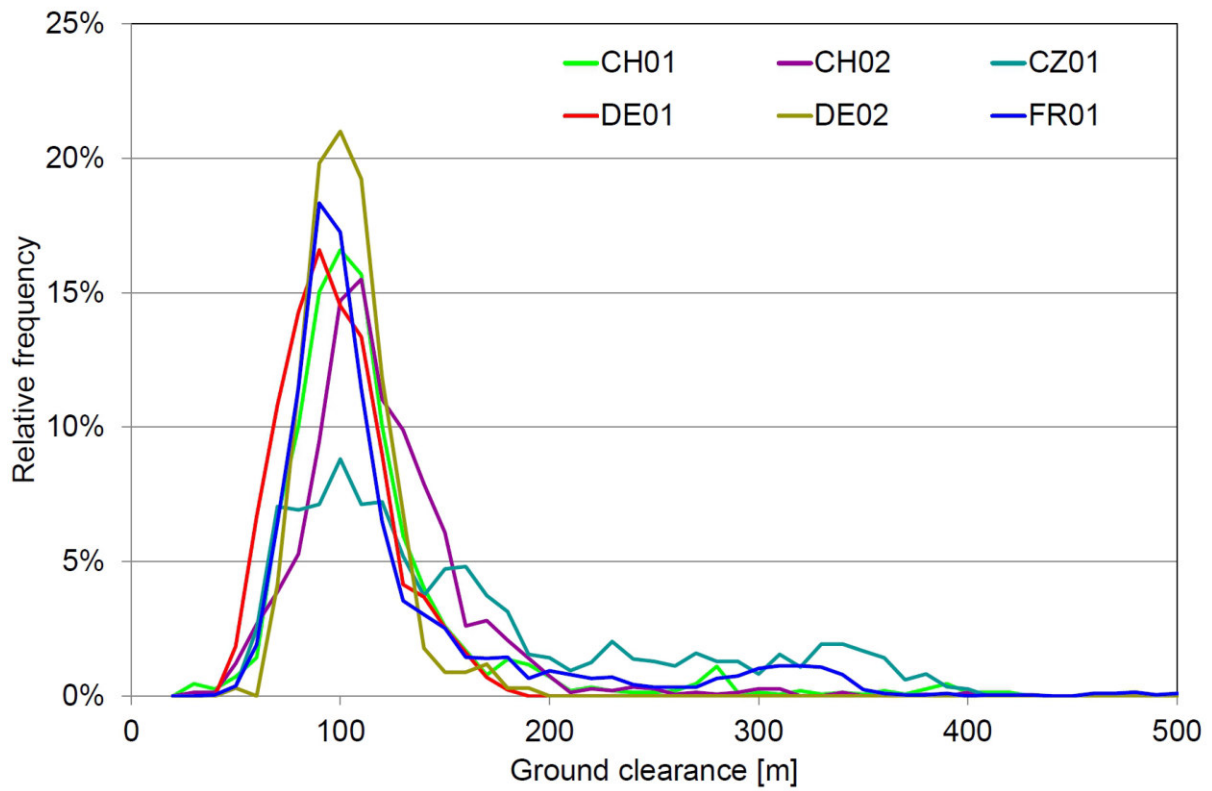
Figure 181: Frequency distributions of ground clearance on the transversal from Neubrunn to Wartau.
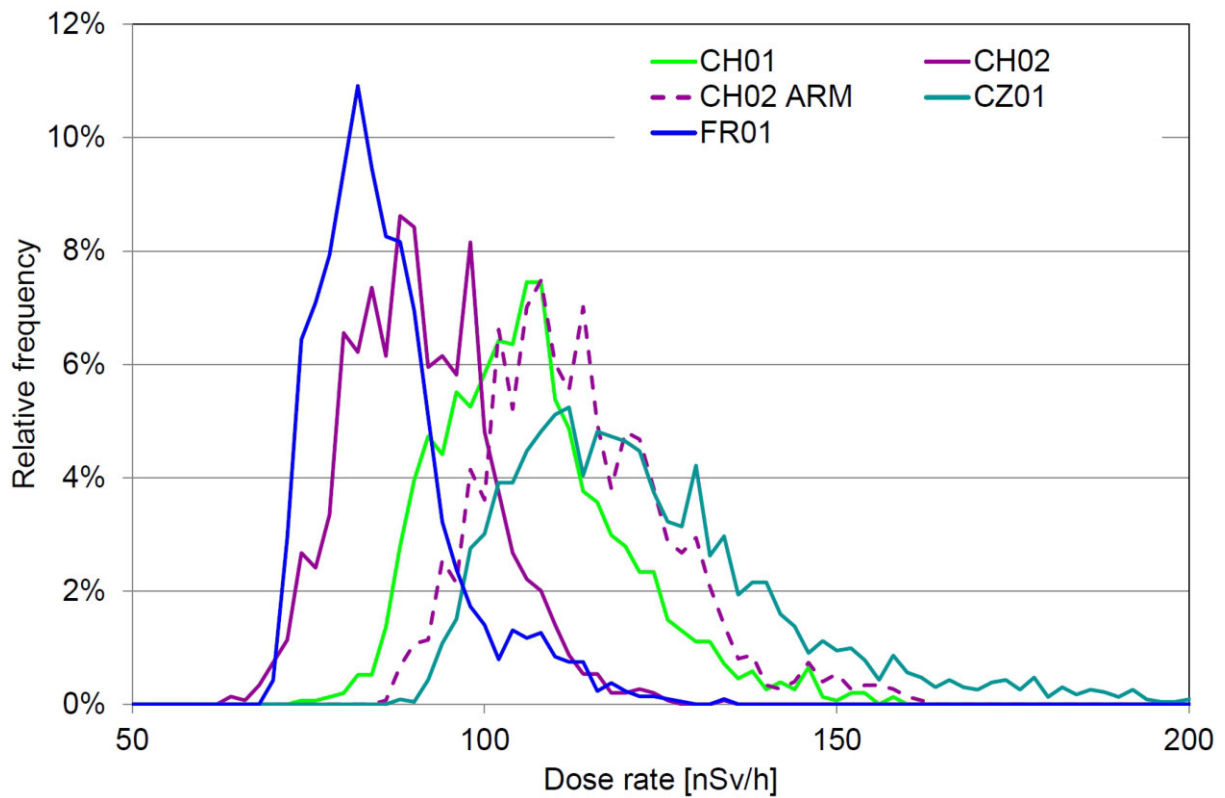
Figure 182: Frequency distributions of dose rate on the transversal from Neubrunn to Wartau.
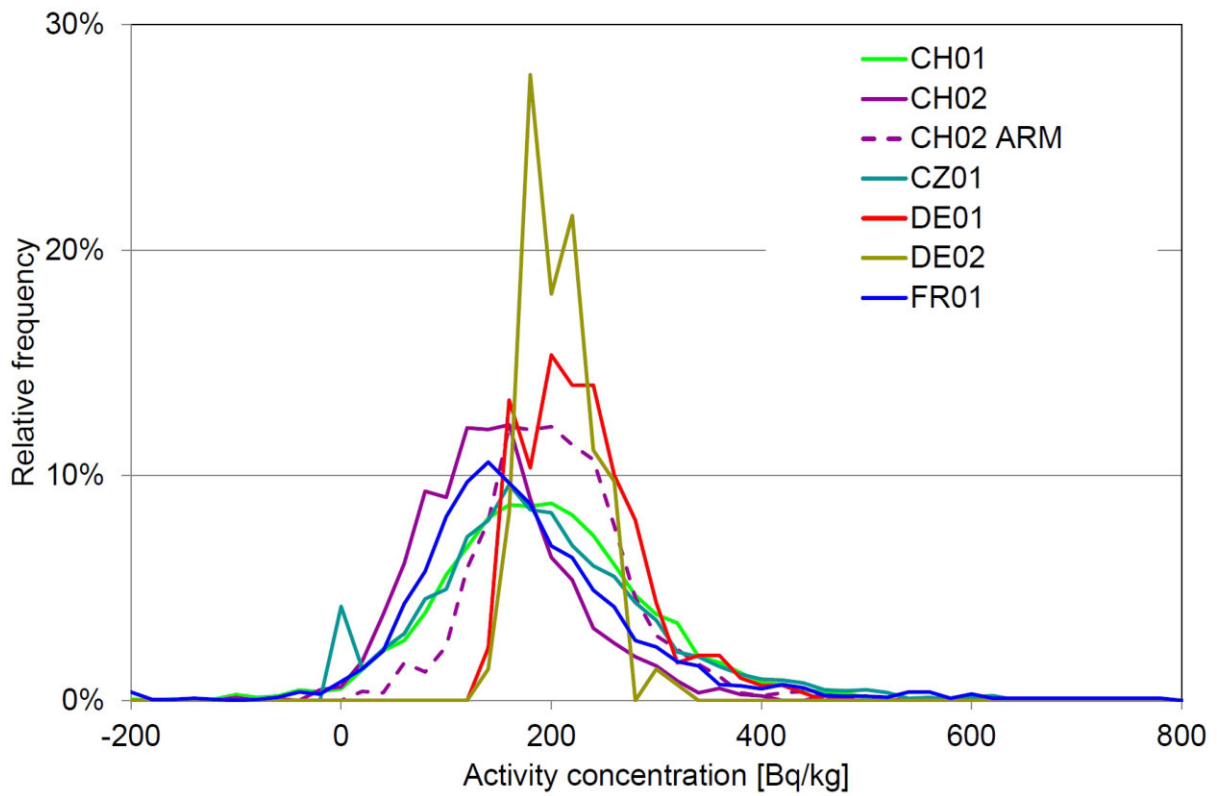
Figure 183: Frequency distributions of ^{40}K activity concentration on the transversal from Neubrunn to Wartau.
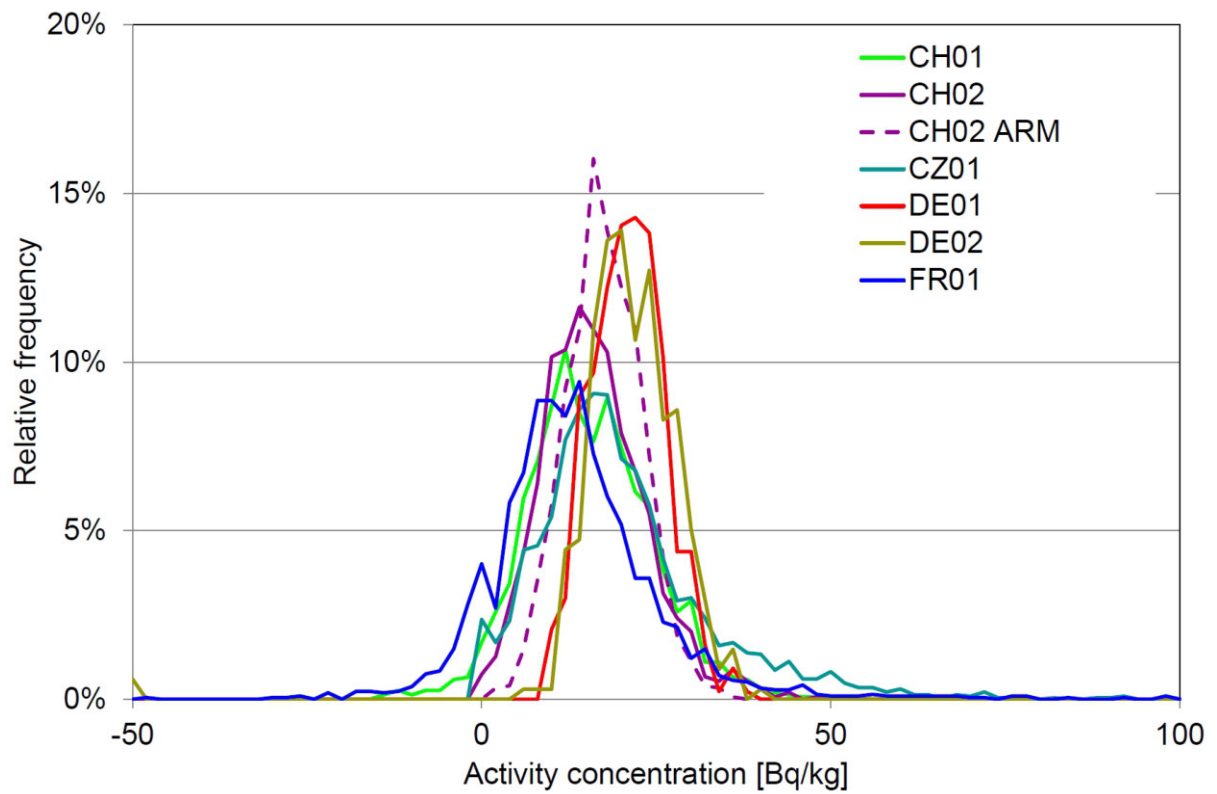
Figure 184: Frequency distributions of ^{232}Th activity concentration on the transversal from Neubrunn to Wartau.
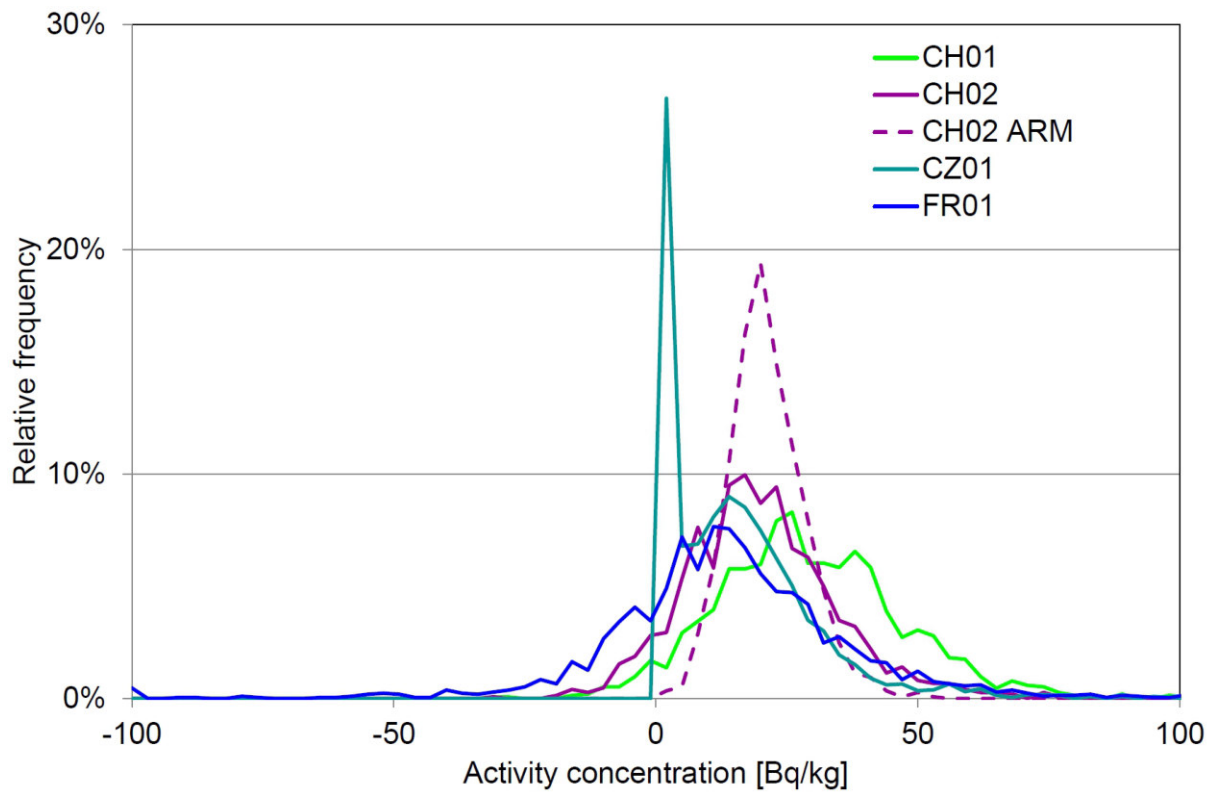
Figure 185: Frequency distributions of ^{238}U activity concentration on the transversal from Neubrunn to Wartau.

11.1.2   Profile diagrams
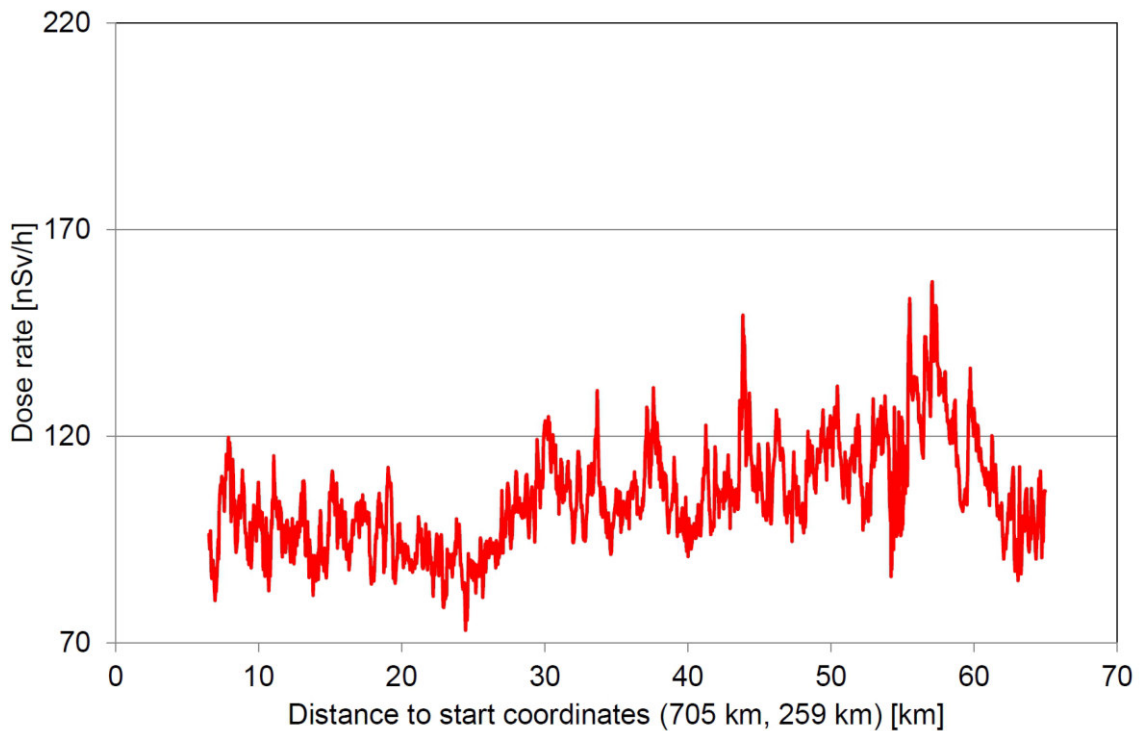
Figure 186: Dose rate along the transversal from Neubrunn to Wartau measured by team CH01.
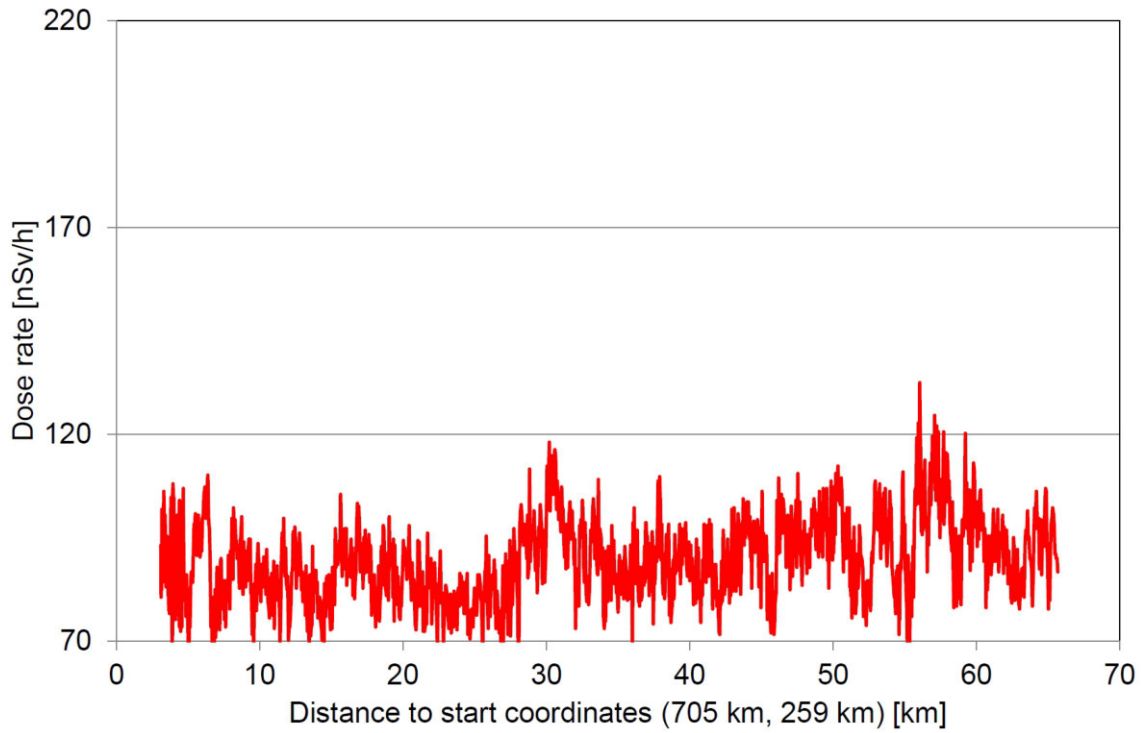
Figure 187: Dose rate along the transversal from Neubrunn to Wartau measured by team CH02.
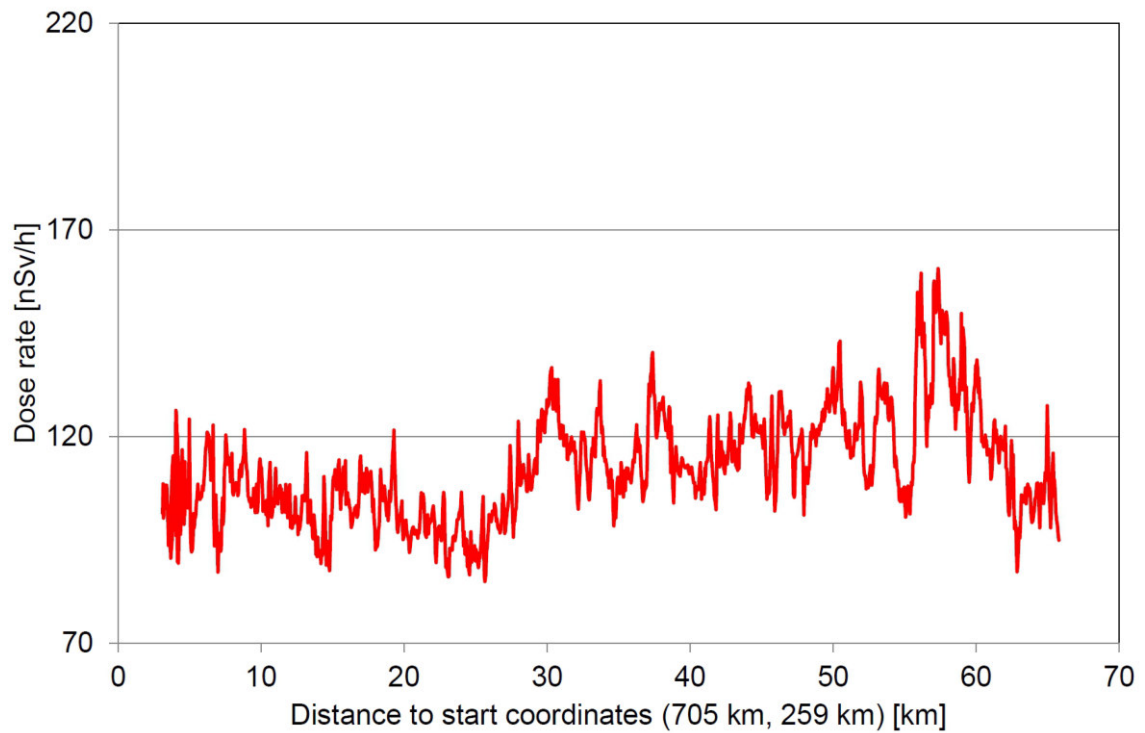
Figure 188: Dose rate along the transversal from Neubrunn to Wartau measured by team CH02. Raw data evaluated with the ARM software.
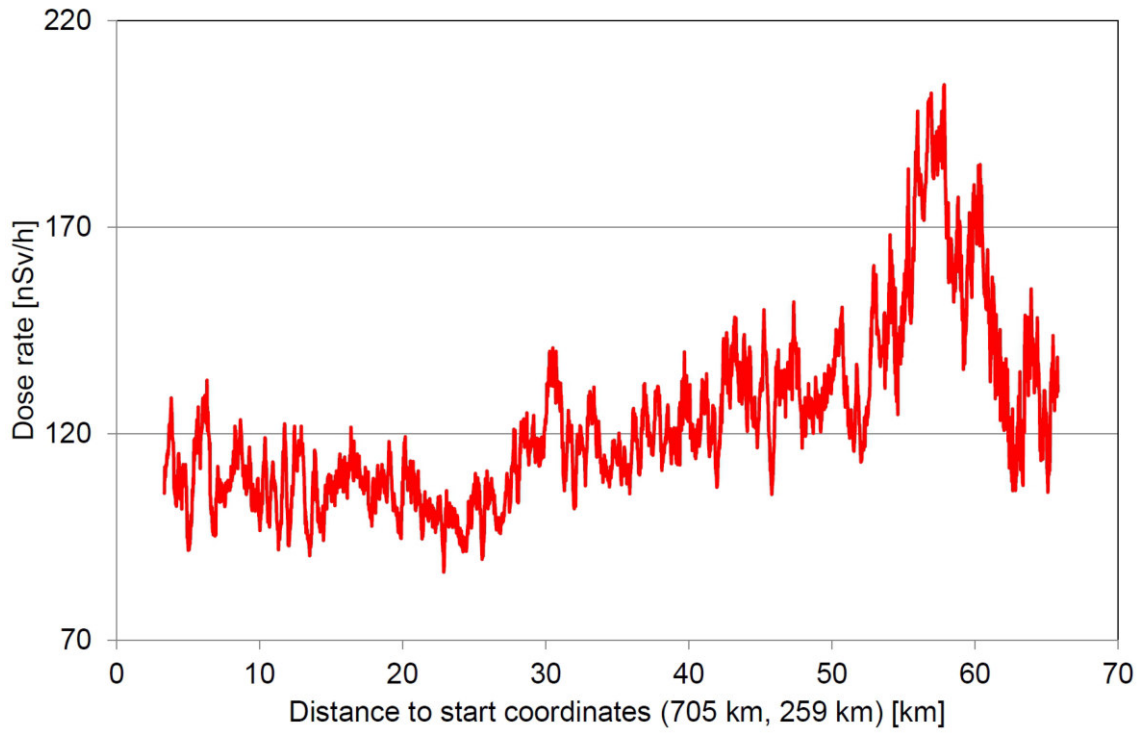
Figure 189: Dose rate along the transversal from Neubrunn to Wartau measured by team CZ01.
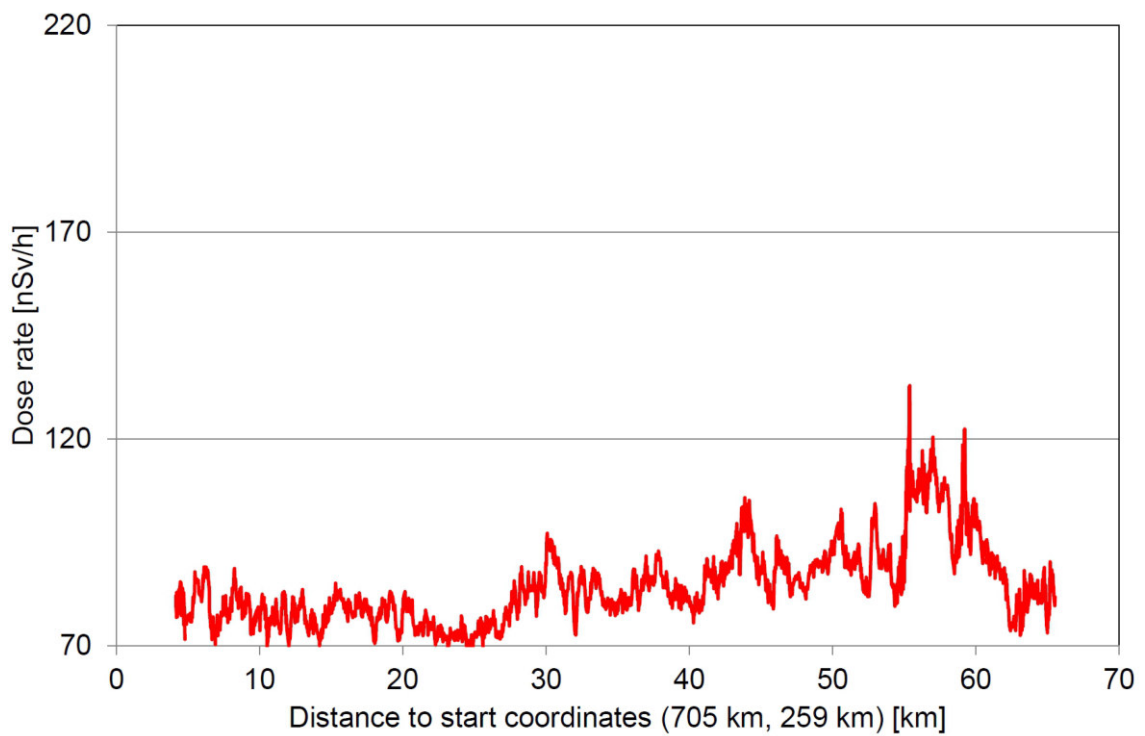
Figure 190: Dose rate along the transversal from Neubrunn to Wartau measured by team FR01.
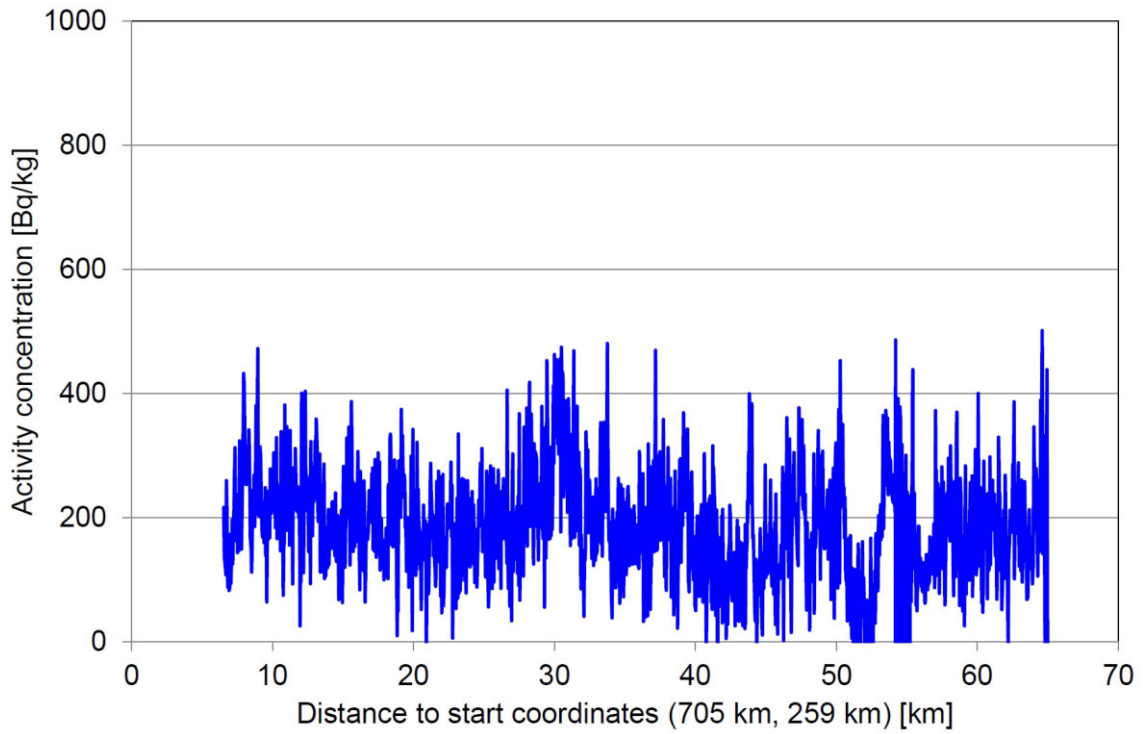
Figure 191: ^{40}K activity concentration along the transversal from Neubrunn to Wartau measured by team CH01.
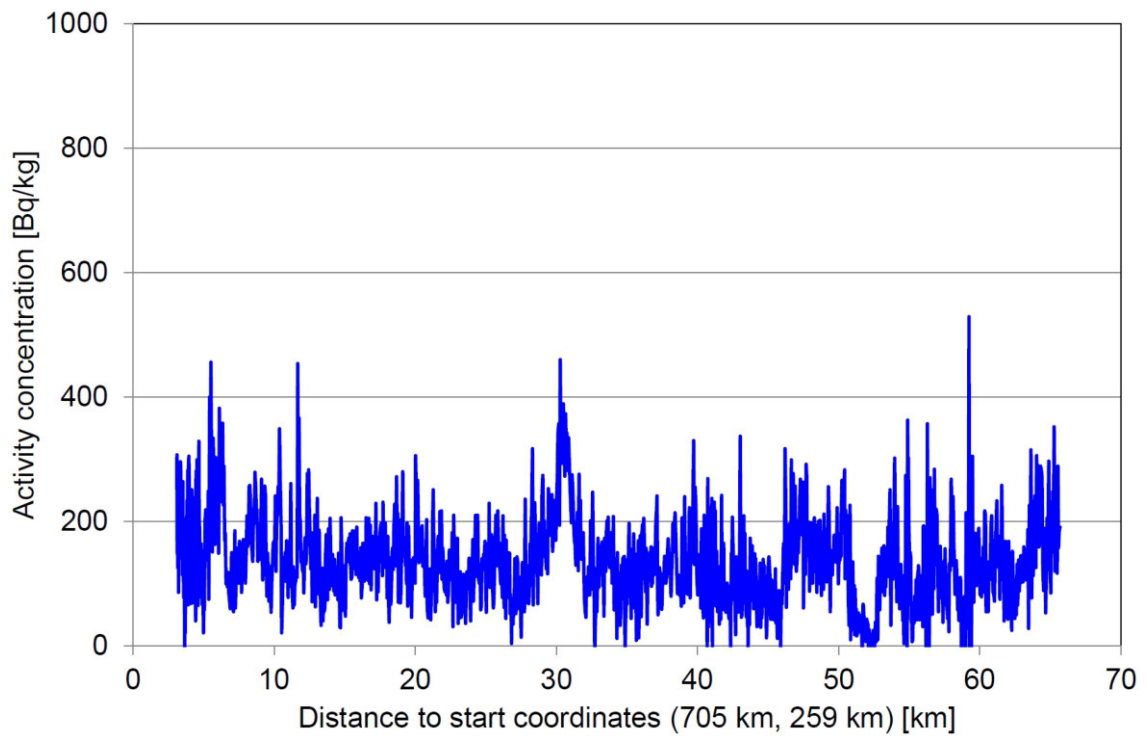
Figure 192: ^{40}K activity concentration along the transversal from Neubrunn to Wartau measured by team CH02.
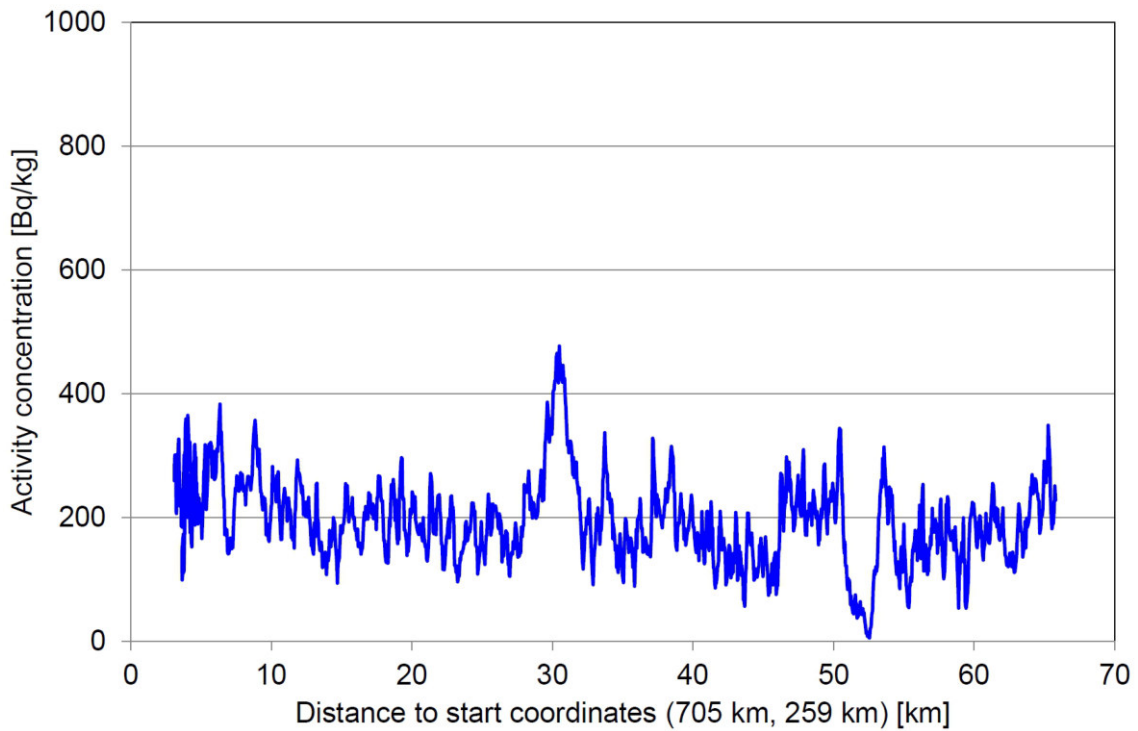
Figure 193: ^{40}K activity concentration along the transversal from Neubrunn to Wartau measured by team CH02. Raw data evaluated with the ARM software.
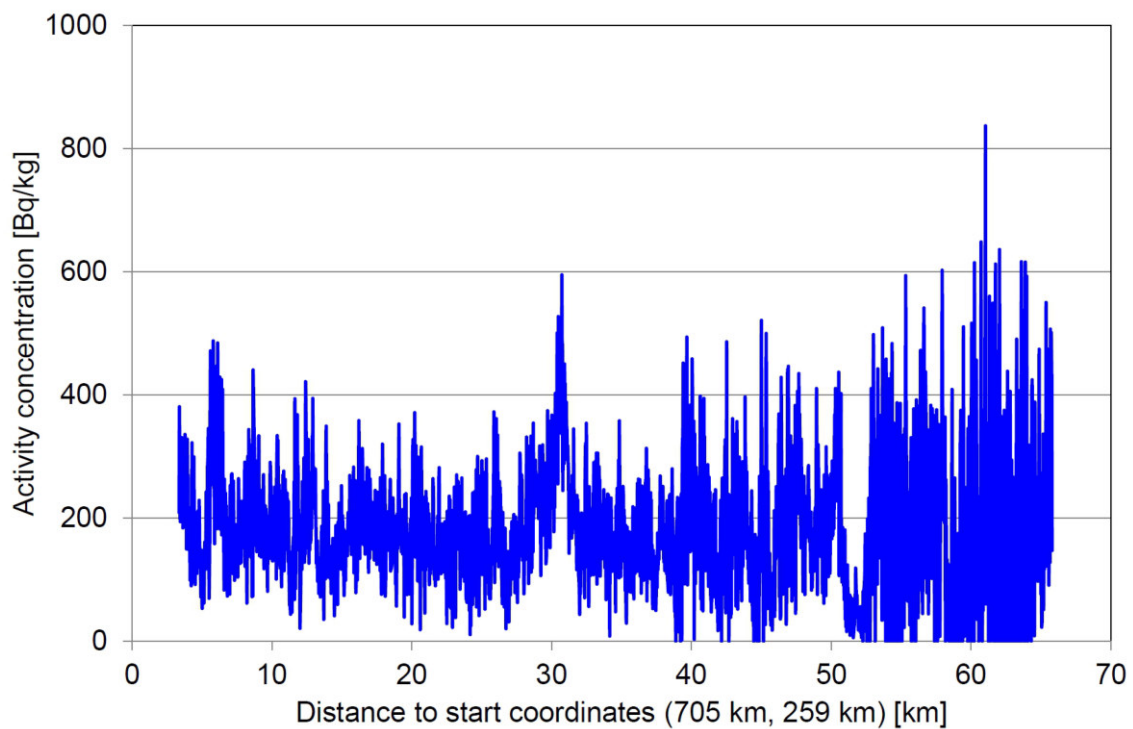
Figure 194: ^{40}K activity concentration along the transversal from Neubrunn to Wartau measured by team CZ01.
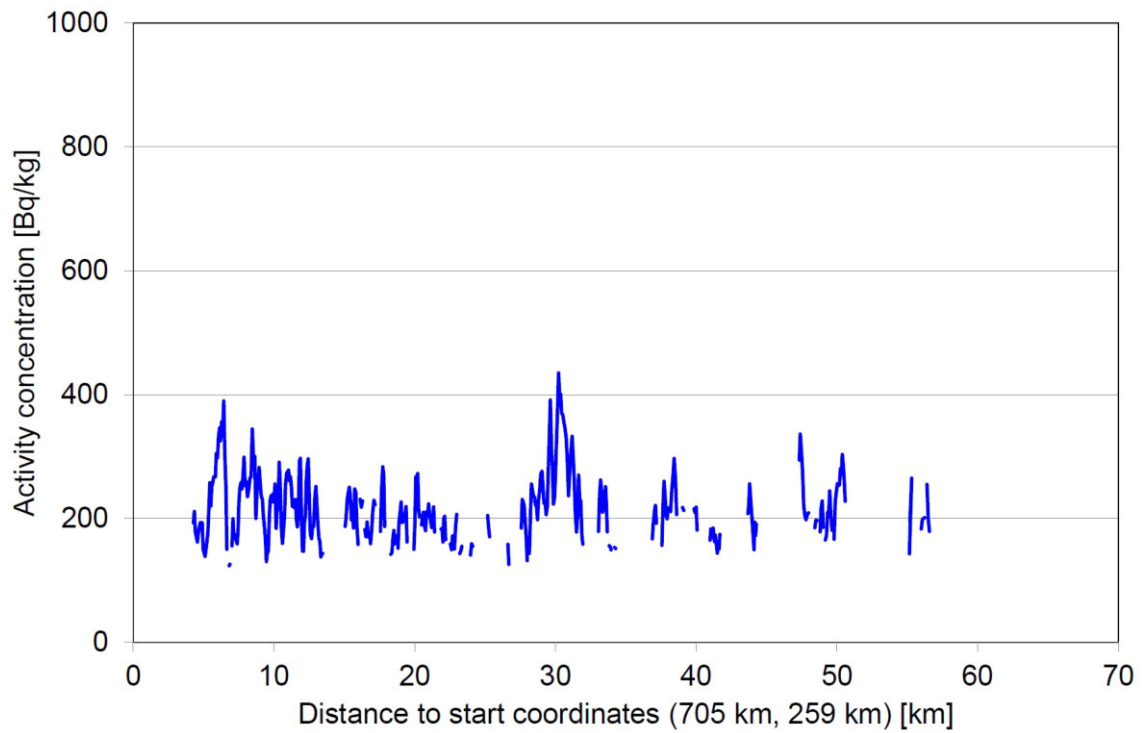
Figure 195: ^{40}K activity concentration along the transversal from Neubrunn to Wartau measured by team DE01.
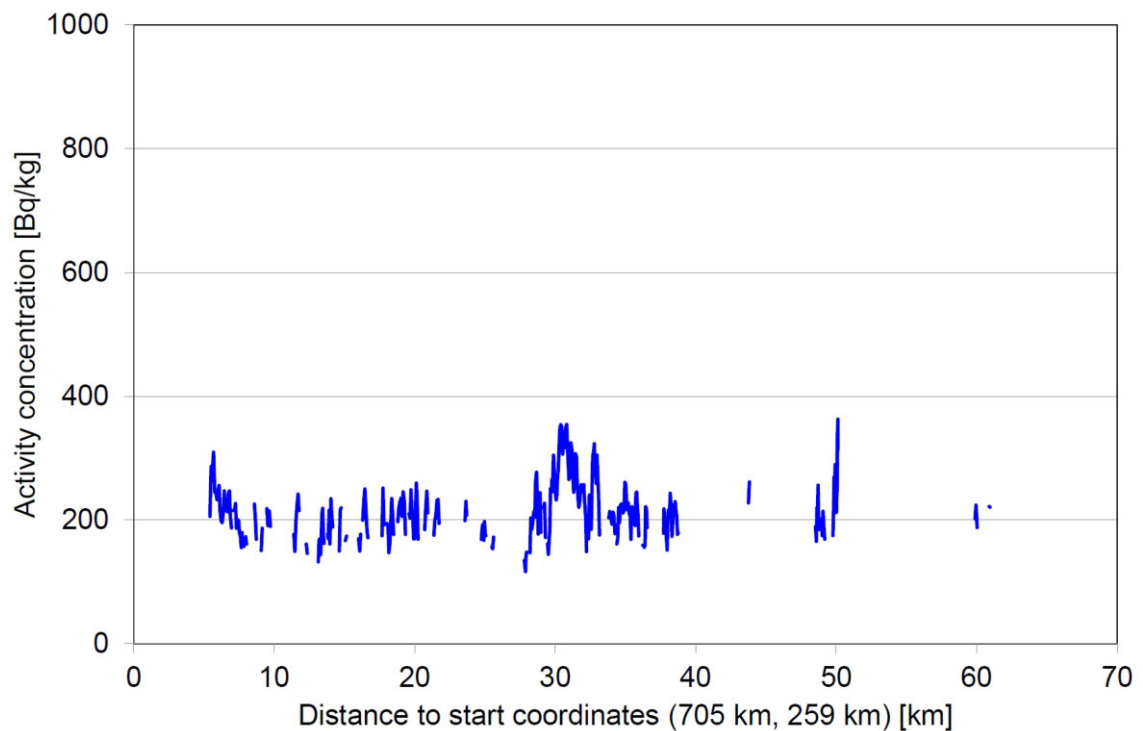
Figure 196: ^{40}K activity concentration along the transversal from Neubrunn to Wartau measured by team DE02.
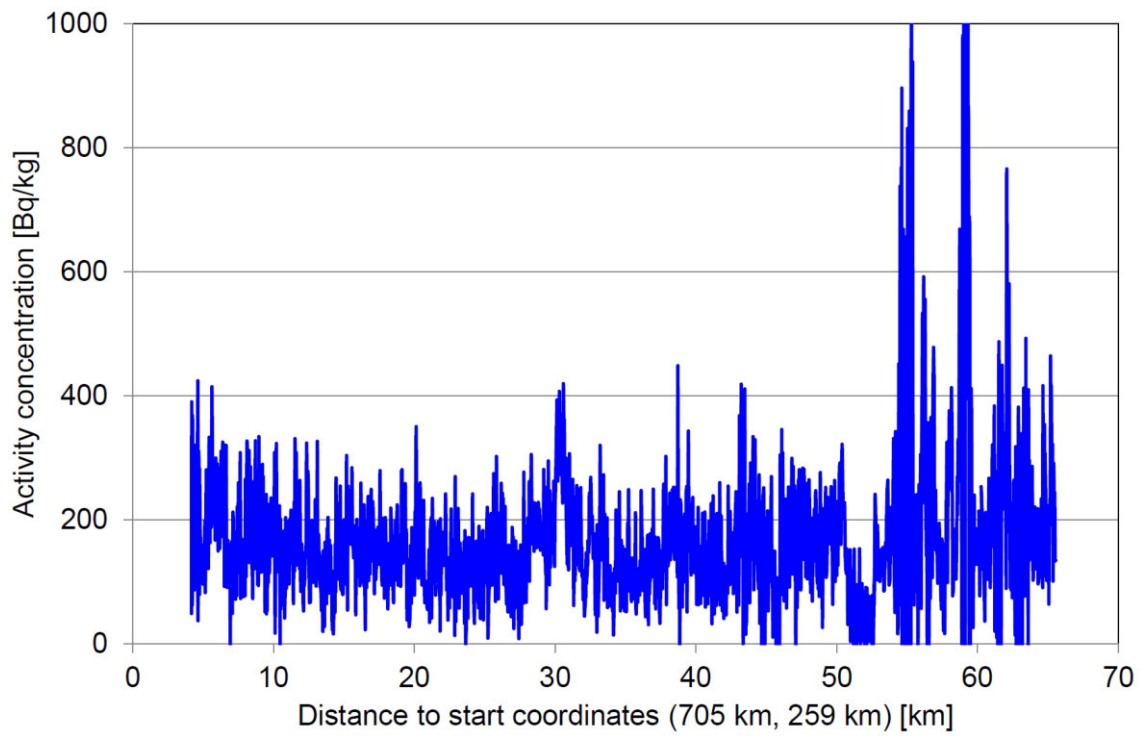
Figure 197: ^{40}K activity concentration along the transversal from Neubrunn to Wartau measured by team FR01.
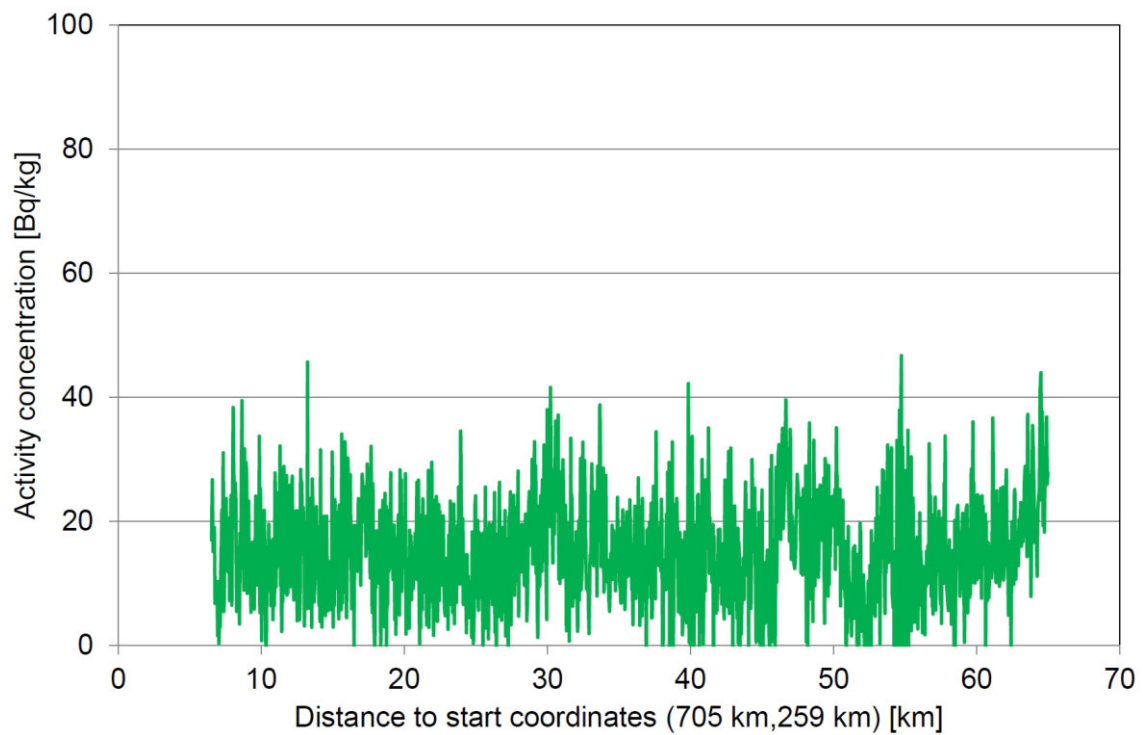
Figure 198: ^{232}Th activity concentration along the transversal from Neubrunn to Wartau measured by team CH01.
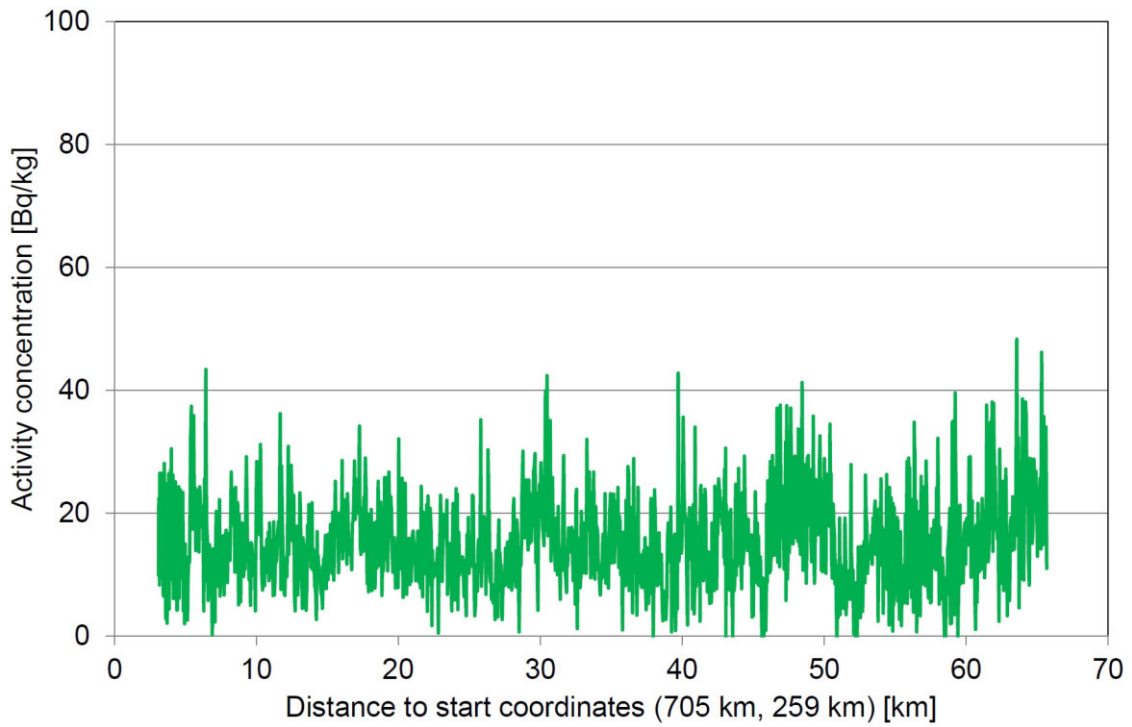
Figure 199: ^{232}Th activity concentration along the transversal from Neubrunn to Wartau measured by team CH02.
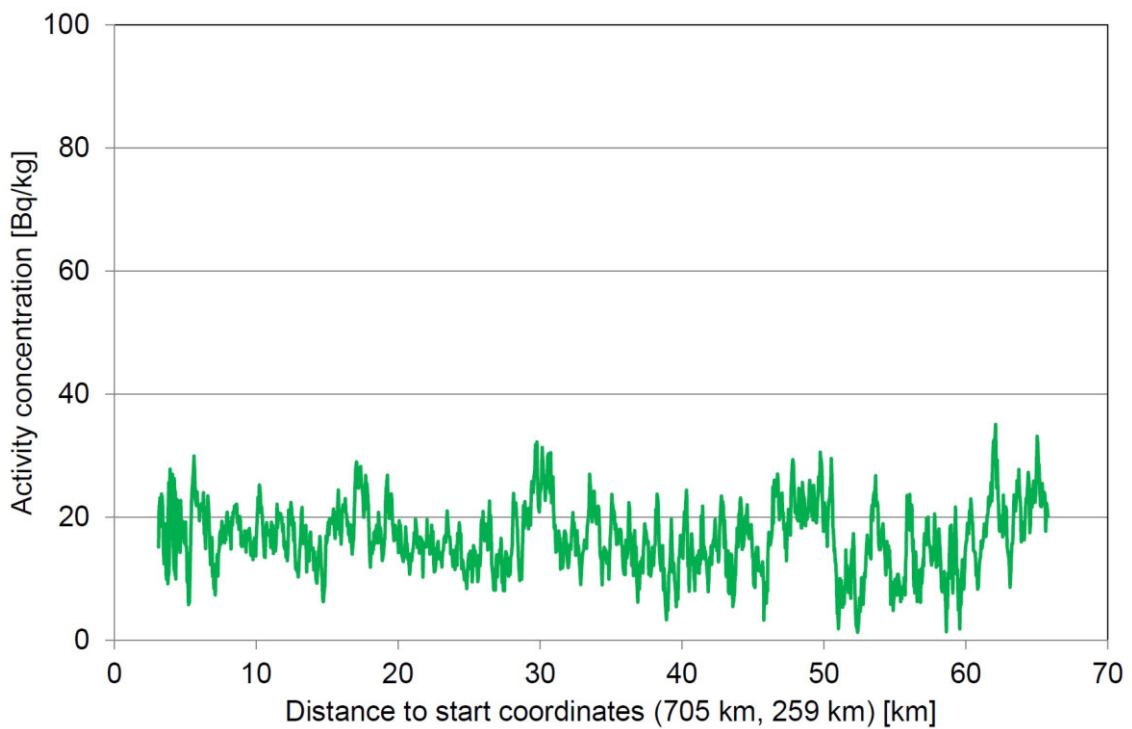
Figure 200: ^{232}Th activity concentration along the transversal from Neubrunn to Wartau measured by team CH02. Raw data evaluated with the ARM software.
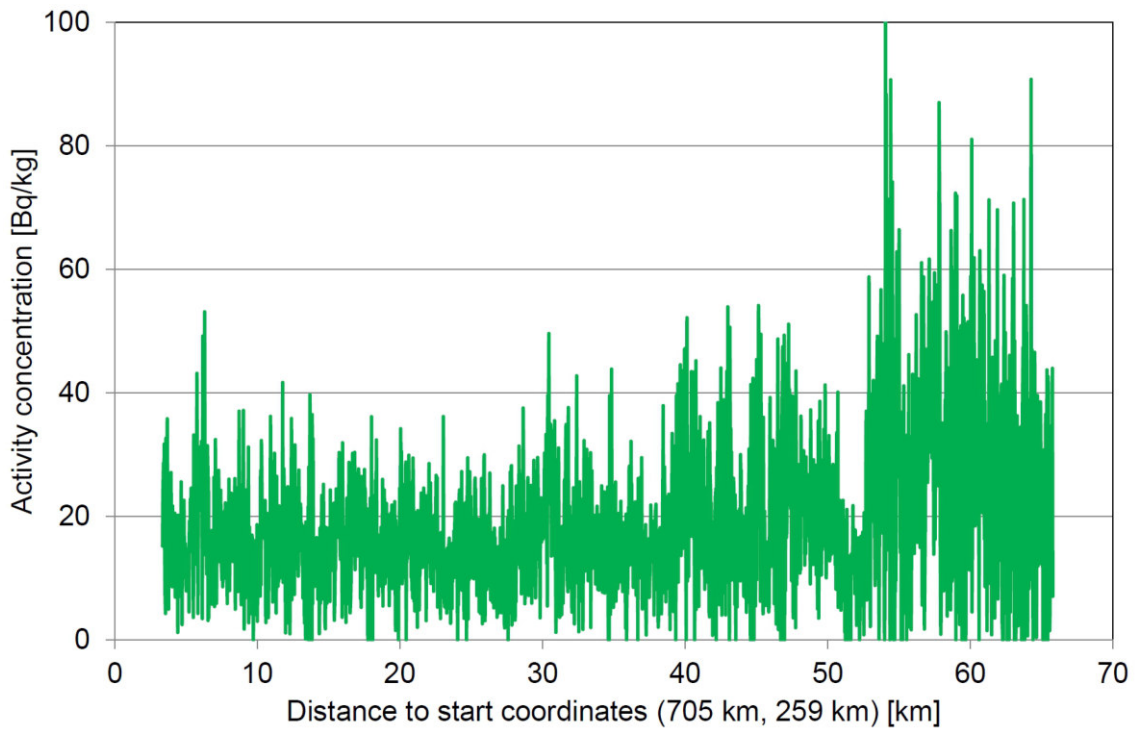
Figure 201: ²³²Th activity concentration along the transversal from Neubrunn to Wartau measured by team CZ01.
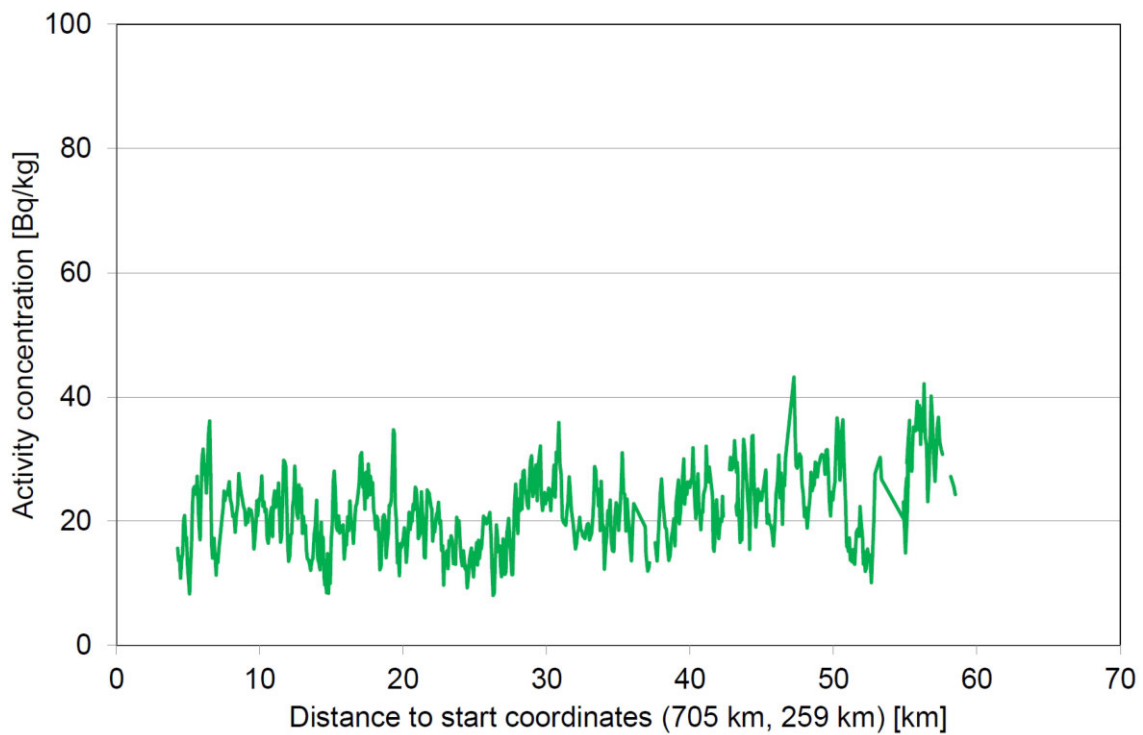
Figure 202: ²³²Th activity concentration along the transversal from Neubrunn to Wartau measured by team DE01.
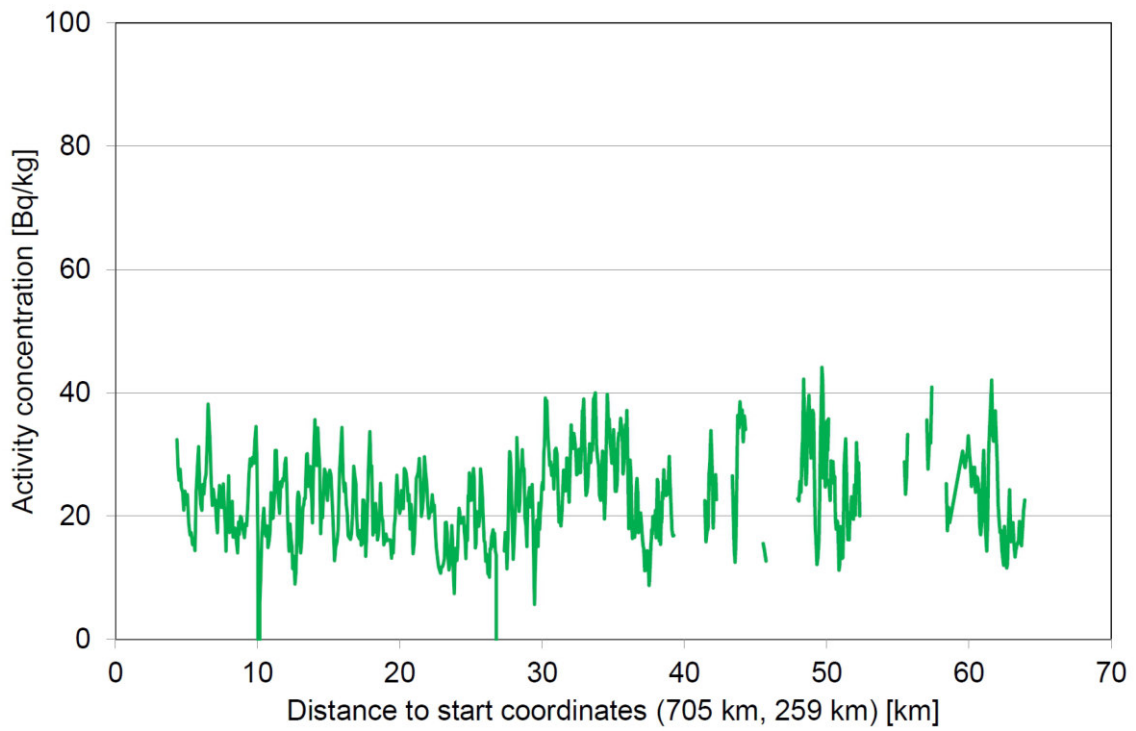
Figure 203: ^{232}Th activity concentration along the transversal from Neubrunn to Wartau measured by team DE02.
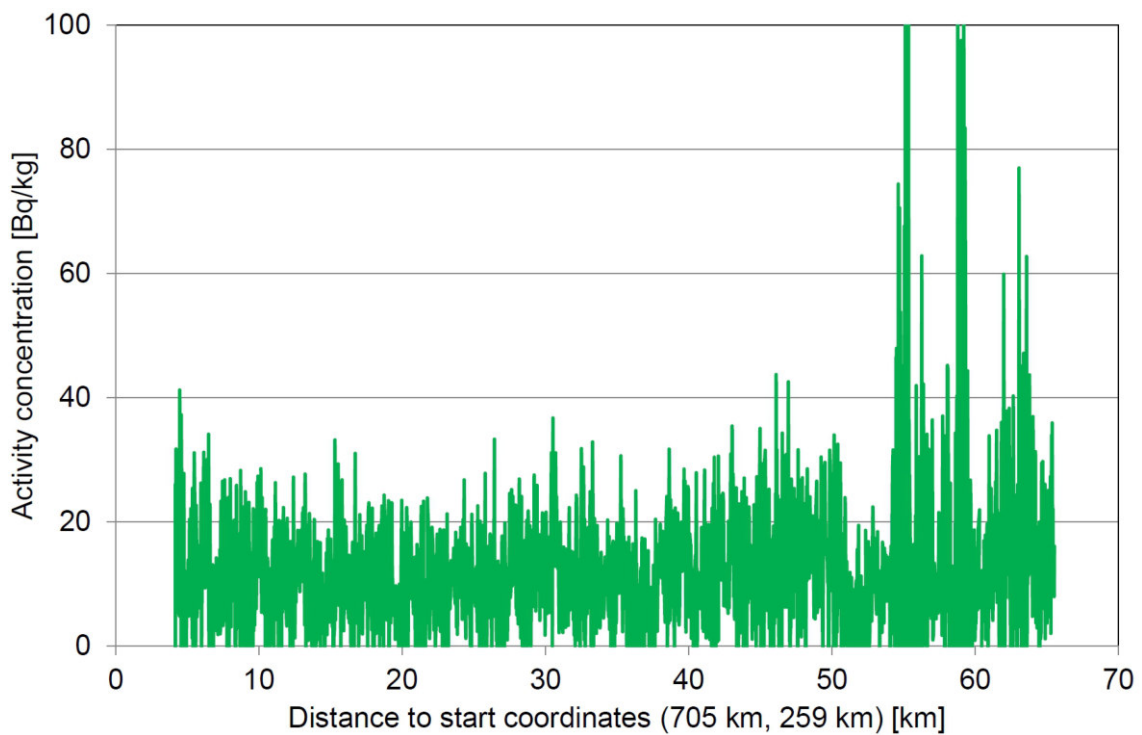
Figure 204: ^{232}Th activity concentration along the transversal from Neubrunn to Wartau measured by team FR01.
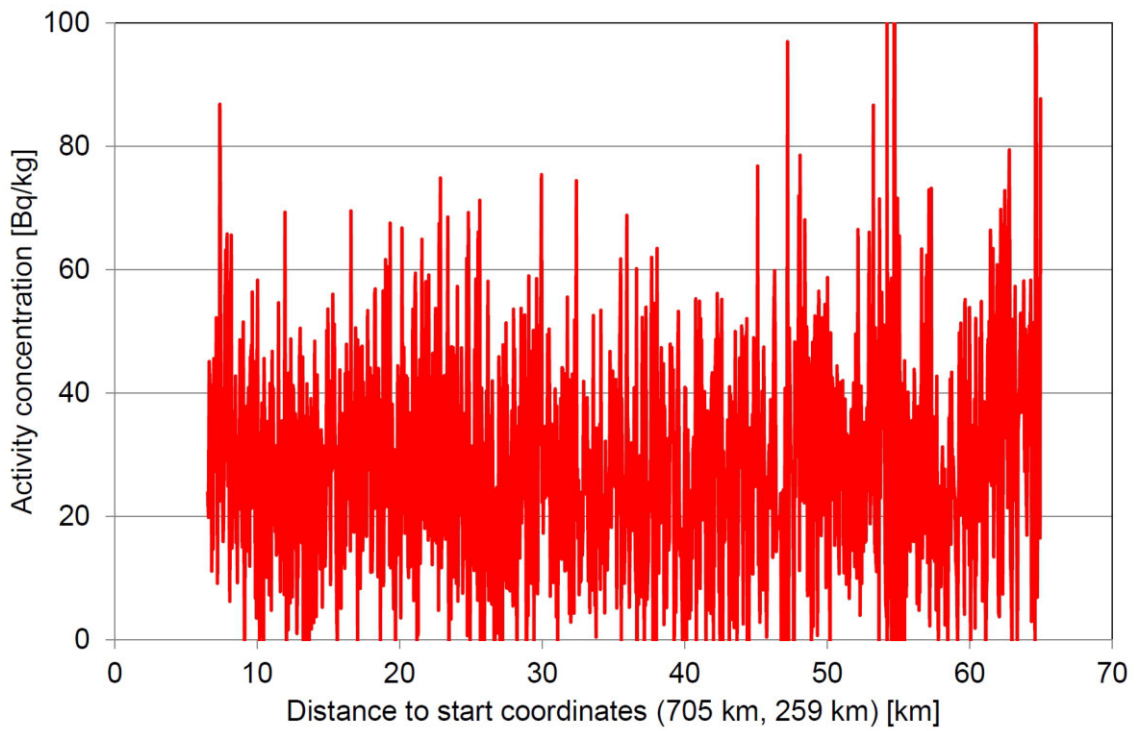
Figure 205: ^{238}U activity concentration along the transversal from Neubrunn to Wartau measured by team CH01.
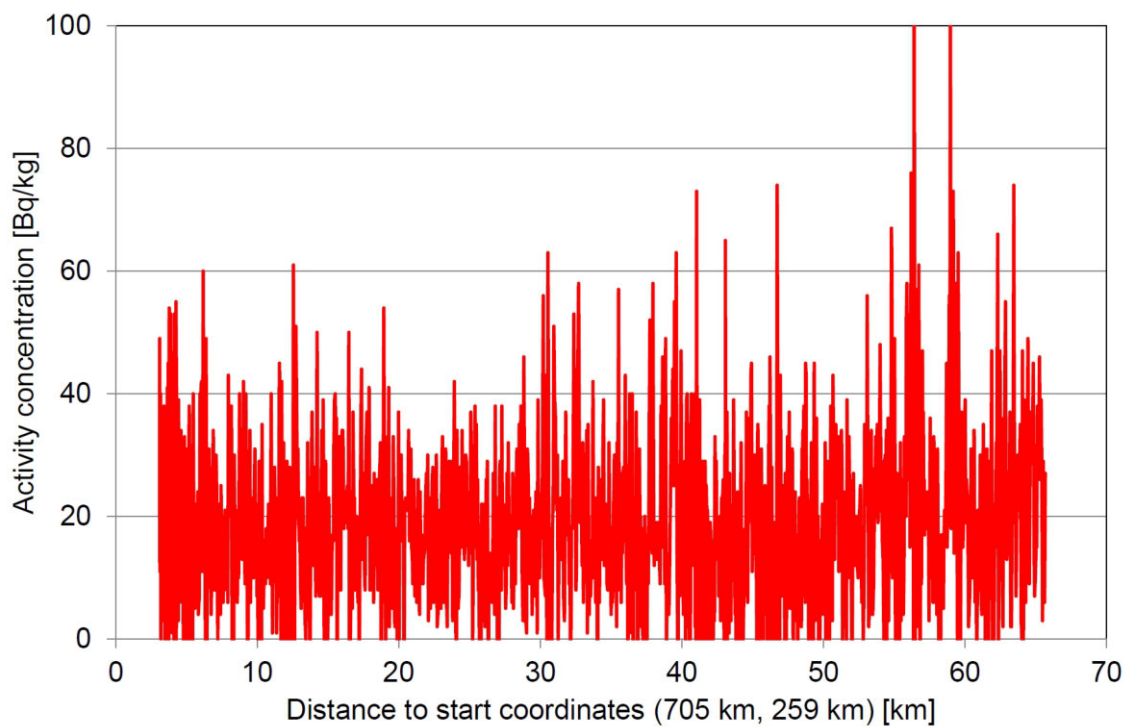
Figure 206: ^{238}U activity concentration along the transversal from Neubrunn to Wartau measured by team CH02.
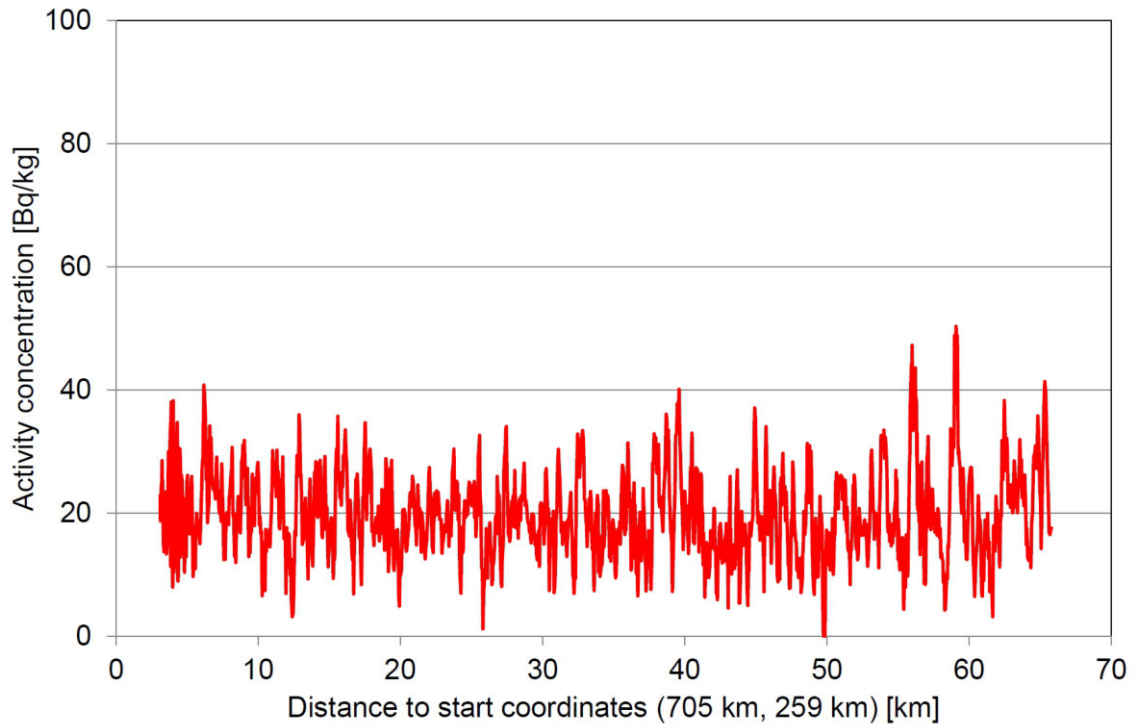
Figure 207: ^{238}U activity concentration along the transversal from Neubrunn to Wartau measured by team CH02. Raw data evaluated with the ARM software.
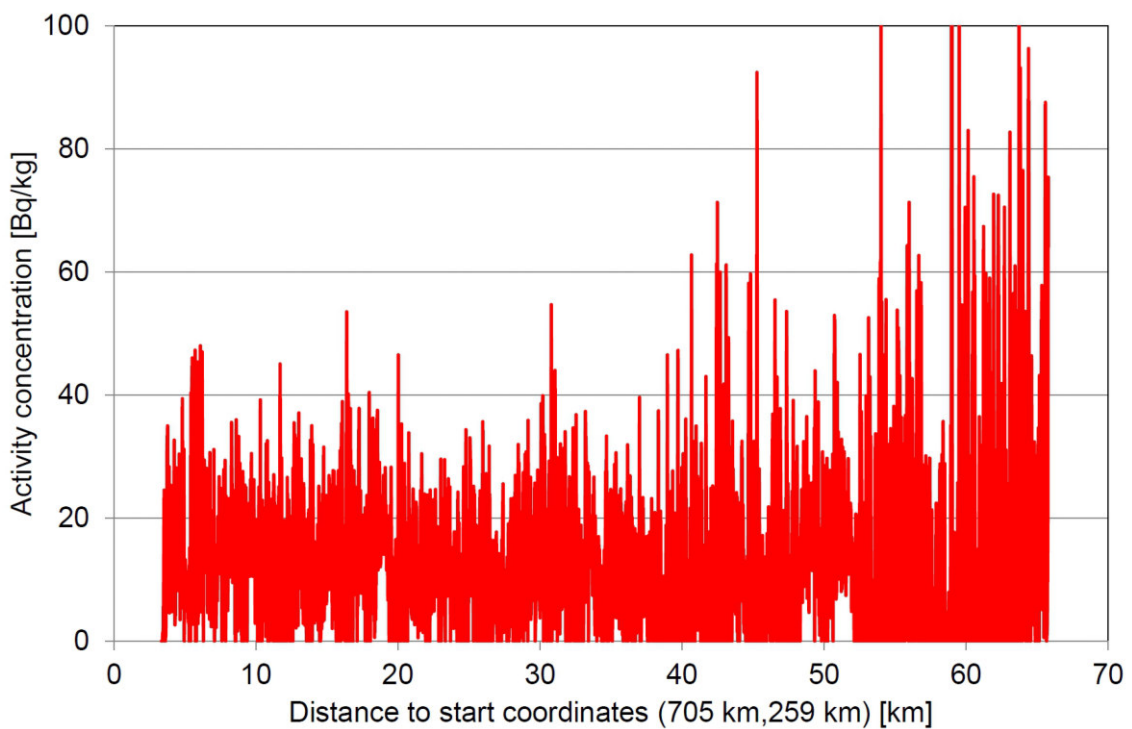
Figure 208: ^{238}U activity concentration along the transversal from Neubrunn to Wartau measured by team CZ01.
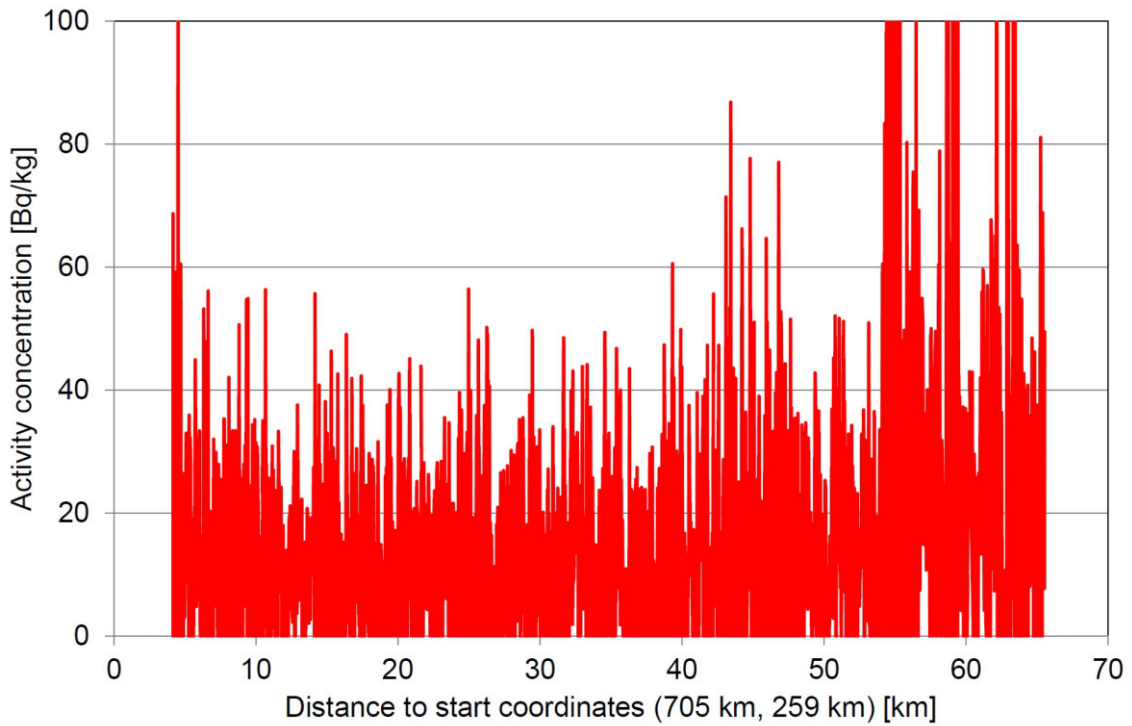
Figure 209: ^{238}U activity concentration along the transversal from Neubrunn to Wartau measured by team FR01.
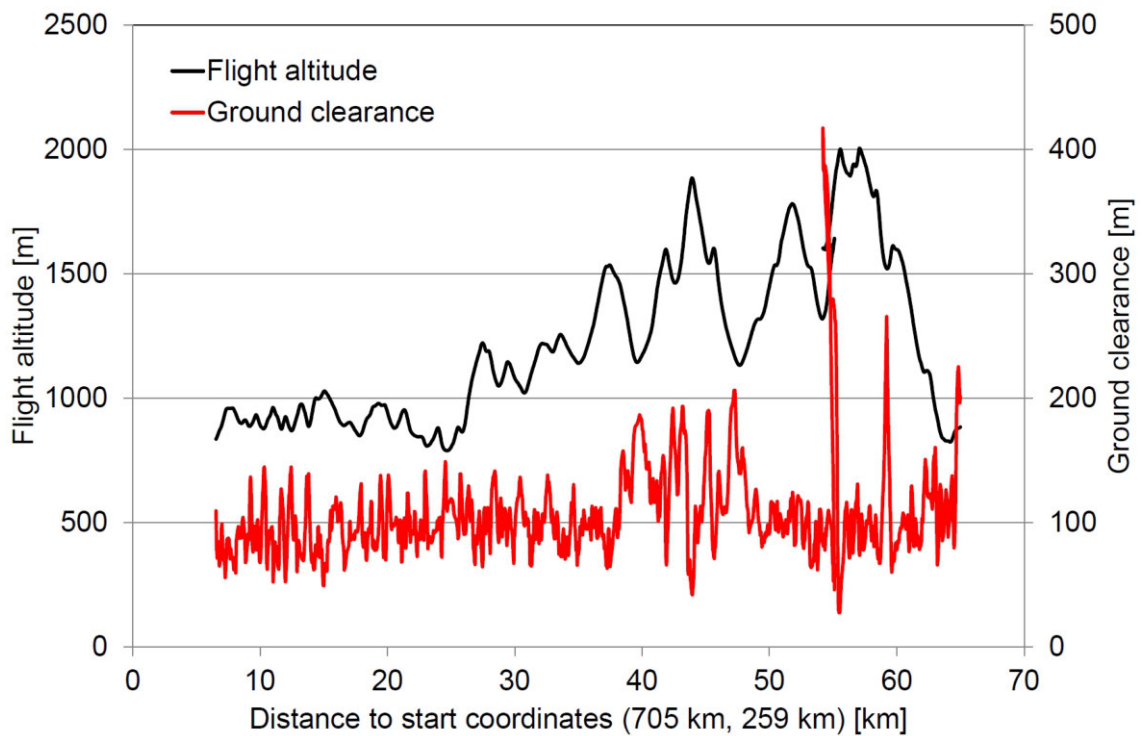
Figure 210: Flight altitude and ground clearance along the transversal from Neubrunn to Wartau measured by team CH01.
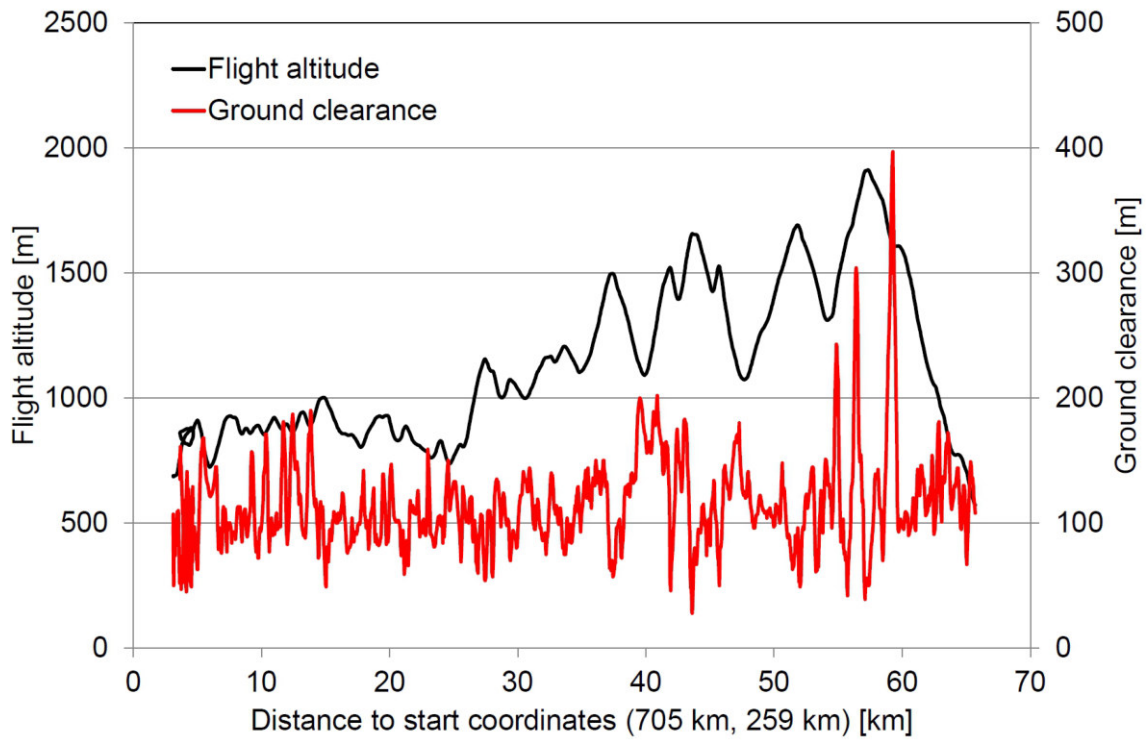
Figure 211: Flight altitude and ground clearance along the transversal from Neubrunn to Wartau measured by team CH02.
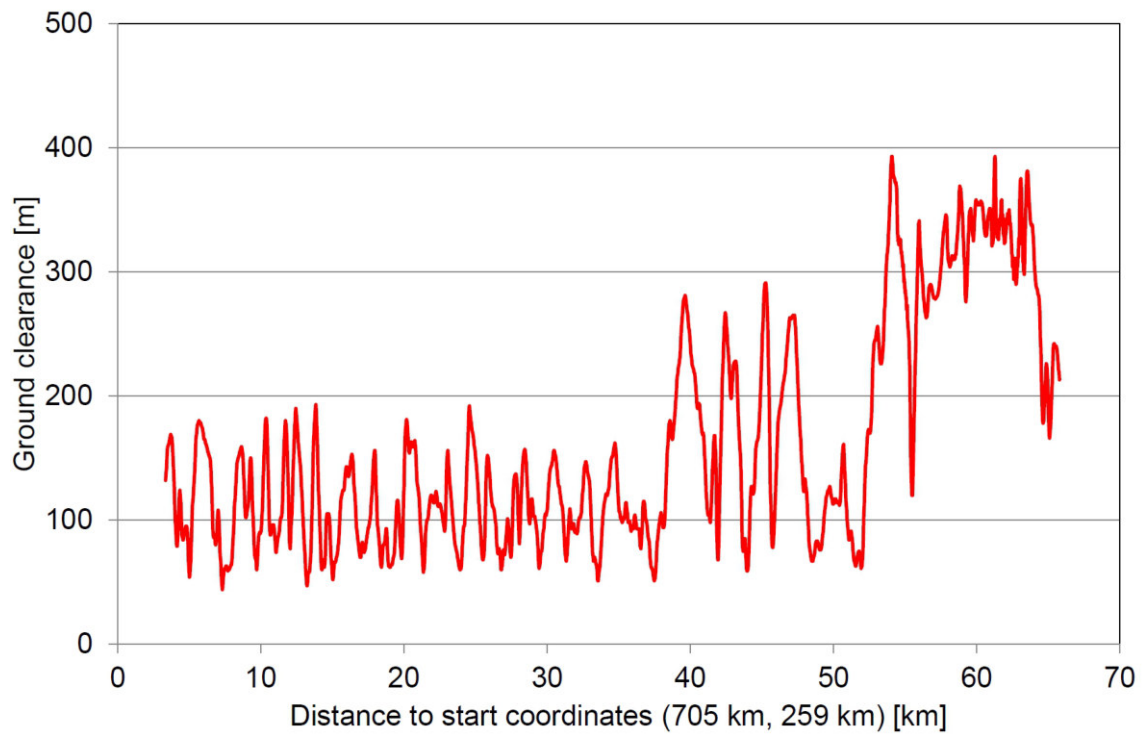
Figure 212: Ground clearance along the transversal from Neubrunn to Wartau measured by team CZ01.
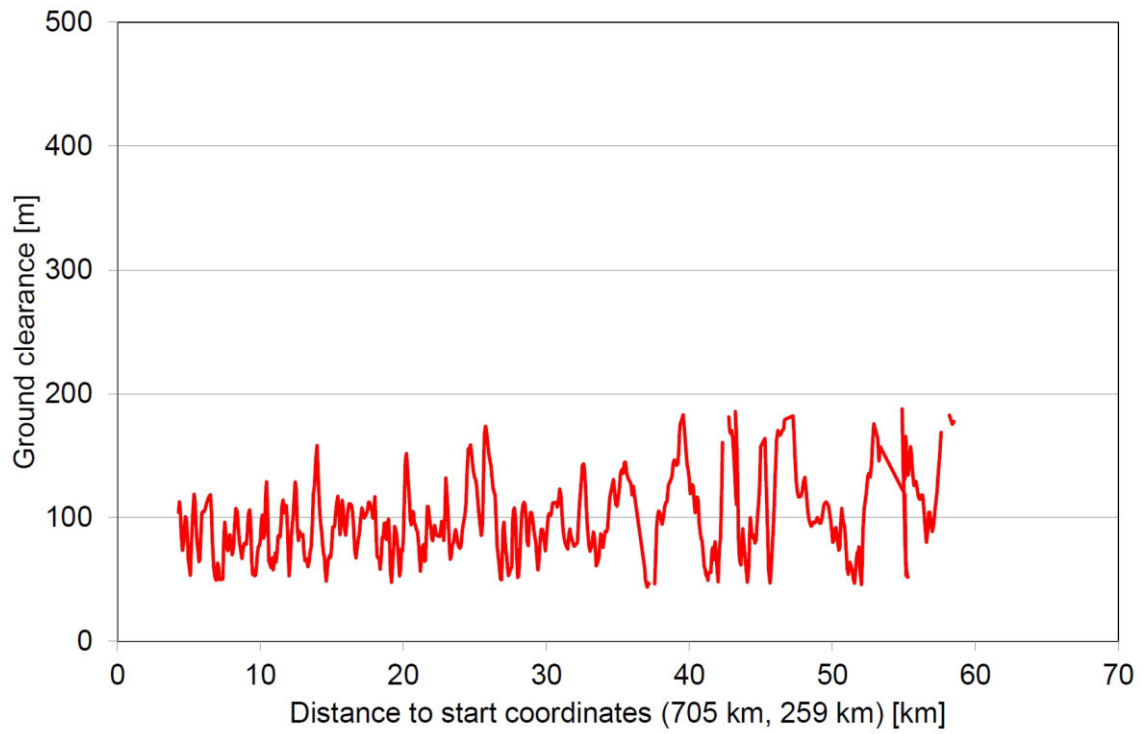
Figure 213: Ground clearance along the transversal from Neubrunn to Wartau measured by team DE01.
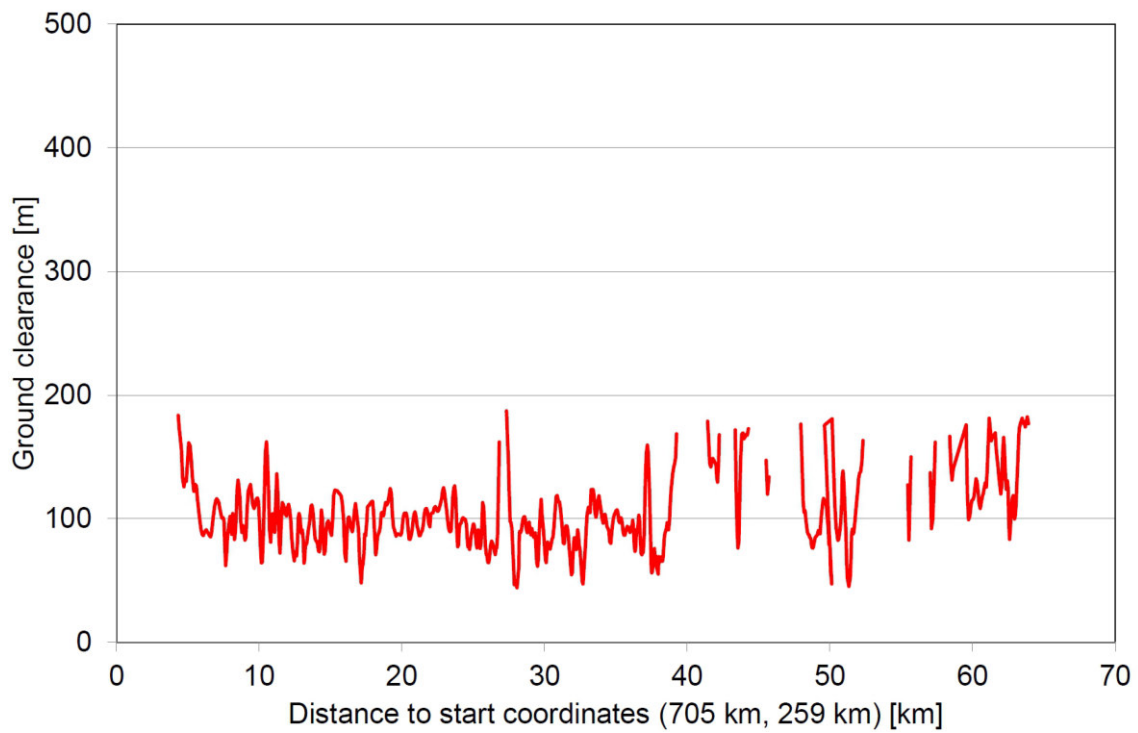
Figure 214: Ground clearance along the transversal from Neubrunn to Wartau measured by team DE02.
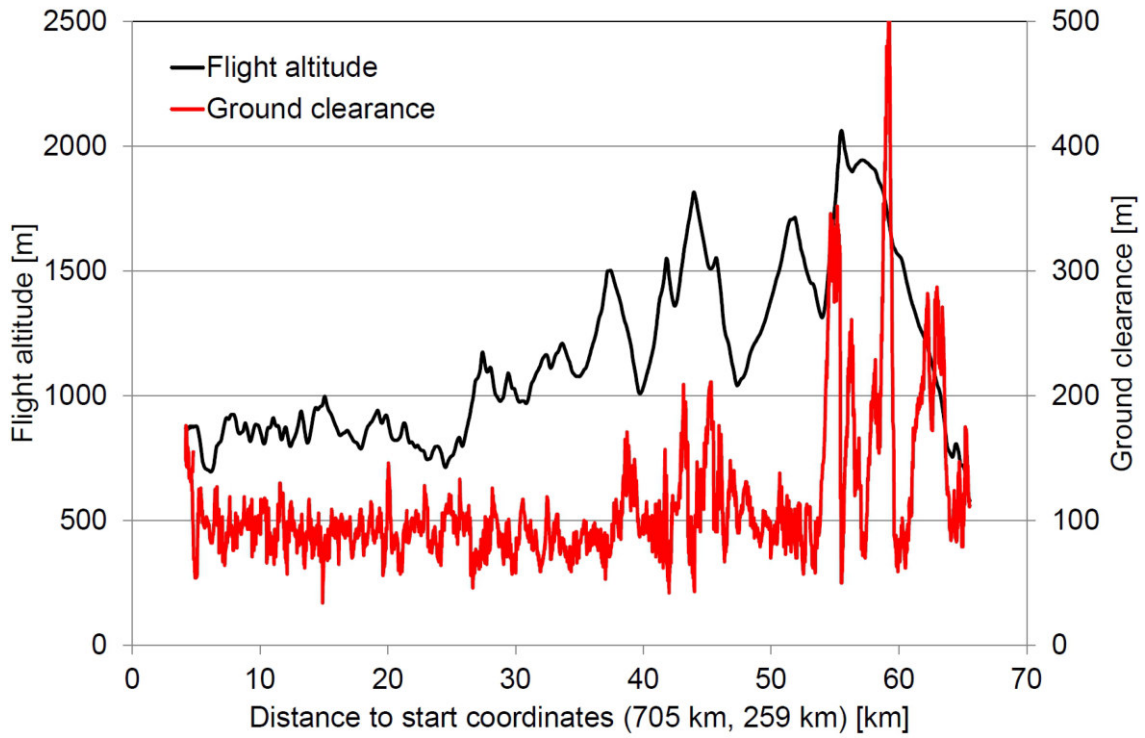
Figure 215: Flight altitude and ground clearance along the transversal from Neubrunn to Wartau measured by team FR01.
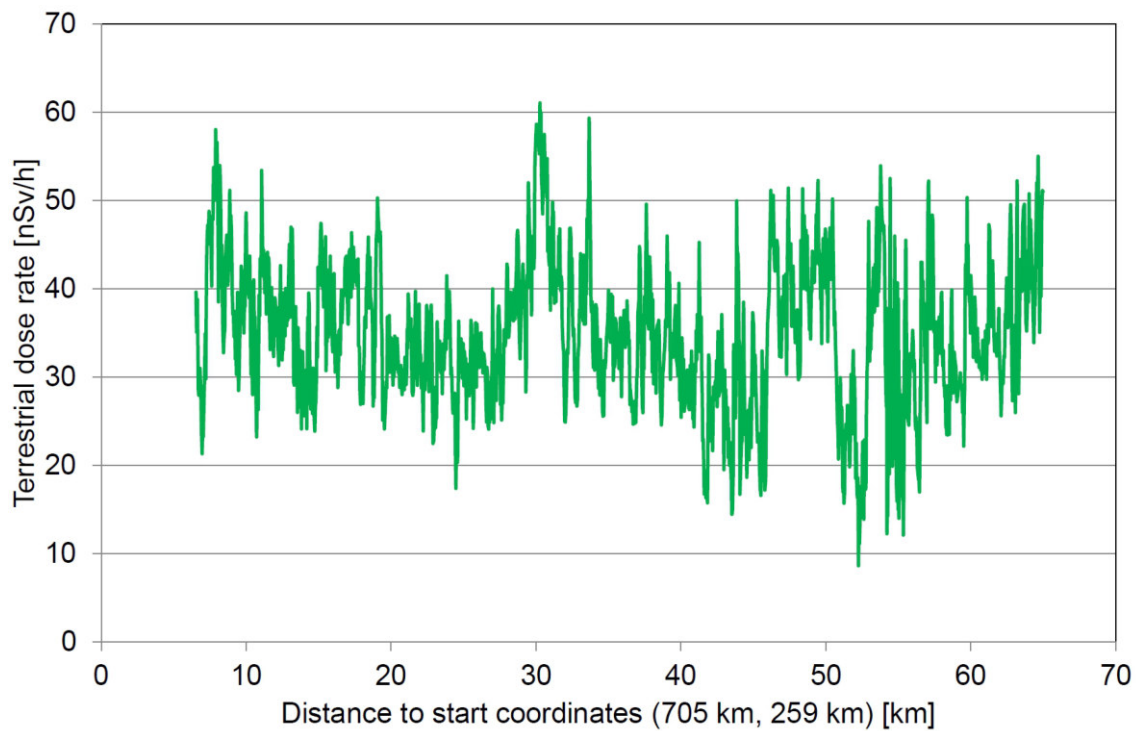
Figure 216: Terrestrial component of the dose rate along the transversal from Neubrunn to Wartau measured by team CH01.

12 Source search and composite mapping

The flight parameters were determined by a command group formed from the heads of the participating measuring teams and the Swiss head pilot. Unfortunately, the apportionment of the search and mapping area to the different teams could not be included. The sections of the measuring area were assigned to the teams in advance by the Swiss head pilot for flight security reasons.

Figure 217 shows the measuring areas assigned to the different teams together with the locations of the sources placed in the area (red asterisks).

The flight lines flown by the different teams are depicted in figure 218. Team DE01 used a spiral pattern and extended the measured area into German territory. Team FR01 had to increase line spacing for some part of the measured area to achive a full covering in the assigned time. For testing the response of their system to a point source, a detour was flown to the source location. Also due to the time restriction, team CZ01 did not cover part of the assigned area.

The geology of the measuring area (figure 219) is dominated by moraines of the Würm glaciation (light green) and weathered loam (brown). The measuring area is bordered in the south east by a region of Tertiary molasse sediments (dark brown). Part of the transversal (section 11) are located in the source search area and are noted as straight red line in figure 219.

Both radioactive sources in the exercise area contained the radionuclide ^{137}Cs and were placed at military training facilities to prevent exposure of the public. The first source with an activity of 19 GBq was placed at the military exercise area in Frauenfeld (coordinate 709950, 270613), located within the area assigned to team DE01. Figure 220 displays an aerial view of the source position at the military exercise area Frauenfeld with the source position marked as green asterisk. The according elevation map (figure221) shows elevation differences less than 15 m in the vicinity of the source position. The second source had a higher activity of 47 GBq and was placed in the military exercise area Herisau (coordinate 740237, 254302). This source was located at the boundary between the areas assigned to teams CZ01 and CH02. The aerial view (figure 222) and the elevation map (figure 223) show a slightly hillier topography compared to the source location at Frauenfeld with maximum elevation differences of about 100 m.
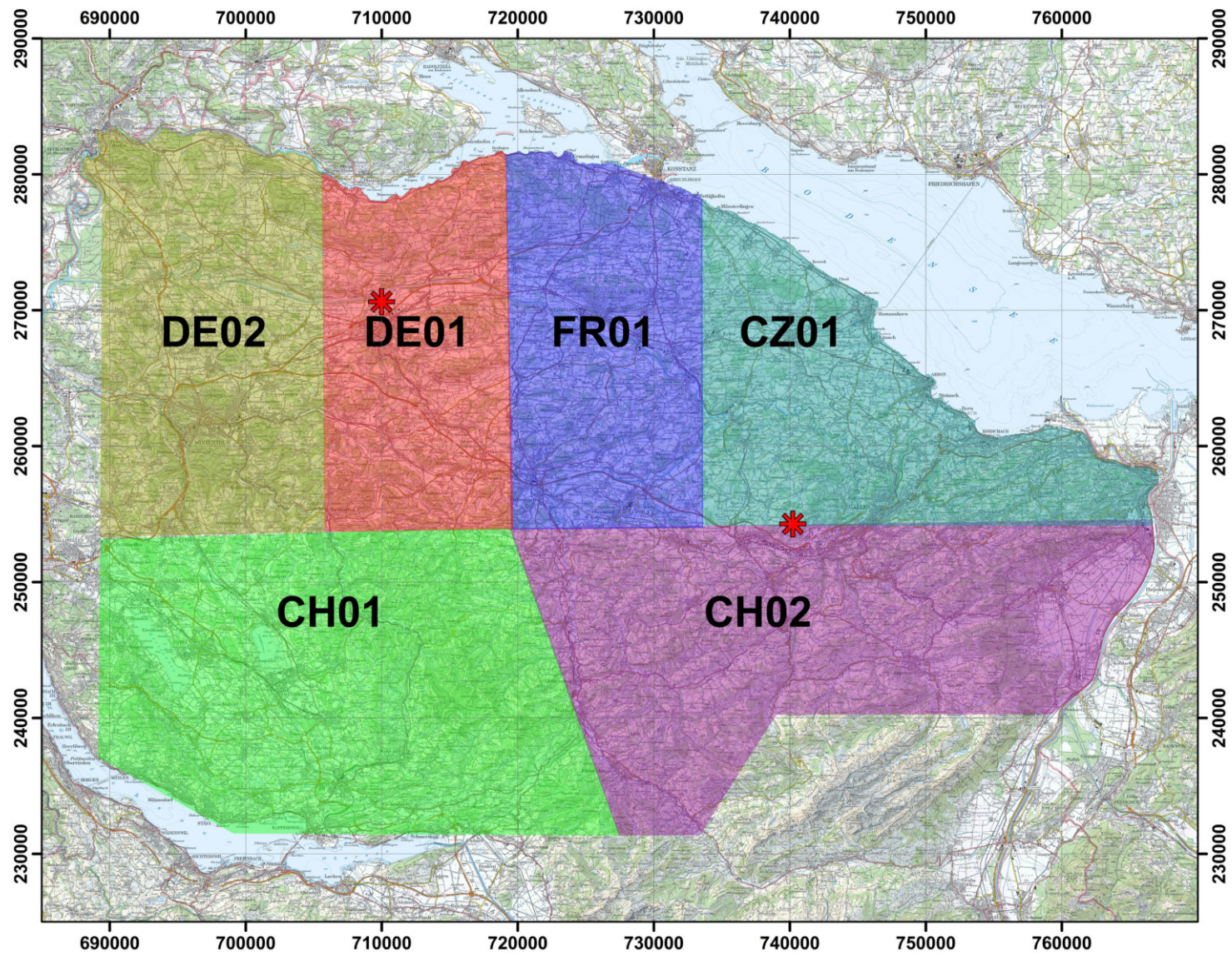
Figure 217: Assigned measuring areas for source search and composite mapping. PK100©2017 swisstopo (JD100042).
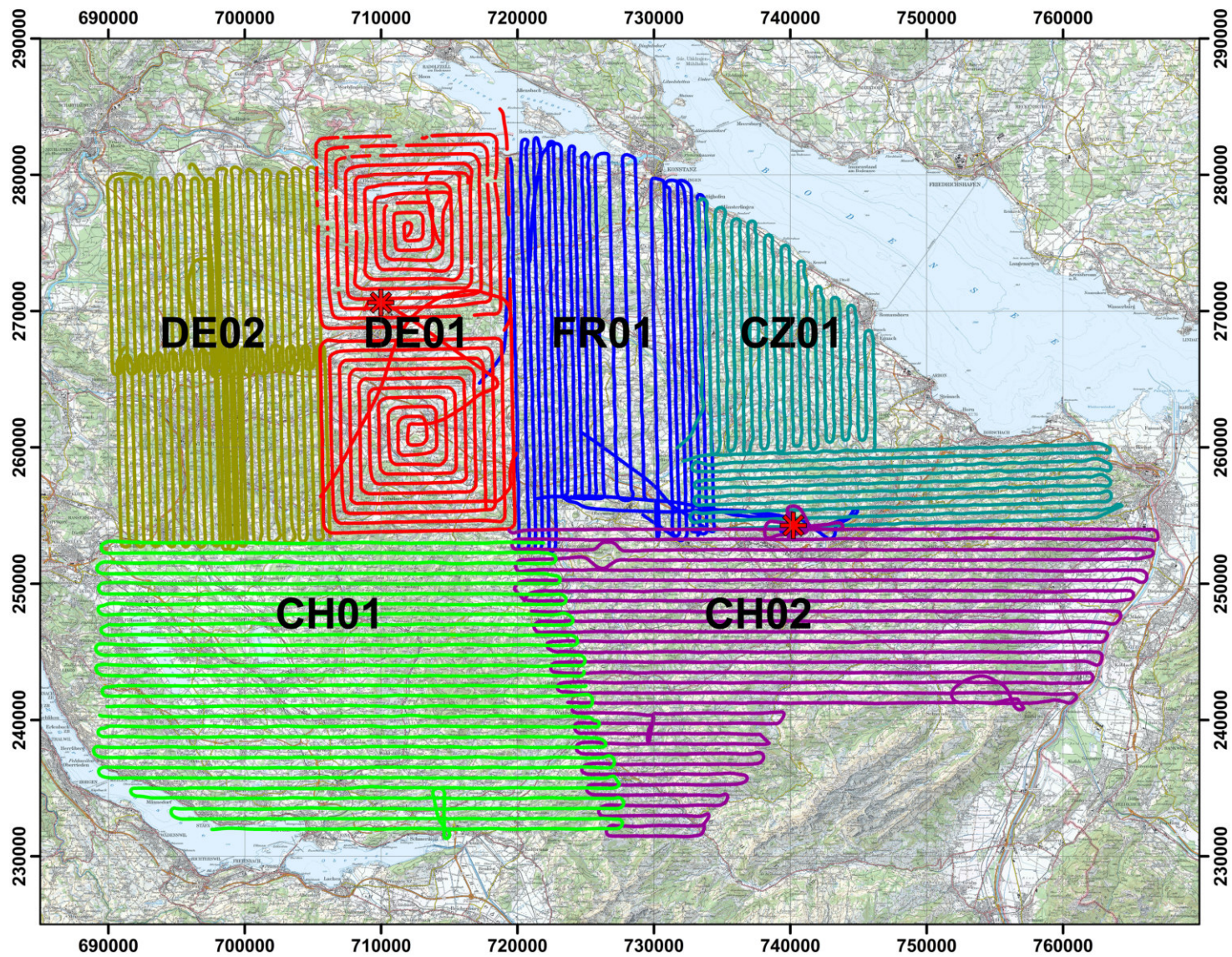
Figure 218: Flight lines of the different teams in the measurement area. PK100©2017 swisstopo (JD100042).
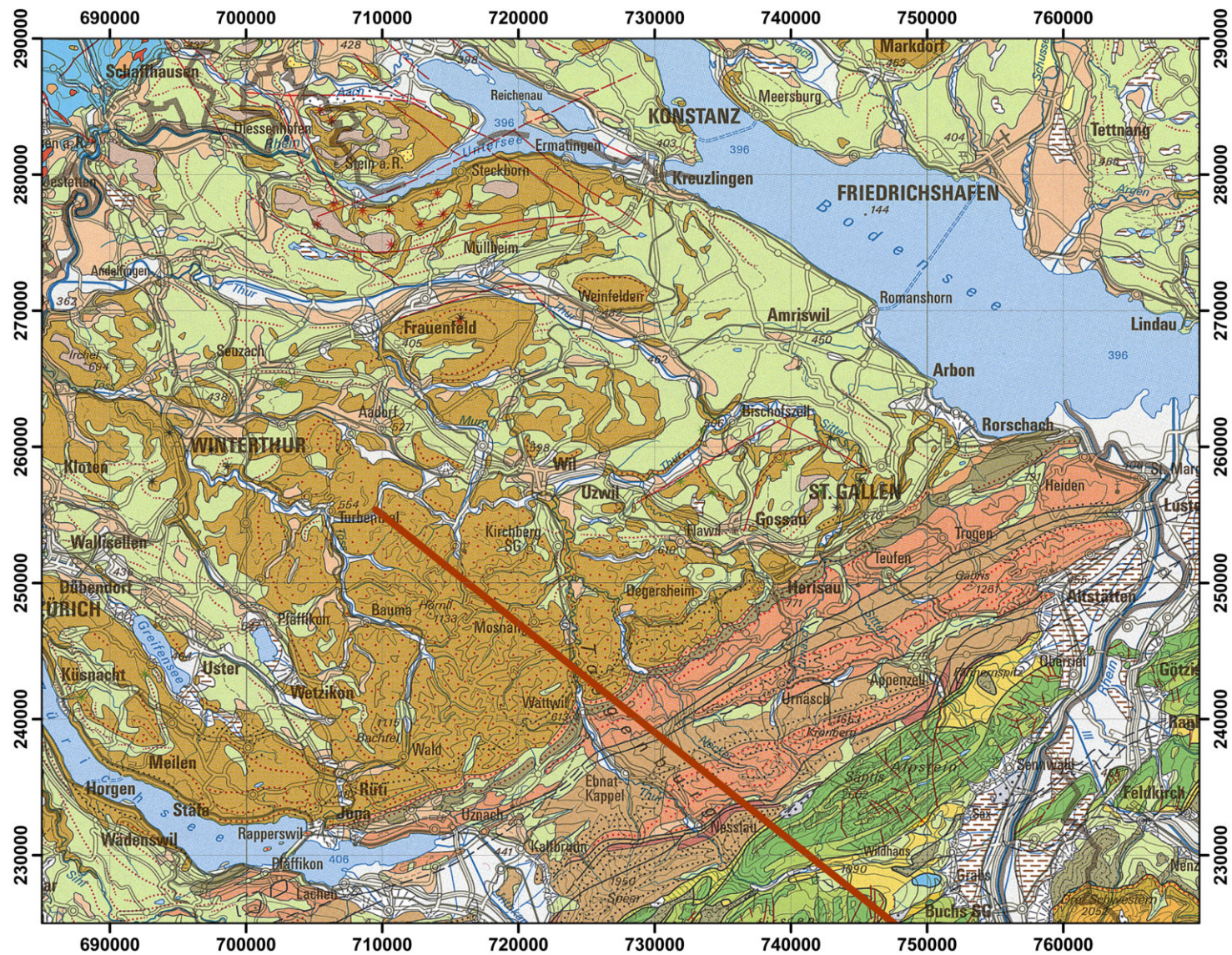
Figure 219: Geology the measurement area. Geologische Karte 1:500000©2017 swisstopo (JD100042).

Figure 220: Arial view of the source location near Frauenfeld. The source position is indicated with a green asterisk. swissimage©2017 swisstopo (JD100042).
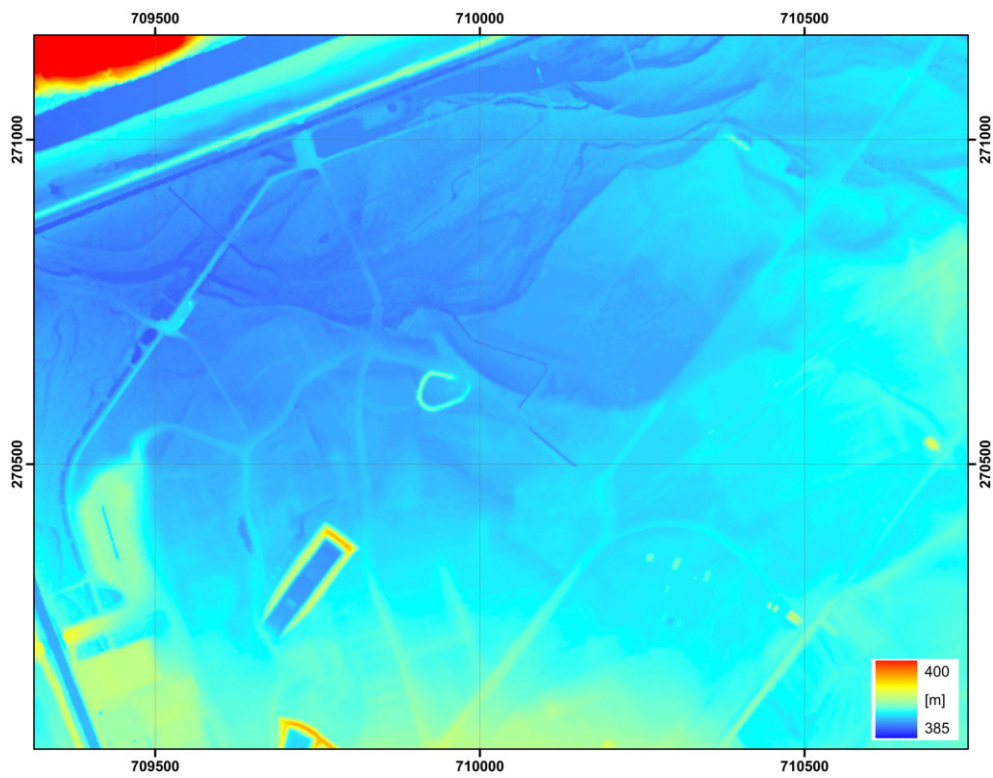
Figure 221: Elevation map of the source location near Frauenfeld. alti3D©2017 swisstopo (JD100042).

Figure 222: Arial view of the source location near Herisau. The source position is indicated with a green asterisk. swissimage©2017 swisstopo (JD100042).
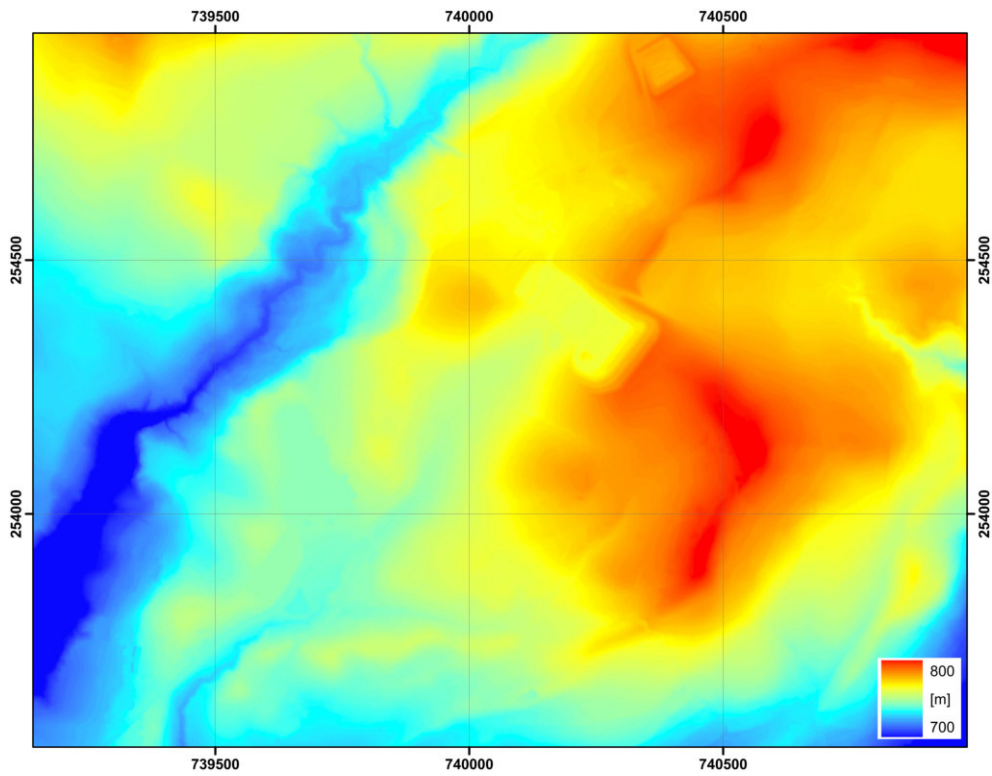
Figure 223: Elevation map of the source location near Herisau. alti3D©2017 swisstopo (JD100042).

12.1 Results

12.1.1 Source search

Teams DE02, FR01 and CH01 had no radioactive sources placed in the assigned measurement areas. Team CZ01 had a clear identification of the ^{137}Cs source from the display of the waterfall spectrum in the helicopter (figure 224). The source was found after 280 seconds flight on the first flight line of team CZ01. Due to a mistake in on-board communication the source location immediately reported to the ground centre was the actual coordinate of the helicopter at the time of report (yellow star in figure 226). This communication error was detected during the off-line data examination and a revised source position (green star in figure 226) was reported. Figure 225 shows the signal peaks of the source in the data record of team CZ01. In a further detailed data analysis performed after the exercise, a time lag of two seconds between GPS and spectrometric data was detected (figure 227).

The measuring system RLL used by team CH02 gave an automated alarm at the source position together with the identification of the radionuclide ^{137}Cs. Figure 228 shows a map with estimated maximum ^{137}Cs point source activities which clearly indicates the position of the placed source near Herisau. After the position of the source was reported by teams CH02 and CZ01, team FR01 flew a detour to obtain a measuring signal from the point source.

Team DE01 had less luck in placing their flight lines as the source near Frauenfeld was positioned right between two flight lines, yielding a minimum distance of 300 m to the source. Combined with the smaller source activity of 19 GBq, the source was not detected during the flight. A detailed post-processing of the data was able to locate and identify the source. Table 35 lists the source positions and estimated source activity reported by the different teams together with the time of reporting for both sources placed in the exercise area.
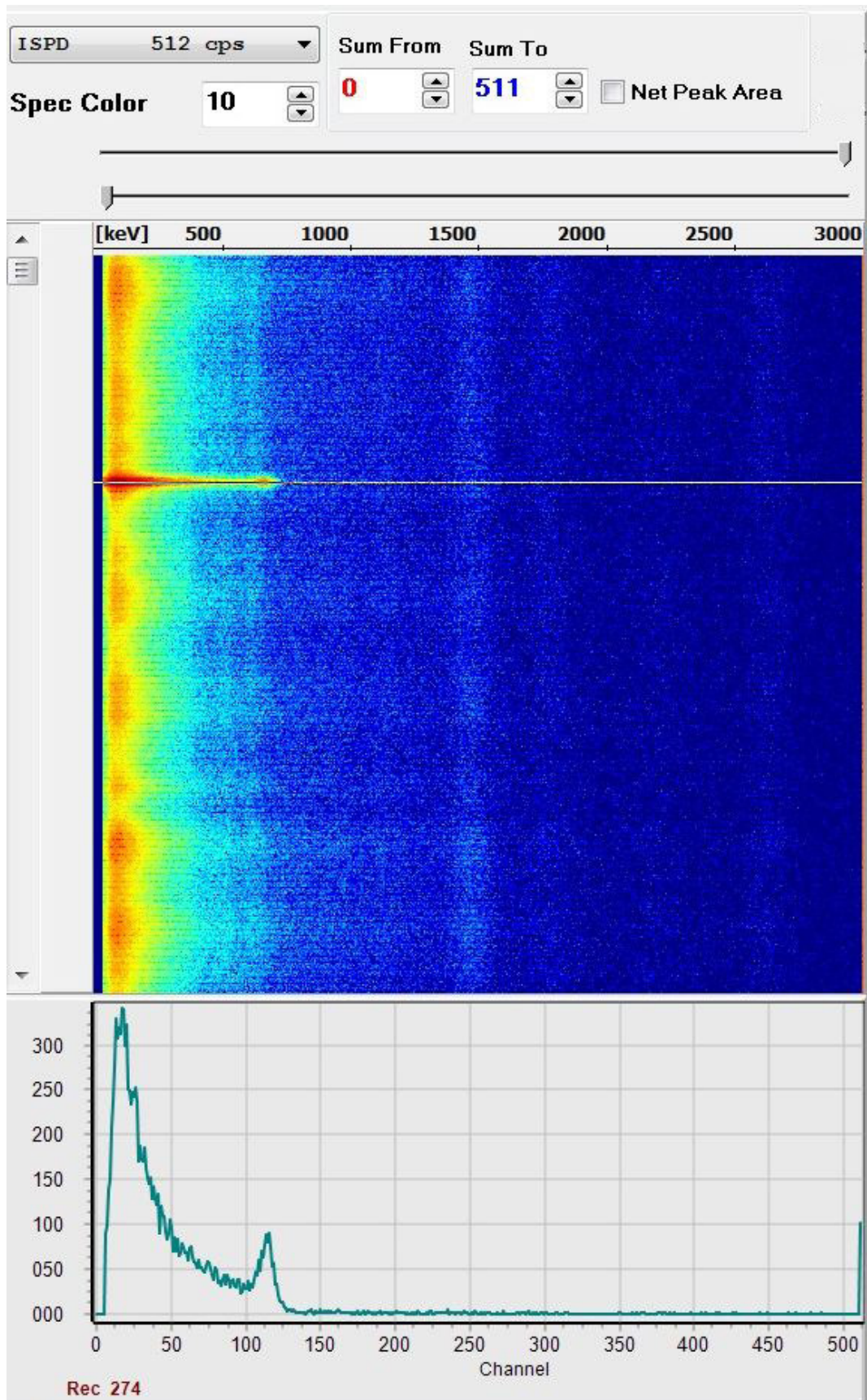
Figure 224: Waterfall spectrum of team CZ01 showing the signal of the ^{137}Cs-source.
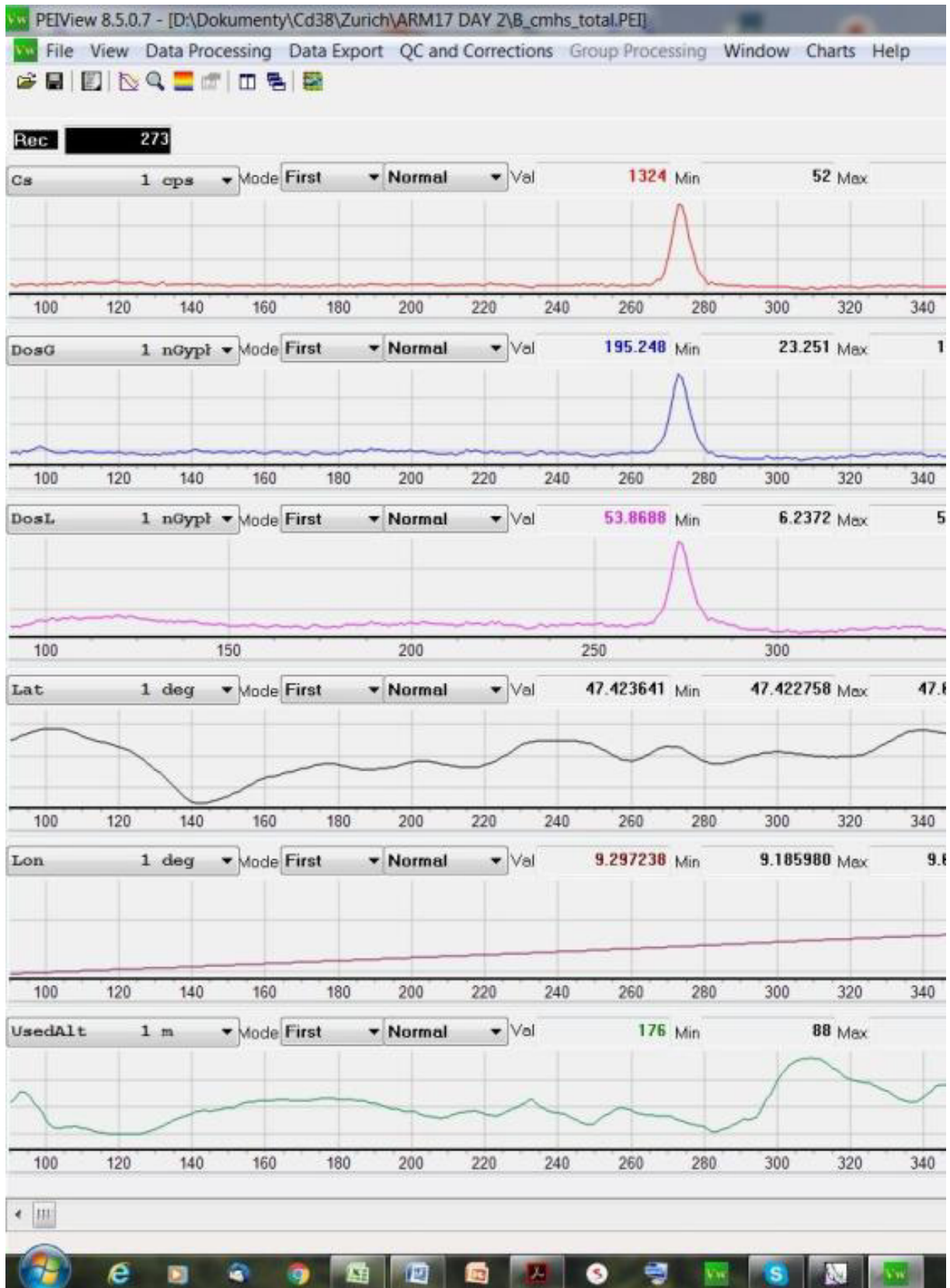
Figure 225: Data record of team CZ01 showing a clear indication of the source.
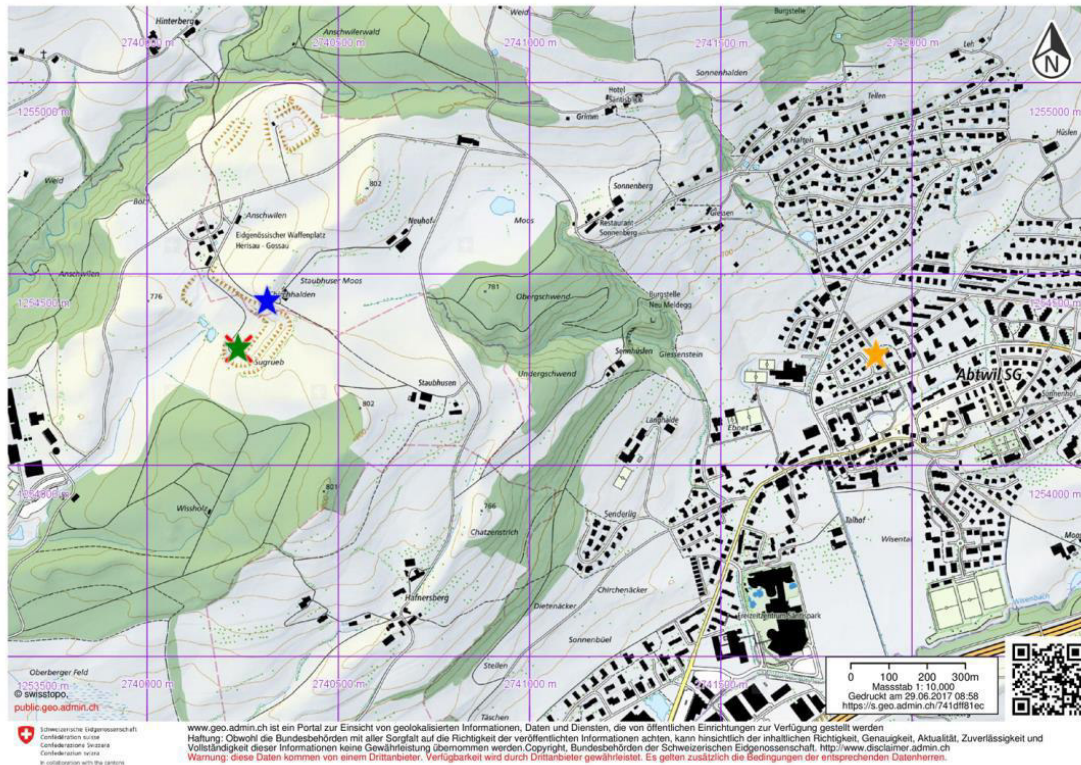
Figure 226: Source positions reported by team CZ01.The red x represents the correct source position, the yellow star is the initially reported position, the blue star is the reported position later during the exercise and the green star the source position reported after off-line data analysis. PK100©2017 swisstopo (JD100042)
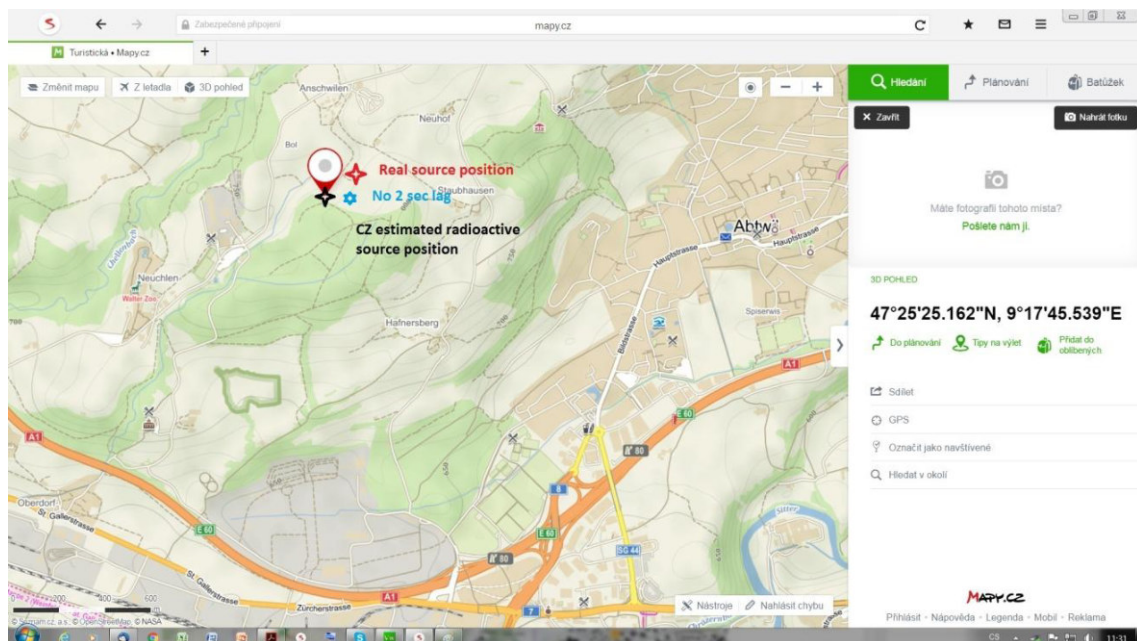
Figure 227: Source position deviation due to GPS time lag.The red cross represents the correct source position, the black cross is the corrected source position reported during the exercise and the cyan asterisk the source position reported in a final analysis after the exercise. PK100©2017 swisstopo (JD100042)

Kompetenzzentrum ABC-KAMIR

Radiometrie System

Mapping		Edition Date :	27.06.2017 17:39:23
Measurement : Cs-137 Pct. CT		**Grid size :**	200m
Type : Maximum			
Extrapolation : 3			
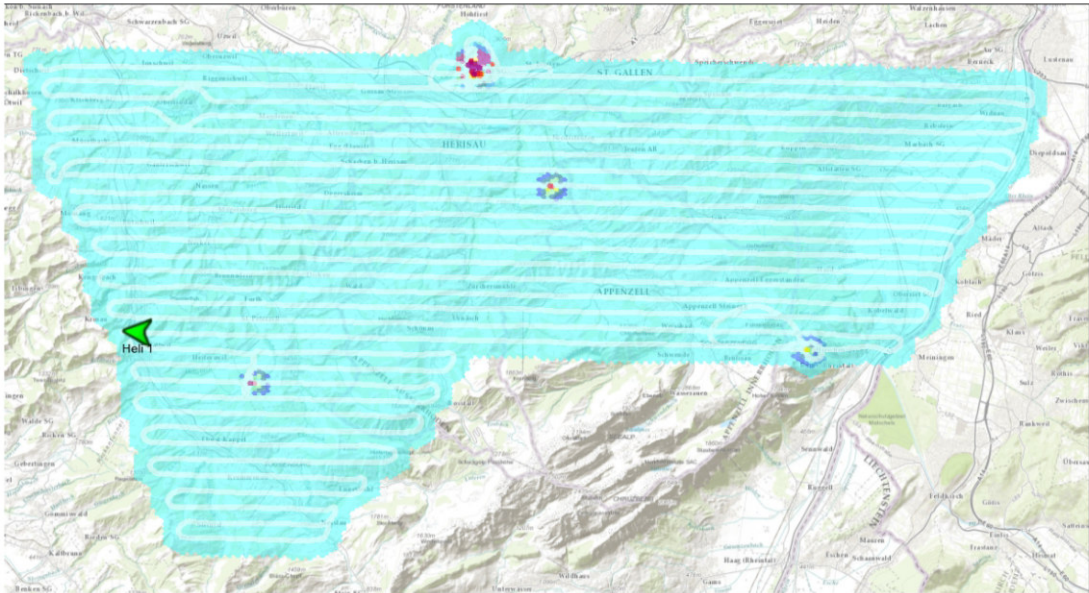
Cs-137 Pct. CT(MBq)

Invalid	1	5	10	20	40	60	80	100	125	150	200	250	300	400	500	1000	5000

Figure 228: Map of the maximum ^{137}Cs point source activity estimated by the RLL software of team CH02

Table 35: Reported locations of the placed sources.

Team	Time of report [MESZ]	Coordinates [m]	Activity [GBq]
Source Herisau; 49 GBq; 740237 m, 254302 m			
CH02	08:40	740234, 254306	39
CZ01	09:40	741902, 254291	-
FR01	10:15	740310, 254431	25
Source Frauenfeld; 19 GBq; 709950 m, 270613 m			
DE02	15:30	709987, 270637	20 - 24

12.1.2 Composite mapping without corrections

Additional to the search for radioactive sources in a large area, composite maps of dose rate and activity distributions of natural radionuclides were part of the exercise. Figure 229 shows a composite map of the dose rates reported of the measurement teams at the end of the exercise. The dose rate increase due to the source located near Herisau can be seen clearly in the map, whereas the source near Frauenfeld with less than half of the activity shows a dose rate increase hardly distinguishable from the background.

The areas with overlapping dose rate data can be clearly identified due to the reduced transparency of the map layers. Additionally, team CZ01 reported higher values compared to the other teams, which can be observed clearly in the map. Further differences between the results of the different teams can be observed in the maps of the natural radionuclides ^{40}K and ^{232}Th (Figs. 230 and 231).

The described differences observed between the different teams would not interfere with a composite mapping in the case of a real emergency. In a real emergency, decisions would be made based on the order of magnitude of the detected activity. The observed deviations can be considered to be more of an academic interest and an indication of possible fields for improvement.
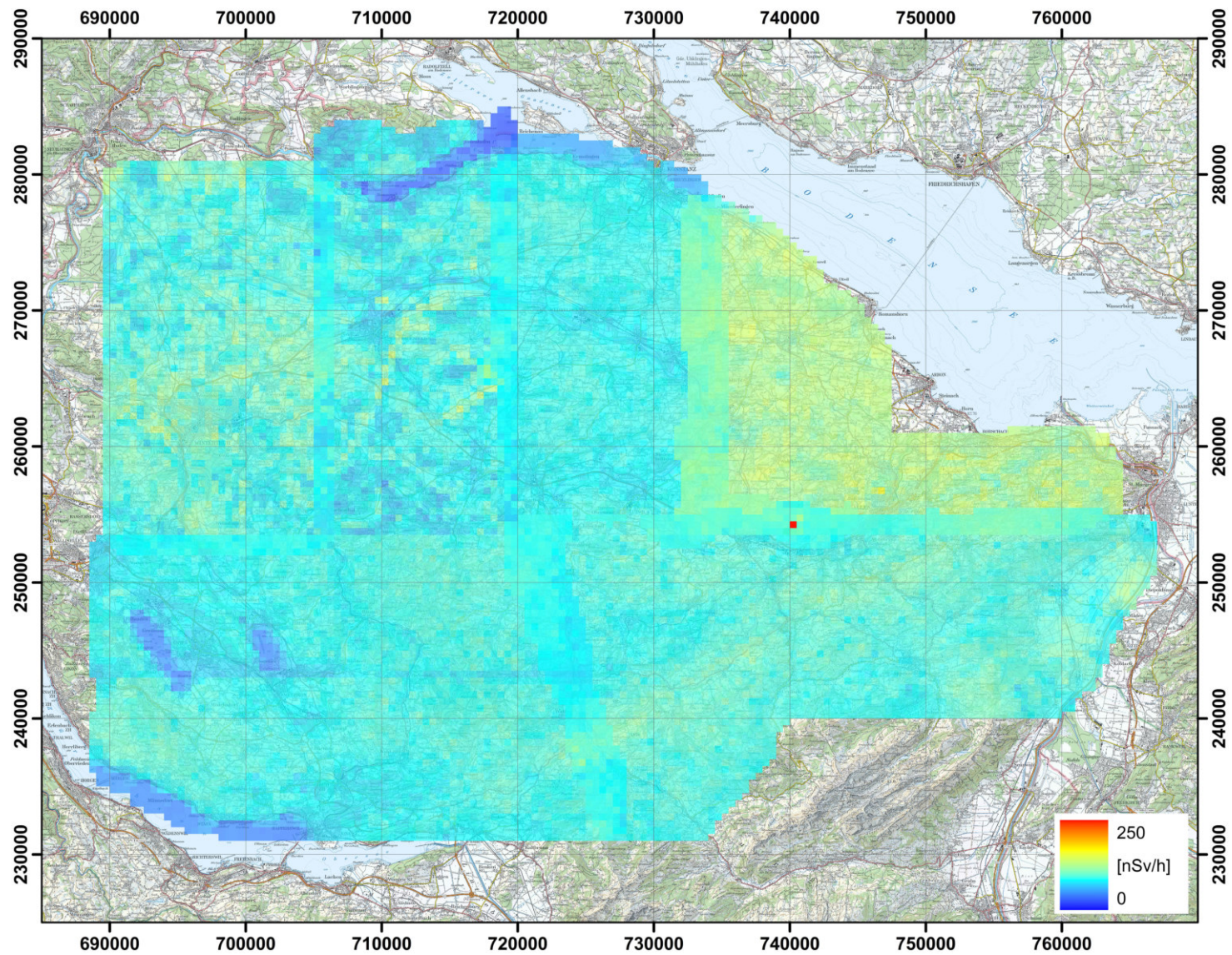
Figure 229: Dose rate in the area between Lake Zurich and Lake Constance. PK100©2017 swisstopo (JD100042).
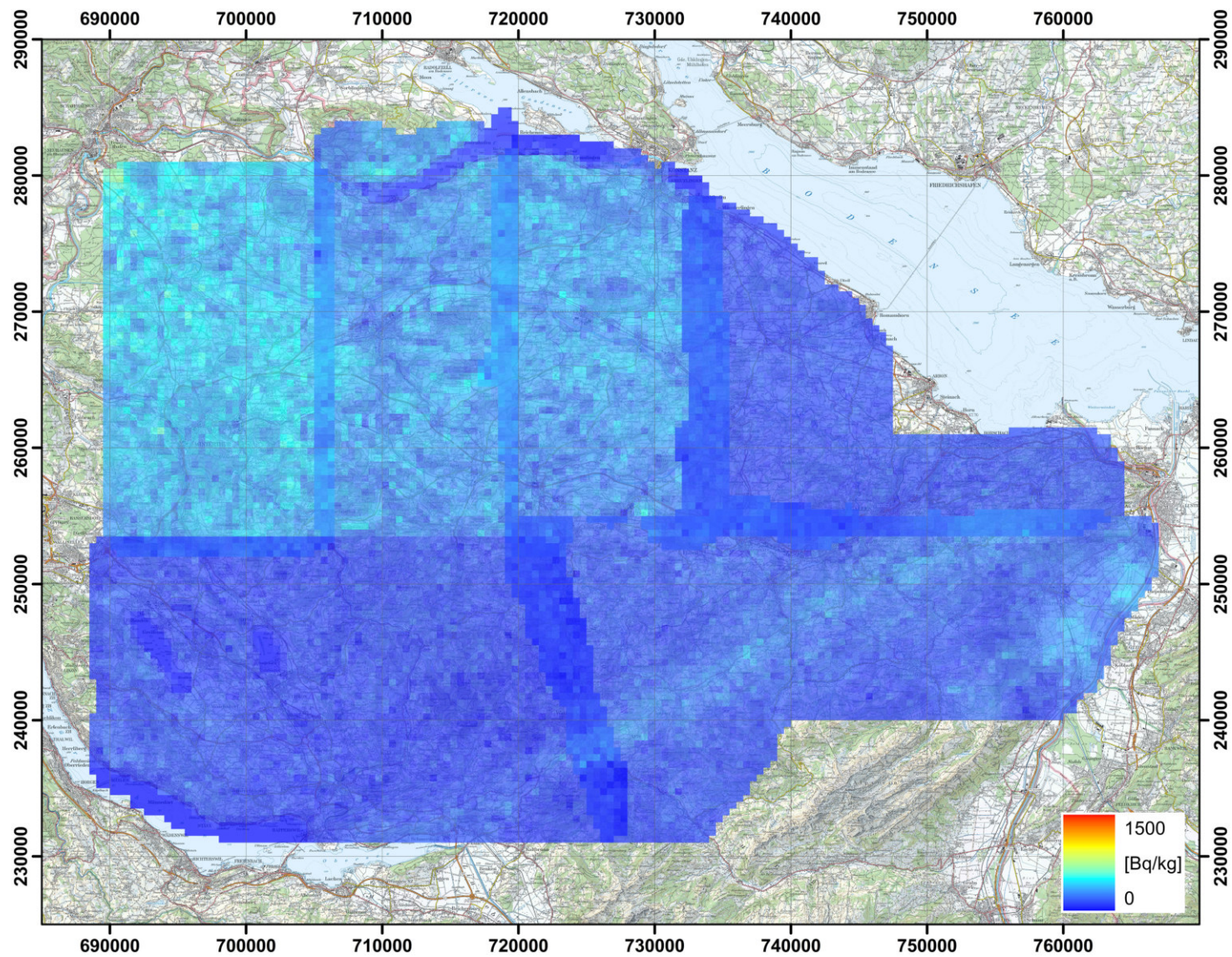
Figure 230: ^{40}K activity concentration in the area between Lake Zurich and Lake Constance. PK100©2017 swisstopo (JD100042).
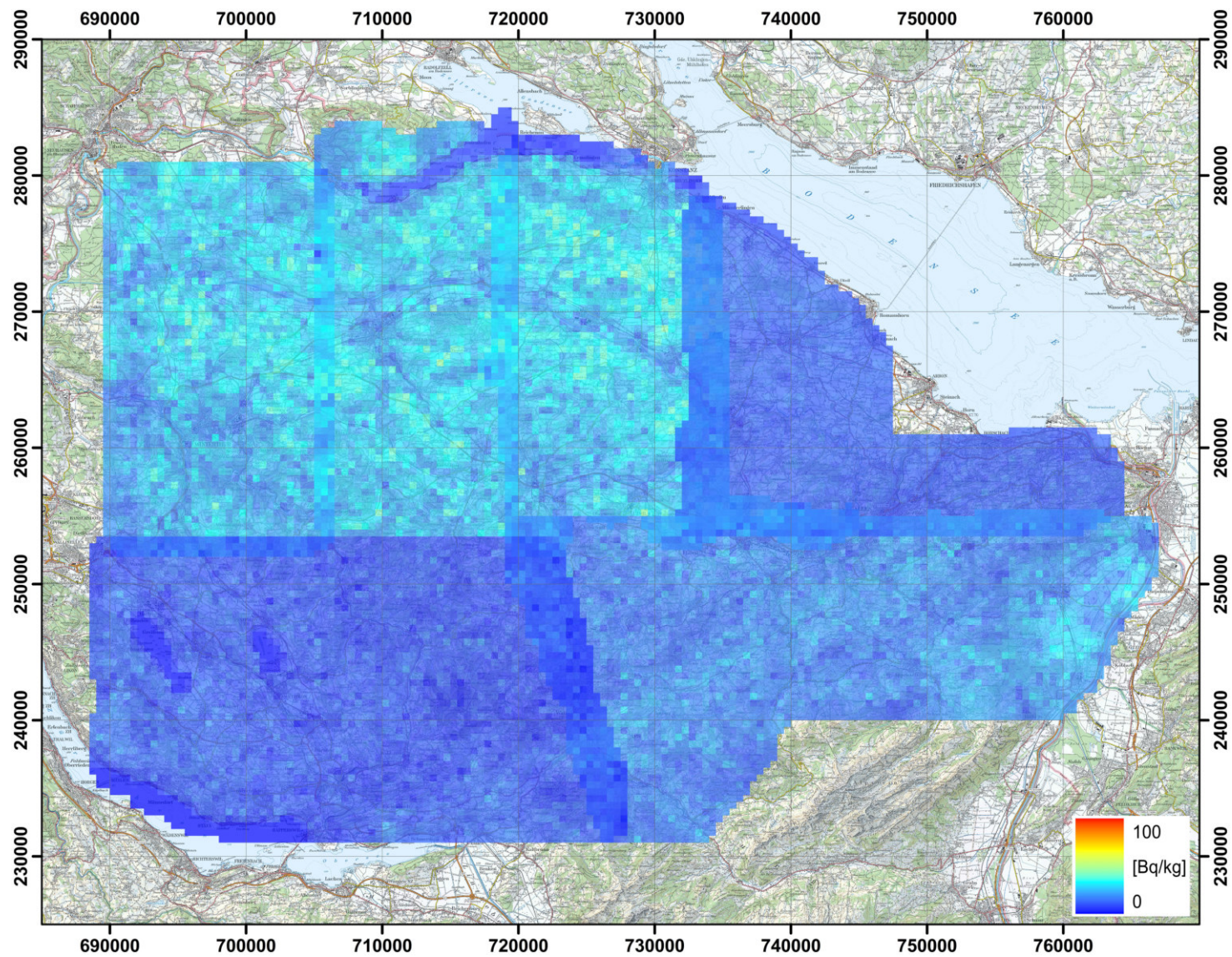
Figure 231: ^{232}Th activity concentration in the area between Lake Zurich and Lake Constance. PK100©2017 swisstopo (JD100042).

12.1.3 Composite mapping with corrections

An altitude profile (section 8) and two reference areas (sections 9 and 10) were added to the exercise to provide additional data for a performance analysis of the measuring systems. The application of corrections derived from these measurements should help to reduce the observed deviations. Teams DE01 and DE02 made corrections based on the altitude profile (section 8) already during the exercise. The elimination of data points below the decision limit during post-processing results leads to gaps in the maps, especially visible in the map of ^{238}U activity concentration (figure 235). Team CH02 did not apply any corrections based on the results of the reference areas. The results calculated from the raw data measured by team CH02 with the ARM software (section3.1) were used instead of results corrected by team CH02. Teams CZ01 and FR01 performed post-processing of the measured data using alternative algorithms without corrections based on the reference areas. The results in the corrected maps of team CH01 include the correction for the faulty detector crystal (section 6.1). Additionally, team CH01 used the results of the reference areas to re-evaluate cosmic stripping, system background (section 8) and calibration factor (section 9) both for the ARM-detector (section 2.1) and the RLL-detector used by team CH02 (section 2.2).

The raster data were merged in the overlapping parts of the measurements for the display of maps after corrections. Figure 232 shows the dose rate after corrections were applied. The derived dose rates of the Swiss and Czech teams yield a consistent map after corrections were applied. The measurement areas of the German and French teams are still identifiable. (figure 229). The differences between measuring teams are reduced in the corrected maps of ^{40}K (figure 233) and ^{232}Th (figure 234) activity concentrations. Elevated potassium concentrations over the tertiary molasse sediments (figure 219) are more visible in the map of the corrected values (figure 233).

The map of the uranium activity concentration (figure 235) shows besides differences between measuring teams also structures reflecting the flight pattern of the individual teams. This "banding" indicates airborne radon progeny interfering with the measurement of ground activity.
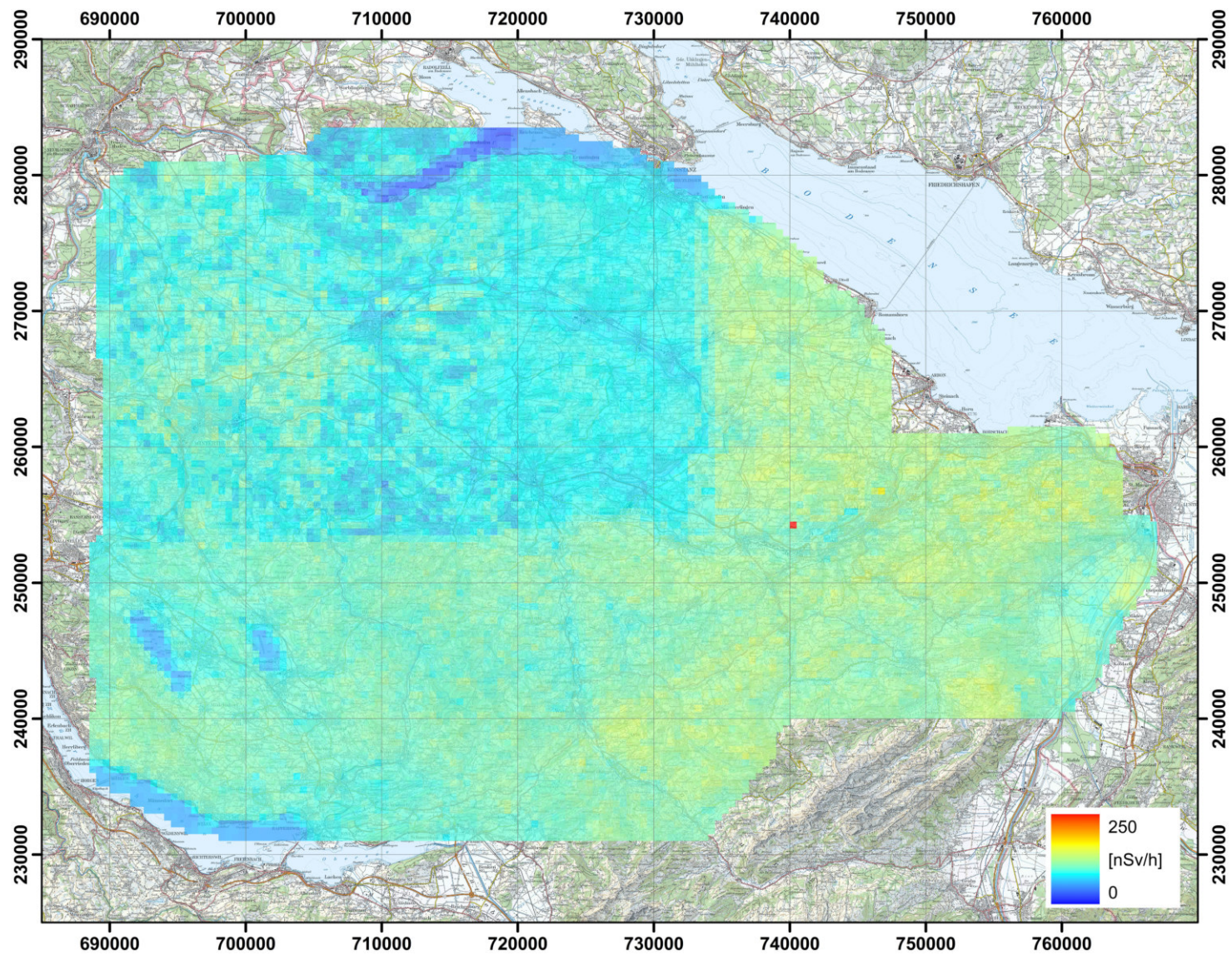
Figure 232: Dose rate in the area between Lake Zurich and Lake Constance after corrections. PK100©2017 swisstopo (JD100042).
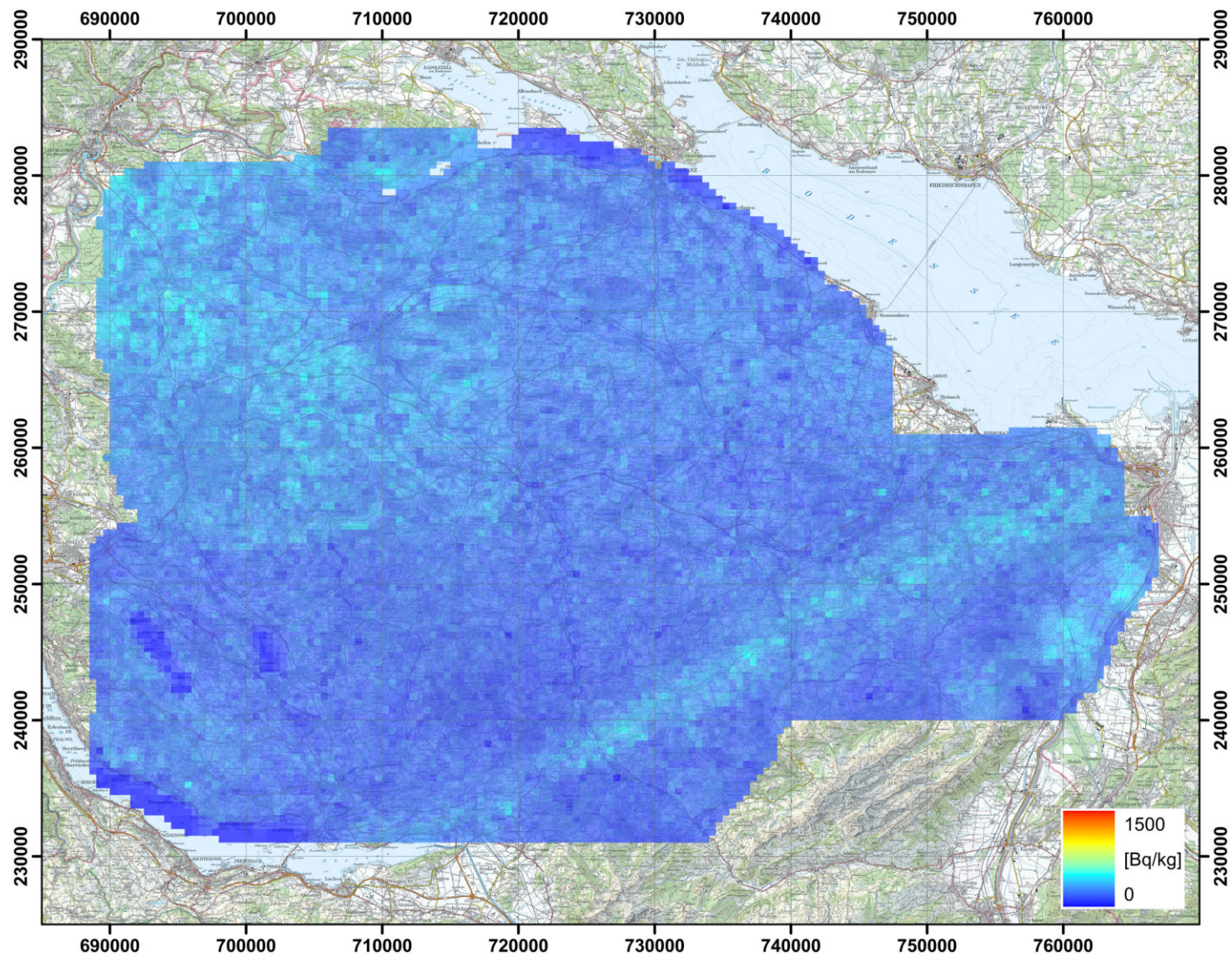
Figure 233: ^{40}K activity concentration in the area between Lake Zurich and Lake Constance after corrections. PK100©2017 swisstopo (JD100042).
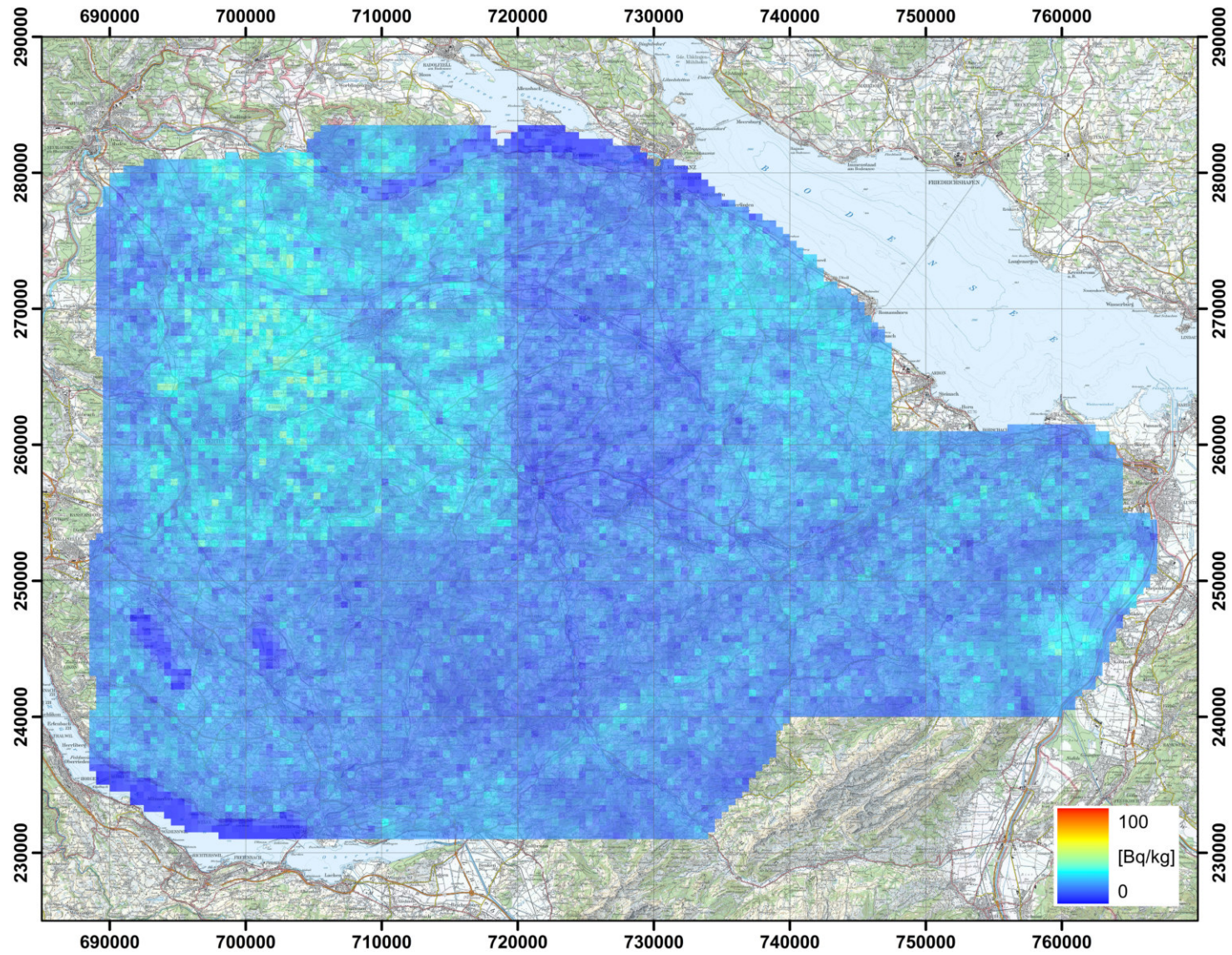
Figure 234: ^{232}Th activity concentration in the area between Lake Zurich and Lake Constance after corrections. PK100©2017 swisstopo (JD100042).
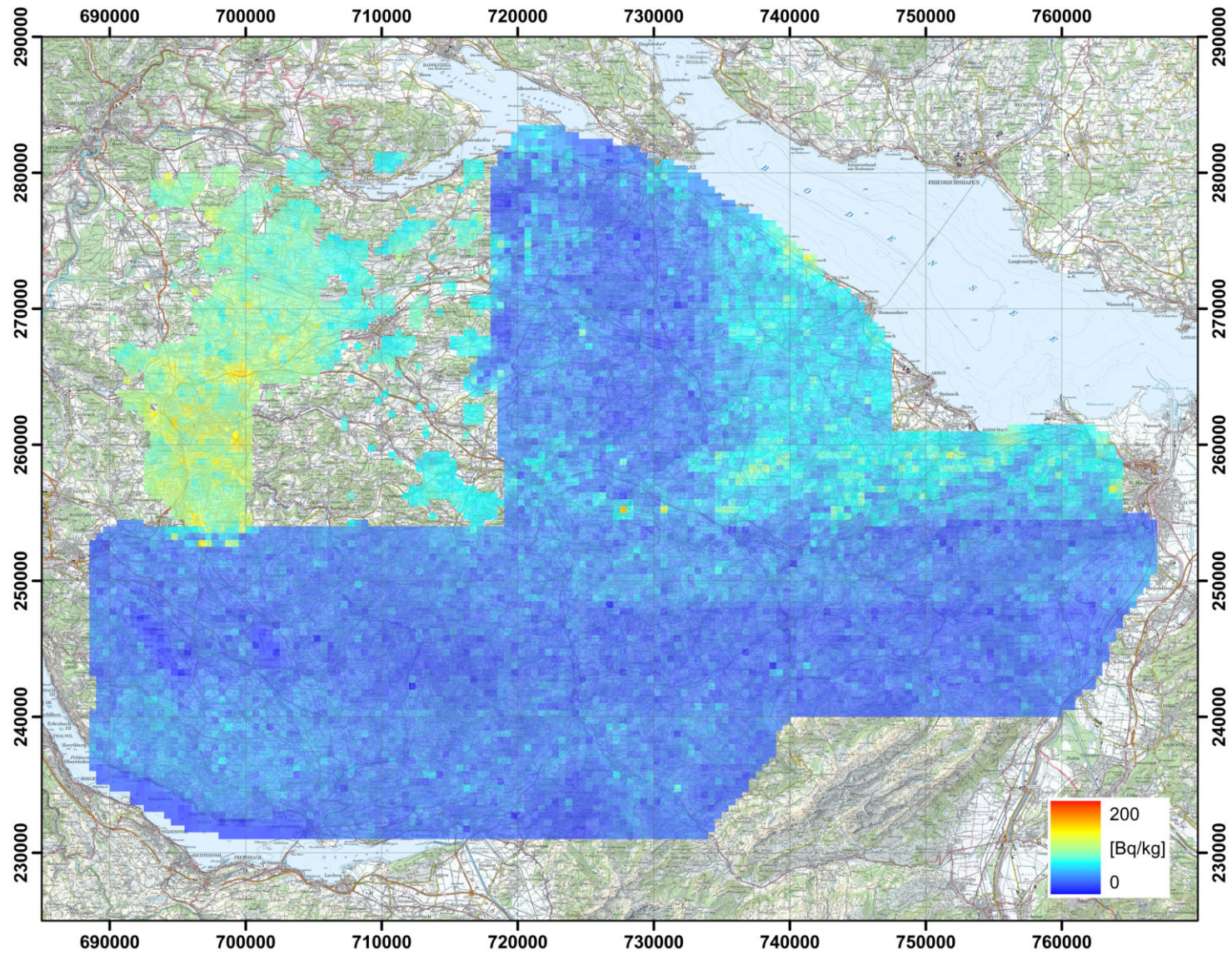
Figure 235: ^{238}U activity concentration in the area between Lake Zurich and Lake Constance after corrections. PK100©2017 swisstopo (JD100042).

13 Conclusions

The recurrent inspection of the vicinity of Swiss nuclear power plants Gösgen and Mühleberg performed prior to the international part of the exercise showed no artificial radionuclides outside the plant premises.

The international intercomparison exercise ARM17 showed clearly the merits of cooperation between measuring teams of different countries. The exercise scenario of a large scale source search represented a realistic case in which international help will be inevitable.

The specifications of the source search of a large area to be searched in a limited time demanded the design of the search strategy prior to the measuring flights, taking into account the individual performance of the used measuring systems and aircraft. The activity of a hidden source detectable in a large area search can not be equalled to the detection limits of the measuring systems. The limiting factor is the estimated maximum distance of the nearest flight line to the hidden source.

Using the measured data in the source search area for the generation of composite radiological maps indicated differences in the results of the different teams. These differences ranging to a maximum of fifty percent were visible, but not of a magnitude where decisions based on the measuring results in a real emergency would be influenced. A detailed analysis of measurements over reference areas was able to improve the results, when applied. A major defect of the detector used by the host team, which was not identified with the standard data processing during the exercise, showed the importance of an extensive post-analysis of the measured data. Unfortunately, an in-depth post-processing of the acquired data was not possible to some of the participants due to lack of man-power. A possible solution to this limitation could be the inclusion of external partners. As airborne gamma-spectrometry systems can be used as valuable research tools, a collaboration with universities or research institutions could be of mutual benefit.

The data exchange between participants based on the ERS-format performed well, but with some room for improvements, especially concerning robustness of the format in the case of errors. The ERS-format was also used by the Swiss teams to exchange raw data for evaluation with a different algorithm. With the exchange of raw data and data evaluation parameters between different teams, the influence of individual evaluation algorithms could be studied. A revised ERS-data format taking these aspects into account was proposed. A recommendation for future intercomparison exercise would be the introduction of a file inventory, where file names, a description of file contents and format are documented together with differences to potential previous versions of the files. With such an inventory, a strict file naming convention would be unnecessary.

The collaboration of the teams was a pleasant experience and the organisers thank all participants for their excellent work, looking forward to the next occasion for working together.

14 Literature

Aarnio, P., Ala-Heikkilä, J., Isolankila, A.; Kuusi, A., Moring, M., Nikkinen, M., Siiskonen, T., Toivonen, H., Ungar, K., Zhang, W.: LINSSI: Database for gamma-ray spectrometry. Journal of radioanalytical and nuclear chemistry, 276, 631-637, 2008.

Bächtiger, K.: Die Kupfer- und Uranerzmineralisationen der Mürtschenalp (Kt. Glarus, Schweiz). Dissertation Nr. 3376, ETH Zürich, 1963.

Bouville, A., Lowder, W.M.: Human Population Exposure to Cosmic Radiation. Radiat. Prot. Dosim. 24(1/4), p. 293 - 299, 1988.

Bucher, B.: Methodische Weiterentwicklungen in der Aeroradiometrie. Dissertation Nr. 13973, ETH Zürich, 2001.

Beck, H.L., DeCampo, J. and Gogolak, C.: In-situ Ge(Li) and NaI(Tl) Gamma-Ray Spectrometry. Report HASL-258, Health and Safety Laboratory, U.S. Department of Energy, Environmental Measurements Laboratory, New York, 1972.

Currie, L.A.: Detection and quantifcation limits: origins and historical overview. Analytica Chimica Acta 391, 127-134, 1999-

Deutsches Institut für Normung: In-situ-Gammaspektrometrie zur nuklidspezifischen Umweltkontaminationsmessung. DIN 25462, 2000.

Deutsches Institut für Normung: Nachweisgrenze und Erkennungsgrenze bei Kernstrahlungsmessungen, Teil 5: Zählende hochauflösende gammaspektrometrische Messungen ohne Berücksichtigung des Probenbehandlungseinflusses. DIN 25482, 1991.

Gilliéron, F.: Zur Geologie der Uranmineralisation in den Schweizer Alpen. Beiträge zur Geologie der Schweiz, Geotechnische Serie, Lieferung 77, Kümmerly und Frey AG, Berne, Switzerland, 1988.

Gilliéron, F.: Bericht über die 1966 - 1984 ausgeführten und mit Bundesmitteln geförderten Uran-Prospektionsarbeiten in den Schweizer Alpen. Schriftreihe des Bundesamtes für Energiewirtschaft, Studie Nr. 41, Bern, Switzerland, 1988.

International Atomic Energy Agency: Airborne Gamma Ray Spectrometer Surveying. IAEA Technical Report Series No. 323, Vienna, 1991.

International Atomic Energy Agency: Guidelines for radioelement mapping using gamma ray spectrometry data. IAEA TECDOC 1363, Vienna, 2003.

International Commission on Radiation Units and Measurements: Gamma-ray spectrometry in the environment. ICRU report 53, Bethesda, 1994.

Kogan, R. M., Nazarov, I.M., Fridman, S. D.: Gamma spectrometry of natural environments and formations: Theory of the method applications to geology and geophysics. Israel Program for Scientific Translations, 1971.

Pavlis, N. K., Holmes, S. A., Kenyon, S. C. and Factor, J. K.: An Earth Gravitational Model to Degree 2160: EGM2008. EGU General Assembly 2008, April 13-18, Vienna, Austria, 2008.

Schötzig, U. and Schrader, H.: Halbwertszeiten und Photonen-Emissionswahrscheinlichkeiten von häufig verwendeten Radionukliden. Bericht PTB-Ra-16/4, Physikalisch-Technische Bundesanstalt, 1993.

Schwarz, G. F.: Methodische Entwicklungen zur Aerogammaspektrometrie. Beiträge zur Geologie der Schweiz, Geophysik Nr. 23, Schweizerische Geophysikalische Kommission, 1991.

Schwarz, G.F., Rybach, L. and Klingelé, E.: Design, calibration and application of an airborne gamma spectrometric system in Switzerland. Geophysics 62, 1369-1378, 1997.

United Nations Scientific Committee on the Effects of Atomic Radiation (UNSCEAR): Sources and Effects of Ionizing Radiation Volume I: Sources. UNSCEAR 2008 Report, United Nations, New York, USA, 2010.

15   National reports covering ARM17

Helbig, A., Hanfland, R., Huber, F., Krol, I., Loske, F., Schkade, U., Strobl, C., Thomas, M.: Internationale Messkampagne ARM17 der Aero-Gammaspektrometrie 2017 vom 25. - 30.06.2017 in der Schweiz - Übungsbericht und Messresultate, Bundesamt für Strahlenschutz, 2017.

16   Previous Swiss national reports

Schwarz, G. F., Klingelé, E. E., Rybach, L.: Aeroradiometrische Messungen in der Umgebung der schweizerischen Kernanlagen. Bericht für das Jahr 1989 zuhanden der Hauptabteilung für die Sicherheit der Kernanlagen (HSK). Interner Bericht, Institut für Geophysik, ETH Zürich, 1990.

Schwarz, G. F., Klingelé, E. E., Rybach, L.: Aeroradiometrische Messungen in der Umgebung der schweizerischen Kernanlagen. Bericht für das Jahr 1990 zuhanden der Hauptabteilung für die Sicherheit der Kernanlagen (HSK). Interner Bericht, Institut für Geophysik, ETH Zürich, 1991.

Schwarz, G. F., Klingelé, E. E., Rybach, L.: Aeroradiometrische Messungen in der Umgebung der schweizerischen Kernanlagen. Bericht für das Jahr 1991 zuhanden der Hauptabteilung für die Sicherheit der Kernanlagen (HSK). Interner Bericht, Institut für Geophysik, ETH Zürich, 1992.

Schwarz, G. F., Klingelé, E. E., Rybach, L.: Aeroradiometrische Messungen in der Umgebung der schweizerischen Kernanlagen. Bericht für das Jahr 1992 zuhanden der Hauptabteilung für die Sicherheit der Kernanlagen (HSK). Interner Bericht, Institut für Geophysik, ETH Zürich, 1993.

Schwarz, G. F., Klingelé, E. E., Rybach, L.: Aeroradiometrische Messungen in der Umgebung der schweizerischen Kernanlagen. Bericht für das Jahr 1993 zuhanden der Hauptabteilung für die Sicherheit der Kernanlagen (HSK). Interner Bericht, Institut für Geophysik, ETH Zürich, 1994.

Schwarz, G. F., Rybach, L.: Aeroradiometrische Messungen im Rahmen der Übung ARM94. Bericht für das Jahr 1994 zuhanden der Fachgruppe Aeroradiometrie (FAR). Interner Bericht, Institut für Geophysik, ETH Zürich, 1995.

Schwarz, G. F., Rybach, L.: Aeroradiometrische Messungen im Rahmen der Übung ARM95. Bericht für das Jahr 1995 zuhanden der Fachgruppe Aeroradiometrie (FAR). Interner Bericht, Institut für Geophysik, ETH Zürich, 1996.

Schwarz, G. F., Rybach, L., Bärlocher, C.: Aeroradiometrische Messungen im Rahmen der Übung ARM96. Bericht für das Jahr 1996 zuhanden der Fachgruppe Aeroradiometrie (FAR). Interner Bericht, Institut für Geophysik, ETH Zürich, 1997.

Bucher, B., Rybach, L., Schwarz, G., Bärlocher, C.: Aeroradiometrische Messungen im Rahmen der Übung ARM97. Bericht für das Jahr 1997 zuhanden der Fachgruppe Aeroradiometrie (FAR). Interner Bericht, Institut für Geophysik, ETH Zürich, 1998.

Bucher, B., Rybach, L., Schwarz, G., Bärlocher, C.: Aeroradiometrische Messungen im Rahmen der Übung ARM98. Bericht für das Jahr 1998 zuhanden der Fachgruppe Aeroradiometrie (FAR). Interner Bericht, Institut für Geophysik, ETH Zürich, 1999.

Bucher, B., Rybach, L., Schwarz, G., Bärlocher, C.: Aeroradiometrische Messungen im Rahmen der Übung ARM99. Bericht für das Jahr 1999 zuhanden der Fachgruppe Aeroradiometrie (FAR). Interner Bericht, Institut für Geophysik, ETH Zürich, 2000.

Bucher, B., Rybach, L., Schwarz, G., Bärlocher, C.: Aeroradiometrische Messungen im Rahmen der Übung ARM00. Bericht für das Jahr 2000 zuhanden der Fachgruppe Aeroradiometrie (FAR). Interner Bericht, Institut für Geophysik, ETH Zürich, 2001.

Bucher, B., Rybach, L., Schwarz, G., Bärlocher, C.: Aeroradiometrische Messungen im Rahmen der Übung ARM01. Bericht für das Jahr 2001 zuhanden der Fachgruppe Aeroradiometrie (FAR). Interner Bericht, Paul Scherrer Institut, Villigen, Schweiz, 2002.

Bucher, B., Rybach, L., Schwarz, G., Bärlocher, C.: Aeroradiometrische Messungen im Rahmen der Übung ARM02. Bericht für das Jahr 2002 zuhanden der Fachgruppe Aeroradiometrie (FAR). Interner Bericht, Paul Scherrer Institut, Villigen, Schweiz, 2003.

Bucher, B., Rybach, L., Schwarz, G.: Aeroradiometrische Messungen im Rahmen der Übung ARM03. PSI-Bericht 04-14, ISSN 1019-0643, Paul Scherrer Institut, Villigen, Schweiz, 2004.

Bucher, B., Butterweck, G., Rybach, L., Schwarz, G.: Aeroradiometrische Messungen im Rahmen der Übung ARM04. PSI-Bericht 05-10, ISSN 1019-0643, Paul Scherrer Institut, Villigen, Schweiz, 2005.

Bucher, B., Butterweck, G., Rybach, L., Schwarz, G.: Aeroradiometrische Messungen im Rahmen der Übung ARM05. PSI-Bericht 06-06, ISSN 1019-0643, Paul Scherrer Institut, Villigen, Schweiz, 2006.

Bucher, B., Butterweck, G., Rybach, L., Schwarz, G.: Aeroradiometrische Messungen im Rahmen der Übung ARM06. PSI-Bericht 07-02, ISSN 1019-0643, Paul Scherrer Institut, Villigen, Schweiz, 2007.

Bucher, B., Guillot, L., Strobl, C., Butterweck, G., Gutierrez, S., Thomas, M., Hohmann, C., Krol, I., Rybach, L., Schwarz, G.: International Intercomparison Exercise of Airborne Gammaspectrometric Systems of Germany, France and Switzerland in the Framework of the Swiss Exercise ARM07. PSI-Bericht Nr. 09-07, ISSN 1019-0643, Paul Scherrer Institut, Villigen, Schweiz, 2009.

Bucher, B., Butterweck, G., Rybach, L., Schwarz, G.: Aeroradiometrische Messungen im Rahmen der Übung ARM08. PSI-Bericht Nr. 09-02, ISSN 1019-0643, Paul Scherrer Institut, Villigen, Schweiz, 2009.

Bucher, B., Butterweck, G., Rybach, L., Schwarz, G., Strobl, C.: Aeroradiometrische Messungen im Rahmen der Übung ARM09. PSI-Bericht Nr. 10-01, ISSN 1019-0643, Paul Scherrer Institut, Villigen, Schweiz, 2010.

Bucher, B., Butterweck, G., Rybach, L., Schwarz, G., Mayer, S.: Aeroradiometrische Messungen im Rahmen der Übung ARM10. PSI-Bericht Nr. 11-02, ISSN 1019-0643, Paul Scherrer Institut, Villigen, Schweiz, 2011.

Bucher, B., Butterweck, G., Rybach, L., Schwarz, G., Mayer, S.: Aeroradiometric Measurements in the Framework of the Swiss Exercise ARM11. PSI-Report No. 12-04, ISSN 1019-0643, Paul Scherrer Institut, Villigen, Switzerland, 2012.

Butterweck, G., Bucher, B., Rybach, L., Schwarz, G., Hödlmoser, H., Mayer, S., Danzi, C. Scharding, G.: Aeroradiometric Measurements in the Framework of the Swiss Exercise ARM12. PSI-Report No. 13-01, ISSN 1019-0643, Paul Scherrer Institut, Villigen, Switzerland, 2013.

Butterweck, G., Bucher, B., Rybach, L., Schwarz, G., Hohmann, E., Mayer, S., Danzi, C. Scharding, G.: Aeroradiometric Measurements in the Framework of the Swiss Exercise ARM13. PSI-Report No. 15-01, ISSN 1019-0643, Paul Scherrer Institut, Villigen, Switzerland, 2015.

Butterweck, G., Bucher, B., Rybach, L., Schwarz, G., Hohmann, E., Mayer, S., Danzi, C. Scharding, G.: Aeroradiometric Measurements in the Framework of the Swiss Exercises ARM14 and FTX14. PSI-Report No. 15-02, ISSN 1019-0643, Paul Scherrer Institut, Villigen, Switzerland, 2015.

Butterweck, G., Bucher, B., Rybach, L., Schwarz, G., Hofstetter-Boillat, B., Hohmann, E., Mayer, S., Danzi, C. Scharding, G.: Aeroradiometric Measurements in the Framework of the Swiss Exercises ARM15, GNU15 and the International Exercise AGC15. PSI-Report No. 15-04, ISSN 1019-0643, Paul Scherrer Institut, Villigen, Switzerland, 2015.

Butterweck, G., Bucher, B., Rybach, L., Poretti, C., Maillard, S., Schwarz, G., Hofstetter-Boillat, B., Hohmann, E., Mayer, S., Scharding, G.: Aeroradiometric Measurements in the Framework of the Swiss Exercises ARM16 and LAURA. PSI-Report No. 17-01, ISSN 1019-0643, Paul Scherrer Institut, Villigen, Switzerland, 2017.

The reports since 1989 can be found and downloaded from the FAR website `http://www.far.ensi.ch.`

17 ERS 2.0 format

The ERS 1.0 format was developed in the framework of the European ECCOMAGS project. A description of the ERS 1.0 format was reproduced in the report on the international intercomparison exercise performed in 2007 (PSI-Report No. 09-07, see previous reports section). The ERS 1.0 format was designed for the data exchange of all measurements related to the radiological environment. In the time since the formulation of the format, the ERS-format was only adapted for measurements with mobile systems. For other purposes, different formats like EURDEP or ANSI 42.42 asserted themselves. Thus, prior to the revision of the ERS-format, a complete discontinuation and replacement with a more widely used format like e.g. ANSI 42.42 was discussed. Whereas the replacement would be possible, a major advantage of the ERS-format would be lost. Mistakes in the ERS-representation of data are easily detectable and can be usually corrected rapidly using a simple text editor. This benefit of the ERS-format was extremely helpful in past comparison exercises for airborne gammaspectrometry. Thus, a revision to a ERS 2.0 is performed focussing on data originating from mobile measurement systems.

The possibility in the ERS 1.0 format to enter raw data and parameters used for data evaluation is strengthened targeting the exchange of raw data and the possibility to evaluate these with algorithms used by other measurement teams. Archiving all data used in the data evaluation to a single file is considered advantageous for the assurance that the data can be re-evaluated in the future. Additionally, the revision tries to remove inconveniences encountered in the application of the format, to remove outdated or confusing quantities, to clarify some of the identifier descriptions, to add identifiers for useful quantities applied in the field and to increase robustness of the format.

17.1 General changes

The ERS 1.0 format uses a space character as delimiter both between different identifier - data groups and between different data items associated to one identifier. Thus, a mistake in the structure for one identifier can infect other identifier - data groups. The ERS 2.0 format is based on the utilisation of a semicolon or line end as external delimiter between different identifier - data groups and a space character between different data items associated with a given identifier. As the semicolon is used as external delimiter, this character cannot be used in data fields or comments. This restriction is considered to be marginal for practical purposes.

Storing spectral data, the ERS 1.0 format recommends a line break after 128 channel data. This recommendation targeted better readable printouts and easier import into spreadsheets. Since the capacity of spreadsheets has increased significantly since the development of the ERS 1.0 format, it is recommended for the ERS 2.0 format to use one line per data point including raw data. Nevertheless, the "#S_+"-identifier for continuation of spectral data is still included in the ERS 2.0 format.

The distinction between windows defined in the header and ROIs for spectral analysis defined for each data point was omitted. The naming of windows or ROIs was generalised, allowing energy windows which are not related directly to a specific nuclide. Due to the generalisation of window names, special identifiers addressing the total count window became obsolete.

17.2   Identifiers of the ERS format

Due to the introduction of external and internal delimiters in ERS 2.0, the special provision for values which include space characters is obsolete.

17.2.1   Header identifiers

Identifier-value pairs of the header type should be placed in the beginning of the file. The comment marker should be handled as identifier and the comment as text string, for example:
/* Start of heading section
Identifier-value pairs
/* End of heading section
The identifier HSW was added to the ERS 2.0 format to document the software version used to generate the results stored in the file. An identifier for the time zone used during the survey was added to the header information as the possibility to change time zones for each data point available in the ERS 1.0 format was removed.
An identifier ISD_SDI was added to store the calibration factor for the calculation of dose rate with the spectrum dose index (SDI) method.The energy window used for the calculation is assigned the fixed name SDI.

Table 36: Header identifier V.

V	File format version	Value format or unit
V	The value for this version is 2.0	Text

Table 37: Header identifier H.

H	General header information	Value format or unit
HCTRY	Country	Text
HORG	Organisation	Text
HMODE	Operational mode. Values are REAL, EXERCISE or TRAINING	Text
HTEAM	Team	Text
HSITE	Site (can be used to describe part of a survey)	Text
HFILE	File name or other code	Text
HSW	Identification of software used for evaluation	Text
HSURVEY	Survey information: should include information about survey name, aimed ground clearance, aimed line spacing, speed, etc.)	Text
HTZ	Time zone Specifies the difference of the time used to UTC	h

Table 38: Header identifier IA.

IA(sysid)	Instrumentation, apparatus	Value format or unit
	sysid - system identification is optional. The third character in the code for instrumentation is the same as the EURDEP code for apparatus type Common types are given here Value should describe the apparatus Can be combined with the _D identifier tail	
IAB	Alpha - ZnS scintillator	Text
IAD	Alpha - solid state detector	Text
IAY	Alpha - alpha spectrometry	Text
IAE	Alpha - other	Text
IAG	Beta - Geiger-Muller counter	Text
IAJ	Beta - solid state detector	Text
IAK	Beta - other	Text
IAM	Beta and gamma - other	Text
IA1	Gamma - Geiger-Muller tube	Text
IAN	Gamma - TLD	Text
IAO	Gamma - ionisation chamber	Text
IAP	Gamma - sodium iodide detector	Text
IAU	Gamma - gamma spectrometry scintillator	Text
IAQ	Gamma - solid state detector, Ge(Li) or HPGe	Text
IAR	Gamma - other	Text
IAZ	Other	Text

Table 39: Header identifier IC.

IC(sysid)	Instrumentation, carrier or platform	Value format or unit
	sysid - system identification is optional Value should describe the carrier	
ICA	Airborne (Type and registration number of the aircraft)	Text
ICG	Ground vehicle (Type and registration number of the vehicle)	Text
ICI	In situ	Text
ICP	Portable	Text
ICZ	Other	Text

Table 40: Header identifier IP.

IP(sysid)	Instrumentation, localization	Value format or unit
	sysid - system identification is optional	
	Value should describe the instrument for positioning	
IPR(sysid)	Description of GPS receiver	Text
IPC(coordid)(sysid)	Type of coordinates system (e.g. "WGS84", or "RT90"). Coordid is the identification number of the coordinates system	Text
IPU(coordid)(sysid)	Describes the unit of the coordinates system	Text
IPG	Ground clearance determination system	Text
IPP	Unit of position precision (meters or PDOP etc.)	Text

Table 41: Header identifier &.

&	Additionally defined identifiers	Value format or unit
	Value should describe the identifier and the unit	
DEFINE&idf	Define additional identifier The identifier is &idf This definition must occur before the identifier can be used Example: DEFINE&DRCOSM "Cosmic dose rate, nSv/h" defines a new identifier &DRCOSM	Text
&idf	An additional identifier &idf that can be used anywhere in the file	Unit as defined by DEFINE

Table 42: Header identifier /*.

/*	Comment marker	Value format or unit
/*	Start of comment	Text

Table 43: Header identifier IS.

IS(sysid)	Spectral processing parameters	Value format
	sysid - system identification is optional	or unit
ISE0	Basic energy calibration intercept	keV
ISE1	Basic energy calibration linear term	keV/channel
ISE2	Basic energy calibration quadratic term	keV/channel^2
ISW	Name winname of window or ROI Examples for winname: Cs-137, MMGC, TOTAL	Text
ISWE1_winname	Lower energy of window or ROI winname	keV
ISWE2_winname	Upper energy of window or ROI winname	keV
ISWC_winname	Cosmic ratio between window or ROI winname and the cosmic window	Numeric
ISWB_winname	Background count rate in winname	cps
ISWRA1	Radon correction sky shine A1	cps
ISWRA2	Radon correction sky shine A2	cps
ISWRA_winname	Radon correction sky shine AXx for winname	Numeric
ISWRB_winname	Radon correction sky shine BXx for winname	Numeric
ISWS_winname1 _winname2	Stripping factor winname1 to winname2	Numeric
ISWT	Attenuation model Example: exp(-mu*h)	Text
ISWT_winname	Attenuation parameter mu for window or ROI winname	1/m
ISWA_Identifier _winname	Calibration factor for activity measured in winname Identifier describes type of distribution Example: ISWA_AD_K-40 7.95	Unit of activity distribution per cps
ISWA0_Identifier _winname	Calibration factor intercept for activity measured in window or ROI winname Example: ISWA0_AD_K-40 -4	Unit of activity distribution
ISWD_winname	Calibration factor for dose rate DHSR calculation using the count rate in window or ROI winname	μSv/h per cps
ISD_SDI	Calibration factor for dose rate DHSR calculation using the SDI method in energy window SDI	μSv/h per (cps * keV)
ISC	Number of channels per spectra	Numeric
ISMmethodid	Identification of a method different than the window method.	Text

17.2.2 Weather and environment identifiers

Can be placed anywhere in the file, but preferably in the header. Identifiers WAT, WAP, WAH and WAD refer to the location of the measuring instrument (for example at flight altitude).

Table 44: Identifier W.

W	Weather	Value format or unit
WP	Precipitation Values are Y or N	Text
WPR	Precipitation rate	mm/h
WPS	Snow cover depth	m
WAT	Air temperature	$^\circ$C
WAP	Air pressure	hPa
WAH	Air humidity	%
WAD	Air density	kg/m^3
WGD	Ground density	kg/m^3
WGH	Ground moisture content wet weight/dry weight	Numeric

17.2.3 Measurement data identifiers

Can be placed anywhere in the file after the heading.
The numeric identifier N for the numbering of data points was removed in favour of using the more general identification using the already existing identifiers PA and PB. Thus, identifier PA has to be the first identifier for each data record. The format of date and time values are simplified in the ERS 2.0 format. The reference to ISO8601 is replaced by a specific format instruction. Generally, the date and time informations should be given in Universal Time (UTC). The special indication defined in ERS 1.0 "Z" is therefore obsolete. A deviating date and time zone for the survey can be specified in the header section with the additional identifier HTZ. The possibility in ERS 1.0 to mix time values with different definitions in a single survey has been disposed. The identifiers for exposure and exposure rate describing an outdated quantity have been removed. The definition of effective dose quantities for different source geometries was considered confusing and the according identifiers were removed. The unit for acquisition real time and acquisition live time was changed to milliseconds, as typically used in mobile gamma-spectrometry.

Table 45: Identifier C.

C	Calendar date and time	Value format
	Without identifier tail(s) type 3 referring to the measurement and the middle of the measuring interval	or unit
CD	Date	YYYY-MM-DD
CT	Time	hh:mm:ss
CDT	Date and Time	YYYY-MM-DD hh:mm:ss

Table 46: Identifier A.

A(sysid)	Activity	Value format
	sysid - system identification is optional	or unit
AP	Activity of a point source	Bq
AL	Activity per unit length of a source distributed along a line	Bq/m
AA	Activity per unit area of a source distributed over an area	Bq/m^2
AV	Activity per unit volume of a source distributed in a volume	Bq/m^3
AD	Activity per unit dry weight of a source distributed in a volume	Bq/kg
AW	Activity per unit wet weight of a source distributed in a volume	Bq/kg

Table 47: Identifier D.

D(sysid)	Dose and dose rate	Value format
	sysid - system identification is optional	or unit
	Calculated for a height of 1 m above ground	
	Without identifier tail type 2 referring to the total	
	dose or dose rate including contributions from	
	photons, charged particles and neutrons of all origins	
DHS	Ambient dose equivalent H*(10)	μSv
DHSR	Ambient dose equivalent rate dH*(10)/dt	μSv/h
DHI	Directional dose equivalent H'	μSv
DHIR	Directional dose equivalent rate dH'/dt	μSv/h
DHP	Personal dose equivalent Hp(10)	μSv
DHPR	Personal dose equivalent rate dHp(10)/dt	μSv/h

Table 48: Identifier F.

| F(sysid) | Fluence | Value format |
	sysid - system identification is optional	or unit
F	Fluence	$1/m^2$
FR	Fluence rate	$1/m^2s$

Table 49: Identifier T.

| T(sysid) | Acquisition time | Value format |
	sysid - system identification is optional	or unit
TL	Acquisition live time	ms
TR	Acquisition real time	ms

Table 50: Identifier P.

| P | Position and identification | Value format |
	The coordinate system (map datum) is defined by the IPC identifier that should be given before measured data. The PA identifier should be placed at the beginning of the record for each measurement or sample point	or unit
PA	Name or code for the measurement or sample point	Text or Numeric
PB	Additional description of the measurement or sample point	Text
PN(coordid)	Measurement or sample point coordinate N-S (latitude) Negative values are allowed, when appropriate	Numeric
PE(coordid)	Measurement or sample point coordinate E-W (longitude) Negative values are allowed, when appropriate	Numeric
PZ(coordid)	Measurement or sample point, altitude above sea level	m
PH	Measurement or sample point, ground clearance	m
PP	Position precision	Numeric

Table 51: Identifier PR.

PR	Relative location related to the source	Value format or unit
PRA	Relative position of measurement or sample point, horizontal distance to centre of source	m
PRH	Relative position of measurement or sample point, height above the centre of a source, negative values allowed	m
PRB	Direction (bearing) of the measurement or sample point relative to the North direction (0-360 degrees) Example: A measurement point North of the source is 0 degrees A measurement point East of the source is 90 degrees	degree

Table 52: Identifier #.

#	Raw data	Value format or unit
#C_winname	Counts in window or ROI winname	Numeric
#R_winname	Count rate in window or ROI winname	1/s
#S	Full Raw spectrum. Values separated by spaces. The number of channels is given by ISC.	Numeric
#SC	Checksum of the spectral data Equals the total counts in the spectrum	Numeric

17.2.4   Source description identifiers

Should be placed before processed data.

Table 53: Identifier SG.

SG	Source geometry in ground, general description	Value format or unit
	Description of the source geometry in ground without specification of source coordinates Can be combined with the Q-identifier to specify geographical coordinates The identifier can take on a radionuclide tail Specifies source geometry assumptions used for data processing	
SGP	Point source in ground at depth	m
SGL	Line source in ground at depth	m
SGA	Plane source in ground at depth	m
SGSS	Slab source in ground, start at depth	m
SGSP	Slab source in ground, stop at depth	m
SGV	Uniform source in ground, start at depth	m
SGE0	Exponential source in ground coefficient at air ground interface or zero ground clearance height	m
SGEM	Exponential source exponent coefficient (mass depth)	m^2/kg
SGEL	Exponential source exponent coefficient (linear depth)	1/m
SGM	Description of a measured depth distribution containing information about site, name, position and distribution	Text

Table 54: Identifier SA.

SA	Source geometry in air, general description	Value format or unit
	Description of the source geometry in air without specification of source coordinates Applicable for airborne, mobile, carried and in situ measurements Can be combined with the Q-identifier to specify geographical coordinates The identifier can take on a radionuclide tail Specifies source geometry assumptions used for data processing	
SAP	Point source in air at ground clearance height	m
SAL	Line source in air at ground clearance height	m
SASS	Uniform slab source in air Start at ground clearance	m
SASP	Uniform slab source in air Stop at ground clearance	m
SAV	Uniform slab source in air Start at ground clearance, infinite height	m
SACHH	Cylindrical source in air, horizontal axis Centre at ground clearance height	m
SACHR	Cylindrical source in air horizontal axis Radius	m
SACV	Cylindrical source in air, vertical axis Start at ground clearance height, infinite height	m
SACVS	Cylindrical source in air, vertical axis Start at ground clearance height	m
SACVP	Cylindrical source in air, vertical axis Stop at ground clearance height	m
SACVR	Cylindrical source in air, vertical axis Radius	m
SAE0	Exponential source in air at zero ground clearance	m
SAEM	Exponential coefficient (mass height)	m^2/kg
SAEL	Exponential coefficient (linear height)	1/m

17.2.5 Identifier tails

Should be connected to the body of certain identifiers. A new identifier tail _D is introduced for measuring systems using several detectors in parallel. Raw and evaluated data can be stored individually for each detector using this identifier tail. The detectors can be described individually in the header section combining IA identifiers with _D identifier tails.

Table 55: Identifier tail Type 1.

	Identifier tail Type 1 Detection limit, uncertainty, apparent and estimated values Can be used for activity, dose, dose rate, fluence and fluence rate Should be written before identifier tail Type 2	**Value format or unit**
_LC	Decision limit Example: Decision limit for activity per unit area AA_LC	As identifier
_LD	Detection limit	As identifier
_LQ	Determination limit	As identifier
_UR	Random uncertainty	As identifier
_US	Systematic uncertainty	As identifier
_UT	Combined total uncertainty	As identifier
_URP	Relative random uncertainty	%
_USP	Relative systematic uncertainty	%
_UTP	Relative combined total uncertainty	%
_DXX	Identification of detector For the case that data of more than one detector are stored for a measurement or sample point Examples: #S_D01, DHSR_D02	Numeric
_+	Continuation character (e.g. #S_+, #S_D03_+)	

Table 56: Identifier tail Type 2.

	Identifier tail Type 2 Radionuclide, energy Can be used for activity, dose, dose rate, fluence, fluence rate, source descriptions and source coordinates	Value format or unit
_Xx-000m	Radionuclide, all radionuclides allowed Examples: _Cs-137, _Tc-99m Decision limit for Cs-137 per unit area AA_LC_Cs-137	As identifier
_TOT	Total for all origins (_COS + _GND)	As identifier
_NAT	Natural radionuclides	As identifier
_ANT	Antropogenic radionuclides	As identifier
_GND	Contribution of ground (_ANT + _NAT)	As identifier
_COS	Cosmic contribution Example: DHSR_COS includes contributions of photons, neutrons and charged particles produced by cosmic radiation	As identifier
_Eenergy	Energy (given in keV). Example: _E662	As identifier

Table 57: Identifier tail Type 3.

	Identifier tail Type 3 Specification of date and time	Value format or unit
_RE	Reference date and/or time	As identifier
_SA	Sampling date and/or time	As identifier
_S	Start of measurement or sampling interval Can be combined with _SA Example: CDT_SA_S Start date and time of sampling interval	As identifier
_M	Middle of measurement or sampling interval Can be combined with _SA	As identifier
_P	Stop of measurement or sampling interval Can be combined with _SA	As identifier

17.2.6   Miscellaneous identifiers

This sections contains identifiers for values used already in the field, but not covered in the previous sections.

Table 58: Identifier M.

M	Miscellaneous identifiers	Value format or unit
MR_winname1 _winname2	Ratio of counts in window or ROI winname1 to counts in window or ROI winname2	Numeric
MTC	Topographic correction applied Allowed values are Y or N	Text
MRC	Radon correction applied Allowed values are Y or N	Text
MND	Value indicating no data available Example: -999	Numeric

18 Evaluation parameter files of team CH01

The parameter files used for the evaluation of raw data used by team CH01 are listed below to improve the traceability of the presented results. The detector definition files have been re-evaluated for all detectors in 2014. A software modification was performed to take into account different formats of terrain model files used for topographic correction, leading to a change in the detector definition file.

18.1 DefinitionFile_Processing_ch.txt

This file defines the standard parameters used for the gridding of measured data used througout this report.

```
Definition file Swiss MGS32
"Windows"
10
Total   401.    2997.     0.   0
K-40    1369.   1558.   1460.   1
U-238   1664.   1853.   1765.   1
Th-232  2407.   2797.   2615.   1
Cs-137   600.    720.    660.   2
Co-60   1100.   1400.     0.   2
MMGC1    400.   1400.     0.   0
MMGC2   1400.   2997.     0.   0
LOW       40.    720.     0.   0
MID      720.   2997.     0.   0
"Ratios"
3
MMGCVerhältnis   MMGC1  MMGC2  Ratio_MMGC
LOWHigh          LOW    MMGC2  RatioLowHigh
LowMid           LOW    MID    RatioLowMid
"Conversion factors Activity to Dose Rate"
8
Total       0         NoCalibration   "    "   0
AD_K-40        0.044   DHSR            "nSv/h"  1
AD_U-238       0.55    DHSR            "nSv/h"  1
AD_Th-232      0.77    DHSR            "nSv/h"  1
AD_Cs-137      0.2     DHSR            "nSv/h"  2
Co-60       0         NoCalibration   "    "   0
MMGC1       0         NoCalibration   "    "   0
MMGC2       0         NoCalibration   "    "   0
"Typ des Darstellungsgrenzwertes"
1
Nachweistyp  0
"counts of spectra to stack"
1
Counts 1
"Auszugebende Werte"
```

```
30
"DHSR TOT             ","DHSR_TOT","nSv/h         ",0.00,250.00
"AP_Co-60             ","AP_Co-60","MBq         ",0.00,150.00
"AP_Cs-137            ","AP_Cs-137","MBq         ",0.00,40.00
"Terr. DL             ","DHSR_TOT","nSv/h        ",0.00,250.00
"CR_Caesium           ","CR_Cs-137","cps         ",20.00,120.00
"CR_Cobalt            ","CR_Co-60","cps         ",0.00,100.00
"NR_Caesium           ","NR_Cs-137","cps         ",0.00,120.00
"NR_Cobalt            ","NR_Co-60","cps         ",0.00,100.00
"Total_CR_corr        ","NR_Total","cps         ",200.00,1200.00
"K-40                 ","AD_K-40","Bq/kg        ",0.00,1000.00
"U-238                ","AD_U-238","Bq/kg        ",0.00,120.00
"Th-232               ","AD_Th-232","Bq/kg        ",0.00,120.00
"Cs-137               ","AD_Cs-137","Bq/kg        ",0.00,240.00
"Cobalt_CR            ","NR_Co-60","cps         ",0.00,120.00
"Nat.Terr.DL          ","DHSR_NAT","nSv/h        ",0.00,250.00
"Künst.DL             ","DHSR_ANT","nSv/h        ",0.00,250.00
"MMGC_Ratio           ","&MMGC_Ratio","%         ",4.00,6.00
"Cosmic DL            ","DHSR_COS","nSv/h        ",20.00,60.00
"Cosmic               ","CR_COS","cps         ",000.00,400.00
"Radar                ","PH","m           ",0.00,300.00
"ODL                  ","DHSR","nSv/h        ",0.00,250
"AD_UT_K-40           ","AD_UT_K-40","Bq/kg        ",0.00,200
"AD_UT_U-238          ","AD_UT_U-238","Bq/kg        ",0.00,50
"AD_UT_Th-232         ","AD_UT_Th-232","Bq/kg        ",0.00,40
"AD_UT_Cs-137         ","AD_UT_Cs-137","Bq/kg        ",0.00,20
"Err_Co-60            ","NR_UT_Co-60","cps         ",0.00,40
"Nachweis_Cs-137      ","CR_LD_Cs-137","cps         ",0.00,100.00
"Nachweis_Co-60       ","CR_LD_Co-60","cps         ",0.00,100.00
"Cs-137 beta=0        ","AA_Cs-137","Bq/m2        ",0.00,20000.00
"AA_UT_Cs-137         ","AA_UT_Cs-137","Bq/m2        ",0.00,20
%
```

18.2   Processing_Quellensuche.txt

This file defines the parameters used for a source search.

```
Definition file Swiss MGS32
"Windows"
10
Total     401.    2997.       0.   0
K-40     1369.    1558.    1460.   1
U-238    1664.    1853.    1765.   1
Th-232   2407.    2797.    2615.   1
Cs-137    600.     720.     660.   2
Co-60    1100.    1400.       0.   2
MMGC1     400.    1400.       0.   0
MMGC2    1400.    2997.       0.   0
LOW        40.     720.       0.   0
```

```
MID       720.    2997.      0.   0
"Ratios"
3
MMGCVerhältnis    MMGC1  MMGC2  Ratio_MMGC
LOWHigh           LOW    MMGC2  RatioLowHigh
LowMid            LOW    MID    RatioLowMid
"Conversion factors Activity to Dose Rate"
8
Total       0         NoCalibration    "       "   0
AD_K-40         0.044     DHSR             "nSv/h"    1
AD_U-238        0.55      DHSR             "nSv/h"    1
AD_Th-232       0.77      DHSR             "nSv/h"    1
AD_Cs-137       0.2       DHSR             "nSv/h"    2
Co-60       0         NoCalibration    "       "   0
MMGC1       0         NoCalibration    "       "   0
MMGC2       0         NoCalibration    "       "   0
"Typ des Darstellungsgrenzwertes"
1
Nachweistyp  0
"counts of spectra to stack"
1
Counts 1
"Auszugebende Werte"
30
"DHSR TOT          ","DHSR_TOT","nSv/h       ",0.00,250.00
"AP_Co-60          ","AP_Co-60","MBq         ",0.00,150.00
"AP_Cs-137         ","AP_Cs-137","MBq        ",0.00,40.00
"Terr. DL          ","DHSR_TOT","nSv/h       ",0.00,250.00
"CR_Caesium        ","CR_Cs-137","cps        ",20.00,120.00
"CR_Cobalt         ","CR_Co-60","cps         ",0.00,100.00
"NR_Caesium        ","NR_Cs-137","cps        ",0.00,120.00
"NR_Cobalt         ","NR_Co-60","cps         ",0.00,100.00
"AP_UT_Cs-137      ","AP_UT_Cs-137","MBq      ",0.00,5000.00
"K-40              ","AD_K-40","Bq/kg        ",0.00,1000.00
"U-238             ","AD_U-238","Bq/kg       ",0.00,120.00
"Th-232            ","AD_Th-232","Bq/kg      ",0.00,120.00
"Cs-137            ","AD_Cs-137","Bq/kg      ",0.00,240.00
"Cobalt_CR         ","NR_Co-60","cps         ",0.00,120.00
"Nat.Terr.DL       ","DHSR_NAT","nSv/h       ",0.00,250.00
"Künst.DL          ","DHSR_ANT","nSv/h       ",0.00,250.00
"MMGC_Ratio        ","&MMGC_Ratio","%         ",4.00,6.00
"Cosmic DL         ","DHSR_COS","nSv/h       ",20.00,60.00
"Cosmic            ","CR_COS","cps          ",000.00,400.00
"Radar             ","PH","m               ",0.00,300.00
"ODL               ","DHSR","nSv/h          ",0.00,250
"AD_UT_K-40        ","AD_UT_K-40","Bq/kg      ",0.00,200
"AD_UT_U-238       ","AD_UT_U-238","Bq/kg     ",0.00,50
"AD_UT_Th-232      ","AD_UT_Th-232","Bq/kg    ",0.00,40
"AD_UT_Cs-137      ","AD_UT_Cs-137","Bq/kg    ",0.00,20
```

```
"AP_UT_Co-60          ","AP_UT_Co-60","MBq         ",0.00,1000
"Nachweis_Cs-137      ","CR_LD_Cs-137,"cps         ",0.00,100.00
"Nachweis_Co-60       ","CR_LD_Co-60","cps         ",0.00,100.00
"Cs-137 beta=0        ","AA_Cs-137","Bq/m2       ",0.00,20000.00
"AA_UT_Cs-137         ","AA_UT_Cs-137","Bq/m2       ",0.00,20
%
```

18.3 DefinitionFile_DetD.txt

This file defines the parameter set used for detector D prior to the modifications described in sections 8.1 and 9.1.1.

```
Definition file System
"Koordinaten"
WGS84
"Non-linearity"
4
a0  1.8745
a1  0.082009
a2  0.00000012708
a3  0.0
"Recorder old RDT-Files"
8
Radar  0.00    -61.00
Baro   0.74    457.14
Cosm   0.00    1.00
Dead   5.00    0.00
Time   0.00    1.00
Temp   0.00    1.00
Pitch  0.00    76.20
Roll   0.00    90.91
"Background/Cosmic"
10
Total       98.1000      1.041      0.032
K-40        12.100       0.050      0.004
U-238        2.700       0.043      0.002
Th-232       3.400       0.044      0.001
Cs-137      15.500       0.102      0.005
Co-60       13.900       0.100      0.004
MMGC1       79.540       0.771      0.019
MMGC2       18.500       0.270      0.007
LOW          0.          0.         0.
MID          0.          0.         0.
"Stripping Coefficients"
10
1.000  0.000  0.000  0.000  0.000  0.000  0.000  0.000  0.000  0.000
0.000  1.000  1.025  0.461  0.000  0.106  0.000  0.000  0.000  0.000
0.000 -0.029  1.000  0.347  0.000  0.004  0.000  0.000  0.000  0.000
0.000 -0.020  0.055  1.000  0.000  0.002  0.000  0.000  0.000  0.000
```

```
0.000  0.328  3.235  1.604  1.000  0.202  0.000  0.000  0.000  0.000
0.000  0.637  2.485  0.670  0.001  1.000  0.000  0.000  0.000  0.000
0.000  0.000  0.000  0.000  0.000  0.000  1.000  0.000  0.000  0.000
0.000  0.000  0.000  0.000  0.000  0.000  0.000  1.000  0.000  0.000
0.000  0.000  0.000  0.000  0.000  0.000  0.000  0.000  1.000  0.000
0.000  0.000  0.000  0.000  0.000  0.000  0.000  0.000  0.000  1.000
"Converted Stripping Coefficients Matrix"
10
1.000  0.000  0.000  0.000  0.000  0.000  0.000  0.000  0.000  0.000
0.000  1.042 -0.795 -0.133  0.000 -0.106  0.000  0.000  0.000  0.000
0.000  0.026  1.007 -0.358  0.000 -0.006  0.000  0.000  0.000  0.000
0.000  0.021 -0.067  1.016  0.000 -0.005  0.000  0.000  0.000  0.000
0.000 -0.310 -2.498 -0.488  1.000 -0.158  0.000  0.000  0.000  0.000
0.000 -0.742 -1.950  0.294 -0.001  1.085  0.000  0.000  0.000  0.000
0.000  0.000  0.000  0.000  0.000  0.000  1.000  0.000  0.000  0.000
0.000  0.000  0.000  0.000  0.000  0.000  0.000  1.000  0.000  0.000
0.000  0.000  0.000  0.000  0.000  0.000  0.000  0.000  1.000  0.000
0.000  0.000  0.000  0.000  0.000  0.000  0.000  0.000  0.000  1.000
"Sigma of Converted Stripping Coefficients Matrix"
10
0.000  0.000  0.000  0.000  0.000  0.000  0.000  0.000  0.000  0.000
0.000  0.000 -0.040 -0.017  0.000 -0.016  0.000  0.000  0.000  0.000
0.000  0.000  0.000 -0.028  0.000  0.000  0.000  0.000  0.000  0.000
0.000  0.000 -0.009  0.000  0.000  0.000  0.000  0.000  0.000  0.000
0.000 -0.080 -0.103 -0.037  0.000 -0.008  0.000  0.000  0.000  0.000
0.000 -0.140 -0.068  0.013  0.000  0.000  0.000  0.000  0.000  0.000
0.000  0.000  0.000  0.000  0.000  0.000  0.000  0.000  0.000  0.000
0.000  0.000  0.000  0.000  0.000  0.000  0.000  0.000  0.000  0.000
0.000  0.000  0.000  0.000  0.000  0.000  0.000  0.000  0.000  0.000
0.000  0.000  0.000  0.000  0.000  0.000  0.000  0.000  0.000  0.000
"Attenuation Coefficients"
10
Total       0.00600    1.00000    0.0003
K-40        0.00800    1.00000    0.0008
U-238       0.00550    1.00000    0.0114
Th-232      0.00600    1.00000    0.0044
Cs-137      0.01000    1.00000    0.0100
Co-60       0.00800    1.00000    0.0080
MMGC1       0.00600    1.00000    0.0060
MMGC2       0.00650    1.00000    0.0065
LOW         0.02000    1.00000    0.01
MID         0.01500    1.00000    0.005
"3D Attenuation Coefficients"
10
Total       0.00350    2.00000
K-40        0.00420    2.00000
U-238       0.00320    2.00000
Th-232      0.00350    2.00000
Cs-137      0.00800    2.00000
```

```
Co-60         0.00800     1.00000
MMGC1         0.00600     1.00000
MMGC2         0.00650     1.00000
LOW           0.02000     1.00000
MID           0.01500     1.00000
"Conversion factors Counts to Activity"
11
Total         0         NoCalibration   "     "
K-40          7.95      AD_K-40         "Bq/kg"
U-238         3.87      AD_U-238        "Bq/kg"
Th-232        1.62      AD_Th-232       "Bq/kg"
Cs-137        1.88      AD_Cs-137       "Bq/kg"
Cs-137        32.96     AA_Cs-137       "Bq/m2"
Cs-137        7.2       AP_Cs-137       "MBq  "
Co-60         2.5       AP_Co-60        "MBq  "
Co-60         0         NoCalibration   "     "
MMGC1         0         NoCalibration   "     "
MMGC2         0         NoCalibration   "     "
"Radon"
1
0             0
"Höhenkorrektur"
4
AltMethod     1
GroundAltDGM 1
DGMType       0
PfadDHM25     C:\DATEN\Benno\Aeroradiometrie\Daten\DHM25\
"SDI Constants"
7
Aten          0.0053
Convert       0.00096
CosmicKorr    95.5
Back          12640.0
Gain          12.0
referenz_alt 100.0
Threshold     240.0
%
```

18.4 DefinitionFile_DetD_neu.txt

This file defines the parameter set used for detector D with the modifications described in sections 8.1 and 9.1.1.

```
Definition file System
"Koordinaten"
WGS84
"Non-linearity"
4
a0  1.8745
a1  0.082009
a2  0.00000012708
a3  0.0
"Recorder old RDT-Files"
8
Radar  0.00    -61.00
Baro   0.74    457.14
Cosm   0.00    1.00
Dead   5.00    0.00
Time   0.00    1.00
Temp   0.00    1.00
Pitch  0.00    76.20
Roll   0.00    90.91
"Background/Cosmic"
10
Total       74.800       1.096       0.071
K-40         6.200       0.065       0.011
U-238        2.600       0.048       0.005
Th-232       0.100       0.059       0.008
Cs-137      16.600       0.072       0.009
Co-60        9.600       0.096       0.006
MMGC1       67.700       0.751       0.049
MMGC2        7.100       0.345       0.024
LOW          0.          0.          0.
MID          0.          0.          0.
"Stripping Coefficients"
10
1.000  0.000  0.000  0.000  0.000  0.000  0.000  0.000  0.000  0.000
0.000  1.000  1.025  0.461  0.000  0.106  0.000  0.000  0.000  0.000
0.000 -0.029  1.000  0.347  0.000  0.004  0.000  0.000  0.000  0.000
0.000 -0.020  0.055  1.000  0.000  0.002  0.000  0.000  0.000  0.000
0.000  0.328  3.235  1.604  1.000  0.202  0.000  0.000  0.000  0.000
0.000  0.637  2.485  0.670  0.001  1.000  0.000  0.000  0.000  0.000
0.000  0.000  0.000  0.000  0.000  0.000  1.000  0.000  0.000  0.000
0.000  0.000  0.000  0.000  0.000  0.000  0.000  1.000  0.000  0.000
0.000  0.000  0.000  0.000  0.000  0.000  0.000  0.000  1.000  0.000
0.000  0.000  0.000  0.000  0.000  0.000  0.000  0.000  0.000  1.000
"Converted Stripping Coefficients Matrix"
```

```
10
1.000  0.000  0.000  0.000  0.000  0.000  0.000  0.000  0.000  0.000
0.000  1.042 -0.795 -0.133  0.000 -0.106  0.000  0.000  0.000  0.000
0.000  0.026  1.007 -0.358  0.000 -0.006  0.000  0.000  0.000  0.000
0.000  0.021 -0.067  1.016  0.000 -0.005  0.000  0.000  0.000  0.000
0.000 -0.310 -2.498 -0.488  1.000 -0.158  0.000  0.000  0.000  0.000
0.000 -0.742 -1.950  0.294 -0.001  1.085  0.000  0.000  0.000  0.000
0.000  0.000  0.000  0.000  0.000  0.000  1.000  0.000  0.000  0.000
0.000  0.000  0.000  0.000  0.000  0.000  0.000  1.000  0.000  0.000
0.000  0.000  0.000  0.000  0.000  0.000  0.000  0.000  1.000  0.000
0.000  0.000  0.000  0.000  0.000  0.000  0.000  0.000  0.000  1.000
"Sigma of Converted Stripping Coefficients Matrix"
10
0.000  0.000  0.000  0.000  0.000  0.000  0.000  0.000  0.000  0.000
0.000  0.000 -0.040 -0.017  0.000 -0.016  0.000  0.000  0.000  0.000
0.000  0.000  0.000 -0.028  0.000  0.000  0.000  0.000  0.000  0.000
0.000  0.000 -0.009  0.000  0.000  0.000  0.000  0.000  0.000  0.000
0.000 -0.080 -0.103 -0.037  0.000 -0.008  0.000  0.000  0.000  0.000
0.000 -0.140 -0.068  0.013  0.000  0.000  0.000  0.000  0.000  0.000
0.000  0.000  0.000  0.000  0.000  0.000  0.000  0.000  0.000  0.000
0.000  0.000  0.000  0.000  0.000  0.000  0.000  0.000  0.000  0.000
0.000  0.000  0.000  0.000  0.000  0.000  0.000  0.000  0.000  0.000
0.000  0.000  0.000  0.000  0.000  0.000  0.000  0.000  0.000  0.000
"Attenuation Coefficients"
10
Total        0.00600    1.00000    0.0003
K-40         0.00800    1.00000    0.0008
U-238        0.00550    1.00000    0.0114
Th-232       0.00600    1.00000    0.0044
Cs-137       0.01000    1.00000    0.0100
Co-60        0.00800    1.00000    0.0080
MMGC1        0.00600    1.00000    0.0060
MMGC2        0.00650    1.00000    0.0065
LOW          0.02000    1.00000    0.01
MID          0.01500    1.00000    0.005
"3D Attenuation Coefficients"
10
Total        0.00350    2.00000
K-40         0.00420    2.00000
U-238        0.00320    2.00000
Th-232       0.00350    2.00000
Cs-137       0.00800    2.00000
Co-60        0.00800    1.00000
MMGC1        0.00600    1.00000
MMGC2        0.00650    1.00000
LOW          0.02000    1.00000
MID          0.01500    1.00000
"Conversion factors Counts to Activity"
11
```

```
Total          0         NoCalibration    "      "
K-40        7.20         AD_K-40          "Bq/kg"
U-238       2.46         AD_U-238         "Bq/kg"
Th-232      1.42         AD_Th-232        "Bq/kg"
Cs-137      1.91         AD_Cs-137        "Bq/kg"
Cs-137     33.46         AA_Cs-137        "Bq/m2"
Cs-137       7.2         AP_Cs-137        "MBq  "
Co-60        2.5         AP_Co-60         "MBq  "
Co-60          0         NoCalibration    "      "
MMGC1          0         NoCalibration    "      "
MMGC2          0         NoCalibration    "      "
"Radon"
1
0          0
"Höhenkorrektur"
4
AltMethod     1
GroundAltDGM 1
DGMType       0
PfadDHM25    C:\DATEN\Benno\Aeroradiometrie\Daten\DHM25\
"SDI Constants"
7
Aten          0.0053
Convert       0.000856
CosmicKorr    124.3
Back          6390.7
Gain          12.0
referenz_alt  100.0
Threshold     240.0
%
```

18.5 DefinitionFile_Det002.txt

This file defines the parameter set used for RLL detector 002 derived from laboratory mea-
surements and measurement results described in 8.1 and 9.1.1.

```
Definition file System
"Koordinaten"
WGS84
"Non-linearity"
4
a0  0.000000
a1  0.083333
a2  0.000000
a3  0.000000
"Recorder old RDT-Files"
8
Radar  0.00   -61.00
Baro  0.74   457.14
```

```
Cosm   0.00    1.00
Dead   5.00    0.00
Time   0.00    1.00
Temp   0.00    1.00
Pitch  0.00   76.20
Roll   0.00   90.91
"Background/Cosmic"
10
Total       62.266        5.534        0.463
K-40         6.515        0.270        0.033
U-238        2.434        0.227        0.032
Th-232      -0.013        0.294        0.029
Cs-137      10.974        0.520        0.089
Co-60        7.562        0.540        0.073
MMGC1       56.303        3.910        0.375
MMGC2        5.963        1.624        0.094
LOW           0.           0.           0.
MID           0.           0.           0.
"Stripping Coefficients"
10
1.000    0.000    0.000    0.000    0.000    0.000    0.000    0.000    0.000    0.000
0.000    1.000    0.986    0.468   -0.002    0.085    0.000    0.000    0.000    0.000
0.000   -0.003    1.000    0.374    0.000   -0.002    0.000    0.000    0.000    0.000
0.000   -0.004    0.061    1.000    0.000   -0.001    0.000    0.000    0.000    0.000
0.000    0.462    3.349    1.750    1.000    0.150    0.000    0.000    0.000    0.000
0.000    0.817    2.447    0.686    0.001    1.000    0.000    0.000    0.000    0.000
0.000    0.000    0.000    0.000    0.000    0.000    1.000    0.000    0.000    0.000
0.000    0.000    0.000    0.000    0.000    0.000    0.000    1.000    0.000    0.000
0.000    0.000    0.000    0.000    0.000    0.000    0.000    0.000    1.000    0.000
0.000    0.000    0.000    0.000    0.000    0.000    0.000    0.000    0.000    1.000
"Converted Stripping Coefficients Matrix"
10
1.000    0.000    0.000    0.000    0.000    0.000    0.000    0.000    0.000    0.000
0.000    1.072   -0.828   -0.131    0.002   -0.093    0.000    0.000    0.000    0.000
0.000    0.001    1.019   -0.383    0.000    0.001    0.000    0.000    0.000    0.000
0.000    0.003   -0.068    1.023    0.000    0.001    0.000    0.000    0.000    0.000
0.000   -0.371   -2.646   -0.499    0.999   -0.124    0.000    0.000    0.000    0.000
0.000   -0.879   -1.768    0.343   -0.003    1.073    0.000    0.000    0.000    0.000
0.000    0.000    0.000    0.000    0.000    0.000    1.000    0.000    0.000    0.000
0.000    0.000    0.000    0.000    0.000    0.000    0.000    1.000    0.000    0.000
0.000    0.000    0.000    0.000    0.000    0.000    0.000    0.000    1.000    0.000
0.000    0.000    0.000    0.000    0.000    0.000    0.000    0.000    0.000    1.000
"Sigma of Converted Stripping Coefficients Matrix"
10
0.000    0.000    0.000    0.000    0.000    0.000    0.000    0.000    0.000    0.000
0.000    0.000   -0.040   -0.017    0.000   -0.016    0.000    0.000    0.000    0.000
0.000    0.000    0.000   -0.028    0.000    0.000    0.000    0.000    0.000    0.000
0.000    0.000   -0.009    0.000    0.000    0.000    0.000    0.000    0.000    0.000
0.000   -0.080   -0.103   -0.037    0.000   -0.008    0.000    0.000    0.000    0.000
```

```
0.000 -0.140 -0.068  0.013  0.000  0.000  0.000  0.000  0.000  0.000
0.000  0.000  0.000  0.000  0.000  0.000  0.000  0.000  0.000  0.000
0.000  0.000  0.000  0.000  0.000  0.000  0.000  0.000  0.000  0.000
0.000  0.000  0.000  0.000  0.000  0.000  0.000  0.000  0.000  0.000
0.000  0.000  0.000  0.000  0.000  0.000  0.000  0.000  0.000  0.000
"Attenuation Coefficients"
10
Total        0.00600    1.00000    0.0003
K-40         0.00800    1.00000    0.0008
U-238        0.00550    1.00000    0.0114
Th-232       0.00600    1.00000    0.0044
Cs-137       0.01000    1.00000    0.0100
Co-60        0.00800    1.00000    0.0080
MMGC1        0.00600    1.00000    0.0060
MMGC2        0.00650    1.00000    0.0065
LOW          0.02000    1.00000    0.01
MID          0.01500    1.00000    0.005
"3D Attenuation Coefficients"
10
Total        0.00350    2.00000
K-40         0.00420    2.00000
U-238        0.00320    2.00000
Th-232       0.00350    2.00000
Cs-137       0.00800    2.00000
Co-60        0.00800    1.00000
MMGC1        0.00600    1.00000
MMGC2        0.00650    1.00000
LOW          0.02000    1.00000
MID          0.01500    1.00000
"Conversion factors Counts to Activity"
11
Total        0          NoCalibration    "       "
K-40         7.27       AD_K-40          "Bq/kg"
U-238        2.63       AD_U-238         "Bq/kg"
Th-232       1.50       AD_Th-232        "Bq/kg"
Cs-137       2.00       AD_Cs-137        "Bq/kg"
Cs-137       34.99      AA_Cs-137        "Bq/m2"
Cs-137       7.53       AP_Cs-137        "MBq  "
Co-60        2.61       AP_Co-60         "MBq  "
Co-60        0          NoCalibration    "       "
MMGC1        0          NoCalibration    "       "
MMGC2        0          NoCalibration    "       "
"Radon"
1
0              0
"HÃűhenkorrektur"
4
AltMethod     1
GroundAltDGM 1
```

```
DGMType        0
PfadDHM25   C:\DATEN\Benno\Aeroradiometrie\Daten\DHM25\
"SDI Constants"
7
Aten          0.0053
Convert       0.00087
CosmicKorr    95.5
Back          12640.0
Gain          12.0
referenz_alt 100.0
Threshold     240.0
%
```

Paul Scherrer Institut :: Forschungsstrasse 111 :: 5232 Villigen PSI :: Switzerland :: Tel. +41 56 310 21 11 :: www.psi.ch